Spectral Parameters of Methane for Remote Sounding of the Jovian Atmosphere

by

E. Kimberly Strong
St. John's College

A thesis submitted for the degree of Doctor of Philosophy in the University of Oxford

Hilary Term, 1992

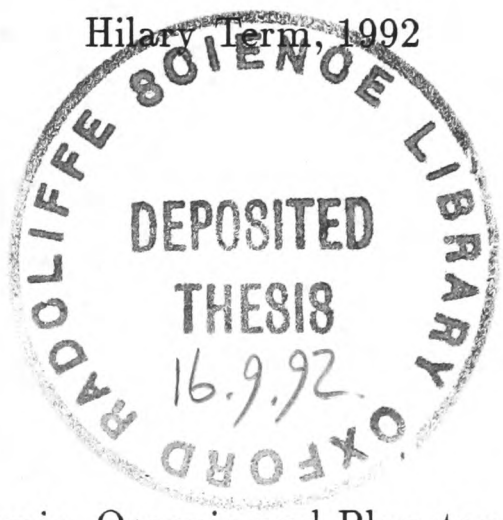

Atmospheric, Oceanic and Planetary Physics
Department of Physics
Clarendon Laboratory
Oxford

Spectral Parameters of Methane for Remote Sounding of the Jovian Atmosphere

E. Kimberly Strong
St. John's College

A thesis submitted for the degree of Doctor of Philosophy
in the University of Oxford

Hilary Term, 1992

Abstract

Spectroscopic measurements in the infrared have proven to be a valuable source of information about the Jovian atmosphere. However, numerous questions remain, many of which will be addressed by the Galileo mission, due to arrive at Jupiter in December, 1995. One of the instruments on Galileo is the Near-Infrared Mapping Spectrometer (NIMS), which will measure temperature structure, chemical composition, and cloud properties. The objective of the work described in this thesis was to investigate the transmittance properties of the Jovian atmosphere and, in particular, to obtain transmittance functions of CH_4 for future use in the planning and interpretation of NIMS measurements.

This thesis begins with a review of our current understanding of the Jovian atmosphere (Chapter 1), and a description of the Galileo mission and the design and objectives of NIMS (Chapter 2). It is then shown (Chapter 3) that absorption bands of CH_4 dominate the near-infrared spectrum of Jupiter, but that line data for CH_4 are currently inadequate over much of the NIMS spectral range (0.7–5.2 μm). For the purposes of NIMS, which has a low resolution of 0.25 μm, the spectrum of CH_4 can be characterised using band models of transmittance as a function of temperature, pressure, and abundance. The theory of band modelling is presented, and previous band-modelling studies of CH_4 are reviewed and are also shown to be inadequate for NIMS (Chapter 4).

An experimental investigation was therefore undertaken to record CH_4 spectra under Jovian conditions of low temperature, large abundance, and H_2-broadening. The experimental resources used to obtain these spectra are described (Chapter 5), the generation of the transmittance spectra is discussed, and their quality is assessed (Chapter 6). The range of frequencies and laboratory conditions covered by these spectra (listed in Appendix A) makes them one of the most comprehensive data sets of this kind yet published.

These spectra were subsequently used to derive transmittance functions for CH_4 (Chapter 7). A variety of models were fitted to the self-broadened CH_4 spectra, and the Goody and Malkmus random band models, using the Voigt lineshape, are shown to provide the best fits. These two models were then fitted to the combined set of self- and H_2-broadened CH_4 spectra. The parameters fitted with the Goody-Voigt model are included in this thesis (Appendices B and C).

Finally, the application of these new band model fits to the problem of Jovian remote sounding is addressed (Chapter 8). This includes an assessment of the reliability of extrapolation to Jovian conditions, a calculation of the level in the Jovian atmosphere that will be sounded by observations of CH_4 absorption, and a calculation of how the uncertainties in the fitted band model will affect the retrieval of atmospheric parameters from NIMS spectra. This thesis concludes with a detailed summary, and with suggestions for future investigations which will help to maximise the return of information from NIMS.

Acknowledgements

I am immensely grateful to the many friends, relatives, and colleagues who have given me support and advice during the course of this work. In particular, I would like to thank the following:

- Prof. Fred Taylor for accepting me as a research student in this department, for acting as my supervisor, for his guidance and encouragement, and most recently for his prompt returning of chapters when reading drafts of this thesis.
- Dr. Simon Calcutt for his advice and comments throughout the course of this work, for allowing me to use his own computer programs, and for kindly reading all of this thesis.
- Dr. John Ballard for making the Laboratory Spectroscopy Facility at the Rutherford Appleton Laboratory available to me, for his help and advice during the period of experimental work, and for working shifts during the spectroscopic experiments.
- Dr. Clive Rodgers for kindly reading all of this thesis, and for his perceptive comments.
- Dr. John Remedios for his help with the experimental work, for working shifts during the spectroscopic experiments, for his many stimulating remarks and suggestions, and for his meticulous reading of the bulk of this thesis.
- Mr. Malcolm Page for his invaluable technical assistance, for his kindness, patience, and encouragement, for willingly working shifts whenever necessary, and for some highly enjoyable cruises on the Thames.
- Mr. George Pullinger for his technical assistance, particularly with the Long White Cell cryogenic system, for readily dealing with my engineering questions, and for his friendliness and sense of humour.
- The numerous technical and engineering personnel at the Rutherford Appleton Laboratory who were always ready to help with a problem, particularly Mr. Bob Coombs, Mr. Peter White, and those at the R12 Workshop, the R18 Engineering and Building Works, and the Safety Section.
- The computing staff at the Rutherford Appleton Laboratory, particularly Dr. Chris Mutlow and Mr. Andy Jackson, for allowing me vast amounts of computer memory and generous use of the computing facilities.
- Mr. Andy Pickering for his help with day-to-day computing problems, and Dr. Bryan Lawrence for answering my questions about LaTeX.
- Mr. Rodney Knight for recording spectra of pump oil with his Perkin Elmer spectrometer, and for working shifts during the spectroscopic experiments.
- Dr. Brian Kerridge and Dr. Graeme Mason for bravely volunteering to work shifts during the spectroscopic experiments.
- Dr. Gilda Ballester, Mr. Tim Kingsmill-Vellacott, and Dr. Peter Read for kindly reading parts of this thesis.

- Dr. David Strong for sacrificing his few days of Christmas holiday to read all of this thesis; his comments are truly appreciated.
- Dr. Bob Watkins for willingly providing advice on engineering problems whenever asked, for reading a chapter of this thesis, and for his interest and encouragement.
- Mr. Paul Morris for so helpfully expediting some rather long GENLN2 jobs!
- Dr. Rod Jones, whose patience and understanding during the final stages of writing this thesis allowed me to avoid the difficult situation of trying to write up while working full-time.
- The many friends who have provided support and encouragement during the course of this work, particularly Dr. Amanda Manning and Dr. Lukas Nellen.
- My parents, whose faith and encouragement over many years helped me to begin and eventually to complete this work, and my sister Joanna, for her loyal support and for (artistically!) trying to keep things in perspective.
- Dr. Richard Hornsey for far too many things to list, but especially for his technical assistance, moral support, electronic mail, telephone calls, and optimism, and for his careful reading of this entire thesis.

I would also like to thank the Rhodes Trust and the Natural Sciences and Engineering Research Council of Canada, whose financial support helped make it possible for me to undertake and complete the research for this thesis.

to Richard and my family

Contents

1 The Atmosphere of Jupiter 1
1.1 The Planet Jupiter . . . 1
1.1.1 Introduction . . . 1
1.1.2 The Origin of Jupiter . . . 2
1.1.3 The Interior of Jupiter . . . 3
1.1.4 The Visible Appearance of Jupiter . . . 4
1.1.5 Dynamics of the Jovian Atmosphere . . . 5
1.2 The Thermal Structure of the Jovian Atmosphere . . . 6
1.2.1 The Effective Temperature and Energy Balance . . . 6
1.2.2 The Horizontal Thermal Structure . . . 8
1.2.3 The Vertical Thermal Structure . . . 9
1.3 The Composition of the Jovian Atmosphere . . . 11
1.3.1 Theoretical Modelling of Composition . . . 11
1.3.2 The Major Constituents . . . 12
1.3.3 Methane . . . 13
1.3.4 Ammonia . . . 14
1.3.5 Other Minor Constituents . . . 16
1.3.6 Isotopic Abundances . . . 19
1.4 The Vertical Cloud Structure of the Jovian Atmosphere . . . 20
1.4.1 Theoretical Modelling of Cloud Structure . . . 20
1.4.2 Models Derived from Observations . . . 21
1.5 Outstanding Problems . . . 24

2 Galileo and the Near-Infrared Mapping Spectrometer 26
2.1 Previous Missions to Jupiter . . . 26
2.1.1 The Pioneer Missions . . . 26
2.1.2 The Voyager Missions . . . 27
2.2 The Galileo Mission to Jupiter . . . 28
2.2.1 Introduction . . . 28
2.2.2 The Spacecraft and Scientific Instruments . . . 30
2.2.3 The Atmospheric Objectives of the Orbiter . . . 31
2.2.4 The Atmospheric Objectives of the Probe . . . 34
2.3 The Near-Infrared Mapping Spectrometer . . . 35
2.3.1 The Scientific Capabilities and Objectives of the NIMS Instrument . . . 35
2.3.2 The Technical Requirements of the NIMS Instrument . . . 37
2.3.3 The Design of the NIMS Instrument . . . 38
2.3.4 The Operational Mode of the NIMS Instrument . . . 40
2.3.5 The Spectroscopic Requirements of NIMS . . . 40

3 Methane and the Near-Infrared Spectrum of Jupiter 42
3.1 The Nature of the Jovian Near-Infrared Spectrum . . . 42
3.1.1 Reflected Solar Radiation: 1 to 4.5 Microns . . . 42
3.1.2 Thermal Emission: The 5-Micron Window . . . 45
3.1.3 Thermal Emission: 10 to 40 Microns . . . 46
3.2 Infrared Spectroscopy of Methane . . . 47
3.2.1 Line Strengths . . . 48
3.2.2 Line Widths . . . 49
3.3 Modelling of the Near-Infrared Spectrum of Jupiter . . . 52
3.3.1 The Basics of Radiative Transfer . . . 52
3.3.2 Line-by-Line Spectral Modelling . . . 55
3.3.3 Available Line Data . . . 56
3.3.4 Line-by-Line Modelling of the Transmittance of Jovian Methane . . . 59

4 Band Modelling of Methane: Theory and Previous Work 65
4.1 The Rationale for Band Modelling of Methane . . . 65
4.2 Band-Modelling Theory . . . 66
4.2.1 Introduction . . . 66
4.2.2 The Single Line Model . . . 68
4.2.3 Regular Band Models . . . 69
4.2.4 Random Band Models . . . 70
4.2.4.1 The Goody Random Band Model . . . 70
4.2.4.2 The Malkmus Random Band Model . . . 72
4.2.4.3 Temperature Dependence in Random Band Models . . . 72
4.2.5 Empirical Models . . . 73
4.3 Previous Band Modelling of Methane . . . 75
4.3.1 Band Modelling in the Visible Region . . . 75
4.3.2 Band Modelling in the Near-Infrared Region . . . 79

5 Experimental Apparatus for the Methane Spectroscopy 84
5.1 The Spectrometer . . . 84
5.1.1 The Bomem Fourier Transform Spectrometer . . . 84
5.1.2 Fourier Transform Spectroscopy . . . 86
5.2 The Long White Cell . . . 88
5.2.1 The Mechanical Design of the Long White Cell . . . 88
5.2.2 The Optical Design of the Long White Cell . . . 89
5.2.3 Optical Components of the Long White Cell . . . 90
5.2.4 The Transfer Optics for the Long White Cell . . . 94
5.2.5 Alignment of the Long White Cell Optics . . . 95
5.2.6 Safety Considerations . . . 96
5.2.7 The Vacuum System . . . 98
5.2.8 The Gas-Handling System . . . 101
5.2.8.1 For the Long White Cell . . . 101
5.2.8.2 For the Transfer-Optics Tanks . . . 103
5.2.9 The Cryogenic Heat Exchanger . . . 104
5.3 Monitoring of Conditions in the Long White Cell . . . 108
5.3.1 The Platinum Resistance Thermometers . . . 108
5.3.2 Temperature Monitoring of the Long White Cell . . . 109
5.3.3 Pressure Monitoring of the Long White Cell . . . 111
5.3.4 Pathlengths in the Long White Cell . . . 112
5.3.5 Gas Supplies for the Methane Spectroscopy . . . 113
5.4 Summary . . . 114

6 Measurement and Initial Processing of the Methane Spectra 115
6.1 The Long White Cell Methane Spectra . . . 115
6.1.1 The Achievable Laboratory Conditions . . . 115
6.1.2 The Achievable Spectral Range . . . 118
6.1.3 The Experimental Procedure . . . 119
6.1.4 The Self-Broadened Methane Spectra . . . 122
6.1.5 The Hydrogen-Broadened Methane Spectra . . . 125
6.2 Initial Processing of the Spectra . . . 127
6.2.1 Background Variability . . . 128
6.2.2 Generation of the Methane Transmittance Spectra . . . 129
6.2.3 Formation of Ice on the Detector . . . 136
6.2.4 The Zero-Signal Level . . . 142
6.2.5 Analysis of Signal-to-Noise . . . 143
6.2.6 Channelling Features . . . 144
6.2.6.1 The 3.2 cm^{-1} Channelling . . . 144
6.2.6.2 The 2.8 cm^{-1} Channelling . . . 146
6.2.6.3 The 80 cm^{-1} Channelling . . . 146
6.2.7 Contamination by Gaseous Impurities and Pump Oil . . . 147
6.3 Summary . . . 152

7 Band-Modelling Analysis of the Methane Spectra 154
7.1 Introduction . . . 154
7.1.1 The Fitting Technique . . . 155
7.2 Band Modelling of the Self-Broadened Methane Spectra . . . 156
7.2.1 Selection of Models and Initialisation of Parameters . . . 156
7.2.2 The Quality of the Fits . . . 159
7.2.2.1 Comparison of the Fits Within Each Sequence . . . 159
7.2.2.2 Comparison of the Five Best Fits . . . 165
7.2.2.3 Comparison of the Fits with the Original Spectra . . . 168
7.2.2.4 Comparison of the Fits with Line-by-Line Spectra . . . 171
7.2.3 The Fitted Parameters . . . 172
7.2.4 Comparisons with the Results of Others . . . 177
7.2.4.1 Comparison of the Quality of the Fits . . . 177
7.2.4.2 Comparison of the Fitted Parameters . . . 180
7.3 Band Modelling of the Hydrogen-Broadened Methane Spectra . . . 186
7.3.1 Selection of Models and Initialisation of Parameters . . . 186
7.3.2 The Quality of the Fits . . . 188
7.3.3 The Fitted Parameters . . . 194
7.3.4 Comparisons with the Results of Others . . . 197
7.4 Summary . . . 197

8 Applications and Conclusions 199
8.1 Applications to Jupiter . . . 199
8.1.1 Extrapolation to Jovian Conditions . . . 199
8.1.2 Remote Sounding Considerations . . . 203
8.2 Summary . . . 208
8.3 Suggestions for Future Work . . . 212

A The Measured Methane Spectra 215

B Band-Model Parameters for the Self-Broadened Methane Spectra 221

C Band-Model Parameters for the Hydrogen-Broadened Methane Spectra 229

References 237

Chapter 1

The Atmosphere of Jupiter

The purpose of this chapter is to present an overview of our current knowledge of the Jovian atmosphere, as the background for subsequent discussions of the Near-Infrared Mapping Spectrometer (NIMS) on the Galileo mission to Jupiter and for the work that has been carried out for this thesis in support of NIMS. It will be shown that numerous questions remain unanswered, many of which will be investigated by Galileo. Particular attention is given to discussions of the thermal structure, the chemical composition, and the cloud structure, as these are the three principal issues to be addressed by NIMS. Later in this thesis, the importance of CH_4 in the near-infrared spectrum of Jupiter, and therefore in the interpretation of NIMS spectra, will be demonstrated. This provides the motivation for the present study, which is concerned with characterising the transmittance properties of CH_4 under Jovian conditions in order to maximise the retrieval of information about the Jovian atmosphere from NIMS spectra.

1.1 The Planet Jupiter

1.1.1 Introduction

As the "giant planet" of our solar system, Jupiter is one of the brightest objects in the night sky and was therefore well-known to the ancient astronomers. In 1610, when Galileo focussed his telescope on Jupiter and discovered four bright satellites revolving around it, the era of telescopic observations began. Since that time, ground-based observations have been joined by those from interplanetary spacecraft, with the latter dramatically improving our knowledge of the Jovian system. Unlike the terrestrial planets, Jupiter is predominantly gaseous, with a complex atmosphere orders of magnitude larger than that of Earth. An understanding of the Jovian atmosphere, like that of any other, requires knowledge of temperature, pressure, composition, cloud structure and dynamics in the horizontal and vertical dimensions. Our current understanding of these variables is the subject of this chapter.

Jupiter, the largest and most massive planet, has a volume and a mass which are, respectively, 1319 and 318 times greater than those of Earth. These figures yield a value of 1.33 g/cm^3

for the mean density, compared with 5.52 g/cm^3 for Earth. This indicates that Jupiter must be largely gaseous and must consist mostly of H_2, because this is the only substance which can be compressed at the high internal pressures of Jupiter and yet give rise to such a low density (Jones, 1984, p.227). This low value, along with the rapid rotation period of approximately 9 hours 55 minutes, results in a noticeable polar flattening, with a dynamic oblateness of 0.0649. Jupiter orbits the Sun at a mean distance of 5.203 A.U., or 778 million km, with an orbital eccentricity of 0.0485 and a sidereal period of revolution of 11.862 years. Further physical data are presented in Table 1.1, including the high albedo which contributes to Jupiter's visibility, and the axial inclination of the equator to the orbit of only 3.12° which results in no significant seasonal variation.

Table 1.1: Fundamental Jovian parameters (Allison and Travis, 1986, p.319; Atreya, 1986, p.20,195; Beatty *et al.*, 1981, p.219; Smoluchowski, 1976, p.20–21.)

Mean distance to Sun	778.3 million km (5.203 A.U.)
Orbital eccentricity	0.0485
Orbital period	11.862 years
Rotation period:	
System I (equatorial band)	9h 50m 30.003s
System II (rest of atmosphere)	9h 55m 40.632s
System III (interior)	9h 55m 29.710s
Inclination of orbit from ecliptic	1.30°
Inclination of equator to orbit	3.12°
Equatorial radius at 1 bar	71,490 km
Oblateness $(R_e - R_p)/R_e$	0.0649
Mass	1.90×10^{27} kg
Mean density	1.33 g/cm^3
Equatorial gravitational acceleration	22.88 m/s^2
Equatorial escape velocity	59.5 km/s
Bond albedo	0.343
Effective emission temperature	124.4 K
1-bar temperature	165 K
Emitted/absorbed radiation	1.67
Equatorial magnetic dipole field	4.28 Gauss
Magnetic dipole tilt	9.6°

1.1.2 The Origin of Jupiter

Various theories have been proposed to explain the formation of the solar system, each with its own assumptions about initial conditions, accretion, gravitational instabilities, removal of angular momentum, radial temperature gradients, and the nature of the primitive solar nebula (*e.g.*, Cameron and Pollack, 1976; Wetherill, 1989). In the case of Jupiter, two principal models have emerged (see Gautier and Owen, 1983). According to the condensation model, Jupiter was formed when matter in the primordial nebula underwent local gravitational condensation, followed by hydrodynamical collapse and slow contraction under hydrostatic equilibrium. Ac-

cording to the nucleation model, condensed solids and ices in the primordial nebula accreted to form the Jovian core, which in turn caused the collapse of the surrounding gaseous envelope to form the atmosphere. These theories are relevant to atmospheric studies because each has different implications for the abundances of elements and isotopes in the Jovian atmosphere. The condensation model predicts a solar composition, whereas the nucleation model predicts a possible enrichment of the gaseous envelope due to the vaporisation of ices during accretional heating of the core. As will be seen in §1.3, current estimates of abundance seem to favour the nucleation model.

1.1.3 The Interior of Jupiter

Models of the Jovian interior, derived from the known mass, radius, and zonal gravity harmonics of the planet, suggest the existence of a central core with a mass 10 to 30 times that of Earth and 0.03 to 0.15 times that of Jupiter, composed of H_2O, CH_4, and NH_3 ices, and SiO_2, MgO, Ni, and Fe (Smoluchowski, 1976, p.17; Stevenson and Salpeter, 1976, p.98). Surrounding the core is an envelope of H_2 and He, differentiated into two distinct zones, as seen in the model of Figure 1.1. In the outer region, the gaseous molecular H_2 becomes gradually denser with increasing depth and pressure until it reaches the liquid phase. At pressures on the order 10^6 bar, there is an abrupt transition to liquid metallic hydrogen as the H_2 molecules break apart (due to attraction between atoms of closely neighbouring molecules) into atoms, which in turn break up (as electrons are attracted to neighbouring atoms) to produce a plasma of protons and electrons (Jones, 1984, p.230).

Figure 1.1: A typical model of the interior of Jupiter (Jones, 1984, p.233).

Support for this model of an electrically conducting liquid interior is provided by the existence of a strong Jovian magnetic dipole field. Hide and Stannard (1976) have shown how this field can be explained by a magnetohydrodynamic dynamo arising from thermally driven fluid motions in both the metallic hydrogen and the inner regions of the molecular H_2. Additional support is provided by the fact that the effective temperature of the planet is almost constant

from equator to pole, despite the equator-to-pole variation in the solar flux. Such a situation is possible if convection in a fluid interior can occur to regulate the internal heat flow so that it compensates for changes in the solar heat flow (Hubbard, 1984, p.268).

1.1.4 The Visible Appearance of Jupiter

The visible appearance of Jupiter is dominated by a series of light-coloured white and yellowish zones alternating with darker blue-gray and brown belts, all aligned parallel with the equator. The nomenclature adopted for these bands is shown in Figure 1.2. Infrared images of Jupiter in the 5 μm region (Terrile and Westphal, 1977) have revealed the zones to have much lower flux levels and brightness temperatures than the belts, suggesting that the zones are colder and higher. The zones appear to be regions of anticyclonic vorticity (clockwise motion in the northern hemisphere, counter-clockwise in the southern) in which warm air masses move upwards and condense into high, cold clouds. Conversely, the belts appear to be areas of cyclonic vorticity relatively free of clouds, where cooler air masses sink downwards (*e.g.*, Keay *et al.*, 1973; Owen and Terrile, 1981; Smith and Hunt, 1976, p.577; Smith *et al.*, 1979a). In the polar regions above 45° latitude, the belt-zone patterns diminish and give way to belt-like dark regions, possibly indicative of clear upper atmosphere free of rising gas (Terrile and Westphal, 1977). The difference in altitude between belts and zones appears to be much less than the scale height (~25 km), being 4 and 10 km for the two highest zones, the North Tropical and South Tropical Zones, respectively (Coffeen, 1974; Smith and Hunt, 1976, p.577).

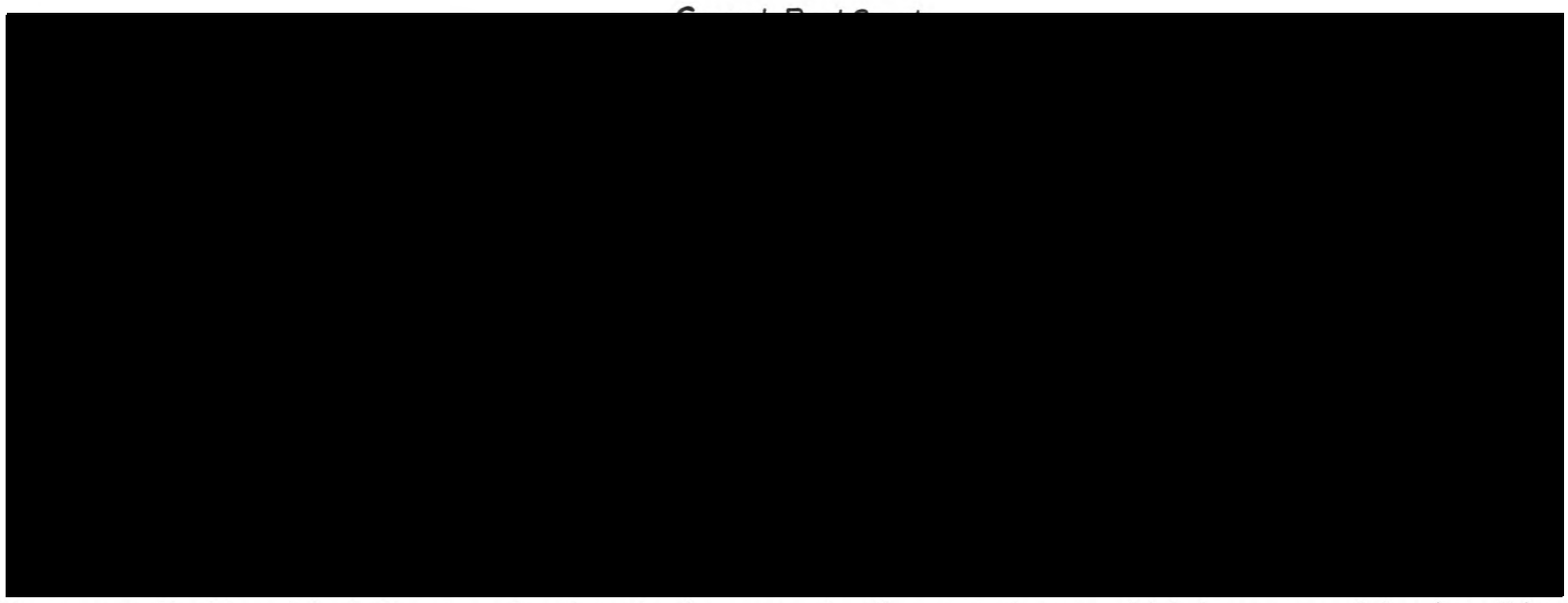

Figure 1.2: Peek's original diagram showing the (now standard) nomenclature which he proposed for describing the belts, zones and regions of the Jovian atmosphere (Peek, 1958, p.22).

Superimposed on the belt-zone structure are various eddies and many smaller, more turbulent features, asymmetrically distributed between the northern and southern hemispheres, with the majority present in the latter (Mitchell *et al.*, 1979). Most notable of the various Jovian eddies is the Great Red Spot (GRS), located within the South Tropical Zone, at ~22°S, and recently measured as ~25,000 km long and ~13,000 km wide (Beebe and Youngblood, 1979). With its anticyclonic vorticity and low infrared brightness temperatures, the GRS seems to

be an area of rising motion, which is rotating with a period of about 6 days and has a mean zonal velocity of -3 m/sec. The colouring of the GRS is thought to be due to chromophores, probably of phosphorus, being forced upwards from the deeper regions of the atmosphere by this rising motion (Prinn and Lewis, 1975).

Three white-coloured eddies known as the South Temperate Ovals (STO's) are also prominent in the Jovian atmosphere, having first appeared in 1938. These ovals are located at 33°S, and are almost 12,000 km long, but are contracting, and may finally disintegrate (Terrile and Beebe, 1979). Additional groupings of smaller white ovals have been discovered at mid-latitudes, again rotating anticyclonically and having a cumulus texture, and believed to indicate high, cool clouds undergoing upward convection (Mitchell *et al.*, 1979). In contrast, darker spots seen in the atmosphere, referred to as "brown barges", exhibit strong emission at 5 μm and may be sinking regions free of obscuring high-altitude clouds. Even stronger sources of 5 μm emission have been detected in the blue-gray hot spots in the equatorial regions, which appear to be the deepest layers that can be seen (Owen and Terrile, 1981).

The many smaller structures visible in the Jovian atmosphere include filaments, chevron morphologies, puffy clouds, rapidly moving jets, and small cloud vortices which rotate about the GRS. One particularly intriguing set of features is a train of regularly spaced white plumes which encircle the planet along the northern edge of the Equatorial Zone at 9°N. These are thought to be generated by intense updrafts of NH_3 which condense and are spread out by horizontal currents (Smith *et al.*, 1979a, 1979b). The fact that only 11 of these plumes were seen with Voyager 2, when 13 had been observed with Voyager 1, provides clear evidence of the variable nature of the Jovian atmosphere.

1.1.5 Dynamics of the Jovian Atmosphere

On a global scale, Jovian dynamics are dominated by two phenomena: zonal winds and long-lived eddies. Analysis of the former requires the definition of a rotating system of reference in order to measure velocities with respect to the mean rotation of the planet. The Jovian atmosphere undergoes differential rotation, the equatorial band between 10°N and 10°S rotating with a period of 9h 50m 30.003s (referred to as System I), and the rest of the atmosphere rotating with period of 9h 55m 40.632s (referred to as System II). Velocities in the Jovian atmosphere are currently specified with respect to the System III period of 9h 55m 29.710s. This is a reference frame rotating with the period of decametric radio emissions which reflect the rotation of Jupiter's internal magnetic field, and it is therefore an indicator of the rotation period of the Jovian interior.

Tracking of Jovian cloud features has revealed a system of counter-flowing eastward and westward winds, with a maximum speed of 140 m/s at 23°N (Ingersoll *et al.*, 1984, p.212). Ingersoll *et al.* (1979, 1981) compared the zonal jet profiles measured by Voyager with those acquired over the past 80 years (summarised by Smith and Hunt, 1976) and found that the

latitudes of the east-west jets have remained essentially constant. They also found that during the four months between the two Voyager encounters, the jet velocities varied by less than the measurement error. Because the visible bands frequently change appearance and lack the same degree of north-south symmetry seen in the zonal jets, it appears that despite the latitudinal similarity between the bands and the zonal winds, they are not strongly inter-related (Hunt *et al.*, 1985, p.108).

Explanations for the zonal jets and their stability can be classified as either shallow or deep atmospheric models. In the former, the upper Jovian atmosphere is assumed to be decoupled from the interior and is treated as a thin shell with a rigid lower boundary. These models generally ignore any vertical heat flow from the interior and are similar to general circulation models of the Earth's atmosphere (Williams, 1978, 1979). In the alternative deep atmospheric models, Jovian circulations are explained by internal convection processes driven by the interior heat source. In the models developed by Busse (1976, 1983), Ingersoll and Miller (1986), and Ingersoll and Pollard (1982), the jets are explained as the surface manifestation of differentially rotating cylindrical structures extending to great depths in the atmosphere. Neither of these theories gives satisfactory explanations of all observations, and there is clearly a need for more detailed measurements of horizontal and vertical Jovian winds.

In addition to the zonal jets, Jovian atmospheric dynamics are characterised by eddy features, from the large quasi-permanent GRS and STO's to small eddies which are formed in the shear zones between jets and last only a day or two. The continual tearing apart of the eddies by the zonal winds helps to drive the latter, as over 10% of the total infrared heat flux is equivalent to the conversion of eddy kinetic energy to zonal kinetic energy (Hunt, 1981). While the smaller eddies appear to acquire their energy through vertical convection of heat from the interior and absorption of solar heat (Ingersoll, 1981, p.124), the explanation for the existence of the larger long-lived eddies in such a turbulent environment remains uncertain. Numerous eddy models have been proposed, and six of the most widely discussed (the Taylor column, hurricane, soliton, modon, intermediate geostrophic vortex, and baroclinic models) are reviewed by Lewis (1988, p.23–41).

1.2 The Thermal Structure of the Jovian Atmosphere

1.2.1 The Effective Temperature and Energy Balance

In order to determine the global energy balance of Jupiter, both its thermal emission and the absorbed solar radiation must be known. The theoretical effective temperature of Jupiter, T_{eff}, can be calculated by equating the energy radiated by the entire surface of the planet, assuming it behaves like a blackbody, to the incident solar energy (*e.g.*, Houghton, 1986, p.2),

$$4\pi r^2 \sigma T_{eff}^4 = \pi r^2 (1 - A) F_s / R^2 \tag{1.1}$$

where r is the radius of the planet,

σ is the Stefan-Boltzmann constant,

A is the Bond albedo of the planet,

F_s is the solar flux at 1 A.U., and

R is the distance of the planet from the sun (in A.U.).

The Bond albedo used in this equation is defined as the ratio of reflected to incident light over the entire surface of a sphere. This differs from the geometric albedo, which is defined as the ratio of the brightness of a planet to the brightness of a perfectly diffusing disk with the same position and apparent size as the planet, when the phase angle between the Sun and Earth, as seen from the planet, is zero (Allen, 1973, p.142). Hanel *et al.* (1981) derived a value of 0.274 $\pm$ 0.013 for the geometric albedo of Jupiter using full disk measurements obtained with the infrared radiometer of the Voyager IRIS instrument (see §2.1.2 for a description of IRIS). Multiplying this by the phase integral of 1.25 measured by the Pioneer photopolarimeter (Tomasko *et al.*, 1978), they calculated the Bond albedo to be 0.343 $\pm$ 0.032.

Substituting this value into Eqn. 1.1 above, the predicted effective temperature of Jupiter is 110 K. This value is significantly less than the equivalent blackbody temperature of 124.4 $\pm$ 0.3 K also derived by Hanel *et al.* (1981) using calculations of the total radiance from 0 to 2300 cm^{-1}. It is also less than other estimates of T_{eff} listed in Table 1.2. This discrepancy provides evidence for the existence of an internal Jovian heat source. In this case, the energy balance equation is more accurately written as

$$E = I + L \tag{1.2}$$

where $L = 4\pi r^2 F_p$, is the internal luminosity of the planet,

F_p is the internal heat flux (power/area) of the planet,

and E and I are the power emission and power insolation, respectively, as defined in Eqn 1.1 (Allison and Travis, 1986, p.299). The internal heat flux of Jupiter can thus be calculated if the effective temperature is known. The energy balance is most commonly expressed as the ratio of the total emitted energy to the absorbed solar energy, E/I, which Hanel *et al.* (1981) have determined to be 1.668 $\pm$ 0.085.

Jupiter thus emits almost twice as much energy as it absorbs from the Sun. The most probable source of this energy is the slow leakage of heat from the hot fluid interior of the planet. This loss of thermal energy decreases the interior pressures, thus causing the planet to contract and converting gravitational potential energy to heat (Lewis and Prinn, 1984, p.325). A contraction of 1 mm per year would generate the observed heating rate. Outwards transfer of this heat occurs through thermal convective overturn, rather than by radiative or conductive processes. Gravitational separation of He in the metallic hydrogen region, by which droplets of He condense and sink to convert gravitational energy into heat, has also been suggested as a possible internal heat source (Stevenson and Salpeter, 1976, p.102). However, this is a less likely hypothesis due to the lack of evidence for the associated depletion of He in the outer

regions of the planet, and due to the fact that Jupiter was probably too hot in the past to allow He condensation (Hubbard, 1984, p.263; Ingersoll, 1981, p.126).

Table 1.2: Measurements of the equivalent blackbody temperature and thermal emission of Jupiter (Hanel *et al.*, 1981; Hildebrand *et al.*, 1985).

REFERENCE	T_{eff} (K)	ENERGY BALANCE	TYPE OF MEASUREMENT
Menzel *et al.* (1926)	130 ± 10		ground-based
Murray and Wildey (1963)	128 ± 2.3		ground-based
Low (1965)	132 ± 6		ground-based
Low (1965)	127 ± 6		ground-based
Aumann and Gillespie (1969)	134 ± 4	2.5 ± 0.5	aircraft
Armstrong *et al.* (1972)	134 ± 4	2.5 ± 0.5	aircraft
Trafton and Wildey (1974)	135 ± 4		ground-based
Murphy and Fesen (1974)	136 ± 5		ground-based
Ingersoll *et al.* (1976)	125 ± 3	1.9 ± 0.2	Pioneer
Erickson *et al.* (1978)	123 ± 2	1.6 ± 0.2	aircraft
Hanel *et al.* (1981)	124.4 ± 0.3	1.668 ± 0.085	Voyager
Hildebrand *et al.* (1985)	126.8 ± 4.5	1.8 ± 0.3	ground-based, aircraft, Voyager

1.2.2 The Horizontal Thermal Structure

As is the case for Earth, the solar radiation incident on Jupiter varies with latitude, contributing 0% of the total energy flux at the poles and about 60% at the equator (Hubbard, 1984, p.267). However, unlike Earth, Jupiter exhibits almost no equator-to-pole temperature gradient. Using measurements made with the Pioneer infrared radiometers, Ingersoll *et al.* (1975, 1976) found that the effective temperature varied by a maximum of only 3.6 K (between 124.1 and 127.7 K) over latitudes from 43°S to 47°N. Similarly, using measurements made with the Voyager infrared experiment, Pirraglia (1984) found that the Jovian thermal emission was roughly uniform with latitude, whereas the absorbed solar radiation was strongly latitude-dependent.

Such observations have been explained in terms of convective energy transport in the interior of Jupiter (Ingersoll and Porco, 1978). Heat flow in the low-viscosity fluid interior is regulated by convection processes which effectively compensate for the changes in absorbed solar radiation. As the solar contribution to the total energy budget decreases towards the poles, the contribution from internal convection increases, thus maintaining an essentially constant total energy budget. Conrath and Gierasch (1984) note that there is about a scale height between the top of the convecting interior (600 mbar) and the level of emission to space (300 mbar). They conclude that, as the temperature at the 300 mbar level does not vary with latitude, some form of dynamical circulation is also necessary in these upper tropospheric regions.

Additional analyses of the horizontal thermal structure have been performed by Hanel *et al.* (1979a, 1979b). From the Voyager 1 infrared measurements, they derived relatively flat isotherms in the troposphere, and determined that the warmest and lowest tropopause is lo-

cated at 15°S latitude, becoming cooler and higher at greater latitudes. The upper stratosphere is generally cooler at high southern latitudes than at high northern latitudes, suggesting a pole-to-pole meridional circulation. Voyager 2 infrared data were used to plot brightness maps of Jupiter at 226 and 602 cm^{-1}, corresponding to the 150 and 800 mbar levels, which showed fairly good correlation with the belt-zone structure and with some of the localised visual features. The local variations in brightness temperature have been attributed to forced vertical motions, horizontal advective transport, and radiative effects of clouds and hazes.

1.2.3 The Vertical Thermal Structure

The mean vertical thermal profile is an important property of a planetary atmosphere, strongly influencing its structure, dynamics, and chemical composition. Jovian temperature profiles were first obtained from ground-based infrared and microwave spectra, then from spacecraft occultation and infrared radiometer data (*e.g.*, Atreya *et al.*, 1981; Hogan *et al.*, 1969; Hunten *et al.*, 1980; Orton and Ingersoll, 1976; Wallace *et al.*, 1974). The temperature profile used later in this present study is that of Orton (1981), which was compiled from observations of the equatorial region of Jupiter made with several instruments on the Voyager spacecraft. In the 1 to 1000 mbar region, the profile was derived from infrared spectra of H_2 and CH_4 absorptions (Hanel *et al.*, 1979a) and from occultations of radio signals as the spacecraft passed behind the planet (Lindal *et al.*, 1981). The profile in the upper atmosphere, where pressures are less than 1 mbar, was derived from stellar and solar occultation measurements made with the Voyager ultraviolet spectrometers (Atreya *et al.*, 1979, 1981; Festou *et al.*, 1981).

Orton's (1981) final temperature profile extends from a maximum pressure of 100 bar to a minimum of 10^{-11} bar. Its accuracy depends on direct measurement errors, uncertainties in the abundances of H_2 and He, and real variations from the nominal temperature at the time of measurement. In order to provide a measure of the temperature variations arising from these errors, Orton (1981) has calculated four additional profiles by adding or subtracting the temperature error due to compositional uncertainties (the "heavy" and "light" models) and that due to the direct measurement error (the "light" and "cool" models) from the nominal temperature profile (see Figure 1.3).

As seen in this figure, the vertical temperature profile of Jupiter is analogous to that of Earth. Like the troposphere of Earth, the lower Jovian atmosphere is a region where the dominant mechanism of vertical heat transfer is convection and the temperature follows an adiabatic gradient. As discussed in §1.2.1, the thermal convection is a consequence of the high heat flux from the interior, with the infrared opacity of the atmosphere reducing the role of radiation as a competing means of heat transfer (Jones, 1984, p.221–222). Thus, although observations have been made only down to about the 1 bar level, the adiabatic gradient is expected to extend far below this, as radiation will not be important at these depths (Ingersoll, 1981, p.121). The adiabatic lapse rate in the troposphere, $-\frac{dT}{dz}$, where T is temperature and z is

Figure 1.3: The nominal composite Jovian temperature profile derived from Voyager data, along with four variations on this model that incorporate compositional and measurement errors (Orton, 1981).

height, is given by (*e.g.*, Houghton, 1986, p.3–5)

$$-\frac{dT}{dz} = \frac{g}{c_p} \tag{1.3}$$

where g is the gravitational acceleration, and

c_p is the specific heat at constant pressure.

From Voyager radio occultations, the adiabatic lapse rate has been measured as 2.1 ± 0.2 K/km at the 1 bar level, where the temperature is calculated to be 165 ± 5 K (Lindal *et al.*, 1981).

At a pressure between 100 and 300 mbar, the temperature gradient falls to zero and the temperature reaches a minimum of about 110 K, marking the Jovian tropopause. Above this is the stratosphere, where the temperature increases with height and convection no longer dominates. In this region, the thinner atmosphere is no longer opaque in the infrared and can therefore be heated by direct absorption of solar radiation. Infrared absorption by CH_4 is thought to be responsible for most of this solar heating, although haze layers may also contribute (Hunt, 1981, p.231; Jones, 1984, p.222). Within this region of temperature increase, there is a small warm inversion layer at about 35 mbar which may be caused by some absorbing minor constituent at that level, or by upward-moving inertia-gravity waves (Eshleman *et al.*, 1979).

The Jovian stratopause is located at the 1 mbar level, where the temperature is about 170–180 K (Hunten, 1976, p.24). Above it is the mesosphere, where there is a radiative balance between the planetary and solar sources of radiation and infrared cooling. At a pressure of about 1 μbar, this merges into the thermosphere, where the temperature again increases. Temperatures in this region are much higher than the 200 K achievable by absorption of solar ultraviolet radiation. This thermospheric heating may be generated by the upward propagation and dissipation of inertia gravity waves or by the precipitation of energetic electrons from the magnetospheric plasma (Atreya *et al.*, 1979). In the uppermost reaches of the thermosphere is

the ionosphere, where solar ultraviolet radiation and energetic magnetospheric ions and electrons are responsible for ionisation, and the temperature, derived from from Voyager radio occultations, is 1450^{+300}_{-250} K at 1500 to 2000 km above the cloud tops (Atreya *et al.*, 1979).

1.3 The Composition of the Jovian Atmosphere

1.3.1 Theoretical Modelling of Composition

Aside from those exceptions discussed below, most elements and isotopes found in the Jovian atmosphere appear to be present in solar abundances. Assuming an adiabatic solar-composition model of Jupiter, it is possible to calculate the thermochemical-equilibrium abundance of any given compound. Lewis (1969b) was the first to do this for about 500 volatile compounds of the 40 cosmically most abundant elements. The resulting distribution is shown in Figure 1.4. A similar calculation was performed nine years later by Barshay and Lewis (1978), when about a dozen new species had been identified in the Jovian atmosphere from observations of absorption features in the 5 μm window (see §3.1.2 for a discussion of the 5 μm window). Barshay and Lewis computed upper limits on the equilibrium abundances of gases being depleted by condensation and suggested that the identification of species predicted to be undetectable would provide evidence of vertical motions. This suggestion is further discussed below.

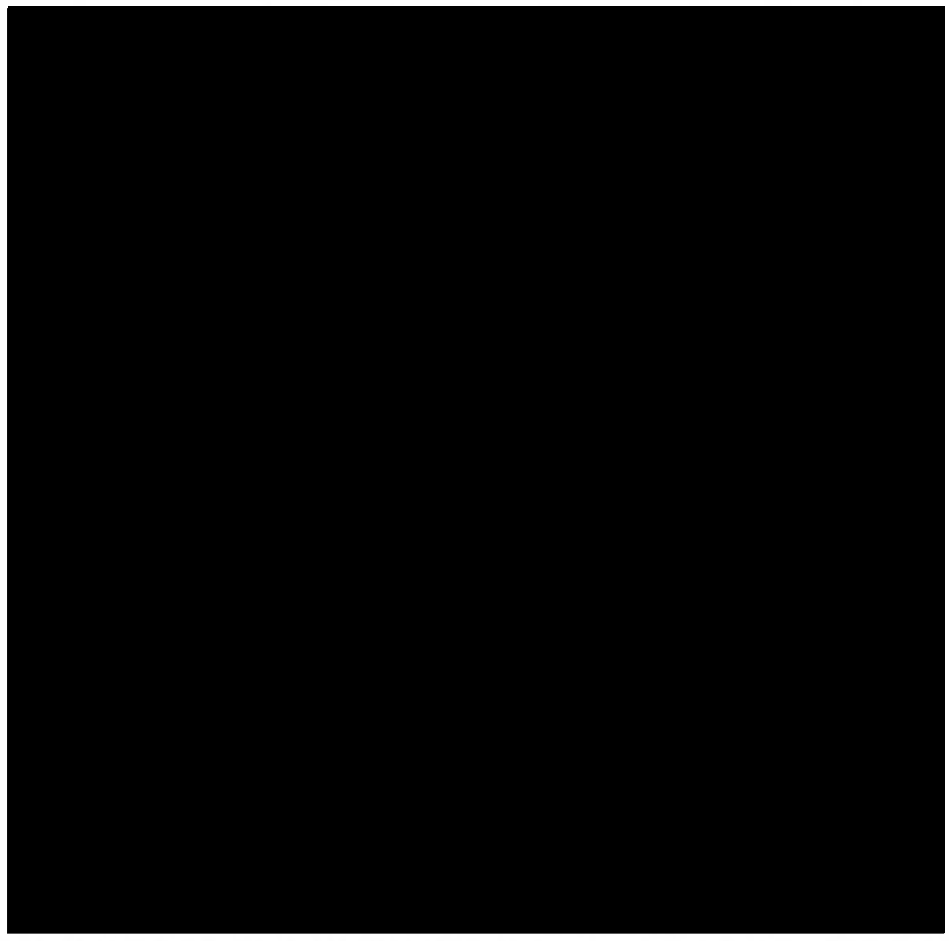

Figure 1.4: The predicted distribution of constituents in a solar-composition thermochemical-equilibrium model of the Jovian atmosphere (Lewis, 1969b).

The remainder of this section is a summary of our current knowledge of the composition of the Jovian atmosphere, as determined primarily from infrared spectroscopic observations. Those abundances which differ from the solar-composition model are of particular interest, as

they provide insight into the evolution and behaviour of the atmosphere. The most recent measurements of abundance are summarised in Table 1.3, in the form of X/H_2 mixing ratios.

Table 1.3: The measured composition of the Jovian atmosphere.

CONSTITUENT	MIXING RATIO relative to H_2	REFERENCE
H_2	0.897 ± 0.030	Gautier *et al.* (1981)
	0.899 ± 0.026	Conrath *et al.* (1984)
	(relative to atmosphere)	
He	0.115 ± 0.037	Gautier *et al.* (1981)
	0.112 ± 0.032	Conrath *et al.* (1984)
CH_4	$(2.5 \pm 0.4) \times 10^{-3}$	Knacke *et al.* (1982)
	$(1.95 \pm 0.22) \times 10^{-3}$	Gautier *et al.* (1982)
	$(3.3 \pm 1.1) \times 10^{-3}$	Bjoraker *et al.* (1986a)
NH_3	$(1.98 \pm 0.99) \times 10^{-4}$	Kunde *et al.* (1982)
	$(2.9 \pm 0.4) \times 10^{-4}$	Bjoraker *et al.* (1986a)
	2.5×10^{-4}	de Pater (1986)
C_2H_6	1.2×10^{-6}	Kostiuk *et al.* (1983)
	$(5.5 \pm 1.5) \times 10^{-6}$	Noll *et al.* (1986)
C_2H_2	$(1.0 \pm 0.3) \times 10^{-7}$	Noll *et al.* (1986)
	1.0×10^{-8}	Drossart *et al.* (1986)
H_2O	$(4 \pm 1) \times 10^{-6}$	Drossart and Encrenaz (1982)
	$(1 - 30) \times 10^{-6}$	Kunde *et al.* (1982)
	$(4 - 30) \times 10^{-6}$	Bjoraker *et al.* (1986b)
PH_3	$(7.8 \pm 1.1) \times 10^{-7}$	Bjoraker *et al.* (1986a)
	6.0×10^{-7}	Lellouch *et al.* (1989)
CO	3×10^{-9}	Larson *et al.* (1978)
	1.1×10^{-9}	Bjoraker *et al.* (1986a)
GeH_4	$10.0^{+2.0}_{-4.0} \times 10^{-10}$	Drossart *et al.* (1982)
	$7.8^{+4.5}_{-2.2} \times 10^{-10}$	Bjoraker *et al.* (1986a)
HCN	$(0.9 \text{ to } < 7) \times 10^{-9}$	Tokunaga *et al.* (1981)
CH_3D	$2.0^{+1.5}_{-1.0} \times 10^{-7}$	Drossart *et al.* (1982)
	$(4.0 \pm 0.6) \times 10^{-7}$	Knacke *et al.* (1982)
	$(2.2 \pm 0.4) \times 10^{-7}$	Bjoraker *et al.* (1986a)

1.3.2 The Major Constituents

H_2 was long thought to be a major constituent of Jupiter because of the low value of the planet's mean density, but it was not until 1960 that H_2 was detected by Kiess *et al.* (1960), who observed the weak quadrupole absorptions of the 3–0 vibrational band. Early estimates of the H_2 abundance, generally expressed as the mole fraction

$$q = \frac{n(H_2)}{n(H_2) + n(He)} \tag{1.4}$$

where n represents the number density (Gautier *et al.*, 1981), have been improved by Pioneer and Voyager data. Orton and Ingersoll (1976, p.211) found that a H_2 mole fraction of 0.88 ± 0.06 provided the best fit to Pioneer infrared radiometer measurements. More recently, Gautier *et al.* (1981) derived H_2 abundances from Voyager data using two different methods. In their first,

they used IRIS infrared data to derive a mole fraction of 0.897 ± 0.030 for the region between 200 and 500 mbar, and in their second, they combined IRIS spectra with Voyager radio occultation profiles to obtain a value of 0.880 ± 0.036. Conrath *et al.* (1984) have revised the second of these estimates to include the error estimate for the radio occultation thermal profile derived by Lindal *et al.* (1981) and the CH_4/H_2 mixing ratio derived by Gautier and Owen (1983), obtaining a value of 0.899 ± 0.026.

Like H_2, long before it was detected He was predicted to be an important element in the Jovian atmosphere (*e.g.*, Owen, 1969). The presence of He was verified when the Pioneer 10 ultraviolet photometer first recorded emission at 584 Å caused by resonant scattering of solar HeI radiation incident on the Jovian atmosphere (Judge and Carlson, 1974). Soon afterwards, Orton and Ingersoll (1976, p.211) estimated a He/H_2 mixing ratio of 0.14 ± 0.08, using the H_2 mole fraction derived from the Pioneer infrared radiometer data. The two H_2 abundances derived by Gautier *et al.* (1981), yield He/H_2 mixing ratios of 0.115 ± 0.037 and 0.136 ± 0.046 respectively, with the latter value revised to 0.112 ± 0.032 using the H_2 abundance obtained by Conrath *et al.* (1984). These results are in good agreement with the solar He abundance of approximately 0.126 (Ross and Aller, 1976), suggesting that little or no He differentiation has occurred in the Jovian atmosphere. However, the estimated uncertainties in the Jovian and solar He abundances remain sufficiently large that He depletion cannot yet be ruled out.

1.3.3 Methane

With its many strong absorption bands dominating the infrared Jovian spectrum, CH_4 was one of the first two species to be identified in the Jovian atmosphere by Wildt (1932), who estimated a column abundance in the tens of m-amagat from observations at 8 μm. (*Note:* 1 m-amagat is the column abundance of an ideal gas at 273.15 K and 1 atm, equivalent to 2.687×10^{21} molecules/cm^2.) This was followed by a much larger estimate of 150 m-amagat obtained by Kuiper (1952) from a comparision of photographic spectra of Jupiter with laboratory spectra of the red CH_4 bands. Because many of the Jovian CH_4 bands are saturated, no further progress was made until the $3\nu_3$ band at 9050 cm^{-1} was identified by Owen (1965), and used by Margolis and Fox (1969a, 1969b, 1969c) to deduce column abundances of 40 to 80 m-amagat. Observations of this band were subsequently used by Maillard *et al.* (1973) and de Bergh *et al.* (1976) to estimate abundances of 38 ± 8 m-amagat and 52 ± 6 m-amagat, respectively. The variation between the early results obtained with the $3\nu_3$ band was due to such factors as telluric absorptions, the complexity of the CH_4 absorption, the presence of unidentified lines, pressure broadening effects, cloud structure, and scattering effects (Ridgway *et al.*, 1976a, p.393). Using typical column abundances of 50 m-amagat for CH_4 and 70 km-amagat for H_2, Prinn and Owen (1976, p.357) calculated the CH_4/H_2 mixing ratio to be 7.1×10^{-4}.

In the visible region of the spectrum, Lutz *et al.* (1976) were the first to measure the laboratory band strengths of the weak CH_4 bands (at 4410, 4860, 5430, and 5760 Å), which

they then compared with visible spectra of Jupiter to derive a value of 150 m-amagat for the column abundance (equivalent to a CH_4/H_2 ratio of 2×10^{-3}). This agreed with Kuiper's original estimate and was several times larger than the $3\nu_3$ values, possibly because of the greater effect of particle scattering at shorter wavelengths. In an attempt to reconcile $3\nu_3$ and visible measurements, Wallace and Smith (1977) used homogeneous scattering models and the new 0.7–1.0 μm CH_4 laboratory data of Dick and Fink (1977) (see §4.3.1) to calculate CH_4 mixing ratios of 1×10^{-3} and 2×10^{-3}. Further support for the higher CH_4 abundance was provided by Fink and Larson (1979), who recorded laboratory spectra of the $3\nu_3$ CH_4 band and demonstrated that the band was more complex and less well understood than previously thought. However, they were able to compare laboratory spectra and Jovian spectra of two broad absorption features at 6400 and 7900 cm^{-1} to derive a column abundance of 130 m-amagat and a mixing ratio of 1.6×10^{-3}.

The visible and infrared bands of CH_4 have been the subject of many more laboratory studies and ground-based Jovian observations over the past 15 years, yielding CH_4 mixing ratios which range from 1.2×10^{-3} to 2.5×10^{-3} (see Cochran, 1977; Knacke *et al.*, 1982; Orton, 1975b; Sato and Hansen, 1979; Smith and Greene, 1980; and West 1979). Voyager infrared spectra of the ν_4 band of CH_4 recorded over 1200 to 1500 cm^{-1} were used by Gautier *et al.* (1982) to derive $(1.95 \pm 0.22) \times 10^{-3}$ for the CH_4/H_2 ratio. Most recently, a value of $(3.3 \pm 1.1) \times 10^{-3}$ was obtained by Bjoraker *et al.* (1986a) using observations of the 5 μm window recorded with the Kuiper Airborne Observatory.

Because most of the carbon on Jupiter is found in CH_4 and most of the hydrogen as H_2, the CH_4 mixing ratio provides a means of determining the Jovian C/H ratio for comparison with the solar value. The C/H ratio can be calculated using (Gautier *et al.*, 1982)

$$C/H \approx 0.5\frac{CH_4}{H_2} \tag{1.5}$$

Measurements of the Jovian C/H ratio made by Combes and Encrenaz (1979), Buriez and de Bergh (1980), and Encrenaz *et al.* (1980), along with values derived from the CH_4 mixing ratios listed above, suggest that C/H is enriched relative to the solar value of 4.7×10^{-4} (Lambert, 1978) by a factor between 1.3 and 3.5. Because CH_4 is the only well-mixed minor constituent in the Jovian atmosphere whose abundance is not altered by cloud or haze condensation or by major chemical reactions with other gases, this C/H enrichment favours the nucleation model of Jovian formation over the condensation model (see §1.1.2), as CH_4 ice initially trapped in an accreted core could later have been released and distributed via heating and convection (Gautier and Owen, 1983). Gautier *et al.* (1982) have shown that this process could provide a C/H enrichment of as much as 20 times the solar ratio.

1.3.4 Ammonia

As is the case for CH_4, strong absorption bands of NH_3 are also found in the infrared, and so NH_3 was the second Jovian species to be identified by Wildt (1932), who estimated a column

abundance of 40 cm-amagat. However, measurements of the Jovian NH_3 abundance are made difficult by the variability of its vertical profile. Photochemical processes in the upper atmosphere, condensation at temperatures below ~145 K, and the formation of clouds of NH_4SH and NH_3–H_2O at pressures of several bar all contribute to this variability (Gautier and Owen, 1983). Measurements at different wavelengths which probe different heights in the atmosphere therefore give quite different values for the abundance.

The NH_3 abundance in the upper regions of the atmosphere above the tropopause has been probed with ultraviolet observations. Jovian spectra recorded by the International Ultraviolet Explorer (IUE) have been used to derive an upper limit of 0.5×10^{-9} on the NH_3/H_2 ratio above the tropopause (Owen *et al.*, 1980), an NH_3 mixing ratio of $(2.5 \pm 1.8) \times 10^{-8}$ in the 100–150 mbar region near the tropopause, and an upper limit of 10^{-9} for pressures <100 mbar in the stratosphere (Wagener *et al.*, 1985). Tomasko (1974) has also demonstrated that photodissociation of NH_3 must occur above the 145 K level, as the decrease in NH_3 mixing ratio with height that results from the NH_3 saturated vapor pressure curve is insufficient to explain the low NH_3 abundances that are observed.

However, estimates of the global Jovian NH_3 abundance require measurments that probe below the levels of condensation and photochemistry. The NH_3 abundance below the tropopause, down to the 5 bar level, has been probed at infrared and visible wavelengths. Values of the NH_3/H_2 ratio in the well-mixed region near 1 bar range between $(1.98 \pm 0.99) \times 10^{-4}$ and $(3.3 \pm 1.7) \times 10^{-4}$ (see Knacke *et al.*, 1982; Kunde *et al.*, 1982; Lindal *et al.*, 1981; and Sato and Hansen, 1979), while the lower region of the troposphere has been probed at 5 μm by Bjoraker *et al.* (1986a), who derived an NH_3/H_2 ratio of $(2.9 \pm 0.4) \times 10^{-4}$ for the 5 bar level. The agreement between this value and those near 1 bar suggests that the NH_3 abundance is fairly uniform in the troposphere, even at the level of NH_4SH clouds (2 bar). These numbers also suggest that the Jovian N/H ratio is between 1 and 2 times its solar value of $9.8^{+2.5}_{-2.0} \times 10^{-5}$ (Lambert, 1978), similar to the enrichment of the C/H ratio and again supporting the nucleation hypothesis.

The NH_3 distribution at pressures greater than 5 bar has been probed by radio measurements, with Marten *et al.* (1980) estimating $1.2 \times 10^{-4} \leq NH_3/H_2 \leq 1.5 \times 10^{-3}$ for pressures greater than 10 to 14 bar. In contrast to the infrared results, the radio observations of de Pater (1986) suggested that there is a decrease in the NH_3 abundance between 1 and 10 bar, with NH_3 undersaturated and uniformly distributed at 0.3 to 0.5 bar, depleted (by a factor of 3 to 8 relative to the solar value) at 0.5 to 1–2 bar, and enriched (by a factor of 2 relative to the solar value) below 2.2 bar. The apparent depletion of NH_3 has been attributed to trapping of NH_3 by reactions with H_2S to form NH_4SH clouds at 1–2.2 bar, but Bjoraker *et al.* (1986a) have calculated that the resulting depletion should only be about 10%, much less than the decrease indicated by the radio data. Clearly, additional measurements of the vertical profile of NH_3 are needed in order to resolve these different results.

1.3.5 Other Minor Constituents

In addition to CH_4 and NH_3, which are the most abundant minor constituents in the Jovian atmosphere and the most important absorbers at visible and infrared wavelengths, various other species have also been detected, with distributions and abundances that provide clues to the past history of Jupiter and to its current physical processes. C_2H_6 and C_2H_2 were the next species to be identified after H_2, NH_3, and CH_4 (Combes *et al.*, 1974; Ridgway, 1974a), and numerous estimates of their abundances have been obtained (see Table 1.3 for some of the most recent). Voyager infrared spectra revealed that the abundance of both species varies with latitude (Hanel *et al.*, 1979a; Maguire *et al.*, 1984), apparently being enhanced towards both poles due to the excitation of CH_4 by precipitating magnetospheric particles (Drossart *et al.*, 1986; Kim *et al.*, 1985; Kostiuk *et al.*, 1983). Both of these hydrocarbons are thought to be generated by the photolysis of CH_4 in the upper stratosphere, then vertically mixed down to the 1 mbar level (where they can be observed), and eventually transported down below the tropopause to be destroyed in chemical reactions in the warmer troposphere (Noll *et al.*, 1986).

Several other hydrocarbons have also been discovered in the Jovian atmosphere. IUE spectra have been used to set upper limits on the mixing ratios of eight different hydrocarbons (Gladstone and Yung, 1983; Wagener *et al.*, 1985), and Kim *et al.* (1985) have made positive identifications of C_2H_4, C_3H_4, and C_6H_6 in Voyager spectra of enhanced infrared emission near the Jovian north magnetic pole. They calculated mixing ratios, relative to H_2, of $(7 \pm 3) \times 10^{-9}$ for C_2H_4, $2^{+2}_{-1} \times 10^{-9}$ for C_6H_6, and $2.5^{+2}_{-1} \times 10^{-9}$ for C_3H_4, and set upper limits of $< 3 \times 10^{-10}$ for C_4H_2 and 6×10^{-7} for C_3H_8. The detection of benzene, the largest molecule to be identified in a planetary atmosphere, is of particular interest because it had not been predicted by chemical modelling. It seems likely that it is produced from the trimerisation of C_2H_2, but studies of this process under Jovian conditions are required to confirm this suggestion (Kim *et al.*, 1985).

H_2O was the first oxygen-bearing molecule to be found in the Jovian atmosphere (Larson *et al.*, 1975) and is of particular importance as a source of atmospheric opacity, a solvent, a participant in cloud formation and chemical reactions, and a source and sink of heat when it changes phase. Estimates of the H_2O mixing ratio have been obtained from Voyager spectra of the 5 μm hot spots, with Kunde *et al.* (1982) deriving values of 1×10^{-6} at 2.5 bar, and 30×10^{-6} at 4 bar, and Drossart and Encrenaz (1982) obtaining a ratio of $(4.0 \pm 1.0) \times 10^{-6}$, averaged over the entire disk for the 230–270 K levels. Using both 2.7 and 5.0 μm spectra, Bjoraker *et al.* (1986b) were able to infer the H_2O profile from 0.7 to 6.0 bar, concluding that H_2O is saturated above 2 bar, and has a mixing ratio of 4×10^{-6} over 2 to 4 bar, which increases to 30×10^{-6} at 6 bar. All of these measurements suggest significant oxygen depletion, with the 6 bar abundance of Bjoraker *et al.* (1986b) giving an O/H ratio 50 times less than the solar value of 8×10^{-4} (Lambert, 1978). The question of whether this depletion is limited to the clearer regions of Jupiter or is representative of the global abundance, remains unresolved and requires measurements of the O/H ratio below the level at which H_2O clouds condense.

The discovery of PH_3 in the Jovian atmosphere (Ridgway, 1974b; Ridgway *et al.*, 1976b) was unexpected because thermochemical-equilibrium calculations predict that, although PH_3 will be stable deep in the atmosphere below 1000 K, phosphorus oxides should predominate at spectroscopically observable levels (Lewis, 1969b). Estimates of the PH_3 mixing ratio have been derived from 5 and 10 μm Voyager IRIS spectra by Drossart *et al.* (1982), Kunde *et al.* (1982), and Lellouch *et al.* (1989), and from ground-based spectra by Knacke *et al.* (1982) and Bjoraker *et al.* (1986a). These values range between $(4.5 \pm 1.5) \times 10^{-7}$ and $(8.3 \pm 2.0) \times 10^{-7}$ in the troposphere, and generally appear to decrease at heights above 1 bar, probably due to photolysis. The most likely explanation for the unexpected presence of PH_3 in the Jovian atmosphere is that rapid vertical convection transports PH_3 from deep in the atmosphere up to observable regions more quickly than it is destroyed by chemical reactions (Prinn and Lewis, 1975). An alternative suggestion is that the abundance of H_2O (the principal oxidising agent of PH_3) is insufficient to oxidise all of the PH_3, allowing PH_3 to remain stable in the upper atmosphere. However, the current estimates of H_2O abundance appear to be more than enough to oxidise PH_3 completely (Bjoraker, 1986a). Simultaneous observations of the temporal and spatial variability in PH_3 and H_2O abundance may allow the correct mechanism to be determined, as PH_3 should vary directly with H_2O if the variability were due to changes in the dynamic mixing rate, whereas PH_3 should vary inversely with H_2O if the variability were due to changes in the H_2O abundance (Drossart *et al.*, 1984).

Like PH_3, CO is a non-equilibrium species predicted to have a negligible abundance under conditions of thermochemical equilibrium. Evidence for the presence of trace amounts of CO was first obtained from observations of the Jovian 5 μm window (Beer, 1975). Subsequent analysis of 5 μm spectra by Beer and Taylor (1978) suggested that CO is uniformly mixed in the stratosphere with a mixing ratio of 1.5×10^{-8}, but absent from the troposphere. However, Larson *et al.* (1978) were able to detect weaker CO lines compatible with the presence of CO in the troposphere, deriving a well-mixed CO/H_2 ratio of 3×10^{-9}. Bjoraker *et al.* (1986a) also found that a well-mixed tropospheric CO distribution gave the best match to their spectra, obtaining a mixing ratio of 1.1×10^{-9}. The most widely accepted explanation for the observed CO abundance is that rapid convection transports CO from levels near 1100 K (where CO is produced by the oxidation of CH_4 by H_2O) up to the visible levels in the upper troposphere more quickly than the CO can be reduced back to CH_4 (Prinn and Barshay, 1977). However, this remains uncertain, as Bar-Nun and Podolak (1985) have calculated a chemical lifetime for CO which is less than the convection time, concluding that the ascending gas will contain 10 orders of magnitude less CO than calculated by Prinn and Barshay (1977). Bar-Nun and Podolak (1985) prefer an alternative mechanism whereby external sources provide the oxygen needed to form CO; both the photolysis of infalling H_2O- and oxygen-containing meteoroidal materials (Prather *et al.*, 1978) and the ejection of oxygen atoms into the Jovian atmosphere from the impact of energetic charged particles on the Galilean satellites (Strobel and Yung, 1979) appear

to be of the right magnitude to provide the necessary flux of oxygen atoms. Again, this is a question yet to be resolved.

For several years, a prominent feature at 2111 cm^{-1} remained unidentified, until Fink *et al.* (1978) discovered that it was matched by the Q branch of the ν_3 band of GeH_4, and then estimated a GeH_4 mixing ratio of 6×10^{-10} for the 300 K, 5 bar hot spots. Using the same feature in Voyager infrared spectra, Drossart *et al.* (1982) derived a GeH_4 mixing ratio of $10.0^{+2.0}_{-4.0} \times 10^{-10}$ in the 200 to 250 K region, while Kunde *et al.* (1982) obtained a value of $(7.8 \pm 2.2) \times 10^{-10}$ at the 2 to 5 bar level. Several more lines in the ν_3 band of GeH_4 were identified by Bjoraker *et al.* (1986a), who inferred a GeH_4 mixing ratio of $7.8^{+4.4}_{-2.2} \times 10^{-10}$. GeH_4 is another species which was predicted to be unobservable by the thermochemical-equilibrium calculations of Barshay and Lewis (1978). They predicted that GeS would be the most abundant Ge compound at altitudes between 300 and 1000 K. This again provides evidence for the existence of a rapid, deep convective cycle by which GeH_4 (like PH_3 and CO) is transported up from about the 900 K level to the 300 K level (Fink *et al.*, 1978).

With its low abundance and weak lines at observable wavelengths, there are few reports on the detection of HCN in the Jovian atmosphere. Tokunaga *et al.* (1981) first identified it from 13.5 μm ground-based infrared spectra, and assuming a uniform tropospheric distribution, they derived a HCN/H_2 ratio of 0.9×10^{-9} to $< 7 \times 10^{-9}$, with an upper limit of 2×10^{-9} in the stratosphere. Vertical convection may be responsible for the observable abundance of HCN, but thermochemical-equilibrium calculations place this abundance at 1500 K, far deeper than the ~1000 K level from which PH_3, CO, and GeH_4 seem to originate (Tokunaga *et al.*, 1981). The alternative theories are that HCN is created photochemically (Kaye and Strobel 1983) and that HCN is a product of lightning discharge on Jupiter, forming during the chemical reactions that occur in the hot shocked atmosphere. Assuming the lightning hypothesis, Bar-Nun and Podolak (1985) have calculated a HCN mixing ratio of the order 3×10^{-10}, suggesting that lightning is sufficient to account for the observed HCN abundance.

All of the minor constituents discussed above have been positively identified in the Jovian atmosphere. However, there are many other predicted species that have yet to be detected. Of particular interest is H_2S, which should be the dominant sulfur-bearing compound between 300 and 2000 K, probably reacting with NH_3 and condensing as NH_4SH clouds above the 2 bar level (Bézard *et al.*, 1983b). Although H_2S has not been detected, its photochemistry in the Jovian atmosphere has been modelled, with emphasis on the possibility of sulfur-bearing compounds being candidates for the observed colouration of Jupiter (Lewis and Prinn, 1970; Prinn and Owen, 1976, p.335–338). Numerous estimations of the upper limit to H_2S abundance have been made, and are summarised by Larson *et al.* (1984), whose own tropospheric upper limit for H_2S/H_2 is 3.3×10^{-8}. The failure to detect H_2S has been attributed to destruction by reactions with NH_3 and by solar photodissociation (Bézard *et al.*, 1983b), and particularly to the trapping of sulphur in the NH_4SH clouds near 1.5–2 bar (Atreya, 1986, p.92–93; Larson

et al., 1984). This latter hypothesis implies that insufficient H_2S will exist at heights where photolysis can generate sulphur-bearing chromophores, leaving only phosphorus compounds and organic polymers as chromophore candidates.

Upper limits on the abundance of currently undetected species can be calculated by selecting the most prominent features present in laboratory spectra, estimating the maximum equivalent width of each feature that would remain undetected in a Jovian spectrum, and deducing the upper limit from the strengths of the features measured in the laboratory. This procedure has been applied to 19 different gases by Treffers *et al.* (1978). The resulting upper limit for SiH_4 suggests that the base of the convective cycle lies at 1500 K, because if SiH_4 were transported from depths below this, it should have a detectable mixing ratio. AsH_3 is the compound most recently detected in the Jovian atmosphere, identified in 4.7 μm spectra by Noll *et al.* (1989). Numerous suspected but currently undetected, gases and isotopes, including Ne, Ar, Kr, Xe, H_2S, HCl, HF, and isotopes of H, He, Ne, Ar, O, S, C, N, and Cl should be detectable with the mass spectrometer on the Galileo probe (see §2.2.4).

1.3.6 Isotopic Abundances

If they could be accurately determined, the abundances of the isotopes D (deuterium), ^{13}C and ^{15}N would provide additional clues to the origin and evolution of Jupiter. The presence of deuterium in the Jovian atmosphere was verified with the discovery of both deuterated hydrogen, HD, (Trauger *et al.*, 1973) and mono-deuterated methane, CH_3D, (Beer *et al.*, 1972). Reviews of the D/H ratios obtained from observations of these two species can be found in Bjoraker *et al.* (1986a), Encrenaz (1984), and Kaye (1987). The D/H ratios vary widely between the extremes of 1.2×10^{-5} and 5.6×10^{-5}. These values are generally consistent with the D/H ratio in the primordial nebula, about 2.5×10^{-5} (Geiss and Reeves, 1972), therefore suggesting that Jovian deuterium did not undergo fractionation during planetary formation. However, more accurate measurements of D/H are needed to confirm this hypothesis.

The carbon-13 isotope, in the form of $^{13}CH_4$, was discovered in the $3\nu_3$ band at 1.1 μm by Fox *et al.* (1972). Their estimate of the $^{12}C/^{13}C$ ratio, as well as those of de Bergh *et al.* (1976) and Combes *et al.* (1977), were revised by Courtin *et al.* (1983) to 87 ± 35, 55^{+35}_{-15}, and 71^{+10}_{-12}, respectively, using new measurements of the ratio of $^{12}CH_4/^{13}CH_4$ intensities in the $3\nu_3$ band made by Brault *et al.* (1981). However, analysis of Voyager IRIS spectra of the ν_4 band of CH_4 by Courtin *et al.* (1983) yielded a value of $^{12}C/^{13}C = 160^{+40}_{-55}$, which is 1.8 times the solar-terrestrial value of 90. This value suggests depletion of ^{13}C relative to the solar and terrestrial value, whereas chemical fractionation or irradiation of Jovian ^{12}C would be expected to increase the abundance of ^{13}C. If the Voyager value is correct, it may represent the true ratio in the primitive solar nebula, with the present ratio in the Sun, inner planets, and asteroids having been reduced by some process that increased the production of ^{13}C in the inner solar system at some period in its evolution (Gautier and Owen, 1983).

The nitrogen-15 isotope was first identified by Lacy *et al.* (1975), who obtained a $^{14}N/^{15}N$ ratio of 280 from the ν_2 feature of NH_3 at 10–13 μm. This value is good agreement with the terrestrial ratio of 270, as are the subsequent measurements by Encrenaz *et al.* (1978) and Tokunaga *et al.* (1980). However, Tokunaga *et al.* (1979) and Drossart *et al.* (1985) obtained much lower values of 170 ± 40 and 125^{+145}_{-75}, respectively. These suggest an enhancement of ^{15}N in the Jovian atmosphere, but the mechanism for this is undetermined (Kaye, 1987). As is true of D and ^{13}C, the uncertainties in the abundance of ^{15}N point to an obvious need for additional and more accurate measurements.

1.4 The Vertical Cloud Structure of the Jovian Atmosphere

1.4.1 Theoretical Modelling of Cloud Structure

The vertical cloud structure of the Jovian atmosphere can be calculated theoretically with a condensation-layer modelling scheme. Starting with the assumption of some initial pressure, temperature, and composition at a point deep in the atmosphere, the temperature and pressure at altitudes above this can be calculated using the dry adiabatic lapse rate and hydrostatic saturation, respectively. These allow the partial pressure and saturation vapor pressure of a gas to be determined at each level, with condensation occuring once the former becomes larger than the latter. At this point, the partial pressure of the condensing gas is set equal to the saturation vapor pressure, the new mole fraction is computed, the altitude is incremented again, and the temperature at the new height is determined from the wet adiabatic lapse rate.

Lewis (1969a) was the first to apply this method to a solar-composition atmosphere, taking into account all possible condensates of the NH_3–H_2O and NH_3–H_2S systems. This showed the clouds to be dominated by aqueous NH_3 solution, with an upper cloud layer of solid NH_3 crystals, a possible intermediate layer of NH_4SH or H_2O ice, and a lower layer of aqueous NH_3 solution. Weidenschilling and Lewis (1973) repeated this modelling using an improved pressure-temperature profile which resulted in condensation at lower temperature levels. As a consequence, H_2O ice became the most important cloud constituent and the aqueous NH_3 cloud was reduced to a marginal amount. Above the H_2O, clouds of NH_4SH and solid NH_3 were predicted, with the base of the latter located at exactly 1 bar for a reference base at 400 K and 25 bar. A repetition of this procedure was performed more recently by Atreya and Romani (1985), who used a thermal profile based on Voyager measurements, a base at 425 K and 200 bar, and a lapse rate of 1.9 K/km, to obtain the profile in Figure 1.5. In this model the bases of the cloud layers are at 0.506, 1.76, and 4.25 bar (equivalent to 143, 207, and 268 K) for the NH_3 ice, NH_4SH, and H_2O ice clouds, respectively, while the major feature of note is the absence of any aqueous NH_3 cloud below the H_2O ice.

Figure 1.5: Theoretical cloud structure of the Jovian atmosphere assuming a solar composition and using a Voyager thermal profile with a base at 400 K and 200 bar (Atreya and Romani, 1985, p.53).

1.4.2 Models Derived from Observations

Although none of the clouds predicted by the theoretical models have been unambiguously detected in the Jovian atmosphere, many more models have been derived from observational data. These can be divided into three groups, defined by the type of observation: (1) models based on remote sensing of reflected sunlight, (2) models based on 5 μm images and their correlation with visible reflectivity, and (3) models based on 5 μm spectra (West *et al.*, 1986).

Models derived from reflection of solar radiation at visible and infrared wavelengths rely on the interpretation of absorptions by gaseous CH_4, NH_3, and H_2. Many such models have been developed, too numerous to present here, but listed in West *et al.* (1986). These models tend to include a cloud, probably of NH_3, which extends up to 200–300 mbar and is present over both the belts and zones. In their comprehensive paper on Jovian cloud structure, Sato and Hansen (1979) made the first attempt to build a coherent model of atmospheric structure by combining the constraints of many observations of CH_4, NH_3, and H_2 absorptions, and proceeding through a series of models of increasing complexity. The best fit to the data was obtained with a ten-parameter model having two cloud layers and a diffuse aerosol haze region overlapping the upper cloud. They concluded that the upper cloud consists of solid NH_3 crystals, has a base at 600–900 mbar, and must extend over both the zones and the belts, while beneath it, separated by a relatively transparent region, is a second cloud, probably of H_2O, with a top at 3–5 bar. This model differs from the theoretical models discussed above, in that no NH_4SH cloud is predicted. However, such a cloud is allowed by the model in the 1 to 3 bar region if it is optically thin enough to permit significant visible radiation to reach the top of the lower cloud.

Similar two-cloud models with a high-altitude haze have been derived from spectra of re-

flected sunlight by others (*e.g.*, Baines *et al.*, 1983; Smith, 1986). More recently, Cunningham *et al.* (1988) also used a two-cloud multiple-scattering radiative transfer model (see Figure 1.6a) to analyse H_2 spectra. In this case, the top of a thick lower cloud layer is located at 2 bar, an upper NH_3 cloud extends from 320 to 700 bar over both the belts and zones, and an upper haze is found at 120 mbar, although the latter is not constrained by the H_2 data, and the solution is not unique. The Jovian cloud models obtained from observations of reflected sunlight thus favour the existence of an overlying NH_3 cloud layer and suggest that there is little difference between the cloud structure in the belts and zones.

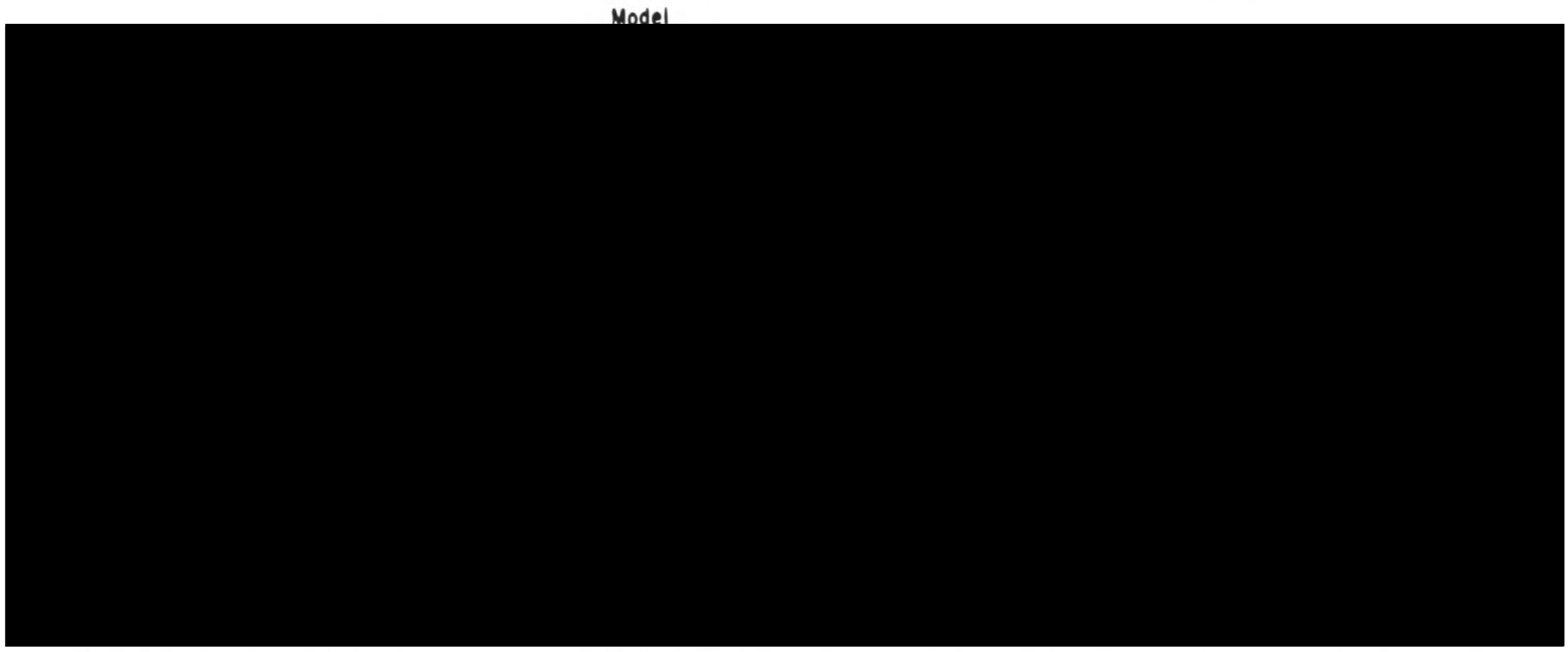

Figure 1.6: (a) Schematic representation of a Jovian two-cloud model with haze derived from observations of reflected sunlight (Cunningham *et al.*, 1988). (b) Schematic drawing of Jovian cloud structure derived from 5 μm images (Owen and Terrile, 1981).

In contrast, cloud models derived from 5 μm images favour three cloud layers with gaps in the upper layers revealing the layers below. Observations of the central area of the Jovian disk recorded from 2.8 to 14 μm by Gillett *et al.* (1969) revealed a particularly high brightness temperature at 5 μm, providing the first indication of an enhancement of radiation at this wavelength. Regions of enhanced 5 μm flux were later found to be correlated with dark brown and blue features (Keay *et al.*, 1973; Westphal, 1969; Westphal *et al.*, 1974). Lewis and Prinn (1970) suggested that regions of 225 K brightness temperature were stable NH_4HS or $(NH_4)_2S$ cloud layers, while regions of 310 K brightness temperature were located deep in the atmosphere and were visible through breaks in the upper clouds.

Additional support for this theory was supplied by 5 μm images of Jupiter obtained by Terrile and Westphal (1977). These were used to construct flux-frequency histograms, plots of the Jovian 5 μm flux versus the number of times a flux value was recorded. The trimodal distribution seen in these histograms indicated that there was a higher probability of seeing three distinct brightness temperatures, with the three peaks corresponding to a low flux level in the Equatorial Zone, an intermediate flux level in the belts, and a high flux level in the 5

μm hot spots of the belts. Comparision of the 5 μm images with colour photographs revealed a correlation between the 5 μm flux and visible colours. The lowest flux was seen over the light-coloured zones and the highest over the dark-coloured belts, thus suggesting that reflection from three different atmospheric levels is responsible for the observed colours.

Both ground-based 5 μm images of Jupiter and Voyager visible pictures (Terrile and Beebe, 1979; Terrile *et al.*, 1979) were used by Owen and Terrile (1981) to refine the 5 μm cloud model to that shown in Figure 1.6b. At the highest altitude, with their tops at 140 K and 0.6 bar, are the white solid-NH_3 cirrus clouds, with the top of the cold GRS at the same height. Below the NH_3 are tawny clouds at the $\sim$2 bar level, which have an intermediate brightness temperature of 220–230 K, and are thought to be NH_4SH. Gaps in these reveal the "brown barges" of a lower layer near 2.4 bar, and at the lowest level are the blue-gray regions, corresponding to the hottest temperatures and visible in the absence of the overlying cloud layers.

However, as shown by West *et al.* (1986), the shape of the Jovian 5 μm spectrum does not match the spectrum of blackbody emission from the cloud at 4.5 bar which is predicted by models derived from 5 μm images. Cloud models derived from 5 μm spectra, such as those of Drossart and Encrenaz (1982), Drossart *et al.* (1982), Kunde *et al.* (1982), and Bézard *et al.* (1983a), therefore differ from those based on 5 μm images, predicting the 5 μm cloud opacity to be distributed throughout a large altitude range or concentrated in the 2 bar region.

The influence of the upper NH_3 cloud on the 5 μm emission was investigated by Bézard *et al.* (1983a), using the NH_3 cloud model derived from IRIS spectra by Marten *et al.* (1981). This suggested that the opacity of the NH_3 ice layer is insufficient to account for the 40 K reduction in the 5 μm brightness temperature seen in the zones. Bézard *et al.* (1983a) concluded that a deep absorbing cloud layer between 1.2 and 4 bar was necessary to account for the large variations in 5 μm emission. A thick cloud layer at the 180–195 K level, which is more likely to be NH_4SH ice than H_2O, provided the best fit to the coldest 5 μm spectra, while a cloud of H_2O ice was possible below the 4 bar level.

In several recent papers, there has been an effort to reconcile the reflected sunlight and 5 μm data. The resulting cloud models obtained by West *et al.* (1985, 1986) are shown in Figure 1.7. West *et al.* (1985) combined high resolution images of the 6190 Å-band CH_4/continuum ratio and contour maps of 5 μm brightness temperature, to formulate a cloud model compatible with both data sets. They concluded that the CH_4/continuum ratio in the hot spots differed little from the ratio in the zones, implying that we are not seeing down to 4 bar in the hot spots at visible wavelengths, but that substantial cloud material exists above 4 bar in such regions, and that cloud stratigraphy based on 5 μm data alone has been interpreted incorrectly. Their cloud model (Figure 1.7a) includes thin scattering haze layers at 80 and 250 mbar, above an NH_3 cloud which has an upper surface is at 320 mbar in both the belts and the zones, a base at 700 mbar, and variable optical thickness. Beneath the NH_3 cloud lies a lower cloud which is sufficiently dense to allow absorption within or below it to be ignored, and which may be

composed of H_2O, H_2O–NH_3 solution, or NH_4SH. The pressure at the top of this lower cloud is a free parameter, and at 5 μm it is treated as a surface with an emissivity of 1.

Figure 1.7: (a) Schematic diagram of the conciliatory Jovian cloud model derived by West *et al.* (1985), along with the pressure-temperature profile of Kunde *et al.* (1982). (b) The essential features of the Jovian tropospheric cloud structure as determined by West *et al.* (1986).

Finally, West *et al.* (1986) have proposed a cloud model which incorporates all of the features that they consider to be essential (Figure 1.7b). At the top of the troposphere is a diffuse haze of NH_3 ice and chromophore particles of radii ≤ 1 μm whose upper surface varies from 0.2 bar at the GRS and equator, to 0.3 at $\pm 10°$ latitude, to 0.4 bar at $\pm 45°$ latitude. This cloud is seen at visible and near-infrared wavelengths, as required by limb darkening, polarimetry, and absorption band data, and it is semi-transparent to thermal radiation. Near the base of the NH_3 cloud, at 0.7 bar, is a layer of patchy clouds of particles between 3 and 100 μm in radius, more optically dense in zones than in belts, and absent from hot spots. Near the 2 bar level is an inhomogeneous, time-variable cloud probably composed of NH_4SH and chromophores, with the possibility of H_2O. The location and the particle size in this cloud are uncertain, but it accounts for 5 μm spectra, modulation of the 5 μm emission, and the observed equivalent widths of CH_4, H_2, and NH_3 lines seen in reflected sunlight. Another cloud of H_2O–NH_3 may exist near the 6 bar level. In addition to being consistent with the reflected sunlight and 5 μm data, this conciliatory model of the Jovian cloud structure is also supported by the model atmosphere calculations of de Pater (1986), which were based on observations at radio wavelengths.

1.5 Outstanding Problems

Our understanding of the average structure of the Jovian atmosphere was greatly increased by the Pioneer and Voyager missions (§2.1), and the mean temperature profile, the bulk chemical composition, the vertical cloud structure, and the nature of zonal winds near the cloud tops

are now known to a first approximation. However, there remain many gaps and incomplete explanations in our knowledge of Jupiter. A recent report by the International Jupiter Watch (Russell, 1988, p.12–16) has emphasised our inability to explain the temporal and spatial variability observed in the appearance of Jupiter, and the changes in cloud colour, albedo, and opacity which occur on scales from tens to thousands of km. In order to allow the development of detailed meteorological models, co-ordinated studies of Jovian meteorological parameters are needed, particularly of cloud albedo and colour, the thermal state of the atmosphere, cloud structure and particle size, and the abundance of NH_3.

As can be gathered from the discussion in this chapter, intriguing problems remain in most areas of Jovian atmospheric science. With regard to the bulk composition, the wide range of values for mixing ratios, and elemental and isotopic abundances needs to be resolved, and the temporal, vertical, and horizontal variability of these quantities determined. Are the C/H and N/H ratios truly enriched, and the O/H ratio depleted, and if so, can these ratios be fully accounted for by models of planetary evolution? Can valid mechanisms be found to explain the presence of non-equilibrium species? What photochemical processes or optical effects cause the colourations of Jupiter?

With regard to the thermal structure, the mean vertical temperature profile needs to be refined and horizontal temperature variations on surfaces of constant pressure investigated. Measurements of both should be extended to higher latitudes for comparison with their equatorial values. The latitudinal variations in solar heating and thermal emission need to be determined in order to determine the global and local energy budgets.

Despite the fact that many models of the vertical cloud structure have been derived from observational data, the true composition and vertical layering of Jovian clouds remains uncertain. Further observations are needed in order to provide sufficient constraints to determine the vertical cloud structure. The horizontal extent of the clouds, their particle size, and the nature of haze layers all need investigation. Furthermore, how is the cloud structure influenced by dynamical processes such as vertical transport and horizontal winds?

Many fundamental questions also exist with regard to large and small scale Jovian dynamics, even the driving mechanisms for the zonal winds and the large eddies remaining uncertain. How does the internal heat source affect dynamics, what are the predominant modes of horizontal and vertical heat transport, and are local dynamical features isolated or part of the general circulation?

These are just a few of the numerous questions about the Jovian atmosphere which require investigation. Most of these will be addressed by Galileo, an ambitious mission to Jupiter that has been designed specifically to resolve many of these issues. The following chapter deals with the Galileo mission and its goals, focussing on the Near-Infrared Mapping Spectrometer, the instrument of particular relevance to the present work.

Chapter 2

Galileo and the Near-Infrared Mapping Spectrometer

In this chapter, the Galileo mission to Jupiter is described and the Near-Infrared Mapping Spectrometer on the Galileo orbiter is introduced. In order to provide an historical context for Galileo, the discussion begins with a brief review of previous spacecraft missions to Jupiter. This is followed by a summary of the goals of the Galileo mission and the instruments that will be used to accomplish them. Finally, the goals and design of the Near-Infrared Mapping Spectrometer are presented, leading to a discussion of the spectroscopic requirements of this instrument and the rationale for the present study.

2.1 Previous Missions to Jupiter

2.1.1 The Pioneer Missions

Pioneers 10 and 11 were the first spacecraft to explore the solar system beyond the orbit of Mars. Their scientific goals were to investigate the interplanetary medium, to study the asteroid belt, and to provide the first *in situ* measurements of the Jovian environment. After the Jupiter encounter, Pioneer 11 also went on to an encounter with Saturn. Pioneer 10 was launched in March, 1972, making its closest encounter with Jupiter on 4 December, 1973, passing 132,520 km above the cloud tops. Pioneer 11 was launched a year later, passing 43,000 km above the Jovian cloud tops on 3 December, 1974.

Pioneer 10 was equipped with eleven scientific instruments, and a twelfth, a magnetometer, was added to the payload of Pioneer 11. These instruments observed micrometeorite fluxes, plasmas, charged particles, magnetic fields, and satellites, as well as the Jovian atmosphere. Three of the instruments, an infrared radiometer, an imaging photopolarimeter, and an ultraviolet photometer, were used for remote sensing of the Jovian atmosphere.

The infrared radiometers on both Pioneers operated in two spectral bands, centered on 20.0 and 45.4 μm, with equivalent widths of 11.6 and 22.7 μm, respectively. Spatial resolutions

from 1/30 to 1/200 of the Jovian diameter were obtained, and more than 75% of Jupiter was mapped by the radiometers (Ingersoll *et al.*, 1975). The design, calibration, and performance of these instruments are described in Bender *et al.* (1974). The goals of this experiment were to measure the net energy flux from the planet, the temperature distribution with latitude, dark-side temperatures, hot or cold spots in the atmosphere, and the H_2/He ratio (Bender *et al.*, 1974). The findings of the Pioneer infrared radiometers are summarised by Ingersoll *et al.* (1976), Orton (1975a), and Orton and Ingersoll (1976).

2.1.2 The Voyager Missions

The Voyager 1 and 2 missions to the outer planets rank as the most ambitious and successful of all planetary missions to date, encountering Jupiter, Saturn, Uranus, Neptune, and numerous satellites before heading out toward interstellar space. Voyager 1, launched in September, 1977, reached its closest approach to Jupiter (348,890 km) on 5 March, 1979, while Voyager 2, launched on a lower-velocity trajectory in August, 1977, arrived at closest approach (721,640 km) on 9 July, 1979. Intensive observations of the Jovian system were made throughout a 98-day fly-by period by Voyager 1, and throughout a 103-day period by Voyager 2 (Stone and Lane, 1979a, 1979b).

Each Voyager carried instruments for eleven scientific investigations, designed for studying the atmosphere, the satellites, and the magnetosphere. Five of these investigations had atmospheric science objectives. These were the infrared radiation, imaging science, photopolarimetry, ultraviolet spectroscopy, and radio science experiments. The two Voyager imaging cameras far exceeded the temporal and spatial resolution of ground-based and Pioneer images, Voyager 1 achieving several kilometres resolution at closest approach.

The infrared spectroscopy and radiometry (IRIS) instruments on Voyagers 1 and 2 have been an invaluable source of information about Jovian atmospheric composition, thermal structure, and dynamics. A description of their design and calibration is given by Hanel *et al.* (1980). The instruments on each spacecraft are identical, consisting of a Michelson interferometer for measuring infrared frequencies from 180 to 2500 cm^{-1} (4 to 55 μm) at a resolution of 4.3 cm^{-1}, and a radiometer for measuring visible and near-infrared frequencies from 5000 to 30000 cm^{-1} (0.33 to 2 μm). These share a 50 cm diameter Cassegrain telescope with a narrow 25° diameter field-of-view which gave a maximum spatial resolution of nearly 1/100 of the Jovian disk diameter at closest approach (Hanel *et al.*, 1979a). IRIS spectra of thermal emission in the 2000 cm^{-1} region (see Figure 2.1), which is free of absorptions by the dominant Jovian gases H_2, CH_4, and NH_3, provided a probe into the deep atmosphere below the upper cloud deck, while IRIS spectra in the 180 to 1500 cm^{-1} range, corresponding to thermal emission from above the 1-bar level, provided a probe of higher altitudes in the Jovian atmosphere. Much of the information derived from IRIS spectra has been mentioned in Chapter 1.

Figure 2.1: Voyager IRIS spectra of thermal emission (a) from 200 to 1400 cm^{-1}, showing strong H_2, NH_3, and CH_4 absorptions, with C_2H_2 and PH_3 absorptions also present, and (b) from 1700 to 2300 cm^{-1}, showing the 5 μm window (Hanel *et al.*, 1979b).

2.2 The Galileo Mission to Jupiter

2.2.1 Introduction

The next spacecraft to explore the Jovian system will be Galileo. The Galileo mission was conceived in the mid-1970's, and originally scheduled for a U.S. Space Shuttle launch during a favourable window in January, 1982. However, a series of problems with the Shuttle program led to delays in the launch, requiring revisions of the planned trajectory, a change in the choice of the upper stage, and redesign of the spacecraft. Eventually, on October 18, 1989, Galileo was successfully launched by the Shuttle and boosted out of Earth orbit by an Inertial Upper Stage (IUS). As a consequence of safety constraints arising from the Challenger Shuttle accident, the solid-fuelled IUS was used instead of the liquid-fuelled Centaur upper stage. Because the less powerful IUS was incapable of sending Galileo on a direct flight to Jupiter, Galileo was launched on a Venus-Earth-Earth gravity-assist trajectory. This is sending it via Venus in February, 1990, Earth in December, 1990, through the asteroid belt for an encounter with asteroid Gaspra in October, 1991, and back to Earth again in December, 1992, before finally arriving at Jupiter in December, 1995. This "VEEGA" route is shown in Figure 2.2.

Galileo is the logical successor to the exploratory Pioneer missions and the subsequent Voyager reconnaissance missions. Because Galileo includes both an orbiter and an entry probe, it will allow the Jovian system to be studied in far greater detail than was possible with either of these preceding fly-by encounters. The orbiter is intended to orbit Jupiter eleven times over a nominal 20-month lifetime, making long-term observations of global and time-dependent features. On each of its revolutions around Jupiter, the Galileo orbiter will follow a different elliptical trajectory, taking it past at least one of the four large Galilean satellites and using gravitational assists from these encounters to alter its orbital period, radius, inclination, or orientation as necessary (Yeates *et al.*, 1985, p.84–88). During these orbits, the orbiter will

Figure 2.2: The Venus-Earth-Earth gravity-assist trajectory to be followed by Galileo on its way to Jupiter (Mitchell, 1988).

maintain a nominal perijove value of 11.5 Jovian radii (R_J), sufficiently far outside the Jovian radiation belts to ensure that the radiation dose does not exceed its maximum allowable value (150 krad for the entire mission; Yeates *et al.*, 1985, p.93).

The Galileo probe, intended to provide the first *in situ* measurements of the Jovian atmosphere, will be released from the orbiter 150 days before entering the atmosphere. The first activation of the scientific instruments on the probe is to occur six hours before entry and about 607,000 km from the centre of Jupiter. The probe will officially "enter" the atmosphere at 450 km above the 1-bar level, at a relative speed of 47.4 km/sec. Atmospheric drag will slow the probe to about Mach 1 (331 m/s), 115 seconds after entry and at a height of about 49 km, at which point the protective aeroshell will be jettisoned and the descent parachute will be deployed. The probe will then begin recording atmospheric data and relaying it to Earth via the orbiter, providing a period of co-ordinated probe and orbiter observations. Measurements are expected to continue until 62 minutes after entry, when the probe nears the 21-bar level, 137 km below the 1-bar level, and is destroyed by the high temperatures (~400 K) and pressures that it encounters (Yeates *et al.*, 1985, p.82–84).

As outlined in the *Galileo Science Requirements Document* (Spehalski *et al.*, 1989, p.I-2-1), the general science objectives of the Galileo mission are as follows:

(1) to investigate the chemical composition and physical state of the Jovian atmosphere,

(2) to investigate the chemical composition and physical state of the Jovian satellites, and

(3) to investigate the structure and physical dynamics of the Jovian magnetosphere.

In each of these categories, a list of more specific objectives has also been drawn up, and those for the Jovian atmosphere (Spehalski *et al.*, 1989, p.I-2-1; Yeates *et al.*, 1985, p.5) are:

(1) to determine the chemical composition of the atmosphere,

(2) to determine the thermal structure of the atmosphere to a depth of at least 10 bar,

(3) to determine the nature of cloud particles and the location and structure of cloud layers,

(4) to determine the radiative energy balance in the atmosphere,

(5) to investigate the circulation and dynamics of the atmosphere, and

(6) to investigate the upper atmosphere and ionosphere.

A discussion of how the instruments on Galileo will meet these objectives is given in §2.2.3 and §2.2.4, below.

2.2.2 The Spacecraft and Scientific Instruments

The design of the Galileo orbiter and probe (detailed in Yeates *et al.*, 1985, p.101–117) is illustrated in Figure 2.3. The Galileo orbiter weighs 1138 kg, of which 103 kg is the payload of scientific instruments. It also carries propellant, which is used by a 400-Newton engine and twelve 10-Newton thrusters to provide attitude control, trajectory correction, orbit insertion, and probe delivery. The power requirement of the orbiter is is 570 Watts, which is supplied by two radio-isotope generators mounted on separate booms, 5 m in length. The parabolic high-gain antenna, 4.8 m in diameter, transmits and receives X-band and S-band signals, and provides a maximum data rate of 134,000 bits/sec.

The orbiter is the first spacecraft to incorporate a dual-spin design, allowing the remote sensing instruments (which require stable and accurate pointing) to remain fixed in inertial space, and the fields and particles experiments (which require a spinning motion) to be spun at 3.15 rpm. Nine scientific instruments are mounted on the Galileo orbiter, and these are listed in Table 2.1. Five of these instruments are designed to measure magnetic fields, charged particles, plasmas, electromagnetic waves, and micrometeoroids. These instruments are mounted along a 10.9 m boom to minimise interference from the main body of the orbiter. The four remaining instruments are for remote sounding and these are discussed in more detail in §2.2.3.

The Galileo probe consists of two parts: a protective deceleration module and a descent module. The probe weighs 335 kg, of which almost half is the heat shield and 28 kg is the scientific payload. As seen in Figure 2.3, the deceleration module, which will provide protection against heat shock and ablation, consists of a conical carbon phenolic aeroshell with a base diameter of 1.25 m and a phenolic nylon aft cover. When the probe reaches the 0.6-bar level during the descent phase, a pilot parachute will be deployed, the aft cover will be released, and the main parachute, 2.5 m in diameter, will open. The descent module is a semicircular compartment fabricated primarily of titanium, protected by Kapton blankets and vented to the atmosphere. It is powered by a Li-SiO_2 battery and four thermal batteries, and communicates with the orbiter in the L-band via a cylindrical antenna, 25 cm in diameter. Seven scientific instruments are mounted on a shelf inside the descent module; these are listed in Table 2.2 and described in §2.2.4.

Figure 2.3: The Galileo orbiter and probe (Yeates *et al.*, 1985, p.4)

2.2.3 The Atmospheric Objectives of the Orbiter

The four remote sensing instruments on the Galileo orbiter are a near-infrared mapping spectrometer (NIMS), a solid-state imaging camera (SSI), a photopolarimeter-radiometer (PPR), and an ultraviolet spectrometer (UVS). Along with the radio science propagation experiment (RS2), these will be used to perform a detailed study of the Jovian atmosphere. Figure 2.4 shows the size of the fields-of-view for each of these four instruments, and their relation to the size of some Jovian features. The following is a summary of the atmospheric measurements to be made by these instruments, excluding NIMS, which is described in greater detail in §2.3.

The SSI is a narrow-angle camera which uses an 800×800 element solid-state silicon CCD sensor, with an angular resolution of 10.16 μrad per pixel (Yeates *et al.*, 1985, p.121-124). A filter wheel can be stepped through seven positions covering the 0.4–1.1 μm spectral range, which overlaps the NIMS range and includes several CH_4 and NH_3 absorption bands. The atmospheric science objectives of the SSI are to study atmospheric energetics, structure, motions, and radiative properties (Spehalski *et al.*, 1989, p.I-2-7). The study of energetics will focus on

Table 2.1: The scientific instruments on the Galileo Orbiter (Yeates *et al.*, 1985, p.6).

ACRONYM	INSTRUMENT	PRIMARY OBJECTIVES
SSI	Solid-State Imaging	Map Galilean satellites at ~1 km resolution and monitor long-term atmospheric circulation
NIMS	Near-Infrared Mapping Spectrometer	Study satellite surface composition, Jovian atmospheric composition and temperature
UVS	Ultraviolet Spectrometer	Measure gases and aerosols in the Jovian atmosphere and search for complex molecules
PPR	Photopolarimeter -Radiometer	Determine distribution and character of atmospheric particles and compare flux of thermal radiation to incoming solar levels
MAG	Magnetometer	Monitor strength and changes in magnetic field
EPD	Energetic Particle Detector	Measure high-energy electrons, protons, and heavy ions in the Jovian magnetosphere
PLS	Plasma Detector	Assess composition, energy, and 3-dimensional distribution of low-energy electrons and ions
PWS	Plasma Wave Spectrometer	Detect electromagnetic waves and analyse wave-particle interactions
DDS	Dust Detector	Measure mass, velocity, and charge of sub-micron-sized particles
RS(1)	Radio Science: Celestial Mechanics	Determine mass and orbit of Jupiter and its satellites
RS(2)	Radio Science: Propagation	Measure atmospheric structure, the radii of atmospheric objects, solar corona and solar wind

Table 2.2: The scientific instruments on the Galileo Probe (Yeates *et al.*, 1985, p.6).

ACRONYM	INSTRUMENT	PRIMARY OBJECTIVES
ASI	Atmospheric Structure Instrument	Determine temperature, pressure, density, and molecular weight as a function of altitude
NMS	Neutral Mass Spectrometer	Determine chemical composition of the atmosphere
HAD	Helium Abundance Detector	Determine the relative abundance of helium
NEP	Nephelometer	Detect clouds and infer states of particles (liquid versus solid)
NFR	Net-Flux Radiometer	Determine ambient thermal and solar energy as a function of altitude
LRD	Lightning and Radio Emission Detector	Verify the existence of lightning
EPI	Energetic Particles Investigation	Measure energetic particle populations in the inner magnetosphere and upper atmosphere

(a) separation of atmospheric mass motions from wave motions at global scales, (b) identification of wave propagation modes and the levels at which they exist, and (c) characterisation of atmospheric flow, cloud, and wave fields. The study of atmospheric structure will (a) examine the vertical structure of atmospheric features by centre-to-limb, multispectral imaging, and (b) characterise the relationship between vertical cloud structure, colour, and morphology. Mea-

surements of the mean vertical wind profile through relative cloud motions, particularly at belt-zone boundaries and in the region of the probe's descent, will reveal atmospheric motions. Finally, the local energy balance will be determined from measurements of the scattering properties of individual features at several wavelengths and many phase angles.

Figure 2.4: The instrumental fields-of-view for the four remote sounding experiments on the Galileo orbiter at a distance of 10 Jovian radii from the planet, with the size of the Jovian features depicted as if directly below the spacecraft (Yeates *et al.*, 1985, p.27).

The PPR is designed to operate in photometry, polarimetry, and radiometer modes, with a fixed circular field-of-view of 2.5 mrad. In the first two modes, it will measure intensity and polarisation of reflected sunlight at ten channels in the visible (between 4100 and 9450 Å) which include strong CH_4 and NH_3 absorption bands. As a radiometer, it will measure thermal infrared radiation over seven intervals extending out to the far-infrared. With the PPR, it should be possible to determine the vertical and horizontal distribution of cloud and haze particles in the Jovian atmosphere, as well as their size, shape, and refractive index. The PPR will also be used to study the energy budget of Jupiter, including the latitudinal variation of reflected solar radiation and emitted thermal radiation, and including the vertical thermal structure from 100 to 500 mbar. Photometric and polarimetric measurements of the CH_4 bands will also be made, which, when combined with the mixing ratio of CH_4 determined by the mass spectrometer on the probe will reveal the pressure levels and vertical structure of cloud layers (Hunten *et al.*, 1986; Spehalski *et al.*, 1989, p.I-2-8).

The UVS will measure ultraviolet radiation over 1150 to 4300 Å in three channels. The first covers 1150–1800 Å at 7 Å resolution, the second covers 1600–3000 Å at 13 Å resolution, and the third covers 2800–4300 Å at 13 Å resolution. The field-of-view is 0.1°×0.4° for the 1600–3000 Å channel, and 0.1°×1.4° for the other two channels. The objectives of the UVS are concerned primarily with atmospheric composition (Spehalski *et al.*, 1989, p.I-2-12 – I-2-

15). These include measurement of the composition and scattering properties at and above the cloud tops, determination of the mixing ratio, spatial distribution, and temporal variability of UV-active molecules in the 1 to 1000 mbar range, and mapping of the distribution of UV-absorbing aerosols. The UVS will also be used to to determine whether there are regions where photodissociation by ultraviolet sunlight or energetic particle precipitation are forming more complex molecules, to determine the abundance of H and H_2 in the upper atmosphere above the turbopause, and to measure the He/H_2 ratio at the level of charged particle penetration.

In the radio science propagation experiment, occultations by the Jovian atmosphere, of the S-band and X-band signals from the orbiter's high-gain antenna will provide an opportunity for atmospheric investigations (Spehalski *et al.*, 1989, p.I-2-32; Yeates *et al.*, 1985, p.140). Measurements of the apparent Doppler shift of the orbiter signal due to atmospheric refraction will be used to study pressure, temperature, and mean molecular mass as a function of altitude. Measurements of the atmospheric absorptivity of radio waves will allow the determination of the location of NH_3 cloud layers, and measurements of the Doppler shift of the probe signal will be used to study turbulence and horizontal wind velocities.

2.2.4 The Atmospheric Objectives of the Probe

Each of the seven instruments on the Galileo probe is designed to perform *in situ* measurements of various properties of the Jovian atmosphere. These are summarised briefly, as follows (from Hunten *et al.*, 1986; and Yeates *et al.*, 1985, p.141–158). Two of the instruments, the Neutral Mass Spectrometer (NMS) and the Helium Abundance Detector (HAD) will be used to investigate composition. The NMS will collect samples of ambient gas and use a mass analyser to determine the bulk composition of the Jovian atmosphere, accurately measuring the abundances and isotope ratios of the major constituents as a function of altitude from 0.1 to 10 bar or greater. In particular, it should be capable of measuring the mixing ratio of CH_4 to an accuracy of 5% (Hansen *et al.*, 1980, p.5). The HAD is designed to determine the value of the helium mixing ratio, currently known to only 3% from Voyager, to an accuracy of 0.1% over 2.5 to 10 bar. Atmospheric samples will be collected and an interferometer will be used to measure the refractive index of the sample relative to that of a reference He/H_2 mixture of known refractive index, thereby allowing the He/H_2 mixing ratio of the atmospheric samples to be determined.

Three more of the probe instruments will be used to investigate atmospheric structure. The Atmospheric Structure Experiment carries temperature and pressure sensors and a three-axis accelerometer, which will be used to define vertical temperature, pressure, and density profiles, to determine the nature of the cloud layering, to define the temperature levels which are responsible for infrared emission, and to measure lapse rates in order to locate regions of convective overturning. The Nephelometer is dedicated to studying the structure and particles of clouds, by measuring the scattering of a beam of light by atmospheric particles. Over the

0.1 to 10 bar range, it will record the vertical cloud profile at intervals of less than 1 km, detecting clouds containing ~1 μm diameter particles at a density of at least 3 particles/cm^3, determining the characteristic dimension and number densities of particles between 0.5 and 20.0 μm in diameter, and discovering whether the particles are liquid or solid. The Net Flux Radiometer will record atmospheric radiation in six infrared bands at altitudes between 0.1 and 10 bar, yielding the net flux and thereby revealing the depth of penetration of solar radiation, the opacity of cloud layers in the visible and thermal regions of the spectrum, and the opacity and abundance of H_2O, CH_4, and NH_3.

The Lightning and Radio Emission Detector is designed to observe lightning in the Jovian atmosphere. It includes two optically sensitive photodiode sensors and a radio frequency sensor. Steady signals received by the optical sensor will be used to measure the brightness and opacity of clouds, and rapidly varying signals will be combined with the radio observations to provide evidence for the existence of lightning. Finally, the Energetic Particles Investigation is concerned primarily with the measurement of electrons, protons, alpha particles, and heavy ions in the inner magnetosphere and the upper regions of the atmosphere.

2.3 The Near-Infrared Mapping Spectrometer

2.3.1 The Scientific Capabilities and Objectives of the NIMS Instrument

One of the four remote sensing instruments on the Galileo orbiter is the Near-Infrared Mapping Spectrometer (NIMS), the first planetary instrument which is capable of performing both imaging and spectroscopy. As is clear from the many references made to infrared measurements in Chapter 1, this region of the spectrum has been particularly valuable in the retrieval of information about the Jovian atmosphere. NIMS, with its dual capabilities, wide spectral range, high spatial resolution, and opportunities for numerous viewing geometries, will offer significant advantages over its predecessors, the Pioneer infrared radiometers and the Voyager IRIS instruments.

NIMS is intended to investigate both the geology of the Jovian satellites and the structure of the Jovian atmosphere. It is the atmospheric measurements to be made by NIMS that are of interest to the present study, and these are (Hunten *et al.*, 1986):

(1) the global distribution and temporal variability of minor atmospheric constituents,

(2) the vertical temperature profile from 1 bar down to the first opaque cloud layer,

(3) cloud coverage and layering,

(4) scattering characteristics and physical properties of the clouds, and

(5) imaging at selected infrared wavelengths.

The ability of NIMS to perform these measurements will be enhanced by a combination of several factors. The spectral range of NIMS extends from 0.7 to 5.2 μm, thus including the critcally important 5 μm window, as well as visible and near-infrared wavelengths not previ-

ously sampled by spacecraft instruments. This spectral region includes both a wide range of wavelengths which can be used to constrain composition and particle size, and a wide range of CH_4, NH_3, and H_2 absorption coefficients which can be used to constrain the vertical distribution of aerosols. Much new information should therefore be retrieved. However, this retrieval will rely heavily on the availability of spectral parameters at these wavelengths, a requirement that is addressed in §2.3.5.

As discussed in §2.3.4, NIMS will attain a maximum spatial resolution of 375 km. This is equivalent to 0.2° of latitude or longitude, significantly smaller than the extent of the major features in the Jovian atmosphere. For comparison, the belts and zones are about 5° wide in latitude, the Great Red Spot is 90° in longitude by 30° in latitude, and the South Temperature Ovals are 9° in longitude by 6° in latitude (Taylor and Calcutt, 1984). NIMS will thus be able to map inside and around these and other cloud features, as well as inside the 5 μm hot spots, reducing the extent of spatial averaging of spectral information. This is a major advantage in the study of a planet with such an inhomogeneous appearance as Jupiter, allowing the spatial dependence of atmospheric parameters to be determined.

Being located on the Galileo orbiter, NIMS will have the opportunity to observe Jupiter from numerous vantage points during the 20-month mission period. This will allow global mapping at different NIMS wavelengths. It will also provide a greater range of viewing angles than has ever been available, particularly valuable in the study of cloud scattering phenomena. NIMS will even be able to use occultations of the Sun, Earth, Galilean satellites, and stars to probe the composition at high altitudes and its variation with latitude and longitude (Hunten *et al.*, 1986). The length of the orbiter mission will obviously be an advantage, providing night-side observations of thermal emission without the interference of solar radiation, and allowing the temporal variability of atmospheric parameters to be investigated. Co-ordinated measurements by NIMS and the probe during the probe descent, and by NIMS and the other orbiter instruments during the extended mission should further enhance the data retrieval.

The feasibility of the NIMS objectives and their implications for the sequencing of NIMS observations has been investigated by Calcutt (1984, Appendix C). He shows that two types of sequencing, cylindrical maps of the entire planet (recorded from beyond $17R_J$ from the planet's centre) and consecutive mosaics of smaller-scale features (recorded from within $17R_J$), will provide for most of the scientific objectives. The cylindrical maps can be used for cloud tracking, determination of global abundances, maximising the coverage of scattering angles, and searching for regions of thermal emission on the dark-side of Jupiter. The small-scale mosaics can be used to perform higher-resolution spectroscopy, to record mosaics of night-side features at high spatial resolution, and to study scattering properties as features move across the limb.

This list of measurements planned for NIMS can be elaborated to provide a more detailed picture of how it will be used to investigate many of the outstanding questions about the Jovian atmosphere. NIMS should contribute significantly to our knowledge of the composition and its

spatial and temporal variability. It will be used to measure the condensible species NH_3 and H_2O, particularly the former above the NH_3 cloud region at 500–700 mbar, and the latter at the top of the H_2O cloud in equatorial hot spots. NH_3 has several bands in the NIMS spectral range, while H_2O can be detected at 2.7 μm and in the 5 μm window. The minor constituents PH_3, CH_3D, and GeH_4 should also be measurable in the 5 μm window. H_2S, whose presence is suspected but not yet confirmed, may be identified in the hot spots using the $\nu_2 + \nu_3$ band at 2.7 μm. Measurements of global abundances may resolve questions about the origin of Jupiter, measurements of vertical profiles may clarify the mechanisms of convective overturn, and measurements of the horizontal distributions may provide tracers of atmospheric motions.

NIMS should be able to probe the vertical temperature profile from 1 bar down to the first opaque cloud layer, extending to depths of 5 bar by observing the 5 μm hot spots. In contrast, the Voyager IRIS instrument was able to probe only from 1 to 600 mbar. Although the temperature gradient is adiabatic below about 1 bar, measurement of the horizontal variation of the temperature at this level (which is used to fix the profile below) will reveal localised heat sources (Taylor and Calcutt, 1984).

A variety of cloud properties will be measured by NIMS. Cloud height and thickness in the 1 to 5 bar region should be obtainable by zenith scanning. Observations of the strongly absorbing CH_4 bands and measurements of emitting temperatures in the 5 μm window are likely to be particularly useful in determining the cloud structure, with the latter useful in probing below the upper NH_3 clouds. Spectra of radiation reflected by cloud layers may be able to reveal their composition. Scattering properties of clouds can be measured as a function of solar phase angle and wavelength, and hence the mean particle size and number density may be retrievable. Finally, the images obtained at many wavelengths, over large regions of the planet, and over long time-scales, will be valuable in tracking the spatial and temporal evolution of the Jovian cloud structure.

2.3.2 The Technical Requirements of the NIMS Instrument

The scientific objectives of the NIMS instrument defined its technical requirements, with these requirements in turn determining its engineering design. The scientific objectives required careful selection of the NIMS spectral range and resolution, angular coverage and resolution, sensitivity and dynamic range, scan timing, and data rates (*NIMS System Description*, 1978, p.2-1–2-2). The spectral range of NIMS was chosen to be 0.7–5.2 μm (1923–14286 cm^{-1}), a range that includes many absorption bands of expected satellite surface materials and atmospheric gases. The spectral resolution is 0.025 μm (equivalent to a resolving power of 28 to 200), adequate to distinguish solid-state features, provide accurate band centres, and resolve gaseous molecular bands without resolving rotational lines. The angular resolution was determined by the need to be able to record full-disk images of satellites at 5 to 30 km resolution, while also being compatible with the scan-platform rates and the SSI experiment. An angular resolution

of 0.5 mrad × 0.5 mrad was selected, with 20 such pixels providing linear angular coverage of 10 mrad.

NIMS was also required to be able to detect spatial variability and changes in composition on the surfaces of satellites. Its dynamic range was therefore defined in terms of the expected range of surface reflectance, and its sensitivity in terms of a lower limit on the detectable reflectance. A dynamic range of 1024:1 was chosen, corresponding to a data encoding of 10 bits per pixel. Calcutt (1984, p.2-4) has demonstrated that a dynamic range of 10,000:1 (17 bits/pixel) would be required to cover the difference in radiance resulting from brightness temperatures varying from 150 to 360 K, (which is expected in the 5 μm window). In order to reduce this required data rate, the three NIMS channels with the longest wavelength are automatically switched to a lower gain if the radiance is greater than a specified value, and all other channels have four selectable gain settings. A signal-to-noise ratio for 1% reflectance of at least 30:1 in the 1 to 3 μm range was also desired and has been achieved, a typical value of 100:1 applying to the 3 μm channel for a surface with an albedo of 0.075 (Hunten *et al.*, 1986).

The scan time for NIMS was chosen to be 4.33 seconds, corresponding to the combination of an angular resolution of 0.5 mrad with the nominal scan-platform motion of 0.12 mrad/sec, and synchronous with the SSI scan time of 60.66 seconds. Finally, the NIMS data rate is 11,520 bits/sec, determined by all of the aforementioned factors, as well as dark-level information, housekeeping, and engineering telemetry.

2.3.3 The Design of the NIMS Instrument

The above technical requirements provided the constraints for the engineering design of the NIMS instrument. The principal components of the instrument are the telescope, optical chopper, grating spectrometer, multidetector focal-plane assembly, passive radiative cooler, and torque-drive motors for the internal scan mirror and the grating, as well as the electronics, controllers, and a microprocessor (see Calcutt, 1984, p.2-4; Taylor and Calcutt, 1984; Yeates *et al.*, 1985, p.124-128; *NIMS System Description*, 1978).

The optical configuration of NIMS is illustrated in Figure 2.5. The telescope is an f/3.5 Ritchey-Chretien reflecting telescope with an entrance diameter of 22.8 cm and a focal length of 80 cm. The secondary mirror is used to scan the input field-of-view (0.5 mrad × 0.5 mrad) through 20 discrete steps with a stepping period of 1/60 seconds. The optical chopper then chops the telescope signal synchronously with the mirror steps, maximising the available signal-integration time and allowing the dark current to be measured.

The f/3.5 collimator, with a focal length of 40 cm, directs the chopped signal onto the spectrometer grating. This is a flat grating, ruled with 40 lines/mm, which can be moved through 12 discrete positions in 4.33 seconds. The light from each of these grating positions passes through the f/1.75 camera optics and reaches the 17 detector elements located on the focal-plane assembly. With each detector sensitive to a different region of the spectrum, 204

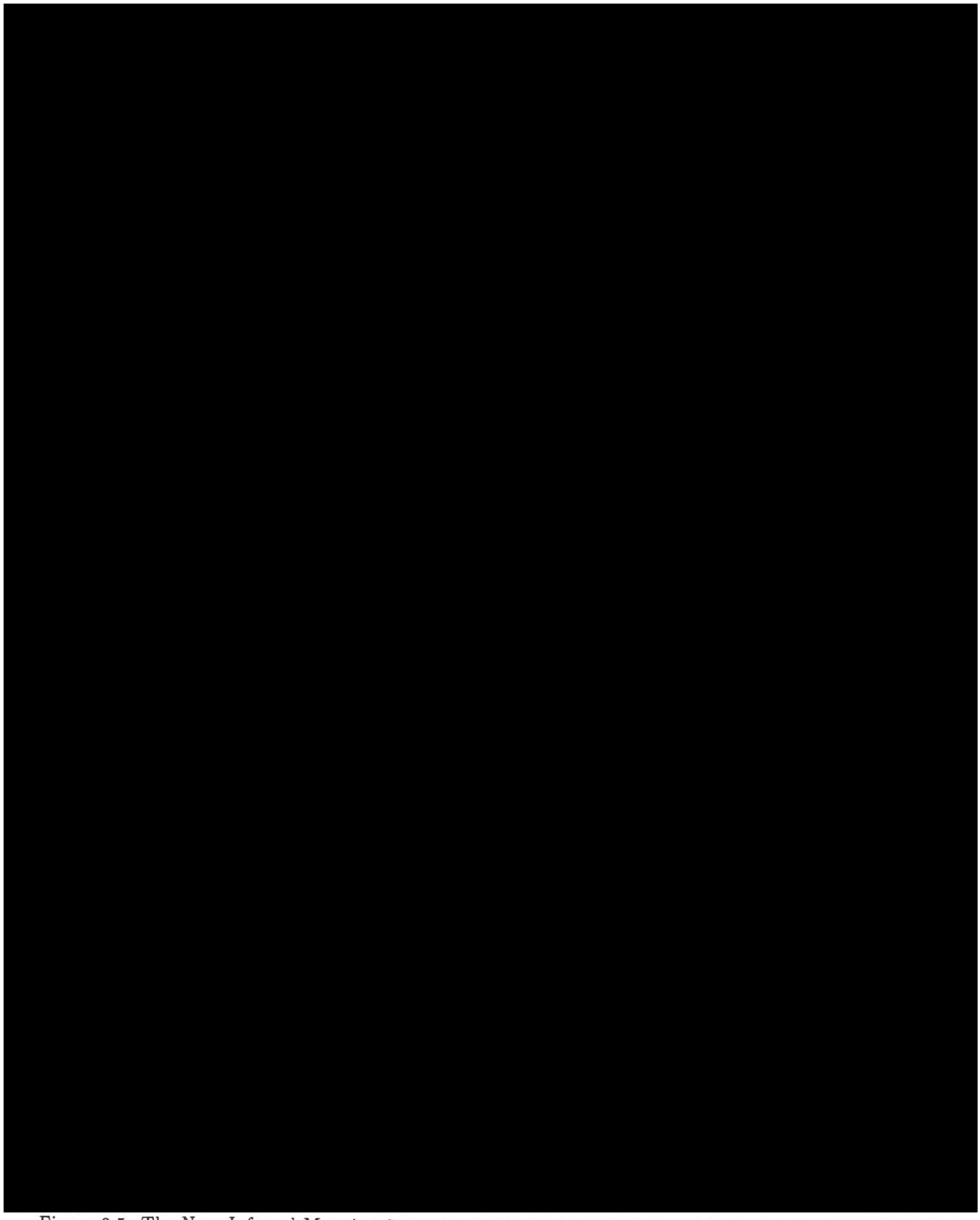

Figure 2.5: The Near-Infrared Mapping Spectrometer and its optical layout (Yeates *et al.*, 1985, p.126).

(12 × 17) discrete wavelengths over the 0.7 to 5.2 μm range are thus sampled. Two of the detectors are silicon photodiodes operating in the second order of the grating, and 15 are indium antimonide photovoltaic elements operating in the first order of the grating. A passive radiative cooler radiates energy to space, maintaining the detectors at 80 K (70 K below the temperature of the NIMS optics) in order to achieve the desired signal-to-noise ratio.

The calibration of NIMS can be monitored during flight using three viewing configurations (Calcutt, 1984, p.4-10; Spehalski *et al.*, 1989, p.I-4-39). The zero level is simply obtained

by viewing to space. Shorter wavelengths are calibrated with a diffuse solar reflecting target mounted on the science boom, which fills the NIMS field-of-view. Longer wavelengths are calibrated with a blackbody at 300 ± 15 K, which is mounted on the scan-platform sunshade and which also fills the NIMS aperture. Because the wavelength ranges of the two calibration targets overlap, any variations between them can be monitored throughout the mission.

The entire NIMS instrument weighs 18.0 kg, and requires 8 Watts average power, 12 Watts peak power. The external dimensions are 82.6 cm × 36.8 cm × 39.1 cm for the optics and 20.3 cm × 25.4 cm × 12.7 cm for the electronics (Hunten *et al.*, 1986).

2.3.4 The Operational Mode of the NIMS Instrument

NIMS images are generated through the combined motions of the grating, the wobbling secondary, and the Galileo scan platform. At each of the 12 grating positions (0.33 seconds/step), the secondary mirror is scanned through its 20 steps (1/60 seconds/step = 0.33 seconds/cycle). Thus, in the 4.33 seconds of the grating cycle, all 204 wavelengths are recorded over a strip of 0.5 mrad × 10 mrad. The Galileo scan platform is also moving, producing an 8 mrad × 8 mrad SSI image frame in 60.66 seconds. During this period, NIMS will have repeated the 4.33 second cycle 14 times to complete a NIMS image frame covering 7 mrad × 10 mrad. Such a frame can be analysed in two ways, either as a spectrum of 204 wavelengths located at one particular 0.5 mrad × 0.5 mrad pixel, or as an image at one particular wavelength located over the entire 7 mrad × 10 mrad spatial area. NIMS can actually be operated in four different modes: with the grating fixed (for mapping), with the secondary mirror fixed (for spectroscopy), with both fixed, and with neither fixed. It is also possible to use 6, 12, or 24 steps of the grating in order to cover the wavelength range, referred to as short, full, and long modes, respectively (Spehalski *et al.*, 1989, p.I-5-52).

The spatial resolution of 0.5 mrad for a NIMS pixel is equivalent to a spatial resolution of 500 km for every 10^6 km from the object, and at a typical perijove distance of $11.5 R_J$ from the centre of Jupiter, this corresponds to 375 km.

2.3.5 The Spectroscopic Requirements of NIMS

In order to retrieve the maximum available information about the Jovian atmosphere from NIMS measurements, and indeed, from any other infrared observations of Jupiter, accurate knowledge of the infrared spectral parameters of Jovian gases is essential. Unfortunately, there are many gaps in this knowledge, as seen for example, in the lengthy list of experimental and theoretical spectroscopic studies recommended in Hornstein *et al.* (1982) at the conclusion of a workshop on vibrational-rotational spectroscopy for planetary atmospheres. In recent years, there have been frequent calls for laboratory measurements of the fundamental spectral parameters required in the application of radiative transfer methods to planetary atmospheres, for example, in many of the papers published in Mumma *et al.* (1982), by Taylor and Calcutt (1984), and in a report

of the International Jupiter Watch, an organisation established to co-ordinate studies of the variability of the Jovian system (Russell, 1988).

For the purposes of NIMS, it is the spectral parameters of those gases with absorption bands in the region from 0.7 to 5.2 μm which are essential. These gases include the dominant absorbers CH_4, NH_3, and H_2, as well as the important minor constituents PH_3, H_2O, CH_3D, GeH_4, and various hydrocarbons. The appearance of these absorptions in the near-infrared spectrum of Jupiter and the quality of the available spectral parameters are the subject of the next chapter, where the importance of CH_4 absorptions in the NIMS spectral region will be discussed and the lack of individual CH_4 line parameters over a large fraction of this region will be demonstrated. As stated in the International Jupiter Watch report (Russell, 1988, p.69–70):

> "The major diagnostics [in remote sensing of the Jovian atmosphere] have been the absorption bands of methane, the dominant absorber in the visible through near-infrared spectrum of Jupiter, ... Across the entire infrared through visible regions, similar gaps in our knowledge of methane line parameters (frequency, strength, pressure broadening and pressure shift coefficients under Jovian conditions) are significant barriers to analysis and interpretation of Jovian spectra and need to be addressed both theoretically and in the laboratory."

Although the preferred form of spectral data is generally a compilation of individual line positions, strengths, shapes, and half-widths, the complexity of the visible and near-infrared spectrum of CH_4 makes such a compilation an enormous task. CH_4 line data need much work, both in the measurement of lines from 1 to 3 μm and the refinement of lines in the 3 to 5 μm region. However, an alternative method of deriving spectral parameters is to record low-resolution laboratory spectra under Jovian conditions and to then fit the transmittance as a function of temperature, pressure, and abundance using band models. As concluded by Hornstein *et al.* (1982, p.755):

> "Spectra obtained with high enough spectral resolution to resolve all features are still not available for some spectral regions for species of interest (notably, methane), and will not become available in the immediate future. Random band models are still necessary in these cases if planetary astronomy is not to simply forego using these spectral regions until the appropriate spectra become available."

In Chapter 4, it will be shown that band modelling of laboratory CH_4 spectra is appropriate for the purpose of retrieving information about the Jovian atmosphere from NIMS spectra.

The importance of CH_4 absorption in the NIMS spectral region, the lack of the relevant CH_4 line data, and the applicability of band modelling to this problem, thus provide the rationale for this thesis, which is concerned with the measurement and analysis of low-resolution near-infrared CH_4 spectra under conditions approximating those in the Jovian atmosphere.

Chapter 3

Methane and the Near-Infrared Spectrum of Jupiter

Most of our knowledge about the composition and structure of planetary atmospheres has been obtained through the interpretation of their spectra. Infrared spectra have been particularly useful because most molecules of interest have rotational-vibrational absorption bands in the infrared. This chapter deals with the significance of CH_4 in the near-infrared spectrum of Jupiter. It begins with a description of this spectrum, which reveals the importance of CH_4 absorptions in the 1 to 4.5 μm region. This is followed by the introduction of some relevant concepts of infrared spectroscopy and radiative transfer, with particular reference to CH_4. Finally, line-by-line methods are used to calculate the transmittance of CH_4 under Jovian conditions, further demonstrating the importance of CH_4 absorption and revealing the inadequacy of CH_4 line data in the NIMS spectral region.

3.1 The Nature of the Jovian Near-Infrared Spectrum

The infrared spectrum of Jupiter, ranging from 1 to 40 μm, can be conveniently divided into three regions, each characterised by a different source of radiation and by different absorption features. These three regions of the spectrum are the subject of this section. A composite Jovian spectrum, providing an overview of the entire 1 to 40 μm range is presented in Figure 3.1.

3.1.1 Reflected Solar Radiation: 1 to 4.5 Microns

In the near-infrared region between 1 and 4.5 μm, the radiation observed at the top of the Jovian atmosphere is solar radiation reflected from the visible cloud layers. Strong absorption bands of CH_4 and NH_3 dominate this region, as seen in Figure 3.1, where the "ALBEDO=1.0" curve is the intensity for a diffusely reflecting planet having no absorptions. The long Jovian pathlengths traversed by the solar radiation cause the CH_4 and NH_3 band centres to be blacked out, leaving a series of narrow transmittance windows. Indeed, as is seen in Figure 3.2 and has

been pointed out by Larson (1982, p.410), the near-infrared spectra of all of the outer planets closely resemble the spectrum of a long-pathlength laboratory CH_4 spectrum. Clearly, CH_4 is the major infrared-active species in these planetary atmospheres.

Figure 3.1: (a) The infrared spectrum of Jupiter, compiled from numerous sources. Two curves are given at 2000 cm^{-1}, the lower for the disk-averaged brightness temperature, and the upper for a possible hot-spot brightness temperature. The expected intensities for a blackbody Jupiter at 125 and 350 K, and the expected intensity for a diffusely reflecting planet with no absorption (the ALBEDO=1.0 curve) are also included. (b) The transmittance of the terrestrial atmosphere under typical good conditions from Kitt Peak (Ridgway *et al.*, 1976a, p.387).

In addition to the many CH_4 bands in the 1 to 4.5 μm region of the Jovian spectrum (see Table 3.3), there are NH_3 bands at 1.6 μm ($2\nu_1$, $2\nu_3$, and $\nu_1+\nu_3$), at 2.0–2.3 μm ($\nu_1+\nu_3$, $\nu_2+\nu_3$, and $\nu_3+\nu_4$), and at 3 μm (ν_1, ν_3, and $2\nu_4$), and pressure-induced H_2 bands at 2.4 and 1.16 μm (the fundamental (1–0) band and the first overtone (2–0), respectively) (Fink and Larson, 1979; Taylor and Calcutt, 1984). Because the centres of the strong bands are saturated, it is the weak wings of these bands and the centres of weak bands that must be used when interpreting such spectra in terms of atmospheric parameters (Taylor and Calcutt, 1984). However, as stated by Larson (1982, p.409–415), the retrieval of information from such absorptions remains limited by the availability of laboratory measurements under the conditions of low temperature, large abundance, and scattering found in the Jovian atmosphere. Lack of knowledge of the CH_4 and NH_3 spectra throughout the 1 to 4.5 μm region has also hindered the detection of absorptions by minor constituents and the identification of new species.

Figure 3.2: A comparison of the near-infrared spectra of the outer planets. The stellar spectrum shows the instrument response and the terrestrial absorptions, while the laboratory spectrum shows how CH_4 absorption dominates the spectra of all of the outer planets (Fink and Larson, 1979).

Below 2 μm, the terrestrial transmittance windows coincide with the Jovian windows, and so this region of the Jovian spectrum has been the subject of many ground-based observations. The $3\nu_3$ band of CH_4 at 1.105 μm has received particular attention, being a band which is sufficiently weak that its absorptions are not heavily saturated and one for which quantum assignments existed as early as 1936 (Childs, 1936). A summary of the earlier ground-based observations of the Jovian $3\nu_3$ band is given by Ridgway *et al.* (1976a), and in §1.3.3 the use of this band in the determination of the CH_4 abundance was discussed. Despite the intensive study of the $3\nu_3$ band in Jovian spectra, it remains poorly characterised in the laboratory (Fink and Larson, 1979). Consequently, additional laboratory studies are essential before this band can be used for reliable investigation of more difficult problems such as the determination of cloud structure and scattering mechanisms.

Near and above 2 μm, the two Jovian transmittance windows are obscured by terrestrial water vapour bands at 1.9 and 2.7 μm. As a result, this region has received much less attention in ground-based studies. The wings of the pressure-induced H_2 absorption band from 2.0 to 2.5 μm are a potential source of information about H_2 abundance and temperature structure, but the lack of knowledge about the adjacent interfering CH_4 bands has proven to be a limitation (Larson, 1982, p.415).

Unlike the Pioneer infrared instruments, whose spectral range did not include the 1–4.5 μm region, and the Voyager IRIS instruments, which only overlapped slightly, covering 4 to 55 μm, NIMS will provide complete coverage from 1 to 4.5 μm. NIMS spectra of the Jovian 1.9 and 2.7 μm windows should be an important new source of information about the Jovian atmosphere. Absorption bands of HCN ($\nu_1 + \nu_3$, $\nu_2 + \nu_3$), H_2S ($\nu_1 + \nu_3$, $\nu_2 + \nu_3$), H_2O ($\nu_2 + \nu_3$,

ν_3, ν_1), and C_2H_2 ($\nu_3 + \nu_4$, $\nu_2 + 2\nu_4 + \nu_5$) (Herzberg, 1945, p.279,283,281,290) are found in these regions and may be detectable by NIMS. It should also be possible to use the NH_3 bands adjacent to these windows to derive vertical NH_3 profiles. Taking advantage of the high spatial resolution of NIMS, the strong CH_4 and NH_3 bands can be used to investigate abundances, temperature profiles, and aerosol and cloud structure at different locations on the planet. In all cases, the dominance of CH_4 and NH_3 absorptions throughout this region makes the laboratory characterisation of the CH_4 and NH_3 bands essential.

3.1.2 Thermal Emission: The 5-Micron Window

The second distinct region of the Jovian infrared spectrum is the 5 μm "window", where the observed flux at the top of the Jovian atmosphere is due to thermal emission. This region is particularly interesting for two reasons:

(1) in areas which are relatively free of cloud cover, the thermal flux originates from deeper levels in the atmosphere, allowing these deeper, hotter regions to be investigated, and

(2) both CH_4 and NH_3 absorption bands are absent, allowing spectral features of other minor constituents to be detected.

The 5 μm window extends from approximately 1800 to 2200 cm^{-1} (4.6 to 5.6 μm; see Figure 2.1). The 1800 cm^{-1} edge is defined primarily by the far wings of the ν_4 band of NH_3, with some contribution from the far wings of the ν_2 and ν_4 bands of CH_4 and the pure rotational lines of H_2. The 2200 cm^{-1} edge is defined primarily by the far wings of the ν_1 and ν_3 bands of PH_3, with some contribution from the far wings of the ν_3 and $2\nu_4$ bands of CH_4 and the fundamental band of H_2 (Kunde, 1982, p.399).

The intensity of the flux at 5 μm, and the depth from which it originates, both depend strongly upon the presence and absence of clouds. The disk-averaged brightness temperature at 5 μm is about 230 K, suggesting that it originates from a level near 2 bar (the level of the NH_4SH clouds). However, observations with a higher spatial resolution reveal local variations in the the 5 μm brightness temperatures. The implications of this variability for the modelling of cloud structure have been discussed in §1.4.2. Areas of lower 5 μm flux are thought to correspond to a real cloud temperature of about 140 K, thus suggesting that we are seeing the tops of the NH_3 clouds, while in the areas of highest 5 μm flux, known as the hot spots, the absence of obscuring cloud cover allows us to see to greater depths in the atmosphere, possibly down to 4–6 bar, corresponding to cloud temperatures of 300 K. Figure 3.1 includes two curves at 5 μm, the lower curve being the disk-averaged flux and the upper curve being the flux for hot spot with a brightness temperature of 350 K.

Because the 5 μm hot-spot emission originates from warmer regions of the atmosphere, minor constituents which condense or freeze out at the colder temperatures above the visible clouds are present here in spectroscopically detectable amounts. In addition, the long atmospheric paths traversed by the 5 μm radiation make it possible to detect constituents which are present in very

small amounts, and to set upper limits for the abundances of gases which are spectroscopically active at 5 μm (Ridgway *et al.*, 1976a, p.396; Taylor and Calcutt, 1984). With no interfering CH_4 or NH_3 absorptions present, spectra of the 5 μm window have been used to successfully identify CH_3D, H_2O, CO, PH_3, GeH_4, and AsH_3 as discussed in §1.3.5. The first spacecraft observations of this region were made by the Voyager IRIS instrument, and NIMS will also provide coverage of the 5 μm window at close to its maximum resolution, 0.025 μm at 5.2 μm corresponding to a resolution of 9.25 cm^{-1}.

NIMS measurements in this region can be used for several investigations. Taylor and Calcutt (1984) have shown that the resolution and signal-to-noise of NIMS will be sufficient to detect and discriminate between the absorptions of NH_3, PH_3, H_2O, and CH_3D, allowing determinations of composition. Mapping of the PH_3 and NH_3 abundances over the Jovian disk will be particularly useful for clarifying the distribution and origin of PH_3 and the role of NH_3 in cloud formation. Mapping of the 5 μm flux can be used to map cloud heights, since the magnitude of the flux is a function of the emitting temperature. The ability of NIMS to perform temperature sounding down to the lower altitudes probed at 5 μm remains uncertain. The retrieval of vertical temperature profiles relies upon a constant mixing ratio, and so the presence of condensible NH_3 and H_2O at the 1800 cm^{-1} edge of the window make retrievals at these wavelengths unlikely. It may be possible to use the 2200 cm^{-1} edge, but this will depend upon the vertical distribution of PH_3 because, as a non-equilibrium species (see §1.3.5), PH_3 may have a variable mixing ratio. However, the lack of horizontal variability seen in the PH_3 abundance in IRIS spectra (Drossart *et al.*, 1982) and the likelihood that PH_3 will be well mixed by convection over 1 to 5 bar both suggest that temperature sounding of these deeper regions may be feasible with NIMS.

3.1.3 Thermal Emission: 10 to 40 Microns

Beyond 10 μm lies another region of thermal emission, this one resembling a blackbody at about 125 K, as seen in Figure 3.1. At these wavelengths, the continuum absorption of the pressure-induced translational and rotational dipole bands of H_2 dominates the spectrum, obscuring the lower atmosphere from view. This thermal flux is emitted from levels in the upper troposphere and the stratosphere, above 0.5 bar and 150 K (Ridgway *et al.*, 1976a, p.386), and has proven to be a useful probe of upper atmospheric structure. Absorption and emission by several other constituents are also superimposed upon this region of the spectrum. The ν_2 band of NH_3 is present from about 9.5 to 12 μm, and an absorbing haze, possibly of NH_3 frost, appears to contribute to the opacity over 8.3 to 9.5 μm.

At 7.7 μm, the brightness temperature rises to ~150 K, apparently due to an atmospheric temperature inversion, whereby solar radiation absorbed by the near-infrared CH_4 bands is re-emitted by the ν_4 band (Gillett *et al.*, 1969). Similar emission features of C_2H_2 and C_2H_6 have also been identified in this region (Combes *et al.*, 1974; Ridgway, 1974a). The usefulness of the ν_4 band of CH_4 for temperature sounding of the Jovian atmosphere over heights from

1 to 1000 mbar was demonstrated by Taylor (1972), and Voyager IRIS thermal profiles were obtained using it and the H_2 lines between 14 and 33 μm (Hanel, 1979a). Both the Pioneer and Voyager infrared instruments made measurements in the 10 to 40 μm region, but NIMS coverage does not extend to these wavelengths.

3.2 Infrared Spectroscopy of Methane

The importance of CH_4 in the near-infrared spectrum of Jupiter has now been demonstrated. Clearly, if we are to take full advantage of the capabilities of NIMS, the near-infrared spectral parameters of CH_4 must be known. In the following section, the availability of such parameters will be reviewed and synthetic spectra of CH_4 under Jovian conditions will be calculated. This section is intended to provide a brief introduction to those spectroscopic concepts used later in this work, with particular reference to CH_4.

The infrared spectrum of a molecule such as CH_4 results from radiative transitions between different vibrational and rotational energy levels. The fundamental theory of vibrational and rotational transitions is well established, being found in such standard texts as Banwell (1983), Goody (1964), and Herzberg (1945, 1950), and is not repeated here. The CH_4 molecule is a spherical top in which the four H atoms form a regular tetrahedron about the central C atom. Having five atoms, the CH_4 molecule has nine degrees of freedom and hence nine normal vibrations (see Herzberg, 1945, p.61,67). These normal vibrations give rise to four fundamental frequencies of vibration, ν_1 at 2917 cm^{-1} (non-degenerate), ν_2 at 1533 cm^{-1} (doubly degenerate), and ν_3 and ν_4, at 3019 and 1311 cm^{-1}, respectively (both triply degenerate).

Simultaneous vibrations and rotations of the CH_4 molecule give its infrared spectrum a characteristic structure. With the energy involved in vibrational transitions being on the order of 1000 times that involved in rotational transitions, the spectrum appears as a series of vibration-rotation bands, each consisting of closely spaced rotational lines located about a central vibrational frequency. The rotational lines in each band group into three branches, referred to as P, Q, and R, which correspond to a change in the rotational vibration number of $\Delta J = -1$, 0, and 1, respectively. The Q branch is located at the centre of the vibrational band where many lines are superimposed upon each other, while the P and R branches consist of almost equally spaced lines on the low and high frequency sides, respectively, of the Q branch.

In addition to the fundamental bands, those resulting from transitions between the first excited level of a normal mode and the ground state (*i.e.*, ν_i), the infrared spectrum of CH_4 is complicated by many overtone, combination, and difference bands. Overtone bands arise from transitions between higher excited levels of a normal mode and the ground state (*i.e.*, $m\nu_i$), combination bands result from simultaneous transitions involving two or more normal modes (*i.e.*, $m\nu_i + n\nu_j$), and difference bands are those arising from transitions for which the lower level is not the ground state (*i.e.*, $m\nu_i - n\nu_j$). The similarity between the ν_1 and ν_3 frequencies, and between these and twice the ν_2 and ν_4 frequencies, results in a large number of sub-bands

in the infrared spectrum of CH_4, as is seen in Table 3.3.

Radiative transitions between different vibration-rotation energy levels may occur by spontaneous emission and by emission and absorption stimulated by the presence of external radiation. Such transitions give rise to spectral lines at frequencies corresponding to the separation of the energy levels, with each line characterised by a line strength and a line width. These line parameters are briefly introduced here, as they are used frequently throughout this thesis.

3.2.1 Line Strengths

When a molecule undergoes a transition between energy levels, an emission or absorption line centered at some characteristic wavenumber, ν_0, results. The strength of this line is defined as the integrated absorption per molecule

$$S = \int_0^\infty k(\nu)\, d\nu \tag{3.1}$$

where $k(\nu)$ is the monochromatic absorption coefficient. The line strength is determined by the transition probability for the levels under consideration, by the population of the initial energy level, and by the amount of gas causing the emission or absorption (Banwell, 1983, p.24–25). An expression for the line strength at temperature T can be derived from first principles (see Penner, 1959, Chapter 2), but it is generally tabulated at a reference temperature T_0 (usually 296 K), allowing the line strength at any other temperature to be calculated using (*e.g.*, Edwards, 1988a)

$$\frac{S(T)}{S(T_0)} = \frac{Q_r(T_0)}{Q_r(T)} \frac{Q_v(T_0)}{Q_v(T)} \frac{exp(-hcE_l/k_BT)}{exp(-hcE_l/k_BT_0)} \frac{[1-exp(-hc\nu_0/k_BT)]}{[1-exp(-hc\nu_0/k_BT_0)]} \tag{3.2}$$

where Q_r is the rotational partition function,

Q_v is the vibrational partition function,

E_l is the energy of the lower level,

h is Planck's constant,

k_B is Boltzmann's constant, and

c is the speed of light.

The first of these terms is the ratio of rotational partition functions, the second is the ratio of vibrational partition functions, the third is the ratio of Boltzmann factors (which partly determines the relative populations of the lower state at each temperature), and the fourth accounts for stimulated emission due to transitions from the upper to the lower state at each temperature. To a good approximation, particularly for T > 100 K, the ratio $Q_r(T_0)/Q_r(T)$ can be evaluated as $(T_0/T)^m$, where m is 1 for linear and diatomic molecules, and is 1.5 for non-linear molecules such as CH_4 (Herzberg, 1945, p.505–506). The vibrational partition function is also molecule-dependent, and in the case of CH_4, $Q_v(T)$ only varies from 1.000 at 175 K to 1.011 at 325 K (McClatchey *et al.*, 1973), and can be approximated by (Edwards, 1987, p.5)

$$Q_v(T) = 1 + 3\exp(-1878.9/T) + 2\exp(-2206.1/T). \tag{3.3}$$

3.2.2 Line Widths

The finite width of a spectral line is determined by three mechanisms: natural broadening, Doppler broadening, and collision (Lorentz) broadening. Natural line-broadening is a consequence of the Heisenberg Uncertainty Principle and determines the fundamental minimum line width. For a typical lifetime of 0.1 seconds for a vibrational transition, the natural line width is only 3×10^{-11} cm^{-1} (Goody, 1964, p.100), which is negligible in comparison to the Doppler and Lorentz line widths under Jovian conditions.

For Doppler and Lorentz broadening, the shape of a line whose central frequency is at wavenumber ν_0 can be described by the normalised lineshape factor, $f(\nu)$. The absorption coefficient at frequencies displaced from ν_0 is then

$$k(\nu) = S f(\nu) \tag{3.4}$$

where $\int_0^\infty f(\nu)\, d\nu = 1$, and S is the line strength.

Doppler line-broadening results from the shifts in absorption and emission frequencies caused by the thermal motion of molecules relative to an observer. For molecules with a Maxwell-Boltzmann distribution of velocities, the normalised Doppler lineshape is

$$f_D(\nu) = \frac{1}{\alpha_D \sqrt{\pi}} \exp\left[-\left(\frac{\nu - \nu_0}{\alpha_D}\right)^2\right] \tag{3.5}$$

where

$$\alpha_D = \frac{\nu_0}{c}\sqrt{\frac{2RT}{m}} = 4.301 \times 10^{-7} \nu_0 \sqrt{\frac{T}{m}} \tag{3.6}$$

is the Doppler half-width of the line, and m is the molecular mass of the molecule (*e.g.*, Goody, 1964, p.97–98). This Doppler half-width is the half-width at the point where k(ν) has fallen to 1/e of its the maximum height, and should be distinguished from the Doppler half-width at half-height which is also found in the literature and which is equivalent to $\alpha_D\sqrt{\ln 2}$ (Jones, 1983, p.30; Rodgers, 1976, p.4).

Lorentz line-broadening (also known as collision or pressure broadening) occurs when the forces of interaction between colliding molecules perturb their internal energy levels and change the emitted and absorbed frequencies. Analysis of Lorentz broadening is complex, requiring details of the interactions between the molecules and of their energy levels. A classical impact approach, such as that of Lorentz (1906) and Michelson (1895), which assumes that the phase of the emitted radiation is randomised upon collision, yields a Lorentz lineshape factor of

$$f_L(\nu) = \frac{\alpha_L/\pi}{(\nu - \nu_0)^2 + \alpha_L^2} \tag{3.7}$$

where

$$\alpha_L = \frac{1}{2\pi c \tau} \tag{3.8}$$

is the Lorentz half-width at half-maximum, with τ being the mean time between collisions. This approximation is now widely used, as it is in good agreement with experimental results near the

line centre, but it becomes less reliable in the far wings where the lineshape may be influenced by other broadening effects. For more accurate determination of the collisional lineshape, more complex theoretical analysis is required, along with experimental verification (see Davis, 1987, p.46–48, and Remedios, 1990, p.28–30, for brief reviews).

The Lorentz half-width is dependent on the temperature, the pressure, and the nature of the colliding molecules. It can be expressed as (*e.g.*, Edwards, 1987, p.6)

$$\alpha_L(T,P) = \left(\frac{T}{T_0}\right)^n \left[\alpha_{Ls}(T_0,P_0)\frac{P_s}{P_0} + \alpha_{Lf}(T_0,P_0)\frac{P_f}{P_0}\right] \tag{3.9}$$

where P is the total pressure,
T is the temperature,
P_0 is a reference pressure (usually 1 atm),
T_0 is a reference temperature (usually 296 K),
P_s is the pressure of the absorbing gas,
P_f $= P - P_s$, is the pressure of the foreign-broadening gas,
n is the exponent of temperature dependence,
$\alpha_{Ls}(T_0,P_0)$ is the self-broadened Lorentz half-width at T_0 and P_0, and
$\alpha_{Lf}(T_0,P_0)$ is the foreign-broadened Lorentz half-width at T_0 and P_0.

Simple kinetic theory gives a value of –0.5 for the exponent n, but the true temperature dependence is more complex, being determined by the type of interaction between the colliding molecules and by the J-values of transitions. For self-broadened CH_4 lines, n has been calculated to be –2/3 (Tejwani and Varanasi, 1971) and –0.6 (Varanasi and Tejwani, 1972), although measurements by Varanasi *et al.* (1973) yielded a value of –0.81. For H_2-broadened CH_4 lines, n appears to be close to the theoretical value of –0.5 (Varanasi *et al.*, 1973), while the value of n for the air-broadened CH_4 lines listed in the HITRAN and GEISA databases (see §3.3.2) varies between –0.63 and –1.00.

The Lorentz half-width at (T_0,P_0) is dependent upon the intermolecular forces, and therefore upon the presence of a foreign gas. The ratio of self-to-foreign broadening (*SFB*, after the notation in Remedios, 1990, p.31) for a given line is defined as

$$SFB = \frac{\alpha_{Ls}(T_0,P_0)}{\alpha_{Lf}(T_0,P_0)}. \tag{3.10}$$

For problems of Jovian interest, the principal broadening gas is of course H_2, but unfortunately, CH_4 line widths found in the literature are most frequently given for air- or N_2-broadened CH_4, these being of greater relevance to studies of the terrestrial atmosphere. However, there are a few studies which provide sufficient data to allow the CH_4-to-H_2 broadening ratio to be calculated for several bands of the infrared. This has been done for the four regions listed in Table 3.1. This table includes the number of lines used in calculating the average self- and H_2-broadened CH_4 Lorentz half-widths, the average value of *SFB* derived from these half-widths, and the references from which these half-widths were obtained. The CH_4-to-H_2

broadening ratio is seen to be fairly constant, varying between only 1.11 and 1.29, with no obvious systematic dependence on frequency. This is in agreement with Fox *et al.* (1988), who summarised measurements of the Ar-, He-, H_2-, and N_2-broadened CH_4 half-widths made in seven regions of the visible and infrared and concluded that there was no systematic variation of these widths with frequency.

Table 3.1: The average self- and H_2-broadened CH_4 Lorentz half-widths at 295 K and 1.01325 bar, along with the resulting self-to-foreign broadening ratio, as derived from measurements by (a) Ballard and Johnston (1986), (b) Varanasi and Chudamani (1990), (c) Varanasi *et al.* (1973), (d) Rank *et al.* (1966), (e) Margolis (1971), and (f) Fox and Jennings (1990).

BAND (cm^{-1})	NO. LINES IN CALC.	AVG. CH_4 α_L^0 (cm^{-1})	AVG. H_2 α_L^0 (cm^{-1})	AVG. *SFB*	REF.'s
ν_4 (1332–1348)	6	0.0765	0.0592	1.29	a, b
ν_3 (3028–3049)	3	0.083	0.075	1.11	c
$2\nu_3$ ($\sim$ 6000)	4	0.0870	0.0749	1.16	d
$3\nu_3$ (9080–9130)	18	0.0804	0.0727	1.11	e, f

In many cases, Doppler and Lorentz broadening are of comparable magnitude and the lineshape must include the effects of both. If the processes causing the Doppler and Lorentz broadening are uncorrelated and collisional narrowing (the decrease in Doppler width which occurs when the frequency of collisions is larger than the frequency of radiation) is negligible, then the Voigt lineshape provides a useful approximation to the combined lineshape. It is obtained from a convolution of the two contributing lineshapes and has the form

$$f_V(\nu) = \frac{y}{\pi^{3/2}\alpha_D} \int_{-\infty}^{\infty} \frac{\exp(-t^2)}{y^2 + (x-t)^2}\, dt \tag{3.11}$$

where $x = (\nu - \nu_0)/\alpha_D$, and $y = \alpha_L/\alpha_D$.

This expression must be evaluated numerically (*e.g.*, Armstrong, 1967; Drayson, 1976), and approaches the Lorentz lineshape at high pressures and the Doppler lineshape at low pressures.

Figure 3.3 illustrates how the Lorentz and Doppler half-widths of CH_4 vary with height in the Jovian atmosphere. This calculation has been performed using the Jovian temperatures and pressures in the nominal model of the Jovian atmosphere derived from Voyager data and described in §1.2.3 (Orton, 1981). The Lorentz half-width has been calculated using –0.5 for the exponent of temperature dependence, and values of 0.085 cm^{-1} for the self-broadened CH_4 half-width and 1.17 for the ratio of CH_4-to-H_2 broadening. The Doppler half-width has been calculated at two frequencies, 1923 and 14286 cm^{-1}, corresponding to the limits of the NIMS spectral range. This plot shows that the Lorentz and Doppler half-widths are comparable near the tropopause level ($\sim$0.1 bar), indicating that the Voigt lineshape is appropriate for Jovian atmospheric calculations.

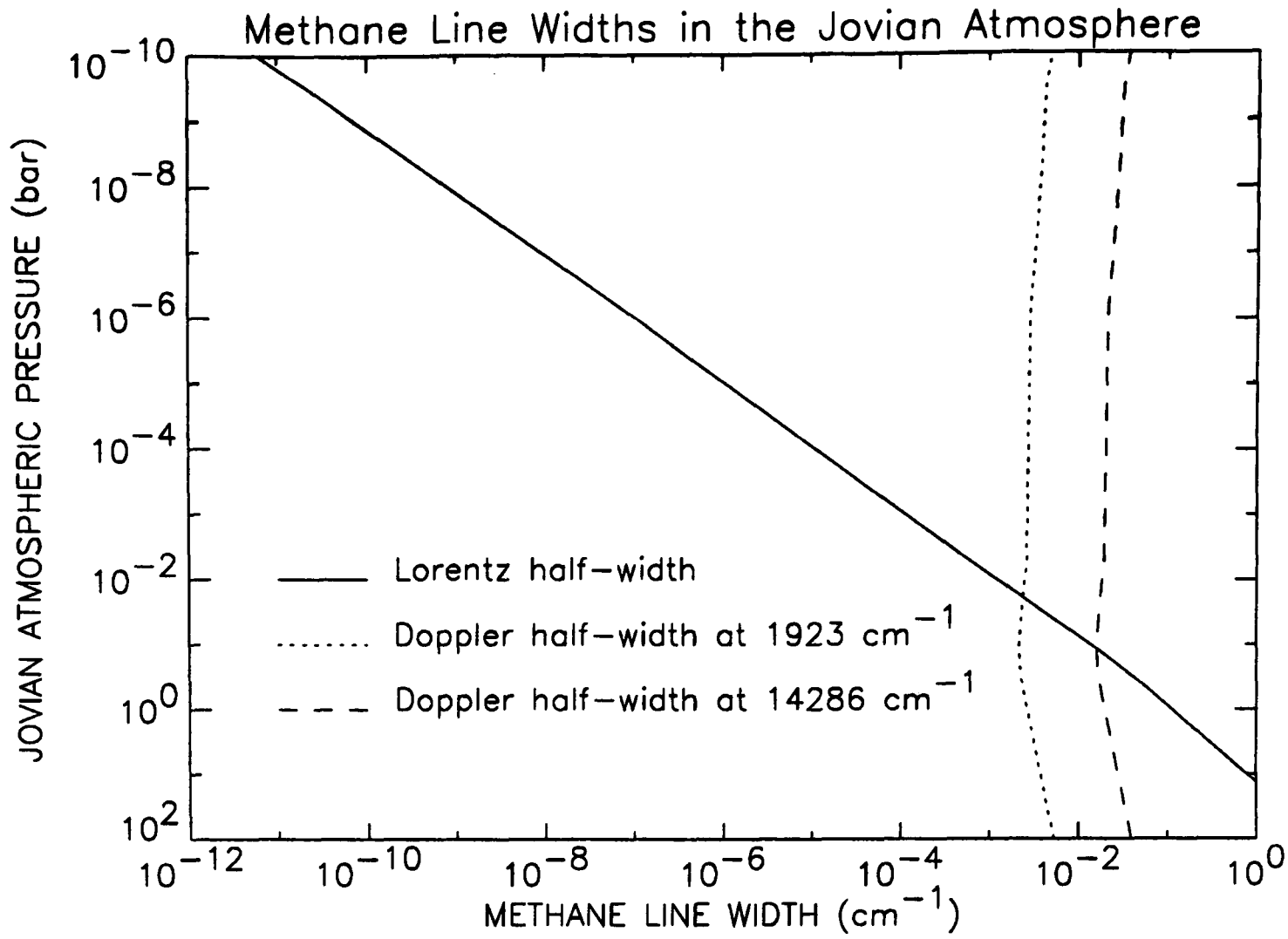

Figure 3.3: The variation of Lorentz and Doppler half-widths with height using the nominal Jovian model atmosphere of Orton (1981).

3.3 Modelling of the Near-Infrared Spectrum of Jupiter

3.3.1 The Basics of Radiative Transfer

The quantitative interpretation of planetary spectra is accomplished with the aid of radiative transfer theory, which provides a representation of spectral radiance as a function of atmospheric parameters. When radiation of intensity $I(\nu)$ passes through a homogeneous path of gas, a fraction $dI(\nu)$ of the radiation is absorbed. This decrease in intensity is proportional to the incident intensity and to the amount of absorbing gas per unit area, dU ($= \rho\, dz$, where ρ is the gas density and dz is the thickness of the path) and is described by the Beer-Lambert Law,

$$dI(\nu)_{absorbed} = -k(\nu, z)I(\nu)\rho(z)\, dz \tag{3.12}$$

where $k(\nu, z)$ is the absorption coefficient of §3.2. Integration of Equation 3.12 yields

$$I(\nu, z_2) = I(\nu, z_1) \exp\left(-\int_{z_1}^{z_2} k(\nu, z)\rho(z)\, dz\right). \tag{3.13}$$

The monochromatic transmittance of the path is then

$$\tau(\nu, z = z_1 : z_2) = \frac{I(\nu, z_2)}{I(\nu, z_1)} = \exp\left(-\int_{z_1}^{z_2} k(\nu, z)\rho(z)\, dz\right) = \exp\left[-\chi(\nu, z = z_1 : z_2)\right] \tag{3.14}$$

where $\chi(\nu, z = z_1 : z_2)$ is defined as the optical depth of the path. Radiation will also be emitted by the absorbing gas, and if it is in local thermodynamic equilibrium, Kirchoff's Law

defines the emitted intensity as

$$dI(\nu)_{emitted} = B(\nu, T)k(\nu, z)\rho(z)\,dz \tag{3.15}$$

where $B(\nu, T)$ is the Planck function for blackbody emission.

Having defined these basic terms, the radiative transfer equation for the outgoing spectral radiance, $I(\nu, \mu)$, at the top of a plane-parallel atmosphere in local thermodynamic equilibrium, can be written as (Conrath, 1982, p.47–51)

$$\begin{aligned} I(\nu,\mu) &= \frac{\mu_0}{\pi} A(\nu) F(\nu) \exp\left[-\left(\frac{1}{\mu_0}+\frac{1}{\mu}\right)\chi(\nu, z_s)\right] \\ &+ [1 - A(\nu)] B(\nu, T_s) \exp\left[-\frac{\chi(\nu, z_s)}{\mu}\right] \\ &+ \int_{z_s}^{\infty} B[\nu, T(z)] \frac{\partial}{\partial z}\left(\exp\left[-\frac{\chi(\nu, z_s)}{\mu}\right]\right) dz \end{aligned} \tag{3.16}$$

where $\cos^{-1}\mu_0$ is the solar zenith angle,

$\cos^{-1}\mu$ is the emission angle,

$A(\nu)$ is the albedo of the lowest boundary of the observable atmosphere,

$F(\nu)$ is the solar flux incident at the top of the atmosphere at the solar zenith angle,

$\chi(\nu, z)$ is the perpendicular optical depth of the atmospheric column between altitude z and the top of the atmosphere, and

s is a subscript denoting values at the lower boundary.

Figure 3.4 shows the geometry for this formulation. The first term in the equation is the direct solar flux reflected from the lower boundary and attenuated by absorption along its two-way path through the atmosphere, the second term is the thermal emission from the lower boundary at temperature T_s, also subject to atmospheric absorption, and the third term is the thermal emission from the atmosphere. Diffuse radiation terms due to particulate and molecular scattering have been ignored. The actual radiance measured by an instrument such as NIMS will then be

$$I(\overline{\nu}, \mu) = \int_{\Delta\nu} \phi(\overline{\nu}, \nu) I(\nu, \mu)\,d\nu \tag{3.17}$$

where $\phi(\overline{\nu}, \nu)$ is the normalised spectral response of the instrument, which defines a pass-band of width $\Delta\nu$ at central frequency $\overline{\nu}$.

Quantitative knowledge about an atmosphere is obtained from its measured spectrum by determining a set of atmospheric parameters which predict theoretical radiances to within some specified deviation from the measured radiances. Two approaches may be used to solve the radiative transfer equation in terms of the atmospheric parameters (*e.g.*, Conrath, 1982, p.54; Hanel, 1982, p.36). The first is direct modelling, in which a synthesized spectrum is calculated from the radiative transfer equation, using some atmospheric model for which a vertical temperature profile and distribution of constituents has been assumed. This spectrum is compared to the measured one, adjustments are made to the parameters, and the process

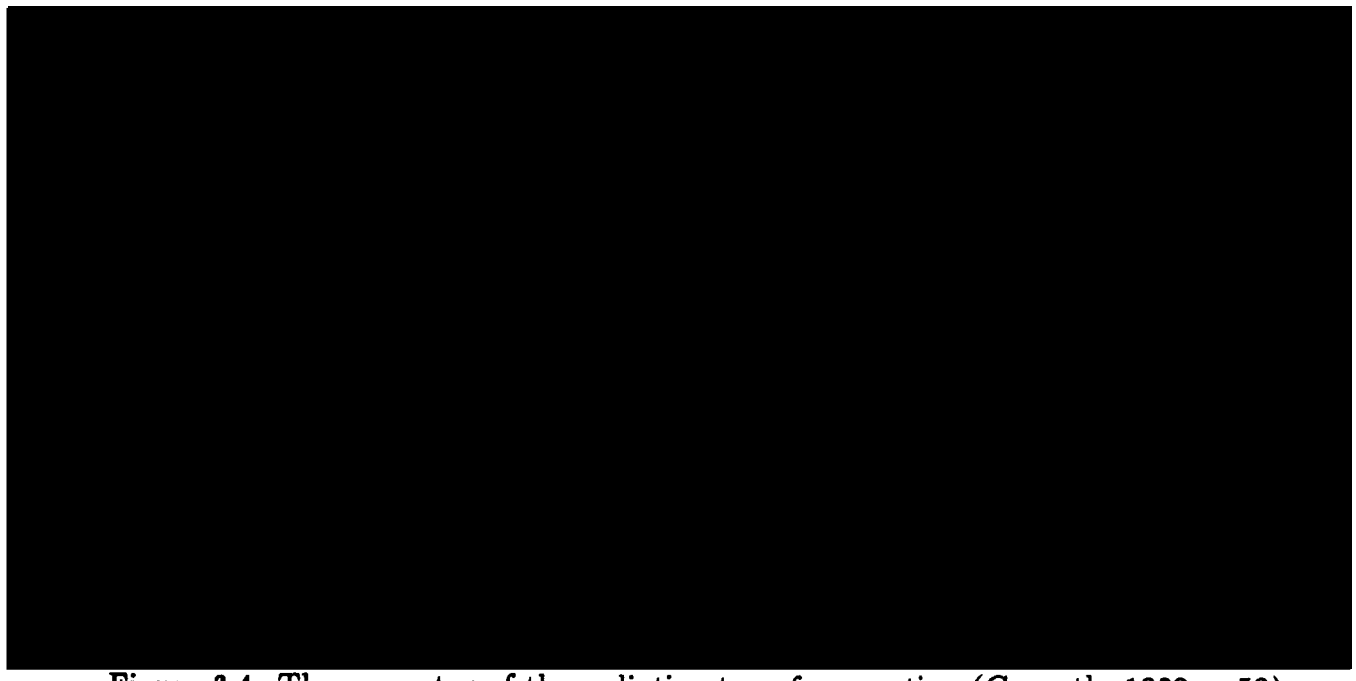

Figure 3.4: The geometry of the radiative transfer equation (Conrath, 1982, p.50)

is repeated until a best fit is obtained. The second is the inversion technique whereby the measured radiances are inserted into the radiative transfer equation to generate an integral equation for the temperature or composition profile. Some form of inversion algorithm is then required in order to solve for the desired profile (*e.g.*, Goody, 1964, Chapter 2). While inversion is most frequently used for determining thermal structure and vertical density profiles, direct modelling is applied in situations where the explicit integral equation is too difficult to set up, for example, when obscuring clouds are present in the atmosphere.

Practical applications of such analyses to the Jovian atmosphere have encountered numerous difficulties (Owen, 1972; Prinn and Owen, 1976). Clouds and aerosols scatter light and mask the lower atmosphere, the reflecting lower boundary is poorly defined, and many spectra consist of such a large number of closely spaced lines that it is difficult to distinguish between them or assign quantum states to the transitions. In particular, interpretation of Jovian spectra relies upon the atmospheric model chosen for the analysis. Because no single comprehensive atmospheric model has yet been adopted for Jupiter (as seen in §1.4), there are often inconsistencies between the results of different authors. The simplest approach is to use a reflecting-layer model, which assumes a plane-parallel atmosphere above a uniformly reflecting Lambertian surface and ignores scattering effects. Although this model has limitations, it can provide useful insights. A more sophisticated model is the homogeneous cloud model which treats the atmosphere as a cloudy mix of gas and particles, and takes account of multiple scattering. More realistic approximations of the Jovian atmosphere are obtained with inhomogeneous cloud models and two-cloud models.

Regardless of the atmospheric model used to interpret planetary spectra, the atmospheric transmittance is crucial in relating the state of the atmosphere to the measured radiance. In the ideal case, the transmittance at any frequency is calculated from the fundamental line parameters for all absorption lines at the frequency of interest; this is the approach taken in the next section. However, in Chapter 4, the alternative method of determining the transmittance using band models will be discussed.

3.3.2 Line-by-Line Spectral Modelling

The solution of the radiative transfer equation requires calculation of the transmittance, and hence of the absorption coefficient. The most accurate method of calculating the transmittance is to use line-by-line models which consider the absorption by each molecular transition within the spectral region of interest. These models require knowledge of the line-centre frequency, the line strength, the energy of the lower state of the transition, the self- and foreign-broadened half-widths, and the exponent of temperature dependence, for every line in the spectral region. One such line-by-line model is GENLN2 (Edwards 1987, 1988a, 1988b), a general purpose model which may be used to perform both atmospheric transmittance and radiance calculations.

In addition to the line-parameter data, the GENLN2 spectral calculation requires specification of the absorbing paths and of certain spectral variables. If the GENLN2 calculation is simulating a laboratory experiment where a homogeneous gas is contained in a cell, then the absorption path is simply specified by the amount of gas, the partial pressure of the gas, the total pressure, and the temperature. A typical atmosphere is inhomogeneous, but it can be approximated by a series of homogeneous layers, each subdivided into a set of "paths" which contain a single absorbing gas for which the same four conditions are specified. One such approximation is that of Curtis (1952) and Godson (1954, 1955). In this approximation, a non-isothermal inhomogeneous path with absorber amount $U(z)$, pressure $P(z)$, and temperature $T(z)$ is represented by an equivalent path with weighted means $\overline{U}$, $\overline{P}$, and $\overline{T}$, such that the equivalent widths of weak and strong Lorentz lines are the same for both paths. The weighted means for a path between altitudes z_1 and z_2 are

$$\overline{U} = \int_{z_1}^{z_2} \frac{dU}{dz}\, dz, \qquad \overline{P} = \frac{1}{\overline{U}} \int_{z_1}^{z_2} P(z) \frac{dU}{dz}\, dz, \qquad \overline{T} = \frac{1}{\overline{U}} \int_{z_1}^{z_2} T(z) \frac{dU}{dz}\, dz. \tag{3.18}$$

The spectral variables required by GENLN2 are those specifying the frequency range and the wide- and fine-mesh parameters. The transmittance calculation is performed in two stages, involving a wide pass and a fine pass. The frequency range is first divided into a specified number of wide-mesh intervals whose width (*DELTA* cm^{-1}) provides the basic frequency division over which the integrated transmittances are calculated. In each of these intervals, the absorption due to the wings of lines whose line centre lies in a specified range (more than *FEXC* cm^{-1} outside *DELTA* and less than *FWIND* cm^{-1} outside *DELTA*), is calculated at three points, these contributions are summed at these points, and a quadratic interpolation is performed to interpolate the total line-wing absorption at intermediate points in the wide-mesh interval. Each wide-mesh interval is then divided into a series of *NDIV* equally spaced fine-mesh intervals, with *DELTA/NDIV* effectively determining the resolution of the calculation. The fine mesh must be sufficiently small that narrow lines are not omitted from the calculation. The absorption is calculated at each of the fine-mesh points by summing the absorption contributions from all nearby lines lying in a specified range (within the interval *DELTA* and within *FEXC* cm^{-1} of *DELTA*).

The total monochromatic absorption coefficient at each of the fine-mesh points is then obtained by adding the interpolated far-wing absorption to the line-by-line absorption of nearby lines. This is performed for each path, allowing the individual path transmittances to be calculated, and the individual path optical depths to be combined to obtain optical depths for user-defined mixed paths of several gases and/or several layers, thus providing the total atmospheric transmittance. Once the total transmittances have been calculated for the fine-mesh points, they are integrated over the wide-mesh intervals, which thus determine the output frequency-resolution.

Although the GENLN2 line-by-line program was originally written for terrestrial applications, in this work it was used to model Jovian atmospheric transmittance. Such calculations were undertaken in order to determine the transmittance of CH_4 in the Jovian atmosphere from the upper surface of each of the three cloud layers to the top of the atmosphere. Before presenting the results of these calculations, the relevant line data available for use will be discussed.

3.3.3 Available Line Data

Line parameters for gases of interest in atmospheric applications have been compiled in two extensive databases, the AFGL/HITRAN and GEISA listings. The AFGL/HITRAN database (McClatchey *et al.*, 1973; Rothman and McClatchey, 1976; Rothman, 1978, 1981; and Rothman *et al.*, 1983, 1987, 1991) includes line parameters for 28 species at frequencies ranging from 0 to 17900 cm^{-1}. It originally included only the line-centre frequency, the strength at 296 K, the air-broadened Lorentz half-width at 296 K, the lower state energy, and quantum identifications, but the 1986 edition made provision for the self-broadened half-width, the exponent of temperature dependence of the air-broadened half-width, and the transition probability. The GEISA database (Chedin *et al.*, 1980, 1981, 1985; Husson *et al.*, 1982, 1986) is similar to the HITRAN database, but is oriented towards gases of interest in planetary atmospheres, including line parameters for 36 species at frequencies from 3×10^{-6} to 17879 cm^{-1}. Values for the exponent of temperature dependence of the half-width were added to the 1984 edition, but the self-broadened half-width has not been included. It should be noted that although the HITRAN and GEISA compilations provide invaluable access to the spectral data needed for atmospheric applications, the accuracy of these data is variable (being derived from different sources), and data for many molecular transitions are missing. The latter is particularly true of CH_4, as will be seen below.

Because the NIMS spectral region extends from 0.7 to 5.2 μm (1923 to 14286 cm^{-1}), both the HITRAN 1986 (Rothman *et al.*, 1987) and GEISA 1984 (Husson *et al.*, 1986) databases were searched to determine the availability of line parameters in this region for gases of Jovian interest. The results are presented in Figure 3.5, where line strength has been plotted against wavenumber to show the locations of lines on the databases. HITRAN 1986 lists line parameters

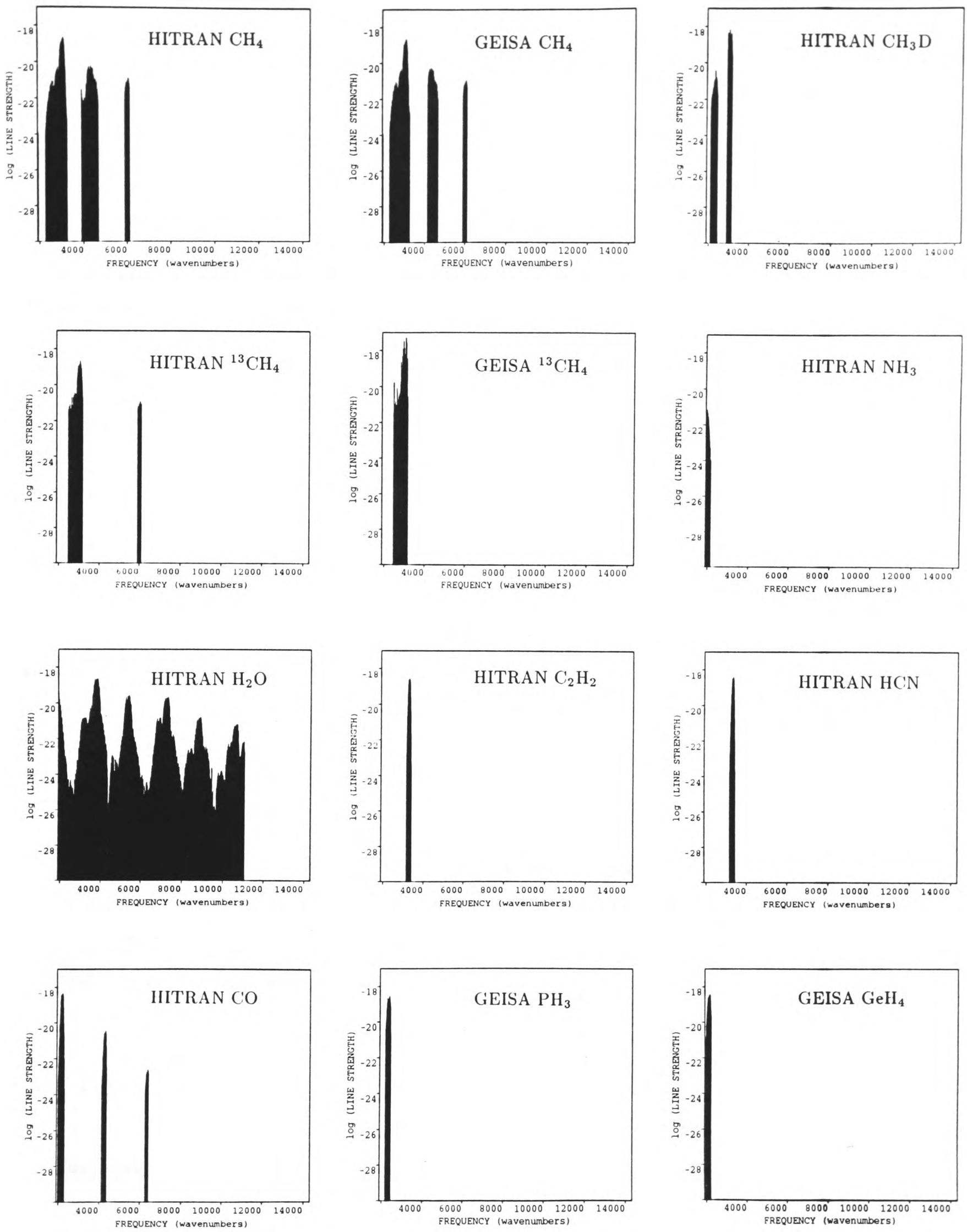

Figure 3.5: Spectral lines listed in the HITRAN 1986 and GEISA 1984 databases over the NIMS spectral range (1923 to 14286 cm^{-1}), for gases of Jovian interest. GEISA data are plotted only when they differ from the HITRAN data.

in the NIMS window for CH_4, CH_3D, $^{13}CH_4$, NH_3, H_2O, C_2H_2, HCN, and CO, while GEISA 1984 includes these gases as well as PH_3 and GeH_4. Several other Jovian gases are also listed on the databases (C_2H_6 and PH_3 on HITRAN, C_2H_4, C_2H_6, C_3H_8 and H_2S on GEISA), but no line data are provided in the NIMS window. This absence of line data for gases which have been identified in the Jovian atmosphere from their absorptions in this region demonstrates that these databases are by no means comprehensive. Furthermore, Figure 3.5 shows that for the two gases which dominate absorption in the near-infrared spectrum of Jupiter, the availability of CH_4 line parameters is limited to 1900–6110 cm^{-1} and the availability of NH_3 line parameters is limited to 1900–2160 cm^{-1}. Since both of these gases are known to have significant absorptions elsewhere in the NIMS window (as seen in Figure 3.1), there is clearly a critical lack of CH_4 and NH_3 line data.

Being the dominant absorber in the Jovian near-infrared spectrum, CH_4 is the gas of interest in this work. The HITRAN 1986 database lists line parameters for 32 bands of CH_4, CH_3D, and $^{13}CH_4$ between 0 and 6107 cm^{-1}. These have been compiled from a combination of theoretical calculations and experimental measurements, and are of varying quality. Table 3.2 summarises the accuracy of the HITRAN 1986 line positions and strengths, as assessed by Rothman *et al.* (1987). Not only are many bands missing from the compilation, many weak lines are either omitted or of poor accuracy. The HITRAN database actually excludes any CH_4 lines whose strength is less than 3.3×10^{-24} $cm^{-1}/(molec \cdot cm^{-2})$, because such weak lines yield less than 10% line-centre absorption in the terrestrial atmosphere. At the longs paths traversed in the Jovian atmosphere, it is the weak lines that are of greater importance because the strong lines are saturated, and so the poor quality of the weak line parameters presents a major limitation in using HITRAN line data to interpret Jovian spectra.

Table 3.2: The accuracy of the HITRAN 1986 CH_4 line parameters, as assessed by Rothman *et al.* (1987), except †, for which accuracies were obtained from the original source (Brown and Rothman, 1982).

REGION (cm^{-1})	ACCURACY of POSITIONS (cm^{-1})	ACCURACY of STRENGTHS	COMMENTS
1000–1950	0.0005–0.005	4%–15%	Several hot bands are missing.
2255–3255	0.0006–0.005	$\leq$ 2%–50%	Accuracy $\leq$ 2% for ν_3 P-branch, 15% for strengths $< 10^{-23}$ $cm^{-1}/(molec \cdot cm^{-2})$, and 50% for very weak lines.
3500–5000 †	0.003–0.0002	2%–15%	No lines weaker than 2×10^{-23} $cm^{-1}/(molec \cdot cm^{-2})$ are included. Only 3 bands of a possible 8 listed.
5000–6500	0.005–0.020	5%–20%	Only 1 band of a possible 12 listed.

The GEISA 1984 database includes line parameters for the same CH_4 bands, but does not impose a minimum line-strength criterion. It therefore lists many more weak CH_4 lines, although the accuracy of their line parameters may be poor. Only a qualitative assessment of

their accuracy is provided by Chedin *et al.* (1985), who conclude that improvements in the line strengths and line widths are needed throughout the 900 to 6100 cm^{-1} region for which data are available. Table 3.3 lists the major infrared bands of $^{12}CH_4$, including the 14 on HITRAN 1986 and GEISA 1984 and an additional 31 obtained from other sources.

In recent years, with the realisation of the importance of CH_4 in the remote sounding of planetary atmospheres, there have been increased efforts to measure the positions, strengths, and half-widths of CH_4 lines, and to assign appropriate quantum numbers. These include studies in each of the four regions listed in Table 3.2: 1000–1950 cm^{-1}, 2255–3255 cm^{-1}, 3500–5000 cm^{-1}, and 5000-6500 cm^{-1}. The HITRAN 1991 database (Rothman *et al.*, 1991), which is in preparation at the time of writing this chapter, includes updates in each of these regions. However, although measurements and calculations are improving the available CH_4 line parameters, they remain restricted to frequencies below 6200 cm^{-1}. Aside from some measurements of line widths in the $3\nu_3$ band near 9000 cm^{-1} by Fox (1984) and Fox *et al.* (1988), very little work has been done in the 6200 to 14286 cm^{-1} region of the NIMS window. Clearly there is a critical need for NIMS-oriented laboratory spectroscopy of CH_4, particularly of both weak and strong lines in the 6200 to 14286 cm^{-1} region, and of weak lines in the 1923 to 6200 cm^{-1} region.

3.3.4 Line-by-Line Modelling of the Transmittance of Jovian Methane

Using the GENLN2 line-by-line program and the available line data, the transmittance of CH_4 in the Jovian atmosphere was calculated for a variety of conditions. The aims of this calculation were to investigate:

(1) the nature of the CH_4 transmittance from the upper surface of each of the three Jovian cloud layers to the top of the atmosphere,

(2) the effect of the CH_4 far-wing contribution on the transmittance, using the Voigt lineshape under Jovian conditions, and

(3) the importance of the differences between the CH_4 line data available on the HITRAN 1986 and GEISA 1984 databases.

The Jovian atmosphere used in the modelling was again the nominal model derived from Voyager data and described in §1.2.3 (Orton, 1981). The Curtis-Godson weighted mean parameters were calculated for 130 layers from 100 bar up to 10^{-11} bar, each of equal thickness in terms of $\Delta ln(P)$ ($ln[P_1/P_2] = 0.23026$). Nadir viewing was assumed, with the total atmospheric paths defined as the combination of all of the layers from the base of a given layer up to the top of the atmosphere. GENLN2 assumes terrestrial isotopic abundances in weighting the line strengths, and given the uncertainty in the Jovian abundances of $^{13}CH_4$ and CH_3D relative to $^{12}CH_4$, the terrestrial values were used in this calculation.

Table 3.3: Principal infrared $^{12}CH_4$ bands: H = HITRAN 1986 (Rothman *et al.*, 1987), G = GEISA 1984 (Chedin *et al.*, 1985), and other bands are from Herzberg (1945, p.308), Taylor and Calcutt (1984), and Brown (1988). The no. of lines in each band is given as HITRAN and (GEISA). The range is the maximum of the two.

BAND	CENTRE (cm^{-1})	SOURCE	RANGE (cm^{-1})	No. of LINES
ν_4	1310.7606	H, G	944–1628	1420 (4671)
ν_2	1533.3367	H, G	1163–1866	810 (3117)
$\nu_3 - \nu_4$	1720.	H, G	1474–1932	462 (2176)
$2\nu_4$	2596.	H, G	2458–2682	41
$2\nu_4$	2612.	H, G	2254–2848	1266 (1289)
$\nu_2 + \nu_4$	2830.	H, G	2572–3185	2300 (2347)
ν_1	2917.	H, G	2741–3092	52 (85)
$\nu_2 + \nu_3 - \nu_2$	3010.	H, G	2898–3106	264 (275)
$\nu_3 + \nu_4 - \nu_4$	3010.	H, G	2880–3136	712 (742)
ν_3	3018.9205	H, G	2809–3210	1903 (1908)
$2\nu_2$	3062.	H, G	2905–3254	755 (744)
unassigned lines		H	2511–3176	847
$3\nu_4$	3868.	Brown		
$\nu_2 + 2\nu_4$	4123.	Herzberg		
$\nu_1 + \nu_4$	4223.497	H, G	4136–4279	151 (172)
$\nu_3 + \nu_4$	4340.	H, G	4147–4490	958 (958)
$2\nu_2 + \nu_4$	4370.	Brown		
$\nu_1 + \nu_2$	4450.	Brown		
$\nu_2 + \nu_3$	4540.	H, G	4409–4667	388 (386)
unassigned lines		H, G	3900–4667	2116 (537)
$3\nu_2$	4600.	Brown		
$\nu_3 + 2\nu_4$	5585.	Herzberg		
$\nu_1 + \nu_2 + \nu_4$	5775.	Herzberg		
$\nu_2 + \nu_3 + \nu_4$	5861.	Herzberg		
$2\nu_3$	6004.991	H, G	5891–6107	142 (142)
$2\nu_2 + \nu_3$	~6086	Taylor&Calcutt		
$2\nu_1 + \nu_4$	~7145	Taylor&Calcutt		
$\nu_1 + \nu_3 + \nu_4$	~7247	Taylor&Calcutt		
$2\nu_3 + \nu_4$	~7349	Taylor&Calcutt		
$\nu_1 + \nu_2 + \nu_3$	~7469	Taylor&Calcutt		
$\nu_2 + 2\nu_3$	7514.	Herzberg		
$\nu_2 + 2\nu_3$	~7571	Taylor&Calcutt		
$2\nu_1 + 2\nu_4$	8421.	Herzberg		
$2\nu_3 + 2\nu_4$	8604.	Herzberg		
$2\nu_1 + \nu_3$	8807.	Herzberg		
$\nu_1 + 2\nu_3$	8900.	Herzberg		
$3\nu_3$	9047.	Herzberg		
$2\nu_1 + \nu_2 + \nu_3$	10114.	Herzberg		
$\nu_1 + \nu_2 + 2\nu_3$	10300.	Herzberg		
$\nu_2 + 3\nu_3$	~10590	Herzberg		
$3\nu_1 + \nu_3$	11270.	Herzberg		
$2\nu_1 + 2\nu_3$	11620.	Herzberg		
$\nu_1 + 3\nu_3$	11885.	Herzberg		
$4\nu_3$	~12076	Herzberg		
$3\nu_1 + \nu_3 + \nu_4$	12755.	Herzberg		
$2\nu_1 + \nu_2 + 2\nu_3$	~13405	Herzberg		
$4\nu_1 + \nu_3$	13790	Herzberg		
$3\nu_1 + 2\nu_3$	~14789	Herzberg		

The spectral range chosen for the calculations was 1800 to 6200 cm^{-1}, the lower bound being just below the edge of the NIMS window and the upper bound marking the limit of the available line data. A wide-mesh interval of 1.0 cm^{-1} was used, as recommended by Edwards (1987, p.19), a value sufficiently small enough to ensure accurate quadratic interpolation of the far-wing contribution at the three points in the interval. Since this is the output interval for the integrated transmittances, these transmittances were subsequently degraded to 10 cm^{-1} resolution using a square weighting function, and then sampled every 5 cm^{-1}. This is consistent with the resolution of the band models of Chapter 7, and is similar to the maximum resolution of NIMS. The number of fine-mesh intervals within each wide-mesh interval was chosen to ensure that no narrow lines were missed in the fine-pass calculation. The smallest line width of a Doppler-broadened CH_4 line (formed at 110 K and 1800 cm^{-1}) in the Jovian atmosphere was calculated to be 0.002 cm^{-1}, and so the number of fine-mesh frequency points was set at 1000, giving a resolution of 0.001 cm^{-1}. The limit for the fine-pass calculation was set at 2.0 cm^{-1}, and the limit for the wide-pass far-wing calculation was left as a variable. The Voigt lineshape was used, as suggested by Figure 3.3.

Two independent sets of line-by-line transmittance spectra were calculated, one using the HITRAN 1986 CH_4 data and one using the GEISA 1984 CH_4 data. For each of these databases, four subsets of spectra were generated using values of 25, 100, 500, and 1000 cm^{-1} as the limit for the wide-pass far-wing calculation. Finally, for each of these values, individual spectra were calculated using three mixed paths extending from 0.32, 2.0, and 5.0 bar, to the top of the atmosphere. These three pressures correspond to the approximate levels of the three Jovian cloud layers (see §1.4), and so the transmittances obtained with these three mixed paths represent the CH_4 transmittance from the top of each cloud layer to the top of the atmosphere. The resulting transmittances are seen in Figures 3.6 and 3.7.

These figures demonstrate several interesting results. Firstly, both the HITRAN and GEISA plots show how the CH_4 transmittance to the top of the atmosphere decreases as the level of the reflecting or emitting cloud layer is located deeper in the atmosphere. This is as expected, since the radiation originating from deeper in the atmosphere must traverse longer absorption paths. For the 0.32 bar cloud, structure is present in all three band centres, however, for the 2.0 and 5.0 bar clouds, the band centres are essentially saturated with significant structure present only in the wings of the 3000 cm^{-1} band.

Secondly, the transmittance in the window regions between the bands is seen to be strongly affected by the far-wing contribution. As the limit for the calculation of the absorption due to the wings of far lines is increased from 25 through 100 and 500 to 1000 cm^{-1}, the continuum absorption in the windows increases substantially. This continuum absorption is less significant for the 0.32 bar calculation, but is considerable for the larger CH_4 abundances. The value of 25 cm^{-1} recommended for the line-wing calculation (Edwards, 1988a) therefore may be open to question for line-by-line modelling of the large CH_4 abundances found in the Jovian

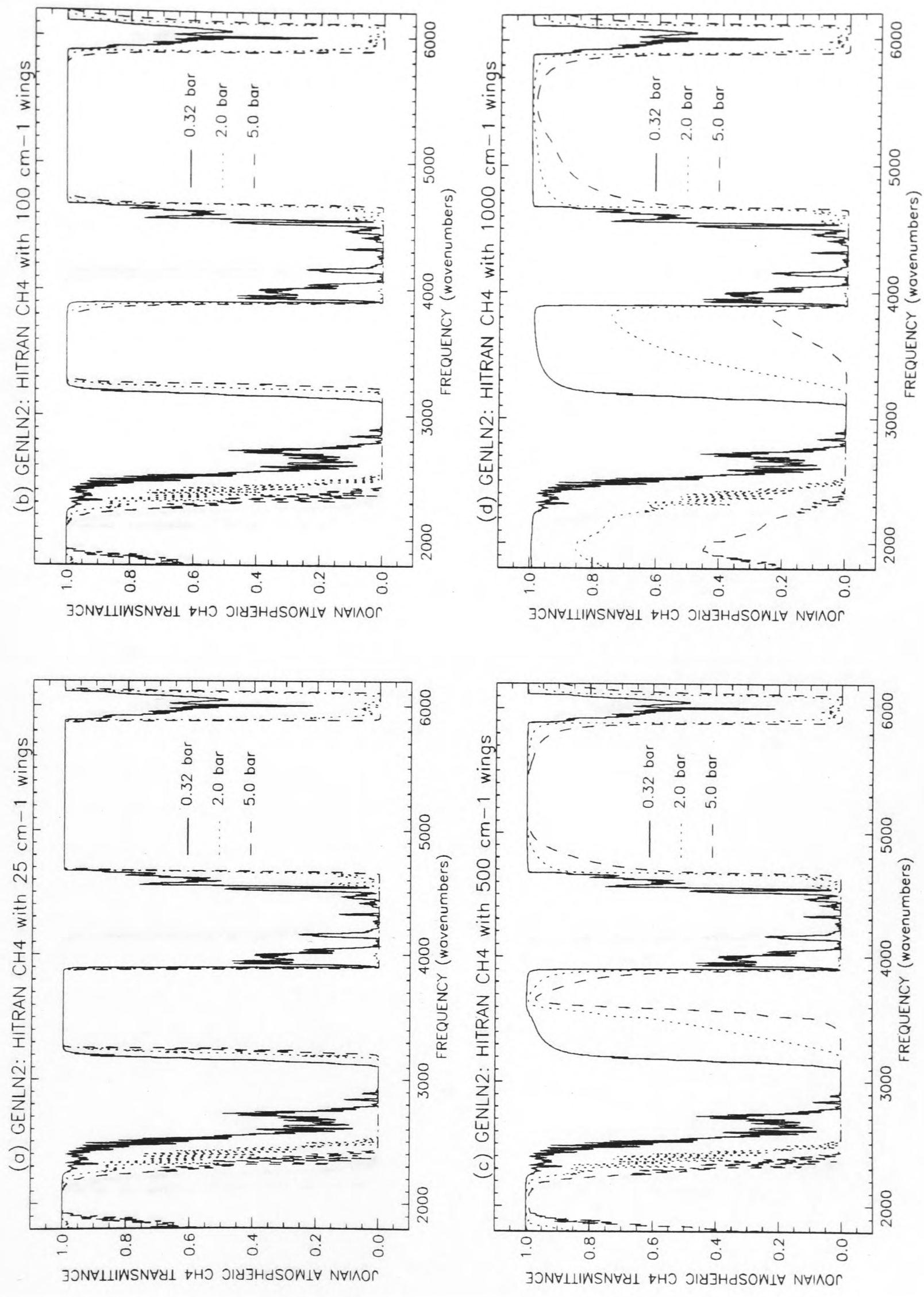

Figure 3.6: The transmittance of CH_4 in the Jovian atmosphere from the 0.32, 2.0, and 5.0 bar levels up to the top of the atmosphere at 10^{-11} bar. The transmittance has been calculated with the GENLN2 line-by-line model, using HITRAN 1986 line data, and including the contribution of far wings out as far as (a) 25, (b) 100, (c) 500, and (d) 1000 cm^{-1} from the wide-mesh intervals.

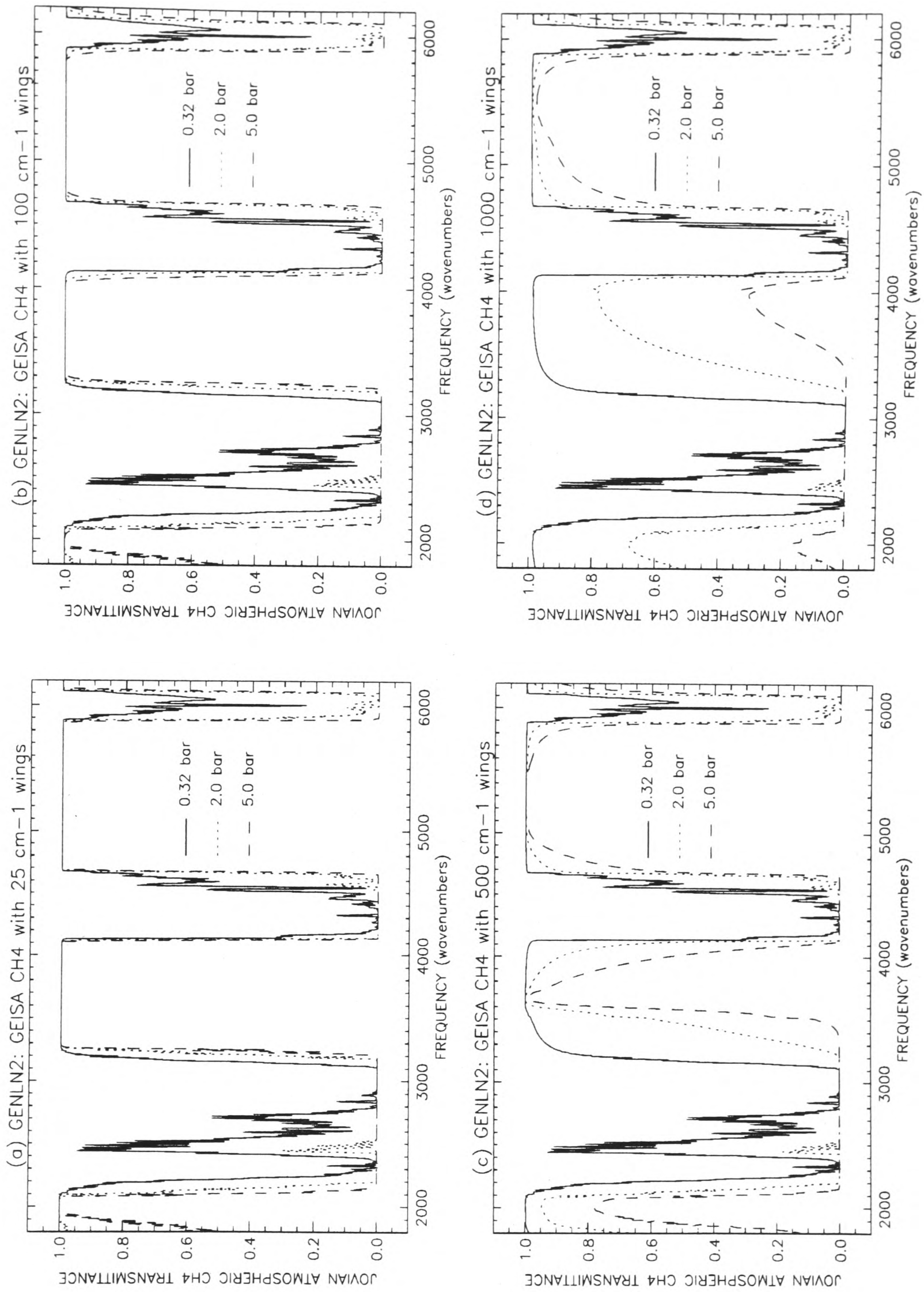

Figure 3.7: The transmittance of CH_4 in the Jovian atmosphere from the 0.32, 2.0, and 5.0 bar levels up to the top of the atmosphere at 10^{-11} bar. The transmittance has been calculated with the GENLN2 line-by-line model, using GEISA 1984 line data, and including the contribution of far wings out as far as (a) 25, (b) 100, (c) 500, and (d) 1000 cm^{-1} from the wide-mesh intervals.

atmosphere. However, it is more likely that the Voigt lineshape is inappropriate in the far wings of CH_4 lines, where they may become sub-Lorentzian (*e.g.*, Lellouch *et al.*, 1991), resulting in an over-estimation of the absorption.

Thirdly, comparison of the spectra generated with the HITRAN and GEISA line data reveals several major differences. The greater number of unassigned lines listed on HITRAN for the 3900 to 4667 cm^{-1} region (see Table 3.3) is reflected in the lower frequency edge of the 4200 cm^{-1} absorption band, which is located near 4100 cm^{-1} in the GEISA spectra, but extends down to 3900 cm^{-1} in the HITRAN spectra. Absorptions present between 3900 and 4100 cm^{-1} in the latter are completely absent from the GEISA spectra. A potentially more significant difference between the spectra is the effect of the weak CH_4 lines which are present on GEISA, but not on HITRAN. As seen in Table 3.3, these additional lines are located mostly below 3000 cm^{-1}, and it is over approximately 2000 to 2600 cm^{-1} that the GEISA spectra exhibit significantly more absorption than the HITRAN spectra. This is true for all three absorber amounts, and is evidence that weak CH_4 lines give rise to measurable absorptions in the Jovian atmosphere. These unsaturated weakly absorbing regions are precisely the most important in Jovian spectra, and so the lack of data about weak lines elsewhere in the NIMS window will be a significant limitation on the retrieval of information from NIMS spectra. A third, but related difference between the HITRAN and GEISA spectra is their appearance when the far-wing contribution is varied. The unassigned HITRAN lines and the weak GEISA lines result in different continuum absorptions in the window regions. Both spectra show similar absorption from 4700 to 5900 cm^{-1}, but from 3100 to 4100 cm^{-1} the continuum absorption is greater in the HITRAN spectra, and from 1800 to 2600 cm^{-1} the continuum absorption is greater in the GEISA spectra.

These results prove that the use of line-by-line modelling as a means of calculating CH_4 transmittance in the Jovian atmosphere is severely limited by the availability of line data. Both weak lines and unassigned stronger lines of CH_4 are seen to be important under Jovian conditions, both for their line-centre and line-wing contributions to the total absorption. The poor quality of the weak line data from 1800 to 6200 cm^{-1}, the known omission of certain strong line data from 1800 to 6200 cm^{-1}, and the complete lack of line data above 6200 cm^{-1} are all proof of the need for laboratory spectroscopic studies of CH_4, not only in support of NIMS, but for any applications requiring accurate knowledge of CH_4 spectral parameters.

Chapter 4

Band Modelling of Methane: Theory and Previous Work

4.1 The Rationale for Band Modelling of Methane

In the previous chapter, the importance of CH_4 in the near-infrared spectrum of Jupiter was discussed and line-by-line calculations of the transmittance of CH_4 under Jovian conditions were presented. Such calculations rely upon the availability and accuracy of CH_4 line parameters. The absence of CH_4 line data for frequencies above 6200 cm^{-1} and the inaccuracy of the available weak line data were demonstrated. This lack of spectral data for CH_4 presents a serious problem for the interpretation of NIMS spectra of Jupiter, both because the NIMS spectral range extends well beyond 6200 cm^{-1} and because the strong CH_4 lines for which parameters have been measured will be saturated at Jovian abundances, making weak bands and weak wings of strong bands far more important in analysis of Jovian spectra. Without information on the atmospheric transmittance of such an important Jovian gas as CH_4, the retrieval of atmospheric parameters from NIMS observations will be extremely restricted.

The ideal form of CH_4 spectral data would be individual line parameters for all CH_4 lines in the NIMS spectral range, allowing the absorption coefficient to be determined to infinite resolution as a function of frequency for input into any atmospheric model calculation. However, this is an impossible objective on the time-scale of the Galileo mission. The large number of near-infrared vibration-rotation overtone and combination bands of CH_4 gives rise to thousands of lines, the measurement and analysis of which, is a massive undertaking, unlikely to be complete for some time. This is particularly true of the weak CH_4 lines, for which large abundances are required, making laboratory studies more difficult. In addition, the overlapping of and interactions between bands increases the difficulty of determining the quantum number assignments of lines, so that many CH_4 lines have yet to be identified. Furthermore, the complexity involved in modelling the spectrum of a tetrahedral spherical top, such as CH_4, also makes it difficult to calculate theoretical line parameters.

Fortunately, the nature of the near-infrared CH_4 spectrum and the low resolution of NIMS allow an alternative to the line-by-line tabulation of spectral data and the line-by-line calculation of atmospheric transmittance. The monochromatic transmittance of Equation 3.14 can be replaced with a wavelength- or frequency-averaged transmittance, represented by a mathematical function of temperature, pressure, and abundance which may be a physical or an empirical approximation of the spectrum. Such functions are known as band models and can be derived from spectral data in two ways. In the first, the band model is fitted to individual line data over a specified spectral interval, thereby generating a set of fitted spectral parameters. These parameters can then be used to calculate transmittances, with the reduced use of computing resources, compared to those required for line-by-line calculations, compensating for the loss of accuracy resulting from the use of fitted parameters. The second application of band modelling is to fit laboratory measurements of the frequency-averaged transmittances directly as a function of the laboratory temperatures, pressures, and abundances.

Because the near-infrared spectrum of CH_4 has such a complex and irregular structure, it is an appropriate candidate for the application of band models, particularly of the random band models described below. In addition, for practical purposes, the spectral resolution of NIMS (0.025 μm) is such that wavelength- or frequency-averaged transmittances are sufficient. Even if a comprehensive set of line parameters were available, these parameters would have to be input into low-resolution transmittance models in order to retrieve atmospheric data from NIMS spectra. It is therefore more efficient to proceed directly from low-resolution spectra to band models than to perform high-resolution measurements to determine line parameters and to then degrade them.

The approach taken in the present study was therefore to measure laboratory spectra of CH_4 over the NIMS spectral range under a variety of conditions which simulated the Jovian atmosphere as closely as possible. The transmittance was then fitted with several different band models, allowing an evaluation of which one provided the best fit to the spectra. The following section introduces the models that are used in Chapter 7, and this is followed by a review and assessment of previous band-modelling studies of CH_4 that have been conducted in the NIMS spectral region.

4.2 Band-Modelling Theory

4.2.1 Introduction

Band models have long been used in radiative transfer calculations for the terrestrial atmosphere, the principle of the random band model having first been suggested by Mayer (1947) and Goody (1952). They were originally developed for determining infrared transmittance and atmospheric heat transfer before gaseous molecular absorption parameters were widely available. This has resulted in the development of a variety of models, each with its own assumptions.

The basic principle underlying all such models is that a real spectrum can be approximated by an infinite array of absorption lines having uniform statistical properties (Goody, 1964, p.122). Such an array is divided into a series of intervals, each interval including several lines and being surrounded by statistically similar intervals. The absorption properties of an interval in the real spectrum are then modelled by those of the equivalent interval in the array.

The practice of fitting band models to wavelength- or frequency-averaged laboratory measurements of transmittance is well established, as is seen in the review of §4.3. The following discussion will refer to frequency-averaged intervals, as these are used in the data analysis of Chapter 7. The frequency-averaged transmittance, $\overline{\tau_i}$, for interval i and for a particular temperature T, pressure P, and abundance U, is given by

$$\overline{\tau_i}(T,P,U) = \frac{1}{\Delta\nu}\int_{\Delta\nu} Wt(\nu-\nu_i)\,\tau(\nu,T,P,U)\,d\nu \tag{4.1}$$

where $Wt(\nu)$ is the weighting or instrument function, and ν_i is the frequency at the centre of the interval. Thus, for each interval i, there is a set of transmittances $\overline{\tau_i}(T,P,U)$ corresponding to the set of laboratory conditions, allowing a band model to be fitted to $\overline{\tau_i}$ as a function of T, P, and U.

Although such models can provide accurate fits to the transmittance for homogeneous laboratory paths, some care must be taken when applying the results to inhomogeneous atmospheric paths or paths including several different absorbing gases. In either case, in a real spectrum, the monochromatic transmittance can be computed as the product of several transmittances, whether of a series of homogeneous sub-paths comprising the inhomogeneous path, or of the different absorbing gases, *i.e.*,

$$\tau_\nu(1,2) = \tau_\nu(1)\times\tau_\nu(2) \tag{4.2}$$

where 1 and 2 refer to two homogeneous layers or to two different absorbing gases (Goody, 1964, p.123). However, in general, this multiplicative property does not apply to frequency-averaged transmittances, *i.e.*,

$$\overline{\tau_i(1,2)} \neq \overline{\tau_i(1)}\times\overline{\tau_i(2)}. \tag{4.3}$$

This failure of the multiplicative property can be overcome in several ways. In the case of an inhomogeneous atmospheric path, the path can be replaced by a single equivalent homogeneous path, calculated using the Curtis-Godson approximation (Equation 3.18). In the case of several different absorbing gases, the multiplicative property will still apply if the absorptions of the different gases are uncorrelated.

When fitting a band model to laboratory spectra, two types of transmittance functions may be used; those that attempt to model physical absorption processes, and those that are purely empirical. The latter are often more successful, but the former are preferable since they should give physically based and therefore more reliable transmittances for conditions interpolated and extrapolated from measurement conditions (Calcutt, 1984, p.5-5). The following is a discussion

of the most commonly used physical and empirical models, concentrating on those models used in the fitting of the laboratory CH_4 spectra in this work.

4.2.2 The Single Line Model

The simplest transmittance model is for the case of individual lines which do not overlap. For such a line, the monochromatic transmittance is given by Equation 3.14, and for a homogeneous path, this simply reduces to

$$\tau(\nu) = \exp[-k(\nu)U] \tag{4.4}$$

where $k(\nu) = Sf(\nu)$ is the absorption coefficient,

S is the line strength,

$f(\nu)$ is the lineshape factor, and

U is the amount of absorbing gas per unit area.

The equivalent width of this line is defined as its integrated absorption (Goody, 1964, p.125),

$$W_{single\ line} = \int_{-\infty}^{+\infty} (1 - \exp[-Sf(\nu)U])\, d\nu. \tag{4.5}$$

The term "curve of growth", used in §4.3, is defined as the equivalent width as a function of the the absorber amount.

Evaluation of the equivalent width therefore depends upon the choice of lineshape. Expressions for W using the Lorentz, Doppler, and Voigt lineshapes have been summarised by several authors, including Plass (1958) and Rodgers (1976, p.9–12). The case of the Lorentz lineshape provides a useful illustration of the concepts of weak and strong absorption. Substituting the Lorentz lineshape (Equation 3.7) into Equation 4.5, the equivalent width becomes (Ladenberg and Reiche, 1913)

$$W_{Lorentz\ line} = 2\pi\alpha_L L(x) \;=\; 2\pi\alpha_L x e^{-x}[I_0(x) + I_1(x)] \tag{4.6}$$

where $x \quad = SU/2\pi\alpha_L$,

$L(x)$ is the Ladenberg-Reiche function, and

I_0, I_1 are Bessel functions.

The Ladenberg-Reiche function can be simplified for the cases of small and large x. In the limit as $SU/\pi\alpha_L \to 0$, the optical depth at the the centre of the line approaches zero and the line is described as weakly absorbing. In this case, the equivalent width becomes

$$W_{weak\ limit} = SU. \tag{4.7}$$

In the limit as $SU/\pi\alpha_L \to \infty$, the optical depth at the the centre of the line approaches infinity and the line is described as strongly absorbing. In this case, the equivalent width becomes

$$W_{strong\ limit} = 2\sqrt{SU\alpha_L}. \tag{4.8}$$

In fact, taking the limit $SUf(\nu_0) \rightarrow 0$ in Equation 4.5, it is clear that the equivalent width for the weak limit is independent of lineshape. However, this is not true of the equivalent width for the strong limit.

Returning to the general case, the frequency-averaged transmittance over spectral interval $\Delta\nu$, for a single line j, is simply

$$\overline{\tau_j}_{single\ line} = 1 - \frac{W_j}{\Delta\nu}. \tag{4.9}$$

If the interval includes N_0 such lines, non-overlapping, the total frequency-averaged transmittance becomes (Rodgers, 1976, p.13)

$$\overline{\tau}_{single\ line\ model} = 1 - \sum_{j=1}^{N_0} \frac{W_j}{\Delta\nu} \tag{4.10}$$

In practice, particularly for the complex near-infrared spectrum of CH_4, there are likely to be many overlapping lines in a spectral interval. In such cases, regardless of the lineshape chosen to evaluate W, the single line model does not provide a realistic representation of $\overline{\tau}$. Instead, models that can deal with overlapping lines must be used. Such models are the subject of the remainder of this section.

4.2.3 Regular Band Models

Band models which assume an infinite array of regularly spaced lines are known as regular models and can be used to treat "weakly" overlapping lines (those which do not interact at the quantum mechanical level). The best known of these models is that of Elsasser (1938, 1942), which assumes an infinite array of equally spaced, identical Lorentz lines. The lineshape for this array, at a frequency ν from the centre of such a line is given by

$$f(\nu) = \sum_{j=-\infty}^{\infty} \frac{1}{\pi} \frac{\alpha_L}{(\nu - j\delta)^2 + \alpha_L^2} \tag{4.11}$$

where δ is the line spacing. This infinite sum can be converted into the analytic expression

$$f(\nu) = \frac{1}{\delta} \frac{\sinh(2\pi\alpha/\delta)}{\cosh(2\pi\alpha/\delta) - \cos(2\pi\nu/\delta)}. \tag{4.12}$$

The resulting equation for the frequency-averaged transmittance over an interval δ is thus

$$\overline{\tau}_{Elsasser} = \frac{1}{\delta} \int_{\delta} \exp\left[\frac{-SU\sinh(2\pi\alpha/\delta)}{\cosh(2\pi\alpha/\delta) - \cos(2\pi\nu/\delta)}\right] d\nu. \tag{4.13}$$

In general, this equation must be numerically evaluated, although it can be simplified for the cases of independent lines and weakly or strongly absorbing lines.

Several other regular models also exist (*e.g.*, Goody, 1964, p.144–150) assuming, for example, an infinite array of equally spaced Lorentz lines having different intensities or an infinite array of doublet lines. Again however, these models are not well suited to the irregularly spaced lines of the near-infrared spectrum of CH_4. The Elsasser model, for example, is better suited to the more regular spectra of linear molecules such as CO and N_2O.

4.2.4 Random Band Models

The apparently random nature of the near-infrared spectrum of CH_4, the consequence of the overlapping of many different bands, makes random band models more appropriate for fitting this spectrum. A variety of such models exist, but all assume that the lines in a spectral interval are randomly distributed, and define the model transmittance of the interval to be the transmittance averaged over all possible arrangements of line positions (Rodgers, 1976, p.16).

The expression for the transmittance in the general random model is derived as follows (Goody, 1964, p.154; Rodgers, 1976, p.18–19). The transmittance of a single line j of equivalent width W_j in interval $\Delta\nu \gg W_j$ is

$$\overline{\tau_j} = 1 - \frac{W_j}{\Delta\nu} \approx \exp\left(\frac{-W_j}{\Delta\nu}\right). \tag{4.14}$$

For randomly placed lines, it is possible to show that their frequency-averaged transmittances are multiplicative. With this property, the mean transmittance of N_0 lines in interval $\Delta\nu$, averaged over all possible line positions, is the product

$$\overline{\tau} = \prod_{j=1}^{N_0} \exp\left(\frac{-W_j}{\Delta\nu}\right) = \exp\left(\frac{-1}{\Delta\nu}\sum_{j=1}^{N_0} W_j\right) = \exp\left(\frac{-W}{\Delta\nu}\right) \tag{4.15}$$

where W is the total equivalent width in interval $\Delta\nu$. For cases where $\Delta\nu$ is not $\gg$ than W_j, the same expression will apply if adjacent spectral intervals are statistically similar to the interval of interest, as absorption within $\Delta\nu$ due to the wings of lines outside $\Delta\nu$ compensates for absorption outside $\Delta\nu$ due to the wings of lines inside $\Delta\nu$.

This transmittance can be expressed in terms of a line-strength-distribution function $N(S)$, where $N(S)\,dS$ is the number of lines in interval $\Delta\nu$ which have a line strength between S and $S + dS$. Using the definition of W (Equation 4.5), the general random model becomes

$$\overline{\tau} = \exp\left(\frac{-1}{\Delta\nu}\int_0^\infty N(S)W(S)\,dS\right) \tag{4.16}$$

$$= \exp\left(\frac{-1}{\Delta\nu}\int_0^\infty N(S)\int_{-\infty}^{+\infty}\left[1 - e^{-SUf(\nu)}\right]\,d\nu\,dS\right). \tag{4.17}$$

Evaluation of this expression for the transmittance thus requires specification of the lineshape and the line-strength-distribution function. Ideally, the latter should be a computationally manageable function which provides a good approximation of the line-strength distribution of the real spectrum. The two most widely used distributions are those of Goody and Malkmus, and the band models derived from these are discussed as follows.

4.2.4.1 The Goody Random Band Model

The Goody random band model (Mayer, 1947; Goody, 1952) assumes an exponential line-strength distribution having a total of N_0 lines of mean strength S_0 randomly spaced over the interval $\Delta\nu$. This distribution has the form

$$N(S) = \frac{N_0}{S_0}\exp\left(\frac{-S}{S_0}\right). \tag{4.18}$$

Substituting this expression into Equation 4.17 and integrating over S gives

$$\overline{\tau}_{Goody} = \exp\left(\frac{-1}{\delta}\int_{-\infty}^{+\infty}\frac{S_0 U f(\nu)}{1+S_0 U f(\nu)}\,d\nu\right) \tag{4.19}$$

where $\delta = \Delta\nu/N_0$ is the mean line spacing and is constant over $\Delta\nu$.

If the Lorentz lineshape, given in Equation 3.7, is used, this equation can be analytically integrated over ν to obtain

$$\overline{\tau}_{Goody-Lorentz} = \exp\left(\frac{-S_0 U/\delta}{\sqrt{1+S_0 U/\pi\alpha_L}}\right) = \exp\left(-1/\sqrt{\frac{1}{(S_0 U/\delta)^2}+\frac{1}{\pi S_0 U\alpha_L/\delta^2}}\right). \tag{4.20}$$

Explicitly expressing α_L in terms of T and P, as

$$\alpha_L = \alpha_L^0\frac{P}{P_0}\sqrt{\frac{T_0}{T}}, \tag{4.21}$$

gives the transmittance in the form

$$\overline{\tau}_{Goody-Lorentz} = \exp\left(-1/\sqrt{\frac{1}{(S_0 U/\delta)^2}+\frac{1}{\pi S_0 U\alpha_L^0(P/P_0)\sqrt{T_0/T}/\delta^2}}\right). \tag{4.22}$$

When used to fit experimental data, this averaged transmittance is generally represented in terms of two parameters, an absorption coefficient k_ν, and a pressure coefficient y_ν. These are defined as

$$k_\nu = \frac{S_0}{\delta} = \frac{\text{mean line strength}}{\text{mean line spacing}} \tag{4.23}$$

and

$$y_\nu = \frac{\alpha_L^0}{P_0\delta} = \frac{\text{self}-\text{broadened Lorentz half}-\text{width at } T_0, P_0}{P_0 \times \text{mean line spacing}}. \tag{4.24}$$

The Goody band model with the Lorentz lineshape can thus be expressed as

$$\overline{\tau}_{Goody-Lorentz} = \exp\left(-1/\sqrt{\frac{1}{(k_\nu U)^2}+\frac{1}{\pi k_\nu y_\nu U P\sqrt{T_0/T}}}\right). \tag{4.25}$$

If the Voigt lineshape, given in Equation 3.11, is used, the Goody model becomes

$$\overline{\tau}_{Goody-Voigt} = \exp\left(\frac{-2}{\delta}\int_0^{\infty}\frac{S_0 U V(x,y)}{1+S_0 U V(x,y)/\alpha_D}\,dx\right) \tag{4.26}$$

where x, y, and α_D are as defined in Equation 3.11. $V(x,y) = \alpha_D f_V(\nu)$ is an even function, allowing the limits of integration to be changed to those shown. As was done for α_L, α_D (given in Equation 3.6) can be expressed explicitly in terms of T, as

$$\alpha_D = \alpha_D^0\sqrt{T}. \tag{4.27}$$

Using this equation and substituting in k_ν (which is constant over the interval defining $\overline{\tau}$), the averaged transmittance becomes

$$\overline{\tau}_{Goody-Voigt} = \exp\left(-2k_\nu U\int_0^{\infty}\frac{V(x,y)}{1+k_\nu U\delta V(x,y)/\alpha_D^0\sqrt{T}}\,dx\right). \tag{4.28}$$

Solution of this equation for $\overline{\tau}$ thus requires numerical evaluation of two integrals.

4.2.4.2 The Malkmus Random Band Model

As an alternative to the Goody model, Malkmus (1967) proposed a line-strength distribution with an infinite number of lines, having the form

$$N(S) = \frac{N_0}{S} \exp\left(\frac{-S}{S_0}\right). \tag{4.29}$$

This distribution includes a $1/S$ weighting which provides a more realistic estimate of the number of weakly absorbing lines than the under-estimate of the Goody model. Substituting this expression into Equation 4.17 and integrating over S gives (Rodgers, 1976, p.22)

$$\overline{\tau}_{Malkmus} = \exp\left(\frac{-1}{\delta}\int_{-\infty}^{+\infty} \ln[1 + S_0 U f(\nu)]\, d\nu\right). \tag{4.30}$$

Again, both the Lorentz and Voigt lineshapes can be explicitly introduced into this equation. To obtain the expression with the Lorentz lineshape, the averaged transmittance is first converted to the general form

$$\overline{\tau}_{Malkmus} = \exp\left(\frac{-1}{\delta}\int_{-\infty}^{+\infty} \frac{S_0 U \nu}{1 + S_0 U f(\nu)} \frac{df(\nu)}{d\nu}\, d\nu\right). \tag{4.31}$$

Substituting the Lorentz lineshape into this equation and integrating over ν gives

$$\overline{\tau}_{Malkmus-Lorentz} = \exp\left(\frac{-2S_0 U/\delta}{1 + \sqrt{1 + S_0 U/\pi\alpha_L}}\right). \tag{4.32}$$

Finally, using Equations 4.21, 4.23, and 4.24, the averaged transmittance becomes

$$\overline{\tau}_{Malkmus-Lorentz} = \exp\left(-1/\left[\frac{1}{2k_\nu U} + \sqrt{\frac{1}{(2k_\nu U)^2} + \frac{1}{4\pi k_\nu y_\nu U P\sqrt{T_0/T}}}\right]\right). \tag{4.33}$$

The Malkmus model with the Voigt lineshape is obtained by substituting $V(x,y) = \alpha_D f_V(\nu)$ into Equation 4.30 to get

$$\overline{\tau}_{Malkmus-Voigt} = \exp\left(\frac{-2\alpha_D}{\delta}\int_0^{\infty} \ln\left[1 + \frac{S_0 U}{\alpha_D} V(x,y)\right] dx\right) \tag{4.34}$$

with α_D constant over the interval. Expressed in terms of the absorption coefficient and α_D^0, this becomes

$$\overline{\tau}_{Malkmus-Voigt} = \exp\left(\frac{-2\alpha_D^0\sqrt{T}}{\delta}\int_0^{\infty} \ln\left[1 + \frac{k_\nu U \delta}{\alpha_D^0\sqrt{T}} V(x,y)\right] dx\right). \tag{4.35}$$

Numerical evaluation of two integrals is thus also required in order to evaluate the Malkmus-Voigt model.

4.2.4.3 Temperature Dependence in Random Band Models

The equations that have been derived for the Goody and Malkmus random band models share a common limitation — their only temperature dependence is that of the Lorentz and Doppler line widths. The usual method of band-model analysis has been to fit the averaged transmittance as a function of temperature, pressure, and abundance, but only at a specific temperature.

Calculation of the band-model transmittance at temperatures other than those measured involves extrapolating from or interpolating between the models fitted at different temperatures. This is an unsatisfactory method, being computationally inefficient and liable to inconsistencies between users.

Calcutt (1984, p.5-8) and Calcutt *et al.* (1988) proposed that the temperature dependence of the absorption be explicitly included in the band model by giving the fitted absorption coefficient the same temperature dependence as that of the line strength. Referring back to Equation 3.2, the ratio of the line strength at a temperature T to that at a reference temperature T_0 can be expressed as

$$\frac{S(T)}{S(T_0)} = \left(\frac{T_0}{T}\right)^{1.5} \exp\left[1.439 E_l \left(\frac{1}{T_0} - \frac{1}{T}\right)\right] \tag{4.36}$$

where E_l is energy of the lower level in units of cm^{-1}, the vibrational partition function is assumed to be unity, and the stimulated emission term has been ignored. The expression for the temperature dependence of the band-model absorption coefficient follows directly from this equation, being

$$k_\nu(T) = k_\nu(T_0) \left(\frac{T_0}{T}\right)^{1.5} \exp\left[1.439 E_l \left(\frac{1}{T_0} - \frac{1}{T}\right)\right], \tag{4.37}$$

allowing both $k_\nu(T_0)$ and E_l to be parameters fitted by the model. This expression is easily incorporated into the equations for $\overline{\tau}$ that were derived above, as $k_\nu(T)$ is used wherever k_ν appears.

4.2.5 Empirical Models

Rather than using physically based band models, laboratory measurements of transmittance may be fitted with purely empirical models that make no assumptions about the fundamental line structure of the spectrum. The transmittance functions used in such models have often been extracted directly from the original data, making them more data-specific than the *a priori* analytical functions of the regular and random band models. One empirical model which includes temperature dependence in addition to pressure and abundance dependence is the simple exponential function

$$\overline{\tau} = \exp\left(-k_\nu U^a P^b T^c\right) \tag{4.38}$$

where a, b, and c are fitted exponents. This model has been generalised somewhat by Smith (1969) to the form

$$\ln(-\ln \overline{\tau}_{Smith}) = \ln k_\nu + a \ln U + b \ln P + c \ln T + \text{higher order terms.} \tag{4.39}$$

An intermediate approach is to make an empirical generalisation of an existing band model in an attempt to provide a better fit to laboratory spectra whose physical structure is only approximated by the band model. This approach was followed by Zachor (1968a, 1968b), who suggested that laboratory data could be fitted with an equation of the form

$$\overline{\tau} = g(\tau_{weak}, \tau_{strong}, M) \tag{4.40}$$

where τ_{weak} is the transmittance in the weak limit,

τ_{strong} is the transmittance in the strong limit, and

M is an adjustable parameter.

This function g should be asymptotic in the limits of weak and strong absorption, while the parameter M determines the transition between these two limits, thereby providing a closer fit in the region of intermediate absorption.

Zachor (1968a) rewrote the Goody-Lorentz model (Equation 4.20) in the form

$$\left(\frac{-1}{\ln \overline{\tau}}\right)^2 = \left(\frac{-1}{\ln \tau_{weak}}\right)^2 + \left(\frac{-1}{\ln \tau_{strong}}\right)^2 \tag{4.41}$$

and then generalised this to

$$\left(\frac{-1}{\ln \overline{\tau}}\right)^2 = \left(\frac{-1}{\ln \tau_{weak}}\right)^2 + \left(\frac{-1}{\ln \tau_{strong}}\right)^2 + M\left(\frac{-1}{\ln \tau_{weak}}\right)\left(\frac{-1}{\ln \tau_{strong}}\right). \tag{4.42}$$

Analytic formulation of this equation requires explicit expressions for the transmittance in the weak and strong limits. For the weak limit of absorption, it is easily demonstrated that both the Goody-Lorentz and Malkmus-Lorentz models reduce to $\overline{\tau} = \exp(-S_0 U/\delta)$ as $SU/\pi\alpha_L \to 0$, thus giving

$$\tau_{weak} = \exp(-k_\nu U). \tag{4.43}$$

However, the strong limit of absorption differs from model to model, for example, being $\overline{\tau} = \exp(-\sqrt{\pi S_0 U \alpha_L}/\delta)$ for the Goody-Lorentz model and $\overline{\tau} = \exp(-2\sqrt{\pi S_0 U \alpha_L}/\delta)$ for the Malkmus-Lorentz model, as $SU/\pi\alpha_L \to \infty$.

Zachor (1968a) preferred to use the more general formula for the strong limit of absorption which was derived by King (1964) to account for line distributions which differed from the ideal regular and random cases. In this formula, the transmittance is defined in terms of the incomplete gamma function, $P(n, x)$:

$$\tau_{strong} = 1 - P\left(n, \left[n\Gamma(n)\sqrt{4S_0 U \alpha_L/\delta^2}\right]^{1/n}\right) \tag{4.44}$$

$$= 1 - P\left(n, \left[n\Gamma(n)\sqrt{4k_\nu y_\nu U P\sqrt{T_0/T}}\right]^{1/n}\right) \tag{4.45}$$

where

$$P(n, x) = \frac{1}{\Gamma(n)}\int_0^x t^{n-1}\mathrm{e}^{-t}\,dt, \tag{4.46}$$

$\Gamma(n)$ is the gamma function, and

n is an adjustable parameter.

When $n = 1/2$, this transmittance reduces to the strong limit of the Elsasser model, when $n = 1$, it reduces to the strong limit of the general random band model with Lorentz lines, and $n > 1$ represents clustering of lines. The Zachor-King model thus becomes

$$\left(\frac{-1}{\ln \overline{\tau}}\right)^2 = \left(\frac{1}{k_\nu U}\right)^2 + \left(\frac{-1}{\ln \tau_{strong}}\right)^2 - M\left(\frac{1}{k_\nu U}\right)\left(\frac{1}{\ln \tau_{strong}}\right) \tag{4.47}$$

or

$$\overline{\tau}_{Zachor-King} = \exp\left[-1/\sqrt{\left(\frac{1}{k_\nu U}\right)^2 + \left(\frac{-1}{\ln \tau_{strong}}\right)^2 - M\left(\frac{1}{k_\nu U}\right)\left(\frac{1}{\ln \tau_{strong}}\right)}\right] \tag{4.48}$$

where τ_{strong} is given by Equation 4.45.

An additional generalisation of this model was proposed by Gibson and Pierluissi (1971). They introduced a scaling parameter for the $(-1/\ln \tau_{strong})^2$ term, expressing the transmittance as

$$\left(\frac{-1}{\ln \overline{\tau}}\right)^2 = B_w\left(\frac{1}{U}\right)^2 + B_s\left(\frac{-1}{\ln \tau_{strong}}\right)^2 + B_{ws}\left(\frac{1}{U}\right)\left(\frac{1}{\ln \tau_{strong}}\right) \tag{4.49}$$

where B_w and B_s are positive and $B_{ws}^2 < B_w B_s$. These three coefficients thus provide complete flexibility in weighting the three terms of the model. Comparing this with Equation 4.47,

$$B_w = \left(\frac{1}{k_\nu}\right)^2, \quad B_{ws} = \frac{-M}{k_\nu}, \tag{4.50}$$

and B_s is the additional scaling factor. Like Zachor (1968a, 1968b), Gibson and Pierluissi (1971) used King's (1964) formula for the strong limit of absorption. This model can thus be written simply as

$$\overline{\tau}_{Gibson-Pierluissi} = \exp\left[-1/\sqrt{\left(\frac{1}{k_\nu U}\right)^2 + B_s\left(\frac{-1}{\ln \tau_{strong}}\right)^2 - M\left(\frac{1}{k_\nu U}\right)\left(\frac{1}{\ln \tau_{strong}}\right)}\right] \tag{4.51}$$

with $|M| < \sqrt{B_s}$, and τ_{strong} again defined by Equation 4.45.

4.3 Previous Band Modelling of Methane

As was shown in Figure 3.2, the absorption bands of CH_4 dominate the visible and infrared spectra of all of the outer planets. As a result, CH_4 has been the subject of various laboratory studies aimed at interpreting these planetary spectra. This section presents a review of of these measurements, concentrating on those that were analysed in terms of band models. As will be seen, despite the work that has been done, there is still a serious lack of band-model parameters for CH_4 in the NIMS spectral region. Because the spectral range of NIMS extends from 0.7 to 5.2 μm, the following discussion deals with previous studies in both the visible and the infrared.

4.3.1 Band Modelling in the Visible Region

Early laboratory studies of CH_4 dealt with the visible bands, using photographic plates to obtain long-pathlength spectra for the purposes of identifying features in planetary spectra and estimating CH_4 abundances (Mecke, 1933; Kuiper, 1950; Dunham, 1952). Many features in the visible spectra of the outer planets remained unidentified until laboratory spectra with sufficiently large CH_4 abundances were available. Owen (1967), Lutz and Ramsay (1972), and Owen *et al.* (1974) used spectra recorded with CH_4 abundances of 1000's of m-amagat

to show that several such features near 7500 Å and 6400 Å in the spectra of Uranus and Neptune were due to CH_4 absorptions. However, Lutz and Ramsay (1972) concluded that without low-temperature, long-pathlength laboratory spectra of CH_4 (none being available at that time), accurate determination of planetary CH_4 abundances was impossible. Several years later, Lutz *et al.* (1976) made the first laboratory measurements of curves of growth and integrated band strengths for four CH_4 bands between 4000 and 6000 Å, using spectra recorded at CH_4 abundances ranging from 439 to 4637 m-amagat, although still at room temperature.

Recognising the need for quantitative measurements of the visible spectrum of CH_4, Dick and Fink (1977) undertook a systematic study, recording pure CH_4 spectra from 6200 to 10600 Å at a resolution of $\sim$3 Å, using 35 pressure-pathlength combinations at 298 K to obtain abundances from 0.93 to 960 m-amagat. Pure and H_2-broadened CH_4 spectra were recorded over the less strongly absorbing 4200 to 6200 Å region for a smaller number of large abundances. The H_2-broadened spectra were searched for simultaneous transitions between H_2 and CH_4, whose existence had been suggested by Danielson (1974), but no such features were discovered. The pure CH_4 spectra displayed a series of broad absorption bands, each of which was calculated to consist of hundreds of combination and overtone vibrational sub-bands.

This complexity, and the fact that no quantum number assignments had been made for any of the measured bands, led Fink *et al.* (1977; and also presented by Benner, 1979) to use the Goody random band model with the Lorentz lineshape to analyse their spectra. They averaged the measured transmittances over 10 Å intervals and fitted these degraded spectra with Equation 4.25. Absorption coefficients were fitted for wavelengths between 4400 and 10360 Å, with uncertainties ranging from several percent for the regions of strong and medium absorption for which 35 independent spectra were available, up to as much as 10% for the weaker bands for which fewer spectra were available. Pressure coefficients could only be derived for wavelengths between 8590 and 10190 Å, as the pressure effect was found to be negligible for shorter wavelengths, and an accuracy of $\sim$30% was estimated for the values that were obtained.

Fink *et al.* (1977) drew several conclusions from their fitted parameters. Their values for y_ν (varying from 3 to 14 atm^{-1}) were found to be significantly greater than those previously obtained from band modelling of the infrared bands of CO_2 and H_2O (generally less than 2 atm^{-1}), suggesting that the density of CH_4 lines was much higher than that of either of these two gases. Using a pressure-broadening coefficient of 0.085 cm^{-1}/atm, they estimated an average line spacing of 0.01 cm^{-1}, a value much lower than the line half-width, therefore implying a significant overlap of spectral lines. For all of the bands except the strongest two at 8900 and 9980 Å, a simple exponential absorption law was sufficient to fit the data, but Fink *et al.* predicted that a measurable pressure effect should exist in the infrared region of the CH_4 spectrum, where the number of sub-bands is smaller and a more definite line structure should replace the pseudo-continuous effect of overlapping lines. Despite the resulting inability to derive atmospheric pressures from the band-model results, the fitted absorption coefficients

provided the first quantitative picture of the CH_4 spectrum up to 1 μm. (An earlier tabulation of CH_4 band-model parameters for the bands at 7270, 8610, and 8890 Å, performed by Woodman (1976), gave dubious results, as discussed by Benner (1979, p.36) and Podolak and Giver (1979).) The results of Fink *et al.* (1977) have therefore been used by numerous groups, for example, Wallace and Smith (1977), Benner (1979), Fink *et al.* (1980), Wallace (1980), and Cruikshank and Apt (1984), in the interpretation of visible spectra of the five outer planets and the satellites Titan and Triton.

The measurements by Dick and Fink (1977) were soon followed by those of Giver (1978), who similarly recorded spectra over 4300 to 10900 Å at 0.5–0.6 Å resolution. However, he was able to obtain pathlengths of 50 to 1200 m and pressures of 0.03 to 18.5 atm, thus achieving CH_4 abundances from 3 to 17500 m-amagat. Assuming the absorption to be independent of pressure, absorption coefficients were derived from transmittances sampled at 10 cm^{-1} intervals simply by applying Beer's Law. An attempt to obtain pressure coefficients for the 8890 Å band led to the conclusion that it was generally greater than 5 atm^{-1}. When the pressure coefficients determined by Fink *et al.* (1977) were assumed and the absorption coefficients recalculated, k_ν increased by 6.6% and 7.9% in the 8890 and 9990 Å bands, respectively. This was deemed to be a minor effect and so the absorption coefficients were integrated over bands defined by absorption minima to obtain a set of band intensities. Giver (1978) compared his absorption coefficients with those of Fink *et al.* (1977), revealing good agreement at longer wavelengths, but generally smaller absorption coefficients for his data at wavelengths below 7000 Å. The discrepancies between these two sets of results were attributed to the use of different sampling intervals and to noise in the spectra of Fink *et al.* (1977) due to turbulence caused by changes in the cell temperature.

Additional spectra of the 7270, 8890, and 10000 Å bands of CH_4 were recorded by Podolak and Giver (1979). Five independent spectra were obtained, keeping the CH_4 abundance constant at $\sim$96 m-amagat while varying the pressure from 0.125 to 2 atm and the pathlength from 50 to 800 m. The absorption and pressure coefficients derived from these spectra proved to be in good agreement with those of Fink *et al.* (1977). Podolak and Giver (1979) used these coefficients in both the Goody-Voigt and Malkmus-Voigt band models in their modelling of the atmosphere of Titan. They found that the latter provided greater absorption for a given CH_4 abundance, and suggested that with its inclusion of many more weak lines, it might be more appropriate for modelling of the overtone and combination bands of the visible CH_4 spectrum.

More recently, Lutz *et al.* (1982) continued their laboratory investigation of the visible spectrum of CH_4, extending their measurements into the 6000–7600 Å region. They recorded spectra at 40 pressure-pathlength combinations at room temperature, with CH_4 abundances ranging from 24 to 3897 m-amagat. As before, these spectra were used to derive equivalent widths, curves of growth, and integrated band strengths for four red bands, demonstrating that the curves of growth were independent of pressure. This was found to be true over a pressure

range of 0.1 to 2.0 atm, again supporting the hypothesis that the CH_4 lines in the visible spectrum are so densely packed that a pseudo-continuous absorption results.

All of the laboratory studies of visible CH_4 spectra discussed thus far have been conducted at room temperature. However, several authors have tried to predict the behaviour of the visible absorption and pressure coefficients of CH_4 at lower temperatures relevant to the atmospheres of the outer planets. Lutz *et al.* (1982) have suggested that the superposition of large numbers of vibrational bands may lead to the curves of growth being independent of temperature, while Benner (1979, p.166) and Fink (1982, p.577) have also suggested that the absorption coefficients of CH_4 are not strongly dependent on temperature. This hypothesis is supported by measurements of the integrated band strengths of liquid CH_4 at 95 K which were made by Ramaprasad *et al.* (1978) for bands between 6190 and 19400 Å. These were converted to gas-phase band strengths and found to be in generally good agreement with the room-temperature band strengths of Lutz *et al.* (1976), Fink *et al.* (1977), and Giver (1978). They differed from the gaseous values by 0.3% to 31%, with these discrepancies probably largely due to uncertainties in the extent of the bands. In general, although the band shapes are expected to change somewhat with temperature, little variation is predicted in the total band strengths. This is because most CH_4 molecules are already in the ground vibrational state at room temperature, and the integrated absorption strength of a band arising from the ground state does not change with temperature.

Some measurements of the absorption coefficient as a function of temperature were finally provided by Smith *et al.* (1990), who measured absorption coefficients for the 6190 Å CH_4 band between 100 and 290 K. They found that the absorption coefficient at the centre of the band increased with decreasing temperature while the absorption strength in the wings decreased, thus resulting in a narrowing of the band profile at lower temperatures. With this narrowing, the temperature dependence of the integrated band strength may have been small, but no calculations of this quantity were performed. Contrary to the suggestion of Fink *et al.* (1977), these measurements suggest that the visible absorption coefficients of methane do exhibit noticeable temperature dependence.

In the absence of any low-temperature measurements, knowledge of the temperature dependence of the pressure coefficients of CH_4 remains even more uncertain. Benner (1979, p.166–169) predicted that it is likely to have a strong temperature dependence, possibly increasing by a factor of 1.5 or decreasing by a factor of 8, depending on the variations in the line spacing and line width. At low temperatures, the total band intensity is likely to be redistributed into a smaller number of low J lines, resulting in an increase in the average line spacing. Benner (1979) calculated that this spacing would increase by factors of 2 to 8 between temperatures of 300 and 80 K, while Fink *et al.* (1980) found that increases of 10, 16.5, and 12 were required for the 10000, 8900, and 7200 Å bands, respectively, in order to match their band-model synthetic spectra with spectra of Pluto (at a nominal temperature of 60 K).

Clearly, although the visible spectrum of CH_4 has been the subject of a series of laboratory studies, there is still a critical need for low-temperature measurements of its spectral parameters. Even the most recent study of this region (Mickelson *et al.*, 1991) has been conducted at room temperature. This work again concentrated on the 6190 Å band, deriving absorption coefficients by applying Beer's Law to spectra recorded using 1400 m-amagat of CH_4. Averaging of the original 1 Å results onto a 10 Å grid gave absorption coefficients that were generally consistent with the results discussed above.

Summarising, quantitative analyses of the CH_4 spectrum do exist for the 0.7 to 1.1 μm region of the NIMS spectral range. However, the lack of low-temperature data appropriate to the Jovian atmosphere remains the major drawback of these studies. In addition, most of these studies have been limited to simply deriving the absorption coefficient from Beer's Law. With the pressure dependence of the visible CH_4 absorption appearing to be weak, only Fink *et al.* (1977) and Benner (1979) have attempted to include it by applying a true band model. In the near-infrared region of the NIMS spectral range, the situation is somewhat different. At these frequencies, the number of overlapping overtone and combination bands decreases and the pseudo-continuous appearance gives way to line structure. Pressure dependence thus becomes measurable and full band modelling more relevant. It is this region of the spectrum which is the subject of the next section.

4.3.2 Band Modelling in the Near-Infrared Region

As was the case for the visible CH_4 spectrum, initial laboratory measurements of the near-infrared CH_4 spectrum were simply used as comparison spectra. For example, Fink and Larson (1979) recorded long-pathlength, room-temperature CH_4 spectra over 0.8–2.5 μm (4000–12500 cm^{-1}) specifically for comparison with spectra of Jupiter, Saturn, Titan, Uranus, and Neptune. This comparison revealed that most of the planetary spectral features seen at 3.6 cm^{-1} resolution in the 4900, 6400, 7850, and 9300 cm^{-1} windows could be identified as CH_4 absorptions (see Figure 3.2). Two additional sequences of laboratory spectra were recorded at a higher resolution (0.42 cm^{-1}), one of the R branch of the $3\nu_3$ band (9000–9200 cm^{-1}), and one of the $2\nu_3$ band (5800–6200 cm^{-1}). These sequences showed how the complexity of the infrared CH_4 spectrum increased as the CH_4 abundance was increased, with the regular line structure of both bands "degenerating into chaos" at the largest absorber amounts (1520 m-amagat for $3\nu_3$, and 47.2 m-amagat for $2\nu_3$). Fink and Larson (1979) also used curves of growth to model two broad absorption features at 6400 and 7900 cm^{-1}. They found that both features were independent of pressure, although being the result of simpler combination and overtone bands, these features did not have the pseudo-continuous nature of the visible bands.

The first band-modelling results for near-infrared CH_4 absorption were published by Apt *et al.* (1981), who used the data of Benner and Fink (1980). Their goal was to compare CH_4 spectra calculated at 10 cm^{-1} resolution using the Goody-Voigt band model with spectra calcu-

lated using line-by-line integration. Synthetic spectra were calculated over the region from 4190 to 4590 cm^{-1}, for temperatures of 296, 153, and 55 K, and CH_4 abundances of 0.013 and 0.40 m-amagat. For the 296 K spectra, the generally lower absorptions of the line-by-line calculation were attributed to the poor quality of the line data. This poor quality also contributed to the differences between the low-temperature spectra, however the lack of temperature dependence in the band-model parameters resulted in a poor extrapolation of the Goody-Voigt model, as it was unable to take account of the depopulation of higher energy levels which occurs at low temperatures. The authors attempted to overcome this problem by increasing the mean line spacing in the band model to make the total equivalent width match that of the line-by-line model at 153 and 55 K. The resulting band-model spectra provided a better match to the line-by-line spectra, but were still unable to match the detailed structure. Apt *et al.* (1981) concluded that although the available CH_4 line and band-model parameters were of insufficient quality to provide accurate analysis of planetary spectra, the actual techniques of both line-by-line and band modelling were valuable in the study of planetary atmospheres, with band modelling being particularly valuable when line data were unavailable.

The long-pathlength, room-temperature laboratory spectra of CH_4 used by Apt *et al.* (1981) are summarised by Benner and Fink (1980), but no qualitative or quantitative analysis is provided. These spectra were recorded from 4000 to 10000 cm^{-1}, and covered a wide range of pressures (0.01 to 6 atm) and CH_4 abundances (0.0003 to 2500 m-amagat), but again were limited to room temperature. Fink (1982) presents several sequences of these spectra, which qualitatively illustrate the complexity of the near-infrared CH_4 spectrum and how the absorption increases to saturation with increasing CH_4 abundance. Unfortunately, no comprehensive band modelling of these spectra has been published.

The first near-infrared low-temperature laboratory spectra of CH_4 to be measured and fitted with a band model were published by Silvaggio (1982). His spectra were recorded from 4000 to 6500 cm^{-1} at a resolution of 0.15 cm^{-1}, with CH_4 abundances of 0.004 to 4.75 m-amagat and temperatures of 273, 191, and 118 K. Both H_2- and He-broadened CH_4 spectra were also recorded, but no details of these are given. Using the theoretical formulation described in Silvaggio *et al.* (1980), the Goody random band model with the Voigt lineshape was used to fit transmittances averaged over intervals of 10 and 100 cm^{-1}. This allowed the mean absorption coefficient, line spacing, and Lorentz self- and foreign-broadening coefficients to be obtained from the data, although the self-broadened Lorentz half-width was fixed at 0.085 cm^{-1}. Unfortunately, only the 273 K spectra were fitted, and only for the regions 4000–4800 cm^{-1} and 5600–6500 cm^{-1}, although the transmittances predicted by the model were apparently in excellent agreement with the measured transmittances for the spectra that were fitted. The 273 K H_2-broadened CH_4 spectra were similarly fitted at 100 cm^{-1} intervals over 4100 to 4700 cm^{-1}, yielding an overall H_2-broadening coefficient of 0.03 cm^{-1}/atm $\pm$ 50% for the band. Equivalent width calculations performed by Cruikshank and Silvaggio (1979) using the Goody-

Voigt parameters fitted to the 273 K self-broadened CH_4 spectra at 100 cm^{-1} intervals provided evidence for the existence of a CH_4 atmosphere on Triton

The spectroscopy and band modelling performed in the present work are a logical extension of the work of Calcutt (1984). He undertook measurements of self- and H_2-broadened CH_4 spectra using the Short White Cell at the Rutherford Appleton Laboratory (see Chapter 5) specifically in support of the NIMS instrument. These spectra were recorded over 4000 to 10000 cm^{-1} at an original resolution of 0.25 cm^{-1}. For the self-broadened CH_4 spectra, six pressures from 0.1 to 1 bar, three pathlengths of 9.7, 14.5, and 19.3 m, and three temperatures of 296, 250, and 213 K were used, giving CH_4 abundances from 0.89 to 24 m-amagat. These conditions are illustrated in Figure 6.1, which also shows the greater range of laboratory conditions that was achieved in the present study.

In his original analysis, Calcutt (1984) degraded the spectra to NIMS resolution, convolving them with a triangle of 0.025 μm full-width half-maximum and sampling every 0.005 μm. For each temperature, these wavelength-averaged transmittances were fitted with four band models, the Goody-Lorentz, Goody-Voigt, simplified Zachor-King ($M = 0$), and Gibson-Pierluissi models. In addition, the Smith model was used to fit the transmittances for all three temperatures simultaneously. These fits showed that, for the range of frequencies and pressures covered by the data, the replacement of the Lorentz lineshape with the Voigt lineshape provided a significant improvement in the fit obtained with the Goody random band model. Even better fits were obtained for the Zachor-King, Gibson-Pierluissi, and Smith models, but their empirical nature made extrapolation outside the laboratory conditions unreliable. Calcutt (1984, p.5-9) tested the behaviour of the models when extrapolated, and found that when the pressure was extrapolated to 5 bar for the maximum measured absorber amount, the transmittances predicted by the Goody-Lorentz, Goody-Voigt, and Zachor-King models agreed to within the errors in the fits. When the CH_4 abundance was extrapolated to a typical Jovian abundance of 372 m-amagat at 5 bar, these three models agreed to within 0.05 in transmittance over 1.2 to 1.8 μm, but outside this range, this agreement was reduced, particularly above 1.8 μm. These findings emphasised the need for laboratory measurements and band modelling of CH_4 spectra under conditions simulating those of Jupiter, a need that has been partly fulfilled in this work.

Calcutt (1984) also recorded several H_2-broadened CH_4 spectra, using CH_4 pressures of 10, 20, and 76 torr, and several H_2 pressures up to 1 bar. The resulting CH_4 abundances were less than those obtained in the self-broadened experiment, requiring extrapolation of the Goody-Lorentz band model. The insensitivity of the transmittance to pressure resulted in large errors in the value of α_{Lf}/α_{Ls}, and so only a mean value was reported. This was found to be 0.69 ± 0.14, corresponding to a CH_4-to-H_2 broadening ratio of 1.4.

Using the same self-broadened CH_4 laboratory spectra, Calcutt *et al.* (1988) later re-analysed them for more general applications. In this case, the spectra were degraded using a triangular instrument function of 10 cm^{-1} full-width half-maximum, and sampled at 5 cm^{-1} intervals.

These degraded spectra were then fitted with a series of progressively more complex band models, beginning with the Weak Limit, followed by the Goody-Lorentz model, and then the Goody-Voigt model. For each of these models, the temperature dependence of the absorption coefficient was added. This explicit temperature dependence was found to give a satisfactory fit to the data, thereby allowing easy calculation of the transmittance at temperatures other than those measured. This improved upon the usual method of interpolating between models fitted at different temperatures. The Goody-Voigt model with $k_\nu(T)$ provided the best fit to the spectra, with the root-mean-square error between the fitted and measured transmittances generally less than 0.01. However, this fit could be obtained only by letting the Lorentz half-width vary unrealistically, indicating that although the Goody model is physically based, some caution must be applied to the interpretion of the fitted parameters.

In recent years, a widely used set of near-infrared CH_4 band-model parameters has been that of Giver *et al.* (1984; see also, Giver *et al.*, 1990). They recorded laboratory spectra of self-broadened CH_4 over 3760 to 9200 cm^{-1} at an original resolution of 1 cm^{-1}. These spectra were measured at temperatures of 295, 188, and 112 K, pathlengths of 3 to 61 m, and pressures from 0.0020 to 12.4 bar (although only up to 0.538 bar at 112 K), giving abundances of 0.0149 to 192.8 m-amagat. The Malkmus band model with the Voigt lineshape was used to fit the transmittances at each temperature at 10 cm^{-1} intervals. Only two parameters, the absorption coefficient and the pressure coefficient, were derived from the fits. The band-model parameters fitted to the 112 K spectra are the only such data currently available for near-infrared absorption of CH_4 at such a low temperature. Giver *et al.* (1984) note that the principal difference between their 112 K and 295 K spectra is a noticeable narrowing of the major absorption bands at the lower temperature.

Giver *et al.* (1988) later expanded on their earlier work by measuring more self-broadened CH_4 spectra at 112 K, 188 K, and room temperature, using a short-pathlength (5.7 cm) absorption cell. These low-abundance spectra were recorded from 4000 to 4760 cm^{-1}, specifically for the purpose of interpreting Triton spectra at these frequencies. They were combined with the previous spectra of Giver *et al.* (1984) in a Malkmus band-model fit, and the resulting band-model parameters were extrapolated to 55 K for use in a reflecting layer model. Cruikshank *et al.* (1989) also used this extrapolation in their analysis of Triton spectra. Unfortunately, no estimate of the reliability of this extrapolation was provided.

McKellar (1989) has recently recorded near-infrared, long-pathlength laboratory spectra of CH_4-N_2 mixtures at 77 K, the lowest temperature yet achieved for such measurements. These cover the region from 3800 to 9100 cm^{-1} at an original resolution of 0.14 cm^{-1}. At such a low temperature, the vapour pressure of CH_4 is only about 0.013 bar, and so with pathlengths of 66 and 88 m, the CH_4 abundances were limited to less than 4 m-amagat. The N_2 was included to pressure-broaden the CH_4 lines, allowing the spectrum to be fully resolved at 0.14 cm^{-1} resolution. Only three spectra were recorded, the first covering 3800–4800 cm^{-1} at 66 m with

0.29 m-amagat CH_4 and 0.064 bar N_2, the second covering 5000–6300 cm^{-1} at 88 m with 2.5 m-amagat CH_4 and 0.355 bar N_2, and the third covering 6700–9100 cm^{-1} at 88 m with 2.5 to 3.5 m-amagat CH_4 and 0.368 bar N_2. No band-model analysis was possible with such a small data set, but plots of all three spectra were presented at resolutions of 0.14, 2, 10, and 20 cm^{-1}. These can be used for comparison with spectra extrapolated from band models fitted to data at higher temperatures, thereby providing a means of testing the reliability of the band-model extrapolation.

In summary, quantitative analysis of the near-infrared spectrum of CH_4 over the NIMS spectral region remains incomplete. Although various sets of laboratory CH_4 spectra have been measured, only a few have been the subject of systematic analysis. Where long-pathlength spectra appropriate to Jovian conditions have been recorded (*e.g.*, Fink and Larson, 1979; Fink, 1982), they have been recorded at room temperature and no band-model analysis has been conducted. Where low-temperature spectra have been measured and modelled, the pathlengths have been short and the abundances small. The 77 K spectra of McKellar (1989) were insufficient for modelling, while the 118 and 191 K spectra of Silvaggio (1982) were omitted from the band-modelling analysis applied to his 273 K spectra, and even this was only performed from 4000 to 6500 cm^{-1}. Only Calcutt (1984) and Giver *et al.* (1984, 1988) have performed band-model analyses of low-temperature CH_4 spectra over a significant range of the near-infrared, and only Calcutt *et al.* (1988) have attempted to include temperature dependence. Even so, the spectra of Calcutt are limited to 4000–10000 cm^{-1} and those of Giver *et al.* to 3760–9200 cm^{-1}, so that neither extends as far as the 5 μm Jovian window. Furthermore, Calcutt's spectra are limited to a maximum abundance of 24 m-amagat and a minimum temperature of 213 K. Although Giver's largest abundance and lowest temperature were 192.8 m-amagat and 118 K, respectively, only 8 of his 98 spectra have CH_4 abundances greater than 40 m-amagat. With Jovian Curtis-Godson weighted mean temperatures and CH_4 abundances being as low as 107 K and as high as 773 m-amagat, respectively, at heights relevant to atmospheric sounding (see §6.1.1), there is clearly a need for more spectroscopy of CH_4 covering as wide a range as possible of the NIMS spectral region and of laboratory conditions relevant to Jupiter. The following chapter describes the laboratory resources used in the experiments which were performed in the present study to meet this need.

Chapter 5

Experimental Apparatus for the Methane Spectroscopy

The experimental spectroscopy described in this thesis was performed at the Laboratory Spectroscopy Facility at the Rutherford Appleton Laboratory (RAL). This facility includes a Fourier transform spectrometer and several gas absorption cells with their associated internal optics, transfer-optics tanks, and gas handling, vacuum and cryogenic systems. These cells allow the measurement of spectra over a range of temperatures, pressures, and optical pathlengths relevant to the atmospheres of Earth and other planets. The largest of these gas absorption cells is known as the Long White Cell, hereafter referred to as the LWC. This cell was used because it provided the longest pathlength (512 m) and lowest temperature (190 K) achievable at the facility, and therefore the closest simulation of conditions found in the Jovian atmosphere. For this study, the LWC was employed to measure near-infrared spectra of self- and H_2-broadened CH_4 in three stages, first at ~296 K, then at ~190 K, and finally at ~240 K, using pathlengths from 64 to 512 m, and pressures from 0.2 to 700 torr at each temperature.

This chapter describes the experimental resources that were used in obtaining the CH_4 spectra. Particular attention is given to the LWC, both because considerable effort was required in preparing it for use with flammable gas and in commissioning the new cryogenic heat exchanger, and because much of this information is not found elsewhere. Other elements of the experimental apparatus and design are also discussed where relevant, beginning with a brief discussion of the spectrometer.

5.1 The Spectrometer

5.1.1 The Bomem Fourier Transform Spectrometer

The spectra presented in this work were recorded with a commercial Bomem DA3.002 Fourier transform spectrometer having a maximum unapodised resolution of 0.0024 cm^{-1}. Figure 5.1 shows the optical layout of this instrument, which is described in the *Bomem DA3.002 Spec-*

trophotometer System Manual (1981). It operates as a Twyman-Green interferometer, which is similar to the basic Michelson interferometer but uses a point source instead of an extended source and a collimated beam instead of a non-collimated beam (Chamberlain, 1979, p.95; Hecht and Zajac, 1974, p.288,323).

Figure 5.1: The optical configuration of the Bomem DA3.002 spectrometer, with the interferometer on the left and the sample compartment on the right (Remedios, 1990, p.89).

As illustrated, an ellipsoid mirror focusses light from the source (which can be switched between a globar and a quartz-halogen lamp) through the filter wheel onto an iris with an adjustable diameter. A flat mirror then directs the light onto a paraboloid mirror which has a focus at the iris and which therefore generates a collimated beam. This beam is directed to the beamsplitter, where it is divided into two beams, the first transmitted towards a fixed flat mirror and the second reflected towards a flat mirror which moves in the vertical direction. These mirrors reflect the beam back to the beamsplitter where they recombine to form an interferometrically modulated beam whose intensity is dependent on the optical path difference between the two arms of the interferometer and on the frequency of the radiation. The modulated beam then leaves the interferometer section of the Bomem and enters the sample compartment, where a flat rotateable mirror, mounted at 45° to the incoming vertical beam, can send the beam in one of five possible directions. For experiments with the LWC, the collimated beam is directed out through the back of the sample compartment and travels via the transfer optics and the LWC optics (see §5.2.5) to a paraboloid mirror identical to that in the interferometer. This mirror focusses the beam onto the first focus of an ellipsoid mirror which finally focusses the beam onto the detector.

The signal recorded by the detector is the interferogram, the intensity as a function of the optical path difference between the two components of the modulated beam. An analogue-to-digital converter generates a digital version of the interferogram from the analogue output of the detector preamplifier. The digitised signal is sent to a High Speed Vector Processor (HSVP), where it is numerically filtered and phase corrected in real time. The HSVP then Fourier analyses the interferogram to produce the spectrum, the intensity as a function of frequency. Both the interferogram and the spectrum are stored on a PDP 11/73 computer, which is also used to set up the operating parameters and to run the Bomem.

The alignment of the moving mirror is of critical importance in ensuring optimum interference modulation. Precise parallel displacement of the moving mirror in the Bomem spectrometer is achieved with a technique called "dynamic alignment", whereby the mirror alignment is monitored with the aid of a HeNe laser beam which is also directed through the Bomem optical path (*Bomem System Manual*, 1981, p.3-16–17). This provides an interferogram which can be used to determine any deviations from optimal alignment, generating voltages which operate electromagnetic tilt transducers on the moving mirror. This method is designed to provide less than 10^{-6} radians root-mean-square angular deviation from optimum alignment, and if the alignment is worse than this, the current scan is aborted and a new one begun. The Bomem also generates a third interferogram from an internal white light source which is used to determine the zero path difference between the two mirrors and to start the recording of the infrared interferogram. Further details of the Bomem design and operation, and of the associated computer software can be found in the the *Bomem System Manual* (1981).

5.1.2 Fourier Transform Spectroscopy

The basic principle of Fourier transform spectroscopy (hereafter, FTS) is that the interference pattern generated by a two-beam interferometer (as a function of the optical path difference between the two beams) is the Fourier transform of the power distribution of the light incident upon the interferometer (as a function of frequency). FTS is of particular advantage to the present work because it allows spectra to be recorded over thousands of wavenumbers, with the entire spectral range measured simultaneously. Comprehensive discussions of FTS theory can be found in many texts (*e.g.*, Chamberlain, 1979; Griffiths and de Haseth, 1986; Richards, 1967), and Remedios (1990) provides a concise review with particular reference to those aspects relevant to operations with the Bomem spectrometer.

The following is a very brief treatment of the underlying theory, introducing some concepts referred to in Chapter 6. Derivation of the intensity of the interferometrically modulated output beam in an ideal two-beam interferometer leads to the equations for the interferogram-spectrum Fourier transform pair

$$I(\delta) \;=\; \frac{1}{2}\int_{-\infty}^{\infty} B(\nu)\cos(2\pi\nu\delta)\,d\nu \quad Watts \tag{5.1}$$

$$B(\nu) \;=\; 2\int_{-\infty}^{\infty} I(\delta)\cos(2\pi\nu\delta)\,d\delta \quad Watts/cm^{-1} \tag{5.2}$$

where $I(\delta)$ is the interferogram,

$B(\nu)$ is the spectral intensity,

δ is the optical path difference, and

ν is the frequency in wavenumbers.

The signal measured by an a.c.-coupled detector is thus $I(\delta)$, allowing the spectrum $B(\nu)$ to be calculated by computing the inverse Fourier cosine transform of the interferogram.

In practice, the two-beam interferometer is never ideal and the transform pair never exact. Because the interferogram is recorded over a finite optical path difference $\pm D$ rather than over $\pm\infty$, the computed spectrum becomes a convolution of the source function with an instrumental lineshape function, thereby limiting the achievable resolution. The lineshape function can be shown to be a $\mathrm{sinc}(2\pi\nu D)$ function, which gives rise to alternating negative and positive side lobes which introduce errors into the computed spectra. These side lobes can be suppressd by multiplying the interferogram by a smooth cut-off function before taking the inverse Fourier transform, a technique known as apodisation, which has the additional effect of increasing the width of the central peak and reducing the resolution. Numerous apodisation functions exist (*e.g.*, Griffiths and de Haseth, 1986, p.16–25; Norton and Beer, 1976) which vary in how well they suppress the side lobes and how much they degrade the resolution. The choice of function depends on the desired compromise, and in this work, as discussed in §6.1.2, the strongest apodisation available with the Bomem was used because the CH_4 spectra were already being recorded at a low resolution.

An additional practical problem with FTS is that there is usually a phase difference between the optical paths traversed in the two arms of the interferometer. Although a compensating plate can be introduced into the fixed mirror arm to ensure that both beams pass through the same thickness of glass, frequency-dependent phase errors can still be present. In the case of the Bomem, phase correction is performed with the aid of a low-resolution interferogram. The phase angle, which is a slowly varying function of frequency, can be calculated after performing a complex Fourier transform of this interferogram, using

$$\tan[\phi(\nu)] = \frac{\mathrm{Imag}[B\ (\nu)]}{\mathrm{Real}[B\ (\nu)]} \tag{5.3}$$

where $\phi(\nu)$ is the phase angle spectrum, and the imaginary component results from the addition of sine components to the interferogram due to the phase errors (Chamberlain, 1979, p.175; Griffiths and de Haseth, 1981, p.26,94). By convolving the Fourier transform of this spectrum with a high-resolution interferogram, a phase-corrected interferogram is generated to which only a cosine Fourier transform need be applied in order to obtain the final high-resolution phase-corrected spectrum. During the spectroscopic measurements of this work, a low-resolution phase spectrum was recorded before every CH_4 spectrum, in order to perform this phase correction.

Further discussion of the practicalities of FTS can be found in the texts referenced above. For the purposes of this work, the CH_4 spectra recorded with the Bomem were of relatively low resolution (0.25 cm^{-1}), as seen in Chapter 6, and were further degraded for the purposes of band modelling. Hence, the high-resolution capability (with a corresponding need for great accuracy) of the Bomem was never utilised, however, the extensive spectral range of the Bomem was used to full advantage.

5.2 The Long White Cell

5.2.1 The Mechanical Design of the Long White Cell

The LWC is a multiple-pass gas absorption cell designed for use with flammable, toxic, and corrosive gases. It consists of two stainless steel cylindrical shells with one mounted concentrically inside the other. The volume within the inner cylinder is the gas absorption cell, and the volume between the two cylinders is the vacuum annulus, which thermally isolates the inner vessel during operations at low temperature. The outer cylinder is 9000 mm long, has an internal diameter of 1000 mm, and is mounted on a support frame whose feet are bonded to anti-vibration pads. The endplates of the outer cylinder are flat stainless steel plates 25 mm thick, reinforced by ribs welded to the inside face, and including ports for the viewing and beam windows, the mirror adjustors, and a gas feedthrough.

Welded at fixed points along the inside of the outer cylinder are two tubes which serve as support rails for the inner cylinder. This cylinder is 8635 mm in length, 750 mm in internal diameter, and 3.81 m^3 in volume, making the volume of the vacuum annulus 3.25 m^3. The inner vessel is designed to the 1977 A.S.M.E. Pressure Vessel Code Section VIII, Division 1, for a maximum working pressure of 5 bar over temperatures from 80 to 300 K. The inner cylinder is mounted on PTFE-insulated support feet welded to its outer surface, which position it concentrically within the outer cylinder and allow movement when the inner vessel contracts or expands. A PTFE-insulated bracket, bolted to the inner endplate at the single-mirror end, and welded to one of the outer-vessel support rails, positions the inner vessel axially and keeps its single-mirror end fixed during contraction and expansion. The endplates for the inner vessel are 38 mm thick, also reinforced by ribs on the inside face and including ports equivalent to those on the outer endplates.

Prior to starting the low-temperature experiments, all of the seals on the inner vessel were checked, and all rubber O-rings in contact with the inner vessel were replaced by indium seals and Raco spring-loaded PTFE seals (both rated down to 77 K). Indium seals were used on the inner-vessel endplates, the gas-handling input bellows, and the inner-vessel vacuum port. Raco seals were used for the CaF_2 windows, their housings, the inner-vessel vacuum port, and the shafts for the inner-vessel mirror adjustors. The housings for the mirror adjustors and the viewing windows were cemented in place with Silastic silicon rubber sealant (rated for 208 to

493 K, but known to work to far lower temperatures). As the outer vessel did not become significantly cold, pernuban rubber O-rings (rated for 240–300 K) and silicon rubber O-rings (rated down to 210 K) were sufficient for the outer-vessel seals.

5.2.2 The Optical Design of the Long White Cell

An overview of the optical layout of the Laboratory Spectroscopy Facility is provided in Figure 5.2, and the nomenclature introduced in this figure will be used in the discussions that follow. The optical design of the LWC is based on the multiple-pass cell first described by White (1942), providing a non-magnifying image relay system which allows long optical pathlengths to be obtained over a much shorter physical cell length. This is of particular advantage in the simulation of the atmospheres of the outer planets, for which long optical pathlengths are essential.

Figure 5.2: The optical configuration of the RAL Laboratory Spectroscopy Facility: the beam from the Bomem spectrometer enters the system at the beam switching mirror (Remedios, 1990, p.86).

Figure 5.3 shows the radiation paths through a White cell, which uses three identical concave spherical mirrors. Two of the mirrors, ML1 (the input mirror) and ML3 (the output mirror) are positioned next to each other at one end of the cell, and the third, ML2, is positioned at the opposite end, such that the centres of curvature of ML1 and ML3 are on the surface of ML2, and the centre of curvature of ML2 is midway between ML1 and ML3. With this arrangement, light enters the cell through an aperture next to ML2 and diverges to fill ML1. ML1 reflects and focusses the beam onto ML2, which reflects it back to fill ML3, which focusses it onto ML2 again. This process can be repeated many times, forming a series of focussed images of

the input aperture on ML2, the position of these images being determined by the fact that the object and image points of ML1 (and ML3) must be equidistant on either side of the centre of curvature of ML1 (or ML3). Adjustment of the distance between the centres of curvature of ML1 and ML3 is performed to obtain the desired number of images, n, on ML2, and hence the desired pathlength,

$$L = 2n + 2. \tag{5.4}$$

The first image off the edge of ML2 becomes the exit image, which emerges from the cell on the opposite side of ML2 from the entrance aperture.

Figure 5.3: The optical arrangement of a White cell (White, 1942).

The optical design of the LWC is a variation on that of White (1942) which was suggested by Bernstein and Herzberg (1948). By indenting the top half of ML2 on both sides, the images can be stacked in two parallel rows, thereby doubling the achievable pathlength. The even-numbered images are aligned in the upper row and the odd-numbered are in the lower row, with adjacent images within each row separated by twice the distance between the centres of curvature of ML1 and ML3. As ML1 and ML3 are adjusted to decrease this distance, more images appear, with the odd-numbered images moving towards the exit image, and the even-numbered images moving towards the entrance image so that the former (even) exit image moves onto the mirror and is reflected to produce a new odd-numbered image. This is seen in Figure 5.4, which shows the arrangement of images for the longest pathlength used in the present work.

5.2.3 Optical Components of the Long White Cell

The optical configuration employed for the CH_4 spectroscopy was the double stacking scheme described above. The three spherical mirrors used in the LWC are 305 mm in diameter, with a radius of curvature of 8000 $\pm$ 10 mm. The edges of these mirrors have been machined flat to give a horizontal "diameter" of 294 mm. In addition, the single mirror has been machined

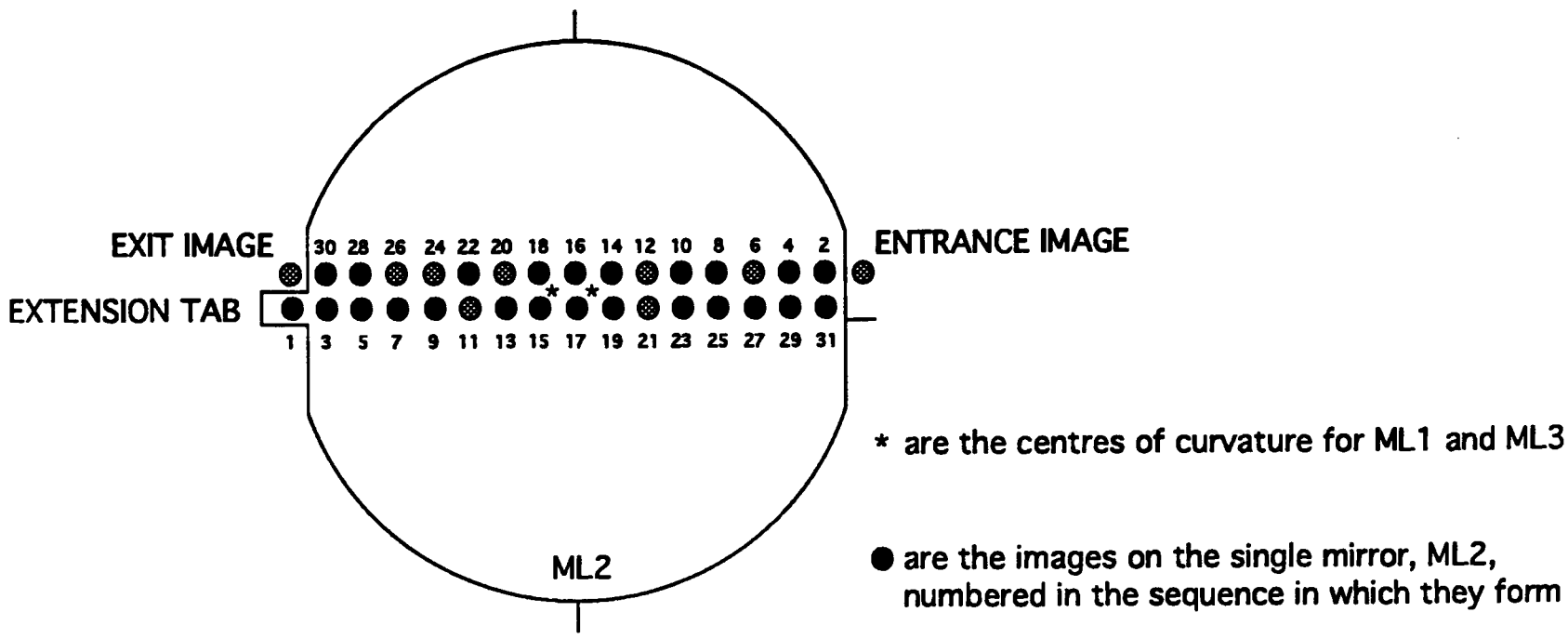

Figure 5.4: The alignment of images on the LWC single mirror (31 images, 512 m).

with a side extension that extends 20 mm beyond the flattened edge of the mirror and 15 mm above the horizontal axis of the mirror. This extension, or tab, is located on the exit side of ML2 and serves to fix the location of the first image (for three or more images), as illustrated in Figure 5.4. All three mirrors are manufactured from Zerodur glass ceramic which has a low coefficient of thermal expansion, thus minimising deformation of the optical surfaces when the LWC is cooled. The mirror surface form is specified spherical to $\lambda/10$ (for $\lambda = 546.1$ nm) to within 2 mm of the edge, including the 20 mm tab. The mirrors are coated with a gold finish which has a high reflectivity, typically 0.97–0.99, and is independent of wavelength over 1–10 μm (Wolfe and Zissis, 1978, p.7-81). The maximum LWC pathlength of 512 m was determined by the number of images which could be fitted onto the single mirror without overlapping (in turn determined by the input image size and by astigmatic and diffractive image spread) and by cumulative reflection losses which made images too faint to see.

The LWC mirrors are held in kinematic mounts which are designed to provide support with minimal deformation of the reflecting surfaces. At each end of the LWC, a horizontal platform welded to the inside of the inner vessel serves as a base for the mounts. The holder for each of the two adjacent mirrors is attached to the main body of its mount by three adjustable springs counter-balanced against the two pivots of the mirror adjusting mechanisms (see Figure 5.5), whereas the holder for the single mirror is firmly bolted to the main body of the mount. A series of five spring plungers and two positioning screws fit into a vee-shaped groove machined around the circumferential edge of the mirrors, fixing the mirrors in their holders.

During tests of the cryogenic system (§5.2.9), the LWC was found to be highly sensitive to vibrations of the cryogenic circulating pump. This sensitivity was reduced by bolting the baseplates of the mirror mounts more tightly to the support base and tightening the two positioning screws and the top spring-loaded screw for each of the mirrors. A piece of PTFE

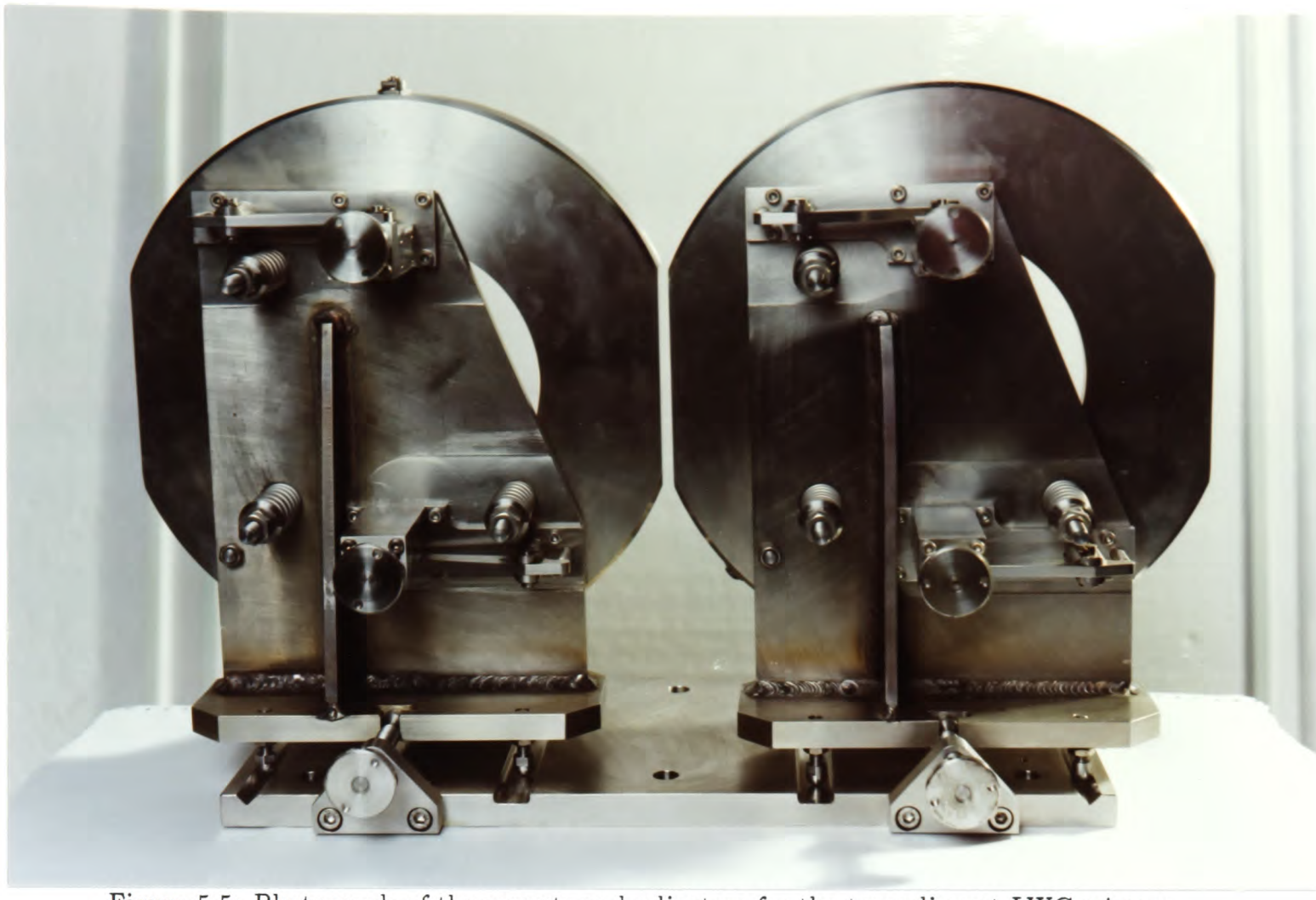

Figure 5.5: Photograph of the mounts and adjustors for the two adjacent LWC mirrors.

was clamped between the top screw and the mirror vee-groove in order to offset any possible differential contraction of the mirror mount relative to the mirror. These adjustments were also found to increase the stability of the mirrors during subsequent external adjustments, as they became less sensitive to very small adjustments and underwent less relaxation when the mirror adjustors were released.

The three mirrors can be adjusted from outside the LWC by simple rotation of control rods that feed through the inner and outer endplates and interlock with pivot, lever, and spring mechanisms at the back of the mirrors. Two of the adjustors for each mirror provide tilt around the vertical and horizontal axes in order to obtain the desired pathlength, while the two adjacent mirrors each have an additional focus adjustor that can be used to change their axial position to compensate for contraction and expansion of the inner vessel. The control rods through the outer endplate can be retracted and disengaged from those through the inner endplate in order to minimise thermal losses during cryogenic operations. During the low-temperature spectroscopy, it was also discovered that the signal at the detector was more stable when the adjustors were disengaged, suggesting that relaxation of the adjustors or gradual expansion of the LWC were causing movement of the adjustors and therefore of the mirrors. Thereafter, the adjustors were disengaged whenever spectra were being recorded.

Due to the weight of the mirrors (18 kg each) that is borne by the adjustors, they are sensitive to the alignment between the inner and outer mechanisms. Both the housings and rods became badly scratched during rotation and disengagement, making several adjustors too stiff to rotate and causing vacuum leaks. As a result, new housings and rods were machined

to replace the damaged ones. In a further effort to reduce the scratching and seizing up of the most heavily used adjustors, several of the new rods were machined from phosphor bronze rather than stainless steel and the diameter of the hole for the rod feedthrough in the housings was increased slightly.

The lubrication of the adjustors and the moving mirror-mount mechanisms also proved to be important. During one of the LWC cooling tests, all of the mirror adjustors seized up and became completely immovable. After removing both the mirror-adjustor housings with their rods and the mirror-mount adjusting screw mechanisms from the LWC and dipping them in liquid N_2 (LN_2), the latter were found to seize up when cold. It was discovered that these screw mechanisms had previously been lubricated with pump oil for room-temperature operations, so all eight were dismantled and cleaned with Genklene solvent. Once the oil had been removed, they rotated properly when dipped in LN_2. However, to improve the cryogenic lubrication, a low-temperature molybdenum disulphide lubricant (rated for $-200°C$ to $+450°C$) was applied to all moving parts in the mirror adjustors. All of the screw mechanisms were dipped in LN_2 after this lubrication to ensure that they worked properly, and no further seizure of the screws in the mirror mounts occurred.

The LWC endplates have ports for mounting of both infrared and viewing windows. The infrared windows are required only at the single-mirror end where they allow radiation from the spectrometer to enter and leave the cell. Two infrared windows are mounted in stainless steel housings that bolt to the inner endplate, and two are mounted in aluminium alloy housings that bolt to the outer endplate. For the CH_4 spectroscopy in this work, CaF_2 windows were used, as a single window provides >90% relatively flat transmittance over the entire NIMS spectral range (*e.g.*, *BDH Handbook*, 1988, p.41; Wolfe and Zissis, 1978, p.7-40). These windows were specified flat to $\lambda/2$ (λ=633 nm) on both faces, and polished to a standard spectroscopic finish. The CaF_2 windows were 80 mm in diameter, and 5 mm thick with an additional 1 mm wedge to prevent contamination of the beam by internally reflected components.

The pressure rating of the windows was determined by the equation for maximum stress, S_{max}, in a uniformly loaded circular plate of thickness t (Marks, 1941, p.477–480),

$$S_{max} = \frac{K D^2 P}{4t^2} \tag{5.5}$$

where K is a constant, dependent on the method of support,

$= 0.75$ for the clamped case, and 1.125 for the unclamped case,

D is the diameter of support, and

P is the pressure.

To avoid plastic deformation of crystal materials, S_{max} should be larger than the apparent elastic limit, F_a, by some safety factor, $SF > 1$. For the CaF_2 windows, with $t = 5$ mm, $D = 60$ mm, $K = 1.125$ (worst case), $F_a = 3.654 \times 10^7$ N/m^2 (from *BDH Handbook*, 1988, p.40), a safety factor of 9 is obtained for a pressure of 1.0 bar. This was the maximum pressure

used during the CH_4 spectroscopy.

Viewing windows are required through the inner and outer endplates at both ends of the LWC in order to allow the front surfaces of all three mirrors to be seen from outside the cell for optical adjustments. All eight windows were unwedged disks 12.7 mm thick and 125 mm in diameter, plate pyrex for the inner vessel, and plate glass for the vacuum vessel. For these non-crystalline materials, F_a is the tensile strength, which is 6.3×10^7 N/m^2 for the pyrex and 16×10^7 N/m^2 for the glass. With $D = 115$ mm, these windows were rated to a pressure of 1.0 bar with a safety factor of 27 for the pyrex and 69 for the plate glass.

During the cooling tests prior to the start of the low-temperature CH_4 spectroscopy, a misty film of pump oil condensed on the outer surfaces of the inner-vessel infrared and viewing windows. With all of the metallic surfaces of the inner vessel covered with multilayer insulation, the outer surfaces of these windows were the coldest points in the vacuum vessel. Pump oil present in the vacuum vessel due to backstreaming from the pumps and outgassing from the insulation therefore condensed on these surfaces. This had a double effect because the film on the input CaF_2 window partly scattered the incoming beam, while the film on the viewing windows made it impossible to see the faintest images. Prior to beginning the 190 K spectroscopy, the pump oil was cleaned from the CaF_2 windows, restoring the signal level at the detector to its previous room-temperature value. A new film quickly began to condense once the LWC was cooled down again, but the signal level did not drop, so the spectroscopy proceeded. During the course of the 190 K measurements, the growth of the film on the viewing windows made it increasingly difficult to see the fainter images on the single mirror, limiting the maximum pathlength to 416 m, instead of 512 m. Therefore, before starting the 240 K spectroscopy, the LWC was again warmed up and the viewing windows at the double-mirror end of the LWC were cleaned. Although the visibility through these windows also deteriorated during the 240 K measurements, the 512 m spectra were recorded first and the pathlength was then stepped down through its sequence, so that fewer images were needed on the single mirror as the images became more difficult to distinguish.

5.2.4 The Transfer Optics for the Long White Cell

Transfer-optics tanks are located between the spectrometer and the LWC, and between the LWC and the detector. The first of these is the input-transfer-optics tank which directs light from the spectrometer into the LWC, and the second is the output-transfer-optics tank which directs the output beam from the LWC onto the detector. Figure 5.2 shows the path traversed through the system by the light beam, and the following description uses the nomenclature in that figure. The collimated beam which emerges from the back of the spectrometer passes through a bellows, tube, and VAT pneumatic gate valve assembly into the side of the input tank. There it is reflected through an angle of about 100° by flat mirror F4, and onto spherical mirror M3 at the back of the input tank. M3 is 100 mm in diameter, with a 400 mm radius of curvature.

Its purpose is to reflect the collimated beam back through the tank and a connecting tube and bellows, through the outer input infrared window, the vacuum vessel, the inner window, and into the inner vessel, producing a focussed image of the Bomem iris at the entrance aperture of the LWC optics (200 mm from M3). The mounts for both F4 and M3 include vernier screws for adjusting the mirror positions in the horizontal, vertical, and axial directions in order to optimise the focus of the input image.

Once the beam has undergone multiple reflections within the LWC, it exits on the opposite side of the single mirror, passes back through the inner output infrared window, the vacuum vessel, the outer window, another connecting tube and bellows, and into the output-transfer-optics tank. At the far end of this tank, it is reflected off spherical mirror M4, identical to M3. This collimates the beam and directs it back onto parabolic mirror P1, which is 100 mm in diameter, 28° off axis, and identical to the collimator inside the Bomem. Reflecting the beam via a small flat mirror, F5, this produces a focussed image of the LWC exit aperture on the first focus of the detector-house ellipsoid, which in turn produces an image at its second focus, located on the sensitive element of the detector. M4 has the same three vernier adjustors as M3, and both F5 and P1 have adjusting screws to allow optimisation of the focus on the detector.

5.2.5 Alignment of the Long White Cell Optics

The optical alignment of the LWC is a sequential process involving both the transfer optics and the LWC mirrors. It was performed several times during experimental preparations, using the quartz-halogen source and the CaF_2 beamsplitter in order to provide visible light for monitoring the adjustments. With the VAT valve between the spectrometer and the input-transfer-optics tank open, the collimated beam is directed out of the back port of the Bomem and onto F4. The screws on the mount for F4 are adjusted to make the beam fill M3, and this mirror is then adjusted to give a focussed image of the Bomem iris at the LWC input image position. The adjustment of M3 is best monitored by optimising the filling of the input LWC mirror ML1, ensuring that none of the beam is intercepted by the back of the single mirror ML2, or lost off the edges of ML1.

At this point, the adjustment of the input optics is complete and that of the LWC mirrors begins. Using a telescope to look through the viewing windows at the double-mirror end of the LWC, the focus and tilt adjustors for ML1 are rotated to position the first focussed image on ML2. If the minimum total pathlength is desired, this first image will be near the centre of ML2, but for longer pathlengths it must be centered on the extension tab at the edge of ML2. This image is reflected back down the cell to fill the output mirror ML3, and so the vertical and horizontal tilts of ML2 are adjusted to centre the beam on ML3 with no loss off the edges. Adjustment of the tilts and focus of ML3 is then performed to either direct the beam immediately out through the LWC output infrared windows without any further reflections, or (if the first image on ML2 is located on the tab) to obtain a longer pathlength by aligning the

appropriate number of focussed images on the single mirror.

With ML3 set such that the output beam from the LWC is centered on the spherical mirror M4 in the output-transfer-optics tank, M4 is positioned to fill the off-axis paraboloidal mirror with the newly collimated beam. The detector housing is bolted onto the side port of the output tank, and an aluminium cylinder of the same size as the detector is mounted in it. The first order adjustment of the paraboloidal and flat mirrors P1 and F5 is performed by eye to produce a sharply focussed image on cross hairs centered on a translucent cover over the base of the cylinder. The cylinder is then replaced with the InSb detector, which is mounted in the housing as shown in Figure 5.6. An electrically insulated clamping ring around the detector holds it in place, while an O-ring seal just below the clamping ring allows the detector housing to be evacuated as part of the volume of the output-transfer-optics tank. The d.c. signal level of the detector can be monitored from a test point on the pre-amplifier board, and this provides a means of determining how well the final image is focussed on the detector. When this signal has been maximised by careful positioning of the detector and fine adjustments of the output transfer optics, the optical alignment of the LWC is complete. The detector can be bolted in place, and the transfer-optics tanks sealed. During the CH_4 experiments, the input optics were set up to properly fill ML1, the single mirror was adjusted to properly fill ML3, and the output optics and detector were optimised for a consistently positioned output image, so that only adjustment of the LWC mirrors ML1 and ML3 was needed to change the pathlength and to maximise the signal at the detector.

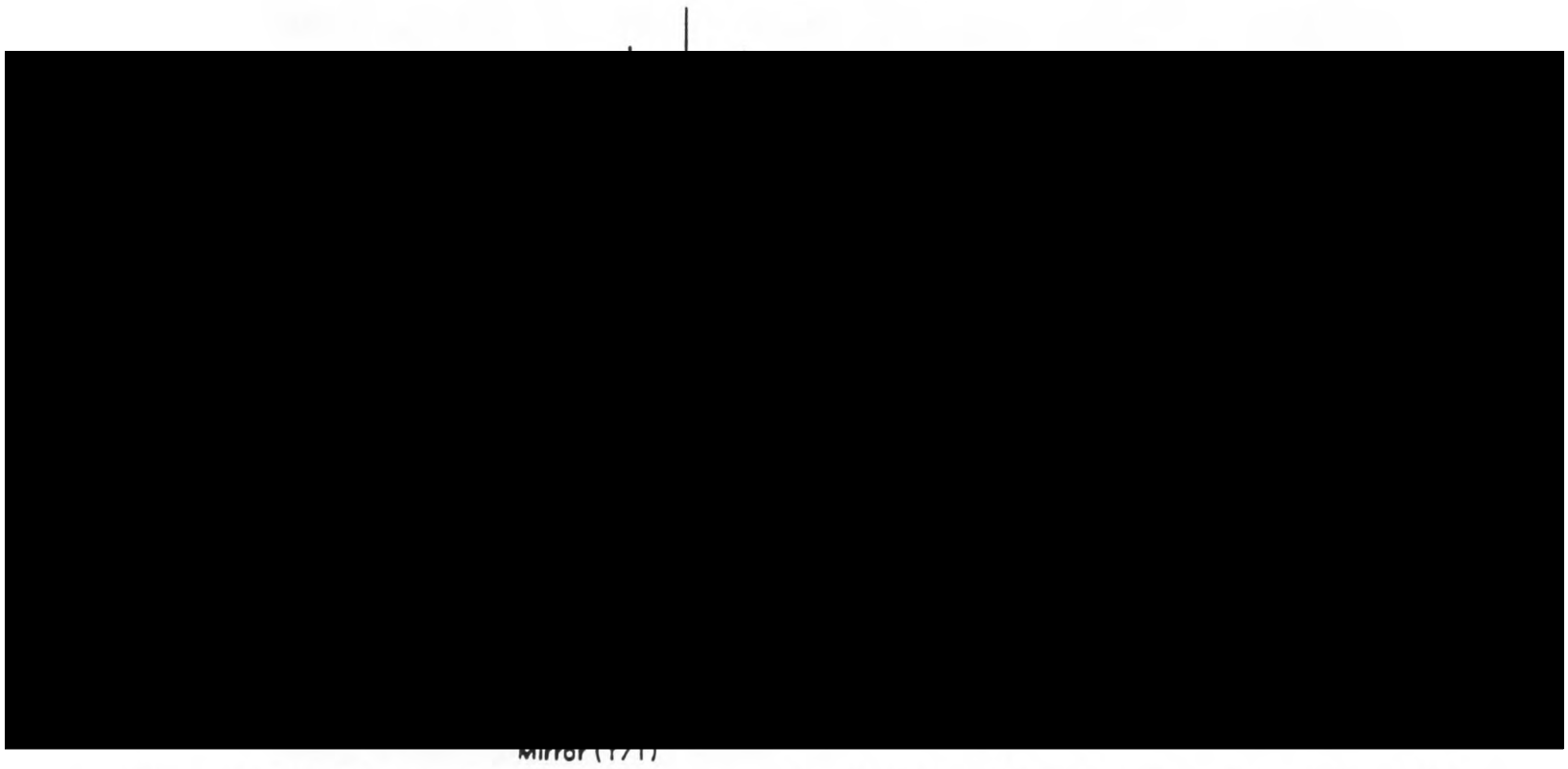

Figure 5.6: The Bomem mounting arrangement for the infrared detector (Remedios, 1990, p.141).

5.2.6 Safety Considerations

Although the LWC was intended for flammable-gas spectroscopy from its inception, the CH_4 and H_2 experiments undertaken for this study were the first such to be conducted. During the

year preceding these experiments, a comprehensive review of safety requirements and procedures was necessary. All existing safety features were checked and upgraded, and many new measures were introduced, aimed at providing safe handling and containment of flammable CH_4 and H_2, and providing the means for recognising and dealing with leaks of these gases. A series of formal safety reviews were held with the RAL Safety Section, leading to the written procedures described below. Commissioning inspections and trial flammable-gas fills and evacuations were conducted with experienced witnesses present, before both the room- and low-temperature experiments. The success and effectiveness of these efforts was demonstrated by the fact that no safety-related accidents occurred throughout the intensive four-month measurement period.

Due to time and effort expended in the identification and implementation of the necessary safety measures and in the writing and formalising of the operating and emergency procedures, this material was prepared as a 176-page report (Operation of the Rutherford Appleton Laboratory Long White Cell Using Methane and Hydrogen: Development and Implementation of Safety Measures and Operating Procedures, *RAL-91-015 Internal Report*, Strong, 1991). This document provided a record of the work undertaken and the procedures developed for the use of flammable gas in the LWC, and it was subsequently adopted by the Atmospheric Sciences Division at RAL, as required reading for all new users of the LWC and as a template for developing procedures for future use of the LWC with gases of a hazardous nature.

In addition to describing the facility and the preparations for the flammable-gas experiments, this report includes an item-by-item Key to the Gas Handling and Vacuum Systems, a Summary of the Implemented Safety Measures, the Emergency Procedures, and the daily operating procedures. In the Emergency Procedures, thirteen potential emergency situations are considered, the means of identifying them are described, and a series of steps to be followed in each situation, whether filling, recording spectra, or evacuating the LWC, are provided. The daily operating procedures included Daily Start- and End-of-Day Checklists, and Filling and Evacuation Checklists, which were completed as necessary during every day of the flammable-gas spectroscopy. In addition, during all flammable-gas operations, the presence of two authorised users was required in the Lab Spectroscopy Area.

Where relevant, the safety features included in the vacuum and gas-handling systems are described in §5.2.7 and §5.2.8. The following is a brief discussion of the original siting of the LWC within the Lab Spectroscopy Area, as this was determined by the need to provide for future flammable-gas operations. It is located in a RAL Division 2 H_2 Area, which is equipped with anti-static floor tiles, a frangible roof of polystyrene panels, sealed fluorescent lights, shutting springs on all four doors, a Crowcon gas warden flammable-gas detection system, and two extraction fans. The gas warden system consists of six detectors distributed around the H_2 Area, which trigger both an audible alarm and an extraction fan when flammable gas is detected. For the experiments in this work, the gas warden was set to detect 10% of the lower explosive limit of H_2 (4% H_2 in air). Before the start of the CH_4 spectroscopy, the integrity of

all of these safety features in the H_2 Area was verified. In addition, the LWC, its support frame, its cranes, and the gas-handling pipework in the H_2 Area were all electrically grounded, and when working with flammable gas in the H_2 Area, anti-static heel tips were worn and H_2-safe torches were used. As a Division 2 Area, no electrical equipment is permitted in this room when flammable gas is in use, and so the vacuum pumps for the LWC are partitioned off in the inner Pump Room. This requirement influenced the design of the gas-handling system, as described in §5.2.8. Surrounding the H_2 Area is the Outer Lab Spectroscopy Area, the general experimental working area where the LWC heat exchanger, the N_2 manifold system, and the control desk for the LWC gas handling, the temperature monitoring, and the master alarm are located. Adjacent to the H_2 Area is the room where the Bomem spectrometer, the Short White Cell (hereafter, the SWC) and its transfer-optics tank, the input- and output-transfer-optics tanks for the LWC, and the gas warden electrical control panel are located.

5.2.7 The Vacuum System

The LWC vacuum system was in place before the start of the CH_4 experiments, but it required repairs and upgrading for operation with flammable gases. A schematic view of the gas-handling and vacuum systems for both the LWC and the transfer-optics tanks is given in Figure 5.7. The main vacuum system includes two diffusion pumps and three rotary pumps. The former are oil diffusion pumps 30 cm in diameter (DP1 for the inner vessel and DP2 for the vacuum vessel), with refrigerated baffles to prevent backstreaming of oil and air-operated quarter swing valves for isolation. The rotary pumps are Edwards ES4000 pumps, with RP1 used to rough out the spectrometer and the transfer-optics tanks, RP2 used to rough out both the inner and vacuum vessels, and RP3 used to back the two diffusion pumps.

These rotary pumps were used to pump the LWC vessels from atmospheric pressure down to 0.01–0.1 torr, taking about 20–30 minutes for the inner vessel, but as long as 24 hours for the vacuum vessel due to outgassing from the multilayer superinsulation wrapped around the outside of the inner vessel. The diffusion pumps were then used to pump the inner vessel and vacuum vessel down to pressures as low as 1×10^{-5} torr, as measured with a calibrated Penning vacuum gauge. When the vessels were isolated from the diffusion pumps, the maximum room-temperature pressure-rise rates were measured to be about 7×10^{-4} torr/hour for the inner vessel (with 700 torr of N_2 in the vacuum vessel), and 5×10^{-5} torr/hour for the vacuum vessel.

Before beginning intensive use of the pumps, they required a general overhaul, which included pump-oil and baffle-refrigerant refills, replacement of RP1 motor bearings, replacement of the diffusion pump temperature control unit and thermostats, checking of the solenoid valves, checking and replacing vacuum gauges, checking and resetting of the pump and vacuum gauge controller units, checking and labelling all fuses in the Pump Room fuse box, and determining the effects of compressed air, demineralised water, and power failures. Additional work performed on the vacuum system for the CH_4 experiments included interlocking each swing valve

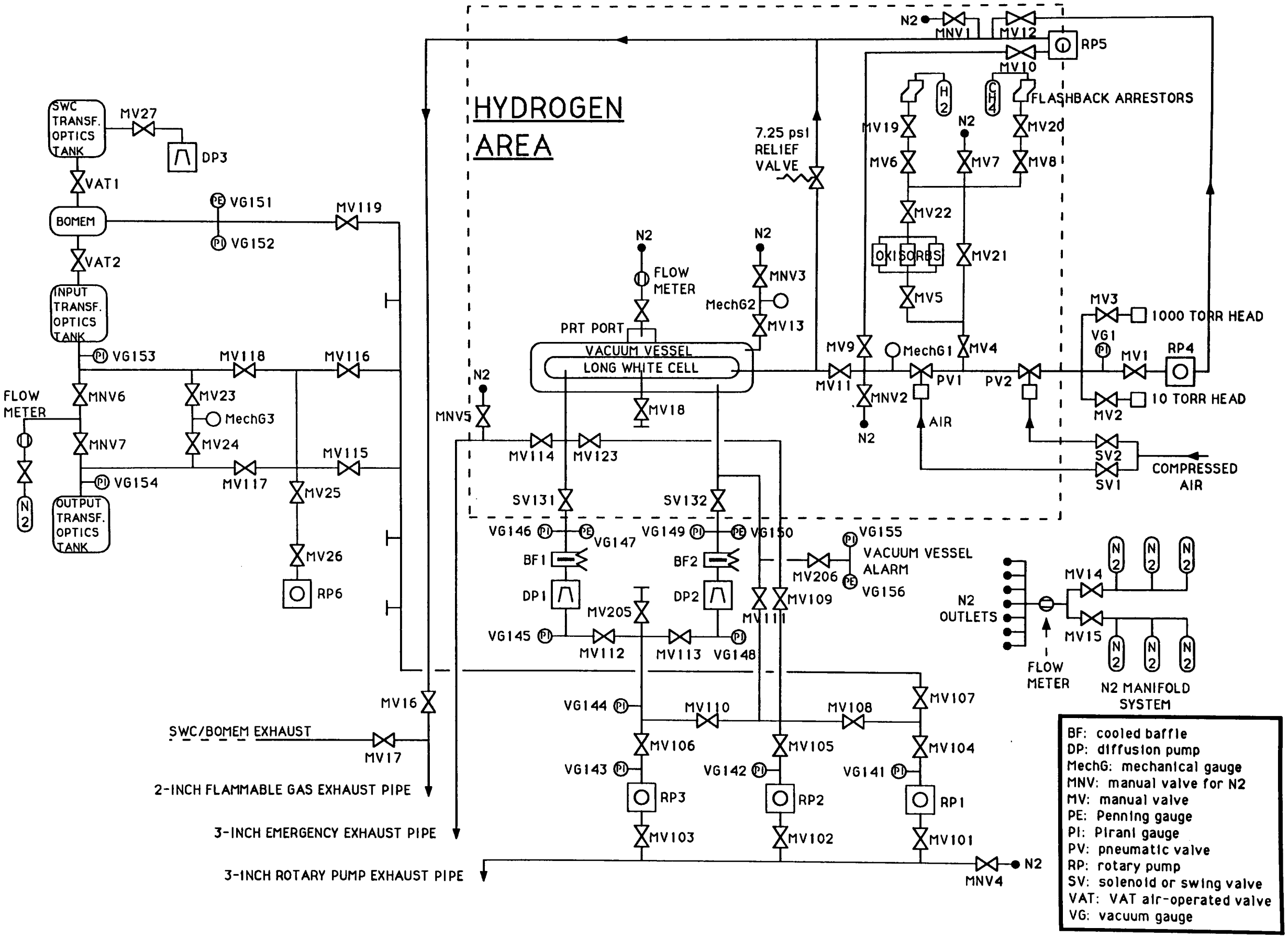

Figure 5.7: Schematic diagram of the Long White Cell gas-handling and vacuum systems.

with its corresponding diffusion pump so that the valve would shut if the pump were turned off or tripped off. Also, both relay delay timers and mains filters were installed on the diffusion pump controller units in order to filter out mains spikes that appeared to be responsible for the frequent tripping off of the pumps prior to the start of the experiments.

The vacuum system includes three exhaust pipes that vent on the roof, one for the large rotary pumps, one for both the gas handling and the Bomem, and one emergency exhaust for the LWC inner vessel which allows the inner vessel to be opened to atmosphere (outdoors) in the event of an emergency. Because the exhaust line from the LWC gas handling joins the exhaust line from the SWC/Bomem, a valve was installed on each of these lines, allowing them to be isolated so that flammable gas could be exhausted from the LWC without travelling back into the SWC/Bomem Area.

All of the pumps and the exhaust pipes were electrically grounded for the experiments. Each of these pipes was already equipped with a non-return valve at the top of the pipe. The H_2 Area extraction fan outlet is also located on the roof, and it is equipped with a coronal shield to prevent the build-up of static charge. For the CH_4 experiments, an alarm system was installed to alert the operators in the event of a fire in one of the vent pipes, or in the extraction fan pipe. This consisted of a fusible link, mounted under tension at the outlet of each of these four pipes, and wired via four-core cables into an alarm box on the control desk in the Outer Lab Spectroscopy Area.

None of these large pumps could be used to pump flammable gas directly out of the LWC, and so an alternative pumping arrangement was devised. Because no electrical equipment was allowed in the H_2 Area in which the LWC was located (see §5.2.6), an opening was made in the wall between the H_2 Area and the Outer Lab Spectroscopy Area and a small rotary pump (RP5) was installed such that the pump was located in the H_2 Area and the electric motor in the Outer Lab Spectroscopy Area. An appropriately cut aluminium sheet was fitted around the pump to re-establish the integrity of the H_2 Area. An Edwards E2M8 rotary pump was used for the room-temperature experiments, and an E1M40 for the cold experiments, these taking 105 and 25 minutes respectively, to pump the inner vessel down from 760 to 20 torr. The method of evacuating flammable gas from the inner vessel began by pumping it down to 20 torr with the small rotary, keeping its exhaust line purged with N_2. Then the flammable gas remaining in the inner vessel was diluted with N_2 until the mixture was below the lower explosive limit (5% in air for CH_4 and 4% for H_2). This safe mixture could then be roughed out with RP2, and finally pumped down with DP1. During low-temperature operations, the Speedivalve above RP5 was found to seize up when cold and so was replaced with a cryogenic Worcester valve to ensure that the inner vessel could be quickly isolated from RP5 in an emergency.

During the first set of measurements, at 296 K, when the LWC vacuum vessel did not have to provide thermal insulation, it was filled and left with 700 torr of "O_2-free" N_2. Spectral tests were performed to assess possible H_2O or CO_2 contamination introduced by the N_2, but they

demonstrated it to be insignificant. Keeping the vacuum vessel filled with N_2 minimised the risks arising from the breakage of the inner-vessel windows or the development of a leak from the inner vessel to the vacuum vessel. In particular, when the transfer-optics tanks were also filled with N_2, this reduced the potential fire risk associated with the exposure of the Bomem sources to flammable gas which could occur if both the inner and vacuum-vessel windows were to break.

However, for the cold LWC measurements, the vacuum vessel had to be evacuated in order to maintain cooling. In this situation, if the vacuum vessel were being pumped when flammable gas was present in the inner vessel, the development of a leak into the vacuum vessel would result in flammable gas being directly pumped. This potential problem was dealt with by leaving the vacuum vessel evacuated but not actively pumped during cold flammable-gas operations, after tests showed that the vacuum vessel would retain its integrity if it were simply isolated during a day of experiments. In addition, a pressure-rise alarm was installed on the LWC vacuum vessel throughout the cold experiments to warn of any leaks of flammable gas from the inner vessel. During the cold measurements, the pressure-rise rate was generally low enough to maintain cooling, but when a small leak developed between the inner and vacuum vessels, a noticeable increase in the LWC temperature-rise rate was observed, and it was sometimes necessary to rough out the vacuum vessel on RP3 during the intervals between spectrometer operations.

Prior to the start of the CH_4 spectroscopy, it was discovered that if the rotary pumps RP1, RP2, or RP3 were on during the recording of spectra, the noise level in the spectra increased significantly. This was true whether or not the pumps were actually pumping the LWC, and appeared to be caused by pump-induced vibration of the LWC and its mirrors. All of the pumps in the Pump Room were therefore turned off whenever spectra were being recorded, as none of them were required during the recording of spectra.

5.2.8 The Gas-Handling System

5.2.8.1 For the Long White Cell

A gas-handling system for the LWC was designed and built specifically for this experiment, incorporating various features to ensure that the LWC was filled, monitored, and evacuated safely. Figure 5.7 illustrates the final design, and Figure 5.8 shows the gas-handling control area. In designing the flammable-gas pipework, it was necessary to locate the flammable-gas cylinders in the H_2 Area, but to keep all electrical equipment out. This was accomplished by using the feedthrough to the inner vessel at the double-mirror end of the LWC as the gas input port, rather than the gas-handling manifold halfway along the side which was less easily accessible and whose high-pressure safety features were not needed for the <1 bar operating pressures. This feedthrough was connected to the gas-handling pumps and the baratron heads (see §5.3.3) in the Outer Lab Spectroscopy Area via 1/4-inch stainless steel pipe. The amount of flammable-gas pipework in this outer area was minimised by removing a glass pane from the

door adjacent to the double-mirror end of the LWC and replacing it with an aluminium panel which could be used for mounting and feedthroughs. The flammable-gas control valves were mounted with the pipework in the H_2 Area and the handles in the Outer Lab Spectroscopy Area, allowing the filling of the LWC to be controlled from outside the H_2 Area.

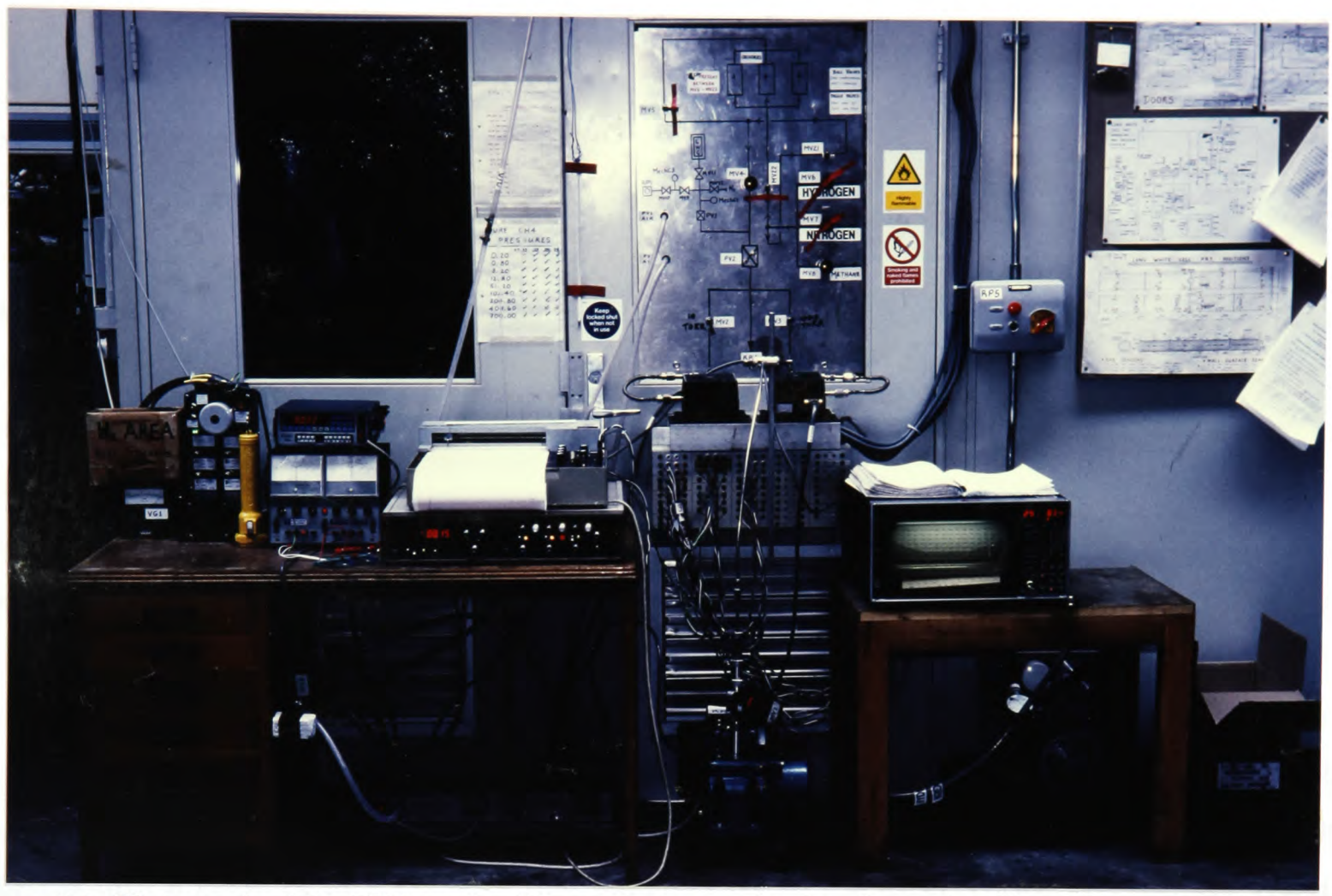

Figure 5.8: Photograph of the LWC gas-handling control area, showing the gas-handling valves mounted on the panel, RP4, the baratrons, the master alarm, the PRT chart recorder and the PRT data logger.

Two air-operated pneumatic valves (PV1 and PV2) were also included in the H_2 Area pipework, operated by two solenoid valves in the Outer Lab Spectroscopy Area which controlled the flow of compressed air. These pneumatic valves allowed the LWC and the pipework outside the H_2 Area to be quickly isolated by an operator in the Outer Lab Spectroscopy Area. The only flammable-gas pipework to be located outside the H_2 Area were 1/4-inch stainless steel lines to the gas-handling rotary pump (RP4) and to the two baratron heads. This pump was a single-stage Genevac rotary pump, which pumped the gas-handling system down to a pressure of about 0.04 torr. When isolated from RP4, the gas-handling pressure would rise at an average rate of about 0.02 torr/hour over several hours. To minimise the length of time that flammable gas was present in the Outer Lab Spectroscopy Area, the gas-handling pipework was used only during filling and evacuation of the LWC. While spectra were being recorded, the LWC was kept isolated with PV1 and the gas-handling pipework was pumped with RP4. In this situation, the pressure of the flammable gas in the LWC was monitored with a mechanical pressure gauge between PV1 and the inner vessel, and the pressure in the vacuum vessel was monitored with another mechanical pressure gauge installed on the vacuum-vessel input port.

The gas-handling system also included several other features. A Pirani vacuum gauge (VG1) was installed above the gas-handling rotary pump for monitoring the pump vacuum, and this gauge was electrically interlocked with PV2, turning on only if PV2 were shut, thus ensuring that VG1 would not come into contact with flammable gas. Three oxisorb cells (for absorbing H_2O and O_2 from the gas supplies; see §5.3.5) were included in the system, being mounted on the inside of the aluminium panel, but a bypass line was also added. The CH_4 and H_2 cylinders were located in the H_2 Area, each equipped with a new Murex 0–2.5 bar regulator, a flashback arrestor which also acted as a non-return valve, and a fine adjustment valve to isolate the cylinders and flashback arrestors from the rest of the system.

A Circle Seal 500 Series 1-inch in-line pressure relief valve was installed on the inner vessel, and was set at a cracking gauge pressure of 7.25 psi. This relief valve was required to vent safely, so 1-inch copper piping was brazed and fitted to feed into the 2-inch exhaust pipe that vents on the roof. Additional copper piping was fitted between the exhaust of RP4 and RP5 and this 2-inch exhaust pipe, and as a pump line between RP5 and the inner vessel. N_2 inputs for purges and fills were required at eight different points in the LWC system. An independent N_2 supply was provided for the transfer-optics tanks, but for the remaining points, a six-cylinder N_2 manifold system was designed and built. This was constructed using 1/4-inch copper pipe, rated to 6000 psi, brazed onto bull-nosed nipples compatible with the N_2 cylinders, a high-pressure regulator, a flowmeter, and two severe-service Union Bonnet valves, thereby dividing the manifold into two independently valved banks of three cylinders, with one regulator. This was fed into a network of PVC hose that supplied N_2 to the inner vessel, the vacuum vessel, the exhaust pipe for RP4 and RP5, the exhaust pipe for Pump Room rotary pumps, the LWC emergency exhaust pipe, and the purge port for the platinum resistance thermometers.

5.2.8.2 For the Transfer-Optics Tanks

An independent gas-handling system was also required for the input- and output-transfer-optics tanks, the final version of which is shown in Figure 5.7. Three flexible stainless steel tubes, 1 inch in diameter, connect the spectrometer and each of the tanks into the 3-inch manifold pipe that leads to the main vacuum system. Each tank has a gas-handling port at the top, and both were equipped with a Pirani gauge, and pipework to a 0–760 torr mechanical gauge, a N_2 supply, and a small rotary pump (RP6). Valves were installed to allow the tanks to be monitored, filled, and pumped both independently and together. The input- and output-transfer-optics tanks were pumped down to a nominal Pirani pressure of 0.65 mbar by RP1, which rose at about 0.1 mbar/hour when the tanks were isolated.

For the room-temperature CH_4 spectroscopy, the transfer-optics tanks and the spectrometer were initially pumped by RP1 each night and refilled with "O_2-free" N_2 each morning, thus minimising the risks involved in a potential flammable-gas leak. However, this was found to introduce significant H_2O and CO_2 contamination in the CH_4 spectra recorded during the first

few days. Several attempts were made to eliminate this contamination during the recording of the 296 K self-broadened CH_4 spectra, but it was reduced significantly only when the spectrometer and the transfer-optics tanks were evacuated during the recording of spectra. Thus, for the subsequent 296 K H_2-broadened CH_4 spectroscopy and for all of the low-temperature CH_4 spectroscopy, the VAT1 valve between the spectrometer and the SWC-transfer-optics tank was opened, allowing the diffusion pump on the SWC-transfer-optics tank to pump the spectrometer through VAT1, and to pump through VAT2 to the two tanks beyond. This pump maintained the pressure in the transfer-optics tanks near 1.2×10^{-4} torr, as registered on the Penning gauge on the spectrometer. Although having both the transfer-optics tanks and the LWC vacuum vessel evacuated meant that leakage through both the inner and outer LWC windows would allow flammable gas to come into contact with the hot light sources in the spectrometer, the absence of O_2 from the system made the likelihood of a fire or explosion negligible.

5.2.9 The Cryogenic Heat Exchanger

The LWC cryogenic system was conceived and designed several years before the start of the experiments undertaken for this work. It was installed by RAL engineers whilst preparations were underway for the room-temperature spectroscopy, and initial cooling tests were performed by a team that included the author, just before the room-temperature CH_4 experiments began. More extensive testing was undertaken, again involving the author, after these experiments were finished. The subsequent 190 K and 240 K CH_4 and H_2 measurements represented the first experimental use of this new cryogenic system. This section provides a brief description of the design and operation of the cryogenic system. Lack of space prevents the inclusion of a more detailed account of the testing and commissioning that was undertaken in preparation for the low-temperature spectroscopy.

The LWC cryogenic system, as used in this work, allowed the inner vessel to be cooled to any temperature between 190 K and 300 K, to be stepped up or down to another temperature, and to be maintained at a given temperature for an extended period of time. A schematic view of the system is seen in Figure 5.9, and a photograph is provided in Figure 5.10. The central feature of the system is the heat exchanger, which uses LN_2 to cool a circulating fluid. The fluid used in this work was halon 2402, dibromotetrafluoroethane, which has a freezing point of 162.7 K. The increase in the viscosity of halon 2402 with decreasing temperature determined the 190 K lower limit of the heat exchanger. In the original design, iso-pentane was considered as a possible circulating fluid because it has a freezing point of 113.5 K, and would therefore have allowed simulation of the coldest temperatures found in the Jovian atmosphere. However, the high volatility and flammability of iso-pentane led to the selection of the safer halon 2402.

The heat exchange occurs in four double-walled vertical stainless steel pipes 400 mm in length, with outer diameters of 54.0 mm for the inner pipe and 66.7 mm for the outer pipe. LN_2 fills the central volume of the pipes and the halon is contained in the surrounding annulus. The

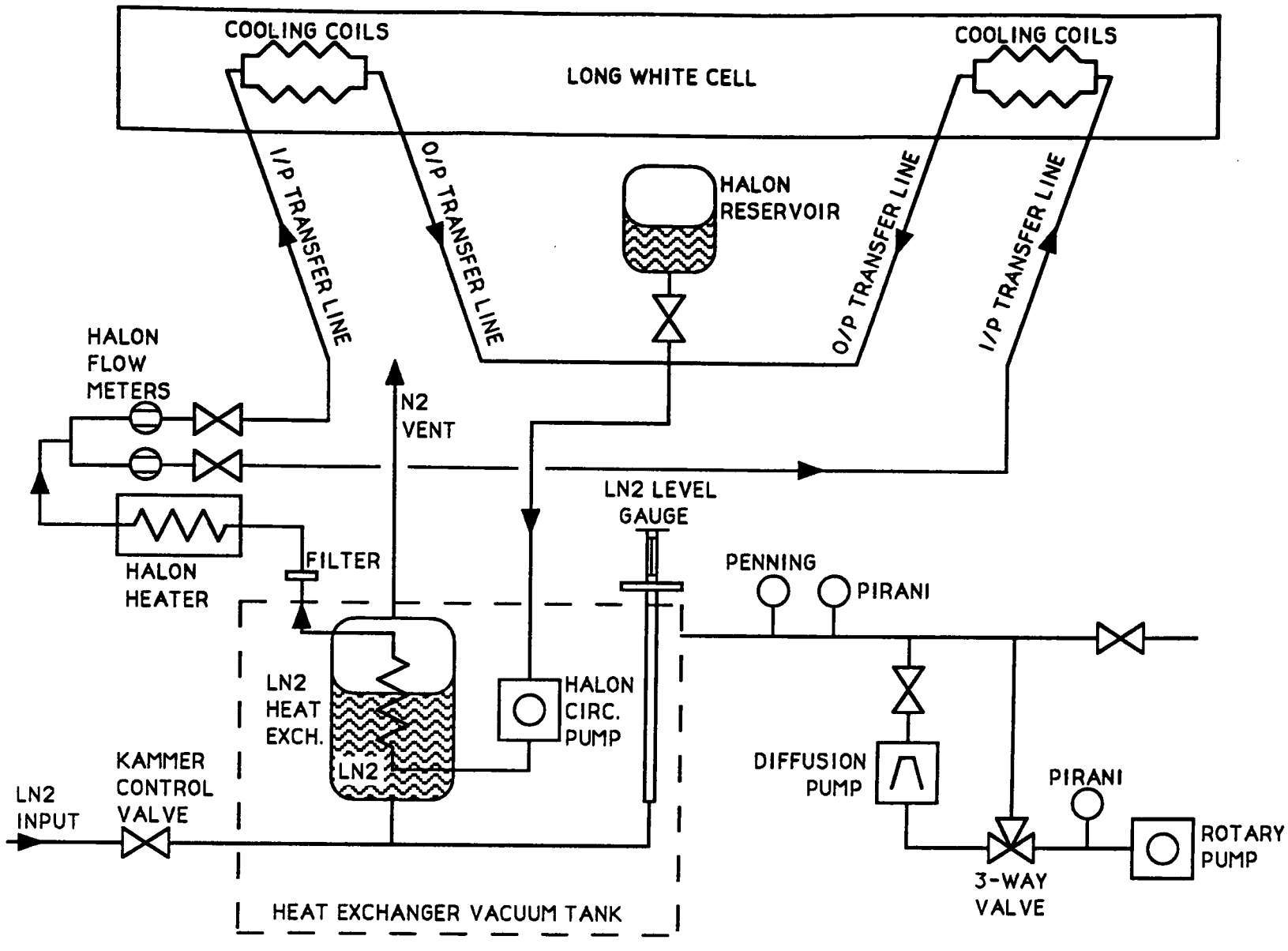

Figure 5.9: Schematic diagram of the Long White Cell cryogenic system.

halon is pumped through the system by a Global Pumping Systems magnetic-drive centrifugal cryogenic pump which circulates the cooled halon through the heat exchanger pipes, past two control valves into two vacuum-insulated transfer lines. Each of these transfer lines contains a flowmeter which provides digital readouts of the cooling-fluid flow rates. These lines lead to two input ports on the top of the LWC, where the halon passes through two flow and return manifolds across the vacuum vessel into two independent cooling circuits. Each of these circuits consists of eight channels welded to the outer surface of the inner vessel, as seen in the photograph of the inner vessel before installation in Figure 5.11. Having passed through these channels, the halon returns back through two output transfer lines and into the heat exchanger.

The conduction of heat between the inner and outer vessels is reduced by the use of low-conductivity supports and connections, and conduction of heat by gas is minimised by operating with the vacuum vessel evacuated. The radiation of heat is reduced by multilayered interleaved aluminium foil and glass paper superinsulation wrapped around the outside of the inner vessel and over its endplates (with holes cut for the windows and mirror adjustors).

Also contained in the cooling-fluid circuit is a 3 kW heater which can be used to speed up the rate of warming when the heat exchanger has been turned off. Both the heat exchanger and the circulating pump are isolated within an insulating vacuum chamber which has its own vacuum system, consisting of an Edwards E2M8 rotary pump and an Edwards 4-inch oil diffusion pump,

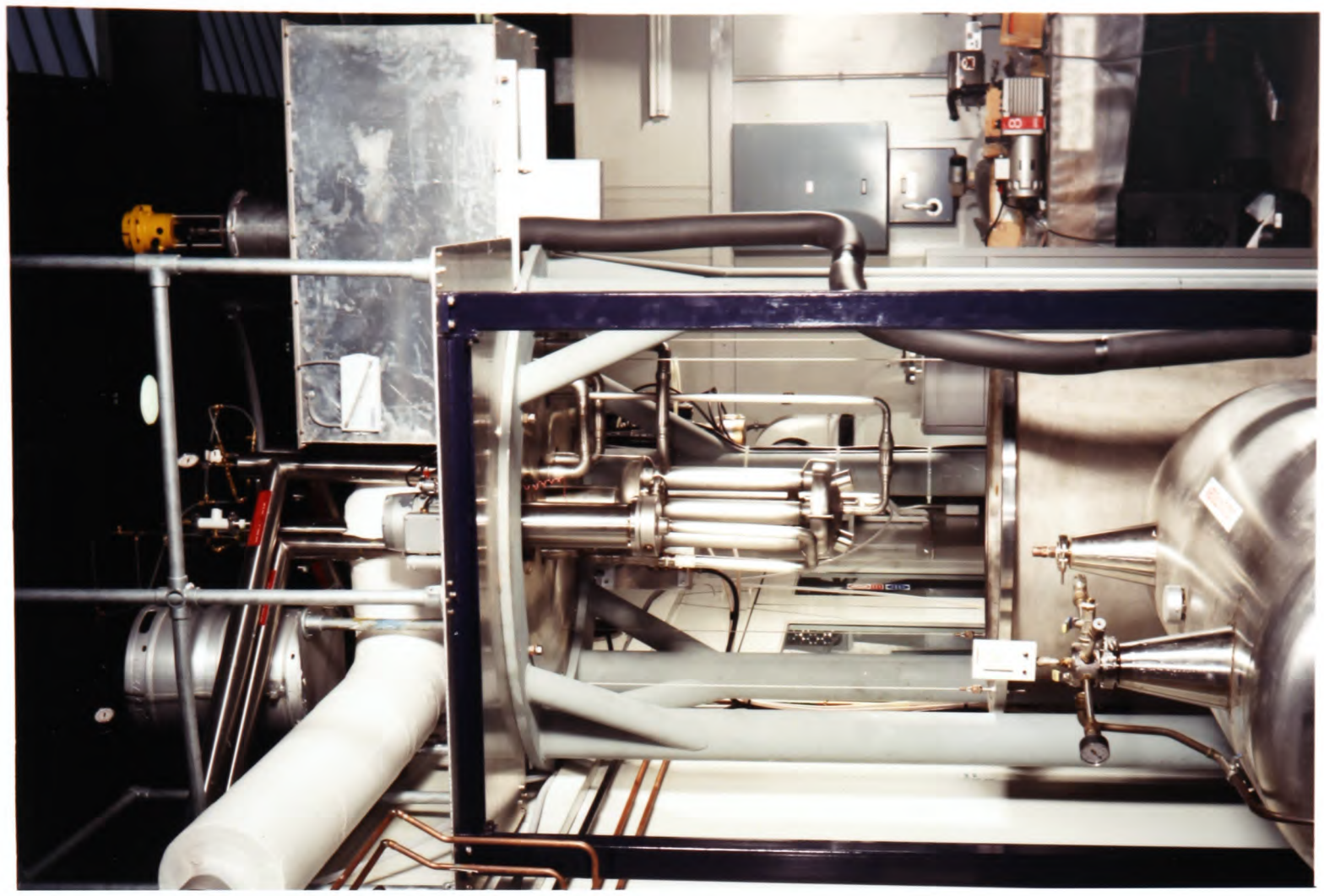

Figure 5.10: Photograph of the LWC cryogenic system, with the vacuum tank lowered to show the pipework in the heat exchanger.

interlocked with an Edwards 1105 vacuum controller unit. At room temperature, the diffusion pump would maintain the tank at a Penning gauge pressure of about 1×10^{-6} mbar, and at 190 K, it would drop as low as 1×10^{-7} mbar.

The temperature of the LWC is determined ultimately by the LN_2 level in the heat exchanger pipes. During the experiments in this work, the LN_2 was supplied from pressurised 200- and 500-litre dewars which were refilled from a 5000-litre tank located outdoors. The N_2 boil-off is exhausted through a partially insulated pipe to atmosphere outside the building. The LN_2 consumption was found to be $\sim$100 l/hr during cooling and $\sim$20 l/hr during stable operation. The LN_2 level is determined by a TCS 6382 microprocessor which controls a Kammer valve, an air-operated, electrically controlled needle valve. The microprocessor receives inputs from a LN_2 level gauge in the heat exchanger and from a platinum resistance thermometer located on the cooling-fluid circuit just beyond the output of the circulating pump. The microprocessor can be programmed to maintain the LN_2 valve at a specified setting, or to adjust the Kammer valve as needed to maintain either the LN_2 level or the cooling-fluid temperature at a specified setting.

With the LWC prepared for cryogenic operations, the vacuum vessel evacuated, and the heat exchanger vacuum tank evacuated, the procedure for cooling down the LWC is as follows. First, the required LWC temperature and the required LN_2 level (usually 80%) are set on the microprocessor, and it is programmed to maintain the latter. With the LN_2 dewar in place and pressurised to 10 psi (for cooling, 5 psi for stable operation), the dewar supply valve is

Figure 5.11: Photograph of the LWC inner vessel prior to installation, showing both the cooling circuits and one set of connection flanges for input and output of the cooling fluid.

opened, the circulation pump is turned on, and the pump current is monitored on the needle display to ensure that the pump does not overheat or stall. This current can be changed by adjusting the two valves that control the flow of the cooling fluid. When the circulating pump is on, relays operate to allow the microprocessor to control the Kammer valve, and thus the flow of LN_2 into the heat exchanger. If the pump fails or trips off, interlocks operate to close the Kammer valve. Once the set temperature of the PRT on the cooling circuit is reached, the microprocessor switches over to vary the LN_2 level in order to maintain this temperature. The LWC can be warmed up by letting the circulating pump run without any LN_2 in the heat exchanger, however, faster warming is achieved by using the halon heater. Interlocks in the system ensure that the heater cannot be operated unless the circulating pump is on, thus avoiding overheating of the halon.

During the cooling tests performed prior to the cold CH_4 spectroscopy, various operating problems were identified and solved and the performance of the cryogenic system was evaluated. The cooling rate was found to be $\sim$10 K/hr, and the temperature-rise rate $\sim$1, $\sim$4, and $\sim$15 K/hr with the cryogenic system shut down, with the circulating pump on, and with both the circulating pump and halon heater on, respectively. The natural temperature-rise rate of the LWC was of particular relevance to the spectroscopy because it was found that when the circulating pump was on, it caused vibration of the LWC which gave rise to unacceptable noise in the recorded spectra. Therefore, whenever CH_4 spectra were being recorded, the cryogenic system was shut down.

5.3 Monitoring of Conditions in the Long White Cell

5.3.1 The Platinum Resistance Thermometers

The LWC temperatures are monitored by a series of platinum resistance thermometers (PRT's), supplied by Heraeus/Nulectrohms. Nineteen PRT's are clipped to the outer surface of the inner vessel to monitor the temperature of the walls, and twenty-seven PRT's are suspended inside the inner vessel to monitor the temperature of the gas. The location and orientation of the PRT's are shown in Figure 5.12.

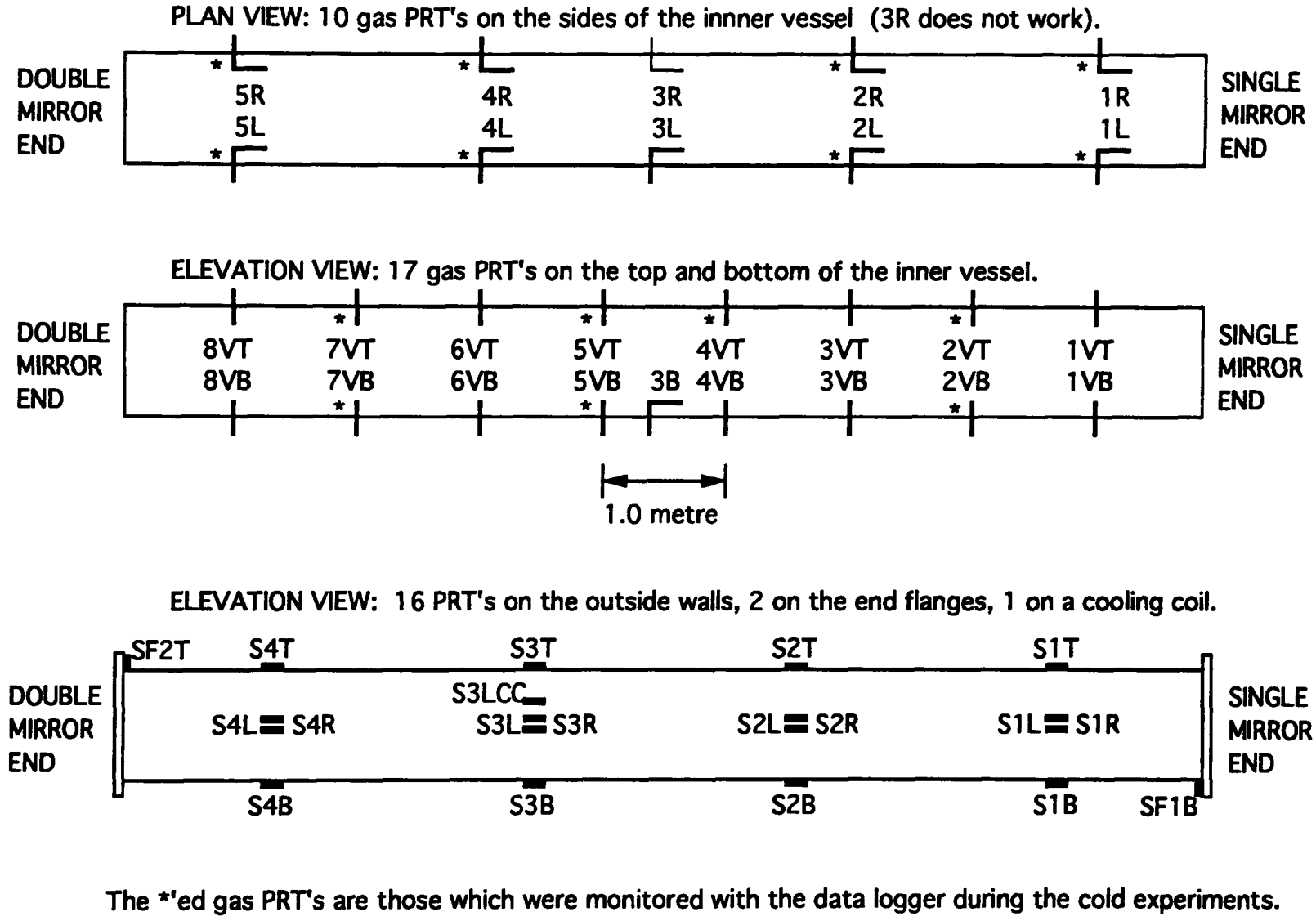

Figure 5.12: The location of the platinum resistance thermometers in the LWC.

Each PRT element is connected to four wires, with all forty-six PRT cables being fed out through a purgeable port on the side of the vacuum vessel and wired into a panel which has four terminals per cable. A d.c. voltage supply is fed into a 1 mA constant current source which supplies current to the 100 ohm PRT resistance element through two of the wires. This produces an output voltage across the remaining two wires which is monitored by a recording device. Knowing the exact value of the input current and the output voltage, the resistance of the PRT can be determined, and as this is linearly dependent on temperature according to the European curve with alpha = 0.00385, the temperature of the PRT can be calculated.

The accuracy of the PRT temperature, as specified by the manufacturers, is ± 0.1 K at 273 and 373 K, and ± 0.3 K at 78 K. Heraeus/Nulectrohms performed a three-point calibration on

a sample of four of the gas sensors and two of the wall sensors, at 77 K, 273 K, and 373 K, and found that these specifications were satisfied. An additional three-point calibration was performed at RAL, in November, 1983, before the PRT's were installed in the LWC. Immersion of each sensor in room-temperature, ice, and LN_2 baths, proved that all of the sensors were within the specifications.

5.3.2 Temperature Monitoring of the Long White Cell

The LWC temperature measurements were performed in two phases. For the room-temperature experiments, when the gas temperature was spatially and temporally stable, a PRT map was recorded once for each pressure-pathlength run, about halfway through the recording of the spectra, using a 1 mA constant current source and a 15 volt d.c. power supply. Tests of the current source, using a precision variable resistor, gave an average current value of 0.9935 mA, with a standard deviation (1σ) of ± 0.0018 mA. This value was therefore used in deriving all of the room-temperature PRT resistances and temperatures from the measured voltages. The standard deviation in the current corresponds to a temperature deviation of ± 0.5 K at room temperature, and so the uncertainty of the room-temperature measurements was taken to be the sum of this value and the quoted accuracy of the PRT's, *i.e.*, $\Delta T = \pm 0.5 \pm 0.1$ K $= \pm 0.6$ K.

For the low-temperature experiments, a Phillips PM8237A/02 Multipoint Data Recorder was used to monitor the LWC temperature. This had a four-terminal input for PT 100 temperature measurements, with an internal 0.7685 mA current source, and internal conversion of PRT resistances to °C, using the DIN 43760 linearisation scale. Tests of all fifteen of the data logger channels, again using the precision variable resistor, showed that the difference between the data logger "temperatures" and those calculated directly from the resistances using the DIN 43760 scale, were always less than ± 0.2 K, within the specified accuracy of the data logger. Additional calculation of the temperatures expected from both the European curve (alpha = 0.00385) to which the PRT's were calibrated, and the DIN 43760 scale used by the data logger, for resistances relevant to the LWC measurements (60–110 ohms), showed that those derived from the European curve were higher, but by less than 0.2 K. As this was also within the accuracy of the data logger, it was considered acceptable. The overall uncertainty of the low-temperature measurements, aside from the variation due to gradients in the LWC, was thus taken to be the sum of the quoted accuracy of the PRT's (± 0.3 K), and the accuracy of the data logger (*Multipoint Data Recorder Operating Manual*, p.10), *i.e.*,

$$\Delta T = \pm 0.3 \pm [0.001 \times |T_{in}| + 0.25 + 0.05|T_{room} - 23|] = \pm[0.7 + 0.001 \times |T_{in}|] \qquad (5.6)$$

with T_{in} in °C and $T_{room} = 20$°C.

For the 190 K and 240 K experiments, the gas PRT's were wired into the data logger, but with only fifteen channels available, only fifteen of the twenty-six gas sensors could be monitored in this way, requiring selection of a representative set. This included all those along the left and

right sides of the LWC (1R, 2R, 4R, 5R, 1L, 2L, 4L, and 5L, excluding 3R because it was broken and 3L because it gave consistently high readings) as these were at approximately the same height as the optical path. Of the vertical sensors, 2VT, 2VB, 4VT, 5VT, 5VB, 7VT, and 7VB were chosen, these being fairly evenly distributed along the length of the LWC. The data logger was programmed to record the temperatures every 10 minutes. In addition, PRT 6VT was wired into a graphical chart recorder to allow continuous monitoring of the LWC temperature. A new 1 mA current source was obtained for this purpose. Its stability was checked with the precision variable resistor and it was found to remain essentially constant at 0.9984 mA.

In order to evaluate the accuracy of the PRT readings at low temperature, a temperature-pressure test was conducted in order to determined the real temperature of the gas in the LWC. Application of the ideal gas law during a cool-down of the LWC from known room temperature, T_o, to some unknown final temperature, T_f, yields the equation

$$T_f = \frac{V_{LWC} T_o}{\frac{P_o}{P_f}(V_{pipes} + V_{LWC}) - V_{pipes}} \tag{5.7}$$

where P_o is the known initial pressure of gas in the LWC,

P_f is the known final pressure of gas in the LWC,

V_{LWC} is the known volume of the LWC, and

V_{pipes} is the unknown volume of the baratron pipework.

An initial test to measure the ratio of V_{pipes} to V_{LWC} showed it to be negligible (1:6392), thus reducing Equation 5.7 to simply

$$T_f = (\frac{P_f}{P_o})T_o. \tag{5.8}$$

The LWC was thus filled with $P_o = 601.1$ torr of N_2, and room-temperature PRT readings were recorded using the new constant current source for all twenty-six gas PRT's, and using the data logger for the fifteen selected gas PRT's. As a check on the reliablity of T_o, the current source was also used to measure the average room temperature of the seventeen wall PRT's, which was found to be 294.4 ± 0.2, in good agreement with the values for the gas PRT's. The LWC was then cooled and six hours later, when the pressure had dropped to $P_f = 496.4$ torr, the temperatures were recorded again. The average measured temperatures and their standard deviations are displayed in Table 5.1, along with the calculated T_f's.

This test showed that the measured PRT cold temperatures were colder than the theoretical values, by 1.7 K for the current source, and by 1.8 K for the data logger. These differences are comparable to the standard deviations in the measured cold temperatures, these being 2.2 K and 1.7 K, respectively. The accuracy of the low-temperature PRT readings was therefore considered acceptable. The slight cold bias of the measured T_f relative to the calculated value suggests that there may be warm pockets in the LWC which contribute to the overall temperature but are not registered by any PRT's. This is supported by the fact that PRT's 3L, 3B, and 4VB, near ports midway along the inner vessel, gave consistently higher temperatures, apparently

due to heat leaks through the ports. The results in Table 5.1 also show that both the room and cold temperatures measured with the data logger were 0.4 K lower than those measured with the current source. This small cold bias of the average data logger temperatures relative to the average current source temperatures suggests that the fifteen PRT's chosen for the data logger were not fully representative of the twenty-six gas PRT's. A similar small bias was also seen in several other tests, but the discrepancies were always within the instrumental uncertainty of the data logger and were therefore also considered acceptable.

Table 5.1: Average LWC temperatures recorded during the LWC temperature-pressure test.

	MEASURED $T_o \pm 1\sigma$ (K)	MEASURED $T_f \pm 1\sigma$ (K)	CALCULATED T_f (K)	ΔT_f (K) (CALC - MEAS)
Current source (26 gas PRT's)	294.5 ± 0.2	241.5 ± 2.2	243.2	+ 1.7
Data logger (15 gas PRT's)	294.1 ± 0.2	241.1 ± 1.7	242.9	+ 1.8
Average ΔT (current source - data logger)	+ 0.4	+ 0.4		

5.3.3 Pressure Monitoring of the Long White Cell

The LWC pressures were measured with MKS Type 390 10-torr and 1000-torr Absolute Baratron Pressure Transducers, along with an MKS Type 270B Signal Conditioner and an MKS Type 274 Three Channel Selector. These baratrons operate as capacitance manometers, having an internal circular inconel diaphragm whose deflection by a pressure differential is a linear function of pressure (Davis, 1987, p.132), and which is mounted inside a thick-walled, temperature-controlled housing maintained at 45°C to reduce the effects of ambient temperature variations.

Both the 10-torr and 1000-torr baratron heads were calibrated by MKS Instruments before being installed in the gas-handling system, and both were found to be accurate to within 0.04%. Before beginning the room-temperature measurements, a set of baratron checks and resets were performed. A barometric test of the 1000-torr head was conducted, exposing it to atmosphere and comparing the reading with that measured by a precision aneroid barometer. The 1000-torr head measured 0.06% higher than the aneroid barometer, slightly worse than its specified calibration error. The performance of the two heads was also compared at five pressures over the range from 0 to 10 torr, giving a maximum difference of 0.31%. The same checks, performed before the start of the cold spectroscopy, showed that the 1000-torr head was 0.05% higher than the aneroid barometer, and that the maximum difference between the two heads was 0.60% over 0–10 torr. In a final check after the cold spectroscopy was finished, the 1000-torr head was 0.09% higher than the aneroid barometer, and the heads were found to differ by as much as 1.1% over 0–10 torr. The individual pressure measurements were therefore considered to be accurate to at least 1.1%.

During the LWC CH_4 experiments, the LWC was kept isolated as much as possible when full of flammable gas. The method of operation was to record the LWC pressure immediately after filling, then to isolate the LWC at PV1 and pump on the gas handling with RP4 while spectra were being recorded, and finally to record the LWC pressure again once the spectra were finished. The intermediate pressures were then interpolated from the initial and final pressures. The initial gas pressure, P_{gas} at time t_i, was calculated simply as

$$P_{gas}(t_i) = P_{meas}(t_i) - P^o_{total}(t_i) \tag{5.9}$$

where the $P_{meas}(t_1)$ is the measured pressure and P^o_{total} is the overall baratron zero for the LWC and the pipework. Calculation of the final gas pressure, P_{gas} at time t_f, required the overall baratron zero at t_f. This could not be measured directly, but could be calculated from the overall baratron zero at t_i, knowing the change in the baratron zero of the pipework and the typical pressure-rise rate of the LWC. However, both of these were found to be negligible, allowing the final gas pressure to be calculated using

$$P_{gas}(t_f) = P_{meas}(t_f) - P^o_{total}(t_i). \tag{5.10}$$

5.3.4 Pathlengths in the Long White Cell

The LWC self- and H_2-broadened CH_4 spectra were recorded at nominal pathlengths of 64, 128, 256, and 512 m, obtained by adjusting the input and output mirrors to get the required number of images on the single mirror. The minimum pathlength of 64 m was chosen as the shortest obtainable when the first image on the single mirror was on the tab. A shorter pathlength of 32 m could have been obtained with only one image on the single mirror, located at its centre. However, due to the erratic performance of the mirror adjustors, it was decided to minimise the amount of adjustment needed by always having the first image on the tab of the single mirror.

The maximum pathlength was determined by the maximum number of images that could be clearly distinguished on the single mirror, these images becoming steadily fainter and beginning to overlap as the number of reflections increased. Figure 5.13 shows the decrease in the d.c. signal level at the InSb detector (see §6.1.2) which occurred due to reflection losses from the LWC mirrors. In this test, using the quartz-halogen source and a 1.0 mm iris, with the inner vessel filled to atmospheric pressure with N_2, the signal level was measured as a function of the LWC pathlength. Although it was just possible to distinguish images for pathlengths greater than 512 m, the "zero" signal level between successive numbers of images became non-zero, suggesting that the large number of images on the single mirror were overlapping. Therefore, 512 m was chosen as the maximum pathlength. However, during the 190 K measurements, the ability to see the the 31 images required for a pathlength of 512 m was severely limited due to the film of pump oil which formed on the outside of the inner-vessel windows, as described in §5.2.3. The maximum pathlength for the 190 K measurements was therefore reduced to 416 m.

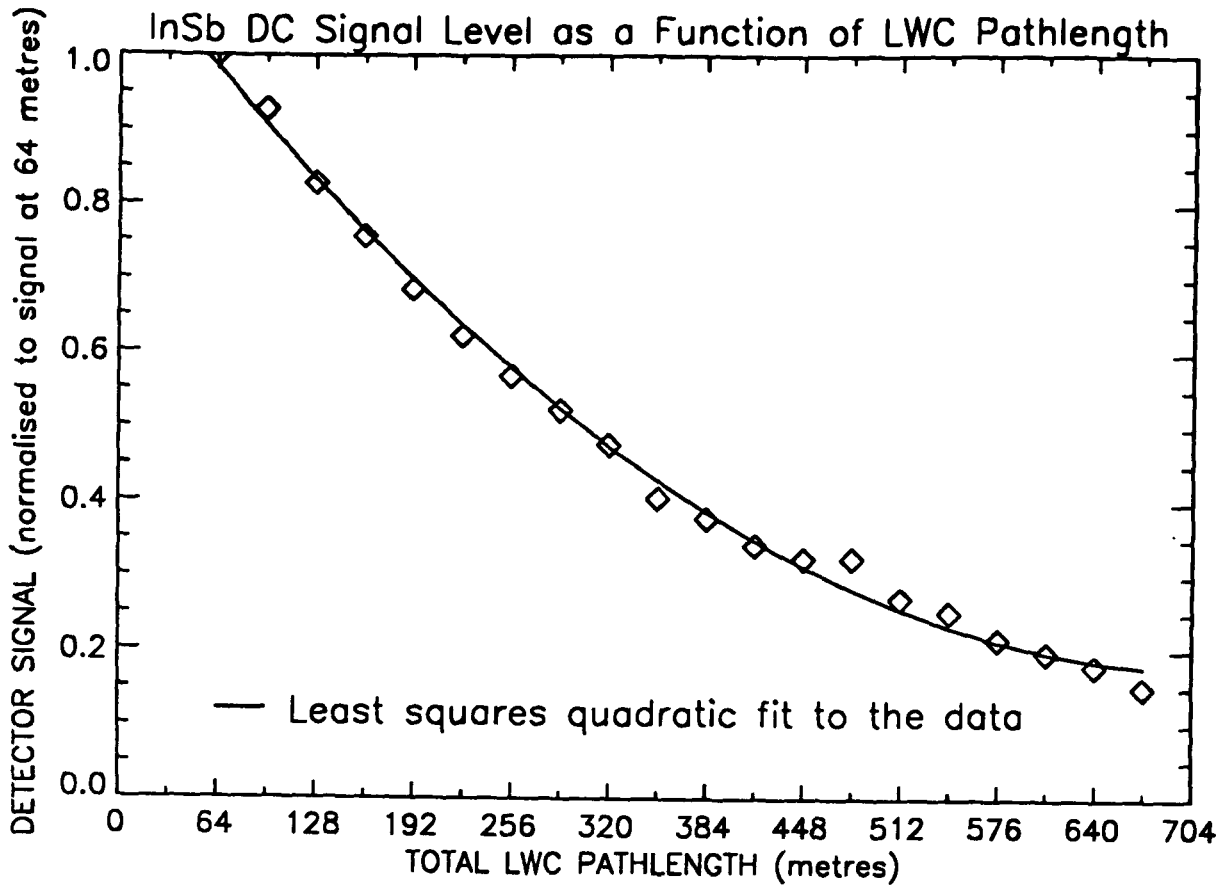

Figure 5.13: The d.c. level of the InSb detector as a function of the pathlength in the Long White Cell.

Calculation of the total gas absorption pathlength requires Equation 5.4 and knowledge of the distance between the front surface of the single mirror and the inner surface of the infrared windows on the inner-vessel endplate. With the latter being 373 mm $\pm$ 10 mm and the radius of curvature of the mirrors being 8000 $\pm$ 10 mm, the total pathlength, in mm, is simply

$$L = 2(373 \pm 10) + (2n + 2)(8000 \pm 10) = 750 + 16000(n + 1), \qquad (5.11)$$

with a cumulative uncertainty of $20(n + 2)$ mm. The pathlengths used during the CH_4 spectroscopy are given in Table 5.2, along with their uncertainties.

Table 5.2: Pathlengths used in the CH_4 spectroscopy

n IMAGES	2n+2 TRAVERSALS	L (m)	ΔL (m)	ΔL/L %
3	8	64.75	0.10	0.15
7	16	128.75	0.18	0.14
15	32	256.75	0.34	0.13
25	52	416.75	0.54	0.13
31	64	512.75	0.66	0.13

5.3.5 Gas Supplies for the Methane Spectroscopy

Because of the long absorption pathlengths of the LWC, the presence of small gaseous impurities in the CH_4 and H_2 could result in appreciable contamination of the recorded spectra, particularly for gases such as H_2O and CO_2, which have strong absorption bands in the spectral region of interest. Therefore, it was desirable to use highly purified gas supplies. To this end, Ultra High Purity CH_4 and H_2 were used throughout the experiments, except in the case of some of

the room-temperature self-broadened CH_4 measurements, when UHP CH_4 was unavailable and High Purity CH_4 was used instead. The supplier's guaranteed maximum impurity specifications for these three gases are given in Table 5.3, with typical analyses generally several ppm lower.

Table 5.3: Impurities in the CH_4 and H_2 gas supplies.

GAS	SUPPLIER'S SPECIFICATION (ppm)		
	HP CH_4	UHP CH_4	UHP H_2
CH_4 or H_2	99.95%	99.995%	99.999%
O_2	10	5	2
N_2	200	20	5
H_2	10	1	—
H_2O	5	5	3
CO_2	10	2	—
Hydrocarbons	200	20	0.1

In order to further minimise any possible contamination of the spectra by impurities in the CH_4 and H_2 supplies, gas-purifying oxisorb cartridges supplied by Messer Griesheim GmbH were integrated into the input line of the gas-handling system. These consist of a carrier material of large surface area, coated with reactive chromium dioxide which acts via chemisorption to remove traces of O_2 (independently of pressure, temperature, and gas flow rate), while a molecular sieve simultaneously adsorbs H_2O. The cartridges used for these experiments each had an absorption capacity of 0.1 litre O_2 and 0.1 litre H_2O vapour, giving guaranteed final purities of <0.1 ppm O_2 and <0.5 ppm H_2O. The cartridges were mounted in re-usable low-pressure units, and in order to increase the overall flow rate (that for each cartridge being a maximum of 1 m^3/hour), three cartridges were mounted in parallel. During installation, "O_2-free" N_2 (5 psi) was blown through both ends of each cartridge, minimising their exposure to air, and once installed, they were always filled with N_2, CH_4, or H_2, as they could not be kept under vacuum.

5.4 Summary

In this chapter, the experimental resources that were used in the CH_4 spectroscopy have been described, including the Bomem Fourier transform spectrometer, the LWC and its component systems, and the apparatus used to monitor temperatures and pressures in the LWC. Commissioning of the RAL Laboratory Spectrosopy Facility for the desired spectroscopic measurements, which involved the use of large volumes of flammable gas at long pathlengths and low temperatures, was a major undertaking in itself. The CH_4 experiments conducted with these resources represented the first use of flammable gas in the LWC and the first use of the new LWC cryogenic system. The self- and H_2-broadened CH_4 spectra that were recorded are described and assessed in the following chapter.

Chapter 6

Measurement and Initial Processing of the Methane Spectra

The lack of spectral parameters for CH_4 in the NIMS spectral region and the corresponding need for laboratory measurements has been discussed in Chapters 3 and 4. Line parameters for CH_4 have been shown to be unavailable above 6200 cm^{-1}, and particularly poor for weak lines below 6200 cm^{-1}, lines which become important at Jovian abundances. Band-model parameters for CH_4 have been shown to provide poor coverage for Jovian conditions, particularly of low temperatures, large abundances, and H_2-broadening. It was therefore established that the maximum range of temperatures, pressures, and pathlengths available with the LWC offered a useful advance over existing data. This chapter describes the self- and H_2-broadened CH_4 spectroscopy that was conducted using the LWC at the RAL facility. It begins with a discussion of both the experimental conditions required by NIMS and those that were achievable with the available resources. This is followed by a discussion of the processing conducted prior to the band-model analysis, and an assessment of the quality of the spectra.

6.1 The Long White Cell Methane Spectra

6.1.1 The Achievable Laboratory Conditions

The approach taken in this work was to record CH_4 spectra at low resolution over a large spectral range for analysis with band models. Ideally, such low-resolution spectra would be recorded under the conditions of pressure, temperature, and abundance that are found in the planetary regime of interest, thereby eliminating the need to extrapolate the band models beyond the laboratory conditions. In order to determine the laboratory conditions appropriate to simulations of the Jovian atmosphere, Curtis-Godson weighted mean parameters were calculated by applying Equation 3.18 to the Jovian atmospheric profile of Orton (1981). The Curtis-Godson pressures, temperatures, and CH_4 abundances were calculated for 130 paths from levels between 100 and 10^{-11} bar up to the top of the atmosphere. This was done for all five of Orton's pro-

files, the "nominal" model, as well as the "cool heavy", "cool light", "warm heavy", and "warm light" models (see §1.2.3). At infrared wavelengths, the Jovian atmosphere is probed primarily at atmospheric pressure levels between approximately 0.01 and 10 bar (Drossart *et al.*, 1989). The Curtis-Godson parameters for the paths from levels between 0.01 and 10 bar, up to the top of the atmosphere, vary from 0.710 to 773 m-amagat, 0.00500 to 5.01 bar, and 107 to 272 K, for the CH_4 abundance, the total pressure, and the temperature, respectively. These parameters define the laboratory regime desirable for simulating the atmospheric regime of interest.

The CH_4 abundance and the total atmospheric pressure have been plotted in Figure 6.1, as functions of temperature for the Curtis-Godson paths to the top of the atmosphere. Three boxes have been superimposed on these profiles, the region within each representing the conditions achievable with a particular laboratory regime. The boxes identified as the "previous SWC conditions" show the range of temperatures, pressures, and CH_4 abundances that were obtained by Calcutt (1984). The boxes identified as the "current LWC conditions" show the range of conditions achieved for the spectra presented in the present study, which clearly provides greater coverage of temperature, pressure, and CH_4 abundance than the work of Calcutt (1984).

Tables A.1 to A.12, in Appendix A, list the the measured spectra and the corresponding laboratory conditions. Temperatures from 189.7 to 293.1 K, CH_4 pressures from 0.0002680 to 0.9477 bar, and CH_4 abundances from 0.01723 to 527.7 m-amagat were obtained in this work. As seen in Figure 6.1, the LWC measurements provide reasonably good coverage of Jovian pressures and CH_4 abundances. Although the maximum values attainable are lower than the Jovian values, the higher pressures and abundances are less important, as the clouds present in the Jovian atmosphere block much of the radiation from the deeper levels. The inability to obtain temperatures lower than 190 K is more unfortunate, because much of the absorption in the Jovian atmosphere does occur below this temperature. However, it is possible that the weaker absorptions in the wings of the CH_4 bands will allow radiation to escape from slightly deeper and warmer regions of the atmosphere (Calcutt, 1984, p.3-2). The long pathlengths available in the LWC therefore allow these weak absorptions to be measured.

Cooling the LWC to the lowest temperatures found on Jupiter may well prove to be impractical. An additional project was therefore undertaken, in parallel with the LWC spectroscopy, for the design and construction of a cooling jacket for the SWC which could achieve such temperatures. This project was awarded a lower priority than the long-pathlength spectroscopy possible with the LWC, as the need for CH_4 spectra with large abundances appears greater than the need for such spectra at the lowest possible temperatures (*e.g.*, the data of Giver *et al.*, 1984; see §4.3.2). In addition, if necessary, it should be possible to extrapolate the large-abundance data over the entire range of Jovian temperatures, as the the theory of temperature dependence of line strength is well established. Although a significant effort was put into the development of the SWC cooling jacket, and construction was completed, time limitations made it impossible to use the jacket to measure CH_4 spectra for this thesis. However, such measurements are

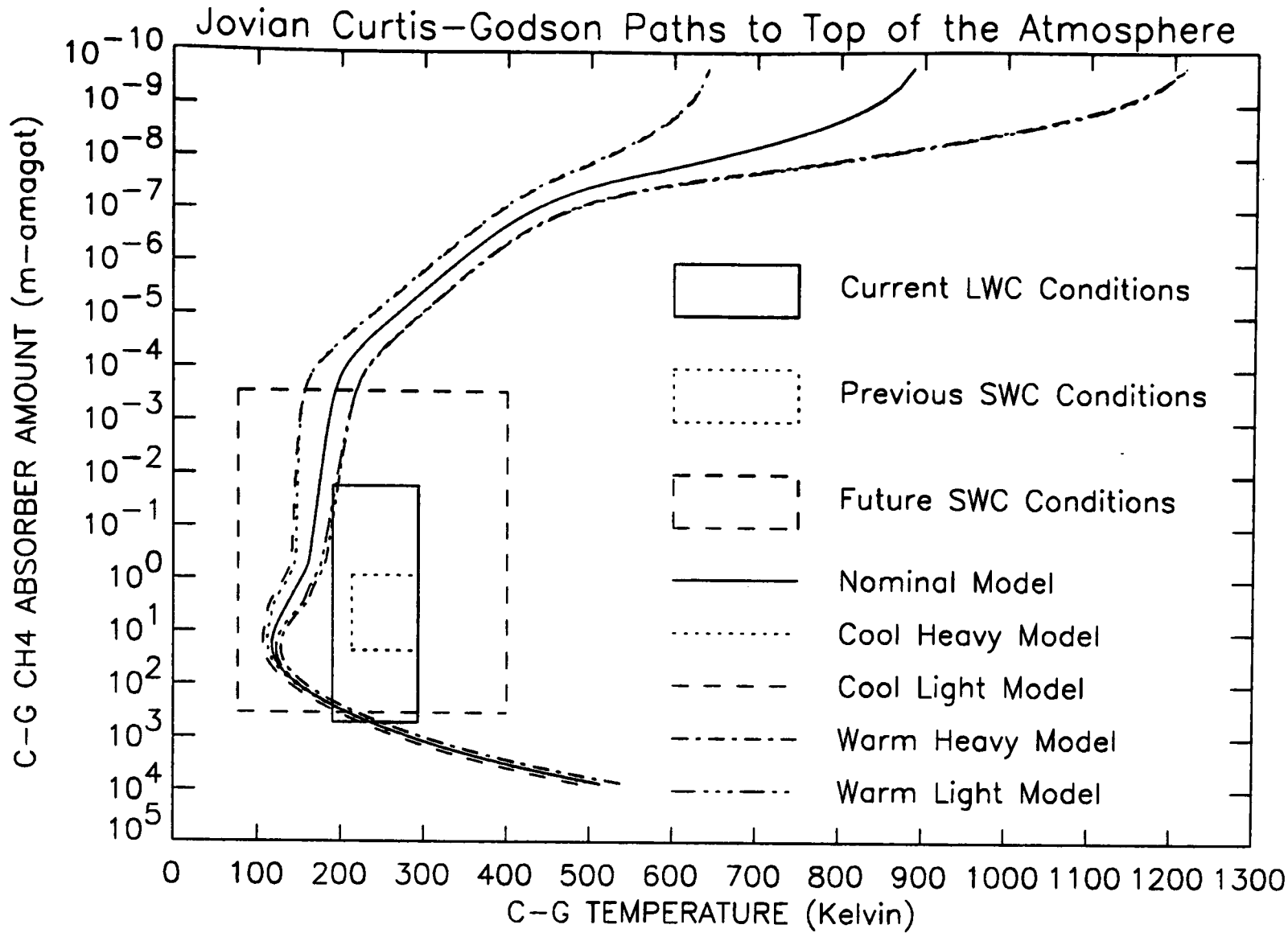

Figure 6.1: The Curtis-Godson parameters for paths to the top of the atmosphere using the five Jovian atmospheric models of Orton (1981). Three laboratory regimes are superimposed on these profiles, representing the range of conditions achieved in this work ("current LWC"), by Calcutt (1984; "previous SWC"), and intended with the new SWC cooling jacket which was designed and built as part of the present study ("future SWC").

intended for the future and are recommended in Chapter 8. The boxes labelled "future SWC conditions" in Figure 6.1 refer to the design parameters of this jacket. It has been designed to operate at pressures up to 5 atm and at temperatures from 77 to 400 K, thus providing low temperatures, high pressures, and fairly large abundances (because the high pressure compensates for the maximum SWC pathlength of 20 m). As seen in Figure 6.1, these conditions encompass a significant portion of the Jovian regime of interest.

6.1.2 The Achievable Spectral Range

The experimental resources employed for the self- and H_2-broadened CH_4 spectroscopy were chosen to provide as extensive coverage as possible of the NIMS spectral region. The latter extends from 1923 to 14286 cm^{-1} (0.7 to 5.2 μm), a very wide range of frequencies that are difficult to cover simultaneously in the laboratory. The spectral range achievable in the laboratory is determined by the choice of optical elements, *i.e.*, the detector, beamsplitter, source, infrared windows, mirrors, and filters. In practice, in this work, it proved possible to obtain spectra from 2000 to 9500 cm^{-1} (1.05 to 5.0 μm), thus providing coverage of nearly all but the visible end of the NIMS region.

The major limiting factors were the spectral responses of the indium antimonide (InSb) detector and the CaF_2 beamsplitter which were used throughout the measurements. The detector is a LN_2-cooled photovoltaic device which provided a nominal coverage of 1800 to 10000 cm^{-1}, with its spectral response dropping towards 10000 cm^{-1}. The InSb detector gave the most extensive coverage of the NIMS region that was possible with a single detector. Coverage out to 14286 cm^{-1} would have required repetition of all of the measurements using a Silicon detector. The CaF_2 beamsplitter was chosen for use in the Bomem spectrometer because it provided more extensive coverage than either the quartz or KCl beamsplitters that were available. It has a specified transmittance of >73% over 1200–8500 cm^{-1}, and thus contributed to the high frequency cut-off. Again, coverage out to 14286 cm^{-1} would have required repetition of all of the measurements with a quartz beamsplitter. The need for measurements at the visible end of the NIMS region was considered less critical, as this region has already been the subject of several laboratory studies (*e.g.*, Dick and Fink, 1977; Giver, 1978; see §4.3.1).

An additional factor influencing the achievable spectral coverage was the choice of light source. The Bomem provided two, a silicon-carbide globar and a quartz-halogen bulb. Neither emitted sufficient radiation over the entire region defined by the InSb detector and the CaF_2 beamsplitter, the globar having a high frequency cut-off near 4000 cm^{-1} and the quartz-halogen bulb having a low frequency cut-off near 3000 cm^{-1}. Both sources were therefore used, because unlike the detector and the beamsplitter, these could be interchanged (via the source-switching mirror in the Bomem) without destroying the integrity of the experimental system. Thus, for each measurement condition, both a set of quartz-halogen spectra and a set of globar spectra were recorded, the latter following immediately after the former. Figures 6.2 and 6.3 show

typical background spectra recorded with each source.

Of the remaining optical elements in the system, the CaF_2 windows and the gold-coated mirrors provided transmittance and reflection, respectively, over the entire NIMS region, as discussed in §5.2.3, and so did not limit the available spectral range. A GaAs filter was also included in the system to eliminate contamination by stray visible radiation of $\lambda < 0.9$ μm. This filter was mounted over the window of the InSb detector rather than in the Bomem filter wheel, thereby ensuring that any visible light entering the system beyond the Bomem was also prevented from falling on the detector.

Before beginning the CH_4 spectroscopy, several additional parameters were selected. Although the maximum resolution of NIMS is 9.25 cm^{-1} at 1923 cm^{-1}, and the intended resolution of the band models was 10 cm^{-1}, the spectra were recorded at the maximum possible resolution within the limitations of the available Bomem computer memory. This allowed better assessment of the quality of the spectra and permits higher-resolution analysis of the spectra if desired in the future. For the spectral range of both the quartz-halogen and globar sources, an apodised resolution of 0.25 cm^{-1} was achievable, and so all of the spectra were recorded at this value. In order to suppress the side lobes due to the instrument lineshape, the strongest available apodisation function was chosen. This minimum three-term Blackman-Harris function reduced the largest side lobes from 22% to 0.04% of the central peak amplitude. This also increased the FWHH of the measured lines to 116% of the specified apodised resolution, but this was judged to be acceptable for the purposes of this low-resolution spectroscopy. Finally, throughout the experiments, a Bomem iris diameter of 1.0 mm was used, as this provided good signal-to-noise (see §6.2.5), without saturating the detector when the quartz-halogen bulb was used. Because the globar produced a smaller flux of radiation at the detector for the chosen combination of optical resources, a higher gain setting of the preamplifier for the InSb detector was used when recording spectra with the globar.

6.1.3 The Experimental Procedure

During the period of spectroscopic measurements, a clearly defined step-by-step procedure was followed each day. The essential steps in this daily experimental procedure are outlined below. As is explained in §6.2.1, five spectra were recorded for every pressure-temperature-pathlength-source combination in order to reduce the effects of random variability. The quartz-halogen spectra were recorded from 2000 to 11000 cm^{-1}, while the globar spectra were recorded from 1400 to 4000 cm^{-1}. Although the spectral coverage extended from 1400 to 11000 cm^{-1}, the signal-to-noise on the spectra limited the useful range to 2000–9500 cm^{-1}. The sequence followed in obtaining each individual spectrum was to first record a "PHAS" spectrum for use in performing the phase correction discussed in §5.1.2. This was immediately followed by a "COAD" operation, in which 30 successive interferograms were recorded and automatically averaged (thereby improving the signal-to-noise) before being phase corrected and numerically

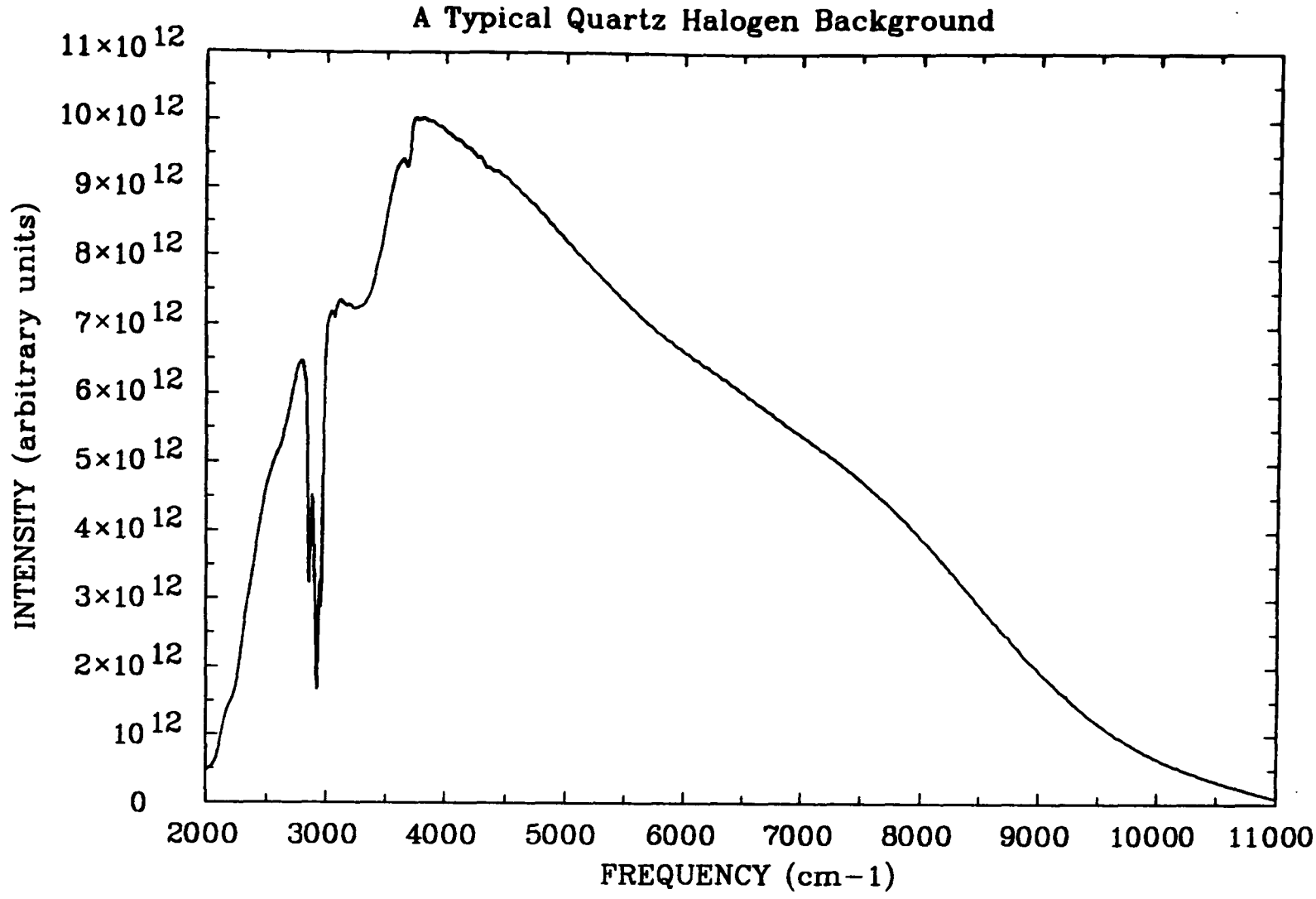

Figure 6.2: A quartz-halogen background spectrum recorded at 64 m and 240 K, plotted at the original resolution: the high frequency cut-off is determined by the InSb detector and CaF_2 beamsplitter, and the low frequency cut-off is determined by the quartz-halogen source.

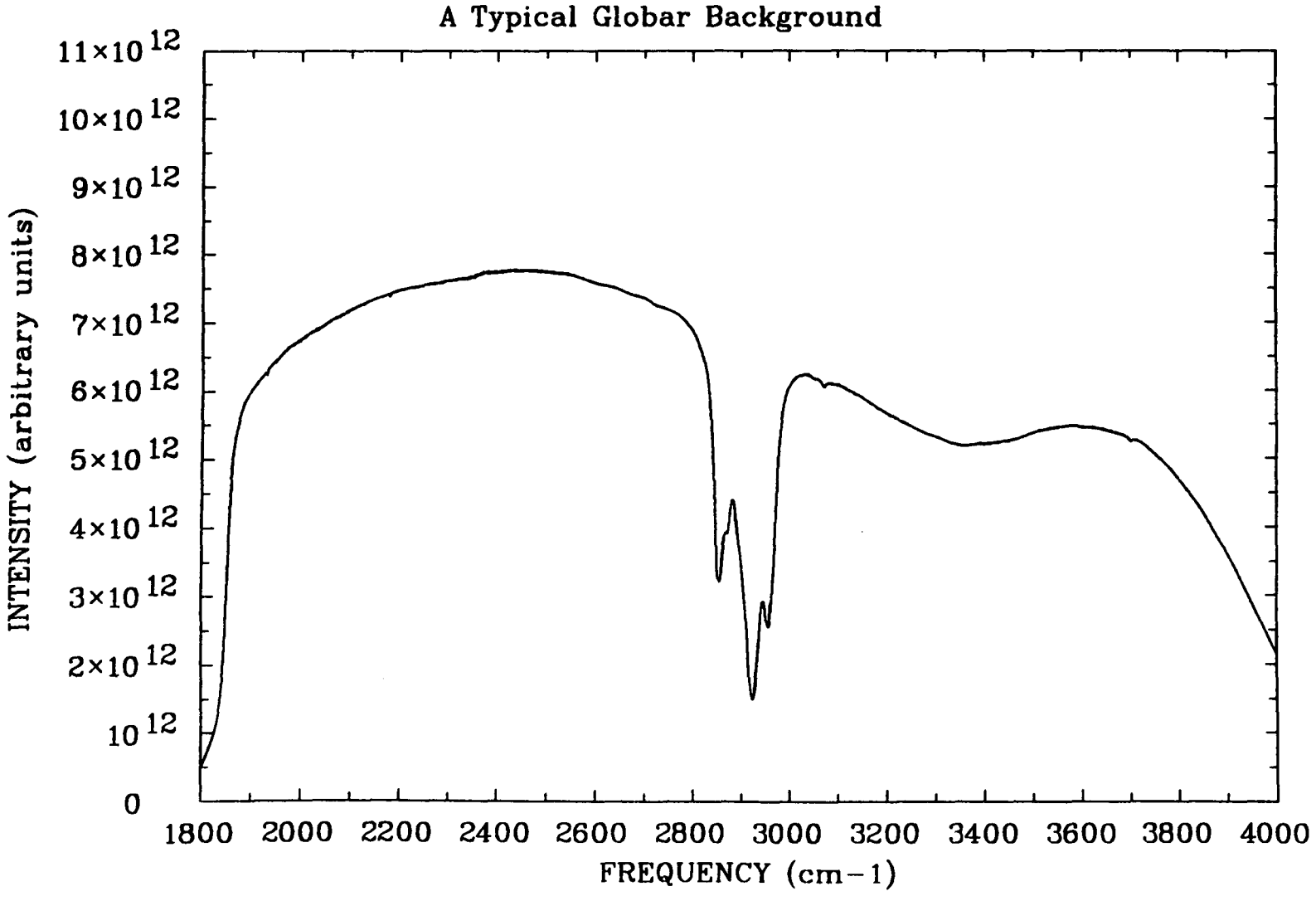

Figure 6.3: A globar background spectrum recorded at 64 m and 240 K, plotted at the original resolution: the high frequency cut-off is determined by the globar source and the low frequency cut-off is determined by the InSb detector.

filtered. Ten minutes were required for each quartz-halogen PHAS–COAD run, and eight minutes for each globar PHAS–COAD run. With the Fourier transform process taking about another ten minutes per spectrum, this was left to be performed by the HSVP overnight.

The CH_4 spectra were recorded in three sets, defined by the nominal LWC temperature. Chronologically, the spectra were recorded first at 296 K, then at lowest possible temperature, 190 K, and finally at an intermediate temperature of 240 K. At each temperature, the usual procedure was to stay at a particular pathlength for several days, stepping through several pressures per day. With each set of five quartz-halogen plus five globar spectra (whether CH_4 spectra or start- and end-of-day backgrounds) taking two hours, each fill taking as long as an hour, and the final evacuation taking at least two hours, between three and five pressures could be measured in a day. The following is a summary of the daily procedure that was carried out each day. The italicised items are the additional steps required for the low-temperature measurements.

(1) Complete a Daily Start-of-Day Checklist to ensure that the spectroscopy facility and LWC system are in a safe state for flammable-gas operations.

(2) Begin the first fill of the day, completing a Filling Checklist as the necesary steps are performed.

(3) Fill the InSb detector with LN_2.

(4) Change the LWC pathlength, if necessary.

(5) Turn off the large pumps (the LWC was generally pumped by DP1 overnight).

(6) *Turn off the LWC heat exchanger circulating pump and vacuum pumps, and shut off the LN_2 supply.*

(7) *Ensure that the data logger is correctly recording the LWC PRT temperatures at 10-minute intervals.*

(8) With the inner vessel under vacuum, but not actively pumped, COAD a set of five empty-cell background quartz-halogen interferograms, followed by a set of five background globar interferograms.

(9) Record the gas handling and inner vessel baratron zeros.

(10) Flush the gas handling system with CH_4.

(11) Fill the inner vessel to the desired CH_4 pressure and record the final baratron readings.

(12) If H_2-broadened CH_4 spectra are to be recorded, flush the gas handling with H_2, fill the inner vessel with the desired pressure of H_2, and record the final baratron readings.

(13) Isolate the inner vessel and resume pumping the gas handling.

(14) COAD a set of self- or H_2-broadened CH_4 interferograms, five with the quartz-halogen source, followed by five with the globar source.

(15) Record a set of PRT temperatures while these interferograms are being recorded (for the room temperature spectra, only).

(16) Once the interferograms have been recorded, open the inner vessel to the gas handling

system and record the baratron readings.

(17) Repeat steps 10 through 16, stepping up in either CH_4 or H_2 pressure, thereby recording spectra at several pressures, but at the same temperature and pathlength, over the course of the day. A new Filling Checklist is completed for each fill.

(18) Once all of the day's CH_4 spectra have been recorded, begin pumping out the inner vessel, completing an Evacuation Checklist as the necesary steps are performed.

(19) After the inner vessel has been pumped with DP1 for about 30 minutes, turn off the large pumps again.

(20) With the inner vessel again under vacuum, but not actively pumped, record a set of end-of-day background interferograms, five with the quartz-halogen source, followed by five with the globar source.

(21) *Resume cooling the LWC, turning on the circulating pump and vacuum pumps, restoring the LN_2 supply, and pumping the LWC vacuum vessel.*

(22) Complete a Daily End-of-Day Checklist to ensure that the spectroscopy facility and LWC system are in a safe state overnight.

(23) Refill the InSb detector with LN_2 to keep it cold overnight.

(24) Leave the inner vessel being pumped, and the day's interferograms being Fourier transformed into spectra overnight.

6.1.4 The Self-Broadened Methane Spectra

A total of 1080 self-broadened CH_4 spectra were recorded, 540 of these using the quartz-halogen light source and 540 using the globar, thereby maximising the spectral coverage. These 540 spectra consist of 108 temperature-pressure-pathlength combinations, for each of which, five independent spectra were recorded. The 108 combinations provided maximum coverage of the achievable conditions, thereby allowing the band models to be fitted to as wide a range of conditions as possible. They correspond to 36 pressure-pathlength combinations at each of three temperatures, these 36 being derived from four pathlengths and nine pressures. The three nominal temperatures were 190, 240, and 296 K, the minimum and maximum achievable, and the midpoint between them. The four nominal pathlengths (see §5.3.4) were 64, 128, 256, and 512 (416 at 190 K) m, again the minimum and maximum, with two intermediate values. The nine nominal pressures were 0.2, 0.8, 3.2, 12.8, 51.2, 102.4, 204.8, 409.6, and 700 torr, chosen in logarithmic steps such that the ratio of successive pressures was 4 up to 51.2 torr and was 2 beyond 51.2 torr, except for 700 torr, which was the highest LWC pressure safely obtainable.

These pressures and pathlengths were chosen to provide CH_4 abundances which were constant for several pressure-pathlength combinations. Figure 6.4 is a plot of CH_4 abundance versus pressure for the 36 pressure-pathlength combinations obtained for the 296 K quartz-halogen self-broadened CH_4 spectra. Similar plots can be constructed for the 240 K and 190 K spectra. This illustrates, for a particular temperature, how the abundance increases with pressure

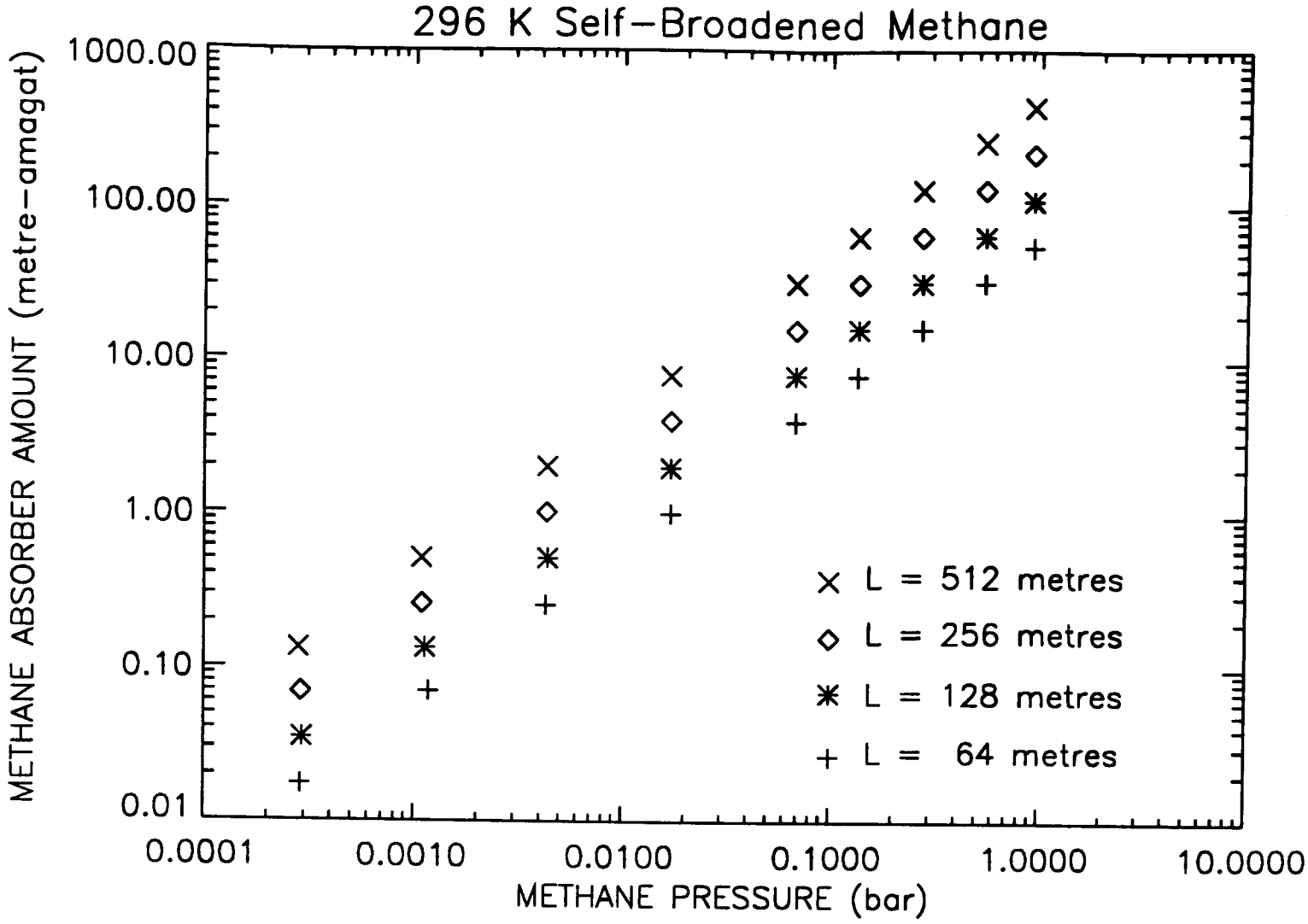

Figure 6.4: The CH_4 abundance as a function of the nine pressures and four pathlengths used in the self-broadened CH_4 spectroscopy. This plot is for the 36 296 K quartz-halogen self-broadened CH_4 spectra.

and pathlength, and is the same for several combinations. Figure 6.5 displays some typical quartz-halogen spectra which have been corrected and degraded to 10 cm^{-1} resolution, as is discussed in §6.2.2. They illustrate how changes in pathlength, pressure, and temperature affect the CH_4 absorption.

Tables A.1 to A.6, in Appendix A, list the 108 averaged self-broadened CH_4 spectra recorded with both the quartz-halogen and globar sources. They have been grouped by source and temperature, and are listed in order of increasing CH_4 abundance within each table. These tables include the LWC pathlength (for which the uncertainties were presented in Table 5.2), the CH_4 absorber amount (calculated using the ideal gas law), and the temperatures and pressures, which were derived as follows.

For the room temperature spectra, a single temperature map of all twenty-six PRT's was recorded once for each pressure-pathlength combination, and so the listed temperatures are the same for both the quartz-halogen and the globar spectra, with the standard deviation being that for the twenty-six PRT readings. The maximum uncertainty in the temperature for each of these 296 K spectra is taken to be the sum of its standard deviation and the instrumental (PRT plus current source) uncertainty of ± 0.6 K, derived in §5.3.2. With the largest standard deviation being ± 0.3, the maximum uncertainty in the 296 K temperatures is ± 0.9 K. For the low temperature spectra, the data logger was used to record the temperature of fifteen PRT's automatically every 10 minutes. For each spectrum in every set of five, linear interpolation in

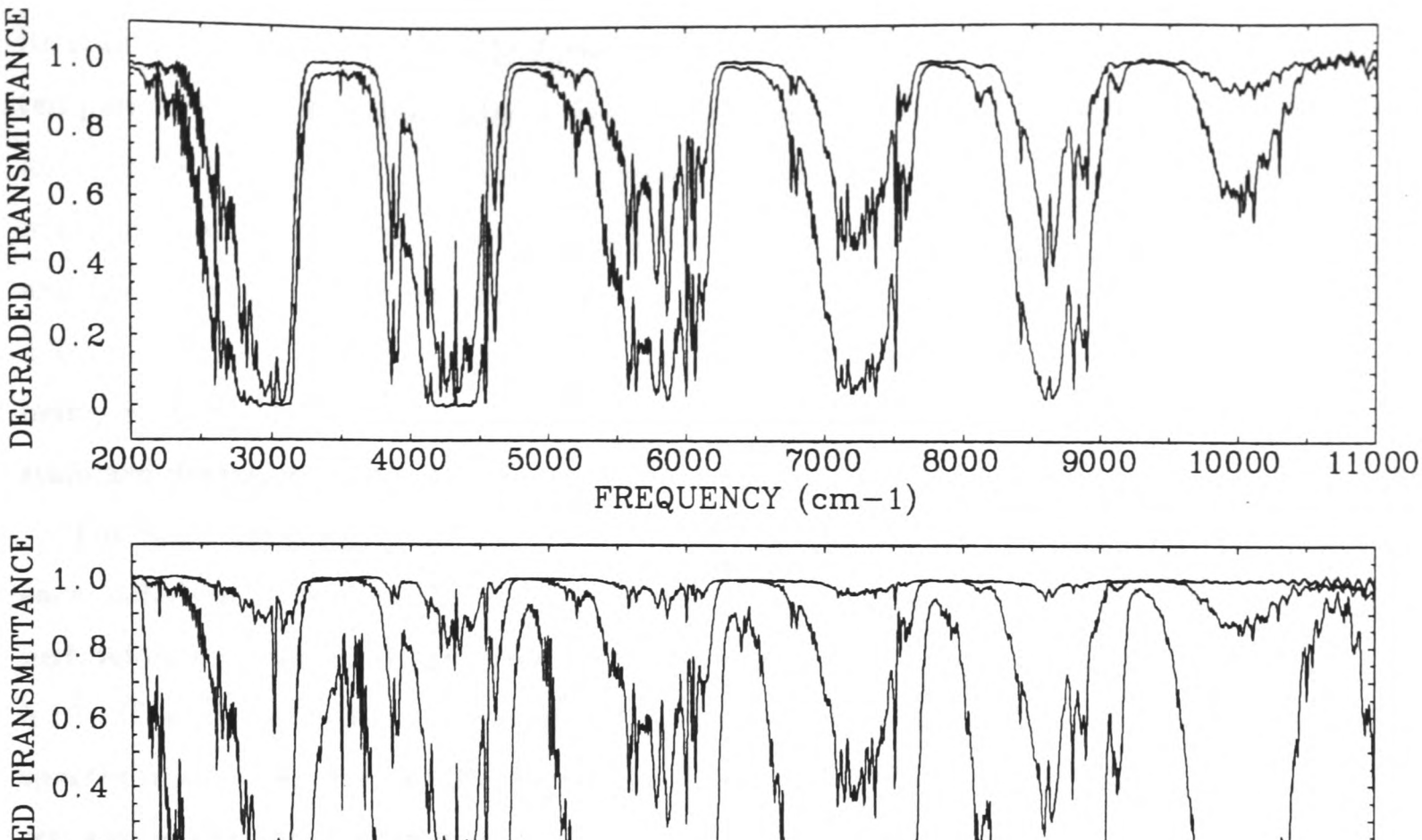

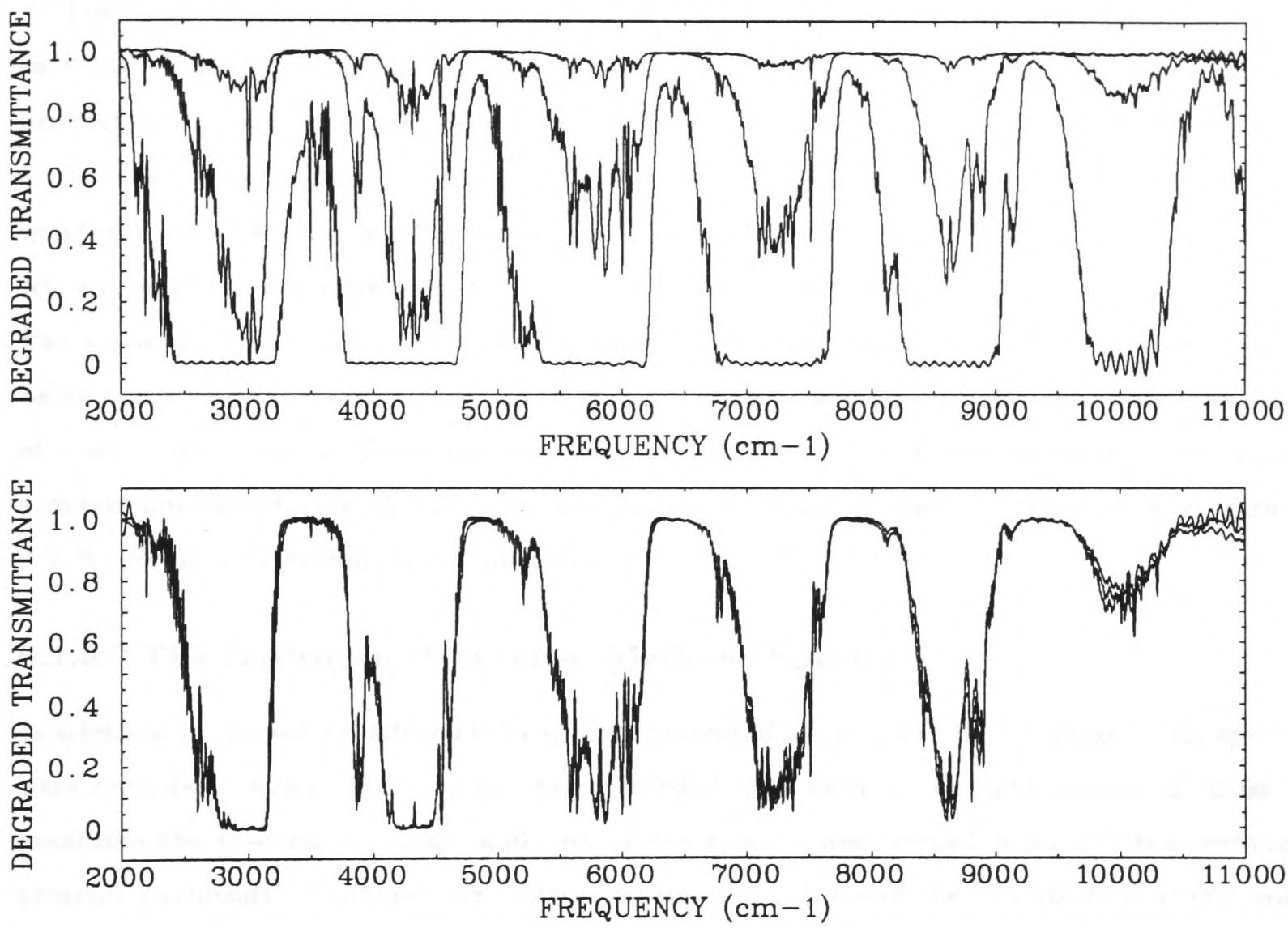

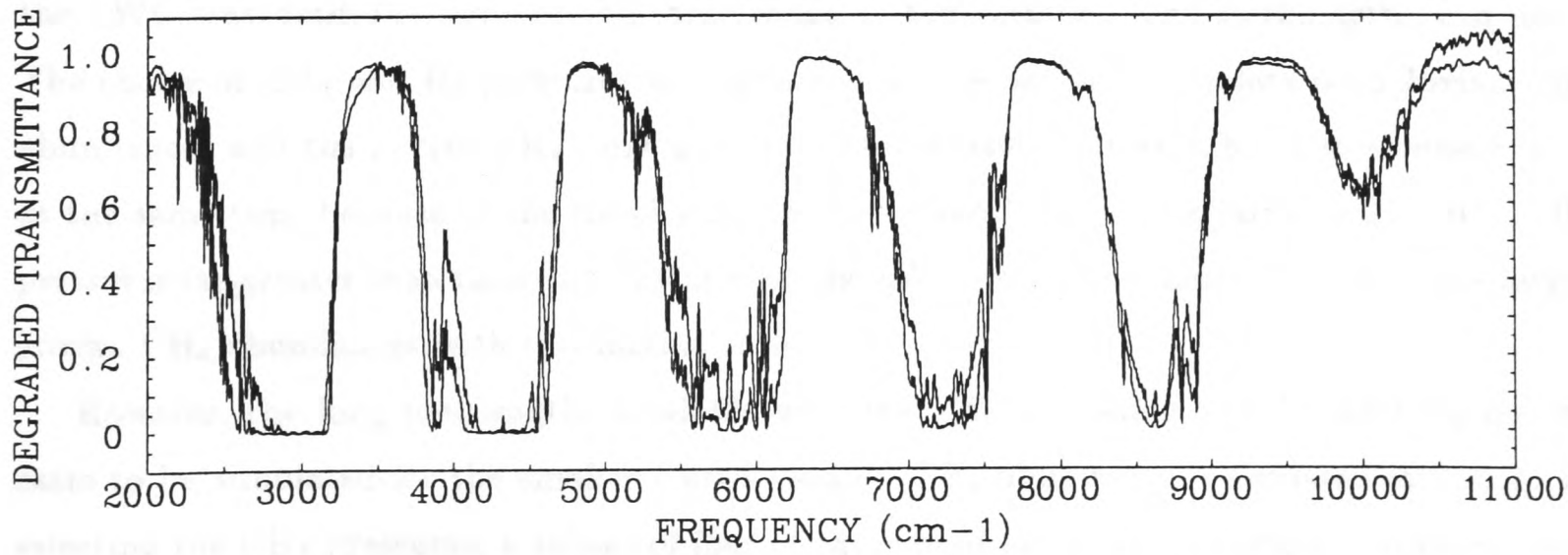

Figure 6.5: Self-broadened CH_4 spectra recorded with the quartz-halogen source, corrected, averaged, and degraded to 10 cm^{-1} as described in §6.2.2. (a) Constant T (~240 K) and P (~51.2 torr), with varying L (64.75 m for upper curve, and 512.75 m for lower curve). (b) Constant T (~240 K) and L (512.75 m), with varying P (~0.2 torr for upper curve, ~12.8 torr for middle curve, and ~700 torr for lower curve). (c) Constant P (~102.4 torr) and L (128.75 m), with varying T (290.8, 239.3, and 193.2 K: barely distinguishable). (d) Constant T (~296 K) and CH_4 abundance (~32.5 m-amagat), with varying P and L (~51.2 torr and 512.75 m for upper curve, ~409.6 torr and 64.75 m for lower curve).

time was used to derive fifteen PRT temperatures. This allowed an average temperature and its standard deviation to be calculated for each spectrum and for each set of five spectra. The temperatures listed in Appendix A are the averages of seventy-five PRT temperatures (fifteen for each of five spectra), with the standard deviation calculated using all seventy-five. The maximum uncertainty in each cold temperature is similarly the sum of its standard deviation and the instrumental uncertainty, but in this case, the latter is given by Equation 5.6 and is $\pm[0.7 + 0.001 \times |T_{in}|]$ for T_{in} in °C. For the 240 K spectra, with the largest standard deviation being ±1.6 K, the maximum uncertainty is ±2.3 K. For the 190 K spectra, with the largest standard deviation being ±3.2 K, the maximum uncertainty becomes ±4.0 K.

For both the room- and low-temperature spectra, the CH_4 pressures were calculated for each individual spectrum by linearly interpolating in time between the pressures measured just before and just after the spectra were recorded ($P_{gas}(t_i)$ and $P_{gas}(t_f)$ of Equations 5.9 and 5.10). The pressures listed in Tables A.1 to A.6 are the averages of the five pressures for the five spectra in each set. For the 296 K spectra, there was negligible change in the pressure within a set, and so the uncertainty is the 1.1% derived in §5.3.3. For the low temperature spectra, there was a gradual temperature rise over the course of the day, due to the LWC cryogenic system being turned off, and so the pressure of gas in the LWC increased slowly during the recording of a set of five spectra. The largest standard deviation for the 240 K spectra is 0.18%, giving a maximum uncertainty of 1.3%, and the largest standard deviation of the 190 K spectra is 0.37%, giving a maximum uncertainty of 1.5%.

6.1.5 The Hydrogen-Broadened Methane Spectra

In addition to the self-broadened CH_4 spectra presented above, 1170 H_2-broadened CH_4 spectra were recorded. Again, 585 of these were recorded with each of the light sources in order to maximise the spectral coverage, and sets of five spectra were recorded for 117 temperature-pressure-pathlength combinations. Again, maximum coverage of the conditions available with the LWC was desirable, and so the same range of temperatures and pathlengths was used. The choice of CH_4 and H_2 pressures was governed by the desire to simulate both Jovian CH_4 abundances and the Jovian CH_4 mixing ratio. Unfortunately, it was difficult to simulate both at the same time because of the small value of the Jovian CH_4 mixing ratio ($\sim 2 \times 10^{-3}$). H_2 pressures far greater than those attainable with the LWC would be required to obtain the larger Jovian CH_4 abundances with this mixing ratio.

However, the long pathlengths available with the LWC did allow the Jovian CH_4 mixing ratio to be simulated for the smaller Curtis-Godson CH_4 abundances calculated in §6.1.1. In selecting the CH_4 pressures, a subset of four of those used in the self-broadened measurements was chosen: 0.2, 3.2, 12.8, and 102.4 torr (nominal values), thus allowing self- and H_2-broadened CH_4 spectra to be compared for the same CH_4 abundances. For the H_2 pressures, three values were chosen, 100, 245 and 600 torr, providing nominal CH_4-to-total mixing ratios ranging from

3.3×10^{-4} to 0.51. Figure 6.6 shows the CH_4 abundances and mixing ratios for the 296 K quartz-halogen H_2-broadened CH_4 spectra that resulted from this choice of pressures, while Figure 6.7 displays two corrected, averaged, and degraded quartz-halogen spectra (see §6.2.2) with and without H_2-broadening. Both of these spectra have the same temperature, CH_4 pressure, and pathlength, but one is self-broadened while the other is broadened by 613.2 torr of H_2.

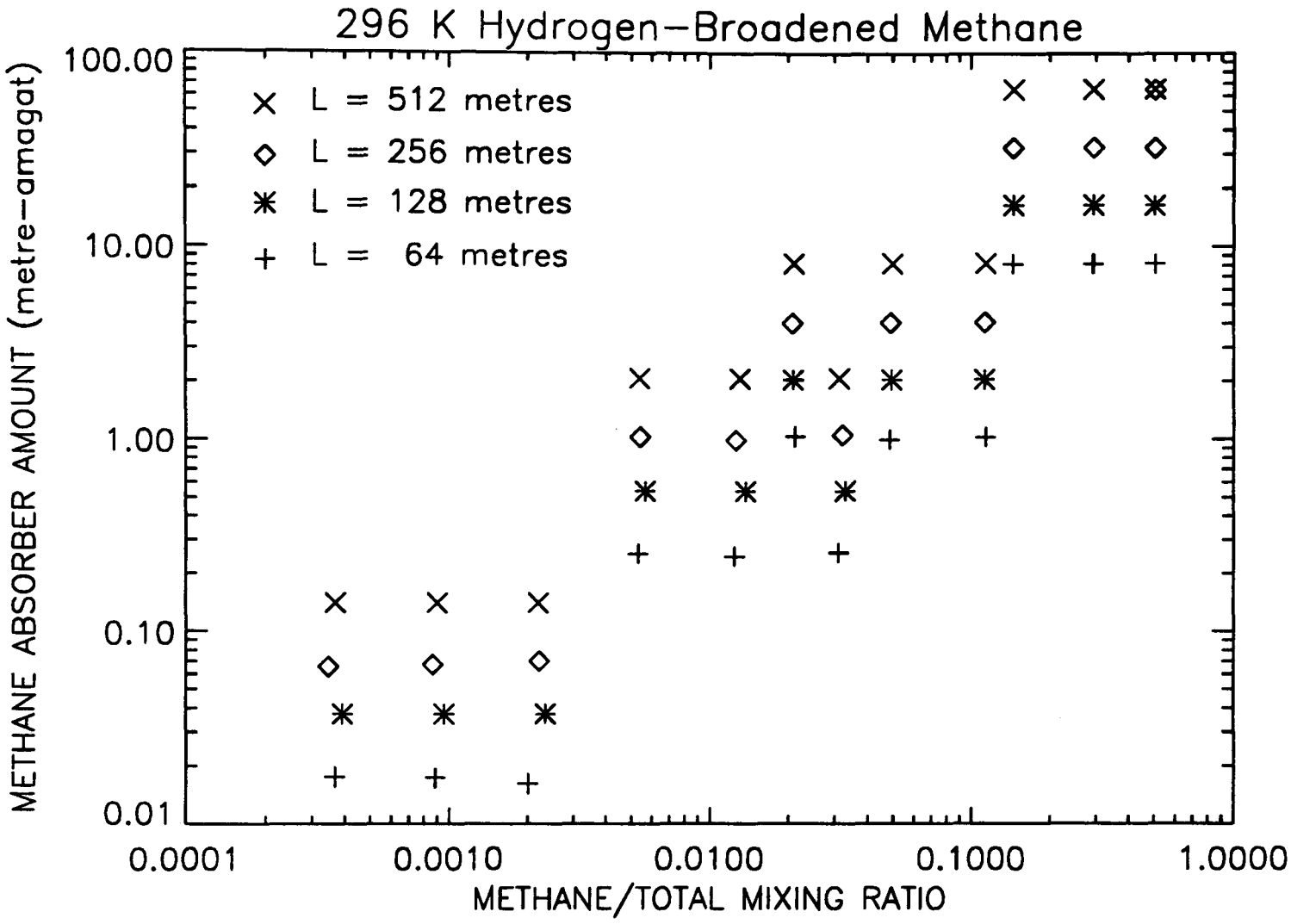

Figure 6.6: The CH_4 abundance as a function of the CH_4 mixing ratio for the four pathlengths used in the H_2-broadened CH_4 spectroscopy. This plot is for the 49 296 K quartz-halogen H_2-broadened CH_4 spectra.

Tables A.7 to A.12, in Appendix A, list the 117 averaged H_2-broadened CH_4 spectra for both the quartz-halogen and globar sources, again grouped by source and temperature, and listed in order of increasing CH_4 abundance within each table. These tables include the total (CH_4 + H_2) pressure, the CH_4-to-total mixing ratio, and the CH_4 abundance, as well as the temperature and pathlength. The temperatures and pressures and their standard deviations have been derived in the same way as those for the self-broadened CH_4 spectra. Taking the largest standard deviations in the temperatures, the maximum uncertainties in the temperatures are $\pm$0.9 K, $\pm$2.1 K, and $\pm$3.4 K for the 296 K, 240 K, and 190 K spectra, respectively. Similarly, taking the largest standard deviations in the pressures, the maximum uncertainties are 1.1%, 1.4%, and 1.5% for the 296 K, 240 K, and 190 K spectra, respectively.

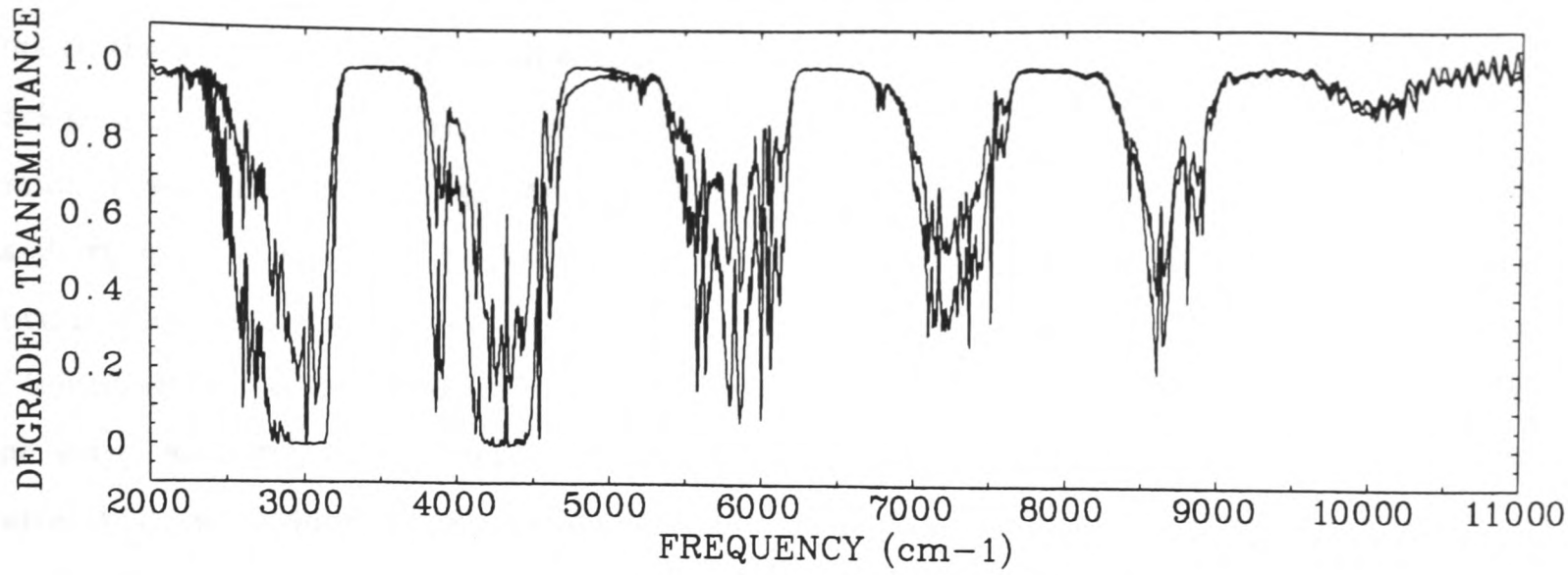

Figure 6.7: Self- and H_2-broadened CH_4 spectra recorded with the quartz-halogen source, corrected, averaged, and degraded to 10 cm^{-1} as described in §6.2.2: constant temperature (~240 K), CH_4 pressure (~12.8 torr), and pathlength (256.75 m), with no H_2 for the upper curve and 613.2 torr of H_2 for the lower curve.

6.2 Initial Processing of the Spectra

Before beginning the band-modelling analysis of the self- and H_2-broadened CH_4 spectra, some initial processing was necessary, involving the generation of a set of transmittance spectra and an assessment of their quality. In principle, a transmittance spectrum is generated simply by ratioing an intensity spectrum recorded with gas in the cell, to a background intensity spectrum recorded with the cell empty but under otherwise identical conditions. In practice, problems caused by changes in the background conditions and by the addition of gas to the cell are frequently encountered in laboratory spectroscopy. Some of these problems affect only small spectral regions, and for some it is relatively simple to apply a correction. The more serious problems are those affecting larger spectral regions, especially when uniform coverage of a wide spectral range is desirable, as was true of this work. Such measurements tend to be particularly vunerable to small changes in the spectrometer or absorption cell which affect the calibration.

In this section, the method of generating the final set of ratioed, averaged, and degraded transmittance spectra is described, and the factors that were found to affect the quality of these spectra are discussed. These factors include:

(1) the background variability,

(2) the formation of ice on the detector,

(3) the zero-signal level,

(4) the signal-to-noise ratio,

(5) the formation of channel spectra, and

(6) spectral features due to the presence of contaminants.

Any errors arising from these factors were minimised as far as possible during the measurement period, using experimental techniques. However, for those cases for which this did not prove feasible, an assessment of the resulting errors was performed, and when possible, the errors were reduced or eliminated computationally.

6.2.1 Background Variability

Due to the long duration of the spectral measurements, and the delay between the recording of background and CH_4 spectra, significant shifts in the background levels were anticipated and found. Preliminary tests suggested variability on the level of 5% of full scale over time scales as short as 10 minutes. It proved impossible to determine the exact cause of such shifts, and optimisation of the spectrometer alignment did not eliminate them. As a consequence, a set of five spectra was recorded for every temperature-pressure-pathlength combination, including the start- and end-of-day backgrounds. This provided a means of assessing the background variability, and reducing any random errors by averaging the five spectra in a set.

The first step in the analysis of the spectra was thus to assess the variability within every set of five background spectra. For both the quartz-halogen and globar backgrounds, this assessment was performed for 53 sets of 296 K spectra, 36 sets of 240 K spectra, and 33 sets of 190 K spectra. For each set, recorded over a period of 40 (for the globar) or 50 (for the quartz-halogen bulb) minutes, the last four intensity spectra were ratioed to the first recorded intensity spectrum to generate four transmittance spectra. Inspection of these ratioed spectra revealed the following deviations from the ideal case of a straight line at 1.0:

(1) A broad ripple with a period of approximately 5000 cm^{-1} was observed in some of the sets, and found to be most noticeable in the 296 K start-of-day backgrounds, significantly reduced in the 190 K backgrounds, and almost negligible in the 240 K backgrounds. This was traced to the formation of ice on the detector, which is discussed further in §6.2.3.

(2) Systematic drifts were present in some of the 190 K sets, primarily for the start-of-day spectra. This was seen as a consistent change in the average transmittance within a set of four ratios, usually decreasing. It appeared to be caused by a relaxation of the LWC mirror adjustors (which was sometimes, but not always, reduced by disengaging the outer handles) after the initial readjustment to maximise the signal at the desired pathlength. These drifts resulted in the average transmittance differing by as much as 0.2 within a set. The presence of such drifts between CH_4 spectra and their backgrounds, would cause the 100% transmittance level to deviate from 1.0 in the ratioed CH_4 transmittance spectra. The method of eliminating this effect is discussed in §6.2.2 below.

(3) In cases where the broad ice ripple was not present, the ratios of quartz-halogen spectra were sometimes lines that sloped from low to high frequencies, indicating changes in signal level with frequency. These slopes were observed at all three temperatures, and both their magnitude and direction varied randomly within each set of ratios. They were thought to be due to an instrumental effect such as misalignment of the mirrors in the spectrometer (Griffiths and de Haseth, 1986, p.39–42), but their exact cause was not determined. The method of dealing with such slopes in the CH_4 transmittance spectra was the same as that used in dealing with the systematic drift, again found in §6.2.2.

(4) The ratioed spectra also exhibited a random variability, clearly seen in those sets not

subject to the systematic drift, and again thought to be due to instrumental effects. The average transmittances for the four ratioed spectra in a set varied randomly from the nominal value of 1.0. This random drift was reduced in the same way as the systematic drift (§6.2.2) and by averaging the five spectra in each set.

6.2.2 Generation of the Methane Transmittance Spectra

The procedure for generating the final set of CH_4 transmittance spectra from the raw intensity spectra is illustrated in Figure 6.8. The following is a description of this procedure, with particular attention to the methods that were used to correct the 100% transmittance level. First of all, for each recorded CH_4 intensity spectrum, a background intensity spectrum was needed in order to compute the ratioed CH_4 transmittance spectrum. These background spectra were generated as follows. For each day of the experiment, a set of five start-of-day and another set of five end-of-day background spectra were recorded with the LWC evacuated, but otherwise using the same Bomem configuration, sources, temperature and pathlength as would be used for the CH_4 spectra recorded that day. The five spectra in each of these sets were averaged to obtain a daily start-of-day and a daily end-of-day averaged background for each source, thereby reducing the random variability within each set. Then the appropriate background for each CH_4 spectrum was computed by linearly interpolating the background intensity in time between the start- and end-of-day averaged backgrounds. Each individual CH_4 intensity spectrum was then ratioed to its interpolated background to generate the CH_4 transmittance spectra.

Examination of these ratioed CH_4 spectra revealed that the 100% transmittance level often varied significantly from 1.0, in both the quartz-halogen and globar spectra. This discrepancy was partly due to the systematic variability caused by the relaxation of the mirror adjustors and to the random variability of the spectra, as described in §6.2.1. Additional systematic variability in the background intensity over the course of a day was introduced by several other factors. The signal level was observed to be highly sensitive to the alignment of the LWC mirrors, and particularly to the position of the first image on the tab, so that small changes in alignment due to the presence of gas in the LWC, mirror movement, or temperature drift, could cause systematic changes in the background intensity. The signal level also fluctuated when gas was introduced into the LWC, the turbulence and change in pressure apparently moving the mirrors slightly. During the 190 K and 240 K measurements, the mirrors were carefully readjusted after each gas fill in order to maximise the signal, but it was not always possible to regain the previous signal (discounting the decrease due to gas absorption) and so this provided another source of variability. Changes in the alignment of the Bomem source-switching mirror, which was frequently switched between the quartz-halogen and the globar sources, and changes in the temperature of the detector or of the source would also have contributed to the overall systematic variability.

With the 100% transmittance level in the CH_4 transmittance spectra varying by as much

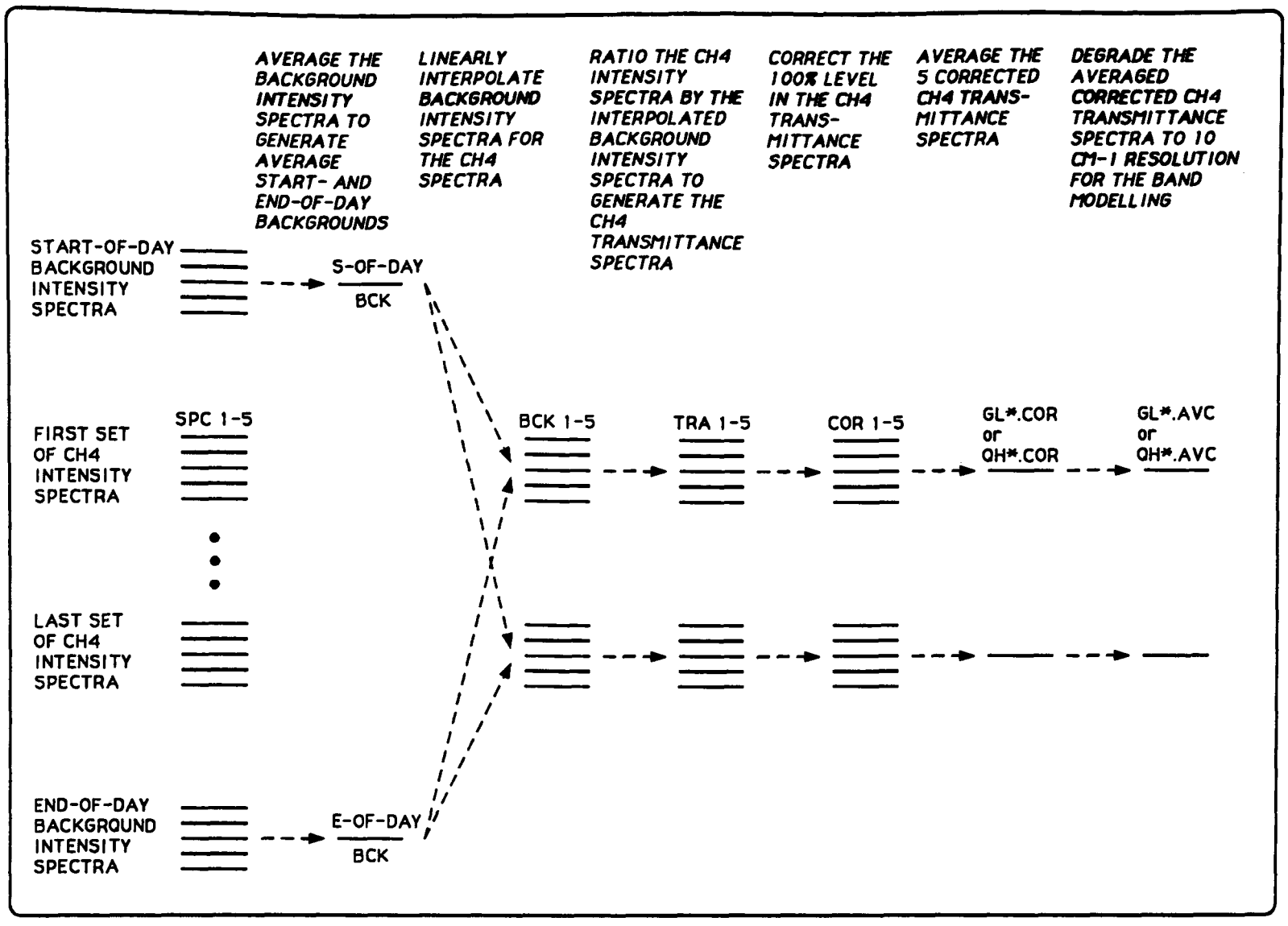

Figure 6.8: The sequence followed in generating the final set of CH_4 transmittance spectra.

as ± 0.3 from 1.0 in the worst cases, some method of normalising the spectra was required. The same problem has been encountered in previous measurements of CH_4 spectra for the purposes of band modelling. Calcutt (1984) dealt with background drift by fitting straight lines to the transmittances (averaged over 100 points) at four frequencies located in regions of zero absorption and ratioing the spectra to these lines in order to correct all points, resulting in corrections of about 2%. Dick and Fink (1977) corrected for slopes in their ratioed spectra and intensity changes in their lamp by similarly dividing their spectra by appropriate normalisation functions. However, both they and Giver (1978) mention the difficulty of determining the "continuum" level for spectra with large CH_4 abundances for which finite absorptions between the main bands eliminated the regions of zero absorption. For these spectra, the "continuum" level was estimated by comparisons with lower abundance spectra, and Giver acknowledged that this was likely to have introduced systematic errors. Benner (1979, p.34) stated that the placement of the "continuum" level was the most difficult problem encountered in assessing the quality of his spectra. His attempts to redefine the "continuum" level by fitting band models and readjusting the most poorly fitted spectra failed, and the level was eventually just defined by eye, introducing uncertainties of several percent and as large as 10 or 15% in the regions between bands.

Similar difficulties were encountered in correcting the 100% transmittance level in this work, due to the large CH_4 abundances of many spectra. It was decided that the spectra could best

be corrected using two different methods, one for the weakly absorbing spectra and one for the strongly absorbing spectra. The "weakly absorbing" CH_4 spectra were defined as those for which there was negligible absorption in the window regions, a convenient dividing point being 25 m-amagat of CH_4 — for spectra with less than this abundance, the transmittance in the windows was assumed to be 1.0. This assumption ignored the possibility of any true CH_4 continuum absorption in these regions, the measurement of which is clearly a difficult problem without a highly stable background level. For these spectra, the correction method of Calcutt (1984, p.5-3), referred to above, was appropriate. The "strongly absorbing" CH_4 spectra were correspondingly defined as those with more than 25 m-amagat of CH_4, and exhibited weak line absorptions in the window regions. For these spectra, a different method of correction was devised. The methods that were used to correct the globar and quartz-halogen CH_4 spectra are described as follows.

The globar CH_4 spectra included two transmittance windows, one centered on 2000 cm^{-1} and one on 3510 cm^{-1}. For the weakly absorbing spectra, there was negligible absorption in both of these windows, allowing a straight line to be fitted to the average transmittances at 2000 ± 5 cm^{-1} and 3510 ± 5 cm^{-1} for each CH_4 spectrum. This line represented the 100% transmittance level, and so ratioing a CH_4 spectrum to this line normalised the regions of maximum transmittance to 1.0. The average shift in transmittance at these two points for globar spectra with less than 25 m-amagat of CH_4 was 0.047 for the 330 self-broadened CH_4 spectra, and 0.074 for the 490 H_2-broadened CH_4 spectra. These values, along with the average shifts for each temperature and the average shifts for the corrected quartz-halogen spectra, are listed in Table 6.1.

Table 6.1: The average shifts in transmittance resulting from correction of the 100% transmittance level in the weakly and strongly absorbing globar and quartz-halogen spectra, tabulated for each temperature and for all three temperatures.

SPECTRA	FOR 296 K	FOR 240 K	FOR 190 K	FOR ALL T's
330 self-broadened CH_4 globar ratioed to fitted line	0.059	0.029	0.053	0.047
490 H_2-broadened CH_4 globar ratioed to fitted line	0.098	0.038	0.074	0.074
210 self-broadened CH_4 globar scaled by max. τ	0.149	0.143	0.113	0.136
95 H_2-broadened CH_4 globar scaled by max. τ	0.195	0.148	0.074	0.143
330 self-broadened CH_4 Q-H ratioed to fitted line	0.047	0.018	0.049	0.038
490 H_2-broadened CH_4 Q-H ratioed to fitted line	0.097	0.040	0.061	0.070
210 self-broadened CH_4 Q-H scaled to match globar	0.084	0.030	0.089	0.067
95 H_2-broadened CH_4 Q-H scaled to match globar	0.140	0.042	0.056	0.083

For the strongly absorbing globar spectra, the transmittance in the 3510 cm^{-1} window was significantly lower than that in the 2000 cm^{-1} window, decreasing to about 85% for the largest CH_4 abundance (and at all three temperatures), due to the presence of weak CH_4 lines at 3510 cm^{-1}. Therefore, fitting a straight line to these two points and using it to correct the globar spectra would have falsely levelled out the two windows. Instead, each strongly absorbing globar spectrum was normalised by scaling it by the maximum transmittance between 2000 and 4000 cm^{-1}. In order to reduce the effects of random noise, the average transmittance over $\nu \pm 5$ cm^{-1} was calculated for every ν, and the largest of these averaged transmittances was used in the scaling. The shift in transmittance (at the ν of maximum transmittance) resulting from this correction was calculated for 210 of the self-broadened CH_4 globar spectra and for 95 of the H_2-broadened CH_4 spectra, and had average values of 0.136 and 0.143, respectively.

Figure 6.9(a) shows two of the corrected globar spectra at the original 0.25 cm^{-1} resolution. These spectra correspond to the largest and smallest CH_4 abundances, showing the extremes of absorption obtained with the globar spectra. This plot also demonstrates how the increase in absorption with increasing CH_4 abundance is significantly greater in the 3510 cm^{-1} window than it is in the 2000 cm^{-1} window, with the latter therefore providing the scaling factor for the more strongly absorbing spectra. Figures 6.9(b) and (c) provide a close-up view of the two window regions for the same two spectra, and include a third spectrum of intermediate CH_4 abundance to show more clearly how the absorption increases in these regions.

The quartz-halogen CH_4 spectra included seven transmittance windows between 2000 and 11000 cm^{-1}, but only five of these were in the region from 3000 to 9500 cm^{-1} which exhibited good signal-to-noise. For the quartz-halogen spectra with less than 25 m-amagat of CH_4, the same method of correction by ratioing to a fitted line was used. Five points (3510, 4870, 6450, 7780, and 9300 cm^{-1}) were selected, each being a frequency of zero absorption in one of the five windows. The average transmittance over ± 5 cm^{-1} about each of these points was calculated and a least squares fitting routine was used to fit a straight line to these five transmittances. The average shift in transmittance at these five points, averaged over the 330 weakly absorbing quartz-halogen self-broadened CH_4 spectra was 0.038. The quartz-halogen H_2-broadened CH_4 spectra were similarly corrected by ratioing to a fitted line, but in this case the line was fitted to only four points as the transmittance at 4870 cm^{-1} lay in the region of H_2 absorption described in §6.2.7. The average shift in transmittance at the four points, averaged over the 490 weakly absorbing quartz-halogen H_2-broadened CH_4 spectra was 0.070.

The strongly absorbing quartz-halogen spectra proved to be more difficult to correct because CH_4 absorptions appeared in all five windows, with no particular window showing consistently stronger or weaker absorption than the other windows. A different method of normalisation was therefore necessary for these spectra, using the fact that each set of globar and quartz-halogen spectra were recorded under the same conditions, and should therefore have the same transmittance in the region of overlapping frequency. This region of overlap included the

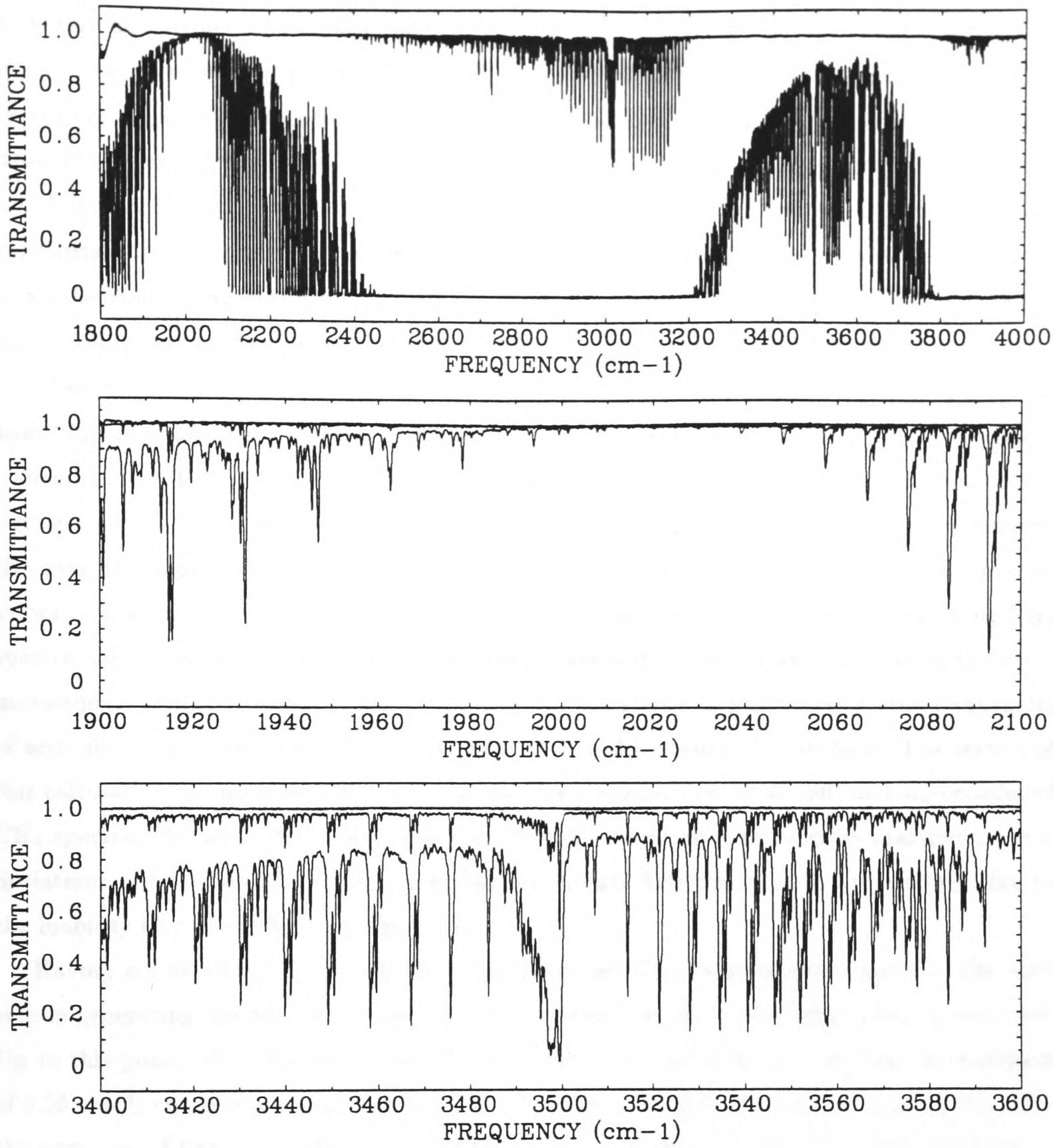

Figure 6.9: Self-broadened CH_4 spectra recorded with the globar, for which the 100% level has been corrected and which are plotted at their original resolution. (a) The entire globar spectral range, extended to 1800 cm^{-1} to more clearly show the shape of the 2000 cm^{-1} window. The upper spectrum is GL01_240K with a CH_4 abundance of 0.02023 m-amagat, and the lower spectrum is GL36_240K with a CH_4 abundance of 527.4 m-amagat. (b) The same two spectra in a close-up of the 2000 cm^{-1} window, with a third spectrum, GL23_240K (38.92 m-amagat of CH_4) also included. (c) The same three spectra in a close-up of the 3510 cm^{-1} window.

3510 cm^{-1} window, and so each quartz-halogen spectra was scaled by the ratio of the corrected globar transmittance at 3510 cm^{-1} to the uncorrected quartz-halogen transmittance at 3510 cm^{-1}. In both cases, the average transmittance over 3510 $\pm$ 5 cm^{-1} was used to reduce the effects of random noise. For the strongly absorbing quartz-halogen spectra, this method of correction resulted in average shifts in transmittance at 3510 cm^{-1} of 0.067 and 0.083 for the 210 self-broadened CH_4 spectra and the 95 H_2-broadened CH_4 spectra, respectively.

The results of these two methods of correcting the 100% level in the quartz-halogen spectra

are compared in Figures 6.10 and 6.11, where both methods of normalisation have been applied to weakly and strongly absorbing spectra. Figure 6.10 shows that the method of ratioing to a fitted line is more appropriate for the weakly absorbing spectrum. If this spectrum is corrected by scaling to match the globar transmittance at 3510 cm^{-1}, the slope seen in the spectrum remains unchanged and regions of zero absorption are not normalised to a transmittance of 1.0. Figure 6.11 shows that the method of scaling to match the globar transmittance is more appropriate for the strongly absorbing spectrum. If this spectrum is corrected by ratioing to a fitted line, "transmittances" significantly greater than 1.0 result, as the line used in the correction is simply the best fit to five points which show considerable scatter.

These figures imply that any slopes present in the 100% transmittance level of the strongly absorbing quartz-halogen spectra are not removed by the method of scaling to match the globar transmittance at 3510 cm^{-1}. Similarly, any slopes in the 100% transmittance level of the strongly absorbing globar spectra are not removed by scaling by the maximum transmittance. However, the figures also suggest a means of assessing the error in transmittance due to residual slopes in the corrected strongly absorbing spectra. By recorrecting the weakly absorbing CH_4 spectra using the method applied to the strongly absorbing spectra and calculating the root-mean-square (r.m.s.) deviation from 1.0 of the recorrected transmittances at the frequencies of zero absorption, an estimate of the uncertainty in this method is obtained. The results of this calculation are presented in Table 6.2. For the combined set of all self- and H_2-broadened CH_4 spectra, the method of correcting the strongly absorbing spectra gives maximum r.m.s. deviations of 0.014 and 0.026 for the globar and quartz-halogen spectra, respectively, due to the inability to remove slopes in the 100% level.

Having corrected all of the self- and H_2-broadened CH_4 transmittance spectra, the next step in generating the final set of spectra was to average the five corrected spectra in every set. Up to this point, all of the processing of the spectra was performed at the original resolution of 0.25 cm^{-1}, creating a complete set of corrected and averaged spectra at this resolution. For the purposes of band modelling, these corrected and averaged spectra were then degraded to a resolution of 10 cm^{-1}. This value was chosen primarily because it represents the highest resolution achievable with NIMS, but also because it facilitates comparison with other band-modelling studies, such as those of Silvaggio (1982), and Giver *et al.* (1984, 1990). The spectra were degraded using a square weighting function and averaging all of the transmittances within ± 5 cm^{-1} of each output frequency. With a spectral increment of 0.1244 cm^{-1} in the original-resolution spectra, the degraded transmittances were the average of 80 or 81 points. In order to avoid undersampling of the degraded spectra, an output frequency spacing of 5 cm^{-1} was selected.

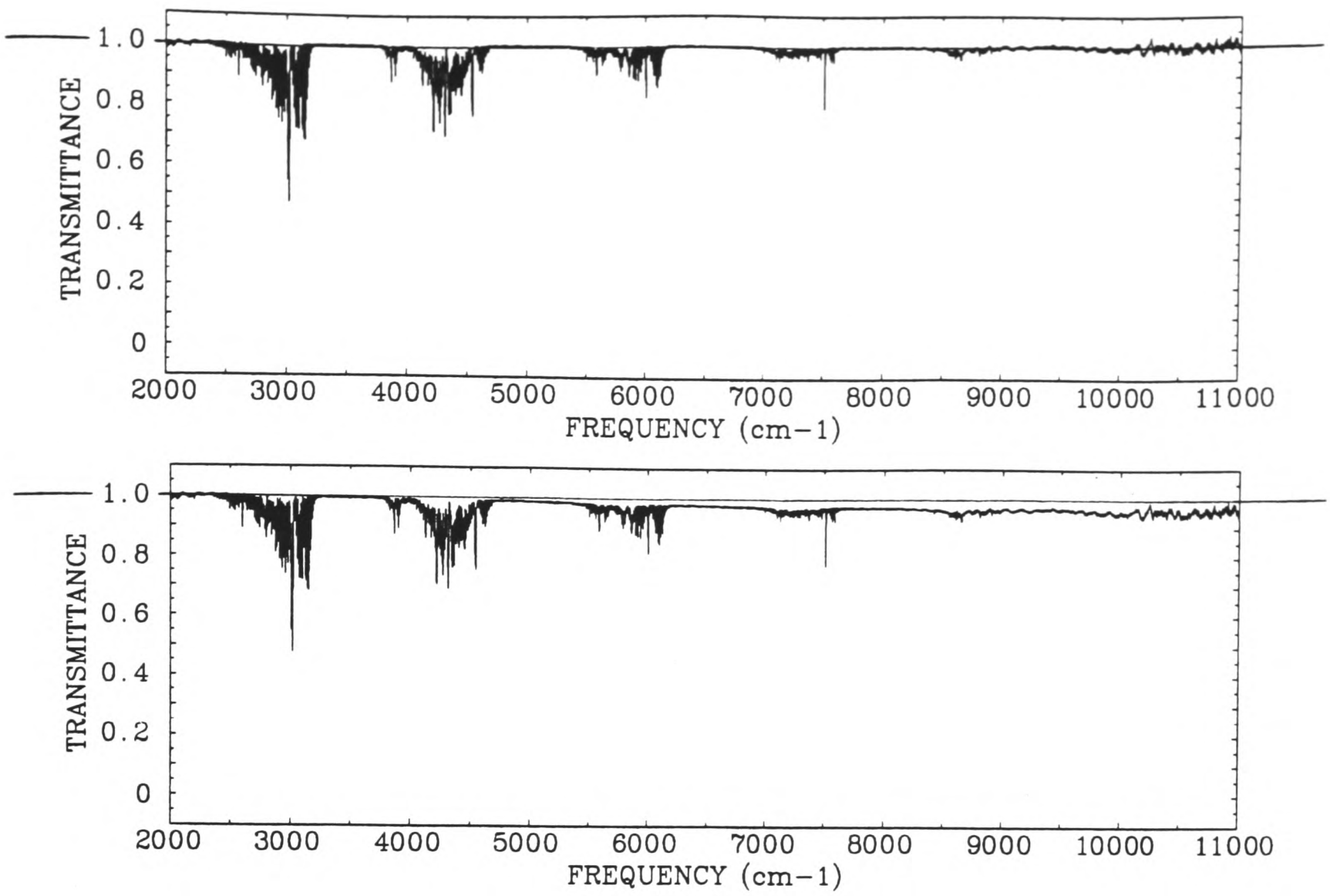

Figure 6.10: A comparison of how the two methods of correcting the 100% transmittance level work for a "weakly absorbing" quartz-halogen CH_4 spectrum (QH03_240K): (a) has been corrected by ratioing the spectrum to a fitted line, (b) has been corrected by scaling to match the globar transmittance at 3510 cm^{-1}.

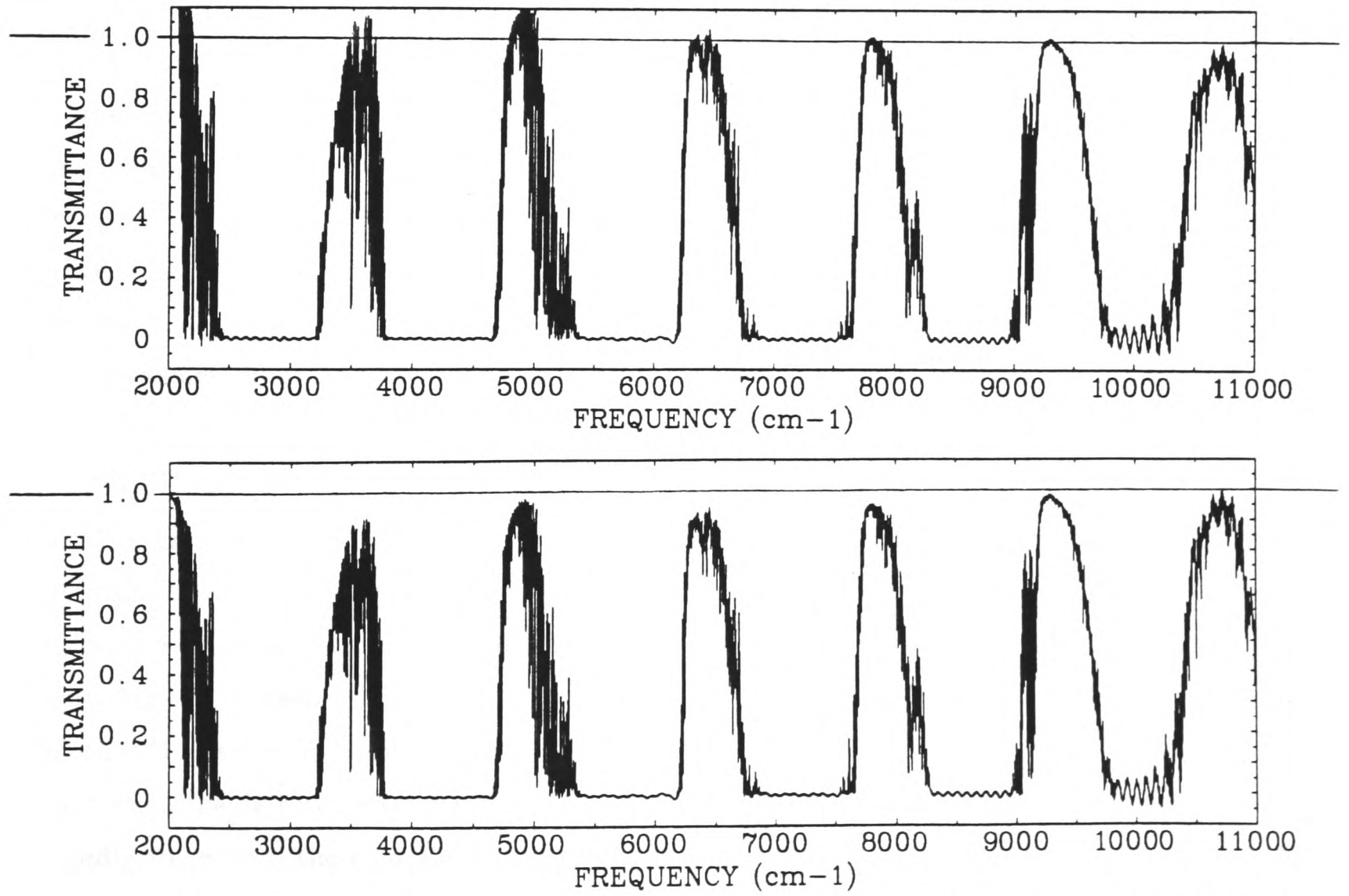

Figure 6.11: A comparison of how the two methods of correcting the 100% transmittance level work for a "strongly absorbing" quartz-halogen CH_4 spectrum (QH36_240K): (a) has been corrected by ratioing the spectrum to a fitted line, (b) has been corrected by scaling to match the globar transmittance at 3510 cm^{-1}.

Table 6.2: The r.m.s. deviation from 1.0 for the weakly absorbing globar and quartz-halogen self- and H_2-broadened CH_4 spectra which were corrected using the methods applied to the strongly absorbing globar and quartz-halogen spectra, thereby not removing any slopes in the 100% transmittance level.

ν (± 5 cm^{-1})	GLOBAR R.M.S. DEVIATION FROM 1			Q-H R.M.S. DEVIATION FROM 1		
	self-broadened CH_4 spectra	H_2-broadened CH_4 spectra	all CH_4 spectra	self-broadened CH_4 spectra	H_2-broadened CH_4 spectra	all CH_4 spectra
2000	0.011	0.015	0.014	—	—	—
3510	0.009	0.014	0.012	0.009	0.014	0.012
4870	—	—	—	0.011	—	0.011
6450	—	—	—	0.013	0.018	0.016
7780	—	—	—	0.017	0.021	0.019
9300	—	—	—	0.020	0.030	0.026

6.2.3 Formation of Ice on the Detector

As was true of the ratios of background spectra discussed in §6.2.1, some of the ratioed CH_4 transmittance spectra were subject to a broad ripple feature, particularly obvious in the 296 K quartz-halogen spectra. When either a background or a CH_4 spectrum was ratioed to a spectrum recorded earlier in the day, this feature appeared as a ripple of varying amplitude, with a minimum at some value between 3500 and 4500 cm^{-1} and another beyond 9000 cm^{-1}, and a maximum at some value between 6000 and 7400 cm^{-1}. The two spectra in Figure 6.12 show how the shape and intensity of the quartz-halogen background changed over one 11-hour period, and how the ratio of these two spectra gave rise to one of the worst examples of the ripple.

Background tests, in which spectra were recorded hourly over the course of a day and ratioed to the first spectrum of the day, showed that the growth of the peak-to-peak amplitude of the ripple and the growth of a broad absorption feature centered on 3220 cm^{-1} (see Figure 6.12) were well correlated. The 3220 cm^{-1} absorption feature was traced to an intense broad band of H_2O ice, centered on 3220 cm^{-1} (*e.g.*, Ockman, 1958), which formed when residual water vapour in the dewar vacuum of the LN_2-cooled InSb detector froze onto the detector element. The presence of H_2O in the detector-dewar vacuum was confirmed by a mass spectrometer scan (performed by the RAL Vacuum Section) which revealed a poor vacuum of the order of 10^{-3}–10^{-4} torr, with a significant H_2O component.

The growth of this 3220 cm^{-1} absorption was found to be strongly dependent on the temperature of the the detector when it was filled with LN_2 at the start of each day. When it was cold (due to being refilled late the previous evening), the absorption at 3220 cm^{-1} increased only slightly between the start- and end-of-day backgrounds, whereas when the detector was at room temperature at the start of the day, the absorption increased significantly. This suggested that when the detector was cooled down from room temperature, the water vapour in the dewar rapidly froze onto the cold element of the detector, causing the 3220 cm^{-1} ice absorption to grow quickly. Then, as the water vapour froze out, the growth of the absorption would level off, and thus, if the detector were cold at the start of a day, the ice layer would already have

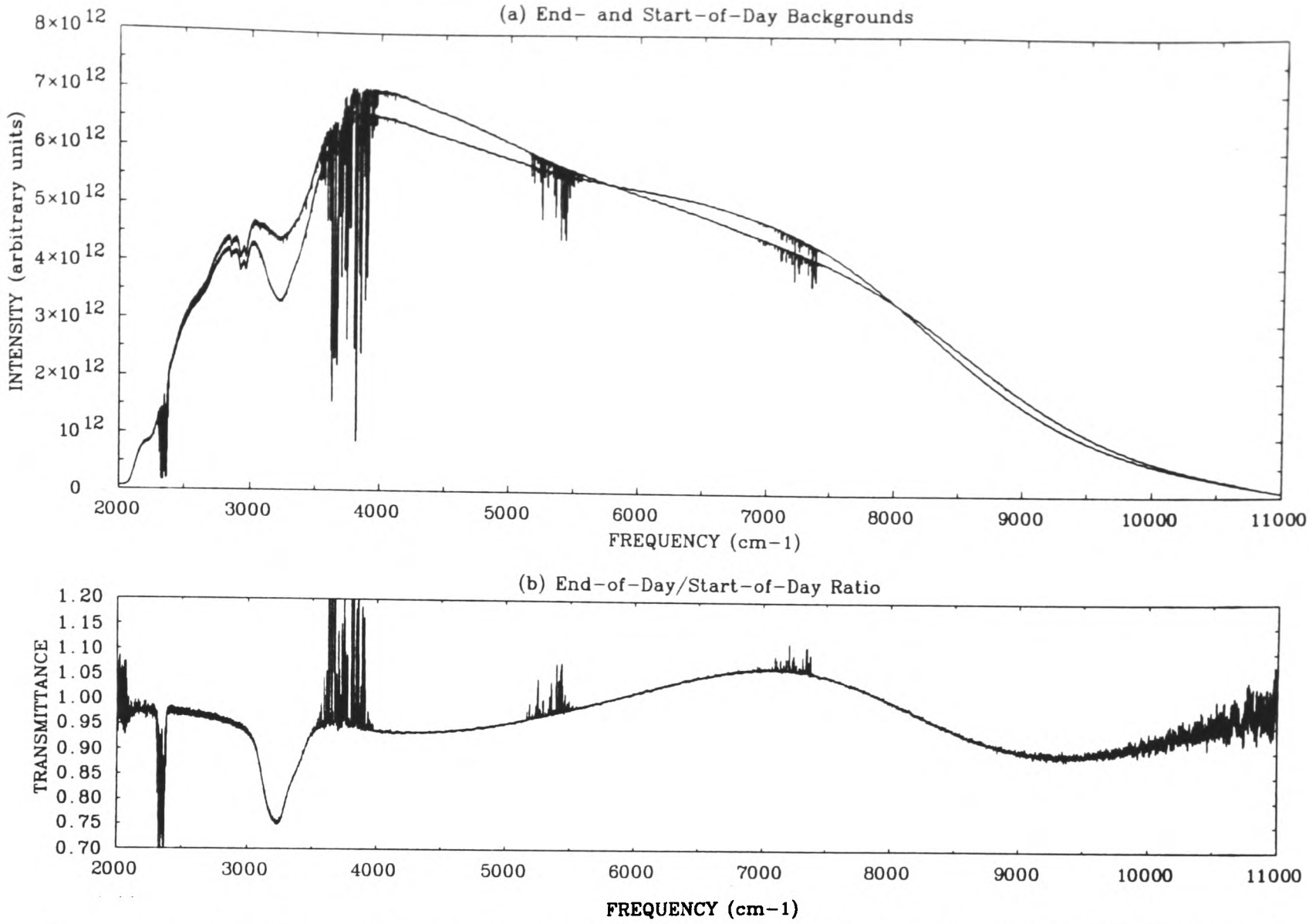

Figure 6.12: (a) Two quartz-halogen background spectra, recorded 11 hours apart, showing how the shape of the background has changed over the course of the day. (b) The ratio of the end-of-day background to the start-of-day background, showing the broad ripple and the growth of the 3220 cm^{-1} absorption feature. (The strong absorption lines are due to H_2O and CO_2 contamination, both being particularly strong on this day.)

formed. This effect is seen in Figure 6.13. The broad ripple correlated with the 3220 cm^{-1} ice absorption appeared to be some form of channel spectrum, produced by the interference of waves which were internally reflected by the sides of the ice layer (see §6.2.6).

Once the cause of the broad ice ripple had been recognised, several attempts were made to reduce the problem. Efforts to remove the contaminating water vapour from the detector-dewar vacuum proved unsuccessful, including pumping it for a week with a turbo-molecular pump (with a nominal ultimate vacuum of 10^{-4} to 10^{-5} torr), and having it pumped (to a nominal vacuum of 10^{-7} to 10^{-8} torr) and baked at 50 °C for three days by the manufacturers, Infrared Associates. With the water vapour thus apparently trapped in the vacuum, attempts were made to rig up a LN_2 header tank for the detector to keep it permanently cold and to thus stabilise the ice formation so that, although still present, it would ratio out in the transmittance spectra. Although none of the trial header tank arrangements worked successfully, due to the small detector opening for the LN_2 input, it did prove possible to keep the detector cold. Once filled with LN_2, it generally remained cold for eight hours or longer, and so, simply by filling it at the end of each day, usually after midnight, and refilling at around 8 a.m. the following morning, the ice deposition was maintained in a stable state overnight. This method was used

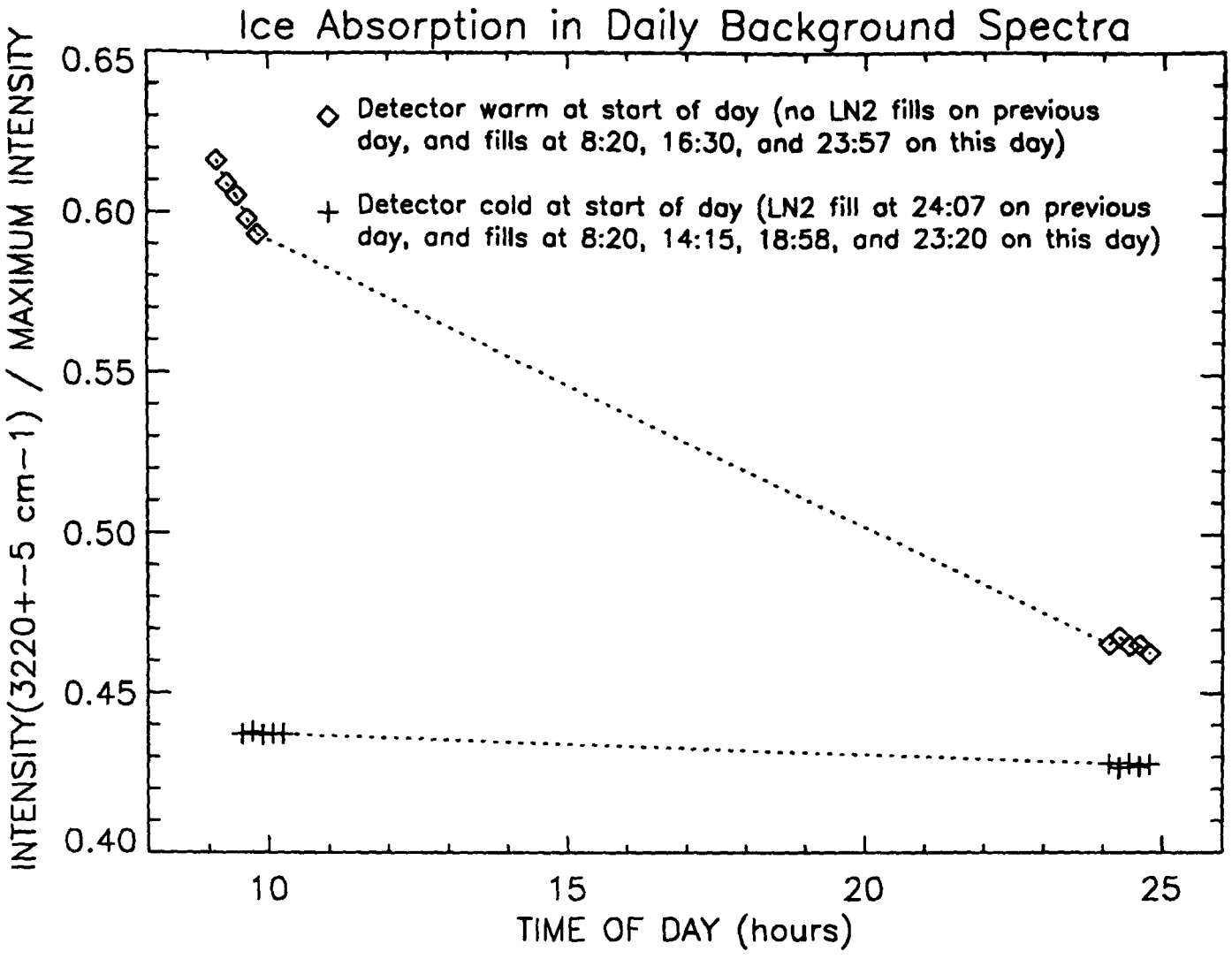

Figure 6.13: The change in the intensity of the ice absorption, for start- and end-of-day background spectra on a day when the InSb detector was at room temperature at the start of the day, and on a day when it was cold at the start of the day.

throughout the 190 K and 240 K spectroscopy.

Additional attempts were made to reduce the broad ice ripple and the 3220 cm^{-1} absorption feature computationally. On days when the detector was warm at the start of the day, the growth of these features was not a linear function of time, and so ratioing a CH_4 intensity spectrum to a background intensity spectrum which had been generated by linear interpolation between the start- and end-of-day backgrounds introduced the residual ripple and 3220 cm^{-1} absorption. Various methods of finding more appropriate background spectra than those generated by linear interpolation in time were therefore tried. In principle, if the growth of the ripple amplitude or of the 3220 cm^{-1} absorption could be modelled as a function of time since filling the detector with LN_2 (*i.e.*, since the ice began to form), then the appropriate backgrounds could be interpolated in time along this fitted curve. In practice, this proved difficult to do.

Fitting such a function (exponential, polynomial, and inverse polynomial) to a set of all of the background spectra proved unfeasible because the magnitude of these features (even when scaled to eliminate background variability) was not consistent from day to day, and because it was difficult to accurately determine the cool-down time (since the detector was sometimes kept cold over several nights, possibly partially warming during some nights). The most successful method of reducing the broad ice ripple involved fitting a series of functions to $I(\nu_{peak} \pm 5)/I(\nu_{trough} \pm 5)$ (where $I(\nu_{peak})$ and $I(\nu_{trough})$ are the intensities at the frequencies

of the ripple peak and trough, respectively, in the ratio of end- to start-of-day background spectra) for the five start-of-day and five end-of-day backgrounds recorded on a single day. These functions were then used to interpolate intermediate backgrounds, and hence a series of ratioed CH_4 transmittance spectra which could be compared to the spectrum generated with the linearly interpolated background to determine which function provided the greatest reduction in the ripple amplitude.

In tests with a weakly absorbing spectrum, a polynomial of degree 3 successfully reduced the ripple amplitude from 0.0063 to –0.0001, while simultaneously reducing the absorption at 3220 cm^{-1} to less than half of its value using the linearly interpolated backgrounds. However, even this method proved unsatisfactory, giving inconclusive results for strongly absorbing spectra, and being difficult to apply, as it involved several interactive decisions, including the selection of ν_{peak} and ν_{trough}, which varied from day to day, and the evaluation of which of the six functions fitted to $I(\nu_{peak})/I(\nu_{trough})$ provided the best reduction of the ripple for each CH_4 transmittance spectrum. Although this method was not applied when generating the CH_4 spectra in this work, if greater accuracy is required in some future analysis of these spectra, particularly for a smaller subset, this method may provide a means of achieving it.

Although it proved difficult to reduce the broad ice ripple computationally, the method of keeping the ice deposition stable by keeping the detector cold did meet with success, as seen in Tables 6.3 and 6.4. These are compilations of the ripple amplitude for the final set of corrected and averaged quartz-halogen self- and H_2-broadened CH_4 transmittance spectra at the original resolution (see §6.2.2). The ripple amplitude has been calculated as the maximum difference between any two of the window transmittances at 3510, 4870, 6450, 7780, and 9300 cm^{-1} ± 5 cm^{-1}, but omitting the transmittance at 4870 cm^{-1} from the calculation for the H_2-broadened spectra as it overlaps the region of H_2 absorption (see §6.2.7). A meaningful estimate of the error due to the ice ripple is provided by the spectra marked by an asterisk, as these are the spectra which have a CH_4 abundance of less than 25 m-amagat, and have zero absorption in the five window regions. The transmittance in these windows ideally should be 1.0, with no difference in transmittance between any two windows. The spectra not marked by an asterisk have larger CH_4 abundances and provide a less reliable measure of the ripple amplitude because weak absorptions appear in the windows.

Calculation of the r.m.s. ripple amplitude for the weakly absorbing spectra provided an estimate of the overall error in transmittance caused by the broad ice ripple. The r.m.s. values at each temperature for the 66 quartz-halogen self-broadened CH_4 spectra and the 98 quartz-halogen H_2-broadened CH_4 spectra are listed in Table 6.5. When all 164 weakly absorbing spectra are taken into account, an r.m.s. error of 0.0154 in transmittance is obtained, so this is therefore the estimate of the overall error introduced into the CH_4 transmittance spectra by the broad ice ripple.

Table 6.3: The peak-to-peak ripple amplitude for the 108 corrected and averaged quartz-halogen self-broadened CH_4 transmittance spectra. The ripple has been calculated for each spectrum as the difference between the highest and lowest of the five window transmittances centered at 3510, 4870, 6450, 7780, and 9300 cm^{-1} and averaged over ± 5 cm^{-1}. The spectra marked with an asterisk are those with less than 25 m-amagat of CH_4 and zero absorption in the window regions.

SPECTRUM	RIPPLE FOR 296 K	RIPPLE FOR 240 K	RIPPLE FOR 190 K
* QH01	0.0072	0.0054	0.0013
* QH02	0.0026	0.0019	0.0027
* QH03	0.0316	0.0036	0.0034
* QH04	0.0095	0.0026	0.0030
* QH05	0.0019	0.0042	0.0060
* QH06	0.0006	0.0029	0.0074
* QH07	0.0243	0.0034	0.0032
* QH08	0.0406	0.0031	0.0022
* QH09	0.0025	0.0022	0.0078
* QH10	0.0029	0.0036	0.0136
* QH11	0.0265	0.0007	0.0053
* QH12	0.0364	0.0015	0.0030
* QH13	0.0011	0.0012	0.0088
* QH14	0.0017	0.0026	0.0145
* QH15	0.0222	0.0050	0.0035
* QH16	0.0282	0.0011	0.0065
* QH17	0.0424	0.0022	0.0044
* QH18	0.0165	0.0058	0.0060
* QH19	0.0089	0.0042	0.0032
* QH20	0.0174	0.0058	0.0070
* QH21	0.0134	0.0077	0.0100
* QH22	0.0083	0.0053	0.0066
QH23	0.0231	0.0195	0.0200
QH24	0.0242	0.0340	0.0271
QH25	0.0291	0.0131	0.0169
QH26	0.0146	0.0056	0.0302
QH27	0.0526	0.0554	0.0608
QH28	0.1343	0.0285	0.0231
QH29	0.0351	0.0052	0.0410
QH30	0.0347	0.0102	0.0357
QH31	0.0669	0.1022	0.0248
QH32	0.0801	0.0368	0.0942
QH33	0.0743	0.0502	0.0573
QH34	0.1426	0.0805	0.0521
QH35	0.0655	0.0559	0.1616
QH36	0.0869	0.1491	0.1868

Table 6.4: The ice ripple for the 117 corrected and averaged H_2-broadened CH_4 Q-H transmittance spectra.

SPECTRUM	RIPPLE FOR 296 K	RIPPLE FOR 240 K	RIPPLE FOR 190 K
QH01_H	* 0.0397	* 0.0060	* 0.0042
QH02_H	* 0.0028	* 0.0009	* 0.0021
QH03_H	* 0.0081	* 0.0066	* 0.0069
QH04_H	* 0.0045	* 0.0072	* 0.0016
QH05_H	* 0.0046	* 0.0067	* 0.0007
QH06_H	* 0.0038	* 0.0086	* 0.0151
QH07_H	* 0.0027	* 0.0077	* 0.0513
QH08_H	* 0.0043	* 0.0042	* 0.0316
QH09_H	* 0.0486	* 0.0084	* 0.0016
QH10_H	* 0.0100	* 0.0026	* 0.0012
QH11_H	* 0.0148	* 0.0025	* 0.0059
QH12_H	* 0.0134	* 0.0039	* 0.0030
QH13_H	* 0.0437	* 0.0018	* 0.0013
QH14_H	* 0.0050	* 0.0033	* 0.0012
QH15_H	* 0.0091	* 0.0074	* 0.0066
QH16_H	* 0.0012	* 0.0007	* 0.0138
QH17_H	* 0.0039	* 0.0044	* 0.0254
QH18_H	* 0.0012	* 0.0028	* 0.0143
QH19_H	* 0.0007	* 0.0042	* 0.0135
QH20_H	* 0.0416	* 0.0022	* 0.0063
QH21_H	* 0.0016	* 0.0072	* 0.0074
QH22_H	* 0.0048	* 0.0036	* 0.0122
QH23_H	* 0.0524	* 0.0053	* 0.0114
QH24_H	* 0.0099	* 0.0055	* 0.0108
QH25_H	* 0.0096	* 0.0064	* 0.0547
QH26_H	* 0.0069	* 0.0043	* 0.0006
QH27_H	* 0.0072	* 0.0071	0.0309
QH28_H	* 0.0133	* 0.0076	0.0409
QH29_H	* 0.0047	* 0.0261	0.0340
QH30_H	* 0.0145	* 0.0059	0.0182
QH31_H	* 0.0050	0.0535	0.0721
QH32_H	* 0.0012	0.0128	0.0070
QH33_H	* 0.0577	0.0047	—
QH34_H	* 0.0181	0.0496	—
QH35_H	* 0.0318	0.0267	—
QH36_H	* 0.0058	0.0704	—
QH37_H	* 0.0105	—	—
QH38_H	* 0.0141	—	—
QH39_H	* 0.0112	—	—
QH40_H	* 0.0172	—	—
QH41_H	* 0.0146	—	—
QH42_H	* 0.0103	—	—
QH43_H	0.0117	—	—
QH44_H	0.0199	—	—
QH45_H	0.0636	—	—
QH46_H	0.0301	—	—
QH47_H	0.0062	—	—
QH48_H	0.0351	—	—
QH49_H	0.0460	—	—

Table 6.5: The r.m.s. ripple amplitude for the weakly absorbing quartz-halogen CH_4 spectra which are marked by an asterisk in Tables 6.3 and 6.4.

SPECTRA	296 K	240 K	190 K	ALL 3 T's
self-broadened CH_4	0.0207	0.0039	0.0128	0.0128
H_2-broadened CH_4	0.0205	0.0072	0.0183	0.0169
both of the above	0.0206	0.0060	0.0143	0.0154

The error in transmittance due to the 3220 cm^{-1} ice absorption feature, which extends from 3000 to 3500 cm^{-1}, was difficult to determine from the CH_4 spectra because of the presence of a strong CH_4 band. However, an estimate of the maximum residual 3220 cm^{-1} absorption was obtained from the hourly background tests mentioned at the start of this section. Three such tests were conducted, for all of which the detector had not been filled at all on the previous day, providing the worst case scenario for linear interpolation of backgrounds. The first and last quartz-halogen background spectra recorded on each day were used to linearly interpolate, in time, backgrounds for each of the intermediate background spectra. Ratioing the recorded background spectra to these interpolated backgrounds then provided a set of "transmittance" spectra. The magnitude of the residual 3220 cm^{-1} absorption in these spectra was quantified as the difference between the average peak-to-peak transmittance and the transmittance at 3220 ± 5 cm^{-1}. It was found to vary from 0.003 to 0.079, 0.017 to 0.061, and 0.025 to 0.051, for each of the three tests. Thus, the maximum residual amplitude of the absorption at 3220 cm^{-1} resulting from using linear interpolation to generate backgrounds for the CH_4 spectra was 0.079. On days when the detector was cold at the start of the day, the amplitudes would be significantly less.

6.2.4 The Zero-Signal Level

The accuracy of the zero-signal level assigned by the Bomem was easily assessed because there were large regions of total absorption in the strongly absorbing CH_4 spectra. The zero-signal level was examined in the five bands of the quartz-halogen spectra and in the two bands of the globar spectra, for those spectra with the largest CH_4 abundances at all the three temperatures. For both the original resolution and the degraded CH_4 spectra, the assigned zero in the transmittance spectra was within 0.01 (*i.e.*, 1% at full scale) of the true zero transmittance level, consistent with previous Bomem results (Remedios, 1990, p.174) and therefore considered acceptable.

However, it was also found that some of the strongest lines at the edges of saturated CH_4 bands showed apparently negative "transmittances" at line centre. Since these lines were obviously very strongly absorbing and likely to be saturated, the option of setting these negative transmittances to zero was considered. In order to assess the effect of this action, averaged transmittances were calculated for several spectra in regions of strongly overshooting lines, and for the same spectra with all negative transmittances set to zero. The averaged transmittances

for the latter spectra were found to be slightly higher, as expected, but by less than 0.01, *i.e.*, within the accuracy of the zero-signal level. Since the random noise in the saturated band centres was evenly distributed about the zero-signal level, forcing all negative transmittances to zero would have produced a small positive offset in these regions. Therefore, no correction was applied to the negative transmittances in the original-resolution spectra. Any degraded "transmittances" which were negative were simply excluded from the band-modelling process.

6.2.5 Analysis of Signal-to-Noise

In order to quantify the random noise on the averaged and corrected original-resolution CH_4 transmittance spectra in a reproducible manner, the average transmittance, τ_{avg}, and its standard deviation, 1σ, were calculated over ± 5 cm^{-1} for selected frequencies in the window regions. The value of the standard deviation provided a measure of the noise, and the ratio of τ_{avg}/σ provided a measure of the signal-to-noise. This calculation was performed at 2000 and 3510 cm^{-1} for the globar CH_4 spectra, and at 3510, 4870, 6450, 7780, and 9300 cm^{-1} for the quartz-halogen CH_4 spectra. Spectra with more than 25 m-amagat of CH_4 were not included in the calculation due to the presence of weak absorptions.

Table 6.6: The minimum and maximum signal-to-noise in the weakly absorbing globar and quartz-halogen self- and H_2-broadened CH_4 spectra.

SPECTRA	S/N FOR 296 K		S/N FOR 240 K		S/N FOR 190 K	
	MIN	MAX	MIN	MAX	MIN	MAX
self-broadened CH_4, globar source	82	330	82	1875	52	1483
H_2-broadened CH_4, globar source	114	749	147	1746	101	1985
self-broadened CH_4, quartz-halogen source	111	3535	82	4471	52	6766
H_2-broadened CH_4, quartz-halogen source	54	3840	165	4825	111	6036

The minimum and maximum signal-to-noise ratios resulting from this calculation are presented in Table 6.6. The signal-to-noise was generally higher in the quartz-halogen spectra, and within these ranges, it exhibited some dependence on frequency and pathlength, decreasing as the background signal dropped off and with an increasing number of reflections off the LWC mirrors. The signal-to-noise was also noticeably better in the 190 K and 240 K spectra compared to the 296 K spectra. This is due to two factors. The first was a reduction in vibration-induced noise due to the securing of the mirrors in their mounts prior to the start of the low temperature spectroscopy. The second was the fact that during the cold spectroscopy, the LWC mirrors were readjusted to maximise the detector DC signal level after every gas fill, an action which was only taken at 296 K if there was a serious loss of signal. In all cases, when the transmittance spectra were degraded to 10 cm^{-1} resolution, the random noise became negligible.

6.2.6 Channelling Features

Several different channel spectra were superimposed on the background and CH_4 intensity spectra. These spectra arise when a beam of light incident on a thin parallel plate undergoes successive internal reflections within it to generate a series of interfering parallel rays which are transmitted through the plate. For approximately normally incident radiation, the resulting interference fringes have a period of

$$\Delta\nu = \frac{1}{2nd} \tag{6.1}$$

where n is the index of refraction of the plate, and

d is the physical thickness of the plate.

The theory underlying this phenomenon is well developed, and can be found in Hecht and Zajac (1974, p.301–307), Jenkins and White (1950, p.254–259), and Rossi (1957, p.137–140).

6.2.6.1 The 3.2 cm^{-1} Channelling

Channelling with a period of approximately 3.2 cm^{-1} was observed in the 296 K self-broadened CH_4 intensity spectra soon after the measurements began. The average period was measured over 30 cm^{-1} intervals in six absorption-free regions of the first quartz-halogen background intensity spectrum recorded each day, showing that it was weakly dependent on frequency, being 3.24, 3.21, 3.16, and 3.09 cm^{-1} at 2200, 3450, 4900, and 6300 cm^{-1}, respectively, and difficult to measure at 7800 and 9300 cm^{-1}. This period was consistent with that calculated from the thickness and the frequency-dependent index of refraction (Palik, 1985, p.439–440) of the GaAs filter which had been mounted horizontally over the window of the detector. When the 296 K self-broadened CH_4 measurements were finished, this filter was removed from the detector and remounted at an angle of $17° \pm 0.5°$ to the face of the detector window. This directed the interfering absorptions away from the detector, reducing the amplitude of the channelling to below the noise level in all subsequently recorded spectra. The 3.2 cm^{-1} channelling therefore appeared only in the 296 K self-broadened CH_4 spectra.

This 3.2 cm^{-1} channelling appeared in both the 296 K CH_4 intensity spectra and in their interpolated backgrounds, but a small phase difference between these spectra prevented the channelling from ratioing out in the CH_4 transmittance spectra. The average channelling amplitude in each of the 30 cm^{-1} intervals described above was also found to be frequency-dependent, decreasing with frequency to become comparable to the random noise level beyond about 7000 cm^{-1}. An attempt was made to remove the interference fringes by applying the spectral subtraction technique described in Clark and Moffat (1978), in which a sine-wave signal is generated and subtracted from the original signal. However, it proved difficult to match the variable period and amplitude of the measured spectra, and so significant channelling remained after the spectral subtraction had been applied.

For the purposes of this thesis, the transmittance spectra were degraded to 10 cm^{-1}, an interval that smoothes out the 3.2 cm^{-1} channelling. If the degrading interval included an integral number of sinusoidal channelling periods, then the degraded transmittance, τ_{deg}, would be identical to the median transmittance through the sinusoid, τ_{median}. However, with a non-integral number of cycles included in the degrading interval, τ_{deg} is offset from τ_{median} by some error, E. This error can be estimated as follows.

For a square weighting function, the degraded transmittance over interval $\Delta\nu$ is

$$\tau_{deg} = \frac{1}{\Delta\nu}\int_{\nu_0}^{\nu_0+\Delta\nu} \tau(\nu)\, d\nu \tag{6.2}$$

where ν_0 is the frequency at the start of the degrading interval. $\tau(\nu)$ can be defined as the sinusoidal channelling term superimposed upon τ_{median}:

$$\tau(\nu) = \tau_{median} + \tau_{channelling}(\nu) \tag{6.3}$$

$$= \tau_{median} + A_c \sin\left[\frac{2\pi}{P_c}(\nu - \nu_c)\right] \tag{6.4}$$

where A_c is the channelling amplitude,

P_c is the channelling period, and

ν_c is the frequency defining the phase of the channelling.

For the purposes of this calculation, ν_c can be defined as ν_0, making the start of a channelling cycle coincide with the start of the degrading interval. This assumption effectively generates the largest possible error by ensuring that the partial cycle included in the degrading interval is not split into positive and negative sections which can cancel each other out. With this simplification, the degraded transmittance reduces to

$$\tau_{deg} = \tau_{median} + A_c \frac{P_c}{2\pi\Delta\nu}\left[1 - \cos\frac{2\pi\Delta\nu}{P_c}\right]. \tag{6.5}$$

The second term in this equation thus represents the absolute error, E, in τ_{deg} introduced by the channelling.

In order to evaluate this error for the 3.2 cm^{-1} channelling in the 296 K self-broadened CH_4 transmittance spectra, the average P_c and A_c were measured in the six quartz-halogen regions defined above, and also for four absorption-free regions in the globar spectra (starting at 1850, 2000, 2200, and 3450 cm^{-1}, and each covering 30 cm^{-1}). This was done for all of the spectra with less than 25 m-amagat of CH_4. Using $\Delta\nu = 10$ cm^{-1}, and the measured values $P_c(\nu)$ and A_c, the maximum value of the error in transmittance was found to be only 0.0002, corresponding to a maximum channelling amplitude of 0.030. This thus defined an upper limit on the error introduced into the degraded transmittance by the 3.2 cm^{-1} channelling. Since this channelling was only present in the 296 K self-broadened CH_4 spectra, it made a negligible contribution to the overall error in the transmittance spectra.

6.2.6.2 The 2.8 cm^{-1} Channelling

A similar sinusoidal channelling with a period of about 2.8 cm^{-1} was discovered in the 240 K and 190 K spectra. Examination of the first background intensity spectrum recorded each day revealed that this channelling was indistinguishable from random noise below 2500 cm^{-1} and above 7000 cm^{-1}, with an apparently frequency-independent period of 2.75 cm^{-1}. The channelling amplitude in these intensity spectra was much weaker than for the 3.2 cm^{-1} channelling. Furthermore, in this case, when the CH_4 transmittance spectra were examined in order to determine the absolute errors as above, the channelling was found to be negligible, ratioing out when the CH_4 intensity spectra were ratioed to the interpolated background spectra. Therefore, no further assessment of this feature was necessary.

6.2.6.3 The 80 cm^{-1} Channelling

A third form of channelling, with a period of approximately 80 cm^{-1} was also discovered, but only in the quartz-halogen spectra. It appeared as a weak sinusoidal oscillation in the quartz-halogen background intensity spectra and in the windows of the quartz-halogen weakly absorbing CH_4 intensity spectra. However, as the CH_4 abundance increased, this channelling appeared to become distorted in these windows, although it was difficult to distinguish from the weak CH_4 absorptions. For CH_4 abundances large enough to saturate the band centres, the channelling in these regions was clearly distorted into an irregular oscillation of varying period and amplitude, which remained in the ratioed CH_4 transmittance spectra.

Because this feature was seen only in the quartz-halogen spectra, and not in the globar spectra, even in the regions of overlapping frequency, it was unlikely to have been a form of true channelling due to thin film interference. Instead, it appeared to be due to a gain change problem in the Bomem spectrometer which generated spikes in the quartz-halogen interferograms and hence oscillations in the spectra. Before the low-temperature CH_4 spectroscopy began, a Bomem engineer tried to eliminate the problem, but his efforts proved unsuccessful. The irregular oscillation in therefore present in all of the quartz-halogen transmittance spectra.

Due to its irregular nature, it was difficult to characterise, reduce, or remove this feature, and so the worst case error in the degraded transmittance due to the oscillation was calculated as part of the total error budget. For cases such as this, where the channelling period is greater than the degrading interval, the maximum possible channelling error is simply the channelling amplitude. Therefore, all of the corrected and averaged original-resolution quartz-halogen self- and H_2-broadened CH_4 spectra were examined to find that the largest amplitude was 0.040. This value was therefore taken to be the maximum error in the degraded transmittances due to the irregular 80 cm^{-1} oscillations. For most of the quartz-halogen spectra, particularly those with lower CH_4 abundances and weaker absorptions, the error in the degraded transmittances due to the irregular oscillation was much less than this value.

6.2.7 Contamination by Gaseous Impurities and Pump Oil

Soon after the recording of the 296 K spectra began, contaminating line absorptions were discovered in the background and CH_4 intensity spectra. These were traced to H_2O and CO_2 impurities in the N_2 purge of the Bomem and the transfer-optics tanks. Using the known pathlength of 5.5 m for the transfer-optics tanks, calculation of synthetic H_2O and CO_2 spectra confirmed that small amounts of these gases could generate significant absorptions. Several attempts were made to remove these impurities, as discussed in §5.2.8.2, but a significant reduction in the contamination was obtained only when the spectrometer and transfer-optics tanks were evacuated. Therefore, the SWC diffusion pump was used to pump out the Bomem and the input- and output-transfer-optics tanks for all of the 190 K and 240 K spectra, and for most of the 296 K H_2-broadened CH_4 spectra.

Although H_2O and CO_2 absorptions are obvious in all of the 296 K self-broadened CH_4 intensity spectra, they ratio out in most of the CH_4 transmittance spectra. It was possible to obtain an estimate of the magnitude of the contaminating absorptions in the degraded CH_4 spectra by examining the low-abundance CH_4 transmittance spectra in which the H_2O and CO_2 were distinguishable from the CH_4 absorptions. The degraded absorption due to the CO_2 was estimated to be ≤ 0.01 in transmittance for all but four days which exhibited very strong CO_2 contamination in their start and end-of-day backgrounds. On these days, the maximum absorption due to CO_2 was 0.04 at 2360 cm^{-1}, with CO_2 absorption affecting the region from 2290 to 2390 cm^{-1}. There is thus a small error in transmittance for some of the 296 K CH_4 spectra in this region. Figure 6.14 is a plot, at the original resolution, of the CH_4 spectrum having the largest CO_2 absorption. It shows both the CO_2 absorption in the interpolated background intensity spectrum, along with the residual CO_2 absorption present in the CH_4 transmittance spectrum generated with this background.

The H_2O contamination in the 296 K self-broadend CH_4 spectra affected three regions, being strongest over approximately 3500–4000 cm^{-1}, weaker over 5150–5550 cm^{-1}, and very weak over 7000–7400 cm^{-1}. However, these H_2O absorptions ratioed out quite well in the CH_4 transmittance spectra, as seen in Figure 6.15. The effect of the small H_2O residual absorptions on the degraded transmittance spectra was assessed for spectra with a CH_4 abundance low enough that H_2O absorptions were distinguishable from CH_4 absorptions. Unlike the CO_2, the residual H_2O absorption was well below 0.01 for all spectra examined.

Examination of all of the daily background spectra proved that only the 296 K self-broadened CH_4 spectra were contaminated by H_2O and CO_2 absorptions arising from impurities in the Bomem and the transfer-optics tanks. However, because of the long pathlengths in the LWC, additional contaminating absorptions may have arisen from the small impurities in the CH_4 and H_2 gas supplies. To determine whether the absorption due to these impurities was significant, the GENLN2 line-by-line program (see §3.3.2) was used to determine the H_2O and CO_2 absorption for the largest CH_4 abundance at room temperature (442.6 m-amagat). The

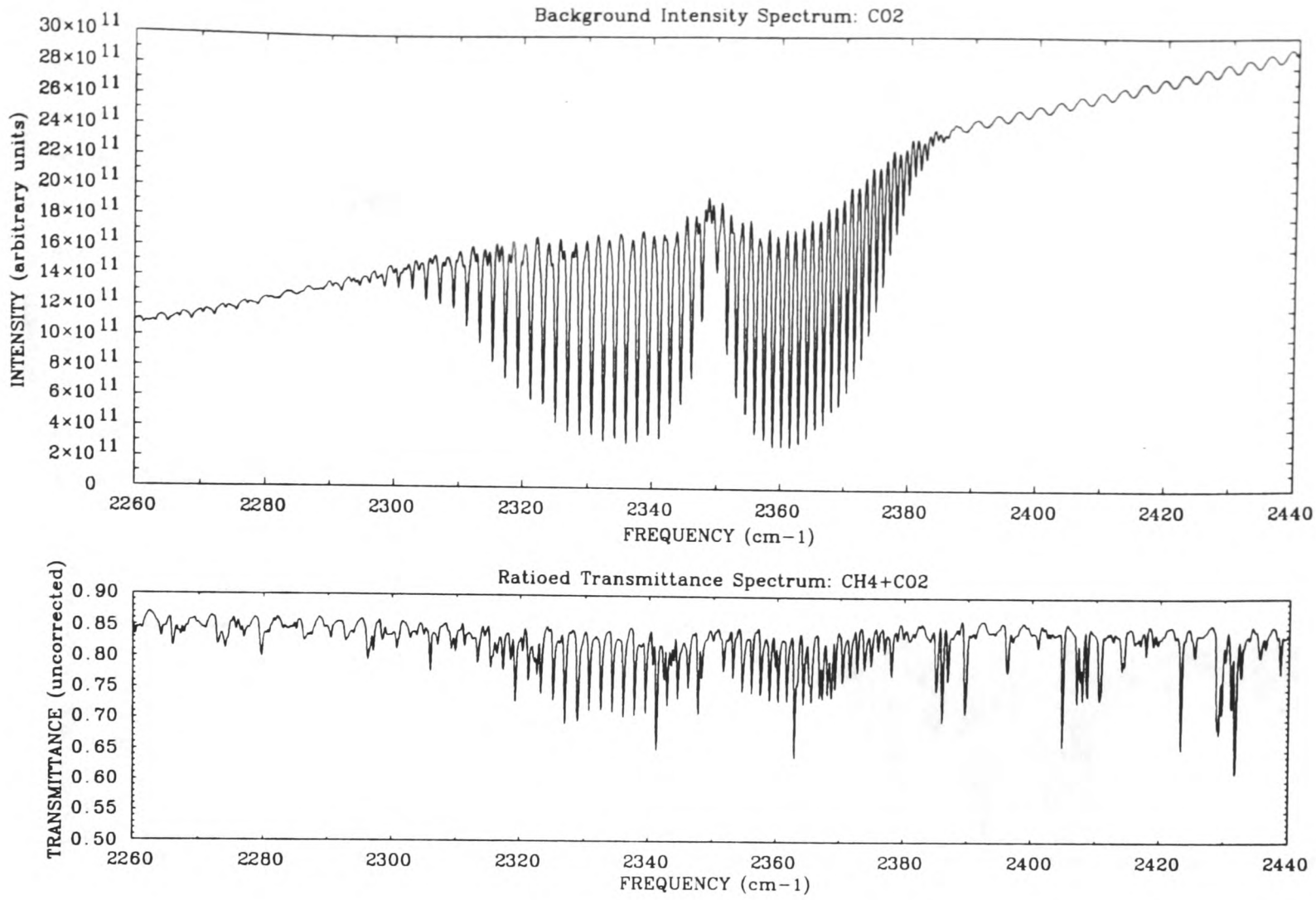

Figure 6.14: Contaminating CO_2 absorption in a background intensity spectrum and in the CH_4 transmittance spectrum generated with this background, both at the original resolution.

calculation was performed over 2000-11000 cm^{-1} and degraded to 10 cm^{-1} resolution. The H_2O absorption was calculated for 0.5 ppm (the specified purity of the oxisorb cells) and for 5 ppm (the specified purity of both the HP and the UHP CH_4 supplies), while the CO_2 absorption was calculated for 10 ppm (the purity of the HP CH_4) and for 2 ppm (the purity of the UHP CH_4).

The resulting synthetic spectra are plotted in Figure 6.16, which shows that for the conditions of maximum abundance, both gases exhibit absorption. In the case of H_2O, the contaminating absorption, present over 3500–4000, 5150–5550, and 7100–7400 cm^{-1}, is much weaker for the specified purity of the oxisorb cells. As these were used throughout the spectroscopy, and as the H_2O absorption will be less for smaller CH_4 abundances, contamination by the H_2O in the gas supplies was not thought to be significant. However, in the case of CO_2, the contaminating absorption, present from 2200 to 2400 and 3550 to 3750 cm^{-1}, is stronger. This is particularly true in the former region, even for the specified purity of the UHP CH_4. Some contamination of these two regions was therefore expected in the CH_4 spectra, although it was not possible to distinguish CO_2 absorption from CH_4 absorption.

In addition to the H_2O and CO_2 absorptions, a strong PQR band was seen only in the CH_4 spectra, centered at approximately 2200 cm^{-1}. This was identified as the ν_2 vibration-rotation band of CH_3D from its line positions and spacings (Chackerian and Guelachvili, 1980, 1983; Rothman *et al.*, 1987). The fact that this band was not present in the background spectra and

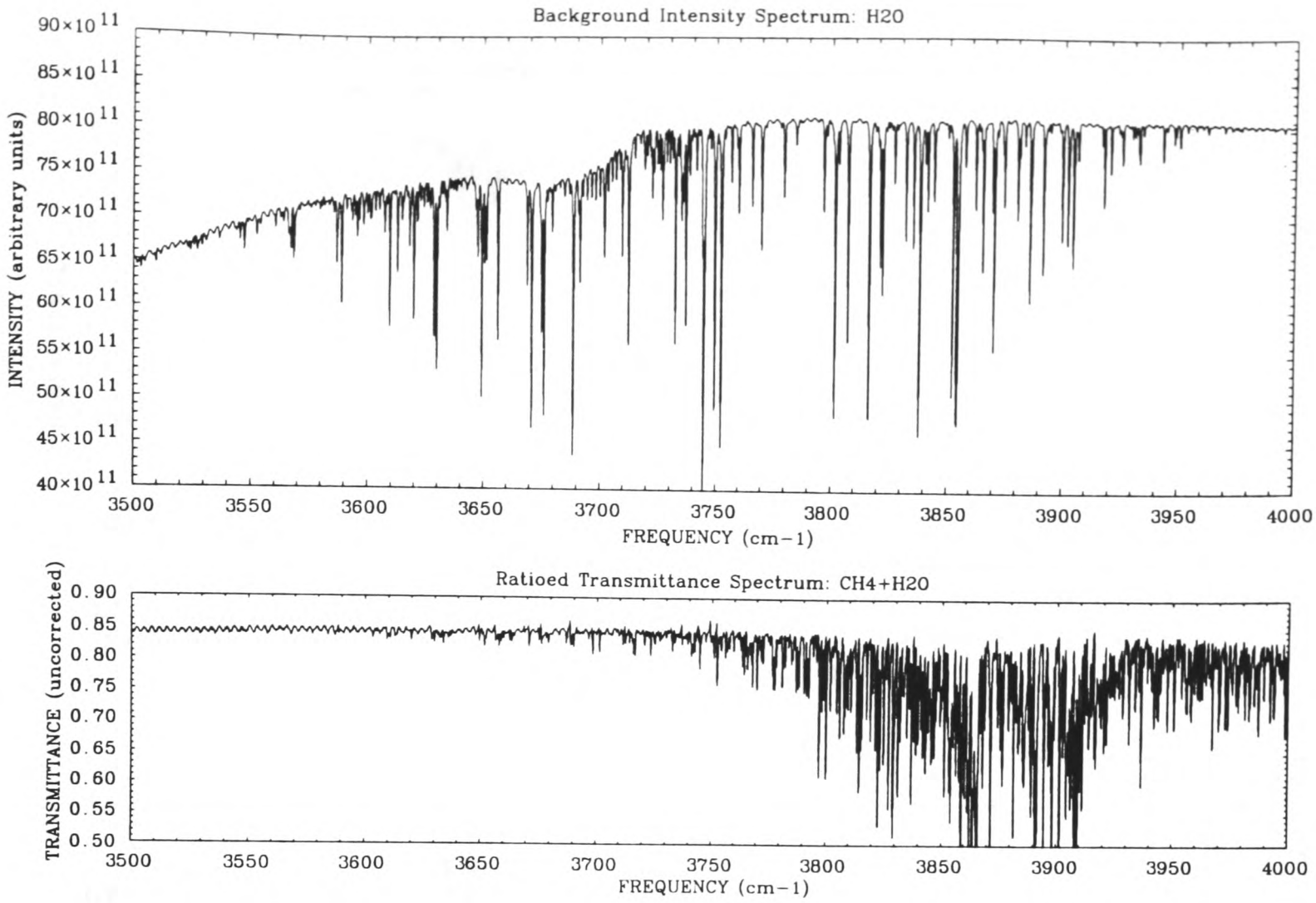

Figure 6.15: Contaminating H_2O absorption in a background intensity spectrum and in the CH_4 transmittance spectrum generated with this background.

increased in strength with increasing CH_4 abundance indicated that it was an isotopic impurity in the CH_4 gas. The terrestrial isotopic ratio of CH_3D to CH_4 is 6.0×10^{-4} (Rothman *et al.*, 1987), and so the CH_3D abundance ranged from approximately 9.3×10^{-6} to 0.33 m-amagat, sufficient to make such a strong band clearly visible. From an examination of spectra with the largest CH_4 abundances, the region from 2039 to ~2324 cm^{-1} was determined to be affected by CH_3D absorption. Lines of the P branch were clearly distinguishable from 2039 cm^{-1} to the Q branch at 2200 cm^{-1}, a region free of CH_4 absorptions, while the extent of the R branch, which overlaps the wing of a methane band, was estimated using the fact that the line at 2323.508 cm^{-1} in the R branch has the same quantum number assignments as the 2039.043 cm^{-1} line in the P branch, and assuming that these two lines are of comparable strength (Chackerian and Guelachvili, 1980).

Weaker absorptions by CH_3D (and similarly, by $^{13}CH_4$), elsewhere in the 2000–9500 cm^{-1} spectral range, were indistinguishable from $^{12}CH_4$ absorptions. However, these isotopic absorptions will be included in the band-model fits. Estimates of the Jovian CH_3D/CH_4 ratio range from 6.6×10^{-5} to 3.1×10^{-4} (based on estimates of the D/H ratio in §1.3.6), consistently smaller than the terrestrial value. Similarly, the Jovian $^{13}CH_4/^{12}CH_4$ ratio is about 0.56 times the terrestrial value (see §1.3.6). Therefore, it should be noted that the band modelling will over-estimate the absorptions of CH_3D and $^{13}CH_4$ relative to those of $^{12}CH_4$, compared to their absorptions relative to $^{12}CH_4$ in Jovian spectra.

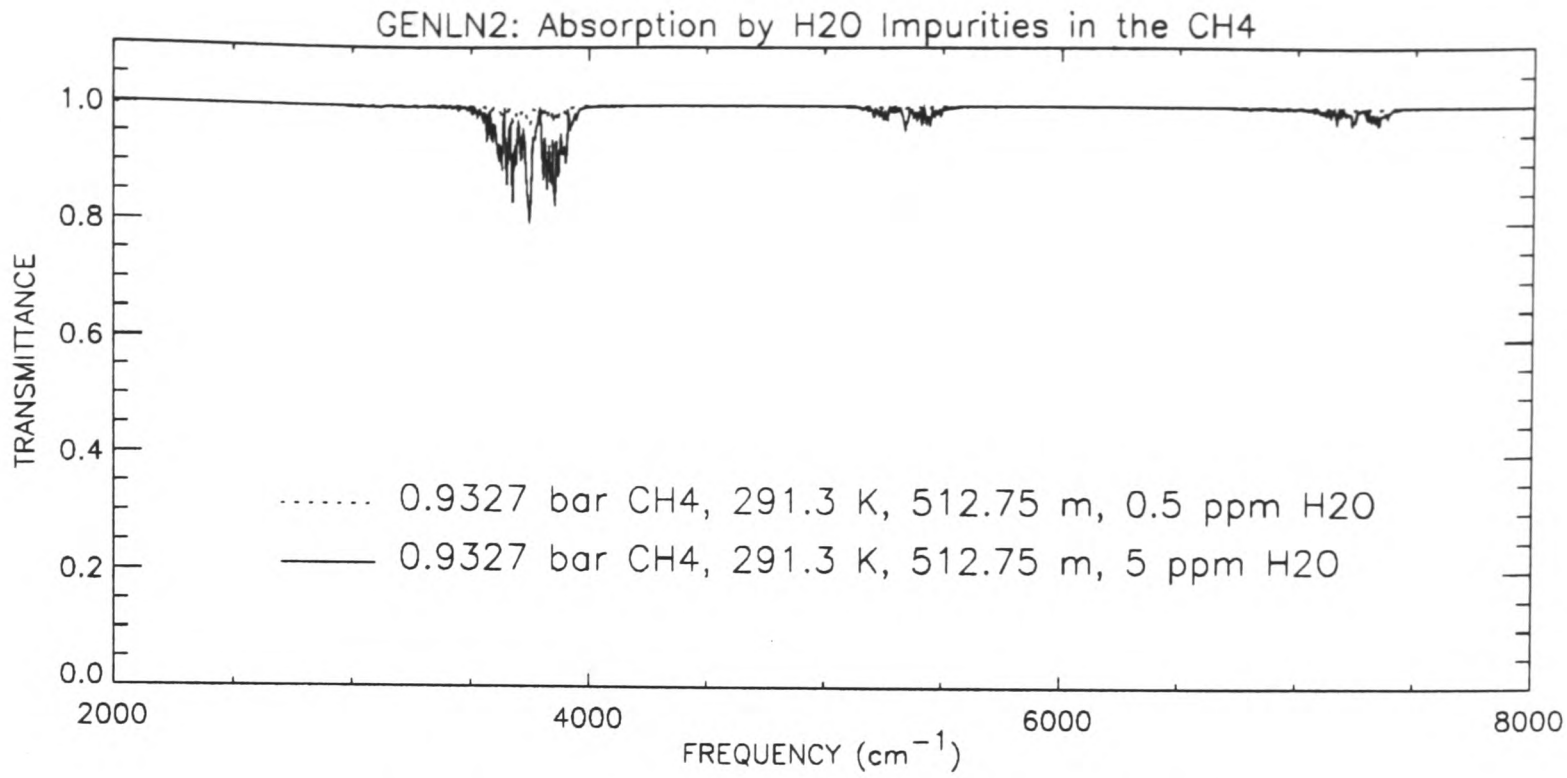

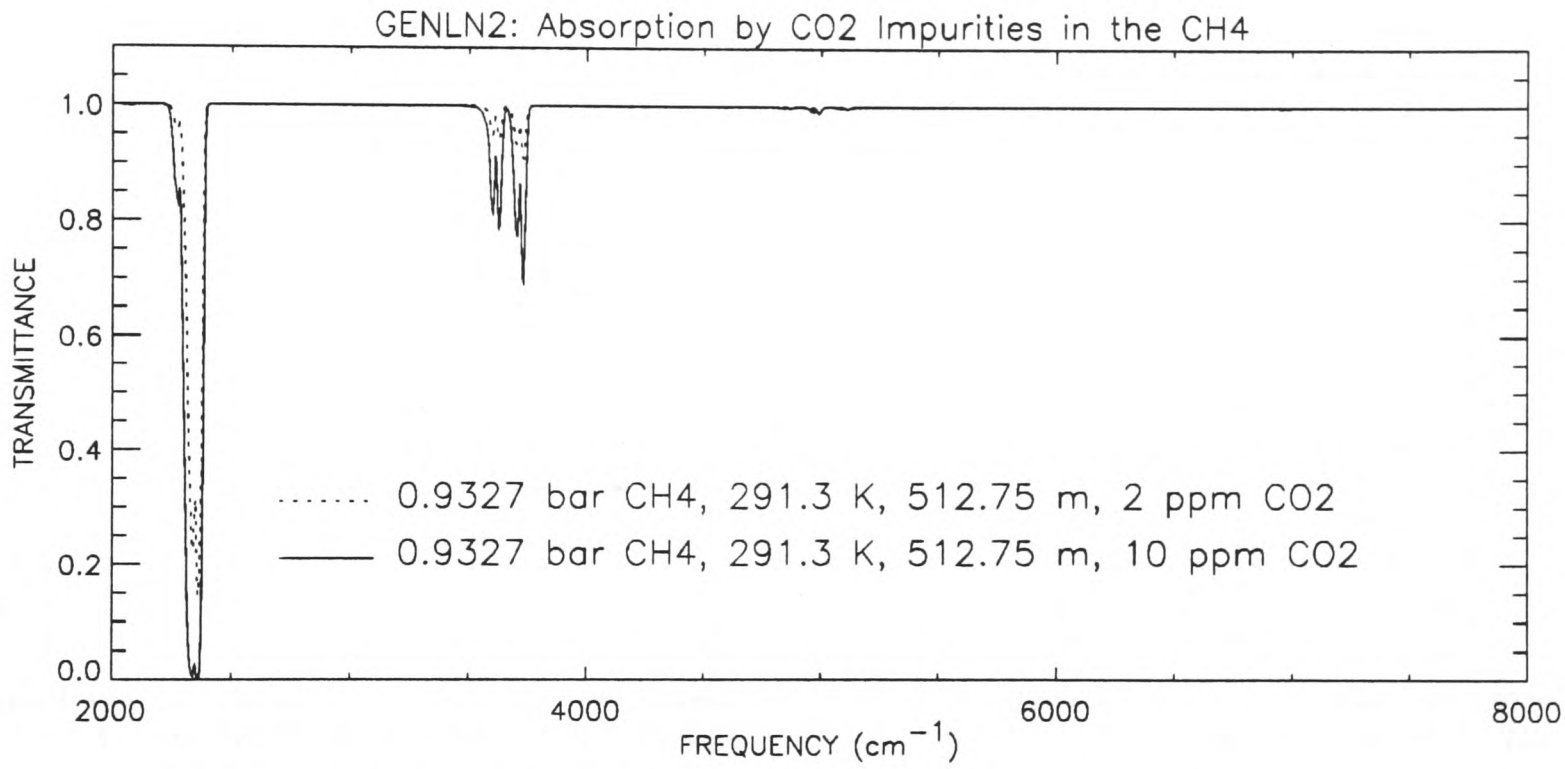

Figure 6.16: GENLN2 calculation of the H_2O and CO_2 absorptions arising from impurities in the CH_4 gas supplies for the largest CH_4 abundance at 296 K. These spectra are at the degraded resolution of 10 cm^{-1}, and no absorption was found beyond 8000 cm^{-1}.

Another absorption feature observed in the H_2-broadened CH_4 spectra was the 1–0 band of H_2. In order to distinguish this band from overlapping CH_4 absorptions and to determine its extent, a set of pure H_2 spectra was recorded at 240 K and 256 m, with the quartz-halogen source, and using the three H_2-broadening pressures of 100, 245, and 600 torr. Figure 6.17 is a plot of the resulting corrected and degraded spectra over the entire quartz-halogen spectral range, which shows the location of the H_2 absorption. Also included in this figure is a close-up view of the absorption feature at the original resolution. It shows six individual absorption lines superimposed on a broad continuum absorption. All six of these lines were identifiable as lines in the 1–0 band of H_2, having line positions in excellent agreement with those listed in Margolis (1982, p.435). The continuum feature extends from approximately 3700 to 5600 cm^{-1}, but is

only significant for 600 torr of H_2. Those CH_4 spectra broadened by 600 torr of H_2 also have H_2 absorption in this region, somewhat less than that seen in Figure 6.17 for pathlengths of 64 and 128 m, and somewhat more for pathlengths of 416 and 512 m.

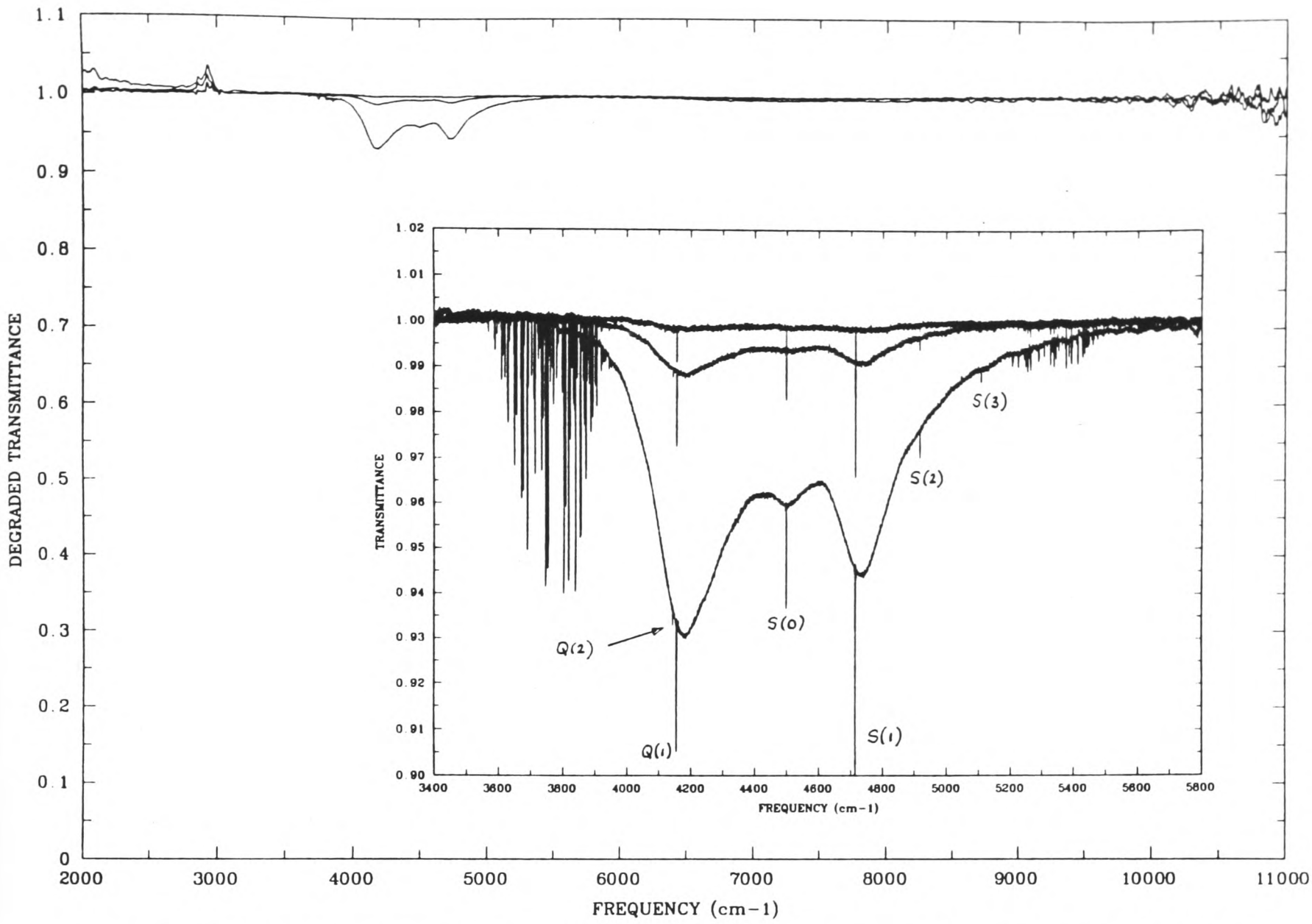

Figure 6.17: Pure H_2 spectra, recorded at 240 K and 256.75 m, and at pressures of 0.1336, 0.3268, and 0.8013 bar. The first spectrum covers the entire quartz-halogen spectral range and has been degraded to 10 cm^{-1}. The second spectrum is a close-up of the 1–0 band at the original resolution, with the six lines identified as shown.

The final contaminating absorption found in the spectra was a broad-band feature, extending from 2820 to 3020 cm^{-1}, and having three sharp absorption maxima at approximately 2850, 2920, and 2960 cm^{-1}. This was first noticed in the 296 K spectra, and was traced to pump oil. A Perkin Elmer spectrometer was used to record some low-resolution spectra of several types of pump oil used in the LWC system. The three-peak structure closely matched the structure present in the spectra of the Apiezon C diffusion pump oil and of the Castrol rotary pump oil (which were indistinguishable at the resolution used). The exact location of the contaminating oil in the 296 K spectra was uncertain, but when the LWC was cooled down, a misty deposit of pump oil condensed on the outside (the vacuum vessel side) of the inner vessel viewing and infrared windows, as described in §5.2.3. Due to backstreaming from the LWC pumps and contamination of the multilayer insulation, the LWC vacuum vessel had become severely contaminated with pump oil over a period of years. This pump oil was cleaned from

the windows prior to the 190 K experiments, and again before the 240 K experiments, but its elimination from the LWC system was a major undertaking beyond the scope of this work.

The pump-oil absorption overlapped the strongest CH_4 band, making it impossible to use the CH_4 transmittance spectra to assess the how well the pump-oil absorption ratioed out. However, the pump-oil absorption in the 296 K spectra remained stable over the course of a day, disappearing completely in the ratios of end- to start-of-day backgrounds. Therefore, there is no error in transmittance due to pump-oil contamination in the 296 K spectra. For the 190 K and 240 K spectra, the pump-oil absorption was much stronger and no longer stable. In order to obtain an upper limit on the error in the CH_4 transmittance for these spectra, the ratio of the end- to start-of-day averaged backgrounds was generated for all 33 days of cold spectra, showing the residual pump-oil absorption. For each of these ratios, the averaged transmittance over ± 5 cm^{-1} at five frequencies in the region of strongest pump-oil absorption (2920 to 2960 cm^{-1}) was calculated. The difference between the smallest of these transmittances and the 100% transmittance level was taken to be the largest error in transmittance due to pump-oil absorption. The maximum error was then calculated as the r.m.s. of these 33 values, giving a value of 0.025. This provides a worst estimate of the error for the 190 K and 240 K CH_4 transmittance spectra due to pump-oil absorption from 2820 to 3020 cm^{-1}. The true error is probably much less, as the pump oil should ratio out better when the CH_4 spectra are ratioed to interpolated background spectra than when end-of-day background spectra are ratioed to start-of-day background spectra.

6.3 Summary

This chapter has presented the self- and H_2-broadened CH_4 spectra that were recorded for the purposes of band modelling, and has provided a discussion of their reduction to transmittance spectra and an assessment of their quality. Within the limitations of the experimental capabilities, the temperatures, pressures, and pathlengths were chosen to obtain coverage of the Jovian regime which was as comprehensive as possible. Similarly, the spectral range and resolution were chosen to provide the maximum possible coverage of the NIMS spectral range. The final set of original-resolution corrected and averaged transmittance spectra, 108 of self-broadened CH_4 and 117 of H_2-broadened CH_4, are a resource in themselves, providing a significant improvement on the data currently available. For the purposes of the present work, these 0.25 cm^{-1} resolution spectra have been taken a step further and degraded to a resolution of 10 cm^{-1} for use in the fitting of band models, which is the subject of the following chapter.

Also discussed in this chapter were various factors, common to spectroscopic measurements, which affected the quality of the data. Not all of the resulting spectroscopic features were found to be significant, and many were reduced or eliminated during the experimental work. Of those unwanted features which did appear in the spectra, some were present in only a subset of the spectra and some affected only a limited spectral region. In addition, by recording such a large

data set, good characterisation of these features was obtained. Where possible, the unwanted features were minimised using computational methods, and the errors in transmittance introduced by each one were assessed. Table 6.7 provides a summary of the factors affecting the spectra, the subsets of spectra and the frequencies that they affected, and either the method used to reduce these effects or the estimated residual or maximum errors in transmittance.

Table 6.7: The factors affecting the quality of the self- and H_2-broadened CH_4 spectra, and the spectra and frequencies that they affected, along with either the method used to reduce the resulting spectroscopic features or the estimated errors in transmittance.

FEATURE	SPECTRA AFFECTED	ν (cm^{-1}) AFFECTED	TREATMENT OR ESTIMATED ERROR IN TRANSMITTANCE
Systematic drifts	All	All	Minimised by scaling or by ratioing to a fitted line
Random variability	All	All	Minimised by averaging the five spectra in a set, and by scaling or by ratioing to a fitted line
Sloping ratios	Weakly absorbing	All	Minimised by ratioing to a fitted line
Sloping ratios	Strongly absorbing globar	All	R.m.s. error $\leq$ 0.014
Sloping ratios	Strongly absorbing quartz-halogen	All	R.m.s. error $\leq$ 0.026
Ripple due to ice	All (worst for 296 K)	All	R.m.s. error $\leq$ 0.015
Ice absorption	All (worst for 296 K)	3000–3500	Maximum error = 0.079
Zero-signal level	All	All	Better than 0.01
3.2 cm^{-1} channelling	296 K, pure CH_4	2000–7000	Negligible after degrading to 10 cm^{-1}
2.8 cm^{-1} channelling	240 K, 190 K	2500–7000	Negligible after ratioing to backgrounds
80 cm^{-1} channelling	Quartz-halogen	All	Maximum error = 0.040
CO_2 in optics tanks	296 K, pure CH_4	2290–2390	Maximum error = 0.010 (0.040 for 4 days)
H_2O in optics tanks	296 K, pure CH_4	3500–4000 5150–5550 7000–7400	Maximum error = 0.01
CO_2 in the CH_4	All	2200–2400 3550–3750	Variable error (see §6.2.7)
H_2O in the CH_4	All	3500–4000 5150–5550 7100–7400	Variable error (see §6.2.7)
CH_3D in the CH_4	All	2039–2324	Variable error (see §6.2.7)
H_2 absorption	H_2-broadened	3700–5600	Variable error (see §6.2.7)
Pump oil	240 K, 190 K	2820–3020	Maximum error = 0.025

Chapter 7

Band-Modelling Analysis of the Methane Spectra

7.1 Introduction

The final output of the data processing described in the previous chapter was a set of corrected, averaged, and degraded spectra, for both self- and H_2-broadened CH_4. These spectra consist of frequency-averaged transmittances for a variety of experimental conditions, averaged over 10 cm^{-1} intervals and sampled every 5 cm^{-1}. In this chapter, transmittance functions are derived for these spectra using the band models that were introduced in Chapter 4.

The fitting of the experimental CH_4 spectra proceeded in two stages. In the first stage, the self-broadened CH_4 spectra were fitted with the Goody and Malkmus random band models, the generalised Zachor-King and Gibson-Pierluissi models, and the empirical Smith model. The Goody and Malkmus models, which are the models most commonly used in fitting CH_4 transmittance, were selected because their assumption of a random line distribution is appropriate to the irregular and complex near-infrared CH_4 spectrum. The three other models were fitted in order to allow a comparison of the results obtained by different models and an assessment of which models provided the best representation of the data. In the second stage of the fitting process, the band models that were most successful at fitting the self-broadened CH_4 spectra were adapted to include foreign-broadening. They were then used to fit both the self- and H_2-broadened CH_4 spectra together.

This chapter begins with a description of the fitting technique that was used in the band modelling, and continues with a presentation of the results, first for the self-broadened CH_4 spectra, and then for the combined set of both the self- and H_2-broadened CH_4 spectra. It includes a discussion of the models fitted, the choice and initialisation of parameters, the quality of the band-model fits, the physical interpretation of the values obtained for the fitted parameters, and a comparison with the previous band-modelling studies described in Chapter 4.

7.1.1 The Fitting Technique

Given a band-model equation for the frequency-averaged transmittance, $\bar{\tau}$, in terms of temperature, pressure, abundance, and several parameters, the aim of a band-model fit is to find the set of parameters for which the band model provides the best match to the measured transmittances. For a set of N_{spec} spectra, each consisting of N_ν frequency-averaged transmittances, N_ν band-model fits are performed. Each of these fits should provide the best possible match between the N_{spec} measured transmittances and the N_{spec} transmittances calculated with the band-model equation.

The problem of representing measured data by a fitted model with adjustable parameters is encountered in many disciplines. The most widely used method of fitting is that of least squares, in which the parameters are adjusted in order to minimise the sum of the squares of the differences between the data and the fitted model at each point. A measure of the deviation between the original data (N points (x_i, y_i)) and the fitted values (using a model $y(x_i; a_1, \cdots, a_M)$ having M parameters) for the final set of best-fit parameters is given by (Press *et al.*, 1986, p.503)

$$\sigma^2 = \sum_{i=1}^{N} \frac{[y_i - y(x_i; a_1, \cdots, a_M)]^2}{N}. \tag{7.1}$$

The method of least squares was used in this study to fit the band models to the measured CH_4 transmittances. As the band models are generally non-linear functions of their parameters, these parameters can be determined only with an iterative method of solution. For this purpose, a commercial non-linear least squares minimisation routine was used, routine E04FDE of the Numerical Algorithms (NAG) Library. This particular routine was chosen as the most appropriate for the problem under consideration, as it finds the unconstrained minimum of the sum of the squares of N non-linear terms with M parameters, given a set of initial estimates for these parameters, and does not require specification of first or second derivatives. This routine uses the corrected Gauss-Newton method described in Gill and Murray (1978). Given an initial set of parameters, $\vec{a} = a_j^1,\ j = 1, \cdots, M$, the routine generates a sequence of points

$$\vec{a}^{k+1} = \vec{a}^k + \alpha^k \vec{P}^k \tag{7.2}$$

where $\vec{P}^k$ is the direction of search, and

α^k is the step-length,

which should converge to minimise the sum of the squares, $\chi^2(\vec{a})$. The step-length is chosen to make $\chi^2(\vec{a}^k + \alpha^k \vec{P}^k)$ approximately a minimum with respect to α^k, while the choice of $\vec{P}^k$ depends upon the reduction in χ^2 during the previous iteration. Further details of this method can be found in the *NAG Manual, Volume 3* (1983, p.3–27) and in Gill and Murray (1978).

7.2 Band Modelling of the Self-Broadened Methane Spectra

7.2.1 Selection of Models and Initialisation of Parameters

The models used to fit the self-broadened CH_4 spectra are summarised in Table 7.1, which includes the equations for $\overline{\tau}$ and a listing of the parameters that were fitted for each model. All of these models have been described in §4.2, where the nomenclature used below has also been defined.

Table 7.1: The band models that were used in fitting the self-broadened CH_4 spectra, along with the parameters that were fitted for each model. (See §4.2 for nomenclature.)

MODEL NAME	EQUATION FOR $\overline{\tau}$	FITTED PARAMETERS
Weak Limit	$\exp\left(-k_\nu U\right)$	$k_\nu(T_0)$, E_l
Goody-Lorentz	$\exp\left(-1/\sqrt{\frac{1}{(k_\nu U)^2}+\frac{1}{\pi k_\nu y_\nu U P\sqrt{T_0/T}}}\right)$	$k_\nu(T_0)$, E_l, y_ν
Goody-Voigt	$\exp\left(-2k_\nu U\int_0^\infty \frac{V(x,y)}{1+k_\nu U\delta V(x,y)/\alpha_D^0\sqrt{T}}\,dx\right)$	$k_\nu(T_0)$, E_l, δ/α_D^0, α_L^0/α_D^0
Malkmus-Lorentz	$\exp\left(-1/\left[\frac{1}{2k_\nu U}+\sqrt{\frac{1}{(2k_\nu U)^2}+\frac{1}{4\pi k_\nu y_\nu U P\sqrt{T_0/T}}}\right]\right)$	$k_\nu(T_0)$, E_l, y_ν
Malkmus-Voigt	$\exp\left(\frac{-2\alpha_D^0\sqrt{T}}{\delta}\int_0^\infty \ln\left[1+\frac{k_\nu U\delta}{\alpha_D^0\sqrt{T}}V(x,y)\right]\,dx\right)$	$k_\nu(T_0)$, E_l, δ/α_D^0, α_L^0/α_D^0
Zachor-King (simplified)	$\exp\left(-1/\sqrt{\left(\frac{1}{k_\nu U}\right)^2+\left(\frac{-1}{\ln\tau_{strong}}\right)^2}\right)$	$k_\nu(T_0)$, E_l, y_ν, n
Gibson-Pierluissi	$\exp\left(-1/\sqrt{\left(\frac{1}{k_\nu U}\right)^2+\left(\frac{-B_s}{\ln\tau_{strong}}\right)^2-\frac{M}{k_\nu U}\frac{1}{\ln\tau_{strong}}}\right)$	$k_\nu(T_0)$, E_l, y_ν, n, B_s, M
Smith (simplified)	$\exp\left(-k_\nu U^a P^b T^c\right)$	$k_\nu(T_0)$, E_l, a, b, c

The self-broadened CH_4 spectra were fitted with four sequences of increasingly complex models, as illustrated in Figure 7.1, using the parameters fitted by one model as the input for the next model. Because the fitting routine is sensitive to the initialisation of the parameters, this method ensured that the value of a parameter was optimised as far as possible before being used as an initial value in a succeeding model. All four sequences began with the fit of the

one-parameter temperature-independent Weak Limit model, fitting the absorption coefficient $k_\nu = k_\nu(T_0)$. Prior to starting the fit, $k_\nu(T_0)$ for each frequency interval was initialised to the average value of $-\ln(\overline{\tau})/U$ for the N_{spec} transmittances in that interval. This fit was followed by the two-parameter Weak Limit model with temperature dependence of k_ν added in the form of Equation 4.37. In this model, both $k_\nu(T_0)$ and E_l were fitted, $k_\nu(T_0)$ being initialised to the best-fit values of the preceding Weak Limit fit, and E_l being given an initial value of 100 cm^{-1} based on a survey of values for CH_4 listed in the HITRAN 1986 database (Rothman *et al.*, 1987).

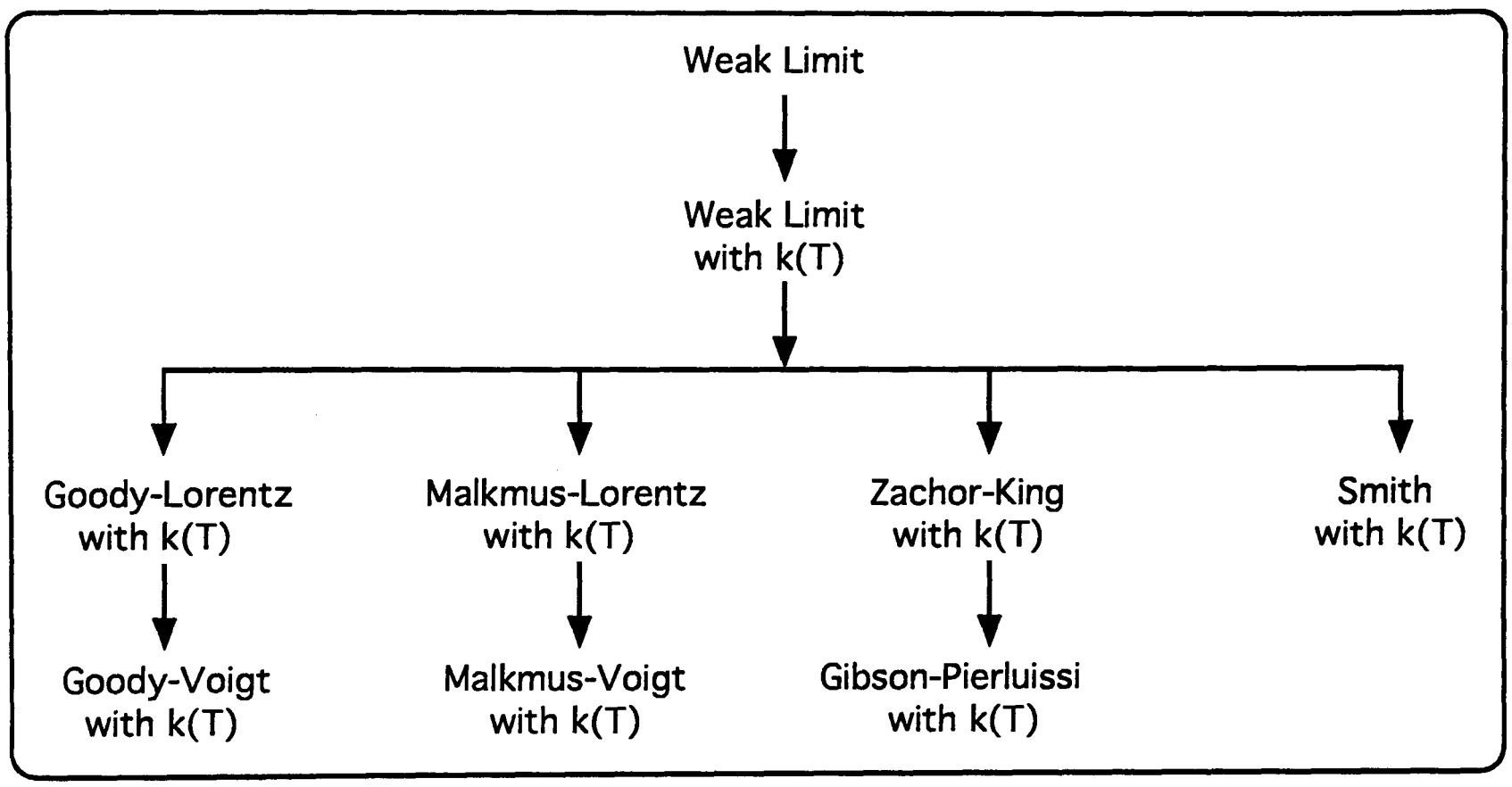

Figure 7.1: The sequences of models used in fitting the self-broadened CH_4 spectra.

These two parameters, thus optimised for the Weak Limit approximation, were then supplied as the initial values for four subsequent independent fitting sequences. In the first sequence, the Goody random band model was fitted to the spectra, first with the Lorentz lineshape and then with the Voigt lineshape. In the Goody-Lorentz model, the pressure coefficient, y_ν, was fitted as the third parameter. This was initialised to give the strong term in Equation 4.25 the same effect as the weak term for the spectrum with the strongest absorption (largest U/P). Calcutt *et al.* (1988) used a similar initialisation, but set the strong term at only 5% of the weak term. In the present study, the optimum initialisation for y_ν was determined from a series of Goody-Lorentz trial fits in which the strong term was initialised to 10, 20, 50, 100, and 200% of the weak term. These fits improved (*i.e.*, the r.m.s. residual error decreased) as the effect of the strong term was increased to 100%, but showed negligible improvement beyond this. Therefore, 100% was chosen as the initialisation factor. The fact that this value was larger than the 5% of Calcutt *et al.* (1988) is attributed to the greater CH_4 abundances and hence the stronger CH_4 absorptions for the spectra fitted in the present study.

Once the Goody-Lorentz model had been fitted, the resulting best-fit parameters were used to initialise the parameters in the Goody-Voigt model. The choice of parameters in the Goody-Voigt model is slightly less obvious than for the Goody-Lorentz model, but follows logically from Equation 4.28. The parameter δ/α_D^0 is found in the denominator of the integrand, while α_L^0/α_D^0 appears in the definition of y in $V(x,y)$:

$$y = \frac{\alpha_L}{\alpha_D} = \left(\alpha_L^0 \frac{P}{P_0}\sqrt{\frac{T_0}{T}}\right)\left(\frac{1}{\alpha_D^0\sqrt{T}}\right) = \frac{\alpha_L^0}{\alpha_D^0}\frac{P}{P_0}\frac{\sqrt{T_0}}{T}. \tag{7.3}$$

$k_\nu(T_0)$ and E_l were directly translated from the Goody-Lorentz fit, α_L^0/α_D^0 was initialised from a given α_L^0, ν, and the molecular mass of CH_4, and δ/α_D^0 was indirectly translated from the Goody-Lorentz fit of y_ν, being equivalent to $y_\nu\alpha_L^0/P_0\alpha_D^0$. The value of the self-broadened Lorentz half-width, α_L^0, chosen for the initialisation was 0.085 cm^{-1}, as used, for example, by Silvaggio (1982) and Giver *et al.* (1984) in their CH_4 band modelling, and consistent with the measured values listed in Table 3.1. Evaluation of the Voigt lineshape $V(x,y)$ was accomplished using the standard computer code of Drayson (1976). Evaluation of the second integral (over x) was performed using Simpson's rule with 101 points computed over both high- and low-resolution grids (*e.g.*, Vandergraft, 1983, p.156).

The second sequence to be fitted from the Weak Limit with $k_\nu(T)$ involved the Malkmus random band model, again using both the Lorentz and Voigt lineshapes. As seen in Table 7.1, the parameters fitted in the Malkmus-Lorentz and Malkmus-Voigt models are equivalent to those in the Goody-Lorentz and Goody-Voigt models, respectively, although the equations for $\bar{\tau}$ differ between the models. The pressure coefficient in the Malkmus-Lorentz model was given the same initial value as it was in the Goody-Lorentz model, after trial fits similar to those described above showed that initialising the strong term to 100% of the weak term again optimised the fit. Thus, all of the parameters in the Malkmus models were initialised in the same way as the equivalent parameters in the Goody models. The evaluation of the Voigt lineshape and of the second integral (over x) were both identical to the methods used for the Goody-Voigt model.

The third sequence of models to be fitted from the Weak Limit with $k_\nu(T)$ were the empirical generalisations of the random band model. The first model to be fitted was a four-parameter Zachor-King model, simplified by setting $M = 0$. The parameters y_ν and n appear in the definition of τ_{strong} given in Equation 4.45. Evaluation of τ_{strong} required evaluation of the gamma and incomplete gamma functions, which was performed using Numerical Recipes routines GAMMLN and GAMMP (Press *et al.*, 1986, p.157,161). The best-fit values obtained with the Zachor-King model were then used to initialise four of the six parameters in the Gibson-Pierluissi model. The additional two parameters, B_s and M, were initialised to 1 and 0, respectively, making the initial model identical to the simplified Zachor-King model.

The last sequence of models to be fitted was simply the empirical Smith model (without any higher order terms) refitted from the Weak Limit. Two such fits were performed. In the first,

the original four-parameter Smith model was refitted from the one-parameter Weak Limit, with the only temperature dependence being in the T^c term. In the second fit, the $k_\nu(T)$ temperature dependence was added to the model and the resulting five-parameter Smith model was refitted from the two-parameter Weak Limit with $k_\nu(T)$. The exponents a, b, and c in the Smith model were initialised to 1, 0, and 0, respectively, making the initial Smith model identical to the Weak Limit model.

The self-broadened CH_4 spectra were thus fitted using all four of the sequences shown in Figure 7.1. Two independent sets of fits were performed, one for the 108 globar spectra and one for the 108 quartz-halogen spectra. Once the fits were completed, the results obtained for these two sources were merged, the globar results being used for the 2000 to 3900 cm^{-1} region and the quartz-halogen results being used for the 3905 to 9500 cm^{-1} region. Before merging these results, the r.m.s. residual error (σ in Equation 7.1) was compared for each source and for each fit in the region of overlap, from 2000 to 4000 cm^{-1}. This comparison showed that σ agreed to within ± 0.01 for the fits with the two sources, except for the region below 2500 cm^{-1} where the signal-to-noise of the quartz-halogen spectra was particularly poor. However, σ for the globar fits was consistently less than or equal to σ for the quartz-halogen fits, particularly for the final fits in each sequence. This was due to the drop in the quartz-halogen signal over this region and the absence of the 80 cm^{-1} channelling in the globar spectra. As a result, the globar fits were adopted for 2000 to 3900 cm^{-1}, 3900 cm^{-1} being chosen as the upper limit because of several spurious points between 3900 and 4000 cm^{-1} in the globar fits. The upper limit of 9500 cm^{-1} was determined by the low quartz-halogen signal level and the corresponding decrease in signal-to-noise above this frequency (see §6.1.2).

7.2.2 The Quality of the Fits

7.2.2.1 Comparison of the Fits Within Each Sequence

The success of each of the fitted models in reproducing the measured transmittances at each frequency was quantified by the r.m.s. residual error, σ, of Equation 7.1. This error is plotted in Figure 7.2 for all ten of the models that were fitted to the self-broadened CH_4 spectra. Considering each of the four sequences of Figure 7.1 in turn, these plots clearly show how the fits improve in each progression.

The first four plots, (a) to (d), are for the four models fitted in the Goody sequence. As expected, the one-parameter Weak Limit model provides a poor fit to the data, particularly in the strongly absorbing band centres (refer to Figure 6.5 for the locations of the bands). The addition of the temperature dependence of k_ν improves the Weak Limit fit, but is still unable to reduce σ significantly. Further improvement is obtained with the addition of the strong term in the Goody-Lorentz model, but the Voigt lineshape is required before σ is consistently reduced across the entire spectrum.

The importance of the Voigt lineshape is illustrated in Figure 7.3, where both the Lorentz

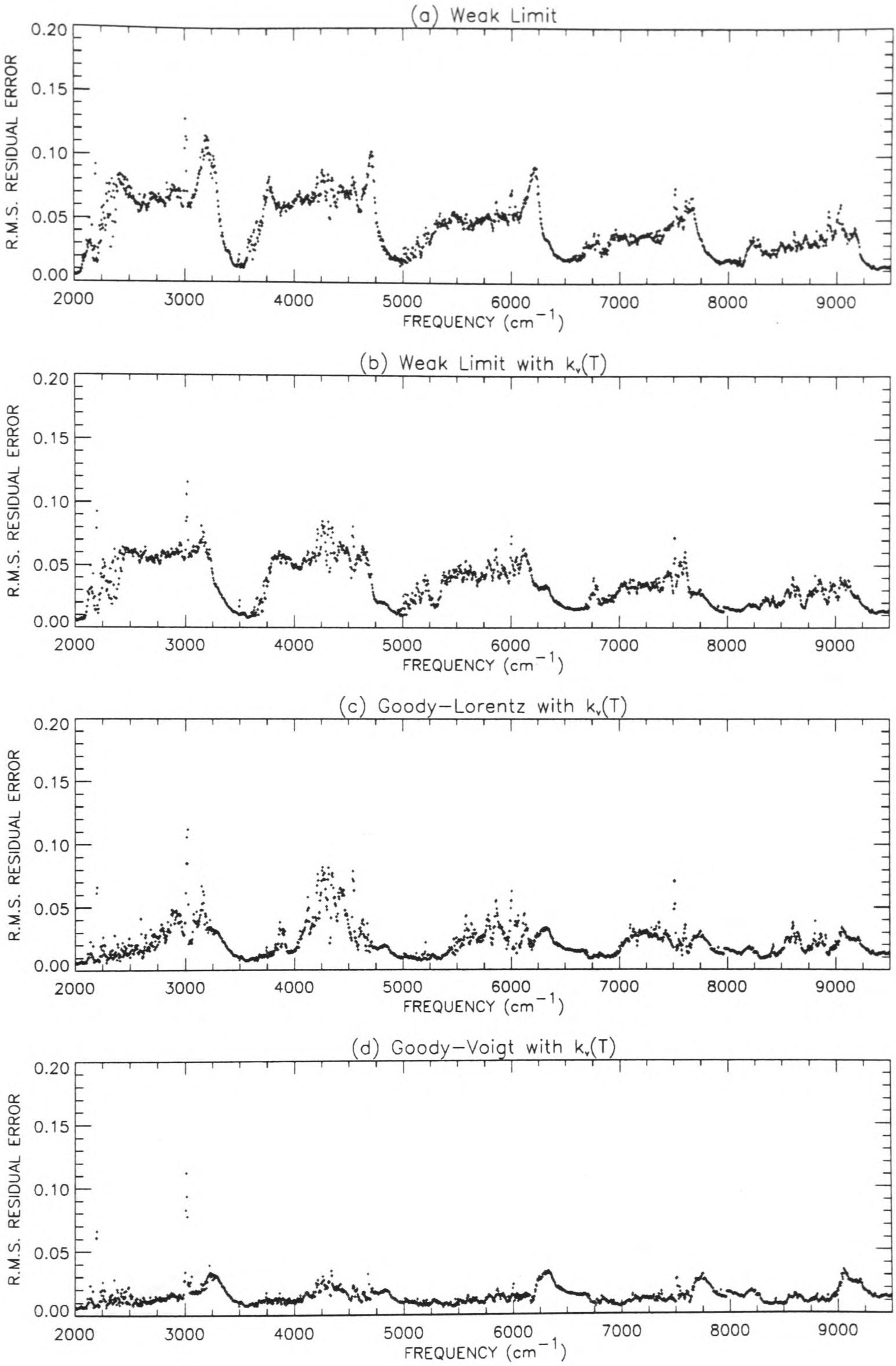

Figure 7.2: The r.m.s. residual error in transmittance for the ten models fitted to the self-broadened CH_4 spectra (continued on following page).

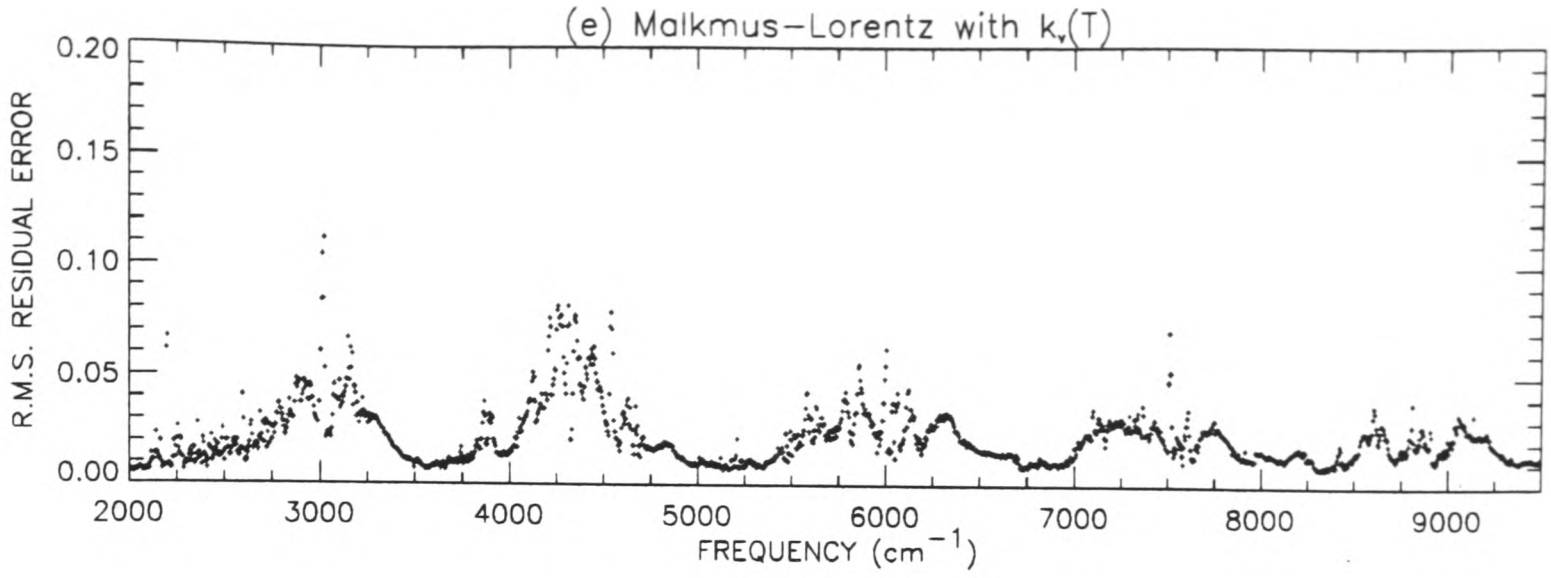
(e) Malkmus–Lorentz with $k_\nu(T)$
R.M.S. RESIDUAL ERROR
0.20
0.15
0.10
0.05
0.00
2000
3000
4000
5000
6000
7000
8000
9000
FREQUENCY (cm^{-1})

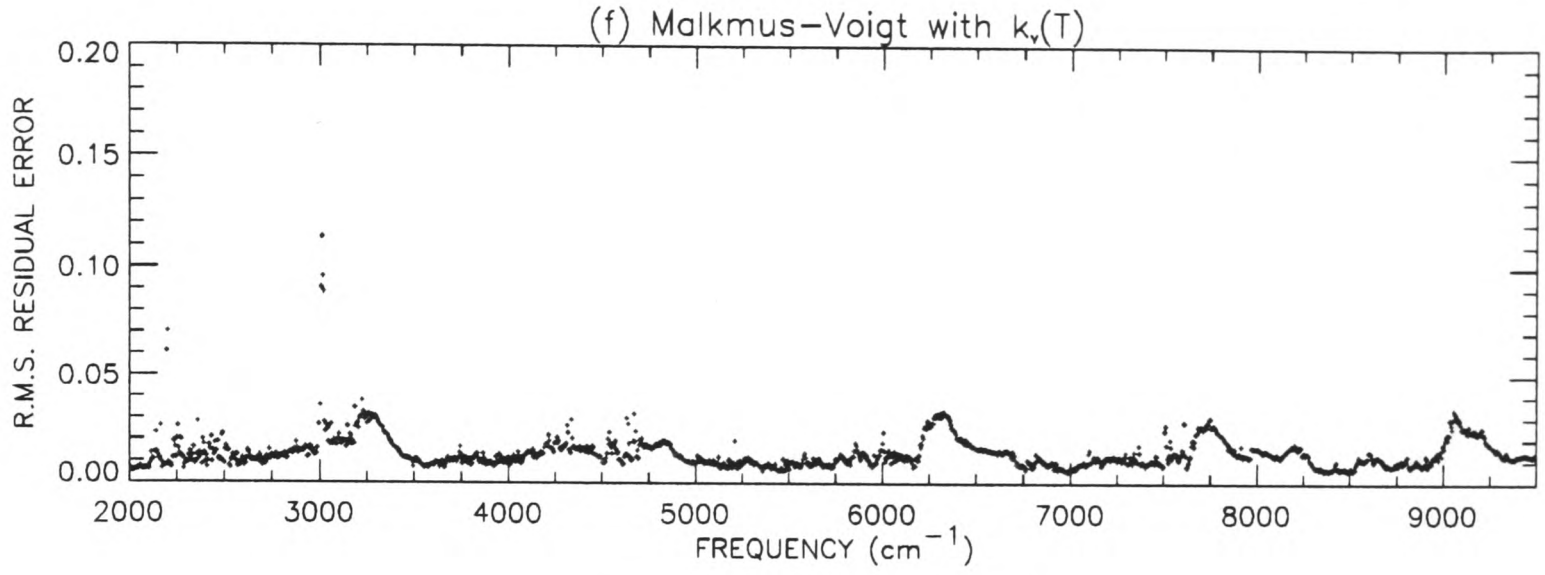
(f) Malkmus–Voigt with $k_\nu(T)$
R.M.S. RESIDUAL ERROR
0.20
0.15
0.10
0.05
0.00
2000
3000
4000
5000
6000
7000
8000
9000
FREQUENCY (cm^{-1})

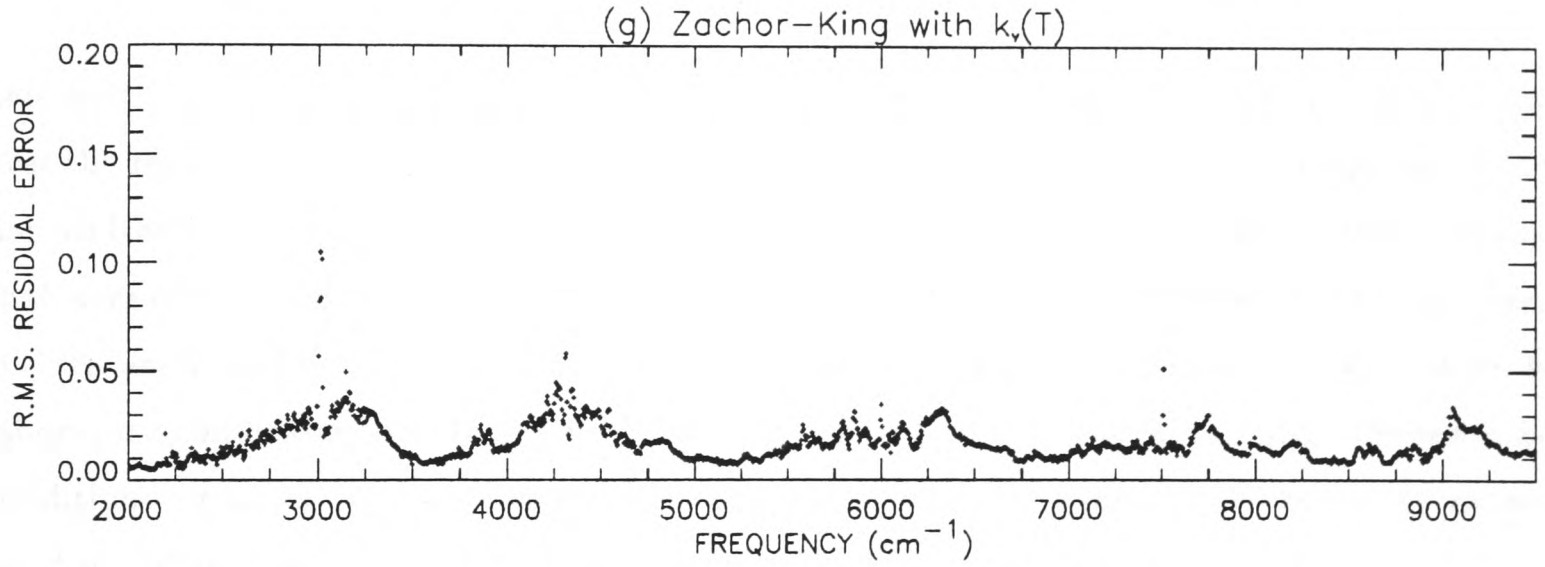
(g) Zachor–King with $k_\nu(T)$
R.M.S. RESIDUAL ERROR
0.20
0.15
0.10
0.05
0.00
2000
3000
4000
5000
6000
7000
8000
9000
FREQUENCY (cm^{-1})

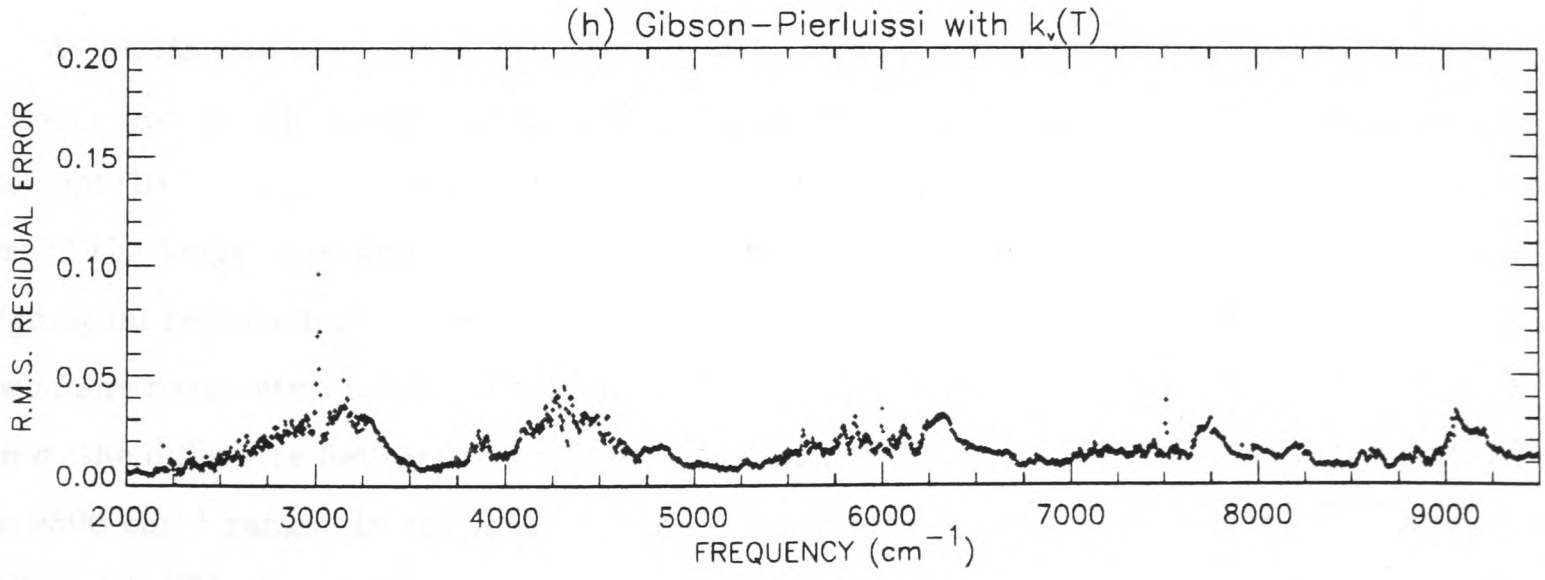
(h) Gibson–Pierluissi with $k_\nu(T)$
R.M.S. RESIDUAL ERROR
0.20
0.15
0.10
0.05
0.00
2000
3000
4000
5000
6000
7000
8000
9000
FREQUENCY (cm^{-1})

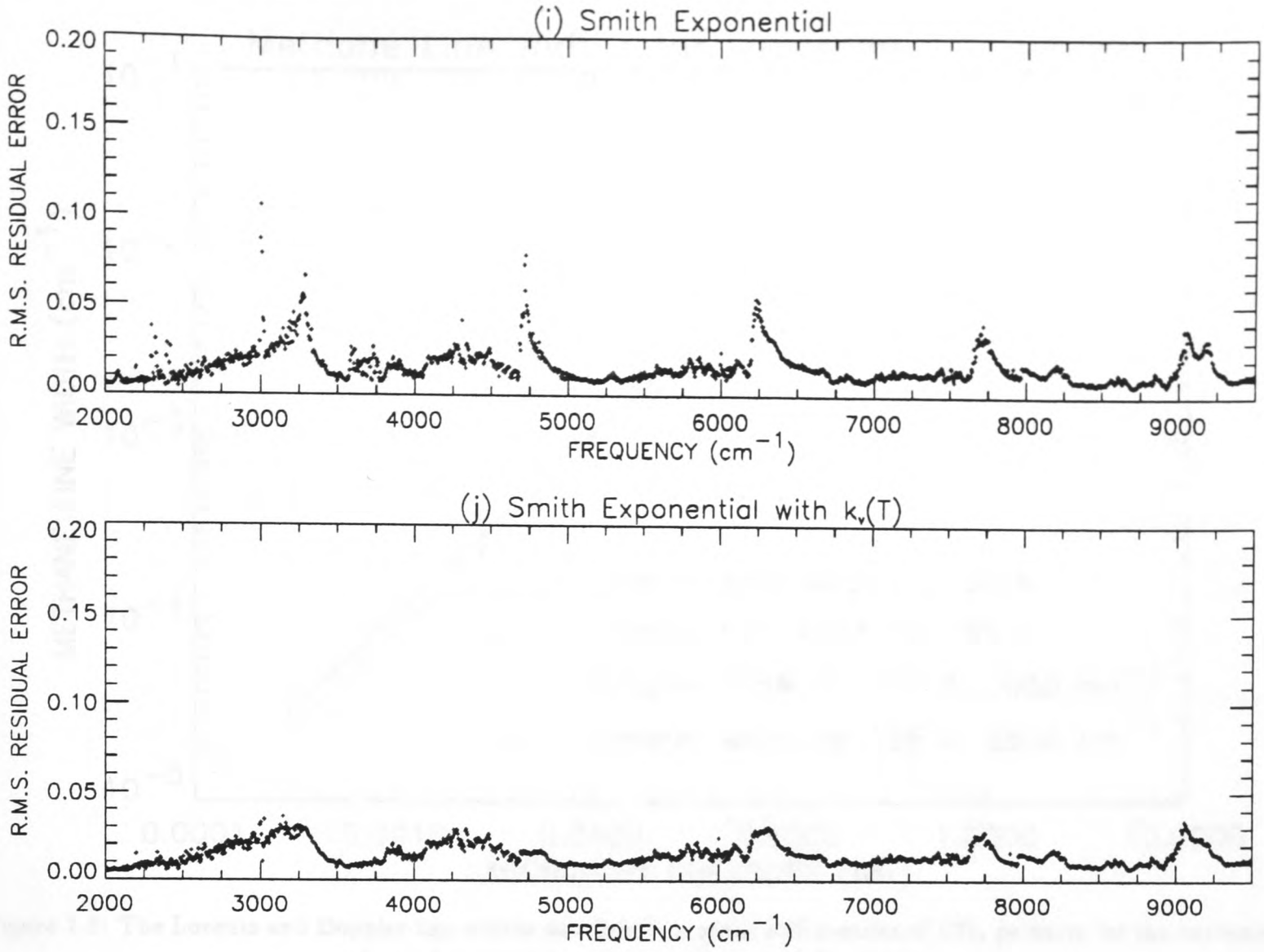

half-width (with $\alpha_L^0 = 0.085$ cm^{-1}) and the Doppler width are plotted as functions of pressure, over the range of pressures used in the self-broadened CH_4 spectroscopy. The extremes of both line widths have been plotted, as determined by the extremes of temperature and frequency that were obtained during the experiments. The range of line widths relevant to the laboratory spectra are therefore those lying in the regions between each pair of lines. Clearly, there are laboratory conditions for which either the Doppler or Lorentz broadening may dominate and conditions for which they are comparable. The use of the Voigt lineshape in the Goody random band model is therefore seen to be appropriate for these experimental conditions.

A similar improvement in σ is seen in the Malkmus fitting sequence. Figure 7.2(e) and (f) shows σ for the Malkmus-Lorentz and Malkmus-Voigt models, again following from the fits in (a) and (b). As was the case for the Goody fit, the Malkmus fit is significantly improved by the use of the Voigt lineshape. In the third sequence, the Zachor-King model, (g), again provides a significant reduction in σ, compared to the preceding Weak Limit fits. However, the addition of two more parameters in the subsequent fit with the Gibson-Pierluissi model, (h), has little effect on σ, the difference between σ for these two models being well below 0.005 over the entire 2000 to 9500 cm^{-1} range. In the final sequence, the Smith exponential model was fitted with and without $k_\nu(T)$. As seen in (i) and (j) of Figure 7.2, the addition of the temperature dependence of k_ν improves the fit at the high frequency edge of each of the five bands.

Another means of illustrating how the fits compare within each sequence is to plot the

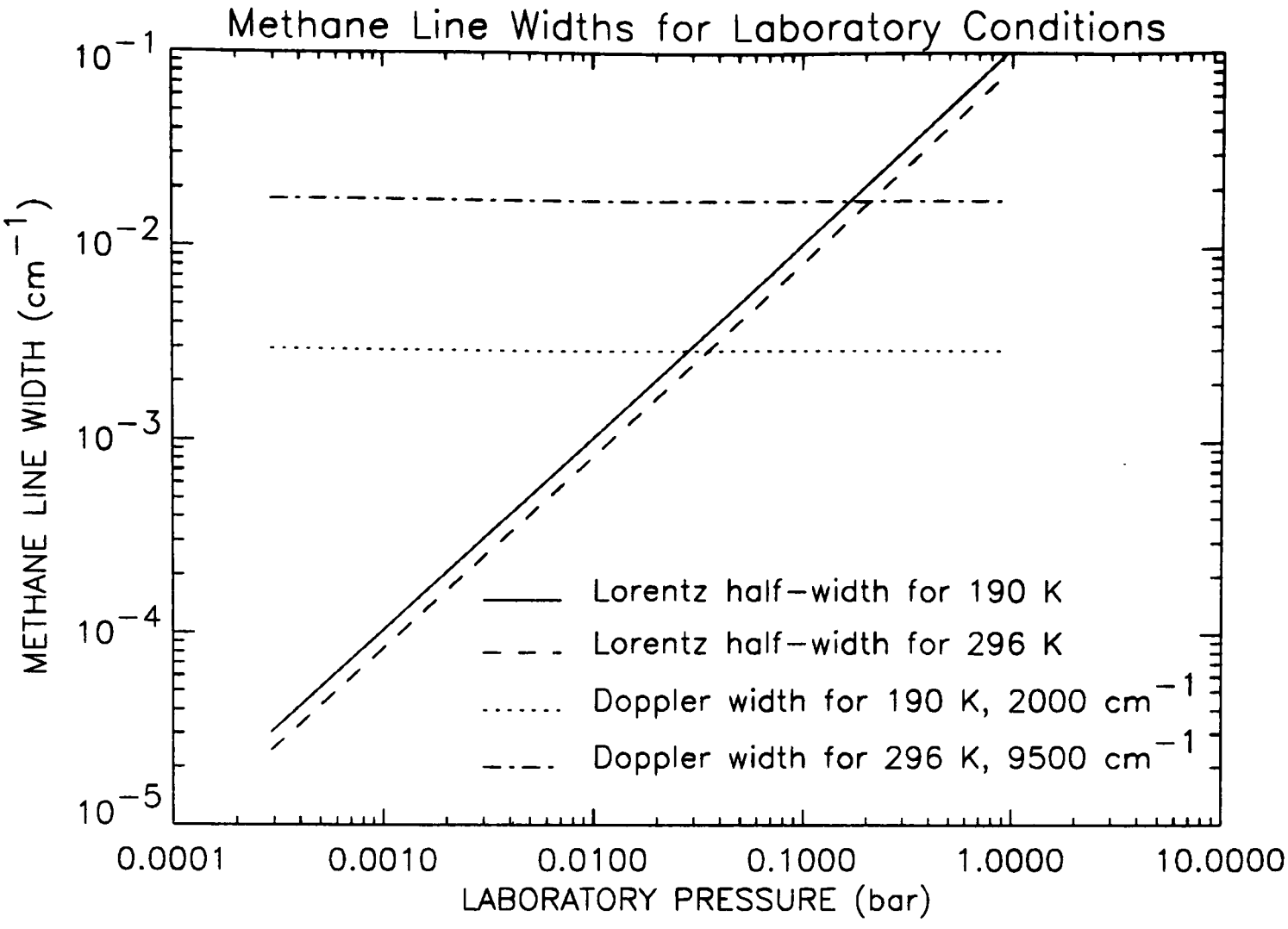

Figure 7.3: The Lorentz and Doppler line widths as a function of the self-broadened CH_4 pressure for the extremes of ν and temperature measured in the laboratory.

original measured transmittances and the fitted transmittances for one particular frequency interval. Such plots are shown in Figure 7.4 for the 2600 cm^{-1} interval and for all ten fitted models. The transmittance has been plotted against CH_4 abundance for all 108 abundances derived from the three temperatures, nine pressures, and four pathlengths. This particular interval was selected because it includes both the weak and strong extremes of absorption, and because it is an interval for which σ is large in the initial Weak Limit fits but is significantly reduced by the more complex models. In the one-parameter Weak Limit model, $\bar{\tau}$ is simply a function of U and so the fitted curve in Figure 7.4(a) is smooth, resulting in a poor match between the measured and fitted transmittances. For the more complex models, $\bar{\tau}$ is also a function of T and P so that the fitted transmittances are no longer smooth functions of U, and therefore provide a closer match to the measured transmittances. For both the Goody and Malkmus models, the match is clearly improved when the Lorentz lineshape is replaced by the Voigt lineshape ((d) versus (c) and (f) versus (e)). However, there is little difference between either the Zachor-King (g) and Gibson-Pierluissi (h) fits, or between the two Smith exponential fits, (i) and (j), as expected from examination of Figure 7.2, which shows that σ at 2600 cm^{-1} changes negligibly between these fits. Plots similar to those in Figure 7.4 can be constructed for every frequency interval fitted by the models, with a good match between the measured and fitted transmittances if σ is small and a poor match if σ is large.

With the exception of the third fitting sequence, the increasingly complex models in each

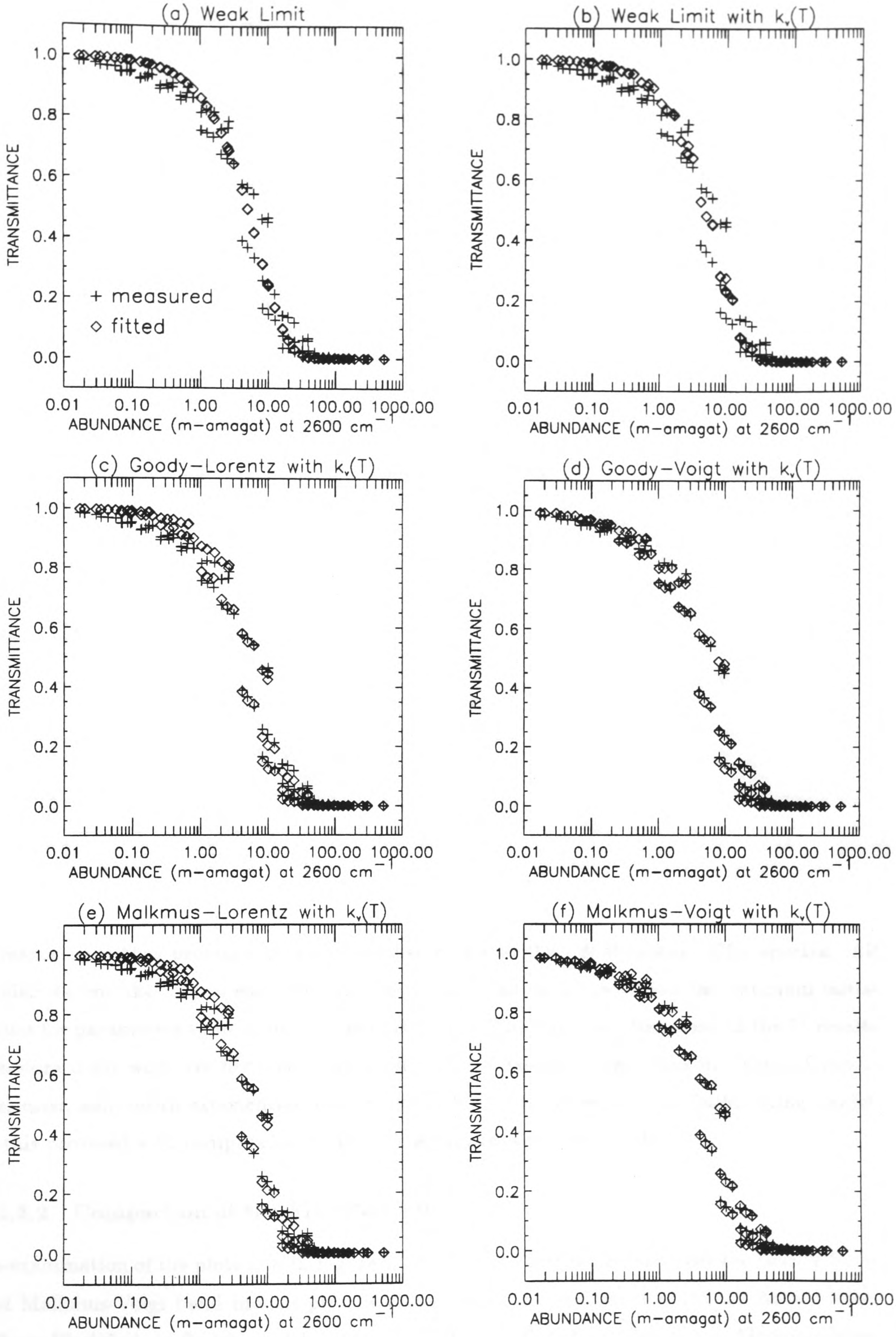

Figure 7.4: The measured and fitted transmittances for the 2600 cm^{-1} interval for the ten models used to fit the self-broadened CH_4 spectra (continued on following page).

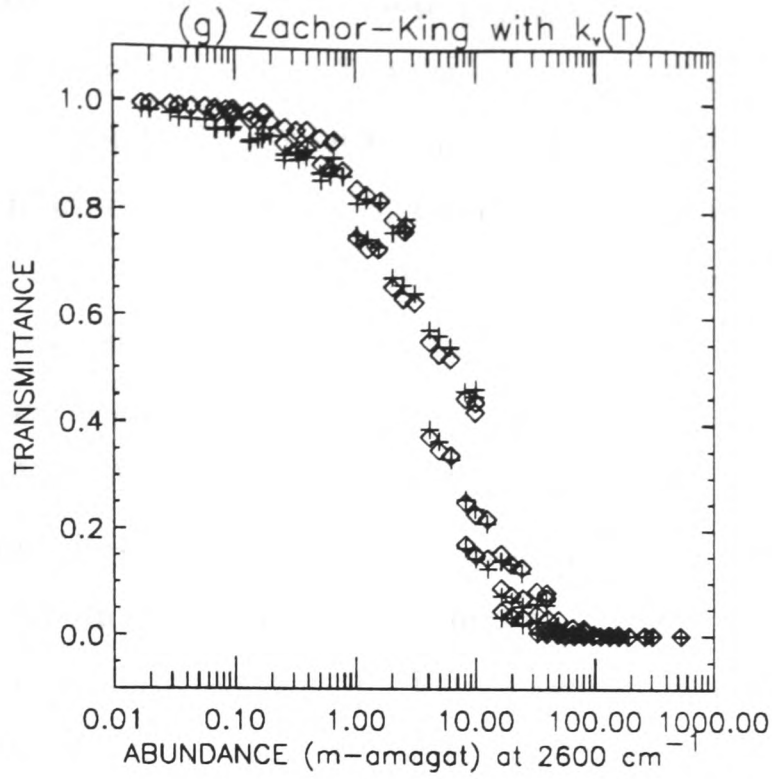

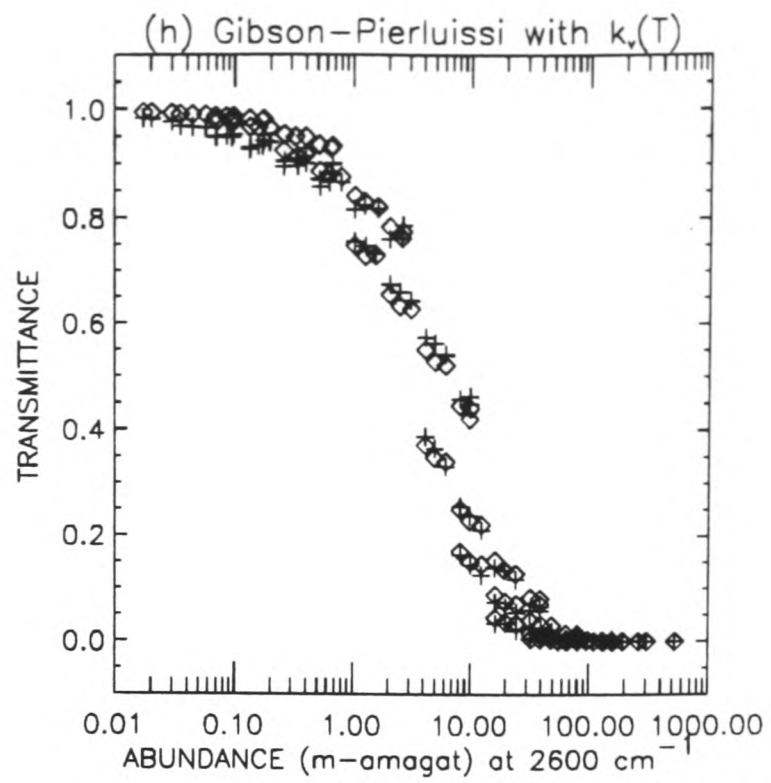

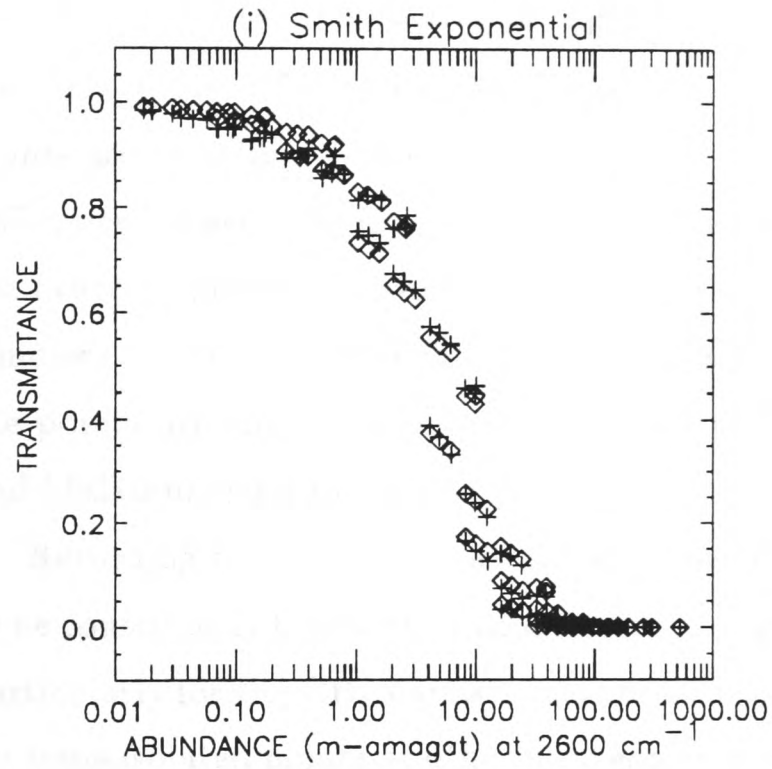

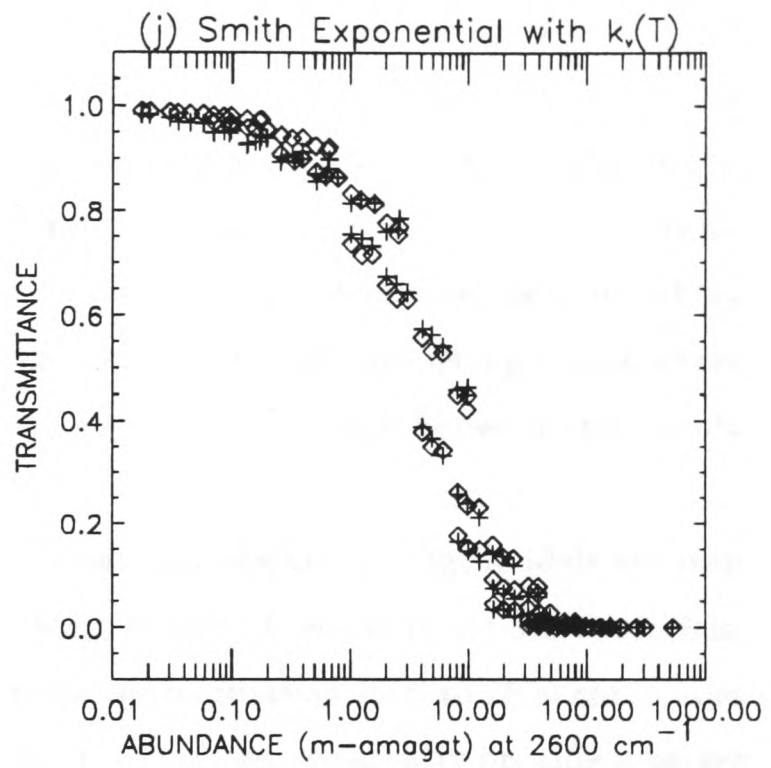

sequence have thus provided progressively better fits to the self-broadened CH_4 spectra. All models except the last in each sequence served as a means of obtaining the optimum initial values for parameters to be fitted by the next model. The following discussion of the fit results therefore deals with five fits, those obtained with the Goody-Voigt, Malkmus-Voigt, Gibson-Pierluissi, and Smith exponential models (all with $k_\nu(T)$), as well as the Zachor-King model, as this provided a fit comparable to that of the Gibson-Pierluissi model.

7.2.2.2 Comparison of the Five Best Fits

Re-examination of the plots of σ in Figure 7.2 for the five best fits reveals that the Goody-Voigt and Malkmus-Voigt band models provide closer fits to the spectra than do the Zachor-King, Gibson-Pierluissi, or Smith models. The value of σ for the Goody-Voigt and Malkmus-Voigt models lies between 0.005 and 0.02 for most of the 2000 to 9500 cm^{-1} range, the exceptions being the region of ice absorption and the sharp edges of bands which were difficult to fit

(discussed below). In these regions, σ remains ≤ 0.035 for both of these models and for the Smith model, and ≤ 0.04 for the Zachor-King and Gibson-Pierluissi models.

In Figure 7.5, the difference between σ for the Goody-Voigt model and σ for each of the other four models is plotted, a negative difference indicating that σ is smaller for the Goody-Voigt fit. The Malkmus-Voigt fit shows the greatest agreement with the Goody-Voigt fit, agreeing to within 0.005 except in the band centre at 4000–4300 cm^{-1}. In this region, σ is slightly larger for the Goody-Voigt fit, but the agreement is still within 0.01. Thus, the $1/S$ weighting and the larger number of weakly absorbing lines included in the Malkmus model offer only a small improvement over the Goody model. The similarity between the fits with the Goody-Voigt and Malkmus-Voigt models is due to the fact that they differ most in the regions of intermediate absorption. This is seen in Figure 7.4, where a comparison of (c) with (e) and (d) with (f) shows that the Goody and Malkmus models provide a similar match to the measured transmittances in these extremes, and only in the region of intermediate absorption is there any detectable difference between the points fitted by the two models. However, these few points are outweighed by the larger number of points in the extremes, and therefore the overall difference between the fits with the two models is small. The same observation can be made for the other frequency intervals in the 2000 to 9500 cm^{-1} range. In fact, for the weakly absorbing windows where the points are clustered near $\overline{\tau} = 1$ and for the strongly absorbing bands where the points are clustered near $\overline{\tau} = 0$, there should be even less difference between the Goody and Malkmus band models.

Returning to Figure 7.5, the fits with the Goody-Voigt and Malkmus-Voigt models are seen to be consistently better than those with the Zachor-King, Gibson-Pierluissi, and Smith models, particularly for the CH_4 bands. Only in the region from approximately 2000 to 2500 cm^{-1}, and for some isolated points at other frequencies, do these three models apparently provide a better fit. The region from 2000 to 2500 cm^{-1} includes the ν_2 band of CH_3D (see §6.2.7). Because this band has a regular PQR structure, seen in the spectra at the original resolution, the assumption of random line spacing made by the Goody and Malkmus models is inappropriate in this region. It is therefore understandable that both of these random band models provide a poorer fit to the spectra in this region than do the empirical models. Furthermore, contamination by CO_2 in this region may also be contributing to the poorer fit. Similarly, the isolated points where σ is better for the empirical models ($\sim$3200, 4600, and 7700 cm^{-1}) are points at the edges of absorption bands where the transmittance drops sharply. Therefore, the assumption of statistically similar intervals on either side of the fitted interval, implicit in the derivation of the random band models, is no longer valid.

Despite the differences in σ from fit to fit, the regions where σ is largest (see Figure 7.2 d, f, g, h, and j) are the same for all five models. Several points near 3000 cm^{-1} are poorly fitted due to contamination by pump oil and the presence of the sharp, strongly absorbing Q branch of the ν_3 band of CH_4. The larger values of σ at $\sim$3200, 6300, 7700, and 9100 cm^{-1},

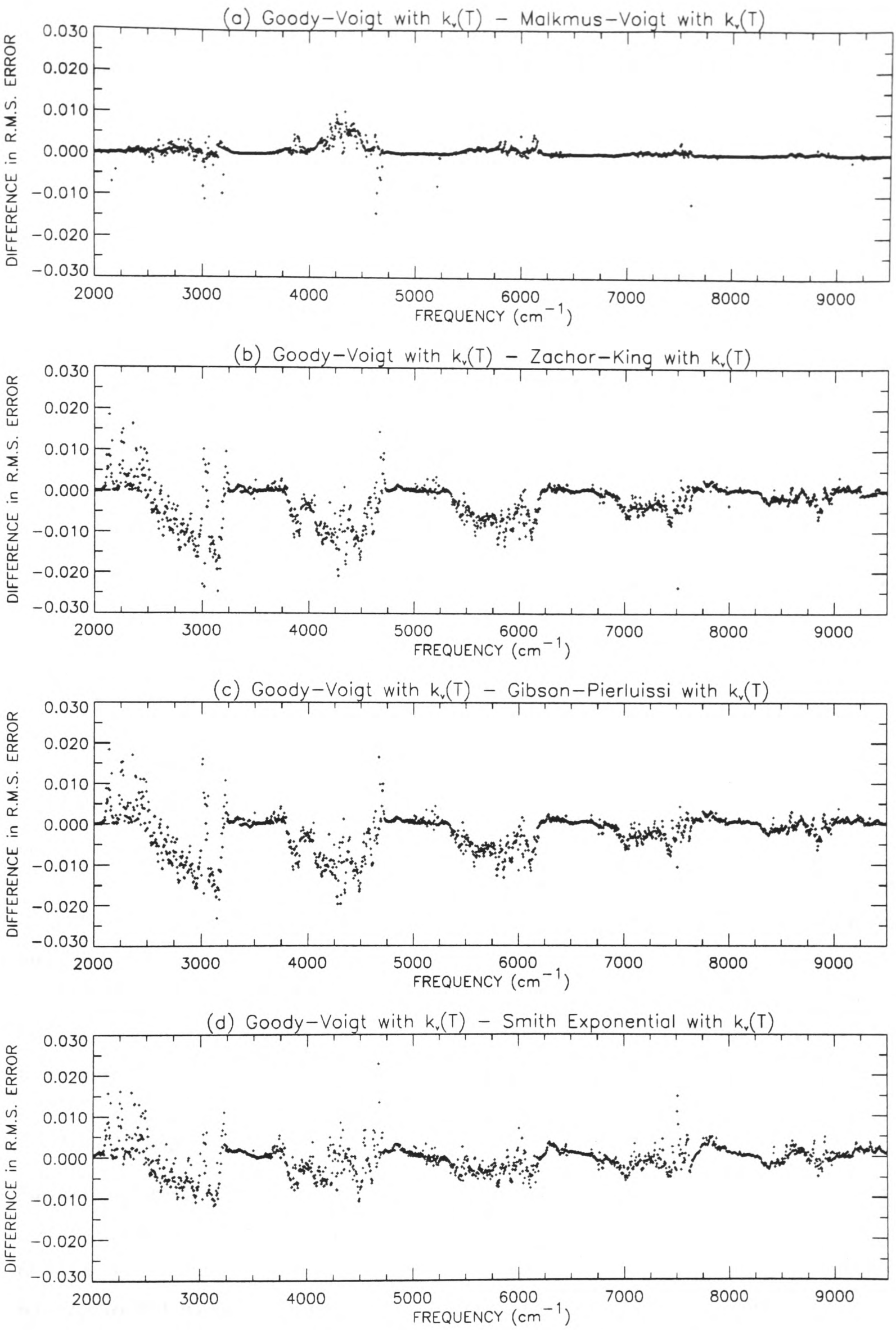

Figure 7.5: The difference between the r.m.s. residual error (σ) for the Goody-Voigt fit and σ for the four other best fits to the self-broadened CH_4 spectra.

which occur at the high frequency edges of strongly absorbing CH_4 bands suggested that the models had difficulty in fitting the sharp change in absorption in these regions. An attempt was made to improve the fits by adding a far-wing continuum term to both the Goody-Voigt and Malkmus-Voigt models, in the form of

$$\overline{\tau} = \exp\left[-C_1 U \left(\frac{P}{P_0}\right)\left(\frac{T}{T_0}\right)^{C_2}\right] \tag{7.4}$$

where C_1 and C_2 are two additional parameters. Such a term might have compensated for the different statistical properties of adjacent fitting intervals in the band edges. However, the resulting fits showed a negligible overall improvement in σ, the only significant reduction (≤ 0.02) being in the suspect 3000 cm^{-1} region and for some points between 2000 and 3000 cm^{-1} — elsewhere, the reduction in σ was generally much less than 0.005.

The similarity between the plots of σ versus frequency for all five models in the regions of maximum σ suggests that errors in the measured transmittances are largely responsible for the larger values of σ. This r.m.s. residual error only provides a measure of the agreement between the fitted and measured transmittances. If the spectra were known to be free of errors, σ would represent the uncertainty in the fit, whereas, if the fit were assumed to be correct, σ would represent the standard deviation in the original data. In this case, σ combines both the measurement errors of the data and the goodness of the fits. As was summarised in Table 6.7, the original spectra were subject to a variety of errors, of which the sloping ratios and the ice ripple had the largest overall effect. With an upper r.m.s. error estimate of 0.020 for the former (Table 6.2) and an r.m.s. error estimate of 0.013 (Table 6.5) for the latter, for the self-broadened CH_4 spectra, these measurement errors account for a significant fraction of the r.m.s. residual error in the fits.

A listing of the parameters fitted to the self-broadened CH_4 spectra using the Goody-Voigt model with $k_\nu(T)$ can be found in Appendix B. As discussed above, the Goody-Voigt and Malkmus-Voigt band models provide the best fits to these spectra, while showing close agreement with each other. As will be shown in §7.3.2 below, the Goody-Voigt model provides the best fit to the H_2-broadened CH_4 spectra. Therefore, the Goody-Voigt parameters have been chosen for inclusion in the Appendices for both the self- and H_2-broadened CH_4 fits.

7.2.2.3 Comparison of the Fits with the Original Spectra

Further insight into the deviation between the fitted models and the original spectra is gained by overplotting the fitted transmittance for a particular model on a measured spectrum, and also plotting the difference between the two. This was carried out for all 108 of the quartz-halogen self-broadened CH_4 spectra, using the fit with Goody-Voigt model. Three such plots are presented in Figures 7.6, 7.7, and 7.8. Because these plots are of quartz-halogen spectra, they include the Goody-Voigt fit over the entire 2000 to 11000 cm^{-1} quartz-halogen spectral range, showing the poor quality of the measured transmittance and therefore of the band-model fit

below 2500 cm^{-1} (for which the fits to the globar spectra were adopted) and above 9500 cm^{-1}.

The first plot, Figure 7.6, was chosen to illustrate the fit to a weakly absorbing spectrum which is badly affected by the broad ice ripple. This plot demonstrates how the ice ripple is eliminated by the band model. In the window regions where there is clearly no absorption, the transmittance has been corrected to 1, despite the deviation from 1 seen in the original spectrum. In these regions, the difference between the fitted and measured transmittance (hereafter, $\Delta\overline{\tau}$) is obviously due to the errors in the latter. Being subject to the ice ripple, spectrum QH12_296K also provides an example of strong ice absorption over 3000–3500 cm^{-1}. Here, the Goody-Voigt model has difficulty in fitting the ice absorption, resulting in a sharp increase in $\Delta\overline{\tau}$, and giving a physical explanation for the large values of σ found in this region. Elsewhere in the spectrum, $\Delta\overline{\tau}$ would be zero in the non-absorbing windows if the ice ripple were not present, but is non-zero in the bands, being as large as 0.04 for some points. Although $\Delta\overline{\tau}$ is positive in these regions (ignoring the effect of ice ripple), thereby indicating that the fitted absorptions are weaker than those measured, this is not true of all the spectra. In some cases, the fit is more strongly absorbing, in some cases, it is less so. The values of $\Delta\overline{\tau}$ obtained in the bands are the best achievable by a least squares fit that is minimising $(\Delta\overline{\tau})^2$ for 108 different points.

The second plot, Figure 7.7, was chosen to demonstrate the fit to a strongly absorbing spectrum. In this case, spectrum QH36_190K, which was corrected by scaling to match the globar transmittance (see §6.2.2), is badly affected by a sloping ratio, and possibly also by the ice ripple. As a result, the windows at approximately 4900, 6400, 7800, 9300, and 10700 cm^{-1} all have anomalously high measured transmittances. For three of these bands, the apparent "transmittance" is greater than 1, however, the fitting procedure ignores any "transmittances" which are ≤ 0 or > 1. Using the transmittances from the other measured spectra, the band-model fit has reduced the transmittances in these windows to values consistent with the other spectra. The large values of $\Delta\overline{\tau}$ in these regions are thus due to errors in the measured spectrum. This plot also shows how the 80 cm^{-1} channelling is effectively eliminated in the fitted band model. This is also seen in Figure 7.6, but the amplitude of the channelling is larger in spectrum QH36_190K, making the effect more obvious. The 80 cm^{-1} channelling present in the measured spectrum is completely absent in the fitted spectrum, and therefore appears as a sinusoidal ripple in $\Delta\overline{\tau}$. The plot of $\Delta\overline{\tau}$ for this strongly absorbing spectrum is effectively the complement of that for the weakly absorbing spectrum. In this case, the CH_4 bands are saturated and $\Delta\overline{\tau}$ is zero (aside from the sinusoidal ripple) in these regions. However, weak absorptions are present in the windows, and it is in these regions that $\Delta\overline{\tau}$ is non-zero. $\Delta\overline{\tau}$ is largest at the high frequency edges of the bands and it is similarly large values in the fits to other strongly absorbing spectra which result in σ for the entire fit being a maximum in these regions.

The third plot in this series, Figure 7.8, has been chosen to demonstrate the fit to a reasonably error-free spectrum of intermediate absorption. Spectrum QH23_240K is essentially

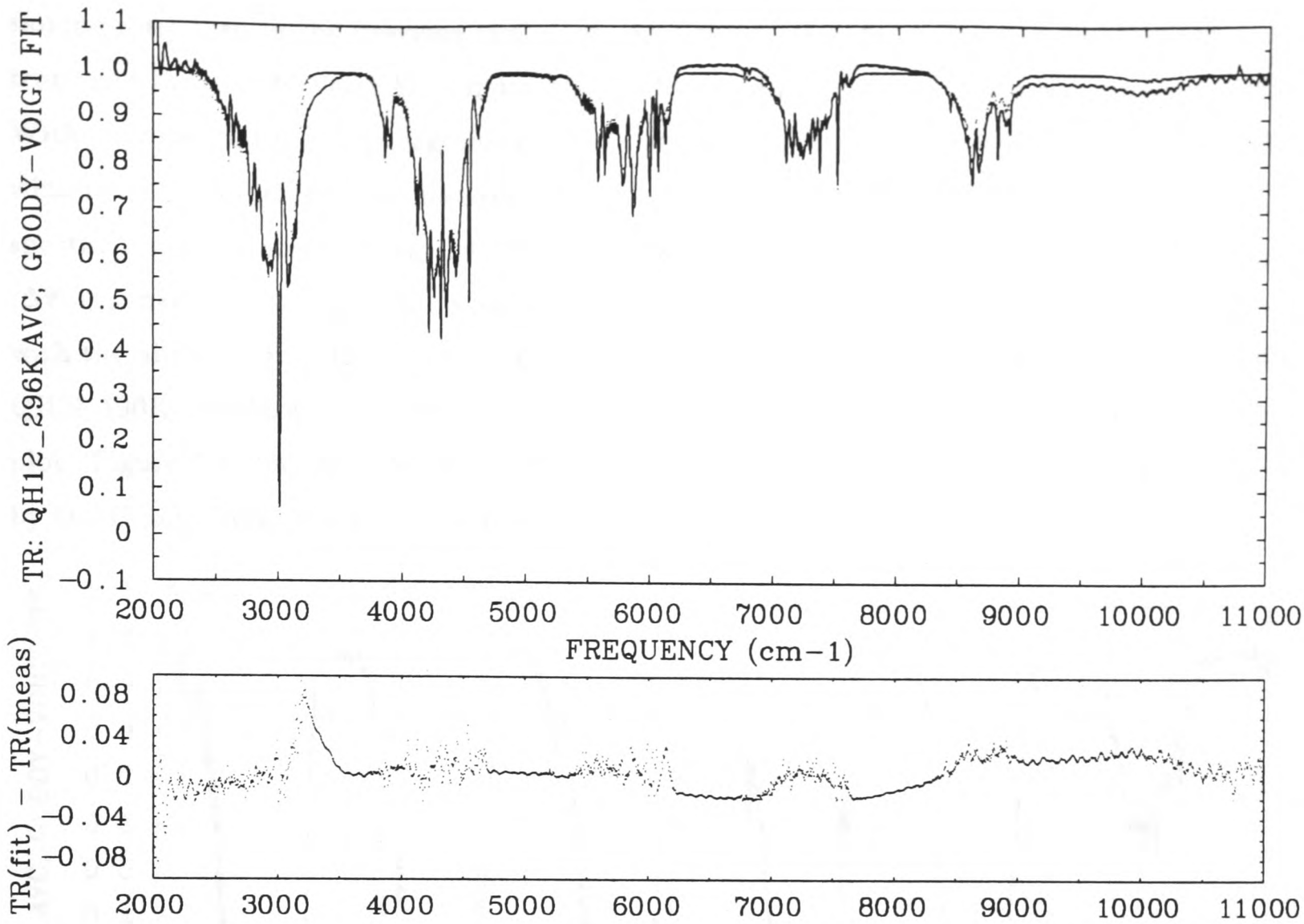

Figure 7.6: (a) Measured spectrum QH12_296K (—) and the Goody-Voigt fit to this spectrum (···). (b) The difference between these two spectra.

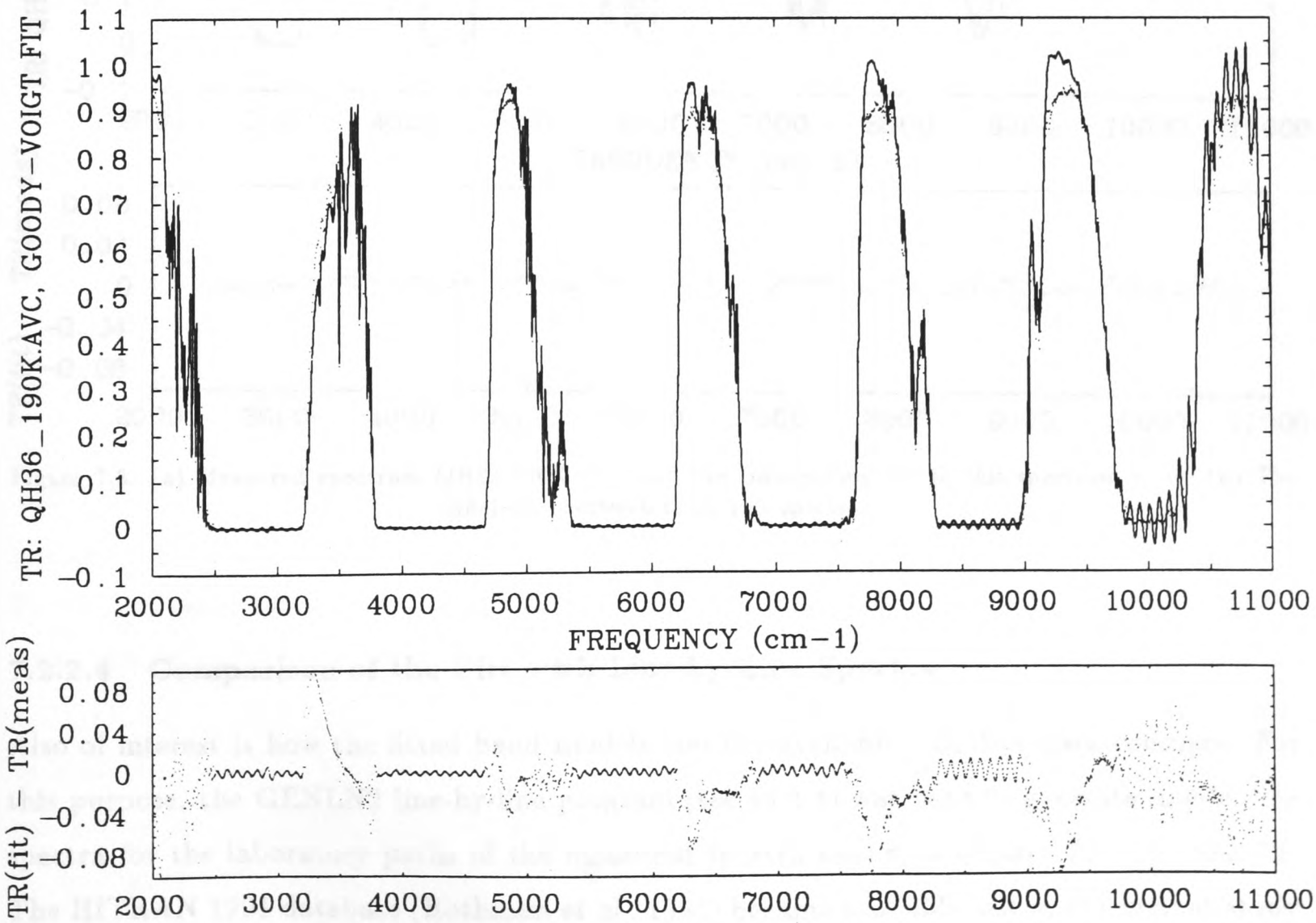

Figure 7.7: (a) Measured spectrum QH36_190K (—) and the Goody-Voigt fit to this spectrum (···). (b) The difference between these two spectra.

free of the ice ripple, the 3000–3500 cm^{-1} ice absorption, the 80 cm^{-1} channelling, and the sloping ratio seen in the previous two plots. As a result, the match between the original spectrum and the Goody-Voigt fit is much better than it was for either of the two previous cases. With only two of the bands beginning to saturate and weak absorptions present in some of the windows, the model is fitting non-zero and non-unity values of transmittance over most of the spectral range. Consequently, $\Delta\bar{\tau}$ is predominantly non-zero across the spectrum. However, $|\Delta\bar{\tau}|$ is generally less than 0.02, while varying positively and negatively about zero. In addition, with the absorption in the bands being weaker and the edges less sharp than was the case for QH36_190K, the large increases in $\Delta\bar{\tau}$ at the band edges seen in that case are absent in this plot. Figure 7.8 thus provides an example of a spectrum which is reasonably well-reproduced by the Goody-Voigt band-model fit.

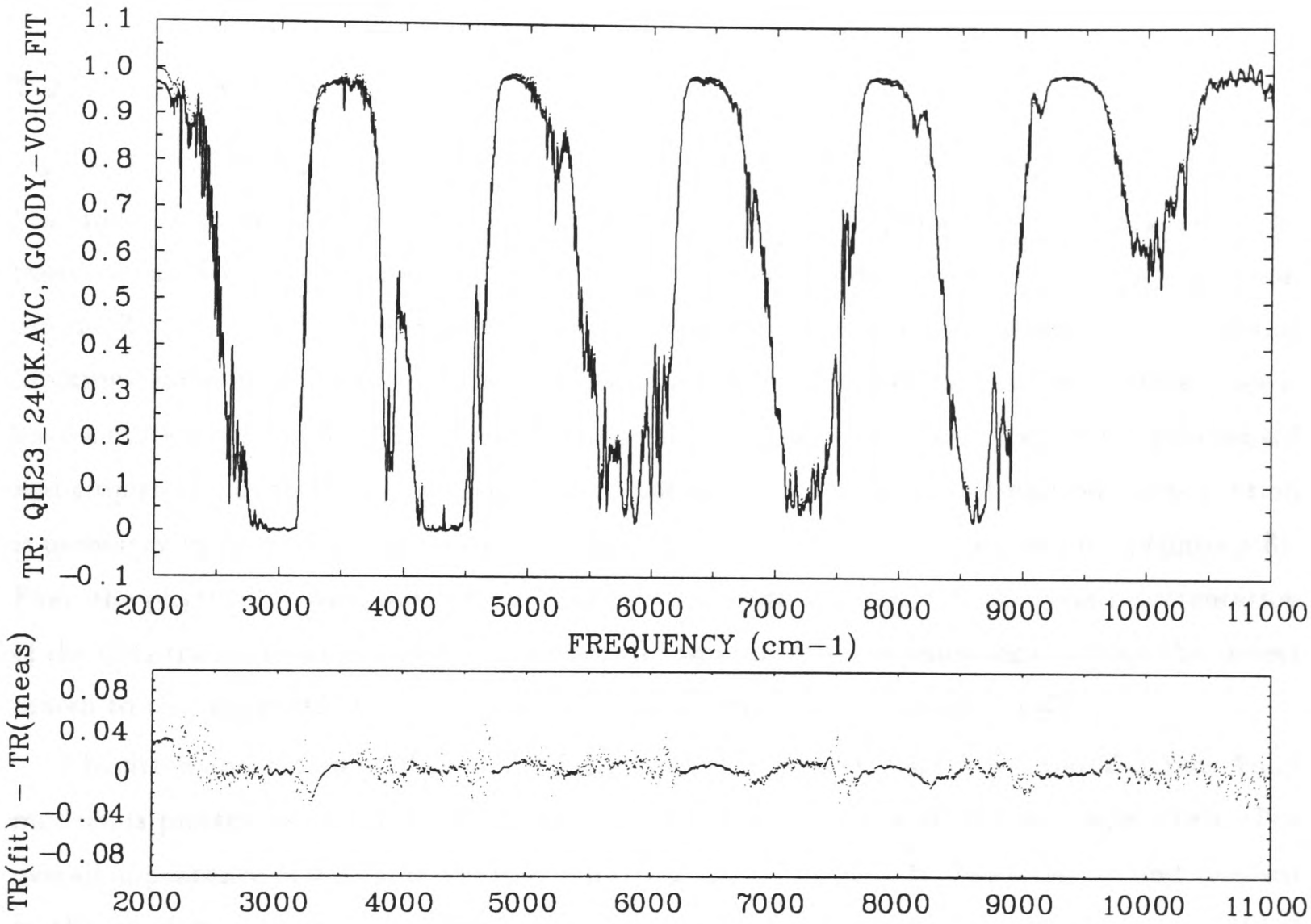

Figure 7.8: (a) Measured spectrum QH23_240K (—) and the Goody-Voigt fit to this spectrum (···). (b) The difference between these two spectra.

7.2.2.4 Comparison of the Fits with Line-by-Line Spectra

Also of interest is how the fitted band models and the available CH_4 line data compare. For this purpose, the GENLN2 line-by-line program (see §3.3.4) was used to generate line-by-line spectra for the laboratory paths of the measured spectra shown in Figures 7.6, 7.7, and 7.8. The HITRAN 1991 database (Rothman *et al.*, 1991) became available just as the present study was being completed and so it was used in these calculations. In Figure 7.9, the three line-by-

line spectra are superimposed on spectra calculated for the same conditions using the fit with the Goody-Voigt model. In these plots, the GENLN2 absorptions are consistently weaker than those of the Goody-Voigt model, most probably due to missing line data, as the Goody-Voigt fit has already been shown to reproduce the three measured CH_4 spectra reasonably well. The line-by-line and band model spectra show the best agreement (within 0.05, 0.15, and 0.10 in transmittance for plots (a), (b), and (c), respectively) in the region below 3255 cm^{-1}, where the greatest number of CH_4 lines in the HITRAN database are found. As expected, poorer agreement is obtained in the 4300 and 5800 cm^{-1} bands, where the CH_4 line data is known to be inadequate (see §3.3.3). Finally, Figure 7.9 clearly reveals the lack of line data for CH_4 in the weakly absorbing 3200–3700 and 4700–5500 cm^{-1} regions, where there are obviously CH_4 absorptions which will be important at Jovian abundances, but no available line parameters, even on the most recently compiled database.

7.2.3 The Fitted Parameters

Figures 7.10 and 7.11 show the parameters that were obtained by fitting the Goody-Voigt and Malkmus-Voigt models, respectively, to the self-broadened CH_4 spectra. The parameters for these two models have been chosen because these models provided better fits to the spectra than did the Zachor-King, Gibson-Pierluissi, or Smith models. Furthermore, because the Goody and Malkmus random band models are physically based, the parameters fitted with these models have a more meaningful physical interpretation than do the parameters fitted by the generalised and empirical models. However, even when a parameter has a physical definition, some caution is necessary in its interpretation, since in practice, it is simply a variable used to optimise a fit. Even the physically based models are unlikely to provide a completely accurate representation of the CH_4 transmittance, and to compensate for this fact while attempting to obtain the closest match to the measured transmittances, the parameters may vary unphysically.

The fitted absorption coefficient, $k_\nu(T_0)$, obtained with the Goody-Voigt and Malkmus-Voigt models, is plotted as a function of frequency in Figures 7.10(a) and 7.11(a), respectively. The overall appearance of $k_\nu(T_0)$ is as expected, being largest in the CH_4 band centres and smallest in the window regions. For the Goody-Voigt model, $k_\nu(T_0)$ varies between 0.0032×10^{-24} and 1400×10^{-24} $(\text{molec/cm}^2)^{-1}$, corresponding to 8.3×10^{-6} to 3.8 $(\text{m-amagat})^{-1}$. For the Malkmus-Voigt model, $k_\nu(T_0)$ ranges up to 1700×10^{-24} $(\text{molec/cm}^2)^{-1}$, or 4.6 $(\text{m-amagat})^{-1}$. In the following section, these results are compared with others that have reported in the literature. A plot of the difference in $k_\nu(T_0)$ between the two models (not shown) reveals that $k_\nu(T_0)$ fitted by the Goody-Voigt model is generally smaller, by as much as 70% in the 2500 to 3000 cm^{-1} region. This is due to the fact that $k_\nu(T_0)$ is not strictly the same for these two models, as seen from the equations in Table 7.1.

In Figures 7.10(b) and 7.11(b), the fitted lower state energy, E_l, is plotted. This parameter is seen to have a jagged appearance on a finer scale than the band structure, probably indicative

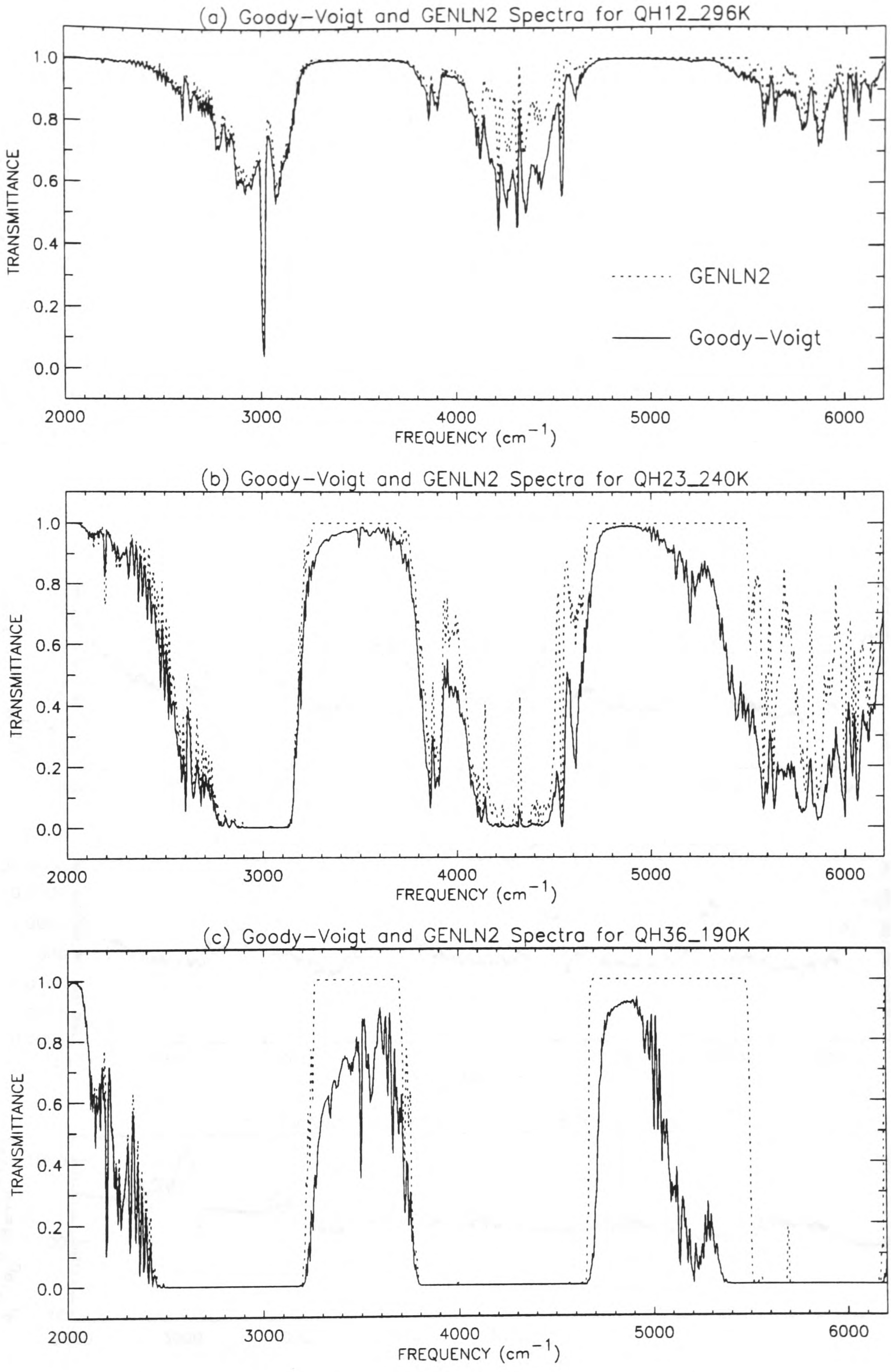

Figure 7.9: Synthetic spectra generated for three laboratory paths, using both the Goody-Voigt model (fitted to the self-broadened CH_4 spectra), and the GENLN2 line-by-line program with CH_4 line data from the HITRAN 1991 database. (See Appendix A for details of the laboratory conditions.)

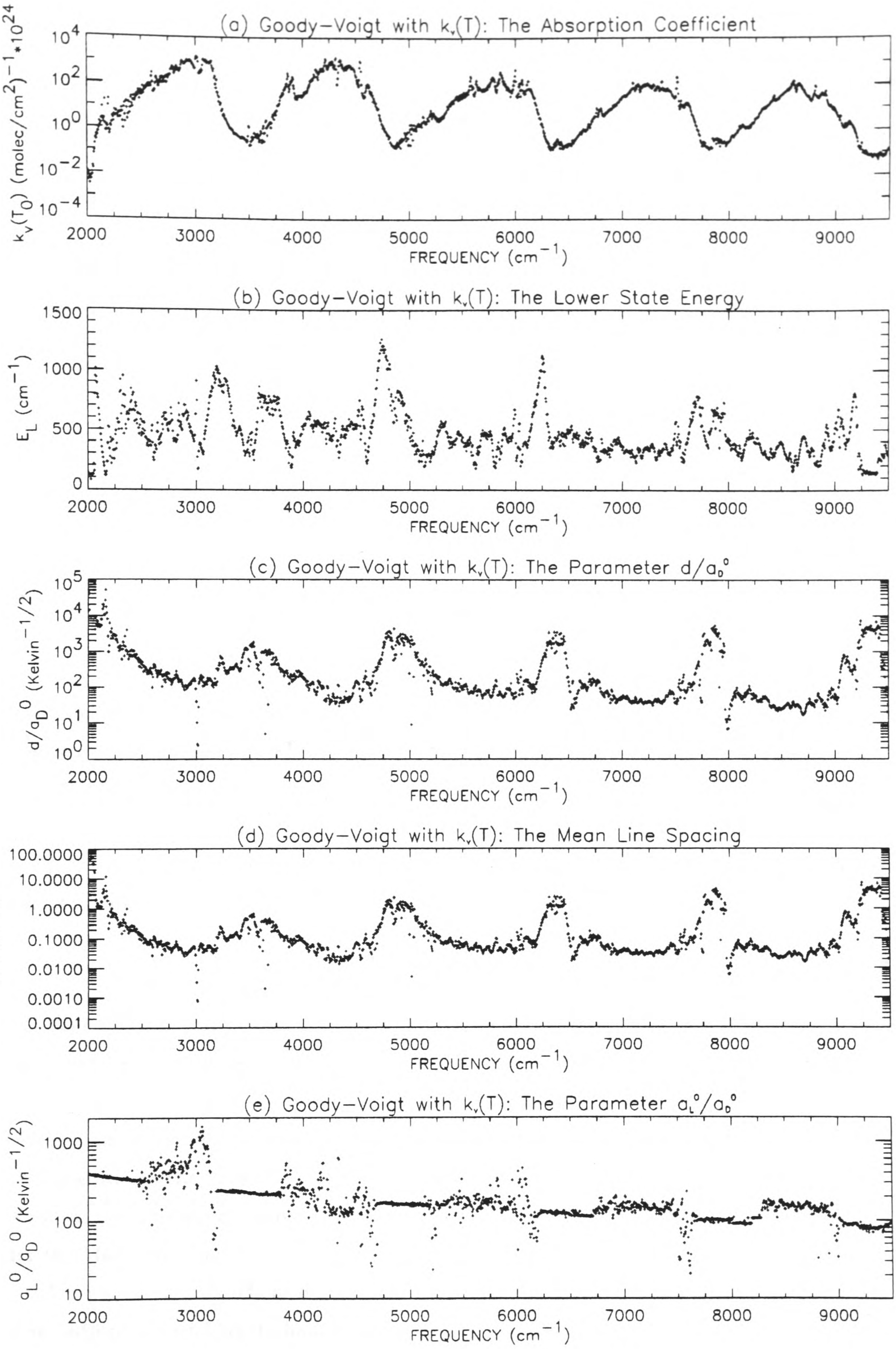

Figure 7.10: The parameters fitted to the self-broadened CH_4 spectra using the Goody-Voigt model with $k_\nu(T)$ (continued on following page).

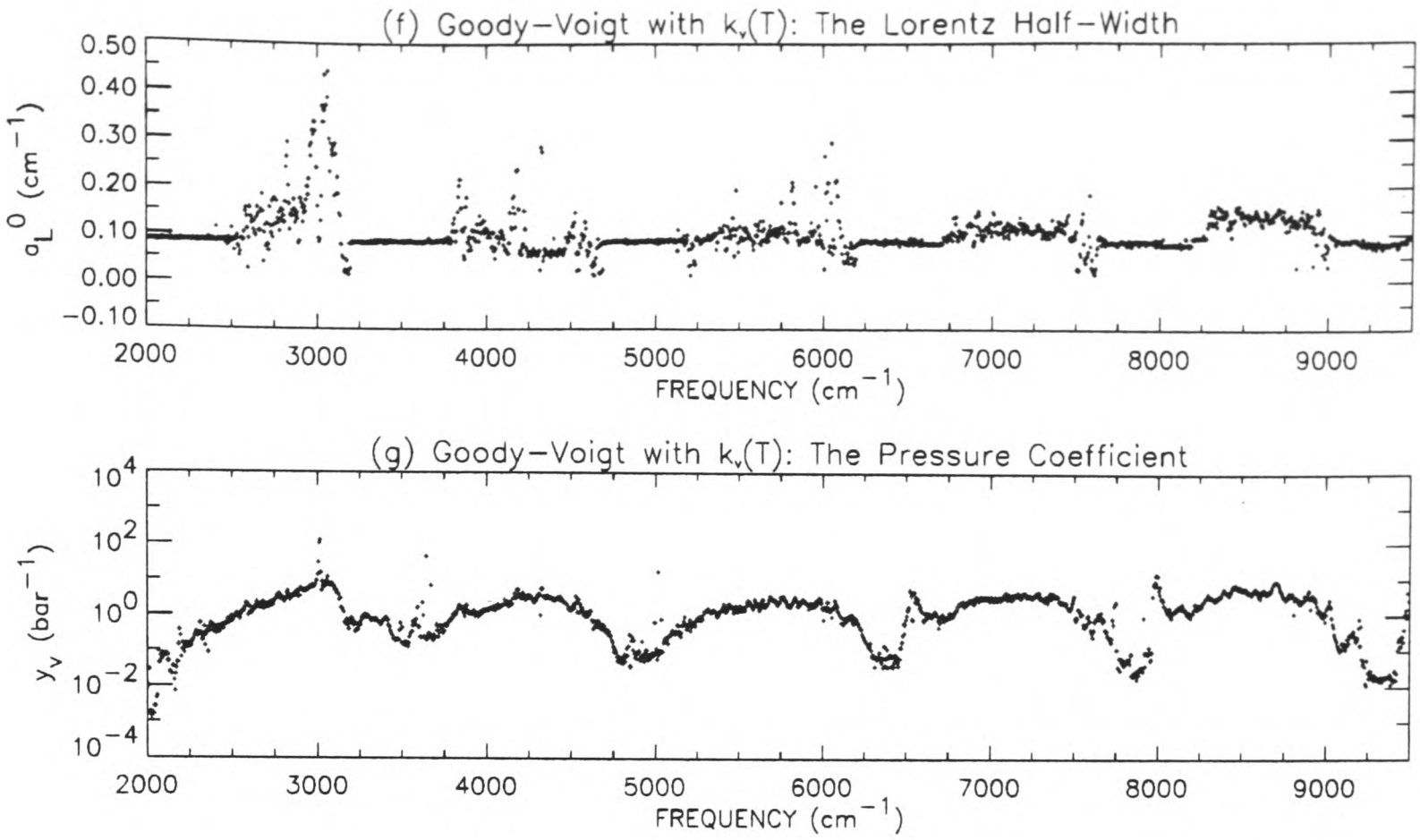

of the differing temperature dependence of J lines within the bands. The values obtained for E_l with the Goody-Voigt and Malkmus-Voigt models are similar, being scattered mostly within $\pm 10\%$ of the Goody-Voigt values. These values vary between 80 and 1260 cm^{-1} for the Goody-Voigt model and between 83 and 1280 cm^{-1} for the Malkmus-Voigt model. These are physically reasonable values, as the HITRAN 1991 database (Rothman *et al.*, 1991) lists values between 10 and 2200 cm^{-1} for CH_4.

The next parameter to be plotted is δ/α_D^0, shown Figures 7.10(c) and 7.11(c). The values of δ/α_D^0 are significantly smaller for the Goody-Voigt fit than for the Malkmus-Voigt fit, implying that δ is also smaller for the Goody-Voigt fit. Knowing

$$\alpha_D^0 = \frac{\alpha_D}{\sqrt{T}} = 4.301 \times 10^{-7} \frac{\nu_0}{\sqrt{m}}, \tag{7.5}$$

α_D^0, and hence δ, can be calculated for each frequency interval. The results of this calculation are presented in Figures 7.10(d) and 7.11(d). In the simpler Goody model, which includes a finite number of lines, δ represents the mean line spacing, whereas in the Malkmus model, which includes an infinite number of lines, δ is an arbitrary parameter with no simple physical interpretation. The values of δ vary between approximately 0.01 and 5.0 cm^{-1} for the Goody-Voigt fit, decreasing in the band centres, and vary between approximately 0.03 and 10.0 cm^{-1} for the Malkmus-Voigt fit.

The parameter α_L^0/α_D^0, as fitted by the two models, is plotted in Figures 7.10(e) and 7.11(e). The self-broadened Lorentz half-width, α_L^0, (at $T_0 = 296$ K, $P_0 = 1.01325$ bar) was calculated from this parameter using the known values of α_D^0. The resulting values of α_L^0 are shown in Figures 7.10(f) and 7.11(f). In the window regions, α_L^0 varies little from its initial value of 0.085 cm^{-1} for both models. However, in the bands, α_L^0 varies between 0.013 and 0.50 cm^{-1}

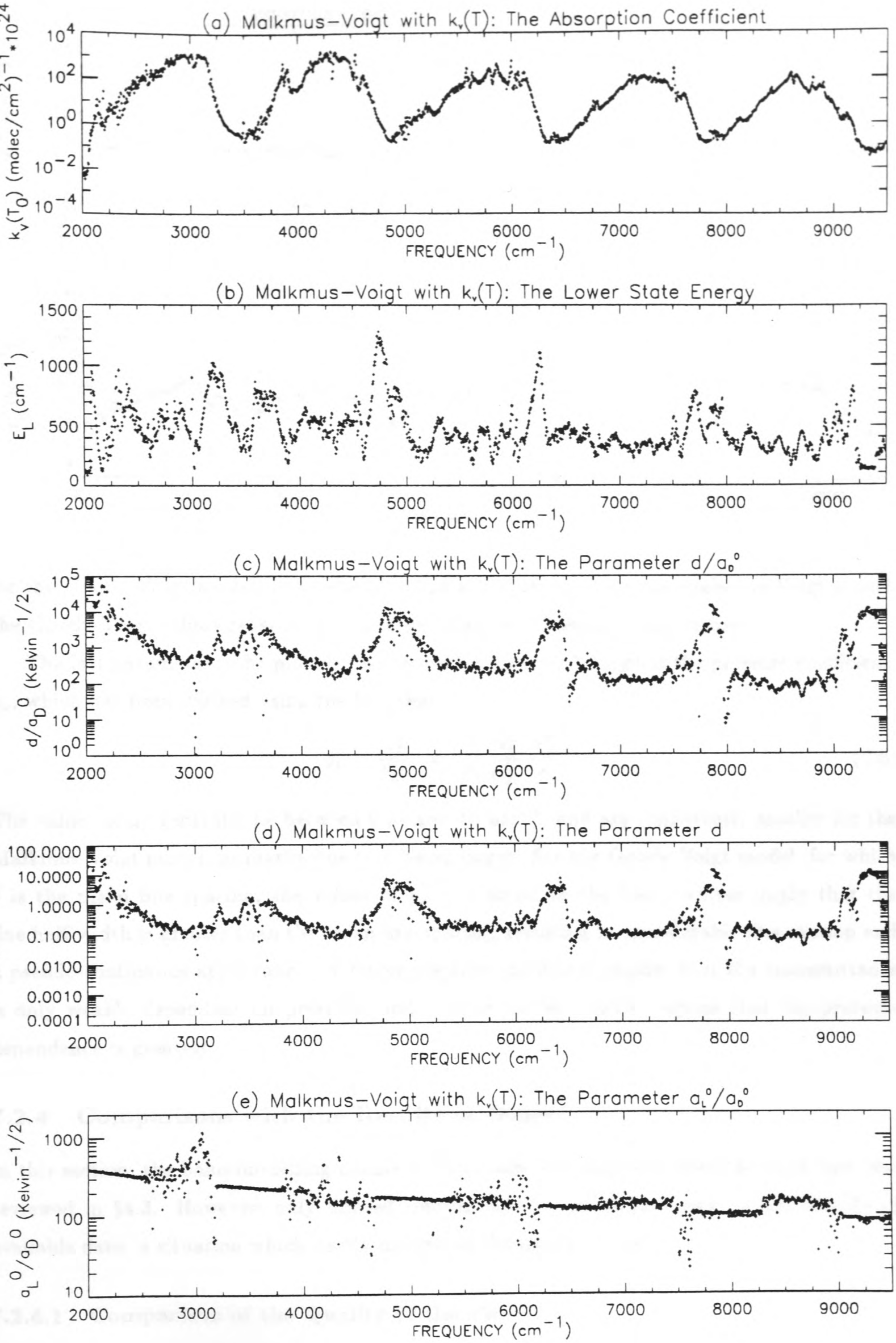

Figure 7.11: The parameters fitted to the self-broadened CH_4 spectra using the Malkmus-Voigt model with $k_\nu(T)$ (continued on following page).

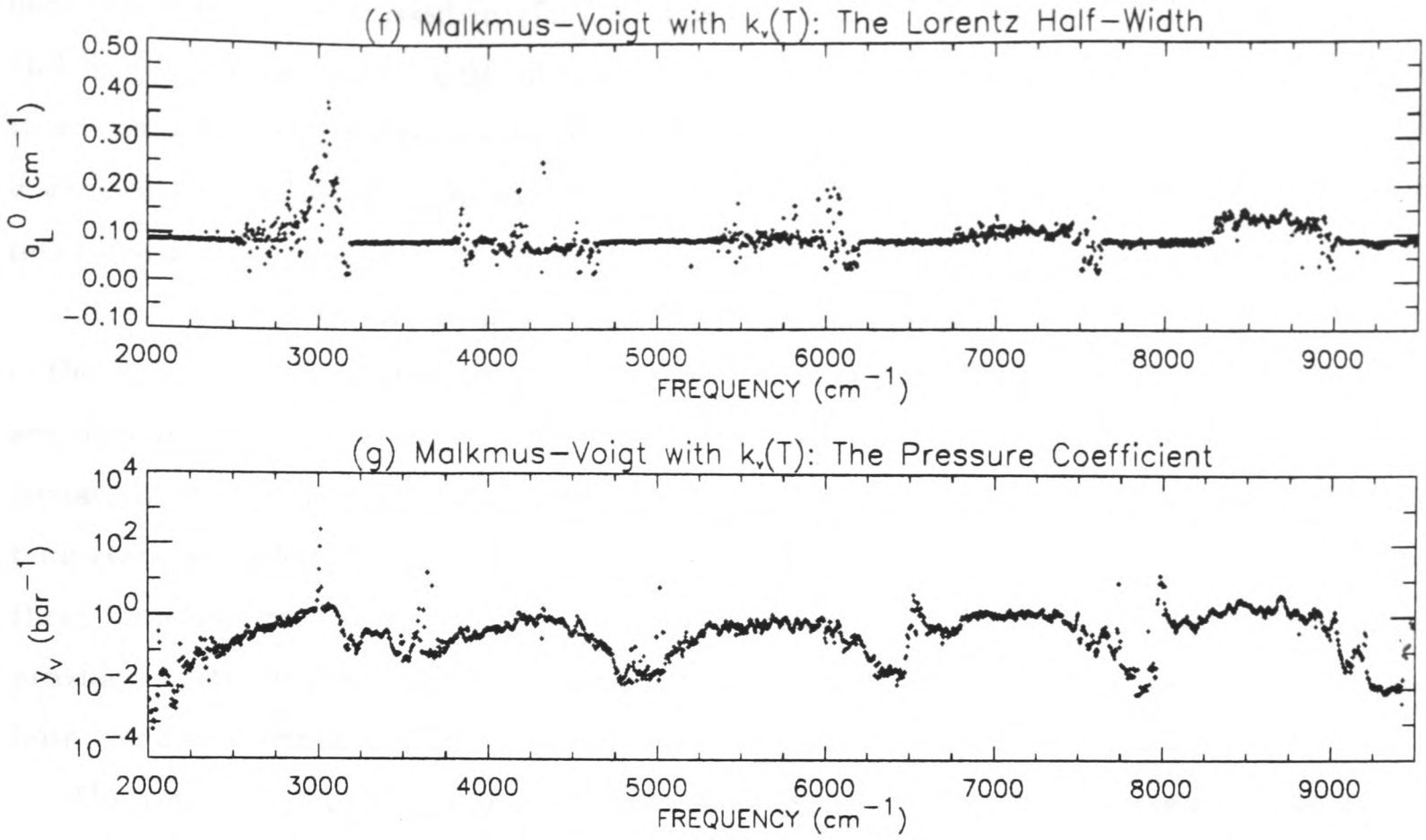

for the Goody-Voigt model, and between 0.016 and 0.38 cm^{-1} for the Malkmus-Voigt model, the Goody-Voigt values generally being larger than the Malkmus-Voigt values.

The last parameter to be plotted, in Figures 7.10(g) and 7.11(g), is the pressure coefficient, y_ν, which has been derived using the fact that

$$y_\nu = \frac{\alpha_L^0}{P_0 \delta} = \frac{1}{P_0} \frac{\alpha_L^0}{\alpha_D^0} \frac{\alpha_D^0}{\delta}. \tag{7.6}$$

The values of y_ν generally lie between 0.01 and 10 bar^{-1}, and are consistently smaller for the Malkmus-Voigt model, primarily due to δ being larger. For the Goody-Voigt model, for which δ is the mean line spacing, the values of $y_\nu > 1$ found in the band centres imply that the line half-width is greater than the mean line spacing, resulting in considerable line overlap and a pseudo-continuous appearance. A larger pressure coefficient implies that the transmittance is only weakly dependent on pressure, and so it is in the window regions that the pressure dependence is greatest.

7.2.4 Comparisons with the Results of Others

In this section, the band-modelling results of this study are compared with the work that was reviewed in §4.3. However, only limited comparisons are possible, owing to the scarcity of available data, a situation which partly motivated the present study.

7.2.4.1 Comparison of the Quality of the Fits

For the work reviewed in §4.3, assessment of the quality of band-model fits to experimental CH_4 data, if provided at all, is often inconsistent from one work to another. In the present study, the overall quality is expressed in terms of the r.m.s. residual error for every frequency

interval fitted. As discussed in §7.2.2.2, σ is $\leq$ 0.035 for the Goody-Voigt, Malkmus-Voigt, and Smith models, and $\leq$ 0.04 for the Zachor-King and Gibson-Pierluissi models. However, these maxima are in the region of ice absorption and at the sharp edges of bands. Elsewhere, σ generally lies between 0.005 and 0.02, considered acceptable, given the uncertainties in the measured transmittances.

Only Calcutt (1984) and Calcutt *et al.* (1988) provide a similar interval-by-interval estimate of the deviation between the fitted and measured transmittances. The results of Calcutt (1984) are only indirectly relevant, as they are expressed as the mean deviation rather the r.m.s. deviation, for fits in wavelength rather than frequency space, and for individual fits at three temperatures rather than a single fit (which includes temperature dependence) to data at all three temperatures. However, as in the present study, the Goody-Voigt model was found to provide a better fit than the Goody-Lorentz model, while unlike the results of the present study, both the Zachor-King and Smith models provided better fits than the Goody-Voigt model.

The results of Calcutt *et al.* (1988) are directly comparable to the results of the current work, as Calcutt *et al.* calculated the r.m.s. error for spectra fitted at 5 cm^{-1} intervals using the temperature-dependent Goody-Voigt model. In order to allow direct comparison of σ between the Goody-Voigt fit of the present study and that of Calcutt *et al.* (1988), σ for both fits has been plotted in Figure 7.12. For the Goody-Voigt fit of Calcutt *et al.*, σ is generally $\leq$ 0.01 (except in the region of quartz absorption at 4500 cm^{-1}), suggesting that it provided a better fit than does the Goody-Voigt fit of the present work. However, σ for the latter fit is comparable to that of Calcutt *et al.* for the three bands common to both spectra (at 5800, 7200, and 8600 cm^{-1}). Furthermore, the spectra fitted by Calcutt *et al.* covered a smaller range of temperatures, pressures, CH_4 abundances, and frequencies, a range of conditions which resulted in insufficient absorption in the windows to allow any band-model fitting in those regions. As a result, not only could the 100% transmittance level be more accurately corrected prior to fitting, but the models also did not have to account for the sharp increases in absorption at the edges of bands. Thus, for example, the poorly fitted 6200–6500 and 7600–7900 cm^{-1} regions of the present study were not fitted by Calcutt *et al.*. The apparently poorer results for σ obtained in the present work can therefore be attributed to the greater range of laboratory conditions achieved, as these resulted in greater experimental difficulties, more frequency intervals to be fitted, and a greater range of transmittances to be fitted at some frequencies.

Of the various other near-infrared CH_4 band-modelling studies discussed in §4.3.2, only a few include brief discussions of the fit quality. Cruikshank and Silvaggio (1979), who fitted the 273 K CH_4 spectra of Silvaggio (1977) at 100 cm^{-1} intervals from 4000 to 4800 cm^{-1} using the Goody-Voigt band model, estimated the goodness of their fit with a reduced χ^2 test, replacing N in Equation 7.1 with $N - 3$. Their final error estimate was equivalent to $\sigma \leq 0.002$ in transmittance. This deviation is significantly better than the values obtained in the present study, and is attributed to three factors. The first is the fact that spectra of Silvaggio (1977)

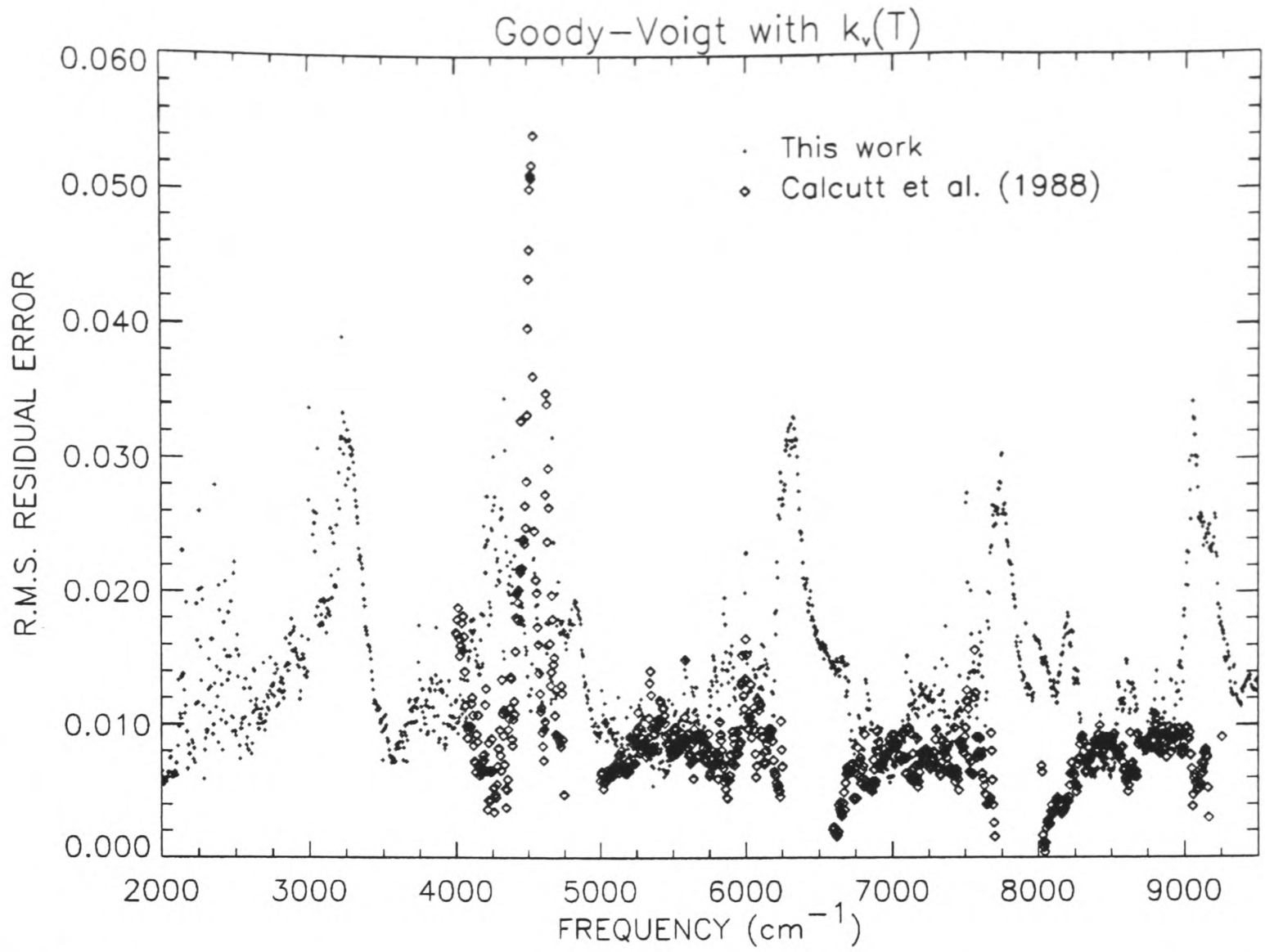

Figure 7.12: The r.m.s. residual error for the Goody-Voigt model with $k_\nu(T)$, as fitted to self-broadened CH_4 spectra in the present study and by Calcutt *et al.* (1988).

were recorded over a smaller range of laboratory conditions, with a single temperature, pressures of only 0.0013 to 0.13 bar, and pathlengths of 3.31 to 36.75 m, therefore a resulting in a smaller range of transmittances to be fitted at each frequency. The second factor, related to the first, is that the spectra were fitted at one temperature with no temperature dependence necessary in the model. The third factor is the larger fitting interval, which may smooth out fluctuations and by increasing the number of lines in an interval may give a better approximation of the statistical distribution assumed by the Goody band model. However, similar values of 0 to 0.003 for $\Delta\bar{\tau}$ in the 10 cm^{-1} interval centred on 4305 cm^{-1} were obtained by Silvaggio (1982, p.592) using the same 273 K CH_4 spectra and again fitting the Goody-Voigt model. In contrast, a value of $\sigma = 0.022$ was obtained for 4305 cm^{-1} using the Goody-Voigt model in this present work. Unfortunately, Silvaggio only presented values of $\bar{\tau}_{measured}$ and $\bar{\tau}_{fitted}$ for this single frequency interval, so no further comparison with his 10 cm^{-1} fits was possible.

A full quantitative assessment of the near-infrared band-model analysis of CH_4 performed by Giver *et al.* (1984, 1988) is also lacking. In this extensive study, the CH_4 spectra were fitted with the Malkmus-Voigt band model at three individual temperatures. The only published data providing any indication of the quality of the fits is a list of the measured and fitted transmittances for the 10 cm^{-1} interval centred on 4650 cm^{-1}, given by Giver *et al.* (1990). Using these values, it was possible to calculate the r.m.s. residual error for the fit at each

temperature, yielding 0.016, 0.015, and 0.008, for the 295, 188, and 112 K fits, respectively. For comparison, the Malkmus-Voigt fit to all three temperatures performed in the present study yielded a value of 0.014 for σ at 4650 cm^{-1}. The similarity of these results thus provides some confidence in the fits of the present study. The larger values of σ obtained by Giver *et al.* (1990) compared to Cruikshank and Silvaggio (1979) above may also be due to the greater range of pressures (0.0020–12.4 bar), pathlengths (3–61 m) and CH_4 abundances (0.0149–192.8 m-amagat) fitted by his model, particularly as the smallest value, 0.008, was obtained for the 112 K spectra for which the pressure was limited to 0.538 bar.

In the visible band-modelling studies of CH_4 described in §4.3.1, the quality of the fits is usually characterised by an error estimate for the fitted parameters rather than a comparison of the fitted and measured transmittances. Thus, Fink *et al.* (1977) and Benner (1979), who used the Goody-Lorentz model, derived standard deviations for their absorption and pressure coefficients and combined these with the errors in the measured spectra, to estimate rather large uncertainties of up to 10% for k_ν and 30% for y_ν. Similar uncertainties of 4–15% for k_ν and 18–31% for y_ν were obtained by Podolak and Giver (1979), for three intervals fitted with the Goody-Lorentz model. If these uncertainties in k_ν and y_ν are converted to uncertainties in transmittance, values of approximately 0.01 in transmittance are obtained, comparable to σ in the present work.

Overall, it appears that the quality of the band-model fits of the present study are generally similar to that of previous studies. When the calculated values of the r.m.s. residual error are greater in the former, this usually occurs in regions which are difficult to fit due to uncertainties in the measured spectra or can be attributed to the greater range of conditions fitted in this work. With the increased spectral coverage and the wider range of laboratory conditions achieved in the current work, these band-model fits represent a significant improvement on the previously available band-model fits of self-broadened CH_4.

7.2.4.2 Comparison of the Fitted Parameters

This comparison of the fitted parameters with those of other authors begins with a consideration of the results of Calcutt *et al.* (1988). In Figures 7.13 to 7.17, the parameters $k_\nu(T_0)$, E_l, δ, α_L^0, and y_ν, derived from the Goody-Voigt fit of Calcutt *et al.*, have been superimposed on plots of the same parameters derived from the Goody-Voigt fit of the present study. The first of these plots, Figure 7.13, is of the absorption coefficient. It reveals excellent agreement between the two fits in the four bands common to both. It also shows clearly how the long laboratory pathlengths and the two light sources used in the present study have led to a significant improvement in spectral coverage, adding data from 2000 to 4000 cm^{-1} and in the four weakly absorbing window regions. This new data should be valuable in the interpretation of NIMS spectra, particularly the data in the window regions, where the CH_4 absorption becomes important for the abundances found in the Jovian atmosphere.

In Figure 7.14, similarly good agreement is seen between the fitted values of the lower state energy obtained by Calcutt *et al.* and in the present study. It should be noted that the fitting technique of Calcutt *et al.* differed slightly from that of the current work in that successively more complex models were only fitted for frequencies having $\sigma > 0.01$ in the preceding model, and as a result, E_l has not been added for all of frequencies fitted by Calcutt *et al.*. In Figure 7.15, the mean line spacing is plotted, having been derived from the fitted parameter δ/α_D^0. Although δ has a similar appearance for the two fits, with closer line spacing in the band centres, δ is generally smaller in the present work. With the maximum CH_4 abundance being 527.7 m-amagat in the present study, compared to only 24 m-amagat in Calcutt *et al.*, the closer line spacing in the former fit may be needed in order to model the resulting stronger absorptions.

Figure 7.16 shows the self-broadened Lorentz half-width, as calculated from the fitted parameter α_L^0/α_D^0. In this plot, the different initialisations used for α_L^0 are obvious, a value of 0.05 cm^{-1} having been used by Calcutt *et al.*, whereas 0.085 cm^{-1} was used in the present study. In Calcutt's fit, α_L^0 remained fixed at 0.05 cm^{-1} if σ were < 0.01 in the preceding models, whereas, in the current work, α_L^0 was allowed to vary for each model. In regions where α_L^0 was fitted in both works, there is no consistent relation between the final values, again emphasising that although α_L^0 has a physical interpretation, it and indeed all of the parameters, are unlikely to be truly representative of reality. The final plot in this sequence of comparisons is Figure 7.17, illustrating the pressure coefficient, y_ν, as derived from δ/α_D^0 and α_L^0/α_D^0 for each of the two Goody-Voigt fits. Because $y_\nu = \alpha_L^0/P_0\delta$, the predominantly larger values of α_L^0 and smaller values of δ obtained in the present study (relative to those of Calcutt *et al.*) combine to make y_ν generally larger in the former. If physically interpreted, this result suggests that a larger number of lines per half-width has been fitted in the present study, consistent with the stronger absorption of the spectra, resulting in a reduced dependence on pressure. Overall, the parameters of the present work, as fitted by the Goody-Voigt band model, appear to be in reasonable agreement with those of Calcutt *et al.*. This is particularly true of $k_\nu(T_0)$ and E_l, while differences between the other parameters can be attributed to the initialisation and to the variation in the original spectra being fitted in each case.

Unfortunately, few of the other band-modelling studies described in §4.3 include values of fitted parameters which can be compared with the parameters fitted in the present study. This is particularly true of the near-infrared studies, with Apt *et al.* (1981), Benner and Fink (1980), Silvaggio (1982), and Giver *et al.* (1984, 1988) all omitting details of their parameters. Cruikshank and Silvaggio (1979) are an exception, as they list the values of k_ν, δ, and α_L^0 which they obtained by fitting 273 K CH_4 spectra with the Goody-Voigt band model. These parameters were fitted over eight 100 cm^{-1} intervals, and so for comparison, the parameters fitted with the Goody-Voigt model in the present study were averaged over the same 100 cm^{-1} intervals. The results are presented in Table 7.2. Although the agreement between the two

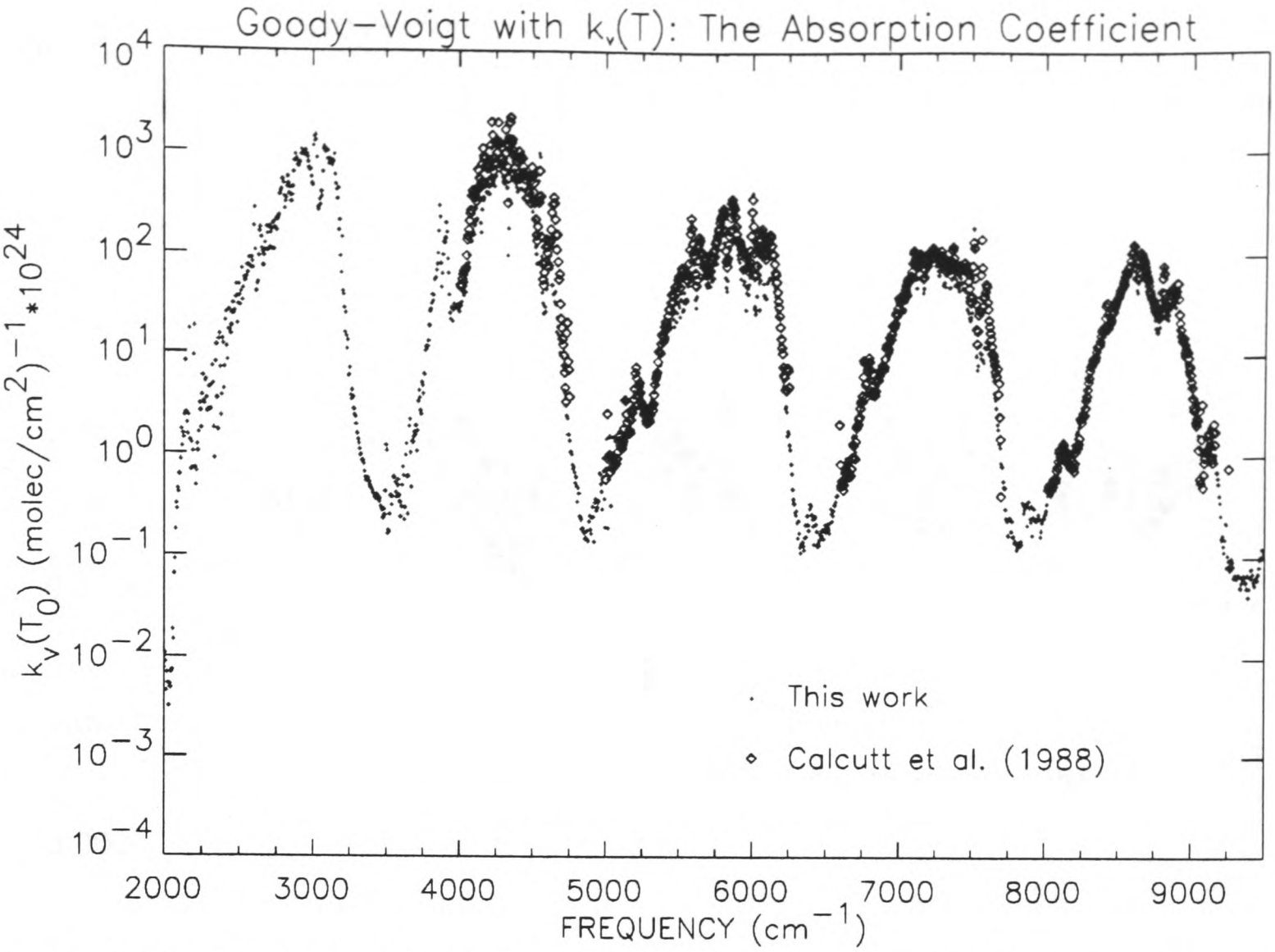

Figure 7.13: The absorption coefficient $k_\nu(T_0)$, as fitted in the present study and by Calcutt *et al.* (1988) using the Goody-Voigt model with $k_\nu(T)$.

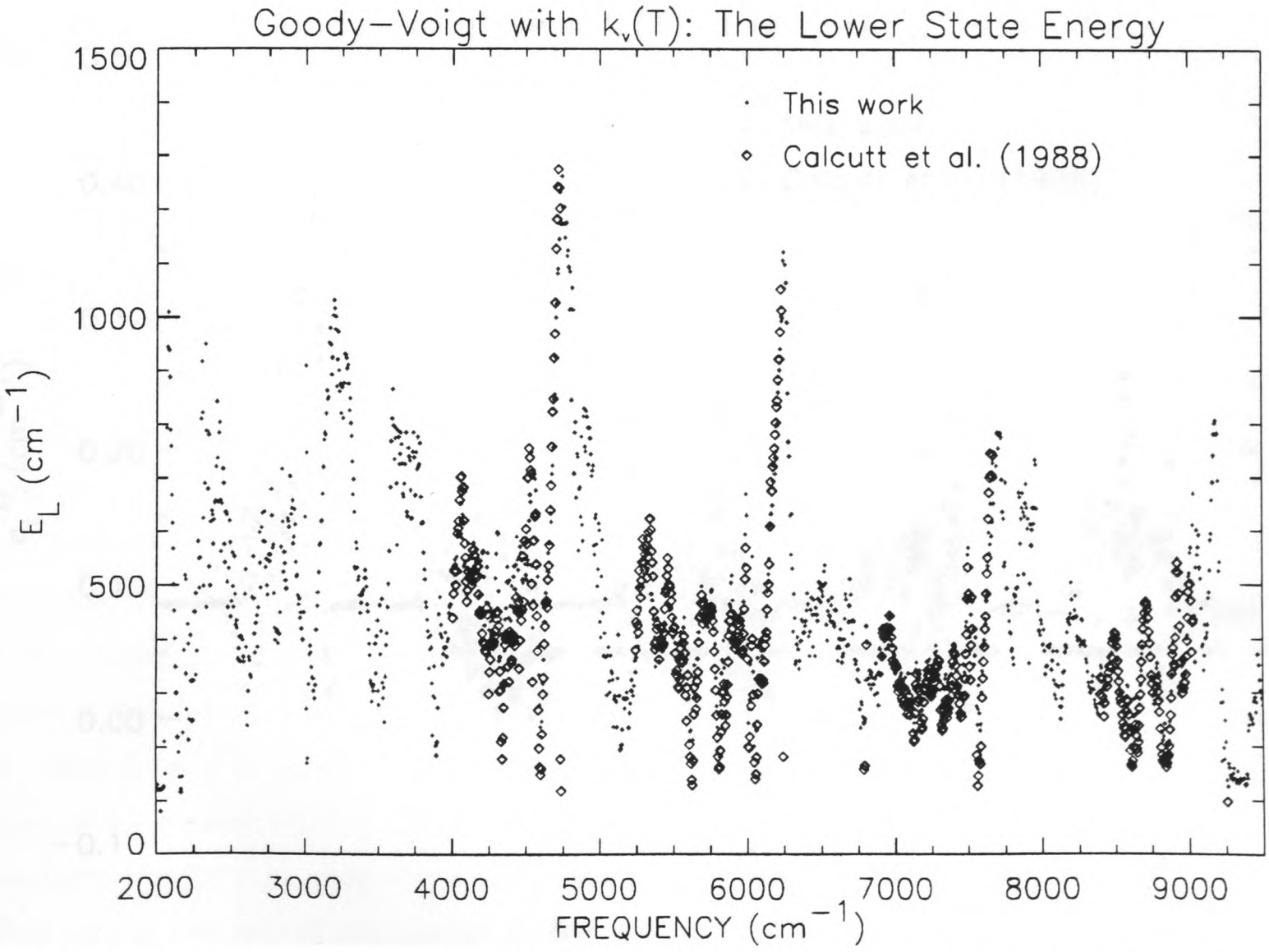

Figure 7.14: The lower state energy E_l, as fitted in the present study and by Calcutt *et al.* (1988) using the Goody-Voigt model with $k_\nu(T)$.

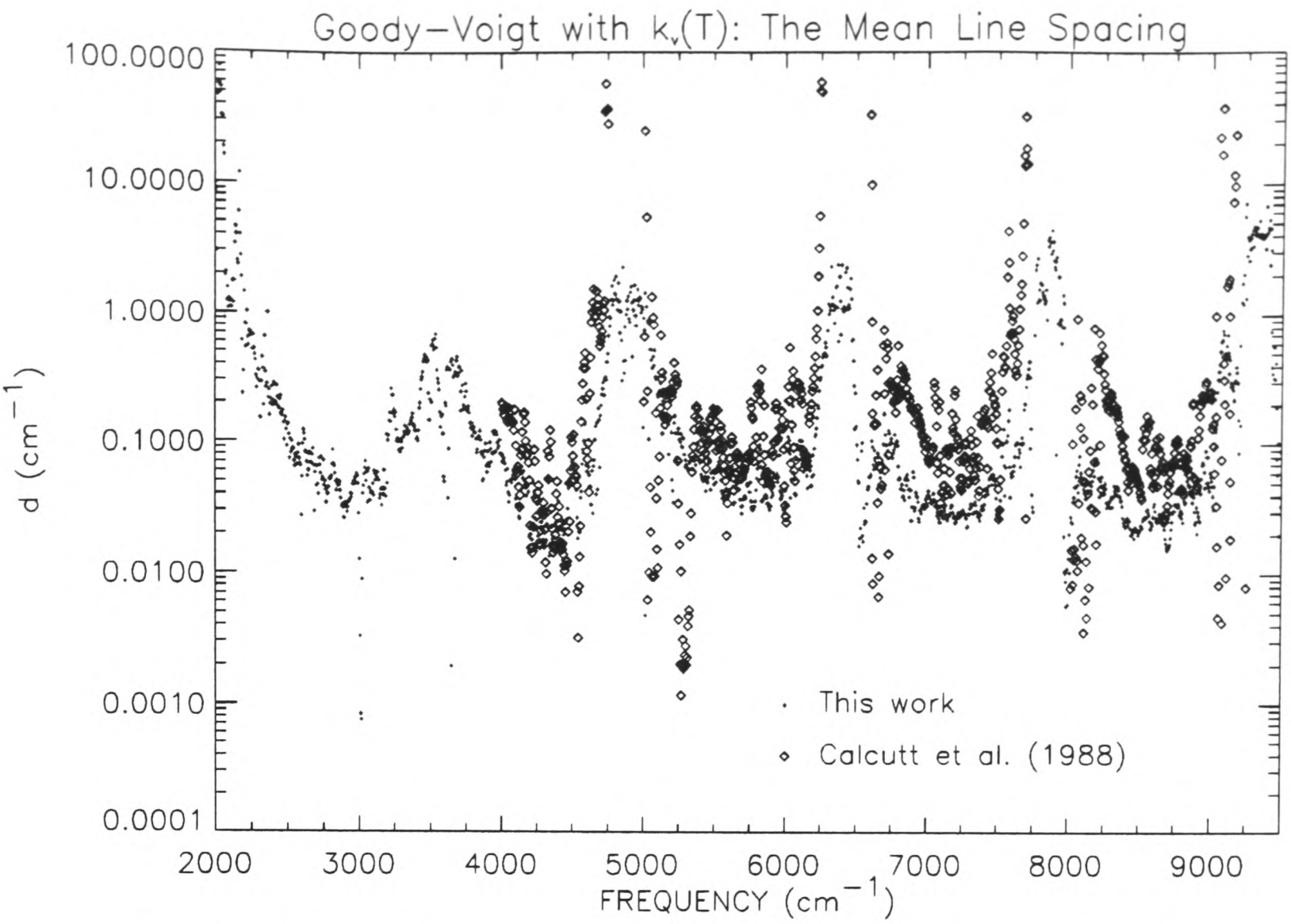

Figure 7.15: The mean line spacing d, as fitted in the present study and by Calcutt *et al.* (1988) using the Goody-Voigt model with $k_\nu(T)$.

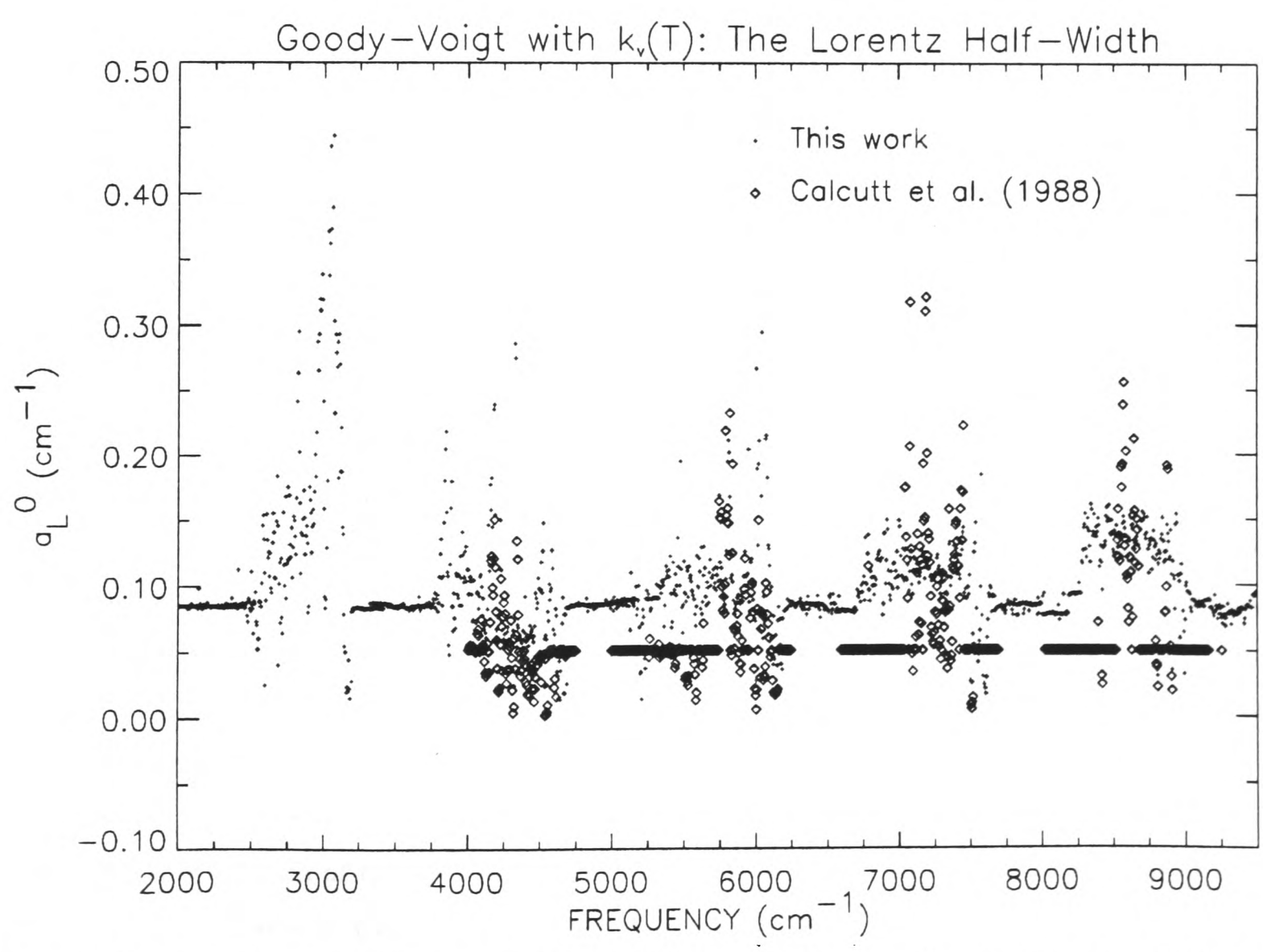

Figure 7.16: The self-broadened Lorentz half-width at 296 K and 1.01325 bar, α_L^0, as fitted in the present study and by Calcutt *et al.* (1988) using the Goody-Voigt model with $k_\nu(T)$.

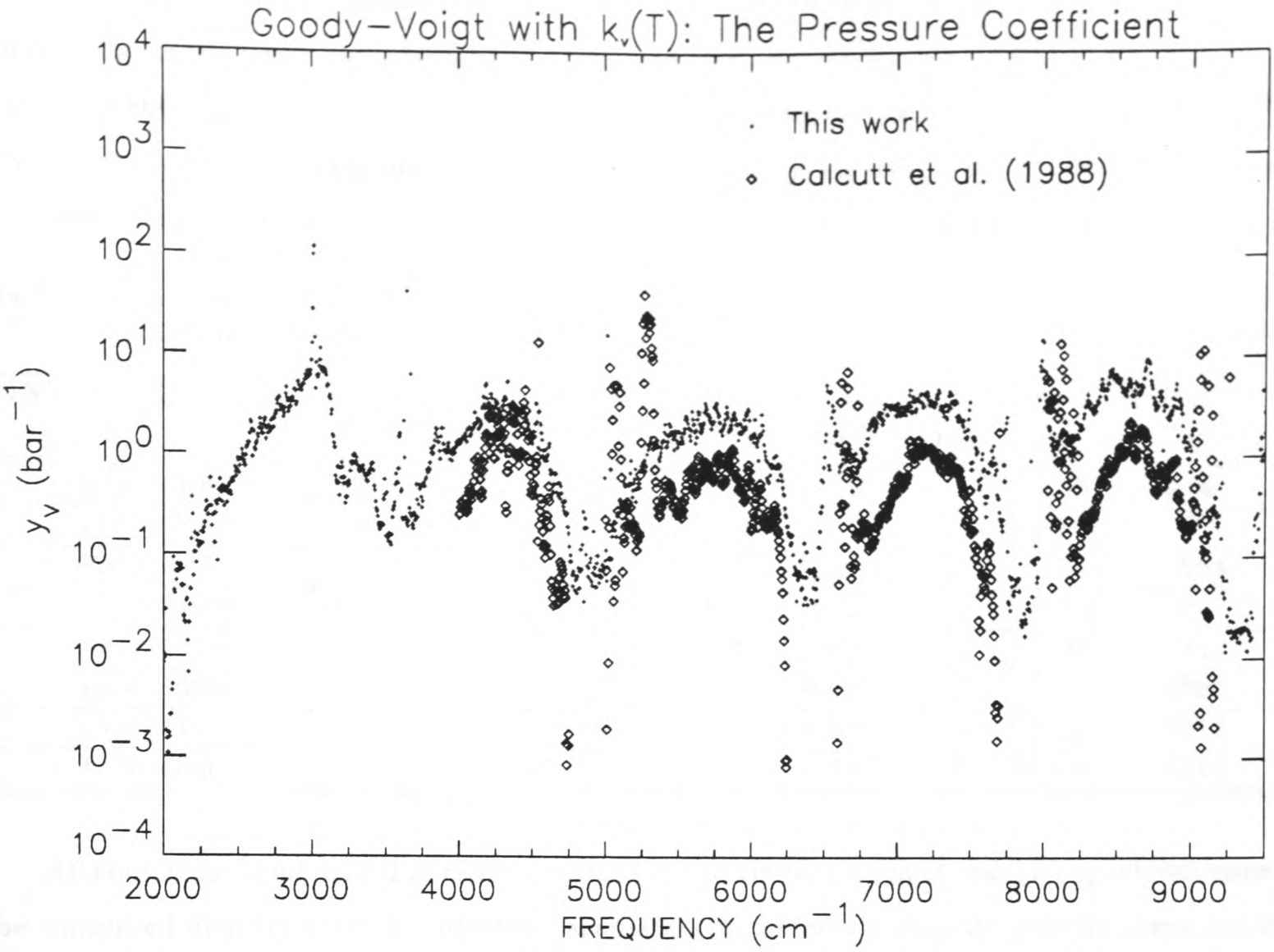

Figure 7.17: The pressure coefficient, y_ν, as fitted in the present study and by Calcutt *et al.* (1988) using the Goody-Voigt model with $k_\nu(T)$.

sets of parameters is poor, this is not surprising considering the different laboratory conditions (the maximum CH_4 abundance of Cruikshank and Silvaggio was 4.7 m-amagat, two orders of magnitude less than the maximum abundance of the present study), the lack of temperature dependence in the Goody-Voigt model of Cruikshank and Silvaggio, and the different interval used in the fitting.

As a further comparison between the results of the present work and the results of Cruikshank and Silvaggio, both sets of parameters were substituted into the Goody-Voigt model to calculate transmittance as a function of abundance. The parameters of the present work were used to calculate the transmittance at the original resolution of 10 cm^{-1}, with these values then averaged over the 100 cm^{-1} intervals of Cruikshank and Silvaggio. This calculation was performed at 273 K, for the lowest and highest pressures measured by Cruikshank and Silvaggio (0.0013 and 0.13 bar), and for each of the eight frequency intervals, giving sixteen plots of $\overline{\tau}$ versus U for each fit. For a given pressure and frequency, the pathlength was stepped through 50 values from 3.31 to 512.75 m (the minimum of Cruikshank and Silvaggio and the maximum of the present study). The resulting abundances were then used to calculate the fitted transmittance for each of the fitted models. For eleven of the sixteen plots, the transmittances fitted by the two sets of parameters agreed to within 0.10 for CH_4 abundances ranging from 0.00425 to 65.8 m-amagat, with no systematic difference between the results of the two models.

Considering the different conditions that were used to derive each set of parameters and the fact that both fits were extrapolated beyond their measurement conditions, this agreement seems to be reasonably good. It also provides proof that different sets of parameters can provide similar transmittances, thus again suggesting that physical interpretation of fitted parameters should be treated with caution.

Table 7.2: The Goody-Voigt band-model parameters fitted by Cruikshank and Silvaggio (1979) ("C+S" below), along with the same parameters fitted in the present work and averaged over the same 100 cm^{-1} intervals.

INTERVAL (cm^{-1})	$k_\nu(T_0)$ (m^{-1}-$amagat^{-1}$)		δ (cm^{-1})		α_L^0 (cm^{-1})	
	C+S	THIS WORK	C+S	THIS WORK	C+S	THIS WORK
4000–4100	0.38	0.222	0.25	0.0553	0.09	0.0898
4100–4200	1.44	0.945	0.10	0.0419	0.098	0.122
4200–4300	6.88	2.07	0.15	0.0232	0.088	0.0694
4300–4400	5.58	1.84	0.157	0.0224	0.087	0.0808
4400–4500	2.09	1.40	0.091	0.0341	0.090	0.0715
4500–4600	7.66	0.566	0.17	0.0590	0.06	0.0866
4600–4700	2.07	0.114	0.32	0.0817	0.09	0.0515
4700–4800	0.003	0.00648	1.00	0.767	0.09	0.0843

Although the band-model parameters fitted in the visible region of the CH_4 spectrum cannot be compared directly with the infrared parameters of this work, they do provide some context for the latter. For example, Fink *et al.* (1977) used Beer's Law and the Goody-Lorentz band model to obtain values of 1.0×10^{-5} to 0.0308 $(\text{m-amagat})^{-1}$ for $k_\nu(T_0)$ and 3 to 14 bar^{-1} for y_ν. Similar values of the visible absorption coefficient (up to 0.032 $(\text{m-amagat})^{-1}$) were obtained by Giver (1978). These values for $k_\nu(T_0)$ lie within the range fitted by the Goody-Voigt and Malkmus-Voigt models in the present work, while these values for y_ν are at the upper end of the 0.01 to 10 bar^{-1} range obtained here. Thus, the densest line spacing in the near-infrared is comparable to that in the visible, but as predicted by Fink *et al.* (1977), the pressure effect appears to be stronger (y_ν smaller) in the infrared, compatible with a better defined line structure than in the pseudo-continuous visible CH_4 spectrum.

Also in the visible, Podolak and Giver (1979) present mean absorption and pressure coefficients at three wavelengths which have values in the same range as those of Fink *et al.* (1977). More interestingly, they used these coefficients and the Voigt lineshape to calculate transmittance with both the Goody and Malkmus band models. Given the same value of δ, the transmittance calculated with the Malkmus model was smaller; conversely, in order to obtain the same transmittance with both models, a larger value of δ was required by the Malkmus model. This is the same effect that is seen in Figures 7.10(d) and 7.11(d), where δ is consistently larger in the Malkmus-Voigt fit. It is due to the fact that δ is a model-dependent fitting parameter, although Podolak and Giver (1979) initially assumed it to be independent of the line-strength distributions of the models.

In summary, this assessment of the values obtained for the fitted CH_4 parameters high-lights the scarcity of near-infrared spectral parameters available in the literature. The band modelling

performed in the present study is therefore clearly extending the availability of such data for CH_4. Where possible, the values fitted in the present work were compared with values obtained in other studies. However, even when parameters were available, a meaningful comparison was hampered by the use of different fitting techniques (particularly the lack of temperature dependence in most models), fitting intervals, and laboratory conditions. The latter probably provides the most important explanation for the variation in parameters between this study and others. In order to provide validation of the results obtained in the present study, measurement of spectra under similar laboratory conditions and the performance of similar band-model fits would be useful.

7.3 Band Modelling of the Hydrogen-Broadened Methane Spectra

7.3.1 Selection of Models and Initialisation of Parameters

As discussed at the start of this chapter, the band modelling of the experimental CH_4 spectra was conducted in two stages. The first stage was the fitting of the self-broadened CH_4 spectra, described above, while the second stage, described in this section, involved the fitting of H_2-broadened CH_4 spectra. The self-broadened CH_4 spectra were fitted with a variety of models, and as has been discussed in §7.2.4.1, this work showed that the Goody-Voigt and Malkmus-Voigt models provided the best fits to the data. Thus, in the second stage of the band modelling, these two physically based models were used to fit the H_2-broadened CH_4 spectra.

In order to provide the greatest possible range of laboratory conditions to these band-model fits, both the self- and H_2-broadened CH_4 spectra were included in this second fitting process. CH_4-to-total mixing ratios from 2×10^{-3} up to 1 were therefore fitted by the models. Two independent fits were again performed, one for the globar spectra and one for the quartz-halogen spectra, each fitting the combined set of 108 self-broadened CH_4 spectra and 117 H_2-broadened CH_4 spectra. Once the fits were completed, the results for each source were merged, with the globar fits again adopted from 2000 to 3900 cm^{-1} and the quartz-halogen fits adopted for 3905 to 9500 cm^{-1}.

As was the case for the self-broadened CH_4 spectra, the combined set of self- and H_2-broadened CH_4 spectra were fitted using sequences of progressively more complex models. The two sequences followed in this case are illustrated in Figure 7.18. The first steps for both the Goody and Malkmus sequences were identical to those in Figure 7.1. Both began with the one-parameter Weak Limit model followed by the two-parameter Weak Limit model with temperature dependence, initialising $k_\nu(T_0)$ and E_l as described in §7.2.1. The resulting optimised values of these parameters were then used to initialise the parameters for the temperature-dependent Goody-Lorentz and Malkmus-Lorentz models, again as described in §7.2.1.

For the next fit in both sequences, a new parameter, the ratio of self-to-foreign broadening,

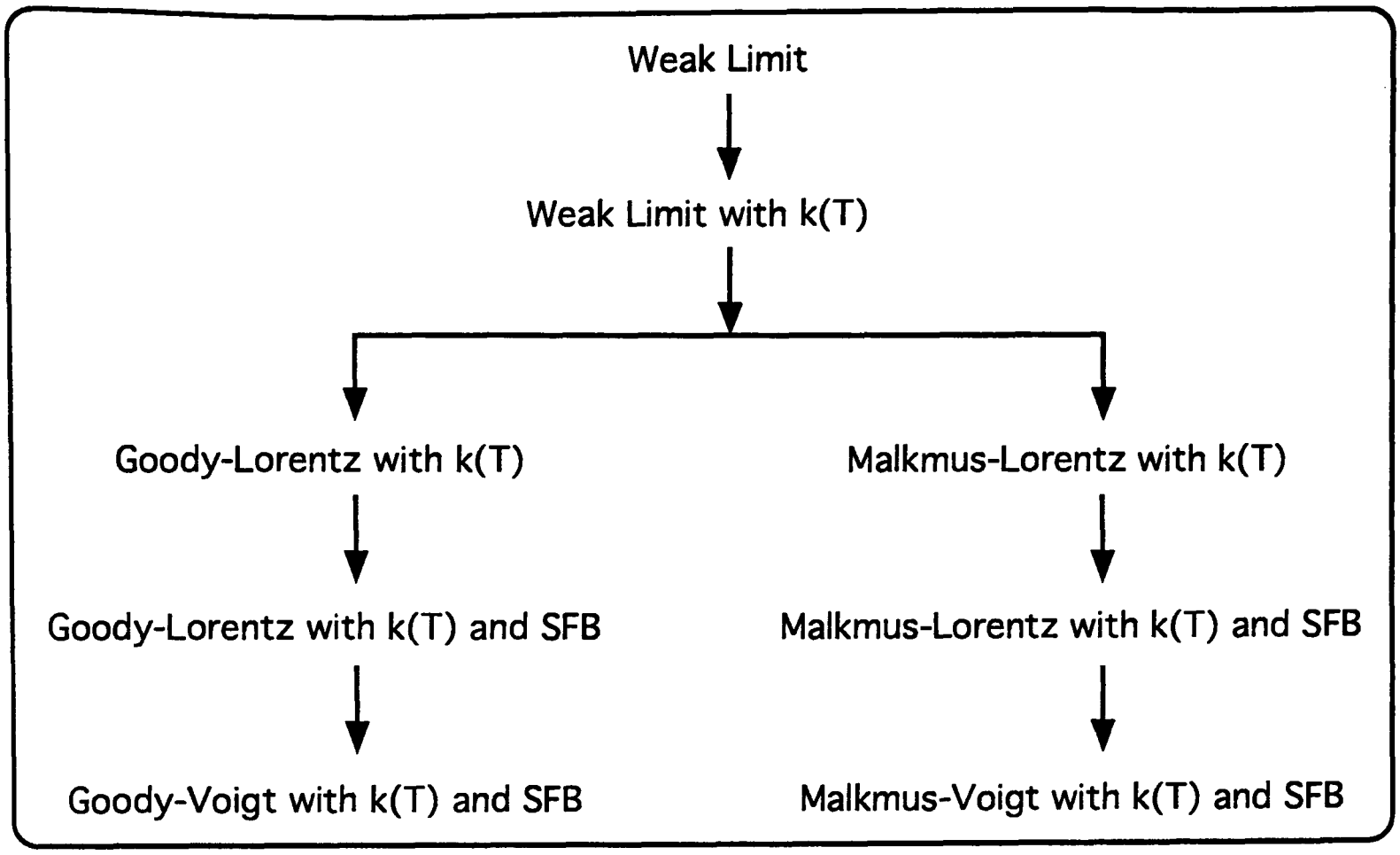

Figure 7.18: The sequences of models used in fitting the H_2-broadened CH_4 spectra.

was introduced into the Goody-Lorentz and Malkmus-Lorentz models. This ratio, *SFB*, has been defined in Equation 3.10 as the ratio of the self-broadened Lorentz half-width to the foreign-broadened Lorentz half-width. This parameter was fitted to the spectra in order to account for the modification of the CH_4 line width due to the presence of H_2. It is introduced into the models in the expression for α_L. In this case, the simplified expression for α_L of Equation 4.21, applicable for self-broadening, is replaced by the more general expression of Equation 3.9. Redefining this latter equation in terms of the CH_4-to-total mixing ratio, q, and the total pressure, P, it becomes

$$\alpha_L(P,T) = \alpha_L^0 \frac{P}{P_0}\sqrt{\frac{T_0}{T}}\left[q + \frac{(1-q)}{SFB}\right] \tag{7.7}$$

where α_L^0 is still the self-broadened Lorentz half-width at T_0 and P_0.

When this expression is introduced into the Goody-Lorentz random band model, $\bar{\tau}$ becomes

$$\bar{\tau}_{Goody-Lorentz} = \exp\left(-1/\sqrt{\frac{1}{(k_\nu U)^2} + \frac{1}{\pi k_\nu y_\nu U P[q+(1-q)/SFB]\sqrt{T_0/T}}}\right). \tag{7.8}$$

In the Goody model, the effect of foreign broadening thus appears in the strong absorption term. Similarly, the Malkmus-Lorentz random band model becomes

$$\bar{\tau}_{Malkmus-Lorentz} = \exp\left(-1/\left[\frac{1}{2k_\nu U} + \sqrt{\frac{1}{(2k_\nu U)^2} + \frac{1}{4\pi k_\nu y_\nu U P[q+(1-q)/SFB]\sqrt{T_0/T}}}\right]\right). \tag{7.9}$$

For both models, *SFB* was initialised to 1, making each model initially the same as the preceding self-broadened model.

Once the Goody-Lorentz and Malkmus-Lorentz models, both with temperature dependence and foreign broadening, had been fitted to all of the self- and H_2-broadened spectra, their final best-fit parameters provided the initial values for the Goody-Voigt and Malkmus-Voigt models. In addition to the newly introduced parameter *SFB*, these models were used to fit the same four parameters $k_\nu(T_0)$, E_l, δ/α_D^0, and α_L^0/α_D^0 that were fitted to the self-broadened CH_4 spectra, with all four parameters being initialised as described in §7.2.1. The ratio of self-to-foreign broadening was again introduced into these models through the definition of α_L, in this case appearing in the definition of y in $V(x,y)$:

$$y = \frac{\alpha_L}{\alpha_D} = \left(\alpha_L^0 \frac{P}{P_0}\sqrt{\frac{T_0}{T}}\left[q + \frac{(1-q)}{SFB}\right]\right)\left(\frac{1}{\alpha_D^0\sqrt{T}}\right) = \frac{\alpha_L^0}{\alpha_D^0}\frac{P}{P_0}\frac{\sqrt{T_0}}{T}\left[q + \frac{(1-q)}{SFB}\right]. \quad (7.10)$$

For these models, *SFB* was initialised directly from the best-fit values obtained with the preceding fits with the Lorentz lineshape.

The combined set of self- and H_2-broadened CH_4 spectra was thus fitted with a total of eight models, culminating in the Goody-Voigt and Malkmus-Voigt models, both of which included both temperature dependence and foreign broadening. The remainder of this section discusses the quality of these fits, the values obtained for the fitted parameters, and how these results compare with others found in the literature.

7.3.2 The Quality of the Fits

Following the methods used with the self-broadened CH_4 spectra, the r.m.s. residual error, σ, was again used to quantify how well the fitted models matched the original measured transmittances. In Figure 7.19, the variation of σ with frequency is plotted for the eight models that were fitted to all of the self- and H_2-broadened CH_4 spectra. The first two fits, using the Weak Limit model (a) and the Weak Limit model with temperature dependence (b), provide poor fits to the data, particularly in the bands. With neither model fitting pressure or foreign broadening, such large values of σ are not surprising for fits to 225 different spectra.

Referring next to Figure 7.19(c), (d), and (e), the three models subsequently fitted in the Goody sequence, the addition of the term for strong absorption in the Goody-Lorentz model is seen to provide a more significant reduction in σ. The addition of the self-to-foreign broadening ratio to the Goody-Lorentz model further improves the fit, but both of the Goody-Lorentz models have trouble fitting points in the 3000 and 4300 cm^{-1} bands. With the introduction of the Voigt lineshape, the large values of σ found in these regions are reduced for all but a few points. With the exception of these points, which correspond to pump-oil contamination and peaks of absorption, σ for the Goody-Voigt fit is less than 0.04 throughout the 2000 to 9500 cm^{-1} spectral range, and less than 0.03 for all frequencies outside the 3000 and 4300 cm^{-1} bands. These values are considered acceptable as they are again comparable to the measurement errors in the spectra, the estimate for the error due to sloping ratios being 0.026

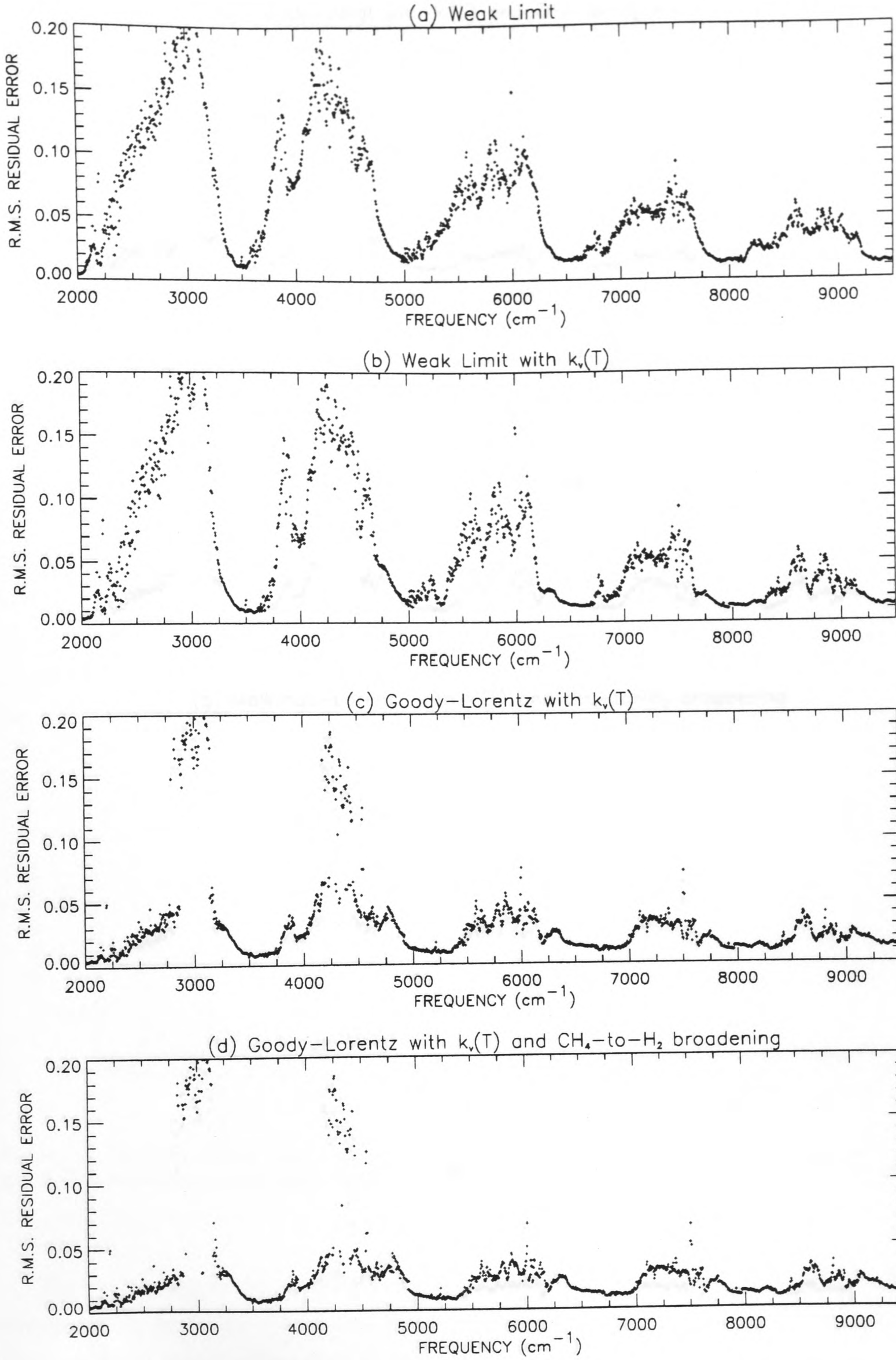

Figure 7.19: The r.m.s. residual error in transmittance for the eight models fitted to the all of the self- and H_2-broadened CH_4 spectra (continued on following page).

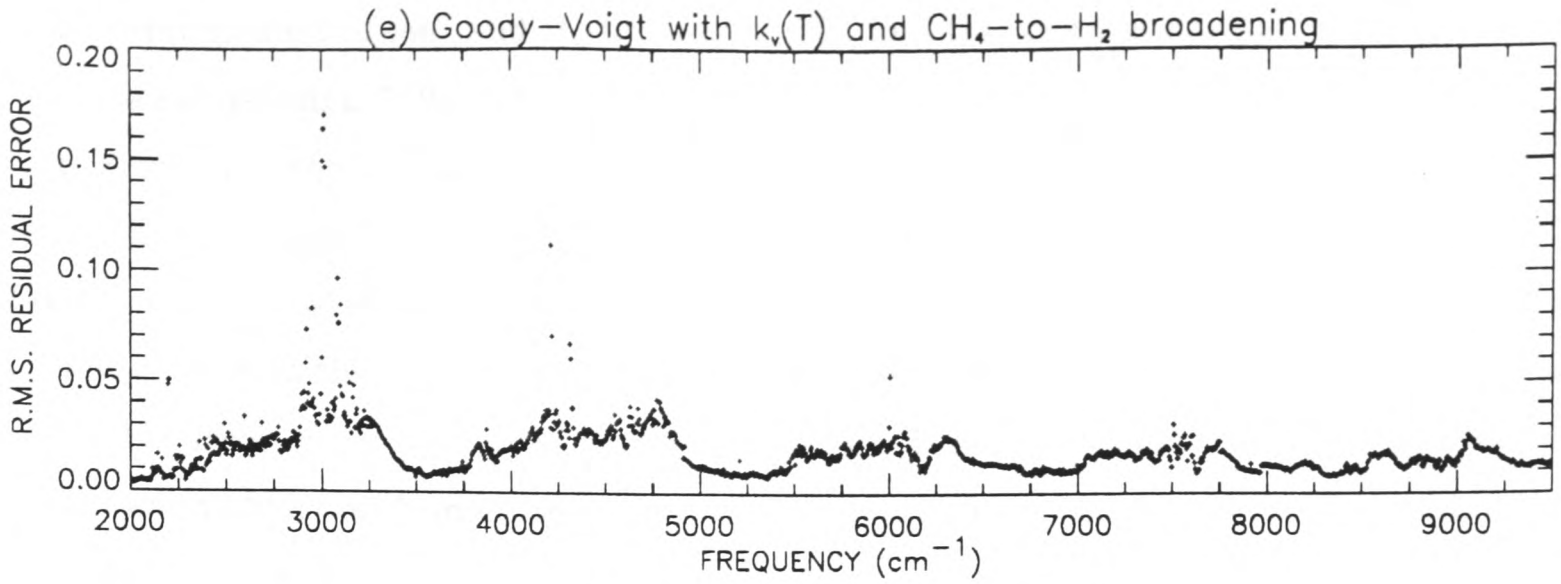
(e) Goody–Voigt with $k_\nu(T)$ and CH_4–to–H_2 broadening
R.M.S. RESIDUAL ERROR
0.20
0.15
0.10
0.05
0.00
2000
3000
4000
5000
6000
7000
8000
9000
FREQUENCY (cm^{-1})

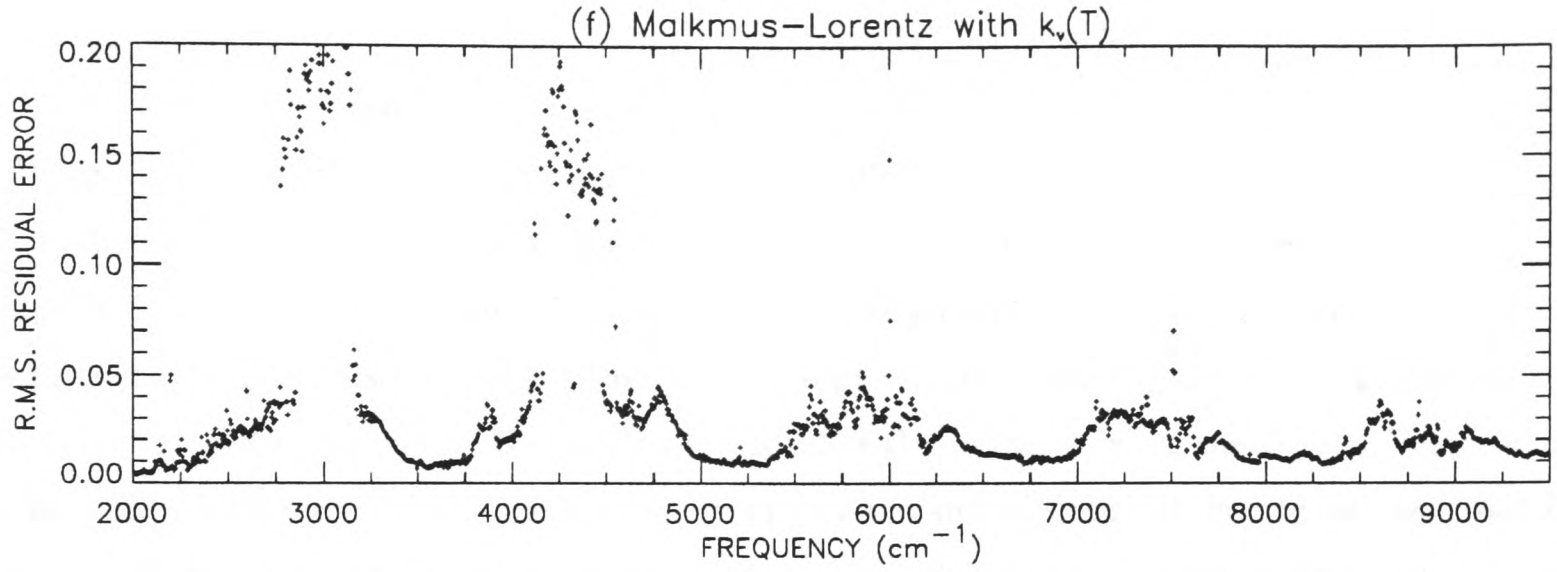
(f) Malkmus–Lorentz with $k_\nu(T)$
R.M.S. RESIDUAL ERROR
0.20
0.15
0.10
0.05
0.00
2000
3000
4000
5000
6000
7000
8000
9000
FREQUENCY (cm^{-1})

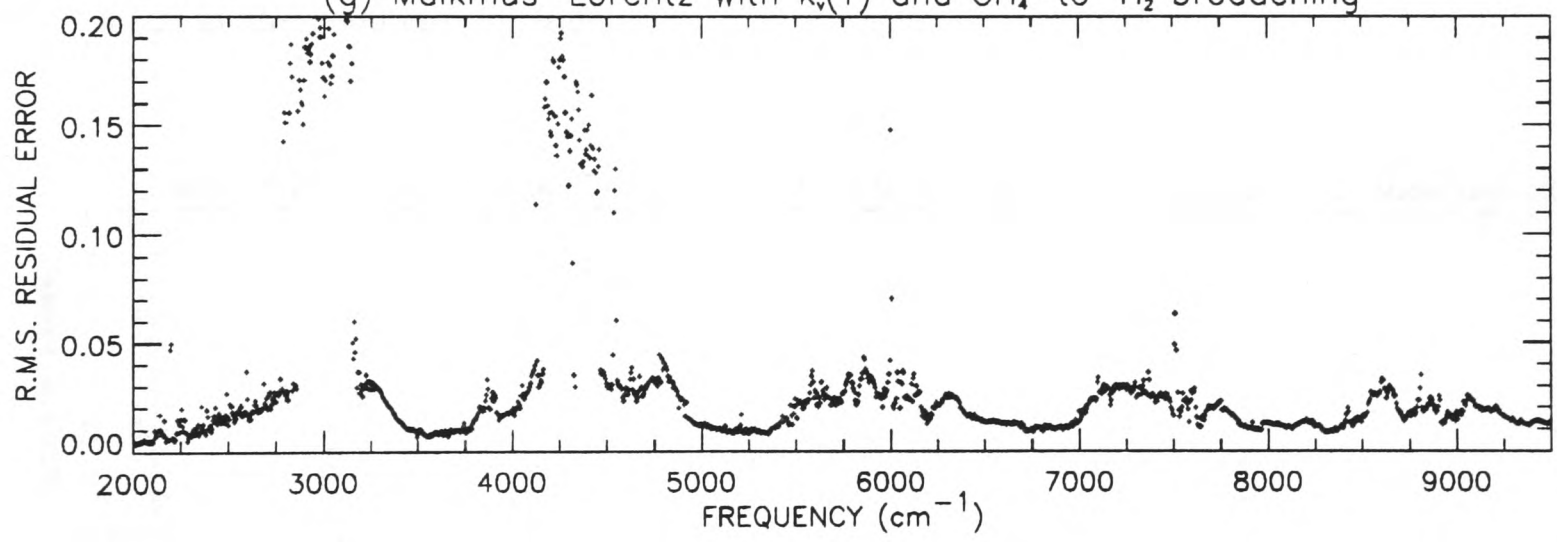
(g) Malkmus–Lorentz with $k_\nu(T)$ and CH_4–to–H_2 broadening
R.M.S. RESIDUAL ERROR
0.20
0.15
0.10
0.05
0.00
2000
3000
4000
5000
6000
7000
8000
9000
FREQUENCY (cm^{-1})

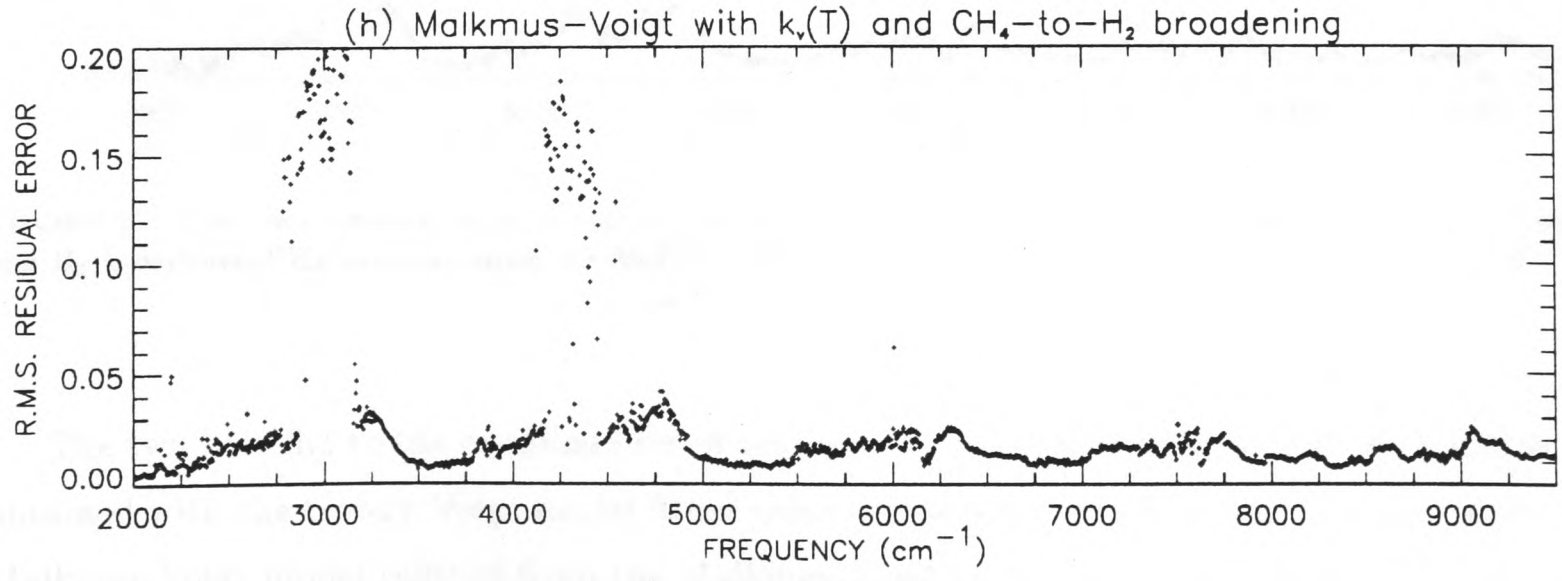
(h) Malkmus–Voigt with $k_\nu(T)$ and CH_4–to–H_2 broadening
R.M.S. RESIDUAL ERROR
0.20
0.15
0.10
0.05
0.00
2000
3000
4000
5000
6000
7000
8000
9000
FREQUENCY (cm^{-1})

for the combined set of self- and H_2-broadened CH_4 spectra, and the estimate for the error due to the ice ripple being 0.015 (see Table 6.7).

In Figure 7.19(f), (g), and (h), a similar improvement in σ is seen in the progression from the Malkmus-Lorentz fit to the Malkmus-Lorentz fit with *SFB* to the Malkmus-Voigt fit with *SFB*. The major exceptions to this are the 3000 and 4300 cm^{-1} bands, where the large values of σ obtained with the Malkmus-Lorentz models have not been reduced by the Malkmus-Voigt model. For frequencies from 2785 to 3145 cm^{-1} and 4125 to 4545 cm^{-1}, σ is > 0.10, and for all of these points, the Numerical Algorithms least squares minimisation routine warned of a convergence problem.

This problem was reduced by refitting the Malkmus-Voigt model with *SFB* to the combined set of self- and H_2-broadened CH_4 spectra, using the Malkmus-Voigt fit to the self-broadened CH_4 spectra (Figure 7.11) to initialise the parameters. The resulting values of σ are plotted in Figure 7.20. With this alternative method of initialisation, the convergence of the fit has improved in both the 3000 and 4300 cm^{-1} bands, particularly in the latter. This same method of initialisation was also tested for the Goody-Voigt model, using the Goody-Voigt parameters fitted to the self-broadened CH_4 spectra to initialise the parameters in the Goody-Voigt model with *SFB*. However, in this case, the resulting r.m.s. residual error differed little from that for the Goody-Voigt model fitted using the progression of Figure 7.18, in fact being slightly worse (by < 0.02) in the 3000 cm^{-1} region.

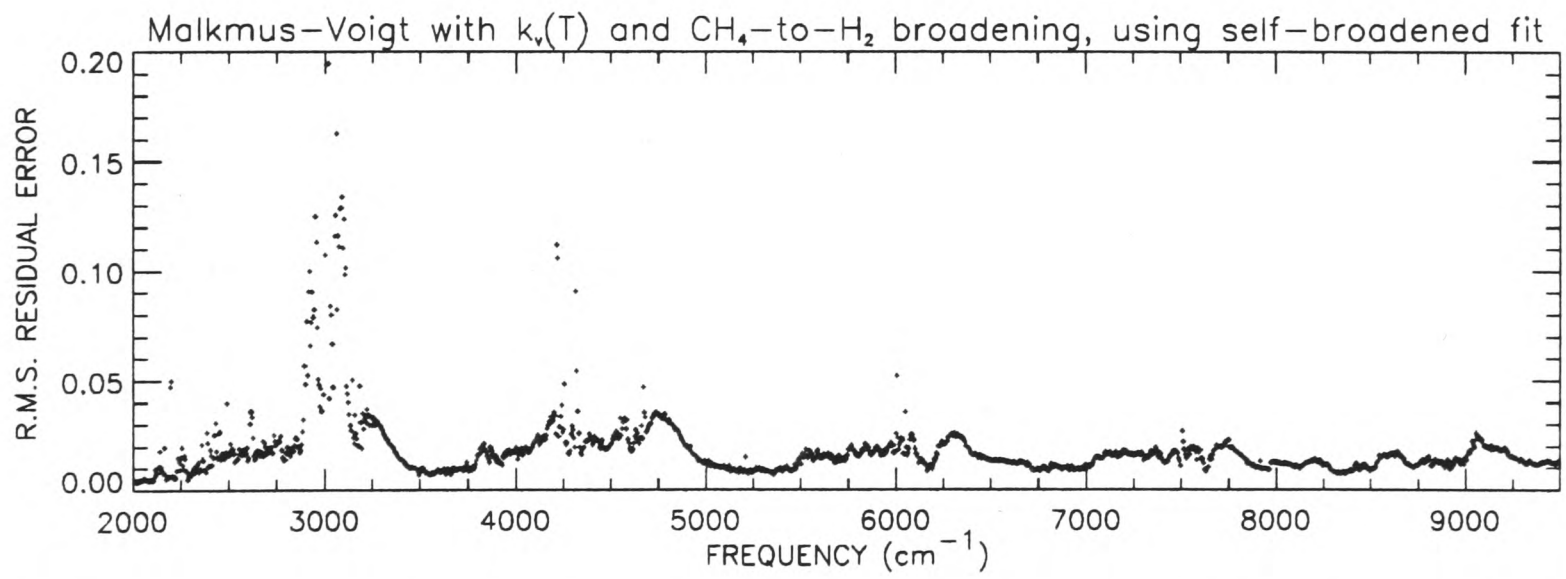

Figure 7.20: The r.m.s. residual error in transmittance for the Malkmus-Voigt model fitted to the all of the self- and H_2-broadened CH_4 spectra, using the Malkmus-Voigt parameters fitted to the self-broadened CH_4 spectra as the initial values.

The two best fits to the combined set of self- and H_2-broadened CH_4 spectra were therefore obtained with the Goody-Voigt model fitted using the progression of Figure 7.18, and with the Malkmus-Voigt model refitted from the Malkmus-Voigt fit to the self-broadened CH_4 spectra. Unless otherwise stated, all further discussion of the Goody-Voigt and Malkmus-Voigt fits to the combined set of self- and H_2-broadened CH_4 spectra will refer to these two best fits. The difference in σ between these two fits is plotted in Figure 7.21. As was the case for the self-

broadened CH_4 spectra, σ is generally similar for these two models, except in the 3000 cm^{-1} band. In this region, the Goody-Voigt model clearly provides a closer fit to the original spectra. Elsewhere throughout the 2000 to 9500 cm^{-1} range, σ for the two fits agrees to within 0.005 except for a few scattered points. Given these findings, the parameters listed in Appendix C, for the complete set of self- and H_2-broadened CH_4 spectra, are those obtained with the Goody-Voigt model. As the Goody model appears to be the band model most commonly used in the literature for the fitting of CH_4 spectra, the inclusion of these Goody-Voigt parameters should also be useful for future comparisons.

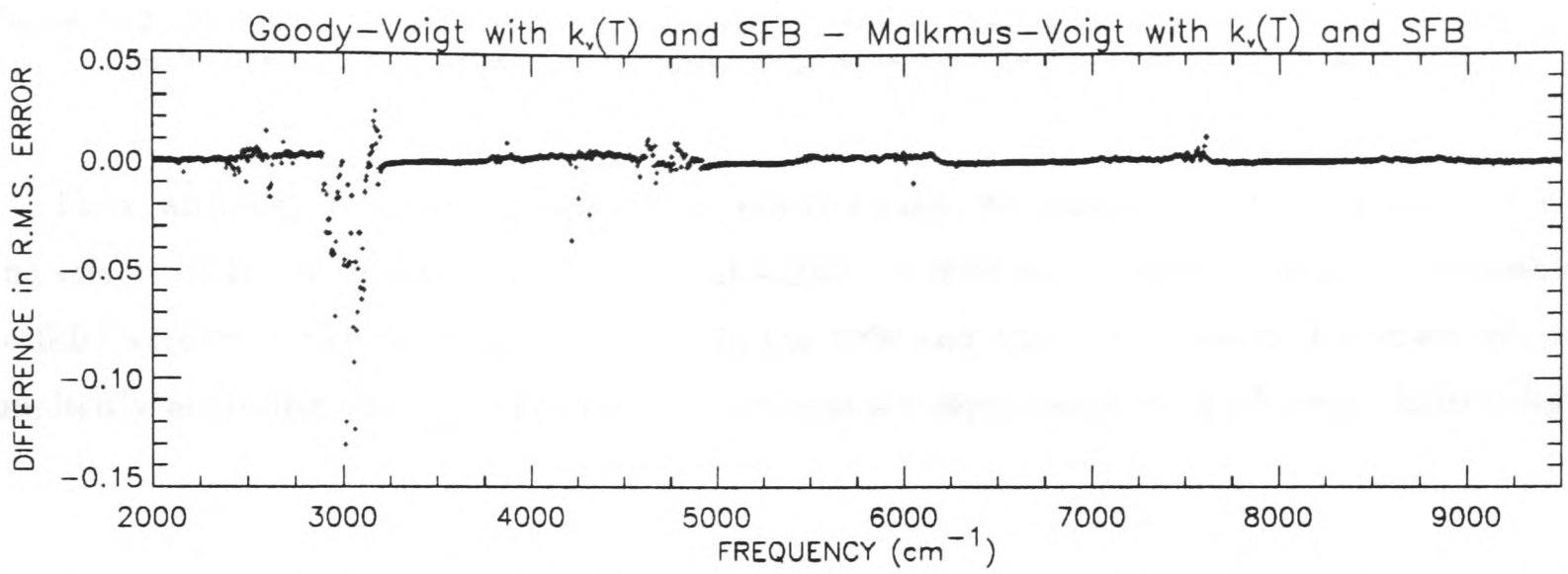

Figure 7.21: The difference between the r.m.s. residual error for the best Goody-Voigt and Malkmus-Voigt fits to all of the self- and H_2-broadened CH_4 spectra.

In order to further assess the quality of the Goody-Voigt fit to all of the spectra, the difference in σ between this fit and the Goody-Voigt fit to the self-broadened spectra was calculated and is plotted in Figure 7.22. This figure shows that σ agrees to within 0.01 between the two fits except in the 3000 and 4300 cm^{-1} bands where σ is as much as 0.03 larger for the Goody-Voigt fit to all of the spectra. Thus, in these two bands, both the Goody-Voigt and the Malkmus-Voigt models are unable to provide as good a fit to all of the spectra as they do to only the self-broadened spectra. The poorer fits in these bands appear to be partly caused by contaminating absorptions (see §6.2.7): pump oil and ice absorption in the 3000 cm^{-1} band, and H_2 absorption in the 4300 cm^{-1} band. The latter is seen in Figure 7.23, where the transmittance calculated with the Goody-Voigt fit to all of the spectra is overlaid on a weakly absorbing quartz-halogen H_2-broadened CH_4 spectrum. This spectrum is for a H_2 pressure of 0.8030 bar and a pathlength of 512.75 m, therefore clearly showing the H_2 absorption which contributes to the poor quality of the fit in the region from 3700 to 5600 cm^{-1}. Similar figures, plotted for all of the H_2-broadened spectra fitted with the Goody-Voigt model, also suggest that in both the 3000 and 4300 cm^{-1} bands, the discrepancy between the fitted and measured transmittances is partly caused by the limitations of the band models, which have difficulty fitting the rapidly varying values of transmittance present in these regions.

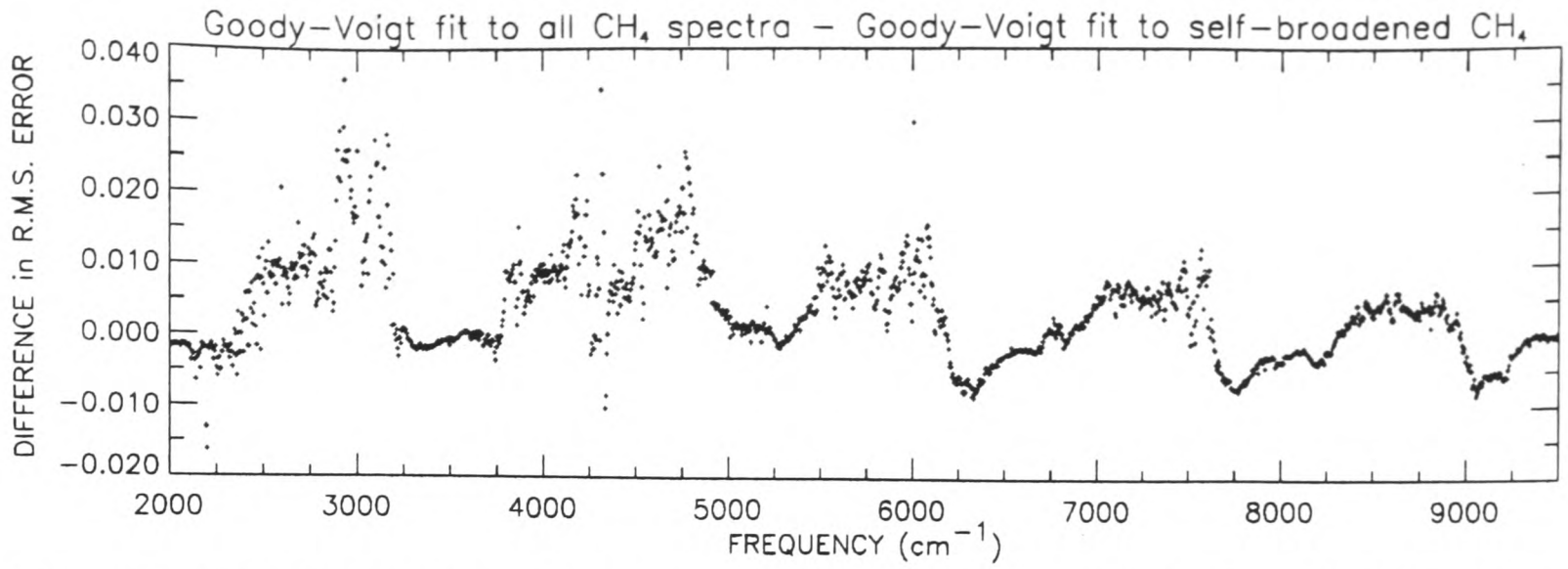

Figure 7.22: The difference between the r.m.s. residual error for the Goody-Voigt fit to all of the self- and H_2-broadened CH_4 spectra and the Goody-Voigt fit to only the self-broadened CH_4 spectra.

Figure 7.23: (a) Measured spectrum QH07_H240K (—) and the Goody-Voigt fit (with $k_\nu(T)$ and SFB) to this spectrum (···). (b) The difference between these two spectra.

Thus, although the introduction of the self-to-foreign broadening ratio has accounted for the effects of H_2-broadening over most of the 2000 to 9500 cm^{-1} spectral range, it is unable to fully account for the strong absorptions in the 3000 and 4300 cm^{-1} bands. For example, by implicitly assuming that the exponent of temperature dependence of the Lorentz half-width,

n, is the same for both self- and H_2-broadened CH_4 lines, *SFB*, as defined in Equation 7.7, is weakly temperature dependent. This has been demonstrated by Varanasi *et al.* (1973), whose measurements of self- and H_2-broadened CH_4 line widths yielded values of 1.11, 1.27, and 1.52 for *SFB* at 295, 250, and 190 K. However, with temperature dependence fitted elsewhere in the model and the number of fitted parameters already being five, no attempt was made to fit n or any temperature dependence of *SFB*. In conclusion, despite the difficulty in fitting the 3000 and 4300 cm^{-1} bands, σ for the Goody-Voigt fit to the combined set of self- and H_2-broadened spectra is less than 0.04 for all but a few points, even in these two bands, and lies between 0.005 and 0.03 for all frequencies outside these regions.

7.3.3 The Fitted Parameters

Figure 7.24 shows both the fitted and derived parameters that were obtained with the Goody-Voigt fit to the combined set of self- and H_2-broadened CH_4 spectra. In (a) through (e), the five fitted parameters, $k_\nu(T_0)$, E_l, δ/α_D^0, α_L^0/α_D^0, and *SFB*, are plotted, while (f) through (h) show the three derived parameters, δ, α_L^0, and y_ν. A comparison of these parameters to those obtained with the Goody-Voigt fit to the self-broadened CH_4 spectra (Figure 7.10) reveals various differences, discussed below. The same comparison, performed for the parameters obtained with the Malkmus-Voigt fits to all of the self- and H_2-broadened CH_4 spectra and to the self-broadened CH_4 spectra, yielded similar results.

For the Goody-Voigt fit to all of the spectra, the absorption coefficient ranges between 1.5×10^{-5} and 12.5 m-amagat, and is found to be significantly larger in the 3000 and 4300 cm^{-1} bands than it is in the Goody-Voigt fit to the self-broadened CH_4 spectra. The lower state energy, while covering a range of values (84–1280 cm^{-1}) similar to those fitted to the self-broadened spectra, is generally smaller, particularly in the 3000 and 4300 cm^{-1} bands where it may compensate for the larger values of $k_\nu(T_0)$. The fitted parameter δ/α_D^0 can be directly translated into the mean line spacing, which ranges between approximately 0.001 and 10 cm^{-1}. This mean line spacing is consistently larger in the fit to all of the spectra, probably biased by the fact that the H_2-broadened spectra are limited to a maximum CH_4 abundance of 78 m-amagat, giving a smaller number of strongly absorbing spectra to be fitted. The fitted parameter α_L^0/α_D^0 can be used to derive the self-broadened Lorentz half-width, which varies between 0.019 and 0.24 cm^{-1}, and it is again in the 3000 and 4300 cm^{-1} bands that values fitted to all of the spectra show the poorest agreement with the values fitted to the self-broadened CH_4 spectra alone. Finally, the derived pressure coefficient, y_ν, although also lying between approximately 0.01 and 10 bar^{-1}, is consistently less in the fit to all of the spectra. This is due to the wider mean line spacing, with the larger number of weakly absorbing spectra giving rise to a stronger pressure dependence.

In theory, if the effects of H_2 broadening were entirely accounted for by the self-to-foreign broadening ratio, then the other CH_4 parameters fitted to the combined set of self- and H_2-

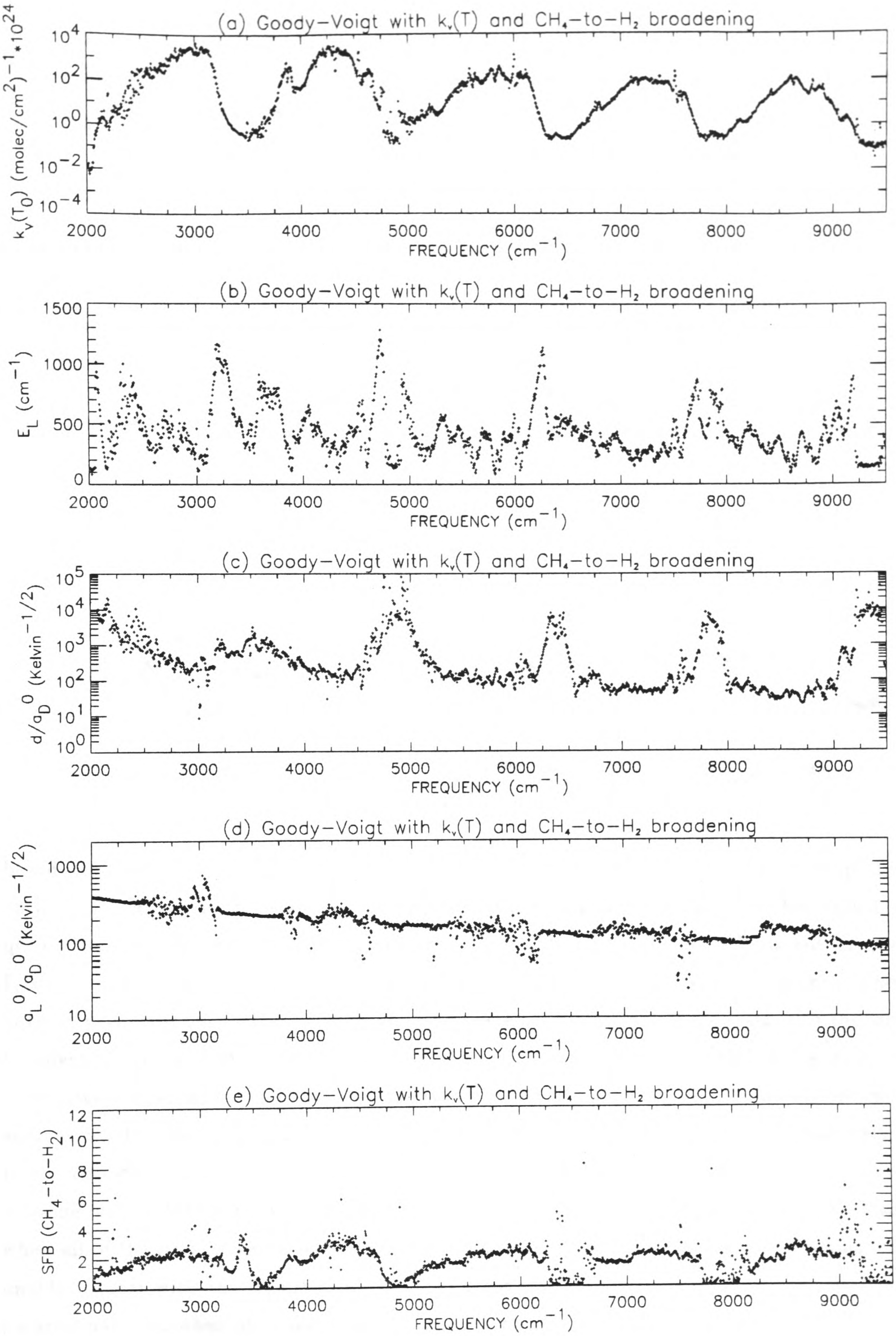

Figure 7.24: The parameters fitted to all of the self- and H_2-broadened CH_4 spectra using the Goody-Voigt model with $k_\nu(T)$ and *SFB* (continued on following page).

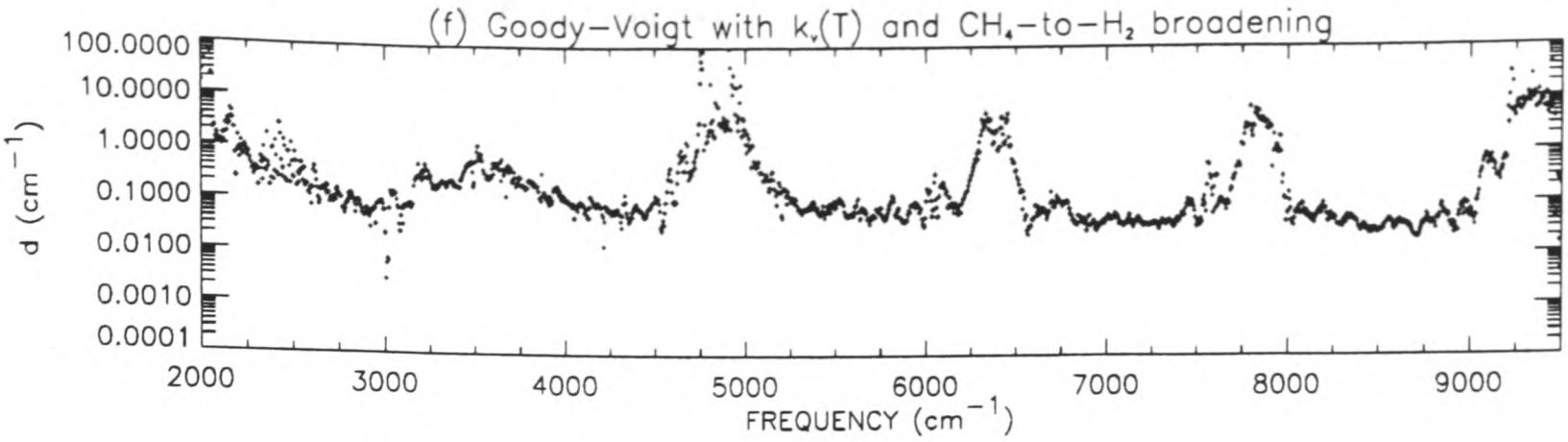

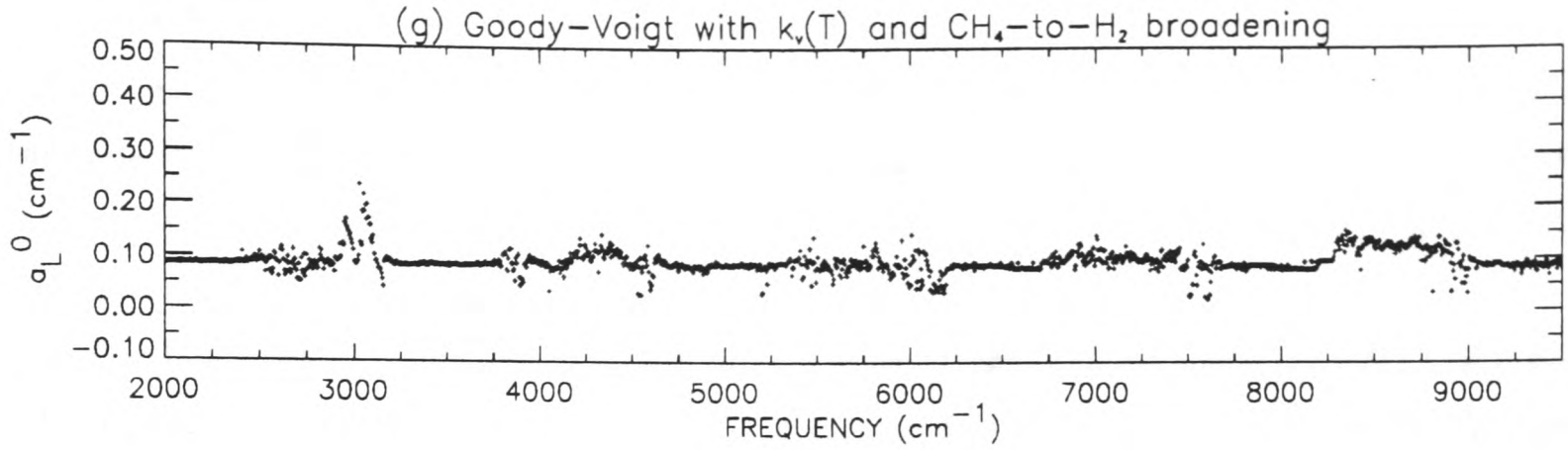

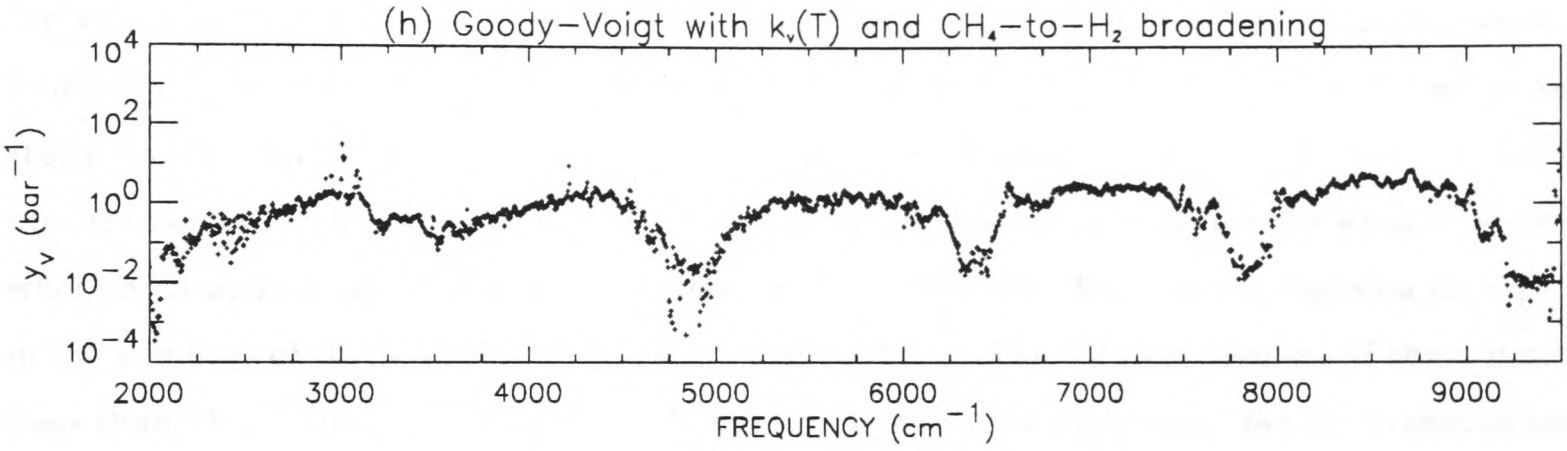

broadened spectra would have the same values as those fitted to the self-broadened CH_4 spectra only. However, as discussed above, the parameters have significantly changed. For each frequency interval, the set of fitted parameters, $k_\nu(T_0)$, E_l, δ/α_D^0, and α_L^0/α_D^0, is not unique. Despite using the same fundamental band model and the same initialisation, different values of these parameters are obtained when the H_2-broadened spectra are fitted along with the self-broadened spectra. Differences in one parameter are compensated for by differences in other parameters. As an additional test, both the Goody-Voigt and Malkmus-Voigt models were once again refitted to the combined set of self- and H_2-broadened CH_4 spectra, fixing the parameters to the best-fit values obtained in the respective fits to the self-broadened CH_4 spectra, and allowing only *SFB* to vary. In both cases, the r.m.s. residual error was significantly worse than when all of the parameters were refitted, thus indicating that the variation in *SFB* alone was unable to deal with the H_2-broadening. This again emphasises the fact that a set of fitted parameters, even when obtained with a physically based random band model, is simply that which optimises the fit to a particular set of measured transmittances.

7.3.4 Comparisons with the Results of Others

Band-modelling data for absorption by H_2-broadened CH_4 is far scarcer than that available for self-broadened CH_4. Only Silvaggio (1982) and Calcutt (1984) have attempted to determine the effect of H_2-broadening on CH_4 absorption using band-modelling methods. Silvaggio (1982) derived a value of 0.03 cm^{-1} $\pm$ 50% for the H_2-broadened Lorentz half-width at 1 atm and 273 K using the Goody-Voigt model to fit transmittances at 100 cm^{-1} intervals over 4100-4700 cm^{-1}. As he kept the self-broadened Lorentz half-width fixed at 0.085 cm^{-1}, this gives a value of 2.8 for *SFB*. Rather than directly fitting models to his H_2-broadened CH_4 spectra, Calcutt (1984) used the Goody-Lorentz fit to his self-broadened CH_4 spectra to extrapolate to the lower CH_4 abundances of the former. He then calculated the value of $\alpha_L(H_2)/\alpha_L(CH_4)$ required to obtain the measured H_2-broadened transmittance. This corresponds to a mean value of $1.4 \pm 20\%$ for *SFB*.

The CH_4-to-H_2 broadening ratio can of course be determined for a specific CH_4 line if both the self- and H_2-broadened line widths for that line are known. This was shown in §3.2.2, where the values listed in Table 3.1 varied between 1.11 and 1.29, with no systematic dependence on frequency. The self-to-foreign broadening ratio fitted by the Goody-Voigt model in the present study was plotted in Figure 7.24(e). It varies between extremes of 0.125×10^{-4} and 10.5, but lies predominantly in the range from 1 to 3. The most notable exceptions are the window regions, where *SFB* approaches 0. These low values are due to the fact that there is minimal absorption in the windows of the H_2-broadened spectra due to the smaller CH_4 abundances of these spectra (less than 78 m-amagat). Thus, as *SFB* tends toward 0, the expression for the transmittance (*e.g.*, Equation 7.8) tends toward the expression for the weak limit of absorption. The values between 1 and 3 obtained for *SFB* in the CH_4 bands encompass the range of values derived from the band-model and line data summarised above, although they are generally higher than the values listed in Table 3.1.

Having derived values for the self-broadened Lorentz half-width, α_L^0, from the fitted parameter α_L^0/α_D^0, the H_2-broadened Lorentz half-width is readily calculated from α_L^0 and *SFB*. The results of this calculation are seen in Figure 7.25. Due to the small values of *SFB* in the windows, the H_2-broadened Lorentz half-width has unrealistically high values in these regions. However, in the CH_4 bands, where the self-broadened Lorentz half-width varies between 0.019 and $\sim$0.15 cm^{-1}, the H_2-broadened Lorentz half-width varies between 0.0061 and $\sim$0.10 cm^{-1}.

7.4 Summary

In this chapter, the results of the band-modelling analysis of the experimental CH_4 spectra have been presented. The 108 self-broadened CH_4 spectra were fitted with four sequences of increasingly complex models, culminating in the Goody-Voigt, Malkmus-Voigt, Gibson-Pierluissi, and Smith models. The first two models gave the best fits to the spectra, generating an r.m.s. resid-

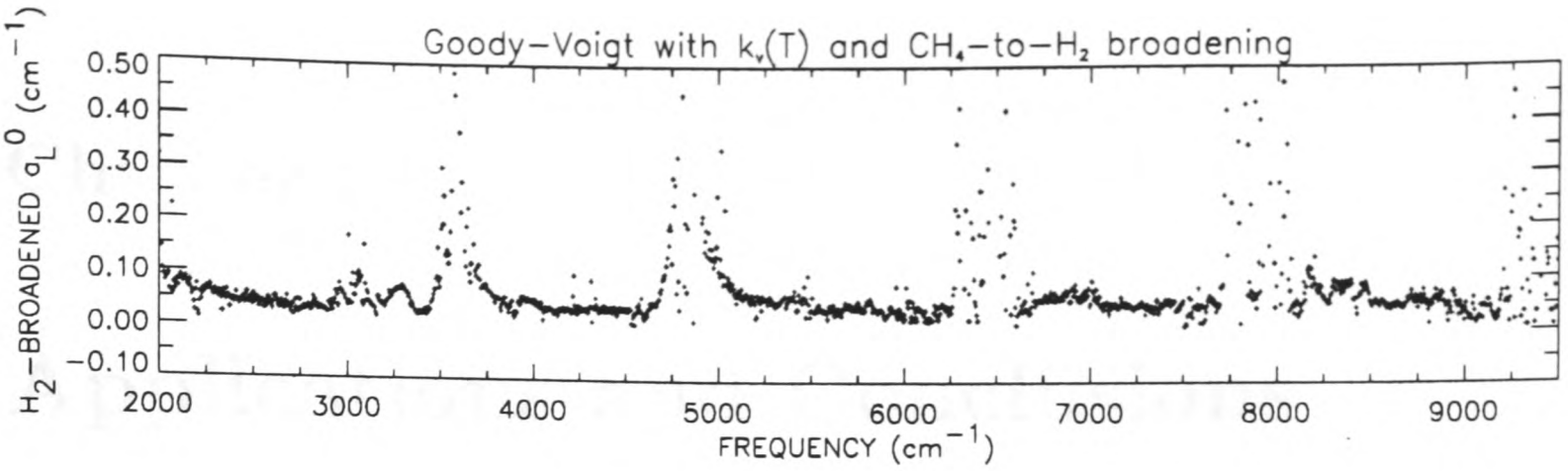

Figure 7.25: The H_2-broadened Lorentz half-width at 296 K and 1.01325 bar, as derived from the Goody-Voigt fit to all of the self- and H_2-broadened CH_4 spectra.

ual error between the fitted and measured transmittances which was less than 0.035 throughout 2000–9500 cm^{-1} and which generally lay between 0.005 and 0.02. This is of the same magnitude as the errors in the original spectra, and comparison of the fitted spectra with the measured spectra showed that the band models eliminated such features as the broad ice ripple, the ice absorption, and the 80 cm^{-1} channelling. The fitted parameters obtained with the Goody-Voigt and Malkmus-Voigt fits to the self-broadened CH_4 spectra have been plotted and discussed, although it has been noted that their physical interpretation should be treated with caution.

Having found that the best fits to the self-broadened CH_4 spectra were obtained with the physically based Goody-Voigt and Malkmus-Voigt band models, these were then used to fit the combined set of 225 self- and H_2-broadened CH_4 spectra. In this case, the Goody-Voigt model was better able to fit the 3000 cm^{-1} band, giving an r.m.s. residual error which was less than 0.04 from 2000 to 9500 cm^{-1}, and between 0.005 and 0.03 for all frequencies outside the 3000 and 4300 cm^{-1} bands, again consistent with the uncertainties in the measured transmittances. As a result, it is the fitted Goody-Voigt parameters which are listed in Appendices B and C.

Where possible, the quality of the fits and the values of the fitted parameters have been compared with data available in the literature. However, this study represents a significant advance on any previous work. In terms of spectral range and the combination of temperatures, pressures, and CH_4 abundances, it provides one of the most comprehesive set of self-broadened CH_4 band-model parameters currently available in the near-infrared. Furthermore, the band-model fits to the combined set of self- and H_2-broadened CH_4 spectra are the first such to be performed. It is these latter parameters, in particular, which should be of value to studies of the Jovian atmosphere and the retrieval of information from NIMS.

Chapter 8

Applications and Conclusions

8.1 Applications to Jupiter

The primary purpose of the work carried out for this thesis was to address the problem of how to obtain adequate atmospheric transmittance functions for use with the NIMS experiment on Galileo. Without knowledge of the transmittance properties of Jovian gases, NIMS would be unable to fulfill its goals of remote sounding of the temperature structure, composition, and cloud properties of Jupiter's atmosphere. In order to achieve the objective of this thesis, self- and H_2-broadened CH_4 spectra have been recorded over the near-infrared spectral range of the NIMS instrument (CH_4 being the dominant Jovian absorber in this region), and then fitted with band models.

To conclude the present study, the application of these new band-model fits to the problem of Jovian remote sounding is briefly considered, focussing on the usefulness of these models in the interpretation of data from NIMS. This includes an assessment of the reliability of extrapolating the band models to Jovian conditions, a calculation of the level sounded in the Jovian atmosphere as a function of wavelength, and a discussion of how the uncertainties in the transmittances derived from the band models will affect the retrieval of atmospheric parameters from NIMS spectra.

8.1.1 Extrapolation to Jovian Conditions

Extrapolation of the band models to Jovian conditions involves some extrapolation in temperature, pressure, and CH_4 abundance beyond the conditions that were achievable in the laboratory. In order to obtain an estimate of the probable errors introduced by this extrapolation, three comparisons were performed. In the first, the spectra generated with the Goody-Voigt model were compared to those generated with the Malkmus-Voigt model for a variety of Jovian paths. This provided a test of of the extent to which the physically based band models give reliable extrapolations. In the second, the spectra generated with the Goody-Voigt model were compared with synthetic line-by-line spectra generated for the same Jovian paths in those regions where

line data were available. This allowed an estimate of how well the best of the models compares to an exact calculation of transmittance under the conditions of interest. Finally, the Goody-Voigt model was extrapolated to the laboratory conditions of some very low-temperature CH_4 spectra available in the literature, allowing a comparison with laboratory data.

Ten Jovian paths were used in the extrapolations, selected from the Curtis-Godson paths to the top of the atmosphere from levels between 0.01 and 10.0 bar, which had been calculated previously from the Jovian models of Orton (1981) (see §6.1.1). Of the ten paths, one was chosen for having the lowest Curtis-Godson temperature of all five Jovian models (107 K, 0.010 bar, and 14.8 m-amagat of CH_4), one for having the highest Curtis-Godson pressure and CH_4 abundance of all five models (262 K, 5.0 bar, and 773 m-amagat), and one for having the lowest Curtis-Godson pressure and CH_4 abundance of all five models (142 K, 0.0050 bar, and 0.710 m-amagat). The remaining seven paths were chosen in logarithmic steps from 0.01 to 10.0 bar, from the nominal model.

In the first test of the reliability of the extrapolation of the Goody-Voigt model, both this and the fitted Malkmus-Voigt model were used to generate spectra over the entire 2000 to 9500 cm^{-1} range for these ten Jovian paths. The Malkmus-Voigt model was chosen for comparison because it is also physically based (and therefore more likely to be reliable when extrapolated), and because the fit with this model was of a similar quality to the fit with the Goody-Voigt model. For each path, both the difference between the transmittances predicted by the two models and the sum of the r.m.s. residual errors for the two fits were plotted as functions of frequency. For the spectra generated from the fits to the self-broadened CH_4 spectra, the agreement was generally excellent, being well within the sum of the fitting errors. The only exceptions to this were some points in the 3000 and 4300 cm^{-1} bands for the two lowest temperature paths, but for these points the differences between the predicted transmittances were still less than 0.08. For the spectra generated from the fits to the combined set of self- and H_2-broadened CH_4 spectra, the agreement between the Goody-Voigt and Malkmus-Voigt transmittances was again generally within the sum of the fitting errors. The only exceptions were a few points in the 3000 cm^{-1} region and in the region of H_2 absorption from 4900 to 5000 cm^{-1}, for which the difference between the predicted transmittances exceeded the sum of the fitting errors for several spectra, and the path with the highest pressure and CH_4 abundance, for which the difference in transmittance was as large as 0.15 in the window regions, although generally much smaller.

Thus, except for a few frequencies under the extremes of Jovian temperature and pressure, the transmittances obtained by extrapolating the Goody-Voigt and Malkmus-Voigt models agreed to within the sum of the fitting errors. However, although this calculation demonstrated consistency between the extrapolations of the two band models, it did not provide any external measure of their reliability. In order to address this question, the GENLN2 line-by-line program (see §3.3.4) was used to calculate synthetic spectra for all ten Jovian paths using CH_4 line

parameters listed in the HITRAN 1991 database (Rothman *et al.*, 1991). It should be noted that the Goody-Voigt model used in this test was that fitted to all of the self- and H_2-broadened CH_4 spectra, while the GENLN2 calculation used the self- and air-broadened half-widths listed in the HITRAN 1991 database. In general, air-broadened CH_4 lines have slightly smaller half-widths than H_2-broadened CH_4 lines (Fox and Jennings, 1990; Fox *et al.*, 1988, 1991) and so the GENLN2 spectra might be expected to slightly over-estimate the absorption at line centre.

Figure 8.1 shows both the Goody-Voigt and GENLN2 spectra calculated for the three extreme Jovian paths described above, over the 2000 to 6200 cm^{-1} region for which CH_4 line data were available. In (a), the weakly absorbing spectra generated for the smallest Curtis-Godson pressure and CH_4 abundance are plotted. In this case, the Goody-Voigt and GENLN2 spectra show good agreement, within 0.05 in transmittance in the 3000 and 5800 cm^{-1} bands and within 0.10 in the 4300 cm^{-1} band. The agreement is poorer for the spectra generated for the lowest temperature path (b), with the GENLN2 absorption being generally larger in the 3000 and 4300 cm^{-1} bands, and the Goody-Voigt absorption being larger in the 5800 cm^{-1} band. It is difficult to determine the extent to which these differences are due to errors in the HITRAN 1991 line data and/or to errors in the extrapolation of the band model. The spectra generated for the largest Curtis-Godson pressure and CH_4 abundance (c) can be compared only in the 2000 cm^{-1} window, where the transmittances again agree to within 0.10 or better, as all of the bands are saturated. Comparisons between the Goody-Voigt and GENLN2 spectra were also made for the seven other Jovian paths, yielding similar results: reasonably good agreement for the weakly absorbing spectra, poorest agreement for the lowest temperature (117.5 K) spectrum, and saturation for the strongly absorbing spectra.

It is also worth noting that Figure 8.1(c) once again demonstrates the inadequacies of the line data currently available for CH_4. Even the most recent complilation of CH_4 line parameters, HITRAN 1991, is completely lacking data in the weakly absorbing regions. Under conditions of high CH_4 abundance, for which the more strongly absorbing bands will be saturated, these regions of weaker absorption will be an important source of information about the Jovian atmosphere. In such cases, little or no information could be retrieved from NIMS using the HITRAN 1991 database, making the transmittance functions derived in the present study particularly valuable.

Unfortunately, there are few low-temperature or high-abundance CH_4 spectra available in the literature, and spectra with sufficient information on their laboratory conditions to allow comparison with the extrapolations of the band models are particularly scarce. One exception is the work of McKellar (1989), whose 77 K spectra were discussed in §4.3.2. The Goody-Voigt fit to the combined set of self- and H_2-broadened CH_4 spectra was used to calculate spectra for each of his three sets of laboratory conditions (66 m, 0.0013 bar CH_4, 0.604 bar N_2; 88 m, 0.0083 bar CH_4, 0.355 bar N_2; and 88 m, 0.0115 bar CH_4, 0.368 bar N_2), again assuming that H_2 and N_2-broadening are similar. For all three paths, the extrapolated spectra were found to

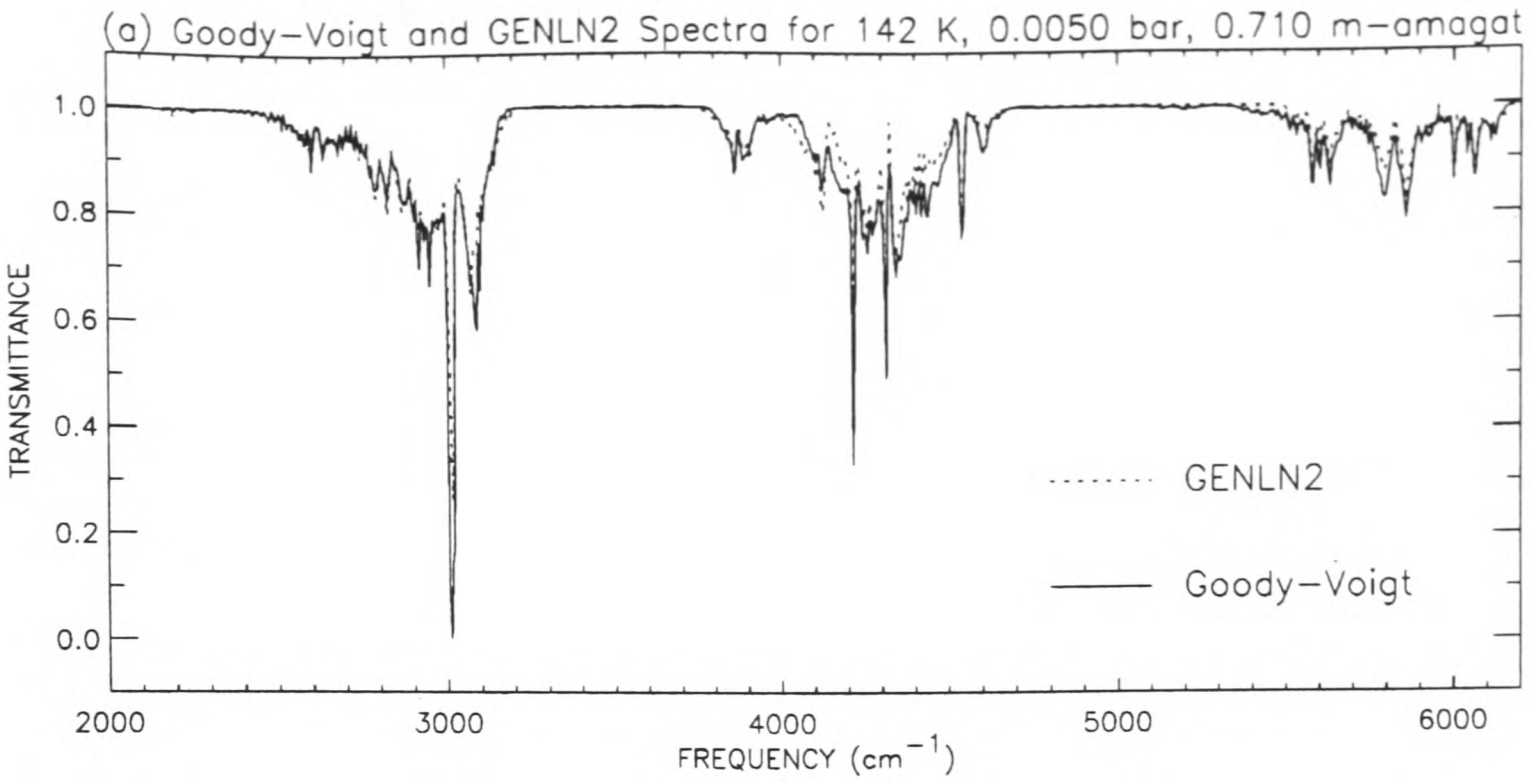

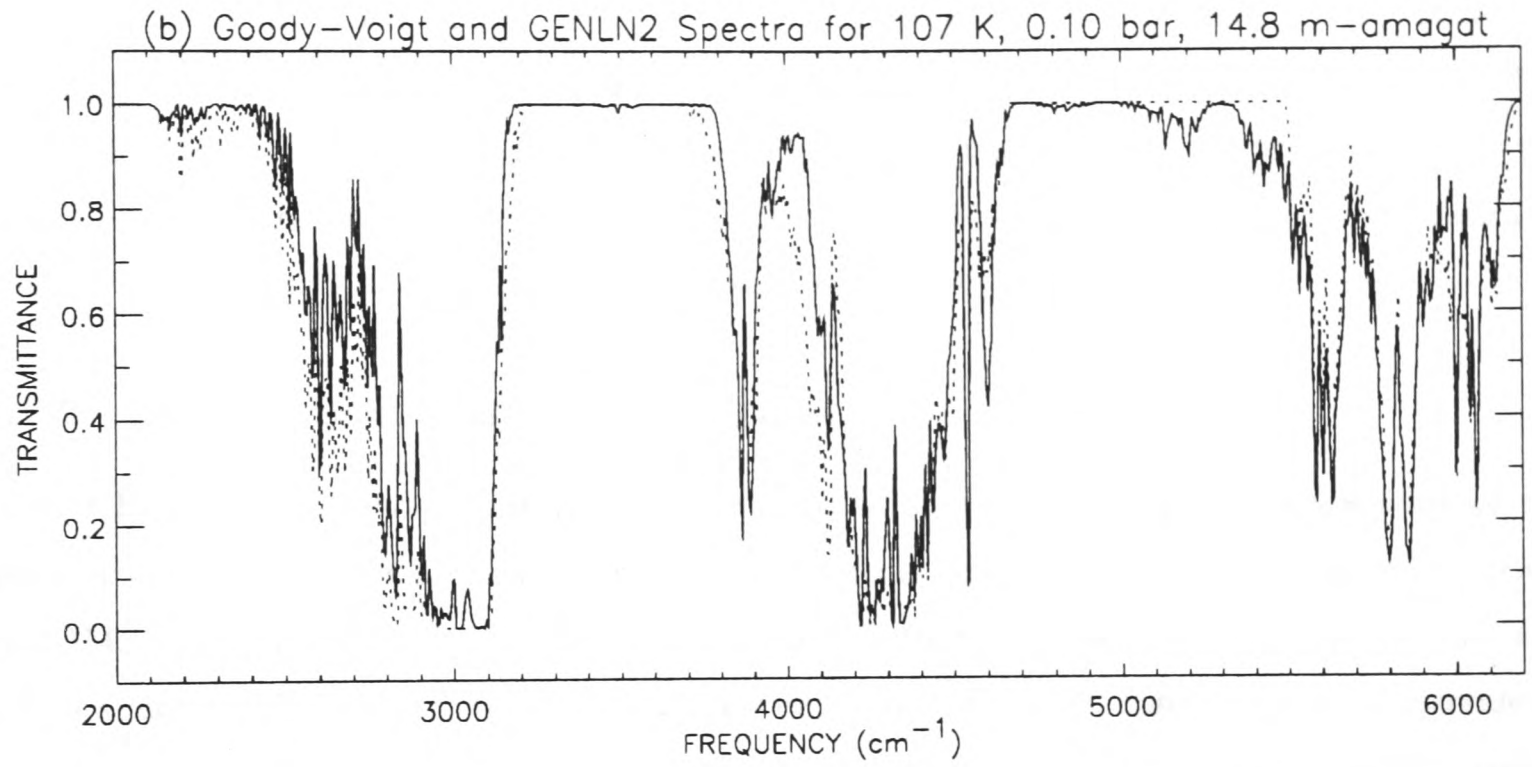

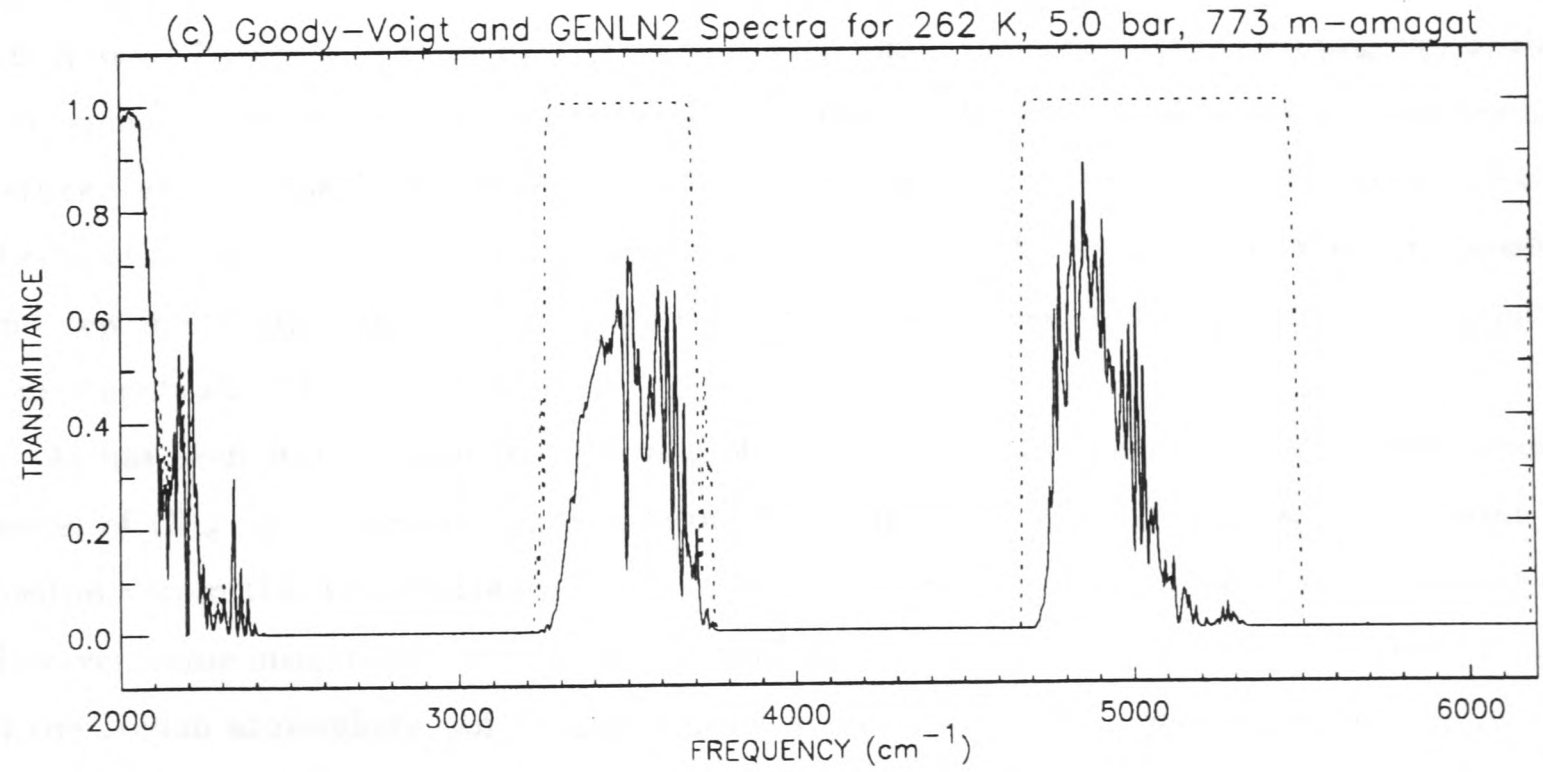

Figure 8.1: Synthetic spectra generated by extrapolating the Goody-Voigt model (that fitted to all of the measured CH_4 spectra) to three extreme Jovian paths, and by applying the GENLN2 line-by-line program to the CH_4 data in the HITRAN 1991 database. All spectra are at 10 cm^{-1} resolution.

under-estimate the absorptions measured by McKellar (1989). This is shown in Figure 8.2(a), in which the Goody-Voigt extrapolation has been superimposed on McKellar's 3800–4800 cm^{-1} spectrum at 10 cm^{-1} resolution (that for his first set of conditions). This figure also includes a line-by-line spectrum, generated using GENLN2 and the HITRAN 1991 database for the same set of conditions, which is seen to be in closer agreement with McKellar's spectrum. In addition to the extrapolation to 77 K, the Goody-Voigt model and GENLN2 were also used to generate synthetic spectra for the same CH_4 abundance and total pressure, but maintaining the temperature at 190 K, *i.e.*, avoiding extrapolation beyond the lowest laboratory temperature. These two spectra have been superimposed on McKellar's original spectrum in Figure 8.2(b). This 190 K Goody-Voigt spectrum is in good agreement with the 190 K GENLN2 spectrum, and provides a closer match to McKellar's original spectrum. These results suggest that the Goody-Voigt band model greatly over-estimates the temperature dependence of the transmittance at low temperatures, which in turn suggests that extrapolation of the band model should be undertaken with caution. While the extrapolation attempted here was very large — 113 K below the lowest laboratory temperature used to derive the model, and 30–40 K below the lowest temperature expected on Jupiter — it is clear that further measurements are desirable over the range from 110 to 190 K. This is discussed further in §8.3.

8.1.2 Remote Sounding Considerations

With CH_4 absorptions dominating the near-infrared spectrum of Jupiter, knowledge of the transmittance properties of CH_4 is a crucial first step in the interpretation of spectra recorded by NIMS. The Goody-Voigt band model which was fitted to the combined set of self- and H_2-broadened CH_4 spectra, thus covering a wide range of Jovian conditions, now provides a convenient means of calculating CH_4 transmittance over most of the NIMS spectral range. Analysis of NIMS spectra is likely to begin with simple models, approximating the Jovian atmosphere as clear (non-scattering) down to the level of the NH_3 cloud tops and in the regions between each of the NH_3, NH_4SH and H_2O cloud layers. In these reflecting-layer models, the band-model transmittances can readily be included in the equation of radiative transfer, and new information about cloud heights, temperature profiles, and the abundances of minor constituents should be retrievable.

As has been stated previously, the goal of the present study was to obtain a transmittance model of CH_4 for future use in interpreting NIMS spectra. The development of retrieval algorithms from this transmittance model is a task which lies outside the scope of this thesis. However, some insight into the usefulness of the fitted Goody-Voigt model for remote sounding of the Jovian atmosphere can be gained from a calculation of the optical depth, χ, of atmospheric CH_4, as a function of wavelength. Most of the information collected by a remote sensing instrument orginates from the level where χ is close to unity. For example, for a satellite instrument viewing vertically downwards, the total radiance $I(\nu)$ received at frequency ν due to

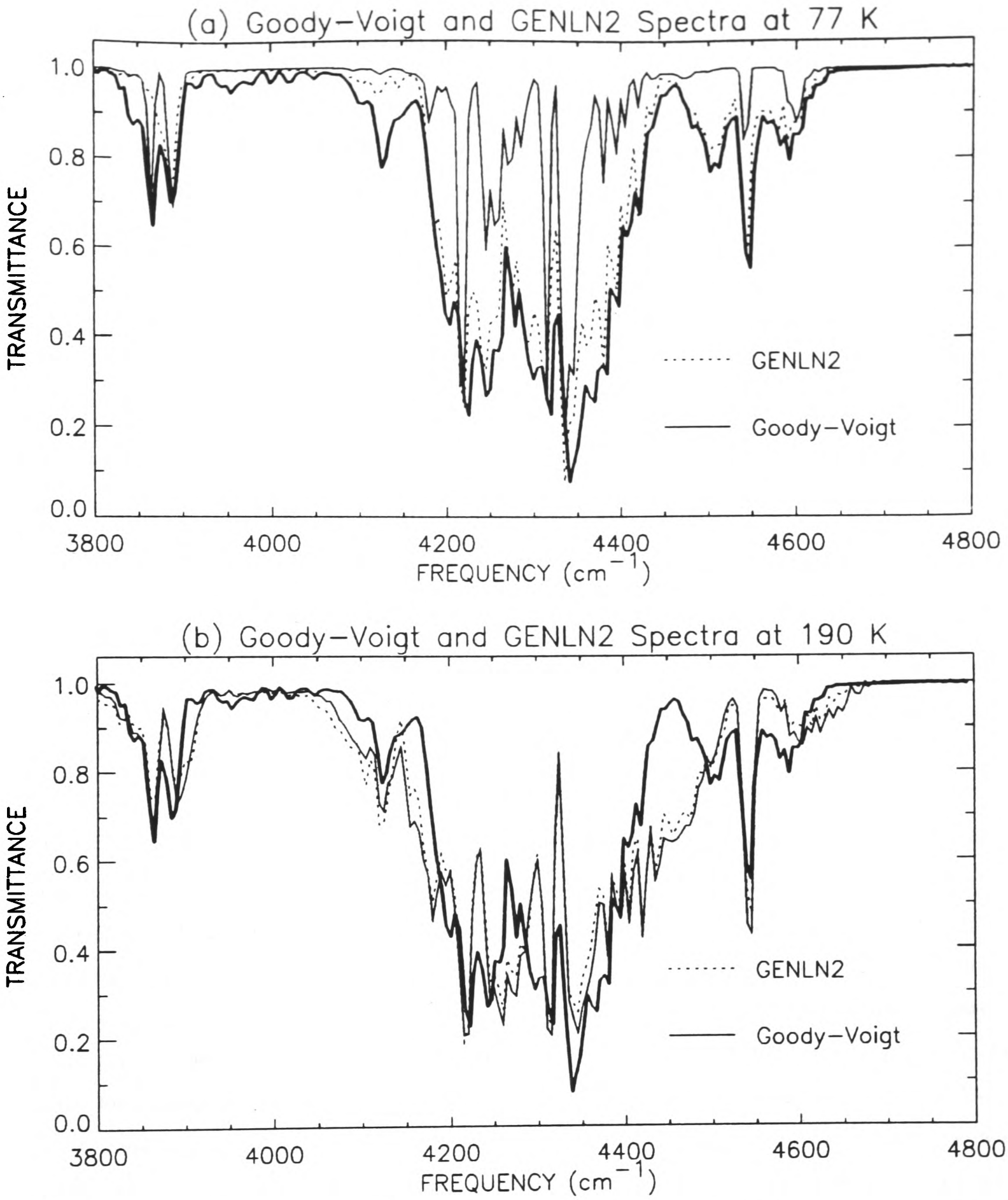

Figure 8.2: The laboratory spectrum (line in boldface) measured by McKellar (1989) at 77 K, 88 m, 0.0115 bar CH_4, and 0.368 bar N_2, along with spectra extrapolated to these conditions using the Goody-Voigt band model and the GENLN2 line-by-line program. In (a) the synthetic spectra have been generated using the correct temperature of 77 K. In (b), the synthetic spectra have been generated using a temperature of 190 K while leaving the total pressure and the CH_4 abundance unchanged.

emission from an absorbing gas in local thermodynamic equilibrium is given by (*e.g.*, Houghton, 1986, p.195; Houghton *et al.*, 1984, p.66)

$$I(\nu) = \int_0^\infty B(\nu,T)\frac{d}{dz}\tau(\nu, z = z:\infty)\,dz = \int_0^\infty B(\nu,T)\kappa(y)\,dy \qquad (8.1)$$

where T is the temperature at height z,

$B(\nu, T)$ is the Planck function for a layer at height z,

$\tau(\nu, z = z : \infty)$ is the transmittance between z and the top of the atmosphere, and

y is defined as $-\ln P$, P being the atmospheric pressure.

The function $\kappa(y) = \frac{d}{dy}\tau$ is known as the weighting function, effectively weighting the blackbody radiance received from each level in the atmosphere. Using Equation 3.14 and the hydrostatic equation, and assuming that the absorption coefficent and the density of the emitting gas are independent of height, it can be shown that the weighting function peaks at that pressure for which the optical depth, χ, to the top of the atmosphere is unity. The largest contribution to the measured radiance thus originates from this $\chi = 1$ level.

Calculation of the mean $\chi = 1$ level for CH_4, which is uniformly mixed in the Jovian atmosphere, will therefore indicate the importance of CH_4 in the determination of the depths to which NIMS will be able to probe. This calculation was performed by first using Orton's (1981) nominal Jovian atmospheric model to generate a fine grid of Curtis-Godson paths to the top of the atmosphere at 0.5 km intervals over the entire 100 to 10^{-11} bar profile. Then for each 10 cm^{-1} frequency interval, the Goody-Voigt fit to all of the measured spectra was used to compute transmittance for each Curtis-Godson path, thereby determining to the nearest 0.5 km, the level at which $\overline{\tau} = \exp(-1)$. The resulting profile of atmospheric height (and pressure) versus frequency was then degraded to NIMS resolution by convolving it with a triangle of full-width-half-maximum of 0.025 μm, and sampling every 0.0125 μm. The final NIMS-resolution profile is plotted on a wavelength scale in Figure 8.3.

From this figure, several interesting points emerge. Firstly, the peak of the weighting function varies significantly with wavelength, being located at pressures between 100 and 0.01 bar over 1 to 5 μm. In the absence of clouds or other absorbing gases, this suggests that CH_4 should be useful in temperature sounding over a height range of more than 300 km. The presence of NH_3 clouds near 0.3 bar, NH_4SH clouds near 2 bar, and H_2O clouds near 5 bar is likely to obscure the deeper levels, but it may be possible to sound to deeper levels through gaps in the clouds. Furthermore, the ability or inability to detect CH_4 at particular wavelengths should provide a means of determining cloud heights and locations. Figure 8.3 also reveals the windows in the CH_4 absorption, the spectral regions in which the concentrations of other minor constituents may be determined. The 5 μm window is obvious, allowing the detection of absorptions by GeH_4, PH_3, H_2O, CH_3D, H_2S, HCN, C_2H_2, C_2H_4, and C_2H_6. Additional windows are located at approximately 2.8, 2.0, 1.6, 1.3, and 1.1 μm. In these regions, the absorption of NH_3 becomes important, as NH_3 bands overlap the 2.8, 2.0, and 1.6 μm CH_4 windows. An analysis of the near-infrared spectral parameters of NH_3, similar to that performed for CH_4 in this work, clearly would be valuable.

The error budget for data retrieved from NIMS measurements will be determined by instrumental errors, assumptions made in the modelling and retrievals, and uncertainties in the knowledge of the transmittance properties of Jovian atmospheric gases. Of particular concern

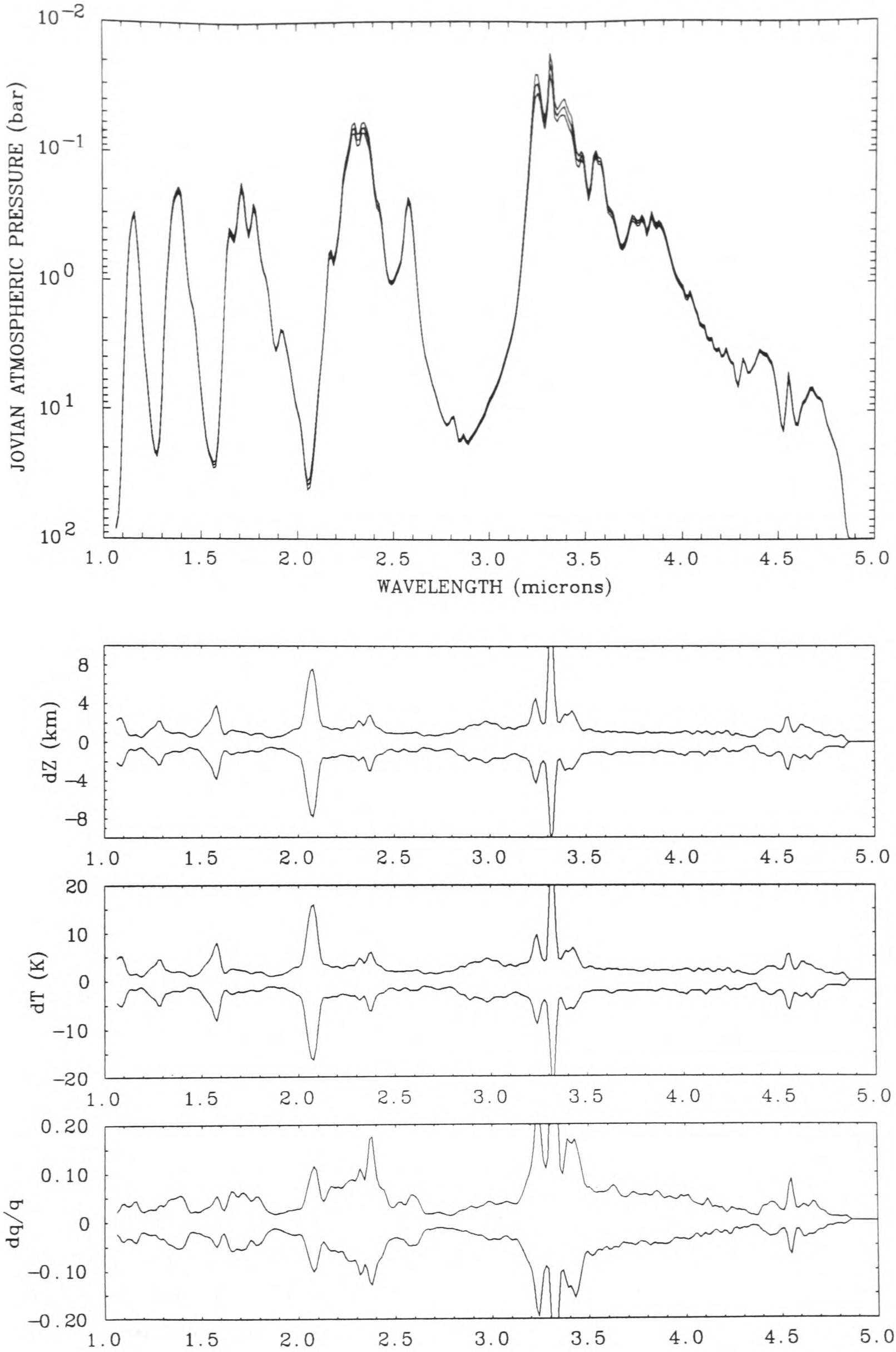

Figure 8.3: The upper plot shows the pressure of the Jovian atmospheric level for which the optical depth to the top of the atmosphere is unity, as calculated using the nominal model of Orton (1981) and the Goody-Voigt fit to all of the self- and H_2-broadened CH_4 spectra. Included in this plot are the levels for which $\overline{\tau} = \exp(-1) \pm \sigma$. The three lower plots show the uncertainties in height, temperature, and CH_4 mixing ratio which arise from the r.m.s. residual fitting errors, σ.

in the present study is how errors in the CH_4 transmittances calculated from the fitted Goody-Voigt model, quantified by the r.m.s. residual error σ, (Figure 7.19(e)) will affect the accuracy of the retrieved atmospheric parameters. The calculation of the mean $\chi = 1$ level, performed above, provides a means of estimating this accuracy. The plot of the $\chi = 1$ level in Figure 8.3 includes two curves for which $\overline{\tau}(\nu) = \exp(-1) \pm \sigma(\nu)$. In the three subsequent plots, these curves of the uncertainty in the $\chi = 1$ level have been translated into uncertainties in height, temperature, and CH_4 mixing ratio. The uncertainty in height, Δz, is simply derived from the atmospheric heights at which $\overline{\tau}(\nu) = \exp(-1) \pm \sigma(\nu)$. As expected, the largest values of Δz are for those wavelengths where σ is large: at $\sim$2.1 μm, where the original spectra were contaminated by H_2 absorption, and at $\sim$3.3 μm, where the spectra were contaminated by pump oil and ice absorption and there was some difficulty in fitting the sharp Q branch of the band. Elsewhere, $|\Delta z|$ is consistently less than 3 km, and is generally closer to 1 km, implying that the uncertainty in the cloud heights retrieved by NIMS due to uncertainties in CH_4 transmittance, will be of this order of magnitude. Considering the current poor understanding of Jovian cloud structure and the large variations in modelled cloud heights (see §1.4), such uncertainties should allow a significant improvement in the determination of the vertical cloud structure.

Below the tropopause, at about 0.1 bar, temperatures in the Jovian atmosphere are believed to follow an adiabatic gradient of 2.1 K/km (Lindal *et al.*, 1981; see §1.2.3). Assuming the CH_4 mixing ratio to be accurately known, and having calculated Δz, the uncertainty in tropospheric Jovian temperatures due to the r.m.s. residual error σ can be estimated as $\Delta T = \frac{dT}{dz}\Delta z$. This uncertainty in temperature has also been plotted in Figure 8.3, and aside from the 2.1 and 3.3 μm regions, $|\Delta T|$ is generally less than 6 K, but mostly closer to 2 K. These values are comparable to current uncertainties in the Jovian temperature profile. For example, according to Orton (1981), errors in the tropospheric temperature profile derived from Voyager include a direct measurement error of $\pm$2 K, and an error of $\pm$1.1 K due to compositional uncertainty. However, larger uncertainties exist in estimates of the temperature at the 1 bar level, which, with the adiabatic gradient, determines the vertical temperature profile. This temperature has been assigned values ranging from 153 to 170 K (Hunten *et al.*, 1980), with Lindal *et al.* (1981) deriving a value of 165 ± 5 K. Thus, uncertainties in the temperatures retrieved by NIMS due to uncertainties in CH_4 transmittance should still allow refinement of the Jovian temperature profile, as well as measurements of horizontal temperature variations.

The third uncertainty plotted in Figure 8.3 is the relative uncertainty in the CH_4 mixing ratio due to σ, in this case assuming the temperature profile to be accurately known. The maxima in $\Delta q/q$ are determined by maxima in σ and minima in the CH_4 abundance. At most wavelengths, $|\Delta q/q|$ is well below 0.10. This compares favourably with the relative uncertainties of 0.22, 0.16, 0.11 and 0.33 in the values of the CH_4 mixing ratio derived by Sato and Hansen (1979), Knacke *et al.* (1982), Gautier *et al.* (1982), and Bjoraker *et al.* (1986a) (see Table 1.3). Thus, the uncertainties in the band model CH_4 transmittance should also allow NIMS to improve

measurements of the Jovian CH_4 mixing ratio. It should also be noted that the accuracy of the cloud heights, temperatures, and mixing ratios can be further increased by sounding the same levels at different wavelengths, thereby narrowing down the range of allowable values for these parameters.

Although the interpretation of NIMS spectra is likely to begin with simple atmospheric models, more sophisticated analyses of NIMS spectra are certain to require the use of scattering models. For these, considering the lack of line data over the NIMS spectral range, some consideration should be given to determining how band-model transmittances can be incorporated into scattering calculations. One approach is to derive the probability distribution of photon paths in a scattering layer using Monte Carlo calculations or inverse Laplace transforms, although these methods appear to be computationally expensive (see McCleese, 1976, p.50–52, for a review). Another possibility is to use the "effective path length" approach of Taylor and McCleese (1977), whereby the atmosphere is treated as clear with layers for which the effective thickness in transmittance, reflection, and emission is calculated for each pair of incident and emergent directions. Alternatively, it may be possible to express the CH_4 transmittance in terms of parameters that can be included directly in scattering models, whether as a weighted sum of exponentials (Rodgers, 1966) as has been tried by McKay *et al.* (1989) and Giver *et al.* (1990), or using the more recently developed correlated-k method which uses cumulative distributions of the absorption coefficient (Goody *et al.*, 1989; West *et al.*, 1990). Investigation of these various methods is recommended in §8.3, below.

8.2 Summary

This thesis began with a review and discussion of our current understanding of the complex Jovian atmosphere. In Chapter 1, a brief overview of Jupiter was provided, followed by a more detailed discussion of the fundamental atmospheric parameters of thermal structure, chemical composition, and cloud layering. It was shown that many questions remain unresolved and that most parameters require refinement, particularly with regard to their spatial and temporal variability.

Although Earth-based observations have a role in deciphering and explaining the nature of the Jovian atmosphere, it is spacecraft observations which have made the most significant contributions to this task. Following the successful Pioneer and Voyager fly-by missions to Jupiter in the 1970's, the Galileo spacecraft is now on its way to this giant planet, scheduled to arrive in December, 1995. Consisting of both an orbiter which will be directed into orbit around Jupiter, and a probe which will be "dropped" into the atmosphere, Galileo will allow detailed investigation of the entire Jovian system.

One of instruments on the Galileo orbiter is NIMS, the Near-Infrared Mapping Spectrometer, a versatile instrument capable of both imaging and spectroscopy. NIMS is a grating spectrometer which will measure radiances over 0.7 to 5.2 μm (1923 to 14286 cm^{-1}) at 0.025

μm resolution. The design of NIMS and its atmospheric goals were described in Chapter 2. With this instrument, it will be possible to detect the many minor constituents which absorb radiation in the near-infrared, particularly those which have absorptions in the 5 μm window. The vertical temperature profile at depths from 1 to 5 bar should also be retreivable from observations of the 5 μm window. NIMS will use the near-infrared CH_4 bands to determine vertical cloud structure and cloud heights, while observations at different wavelengths and viewing angles should provide insight into the microphysical properties of clouds.

Accurate knowledge of the line parameters or broad-band spectral parameters of Jovian gases will be essential in order to make the most of the spectroscopic measurements of NIMS. In Chapter 3, the nature of the near-infrared spectrum of Jupiter was described. It was shown that, over the NIMS range, this spectrum divides conveniently into two regions. Below 4.5 μm, the Jovian spectrum consists of solar radiation reflected from the clouds and dominated by strong absorption bands of CH_4 and NH_3, while above 4.5 μm, thermal emission from deeper atmospheric layers, free of strong CH_4 or NH_3 absorptions, creates the 5 μm window. Figure 3.2 clearly illustrated the importance of CH_4 in determining the appearance of the near-infrared spectra of all of the outer planets.

This therefore led to an investigation of the availability of near-infrared line data for CH_4 on the HITRAN and GEISA databases which revealed a complete lack of such data above 6200 cm^{-1} (below 1.6 μm). The CH_4 line data that were available over 1800 to 6200 cm^{-1} were then used in the computation of line-by-line transmittance spectra for Curtis-Godson paths from each of the three Jovian cloud layers, at 0.32, 2.0, and 5.0 bar, up to the top of the Jovian atmosphere. These spectra provided confirmation of the strength of CH_4 absorptions under the conditions of temperature, pressure, and abundance encountered in the Jovian atmosphere. As expected, the strength of the absorptions increased with the depth in the atmosphere, completely saturating in the band centres for the path from 5.0 bar. Furthermore, as independent calculations were made for the line data on each database, it was found that weak lines listed on GEISA but absent from HITRAN, and unassigned lines listed on HITRAN but absent from GEISA all contributed significantly to the absorption. This suggested that untabulated weak line data in other regions of the NIMS spectral range will also generate measurable absorptions under Jovian conditions.

With CH_4 line data unavailable in the 6200 to 14386 cm^{-1} region of the NIMS window and omissions and uncertainties in the line data which is listed in the 1923 to 6200 cm^{-1} region, there is obviously a critical need for additional measurements of CH_4 spectral parameters. Although individual line parameters would be the most ideal form for such data, allowing the calculation of the monochromatic transmittance, the complexity of the near-infrared spectrum of CH_4 makes this an impossible task on the time-scale of the Galileo mission. However, for the purposes of NIMS, which is a low-resolution instrument (9.25 cm^{-1} at 1923 cm^{-1}, and 510 cm^{-1} at 14286 cm^{-1}), the monochromatic transmittance can be replaced by a broad-

band transmittance which is a well-defined function of temperature, pressure, and abundance. Accordingly, the present study aimed to measure laboratory spectra of CH_4 over the NIMS spectral region for the greatest possible range of Jovian conditions, and to then fit broad-band models to the measured transmittances.

Hence, the theoretical basis of band modelling was introduced in Chapter 4. This was followed by the derivation of the band models intended for use later in this work. Both random and empirical band models were discussed, and a method of fitting temperature dependence in the models was explained. Previous band-modelling studies of CH_4 were then reviewed, setting the scene for the measurements and modelling to follow. Although some work has been performed previously on both the visible (also included in the NIMS spectral range) and near-infrared spectrum of CH_4, it remains inadequate for the purpose of interpreting NIMS data. Particularly lacking are laboratory spectra and systematic band-model analyses of CH_4 transmittance under the low-temperature, high-abundance, H_2-broadened conditions relevant to Jupiter.

Clearly, there was a need for spectroscopic measurements of CH_4 under Jovian conditions which could be used to derive band models of transmittance for future application in interpreting NIMS observations. The practical considerations of performing low-temperature, long-pathlength, flammable-gas spectroscopy were described in Chapter 5. Using the Long White Cell at the RAL Laboratory Spectroscopy Facility, it was possible to achieve temperatures as low as 190 K and pathlengths as long as 512 m. A major part of the work performed for this thesis involved commissioning the Long White Cell and the facility for the required measurements. Considerable effort was necessary to make the system safe for an extended and intensive period of use with flammable gases, with the gas-handling system in particular, being designed and built specifically for this experiment. The cryogenic system was installed immediately prior to the start of the spectroscopic measurements, and another part of the experimental work involved testing and preparing this system before use. The subsequent low-temperature measurements were the first experiments to be conducted with this new cryogenic system.

Once the Long White Cell was fully operational, a Bomem Fourier transform spectrometer was used to record an extensive set of self- and H_2-broadened CH_4 spectra. In terms of frequency, temperature, pressure, and pathlength, the apparatus was pushed to its limits in order to obtain the greatest possible coverage of both the NIMS spectral range and Jovian conditions. Two light sources were used, the globar extending the spectral coverage down to 2000 cm^{-1} and the quartz-halogen bulb extending it up to 9500 cm^{-1}. The self-broadened CH_4 spectra were recorded at nominal temperatures of 190, 240, and 296 K, pathlengths of 64, 128, 256, 416 (for the 190 K spectra) and 512 m (for the 240 and 296 K spectra), and nine pressures between 0.2 and 700 torr. The H_2-broadened spectra were recorded at the same temperatures and pathlengths, using nominal CH_4 pressures of 0.2, 3.2, 12.8, and 102.4 torr and nominal H_2 pressures of 100, 245, and 600 torr. Details of these spectra were presented in Chapter 6,

where it was shown that the experimental conditions provided good coverage of the relevant Jovian pressures and CH_4 abundances, although they did not extend down to the lowest Jovian temperatures. However, the ranges of frequencies, temperatures, CH_4 and H_2 pressures, and CH_4 abundances achieved in this work make these spectra one of the most comprehensive data sets of this kind yet recorded, particularly with regard to the H_2-broadened spectra. A listing of the spectra was provided in Appendix A.

Chapter 6 continued with a discussion of the processing of the spectra that was conducted before the start of the band modelling. The method used to generate the final set of corrected, averaged, and degraded transmittance spectra was described. Each of the original intensity spectra was ratioed to an empty-cell background spectrum interpolated from the appropriate start- and end-of-day backgrounds, and scaled or ratioed to a fitted line in order to correct the 100% transmittance level. Then, the five spectra recorded for each source-temperature-pressure-pathlength combination were averaged to reduce random errors, producing a complete set of spectra at the original 0.25 cm^{-1} resolution. For the purposes of band modelling, these spectra were then degraded to 10 cm^{-1} resolution. Finally, before the start of the modelling, an assessment of the quality of the spectra was undertaken. Various factors were found to affect this quality, and where possible, an estimate of the resulting errors in transmittance was performed, as summarised in Table 6.7.

Chapter 7 dealt with the band-modelling analysis of the measured CH_4 spectra. The least squares method used in fitting the transmittances was described, and the fitted models and their parameters were summarised. The analysis began with the 108 self-broadened CH_4 spectra, which were fitted independently of the H_2-broadened spectra using four sequences of increasingly complex models. The parameters fitted by one model were used to initialise the parameters of the subsequent model, thereby optimising the initial values for each fit. All four sequences began with the simple one parameter Weak Limit model, followed by the same model with temperature dependence (added by giving the absorption coefficient the same temperature dependence as that of line strength and fitting the lower state energy). Then the Goody, Malkmus, Zachor-King/Gibson-Pierluissi, and Smith models, all with temperature dependence included, were used to obtain improved fits to the spectra.

This choice of two random band models, two generalised band models, and an empirical transmittance model allowed an assessment of which provided the best representation of the spectra. The quality of the fit for each frequency interval was quantified by the r.m.s. residual deviation, σ, between the fitted and measured transmittance for each set of laboratory conditions. The values obtained for σ were found to be comparable for the fits with the Goody-Voigt and Malkmus-Voigt models, and consistently better for these two models than for any of the others. Over most of the 2000 to 9500 cm^{-1} range, σ for the fits with the Goody-Voigt and Malkmus-Voigt models was between 0.005 and 0.02, comparable to the errors estimated in the original spectra and therefore considered acceptable. Slightly higher values of up to 0.035 were

obtained at the sharp edges of bands where the models appeared to have some difficulty dealing with the sudden changes in transmittance. Plots of the transmittance fitted by the Goody-Voigt model superimposed on the original transmittance spectra clearly showed that by finding the best fit to the 108 transmittances at each frequency, the band model was able to eliminate many of the flaws in the original data. The parameters that were fitted by the Goody-Voigt and Malkmus-Voigt models were also presented, but it was emphasised that the physical interpretation of these parameters should be treated carefully. The quality and the parameters of the band model fits to the self-broadened CH_4 were compared with previous band-modelling studies of CH_4, primarily revealing the scarcity of relevant data available for such comparisons.

Having found that the two random band models provided the best fits to self-broadened CH_4 spectra, these two models were used to fit all 225 of the self- and H_2-broadened CH_4 together. Again, sequences of models of increasing complexity were fitted, culminating in the Goody-Voigt and Malkmus-Voigt models, each including both temperature dependence and self-to-foreign broadening. For these two models, σ was comparable for all frequencies except the 3000 and 4300 cm^{-1} bands, where the Malkmus-Voigt model was unable to converge to a solution, having difficulty in dealing with the sharp Q branches, and with contamination by pump oil and ice absorption in the 3000 cm^{-1} band and by H_2 absorption in the 4300 cm^{-1} band. Better success was achieved by re-initialising the parameters of the Malkmus-Voigt model with the values obtained in the Malkmus-Voigt fit to the self-broadened CH_4 spectra, and then refitting to the combined set of self- and H_2-broadened CH_4 spectra. However, the Goody-Voigt model still provided a better fit in the 3000 cm^{-1} band, with σ being less than 0.04 throughout the 2000 to 9500 cm^{-1} spectral range, and between 0.005 and 0.03 for all frequencies outside the 3000 and 4300 cm^{-1} bands, values again similar to the measurement errors in the spectra. The parameters obtained with this Goody-Voigt fit were briefly discussed, and the value of the fitted self-to-foreign broadening ratio was compared to values available in the literature.

For the combined set of self- and H_2-broadened CH_4 spectra, the parameters fitted with Goody-Voigt model have been listed in Appendix C. In addition, for the use of those interested only in pure CH_4 absorption, the parameters fitted only to the self-broadened CH_4 spectra have been included in Appendix B — for consistency, it is again the Goody-Voigt parameters which have been listed.

8.3 Suggestions for Future Work

The present study has led to the characterisation of the broad-band transmittance of self- and H_2-broadened CH_4 as a function of temperature, pressure, and abundance over the spectral range from 2000 to 9500 cm^{-1}. The resulting band-model fits are now ready for use in the interpretation of NIMS spectra once they become available. Meanwhile, the work undertaken for this thesis provides the basis for recommending several areas of investigation during the period prior to the December, 1995 arrival of Galileo at Jupiter, investigations that will help

to maximise the return of information from NIMS. These are as follows.

1. The cryogenic system for the Long White Cell is currently limited to 190 K, the lowest temperature achieved in the present work, by the viscous behaviour of the halon cooling fluid at temperatures below this. Upgrading the system to handle a cooling fluid which retains its integrity down to the lowest Jovian temperatures (110 K at the tropopause) is clearly desirable. However, recognising the technical difficulties involved in achieving such extreme cooling of long paths, significant effort was put into overseeing the design and construction of a cooling jacket for the Short White Cell. This is intended to allow measurements at pressures as high as 5 bar and temperatures as low as 77 K. The portion of the Jovian regime covered by these conditions was illustrated in Figure 6.1. With this jacket, CH_4 spectra will be obtainable at the lowest Jovian temperatures and highest relevant pressures. A suite of spectrosocopic measurements of self- and H_2-broadened CH_4 spectra is therefore recommended, covering the same spectral range and at the same resolution as those measured in this work, and also covering the greatest possible range of temperatures, pressures, and pathlengths. Band modelling of these spectra, in combination with the spectra modelled in this work, would reduce the need for extrapolation of the models beyond the original laboratory conditions. This would then provide greater confidence in transmittances generated by the fitted band models.

2. Coverage of the visible region of the NIMS spectral range (9500 to 14286 cm^{-1}) was not possible during the measurements performed in this work. Although band modelling of this region was performed by Fink *et al.* (1977), it was done at room temperature. With a suitable choice of optical components, visible self- and H_2-broadened CH_4 spectra could be measured under the conditions identical to those achieved in the infrared in this work, allowing the temperature-dependent band modelling to be extended across the entire NIMS range.

3. Although not as dominant as CH_4, NH_3 is also a significant absorber in the near-infrared spectrum of Jupiter. The line data available for NH_3 are also poor, while knowledge of the transmittance properties of NH_3 will be important in the analysis of NIMS spectra. Low-resolution spectroscopy of NH_3 using the current LWC system, again over the greatest possible range of conditions, and again followed by band-modelling analysis, would be useful in characterising the near-infrared spectrum of this gas.

4. Scattering effects are likely to be significant in NIMS spectra of the Jovian atmosphere. The issue of reconciling band models with atmospheric scattering models should therefore be addressed. Several potential methods were mentioned in §8.1.2, and investigations of their feasibility might help to resolve a complex issue.

5. Considering the lack of line parameters for individual CH_4 lines over large regions of the near-infrared spectrum and the poor quality of the available weak line data, high-

resolution measurements could be profitably undertaken in many bands. Even where line data are available, the line widths listed are usually for air- or N_2-broadened CH_4, whereas it is H_2-broadened line widths that are relevant to Jupiter. The most useful measurements would probably be in the weak wings of bands which do not saturate under Jovian conditions and would not be contaminated by absorptions of NH_3 or H_2. These include both wings of the 8600 cm^{-1} band, the high frequency wing of the 7200 cm^{-1} band, and both wings of the 5600 cm^{-1} band.

Finally, the measurements and analysis performed for this thesis, although conducted primarily in support of the NIMS instrument, also have applications to other problems. They should be directly applicable to the interpretation of ground-based observations of Jupiter, such as those recently made by Moreno *et al.* (1991) in the regions from 1.4 to 2.4 and 2.9 to 4.1 μm. Furthermore, with CH_4 also dominating the near-infrared spectra of Saturn, Titan, Neptune, and Uranus, the long-pathlength CH_4 spectra recorded in this work should prove to be useful in interpreting observations of all of these planetary bodies. Indeed, Lellouch *et al.* (1991) and Coustenis *et al.* (1991) have already performed a preliminary analysis of the 1.1 μm window of Titan, using some of the original-resolution CH_4 spectra recorded in this work to identify approximately 95 new lines between 9050 and 9160 cm^{-1}. Griffith and Owen (1991) have also used CH_4 spectra from this work to demonstrate that CH_4 is the principal source of atmospheric opacity in the near-infrared spectrum of Titan. Further applications of the original-resolution CH_4 spectra to studies of Titan are currently under consideration, while Yelle (1991, personal communication) has suggested that the low-resolution band-model parameters may be of use in the analysis of CH_4 heating in the atmosphere of Neptune. In conclusion, given the importance of CH_4 in the atmospheres of Jupiter and all of the outer planets, the work conducted for this thesis provides a firm basis for gaining a better understanding of these complex and intriguing neighbours of our own planet.

Appendix A

The Measured Methane Spectra

Table A.1: The "296 K" quartz-halogen self-broadened CH_4 spectra and their measurement conditions.

SPECTRUM	T ± 1σ (K)	P (bar)	L (m)	U(mol/cm^2)	U(m · am)
QH01_296K	292.1 ± 0.2	0.0002884	64.75	4.631×10^{19}	0.01723
QH02_296K	291.2 ± 0.2	0.0002930	128.75	9.384×10^{19}	0.03492
QH03_296K	288.8 ± 0.3	0.0002888	256.75	1.860×10^{20}	0.06921
QH04_296K	291.8 ± 0.2	0.001177	64.75	1.892×10^{20}	0.07041
QH05_296K	293.1 ± 0.3	0.0002814	512.75	3.566×10^{20}	0.1327
QH06_296K	291.7 ± 0.2	0.001128	128.75	3.606×10^{20}	0.1342
QH07_296K	290.6 ± 0.2	0.004278	64.75	6.905×10^{20}	0.2570
QH08_296K	289.3 ± 0.3	0.001091	256.75	7.014×10^{20}	0.2610
QH09_296K	292.7 ± 0.2	0.001084	512.75	1.376×10^{21}	0.5119
QH10_296K	291.8 ± 0.2	0.004362	128.75	1.394×10^{21}	0.5188
QH11_296K	291.4 ± 0.3	0.01709	64.75	2.751×10^{21}	1.024
QH12_296K	289.8 ± 0.3	0.004304	256.75	2.762×10^{21}	1.028
QH13_296K	291.8 ± 0.2	0.01707	128.75	5.456×10^{21}	2.030
QH14_296K	292.4 ± 0.3	0.004320	512.75	5.487×10^{21}	2.042
QH15_296K	291.5 ± 0.2	0.06826	64.75	1.098×10^{22}	4.087
QH16_296K	289.3 ± 0.2	0.01712	256.75	1.101×10^{22}	4.096
QH17_296K	291.8 ± 0.1	0.01708	512.75	2.174×10^{22}	8.091
QH18_296K	291.1 ± 0.2	0.1353	64.75	2.180×10^{22}	8.113
QH19_296K	290.3 ± 0.2	0.06829	128.75	2.194×10^{22}	8.165
QH20_296K	292.4 ± 0.2	0.06833	256.75	4.346×10^{22}	16.17
QH21_296K	290.8 ± 0.2	0.1364	128.75	4.374×10^{22}	16.28
QH22_296K	291.4 ± 0.2	0.2730	64.75	4.394×10^{22}	16.35
QH23_296K	293.0 ± 0.2	0.1364	256.75	8.658×10^{22}	32.22
QH24_296K	292.3 ± 0.2	0.06831	512.75	8.680×10^{22}	32.30
QH25_296K	291.2 ± 0.2	0.2730	128.75	8.743×10^{22}	32.54
QH26_296K	291.2 ± 0.3	0.5461	64.75	8.796×10^{22}	32.73
QH27_296K	291.6 ± 0.1	0.9331	64.75	1.501×10^{23}	55.86
QH28_296K	291.1 ± 0.2	0.1365	512.75	1.742×10^{23}	64.82
QH29_296K	291.0 ± 0.2	0.2726	256.75	1.742×10^{23}	64.84
QH30_296K	291.6 ± 0.2	0.5464	128.75	1.748×10^{23}	65.04
QH31_296K	291.0 ± 0.2	0.9299	128.75	2.980×10^{23}	110.9
QH32_296K	291.9 ± 0.2	0.2730	512.75	3.474×10^{23}	129.3
QH33_296K	290.5 ± 0.2	0.5464	256.75	3.498×10^{23}	130.2
QH34_296K	291.6 ± 0.1	0.9329	256.75	5.950×10^{23}	221.4
QH35_296K	289.2 ± 0.2	0.5461	512.75	7.013×10^{23}	261.0
QH36_296K	291.3 ± 0.1	0.9327	512.75	1.189×10^{24}	442.6

Table A.2: The "296 K" globar self-broadened CH_4 spectra and their measurement conditions.

SPECTRUM	T ± 1σ (K)	P (bar)	L (m)	U(mol/cm^2)	U(m · am)
GL01_296K	291.8 ± 0.2	0.0002888	64.75	4.642×10^{19}	0.01728
GL02_296K	291.2 ± 0.2	0.0002944	128.75	9.429×10^{19}	0.03509
GL03_296K	288.8 ± 0.3	0.0002894	256.75	1.864×10^{20}	0.06936
GL04_296K	291.8 ± 0.2	0.001178	64.75	1.893×10^{20}	0.07047
GL05_296K	293.1 ± 0.3	0.0002821	512.75	3.575×10^{20}	0.1330
GL06_296K	291.7 ± 0.2	0.001130	128.75	3.613×10^{20}	0.1345
GL07_296K	290.6 ± 0.2	0.004280	64.75	6.908×10^{20}	0.2571
GL08_296K	289.3 ± 0.3	0.001092	256.75	7.020×10^{20}	0.2613
GL09_296K	292.7 ± 0.2	0.001085	512.75	1.377×10^{21}	0.5124
GL10_296K	291.8 ± 0.2	0.004366	128.75	1.395×10^{21}	0.5193
GL11_296K	291.4 ± 0.3	0.01711	64.75	2.754×10^{21}	1.025
GL12_296K	289.8 ± 0.3	0.004306	256.75	2.763×10^{21}	1.028
GL13_296K	291.8 ± 0.2	0.01708	128.75	5.459×10^{21}	2.032
GL14_296K	292.4 ± 0.3	0.004321	512.75	5.489×10^{21}	2.043
GL15_296K	291.5 ± 0.2	0.06829	64.75	1.099×10^{22}	4.089
GL16_296K	289.3 ± 0.2	0.01712	256.75	1.101×10^{22}	4.096
GL17_296K	291.8 ± 0.1	0.01709	512.75	2.175×10^{22}	8.096
GL18_296K	291.1 ± 0.2	0.1364	64.75	2.198×10^{22}	8.179
GL19_296K	290.3 ± 0.2	0.06829	128.75	2.194×10^{22}	8.165
GL20_296K	292.4 ± 0.2	0.06835	256.75	4.347×10^{22}	16.18
GL21_296K	290.8 ± 0.2	0.1364	128.75	4.374×10^{22}	16.28
GL22_296K	291.4 ± 0.2	0.2732	64.75	4.397×10^{22}	16.36
GL23_296K	293.0 ± 0.2	0.1365	256.75	8.664×10^{22}	32.24
GL24_296K	292.3 ± 0.2	0.06834	512.75	8.684×10^{22}	32.32
GL25_296K	291.2 ± 0.2	0.2732	128.75	8.750×10^{22}	32.56
GL26_296K	291.2 ± 0.3	0.5461	64.75	8.796×10^{22}	32.73
GL27_296K	291.6 ± 0.1	0.9332	64.75	1.051×10^{23}	55.86
GL28_296K	291.1 ± 0.2	0.1365	512.75	1.742×10^{23}	64.82
GL29_296K	291.0 ± 0.2	0.2728	256.75	1.743×10^{23}	64.89
GL30_296K	291.6 ± 0.2	0.5465	128.75	1.748×10^{23}	65.05
GL31_296K	291.0 ± 0.2	0.9299	128.75	2.980×10^{23}	110.9
GL32_296K	291.9 ± 0.2	0.2732	512.75	3.476×10^{23}	129.4
GL33_296K	290.5 ± 0.2	0.5464	256.75	3.498×10^{23}	130.2
GL34_296K	291.6 ± 0.1	0.9329	256.75	5.950×10^{23}	221.4
GL35_296K	289.2 ± 0.2	0.5461	512.75	7.013×10^{23}	261.0
GL36_296K	291.3 ± 0.1	0.9326	512.75	1.189×10^{24}	442.5

Table A.3: The "240 K" quarts-halogen self-broadened CH_4 spectra and their measurement conditions.

SPECTRUM	T ± 1σ (K)	P(bar)	± 1σ	L (m)	U(mol/cm²)	U(m · am)
QH01_240K	239.1 ± 0.6	0.0002772	± 0.06%	64.75	5.438×10^{19}	0.02024
QH02_240K	238.7 ± 0.6	0.0003032	± 0.04%	128.75	1.185×10^{20}	0.04409
QH03_240K	238.9 ± 0.6	0.0002934	± 0.04%	256.75	2.284×10^{20}	0.08500
QH04_240K	240.0 ± 0.9	0.001294	± 0.04%	64.75	2.529×10^{20}	0.09411
QH05_240K	239.3 ± 1.0	0.001085	± 0.04%	128.75	4.228×10^{20}	0.1574
QH06_240K	239.3 ± 0.6	0.0002938	± 0.05%	512.75	4.560×10^{20}	0.1697
QH07_240K	239.6 ± 0.9	0.001114	± 0.04%	256.75	8.647×10^{20}	0.3218
QH08_240K	240.9 ± 1.2	0.004649	± 0.04%	64.75	9.051×10^{20}	0.3369
QH09_240K	240.1 ± 1.3	0.004289	± 0.04%	128.75	1.666×10^{21}	0.6200
QH10_240K	240.2 ± 0.9	0.001115	± 0.06%	512.75	1.724×10^{21}	0.6416
QH11_240K	240.4 ± 1.3	0.004312	± 0.04%	256.75	3.336×10^{21}	1.241
QH12_240K	241.7 ± 1.3	0.01751	± 0.04%	64.75	3.398×10^{21}	1.265
QH13_240K	240.9 ± 1.5	0.01728	± 0.04%	128.75	6.690×10^{21}	2.490
QH14_240K	241.1 ± 1.2	0.004485	± 0.05%	512.75	6.909×10^{21}	2.571
QH15_240K	242.7 ± 1.3	0.06837	± 0.05%	64.75	1.321×10^{22}	4.917
QH16_240K	241.1 ± 1.4	0.01721	± 0.06%	256.75	1.328×10^{22}	4.941
QH17_240K	242.1 ± 1.4	0.01712	± 0.06%	512.75	2.626×10^{22}	9.775
QH18_240K	241.7 ± 1.5	0.06851	± 0.04%	128.75	2.643×10^{22}	9.838
QH19_240K	239.5 ± 0.7	0.1369	± 0.04%	64.75	2.681×10^{22}	9.977
QH20_240K	241.9 ± 1.3	0.06850	± 0.04%	256.75	5.266×10^{22}	19.60
QH21_240K	239.3 ± 0.7	0.1361	± 0.18%	128.75	5.304×10^{22}	19.74
QH22_240K	240.6 ± 0.8	0.2737	± 0.06%	64.75	5.335×10^{22}	19.86
QH23_240K	243.3 ± 1.4	0.06851	± 0.04%	512.75	1.046×10^{23}	38.92
QH24_240K	242.2 ± 0.8	0.5466	± 0.08%	64.75	1.058×10^{23}	39.39
QH25_240K	240.2 ± 0.8	0.2732	± 0.04%	128.75	1.061×10^{23}	39.48
QH26_240K	239.3 ± 0.6	0.1369	± 0.04%	256.75	1.064×10^{23}	39.60
QH27_240K	244.5 ± 0.6	0.9354	± 0.14%	64.75	1.794×10^{23}	66.78
QH28_240K	241.6 ± 0.8	0.5469	± 0.06%	128.75	2.111×10^{23}	78.57
QH29_240K	239.6 ± 0.8	0.1365	± 0.05%	512.75	2.116×10^{23}	78.75
QH30_240K	240.3 ± 0.7	0.2738	± 0.05%	256.75	2.119×10^{23}	78.86
QH31_240K	243.6 ± 0.7	0.9361	± 0.16%	128.75	3.584×10^{23}	133.4
QH32_240K	241.5 ± 0.9	0.2734	± 0.05%	512.75	4.205×10^{23}	156.5
QH33_240K	241.7 ± 0.7	0.5468	± 0.07%	256.75	4.207×10^{23}	156.6
QH34_240K	243.8 ± 0.7	0.9351	± 0.10%	256.75	7.133×10^{23}	265.5
QH35_240K	243.0 ± 0.8	0.5470	± 0.07%	512.75	8.361×10^{23}	311.1
QH36_240K	245.1 ± 0.7	0.9358	± 0.08%	512.75	1.418×10^{24}	527.8

Table A.4: The "240 K" globar self-broadened CH_4 spectra and their measurement conditions.

SPECTRUM	T ± 1σ (K)	P(bar)	± 1σ	L (m)	U(mol/cm²)	U(m · am)
GL01_240K	239.6 ± 0.8	0.0002777	± 0.04%	64.75	5.436×10^{19}	0.02023
GL02_240K	238.9 ± 0.8	0.0003036	± 0.04%	128.75	1.185×10^{20}	0.04411
GL03_240K	239.2 ± 0.7	0.0002938	± 0.02%	256.75	2.284×10^{20}	0.08501
GL04_240K	240.4 ± 1.0	0.001296	± 0.03%	64.75	2.528×10^{20}	0.09410
GL05_240K	239.6 ± 1.1	0.001086	± 0.03%	128.75	4.227×10^{20}	0.1573
GL06_240K	239.6 ± 0.8	0.0002942	± 0.05%	512.75	4.560×10^{20}	0.1697
GL07_240K	239.9 ± 1.0	0.001115	± 0.03%	256.75	8.644×10^{20}	0.3217
GL08_240K	241.2 ± 1.3	0.004654	± 0.03%	64.75	9.050×10^{20}	0.3368
GL09_240K	240.4 ± 1.5	0.004296	± 0.03%	128.75	1.667×10^{21}	0.6202
GL10_240K	240.6 ± 1.0	0.001117	± 0.04%	512.75	1.724×10^{21}	0.6417
GL11_240K	240.7 ± 1.4	0.004316	± 0.03%	256.75	3.335×10^{21}	1.241
GL12_240K	242.0 ± 1.4	0.01752	± 0.03%	64.75	3.396×10^{21}	1.264
GL13_240K	241.2 ± 1.6	0.01729	± 0.03%	128.75	6.685×10^{21}	2.488
GL14_240K	241.5 ± 1.3	0.004492	± 0.03%	512.75	6.908×10^{21}	2.571
GL15_240K	243.0 ± 1.3	0.06846	± 0.03%	64.75	1.321×10^{22}	4.918
GL16_240K	241.4 ± 1.5	0.01724	± 0.04%	256.75	1.328×10^{22}	4.943
GL17_240K	242.4 ± 1.4	0.01715	± 0.04%	512.75	2.628×10^{22}	9.780
GL18_240K	242.0 ± 1.5	0.06861	± 0.03%	128.75	2.644×10^{22}	9.840
GL19_240K	239.7 ± 0.8	0.1371	± 0.04%	64.75	2.683×10^{22}	9.984
GL20_240K	242.2 ± 1.3	0.06858	± 0.03%	256.75	5.266×10^{22}	19.60
GL21_240K	239.5 ± 0.7	0.1369	± 0.15%	128.75	5.331×10^{22}	19.84
GL22_240K	241.0 ± 0.8	0.2741	± 0.04%	64.75	5.334×10^{22}	19.85
GL23_240K	243.6 ± 1.4	0.06859	± 0.04%	512.75	1.046×10^{23}	38.92
GL24_240K	242.8 ± 0.7	0.5481	± 0.06%	64.75	1.059×10^{23}	39.40
GL25_240K	240.5 ± 0.8	0.2736	± 0.04%	128.75	1.061×10^{23}	39.48
GL26_240K	239.4 ± 0.7	0.1371	± 0.03%	256.75	1.065×10^{23}	39.64
GL27_240K	245.6 ± 0.7	0.9395	± 0.11%	64.75	1.794×10^{23}	66.77
GL28_240K	242.0 ± 0.8	0.5478	± 0.05%	128.75	2.111×10^{23}	78.57
GL29_240K	239.9 ± 0.8	0.1368	± 0.04%	512.75	2.118×10^{23}	78.82
GL30_240K	240.6 ± 0.7	0.2740	± 0.04%	256.75	2.118×10^{23}	78.82
GL31_240K	244.8 ± 0.7	0.9406	± 0.12%	128.75	3.583×10^{23}	133.4
GL32_240K	241.9 ± 0.9	0.2738	± 0.04%	512.75	4.204×10^{23}	156.5
GL33_240K	242.3 ± 0.7	0.5480	± 0.05%	256.75	4.206×10^{23}	156.5
GL34_240K	244.7 ± 0.7	0.9381	± 0.12%	256.75	7.130×10^{23}	265.3
GL35_240K	243.6 ± 0.8	0.5481	± 0.05%	512.75	8.357×10^{23}	311.0
GL36_240K	245.9 ± 0.7	0.9381	± 0.06%	512.75	1.417×10^{24}	527.3

Table A.5: The "190 K" quarts-halogen self-broadened CH_4 spectra and their measurement conditions.

SPECTRUM	T ± 1σ (K)	P(bar)	± 1σ	L (m)	U(mol/cm^2)	U(m · am)
QH01_190K	189.7 ± 1.6	0.0003238	± 0.08%	64.75	8.006×10^{19}	0.02979
QH02_190K	189.9 ± 1.6	0.0003129	± 0.08%	128.75	1.537×10^{20}	0.05719
QH03_190K	190.2 ± 1.7	0.0002680	± 0.10%	256.75	2.621×10^{20}	0.09753
QH04_190K	190.9 ± 2.3	0.001070	± 0.08%	64.75	2.629×10^{20}	0.09784
QH05_190K	191.2 ± 1.9	0.0002986	± 0.09%	416.75	4.714×10^{20}	0.1755
QH06_190K	191.0 ± 2.1	0.001077	± 0.08%	128.75	5.259×10^{20}	0.1957
QH07_190K	192.1 ± 2.9	0.004332	± 0.13%	64.75	1.058×10^{21}	0.3936
QH08_190K	191.3 ± 2.3	0.001089	± 0.08%	256.75	1.059×10^{21}	0.3940
QH09_190K	192.5 ± 2.4	0.001137	± 0.09%	416.75	1.783×10^{21}	0.6636
QH10_190K	192.3 ± 2.8	0.004368	± 0.09%	128.75	2.118×10^{21}	0.7884
QH11_190K	193.5 ± 3.1	0.01717	± 0.10%	64.75	4.162×10^{21}	1.549
QH12_190K	192.6 ± 3.0	0.004492	± 0.08%	256.75	4.338×10^{21}	1.614
QH13_190K	194.0 ± 2.9	0.004537	± 0.07%	416.75	7.060×10^{21}	2.627
QH14_190K	193.5 ± 2.9	0.01720	± 0.10%	128.75	8.290×10^{21}	3.085
QH15_190K	193.9 ± 3.1	0.01711	± 0.10%	256.75	1.641×10^{22}	6.108
QH16_190K	194.9 ± 2.8	0.06859	± 0.09%	64.75	1.651×10^{22}	6.143
QH17_190K	195.6 ± 3.0	0.01727	± 0.09%	416.75	2.665×10^{22}	9.919
QH18_190K	191.4 ± 1.9	0.06838	± 0.09%	128.75	3.332×10^{22}	12.40
QH19_190K	191.6 ± 1.7	0.1370	± 0.11%	64.75	3.354×10^{22}	12.48
QH20_190K	195.5 ± 2.9	0.06845	± 0.09%	256.75	6.512×10^{22}	24.23
QH21_190K	194.0 ± 1.9	0.2738	± 0.11%	64.75	6.619×10^{22}	24.64
QH22_190K	193.2 ± 1.9	0.1373	± 0.11%	128.75	6.628×10^{22}	24.67
QH23_190K	197.6 ± 2.9	0.06865	± 0.09%	416.75	1.049×10^{23}	39.03
QH24_190K	195.6 ± 1.8	0.2736	± 0.13%	128.75	1.305×10^{23}	48.55
QH25_190K	196.9 ± 2.3	0.5497	± 0.18%	64.75	1.309×10^{23}	48.73
QH26_190K	191.2 ± 1.6	0.1370	± 0.10%	256.75	1.333×10^{23}	49.59
QH27_190K	191.8 ± 1.7	0.1369	± 0.12%	416.75	2.155×10^{23}	80.19
QH28_190K	202.1 ± 1.7	0.9331	± 0.27%	64.75	2.165×10^{23}	80.59
QH29_190K	198.7 ± 1.6	0.5474	± 0.16%	128.75	2.569×10^{23}	95.62
QH30_190K	193.5 ± 1.5	0.2738	± 0.24%	256.75	2.632×10^{23}	97.94
QH31_190K	196.7 ± 1.7	0.2740	± 0.37%	416.75	4.205×10^{23}	156.5
QH32_190K	202.4 ± 1.4	0.9334	± 0.20%	128.75	4.301×10^{23}	160.1
QH33_190K	196.9 ± 1.4	0.5469	± 0.20%	256.75	5.166×10^{23}	192.2
QH34_190K	201.2 ± 1.5	0.5476	± 0.20%	416.75	8.216×10^{23}	305.8
QH35_190K	201.7 ± 1.3	0.9374	± 0.25%	256.75	8.643×10^{23}	321.7
QH36_190K	206.0 ± 1.4	0.9361	± 0.22%	416.75	1.372×10^{24}	510.5

Table A.6: The "190 K" globar self-broadened CH_4 spectra and their measurement conditions.

SPECTRUM	T ± 1σ (K)	P(bar)	± 1σ	L (m)	U(mol/cm^2)	U(m · am)
GL01_190K	190.2 ± 1.8	0.0003248	± 0.08%	64.75	8.009×10^{19}	0.02981
GL02_190K	190.3 ± 1.8	0.0003137	± 0.07%	128.75	1.537×10^{20}	0.05721
GL03_190K	190.6 ± 1.9	0.0002686	± 0.08%	256.75	2.621×10^{20}	0.09754
GL04_190K	191.4 ± 2.5	0.001073	± 0.06%	64.75	2.629×10^{20}	0.09785
GL05_190K	191.7 ± 2.0	0.0002994	± 0.09%	416.75	4.715×10^{20}	0.1755
GL06_190K	191.5 ± 2.4	0.001080	± 0.06%	128.75	5.260×10^{20}	0.1957
GL07_190K	192.7 ± 3.2	0.004352	± 0.11%	64.75	1.059×10^{21}	0.3942
GL08_190K	191.8 ± 2.6	0.001091	± 0.06%	256.75	1.063×10^{21}	0.3958
GL09_190K	193.1 ± 2.6	0.001140	± 0.07%	416.75	1.782×10^{21}	0.6633
GL10_190K	192.8 ± 3.0	0.004380	± 0.07%	128.75	2.119×10^{21}	0.7885
GL11_190K	193.9 ± 3.2	0.01720	± 0.07%	64.75	4.160×10^{21}	1.548
GL12_190K	193.1 ± 3.2	0.004504	± 0.06%	256.75	4.338×10^{21}	1.614
GL13_190K	194.5 ± 3.0	0.004548	± 0.07%	416.75	7.059×10^{21}	2.627
GL14_190K	194.0 ± 3.0	0.01725	± 0.06%	128.75	8.292×10^{21}	3.086
GL15_190K	194.4 ± 3.2	0.01715	± 0.06%	256.75	1.641×10^{22}	6.106
GL16_190K	195.4 ± 2.8	0.06878	± 0.07%	64.75	1.651×10^{22}	6.144
GL17_190K	196.2 ± 3.1	0.01732	± 0.06%	416.75	2.665×10^{22}	9.918
GL18_190K	191.9 ± 1.9	0.06857	± 0.07%	128.75	3.332×10^{22}	12.40
GL19_190K	192.2 ± 1.7	0.1374	± 0.09%	64.75	3.353×10^{22}	12.48
GL20_190K	196.0 ± 2.9	0.06863	± 0.07%	256.75	6.512×10^{22}	24.24
GL21_190K	194.9 ± 1.7	0.2750	± 0.09%	64.75	6.618×10^{22}	24.63
GL22_190K	194.0 ± 1.9	0.1378	± 0.09%	128.75	6.624×10^{22}	24.65
GL23_190K	198.2 ± 2.9	0.06885	± 0.08%	416.75	1.049×10^{23}	39.03
GL24_190K	196.4 ± 1.9	0.2746	± 0.12%	128.75	1.304×10^{23}	48.53
GL25_190K	198.5 ± 2.1	0.5532	± 0.14%	64.75	1.307×10^{23}	48.65
GL26_190K	191.8 ± 1.6	0.1361	± 0.08%	256.75	1.320×10^{23}	49.11
GL27_190K	192.8 ± 1.7	0.1377	± 0.10%	416.75	2.156×10^{23}	80.24
GL28_190K	204.0 ± 1.5	0.9410	± 0.21%	64.75	2.163×10^{23}	80.52
GL29_190K	199.7 ± 1.6	0.5501	± 0.13%	128.75	2.569×10^{23}	95.61
GL30_190K	194.7 ± 1.5	0.2754	± 0.12%	256.75	2.631×10^{23}	97.90
GL31_190K	198.3 ± 1.6	0.2760	± 0.12%	416.75	4.202×10^{23}	156.4
GL32_190K	203.7 ± 1.4	0.9391	± 0.15%	128.75	4.300×10^{23}	160.0
GL33_190K	198.2 ± 1.3	0.5504	± 0.16%	256.75	5.165×10^{23}	192.2
GL34_190K	202.7 ± 1.5	0.5514	± 0.16%	416.75	8.212×10^{23}	305.6
GL35_190K	203.9 ± 1.3	0.9477	± 0.19%	256.75	8.644×10^{23}	321.7
GL36_190K	207.5 ± 1.4	0.9429	± 0.18%	416.75	1.372×10^{24}	510.5

Table A.7: The "296 K" quarts-halogen H_2-broadened CH_4 spectra and their measurement conditions.

SPECTRUM	T ± 1σ (K)	P_{total}(bar)	P_{CH_4}/P_{total}	L (m)	U(mol/cm^2)	U(m · am)
QH01_H296K	289.4 ± 0.2	0.1336	2.003×10^{-3}	64.75	4.337×10^{19}	0.01614
QH02_H296K	291.4 ± 0.2	0.3270	8.828×10^{-4}	64.75	4.646×10^{19}	0.01729
QH03_H296K	292.2 ± 0.2	0.8002	3.659×10^{-4}	64.75	4.700×10^{19}	0.01749
QH04_H296K	291.5 ± 0.2	0.1337	2.343×10^{-3}	128.75	1.002×10^{20}	0.03730
QH05_H296K	292.0 ± 0.2	0.3274	9.570×10^{-4}	128.75	1.001×10^{20}	0.03724
QH06_H296K	291.7 ± 0.2	0.8005	3.915×10^{-4}	128.75	1.002×10^{20}	0.03729
QH07_H296K	291.4 ± 0.2	0.1341	2.209×10^{-3}	256.75	1.891×10^{20}	0.07036
QH08_H296K	290.1 ± 0.2	0.3271	8.616×10^{-4}	256.75	1.807×10^{20}	0.06724
QH09_H296K	291.8 ± 0.2	0.8013	3.453×10^{-4}	256.75	1.764×10^{20}	0.06565
QH10_H296K	288.4 ± 0.3	0.1339	2.197×10^{-3}	512.75	3.789×10^{20}	0.1410
QH11_H296K	288.2 ± 0.3	0.3272	8.996×10^{-4}	512.75	3.793×10^{20}	0.1412
QH12_H296K	288.0 ± 0.2	0.8002	3.681×10^{-4}	512.75	3.799×10^{20}	0.1414
QH13_H296K	289.4 ± 0.2	0.1378	3.097×10^{-2}	64.75	6.916×10^{20}	0.2574
QH14_H296K	291.7 ± 0.2	0.3310	1.241×10^{-2}	64.75	6.605×10^{20}	0.2458
QH15_H296K	292.6 ± 0.2	0.8045	5.304×10^{-3}	64.75	6.841×10^{20}	0.2546
QH16_H296K	291.2 ± 0.2	0.1379	3.295×10^{-2}	128.75	1.455×10^{21}	0.5416
QH17_H296K	291.6 ± 0.2	0.3317	1.371×10^{-2}	128.75	1.454×10^{21}	0.5413
QH18_H296K	290.7 ± 0.2	0.8047	5.648×10^{-3}	128.75	1.458×10^{21}	0.5426
QH19_H296K	292.1 ± 0.2	0.1382	3.207×10^{-2}	256.75	2.822×10^{21}	1.050
QH20_H296K	290.3 ± 0.2	0.1507	1.134×10^{-1}	64.75	2.761×10^{21}	1.028
QH21_H296K	290.8 ± 0.2	0.3309	1.257×10^{-2}	256.75	2.660×10^{21}	0.9900
QH22_H296K	291.6 ± 0.2	0.3437	4.849×10^{-2}	64.75	2.681×10^{21}	0.9976
QH23_H296K	292.2 ± 0.2	0.8059	5.394×10^{-3}	256.75	2.767×10^{21}	1.030
QH24_H296K	292.1 ± 0.2	0.8180	2.116×10^{-2}	64.75	2.779×10^{21}	1.034
QH25_H296K	288.0 ± 0.3	0.1379	3.136×10^{-2}	512.75	5.577×10^{21}	2.076
QH26_H296K	289.4 ± 0.2	0.1515	1.127×10^{-1}	128.75	5.502×10^{21}	2.048
QH27_H296K	288.5 ± 0.3	0.3311	1.307×10^{-2}	512.75	5.571×10^{21}	2.073
QH28_H296K	290.4 ± 0.2	0.3440	4.961×10^{-2}	128.75	5.481×10^{21}	2.040
QH29_H296K	289.0 ± 0.3	0.8042	5.381×10^{-3}	512.75	5.561×10^{21}	2.070
QH30_H296K	290.2 ± 0.2	0.8174	2.088×10^{-2}	128.75	5.485×10^{21}	2.041
QH31_H296K	291.5 ± 0.2	0.1511	1.131×10^{-1}	256.75	1.090×10^{22}	4.058
QH32_H296K	290.6 ± 0.2	0.3440	4.931×10^{-2}	256.75	1.086×10^{22}	4.040
QH33_H296K	292.1 ± 0.2	0.8190	2.077×10^{-2}	256.75	1.083×10^{22}	4.031
QH34_H296K	288.3 ± 0.2	0.1509	1.139×10^{-1}	512.75	2.214×10^{22}	8.241
QH35_H296K	290.2 ± 0.2	0.2700	5.051×10^{-1}	64.75	2.204×10^{22}	8.203
QH36_H296K	288.5 ± 0.2	0.3442	4.992×10^{-2}	512.75	2.212×10^{22}	8.232
QH37_H296K	291.2 ± 0.2	0.4630	2.934×10^{-1}	64.75	2.188×10^{22}	8.143
QH38_H296K	289.0 ± 0.3	0.8170	2.103×10^{-2}	512.75	2.208×10^{22}	8.218
QH39_H296K	291.5 ± 0.2	0.9370	1.454×10^{-1}	64.75	2.192×10^{22}	8.158
QH40_H296K	289.2 ± 0.2	0.2700	5.058×10^{-1}	128.75	4.404×10^{22}	16.39
QH41_H296K	288.5 ± 0.2	0.4634	2.951×10^{-1}	128.75	4.421×10^{22}	16.45
QH42_H296K	288.5 ± 0.2	0.9365	1.460×10^{-1}	128.75	4.420×10^{22}	16.45
QH43_H296K	291.1 ± 0.2	0.2706	5.049×10^{-1}	256.75	8.729×10^{22}	32.49
QH44_H296K	290.6 ± 0.2	0.4637	2.945×10^{-1}	256.75	8.740×10^{22}	32.53
QH45_H296K	291.6 ± 0.2	0.9391	1.457×10^{-1}	256.75	8.726×10^{22}	32.47
QH46_H296K	289.4 ± 0.2	0.2700	5.057×10^{-1}	512.75	1.752×10^{23}	65.21
QH47_H296K	290.0 ± 0.2	0.4632	2.950×10^{-1}	512.75	1.750×10^{23}	65.13
QH48_H296K	291.2 ± 0.2	0.5397	5.057×10^{-1}	256.75	1.743×10^{23}	64.87
QH49_H296K	290.5 ± 0.2	0.9363	1.459×10^{-1}	512.75	1.747×10^{23}	65.00

Table A.8: The "296 K" globar H_2-broadened CH_4 spectra and their measurement conditions.

SPECTRUM	T ± 1σ (K)	P_{total}(bar)	P_{CH_4}/P_{total}	L (m)	U(mol/cm^2)	U(m · am)
GL01_H296K	289.4 ± 0.2	0.1337	2.003×10^{-3}	64.75	4.340×10^{19}	0.01615
GL02_H296K	291.4 ± 0.2	0.3271	8.828×10^{-4}	64.75	4.648×10^{19}	0.01730
GL03_H296K	292.2 ± 0.2	0.8003	3.659×10^{-4}	64.75	4.700×10^{19}	0.01749
GL04_H296K	291.5 ± 0.2	0.1337	2.343×10^{-3}	128.75	1.002×10^{20}	0.03730
GL05_H296K	292.0 ± 0.2	0.3275	9.570×10^{-4}	128.75	1.001×10^{20}	0.03725
GL06_H296K	291.7 ± 0.2	0.8006	3.915×10^{-4}	128.75	1.002×10^{20}	0.03729
GL07_H296K	291.4 ± 0.2	0.1341	2.209×10^{-3}	256.75	1.891×10^{20}	0.07036
GL08_H296K	290.1 ± 0.2	0.3271	8.616×10^{-4}	256.75	1.807×10^{20}	0.06724
GL09_H296K	291.8 ± 0.2	0.8015	3.453×10^{-4}	256.75	1.763×10^{20}	0.06563
GL10_H296K	288.4 ± 0.3	0.1340	2.197×10^{-3}	512.75	3.791×10^{20}	0.1411
GL11_H296K	288.2 ± 0.3	0.3273	8.996×10^{-4}	512.75	3.795×10^{20}	0.1412
GL12_H296K	288.0 ± 0.2	0.8002	3.681×10^{-4}	512.75	3.799×10^{20}	0.1414
GL13_H296K	289.4 ± 0.2	0.1379	3.097×10^{-2}	64.75	6.921×10^{20}	0.2576
GL14_H296K	291.7 ± 0.2	0.3311	1.241×10^{-2}	64.75	6.607×10^{20}	0.2459
GL15_H296K	292.6 ± 0.2	0.8047	5.304×10^{-3}	64.75	6.842×10^{20}	0.2546
GL16_H296K	291.2 ± 0.2	0.1379	3.295×10^{-2}	128.75	1.455×10^{21}	0.5416
GL17_H296K	291.6 ± 0.2	0.3318	1.371×10^{-2}	128.75	1.455×10^{21}	0.5414
GL18_H296K	290.7 ± 0.2	0.8049	5.648×10^{-3}	128.75	1.458×10^{21}	0.5428
GL19_H296K	292.1 ± 0.2	0.1383	3.207×10^{-2}	256.75	2.824×10^{21}	1.051
GL20_H296K	290.3 ± 0.2	0.1508	1.134×10^{-1}	64.75	2.763×10^{21}	1.028
GL21_H296K	290.8 ± 0.2	0.3310	1.257×10^{-2}	256.75	2.661×10^{21}	0.9903
GL22_H296K	291.6 ± 0.2	0.3438	4.849×10^{-2}	64.75	2.681×10^{21}	0.9979
GL23_H296K	292.2 ± 0.2	0.8061	5.394×10^{-3}	256.75	2.767×10^{21}	1.030
GL24_H296K	292.1 ± 0.2	0.8181	2.116×10^{-2}	64.75	2.780×10^{21}	1.034
GL25_H296K	288.0 ± 0.3	0.1379	3.136×10^{-2}	512.75	5.577×10^{21}	2.076
GL26_H296K	289.4 ± 0.2	0.1515	1.127×10^{-1}	128.75	5.502×10^{21}	2.048
GL27_H296K	288.5 ± 0.3	0.3312	1.307×10^{-2}	512.75	5.573×10^{21}	2.074
GL28_H296K	290.4 ± 0.2	0.3440	4.961×10^{-2}	128.75	5.481×10^{21}	2.040
GL29_H296K	289.0 ± 0.3	0.8042	5.381×10^{-3}	512.75	5.561×10^{21}	2.070
GL30_H296K	290.2 ± 0.2	0.8174	2.088×10^{-2}	128.75	5.485×10^{21}	2.041
GL31_H296K	291.5 ± 0.2	0.1511	1.131×10^{-1}	256.75	1.090×10^{22}	4.058
GL32_H296K	290.6 ± 0.2	0.3441	4.931×10^{-2}	256.75	1.086×10^{22}	4.041
GL33_H296K	292.1 ± 0.2	0.8192	2.077×10^{-2}	256.75	1.083×10^{22}	4.032
GL34_H296K	288.3 ± 0.2	0.1509	1.139×10^{-1}	512.75	2.214×10^{22}	8.241
GL35_H296K	290.2 ± 0.2	0.2700	5.051×10^{-1}	64.75	2.204×10^{22}	8.203
GL36_H296K	288.5 ± 0.2	0.3444	4.992×10^{-2}	512.75	2.213×10^{22}	8.237
GL37_H296K	291.2 ± 0.2	0.4630	2.934×10^{-1}	64.75	2.188×10^{22}	8.143
GL38_H296K	289.0 ± 0.3	0.8170	2.103×10^{-2}	512.75	2.208×10^{22}	8.218
GL39_H296K	291.5 ± 0.2	0.9367	1.454×10^{-1}	64.75	2.191×10^{22}	8.155
GL40_H296K	289.2 ± 0.2	0.2703	5.058×10^{-1}	128.75	4.409×10^{22}	16.41
GL41_H296K	288.5 ± 0.2	0.4635	2.951×10^{-1}	128.75	4.422×10^{22}	16.46
GL42_H296K	288.5 ± 0.2	0.9363	1.460×10^{-1}	128.75	4.419×10^{22}	16.45
GL43_H296K	291.1 ± 0.2	0.2706	5.049×10^{-1}	256.75	8.729×10^{22}	32.49
GL44_H296K	290.6 ± 0.2	0.4637	2.945×10^{-1}	256.75	8.740×10^{22}	32.53
GL45_H296K	291.6 ± 0.2	0.9390	1.457×10^{-1}	256.75	8.727×10^{22}	32.48
GL46_H296K	289.4 ± 0.2	0.2700	5.057×10^{-1}	512.75	1.752×10^{23}	65.21
GL47_H296K	290.0 ± 0.2	0.4632	2.950×10^{-1}	512.75	1.750×10^{23}	65.13
GL48_H296K	291.2 ± 0.2	0.5397	5.057×10^{-1}	256.75	1.743×10^{23}	64.87
GL49_H296K	290.5 ± 0.2	0.9360	1.459×10^{-1}	512.75	1.746×10^{23}	64.98

Table A.9: The "240 K" quartz-halogen H_2-broadened CH_4 spectra and their measurement conditions.

SPECTRUM	T ± 1σ (K)	P_{total}(bar) ± 1σ	P_{CH_4}/P_{total}	L (m)	U(mol/cm^2)	U(m · am)
QH01_H240K	239.4 ± 0.8	0.1338 ± 0.05%	2.041×10^{-3}	64.75	5.350×10^{19}	0.01991
QH02_H240K	240.3 ± 0.6	0.8014 ± 0.11%	3.644×10^{-4}	64.75	5.700×10^{19}	0.02121
QH03_H240K	239.2 ± 0.7	0.3277 ± 0.06%	9.911×10^{-4}	64.75	6.368×10^{19}	0.02370
QH04_H240K	240.3 ± 0.6	0.8031 ± 0.10%	3.386×10^{-4}	256.75	2.105×10^{20}	0.07832
QH05_H240K	239.3 ± 0.6	0.3269 ± 0.08%	8.576×10^{-4}	256.75	2.179×10^{20}	0.08109
QH06_H240K	239.1 ± 0.7	0.1341 ± 0.05%	2.131×10^{-3}	256.75	2.223×10^{20}	0.08272
QH07_H240K	240.6 ± 0.7	0.8033 ± 0.12%	3.362×10^{-4}	512.75	4.169×10^{20}	0.1552
QH08_H240K	239.4 ± 0.8	0.1338 ± 0.05%	2.051×10^{-3}	512.75	4.257×10^{20}	0.1584
QH09_H240K	239.7 ± 0.7	0.3280 ± 0.06%	9.260×10^{-4}	512.75	4.706×10^{20}	0.1751
QH10_H240K	242.7 ± 0.9	0.8143 ± 0.26%	4.974×10^{-3}	64.75	7.827×10^{20}	0.2913
QH11_H240K	240.2 ± 0.9	0.3330 ± 0.06%	1.303×10^{-2}	64.75	8.472×10^{20}	0.3153
QH12_H240K	240.3 ± 1.0	0.1386 ± 0.06%	3.265×10^{-2}	64.75	8.832×10^{20}	0.3287
QH13_H240K	247.3 ± 1.0	0.8419 ± 0.28%	1.950×10^{-2}	64.75	3.114×10^{21}	1.159
QH14_H240K	240.0 ± 1.0	0.1386 ± 0.06%	3.083×10^{-2}	256.75	3.311×10^{21}	1.232
QH15_H240K	241.6 ± 1.1	0.3476 ± 0.09%	4.918×10^{-2}	64.75	3.319×10^{21}	1.235
QH16_H240K	240.8 ± 0.8	0.3329 ± 0.10%	1.293×10^{-2}	256.75	3.324×10^{21}	1.237
QH17_H240K	242.6 ± 0.8	0.8142 ± 0.15%	5.325×10^{-3}	256.75	3.324×10^{21}	1.237
QH18_H240K	241.6 ± 1.1	0.1520 ± 0.07%	1.133×10^{-1}	64.75	3.343×10^{21}	1.244
QH19_H240K	244.3 ± 1.0	0.8186 ± 0.09%	5.174×10^{-3}	512.75	6.439×10^{21}	2.396
QH20_H240K	240.5 ± 1.0	0.1385 ± 0.09%	3.176×10^{-2}	512.75	6.793×10^{21}	2.528
QH21_H240K	241.1 ± 0.9	0.3342 ± 0.10%	1.363×10^{-2}	512.75	7.017×10^{21}	2.612
QH22_H240K	242.6 ± 1.0	0.3478 ± 0.10%	4.859×10^{-2}	256.75	1.296×10^{22}	4.821
QH23_H240K	241.3 ± 1.1	0.1521 ± 0.07%	1.128×10^{-1}	256.75	1.322×10^{22}	4.921
QH24_H240K	244.9 ± 1.0	0.8342 ± 0.08%	2.006×10^{-2}	256.75	1.271×10^{22}	4.729
QH25_H240K	251.6 ± 1.1	0.9717 ± 0.16%	1.330×10^{-1}	64.75	2.409×10^{22}	8.966
QH26_H240K	246.1 ± 1.1	0.8369 ± 0.11%	2.009×10^{-2}	512.75	2.537×10^{22}	9.443
QH27_H240K	242.8 ± 1.1	0.3485 ± 0.11%	4.770×10^{-2}	512.75	2.543×10^{22}	9.464
QH28_H240K	243.7 ± 1.2	0.4692 ± 0.09%	2.910×10^{-1}	64.75	2.628×10^{22}	9.780
QH29_H240K	242.1 ± 1.2	0.1521 ± 0.07%	1.128×10^{-1}	512.75	2.632×10^{22}	9.796
QH30_H240K	243.3 ± 1.0	0.2729 ± 0.08%	5.039×10^{-1}	64.75	2.651×10^{22}	9.866
QH31_H240K	246.6 ± 1.1	0.9573 ± 0.06%	1.411×10^{-1}	256.75	1.019×10^{23}	37.91
QH32_H240K	244.8 ± 1.2	0.4696 ± 0.06%	2.899×10^{-1}	256.75	1.034×10^{23}	38.49
QH33_H240K	243.1 ± 1.1	0.2724 ± 0.08%	5.018×10^{-1}	256.75	1.046×10^{23}	38.92
QH34_H240K	248.3 ± 1.2	0.9621 ± 0.07%	1.402×10^{-1}	512.75	2.018×10^{23}	75.09
QH35_H240K	244.7 ± 1.3	0.4700 ± 0.06%	2.896×10^{-1}	512.75	2.066×10^{23}	76.89
QH36_H240K	243.9 ± 1.0	0.2728 ± 0.08%	5.023×10^{-1}	512.75	2.087×10^{23}	77.66

Table A.10: The "240 K" globar H_2-broadened CH_4 spectra and their measurement conditions.

SPECTRUM	T ± 1σ (K)	P_{total}(bar) ± 1σ	P_{CH_4}/P_{total}	L (m)	U(mol/cm^2)	U(m · am)
GL01_H240K	239.7 ± 0.9	0.1341 ± 0.04%	2.041×10^{-3}	64.75	5.355×10^{19}	0.01993
GL02_H240K	241.1 ± 0.6	0.8041 ± 0.09%	3.644×10^{-4}	64.75	5.700×10^{19}	0.02121
GL03_H240K	239.5 ± 0.7	0.3282 ± 0.05%	9.911×10^{-4}	64.75	6.370×10^{19}	0.02371
GL04_H240K	241.2 ± 0.7	0.8058 ± 0.08%	3.386×10^{-4}	256.75	2.104×10^{20}	0.07829
GL05_H240K	239.9 ± 0.7	0.3277 ± 0.05%	8.576×10^{-4}	256.75	2.179×10^{20}	0.08108
GL06_H240K	239.5 ± 0.8	0.1343 ± 0.04%	2.131×10^{-3}	256.75	2.222×10^{20}	0.08271
GL07_H240K	243.2 ± 0.7	0.8113 ± 0.09%	3.362×10^{-4}	512.75	4.166×10^{20}	0.1550
GL08_H240K	239.8 ± 0.9	0.1341 ± 0.04%	2.051×10^{-3}	512.75	4.260×10^{20}	0.1585
GL09_H240K	240.1 ± 0.8	0.3286 ± 0.05%	9.260×10^{-4}	512.75	4.707×10^{20}	0.1752
GL10_H240K	245.1 ± 0.9	0.8207 ± 0.20%	4.974×10^{-3}	64.75	7.812×10^{20}	0.2907
GL11_H240K	240.8 ± 0.9	0.3338 ± 0.06%	1.303×10^{-2}	64.75	8.472×10^{20}	0.3153
GL12_H240K	240.8 ± 1.1	0.1389 ± 0.05%	3.265×10^{-2}	64.75	8.833×10^{20}	0.3287
GL13_H240K	249.3 ± 1.0	0.8493 ± 0.22%	1.950×10^{-2}	64.75	3.116×10^{21}	1.160
GL14_H240K	240.5 ± 1.1	0.1388 ± 0.05%	3.083×10^{-2}	256.75	3.309×10^{21}	1.232
GL15_H240K	242.4 ± 1.1	0.3485 ± 0.06%	4.918×10^{-2}	64.75	3.316×10^{21}	1.234
GL16_H240K	241.6 ± 0.9	0.3338 ± 0.08%	1.293×10^{-2}	256.75	3.322×10^{21}	1.236
GL17_H240K	243.8 ± 0.7	0.8179 ± 0.12%	5.325×10^{-3}	256.75	3.322×10^{21}	1.236
GL18_H240K	242.2 ± 1.2	0.1523 ± 0.06%	1.133×10^{-1}	64.75	3.342×10^{21}	1.244
GL19_H240K	245.0 ± 0.8	0.8209 ± 0.07%	5.174×10^{-3}	512.75	6.439×10^{21}	2.396
GL20_H240K	241.1 ± 1.1	0.1389 ± 0.05%	3.176×10^{-2}	512.75	6.796×10^{21}	2.529
GL21_H240K	241.9 ± 0.9	0.3353 ± 0.08%	1.363×10^{-2}	512.75	7.017×10^{21}	2.611
GL22_H240K	243.6 ± 1.0	0.3489 ± 0.10%	4.859×10^{-2}	256.75	1.294×10^{22}	4.817
GL23_H240K	241.9 ± 1.2	0.1524 ± 0.07%	1.128×10^{-1}	256.75	1.322×10^{22}	4.919
GL24_H240K	245.6 ± 0.8	0.8361 ± 0.06%	2.006×10^{-2}	256.75	1.270×10^{22}	4.727
GL25_H240K	253.4 ± 1.0	0.9767 ± 0.12%	1.330×10^{-1}	64.75	2.404×10^{22}	8.948
GL26_H240K	247.0 ± 0.9	0.8398 ± 0.09%	2.009×10^{-2}	512.75	2.537×10^{22}	9.442
GL27_H240K	243.6 ± 1.0	0.3494 ± 0.05%	4.770×10^{-2}	512.75	2.541×10^{22}	9.457
GL28_H240K	244.5 ± 1.0	0.4706 ± 0.08%	2.910×10^{-1}	64.75	2.627×10^{22}	9.777
GL29_H240K	242.7 ± 1.2	0.1525 ± 0.07%	1.128×10^{-1}	512.75	2.632×10^{22}	9.797
GL30_H240K	243.9 ± 1.1	0.2736 ± 0.06%	5.039×10^{-1}	64.75	2.651×10^{22}	9.867
GL31_H240K	247.2 ± 0.9	0.9590 ± 0.04%	1.411×10^{-1}	256.75	1.018×10^{23}	37.89
GL32_H240K	245.3 ± 1.1	0.4705 ± 0.04%	2.899×10^{-1}	256.75	1.034×10^{23}	38.49
GL33_H240K	243.7 ± 1.1	0.2729 ± 0.06%	5.018×10^{-1}	256.75	1.045×10^{23}	38.89
GL34_H240K	248.9 ± 0.9	0.9639 ± 0.05%	1.402×10^{-1}	512.75	2.017×10^{23}	75.05
GL35_H240K	244.9 ± 1.4	0.4708 ± 0.04%	2.896×10^{-1}	512.75	2.068×10^{23}	76.95
GL36_H240K	244.6 ± 1.1	0.2734 ± 0.06%	5.023×10^{-1}	512.75	2.085×10^{23}	77.61

Table A.11: The "190 K" quarts-halogen H_2-broadened CH_4 spectra and their measurement conditions.

SPECTRUM	T ± 1σ (K)	P_{total}(bar) ± 1σ	P_{CH_4}/P_{total}	L (m)	U(mol/cm²)	U(m · am)
QH01_H190K	192.2 ± 1.7	0.3289 ± 0.24%	8.577×10^{-4}	64.75	6.884×10^{19}	0.02562
QH02_H190K	191.5 ± 1.8	0.1339 ± 0.16%	2.185×10^{-3}	64.75	7.166×10^{19}	0.02667
QH03_H190K	192.4 ± 1.7	0.3290 ± 0.22%	8.182×10^{-4}	256.75	2.602×10^{20}	0.09684
QH04_H190K	193.6 ± 1.1	0.8099 ± 0.40%	3.570×10^{-4}	256.75	2.778×10^{20}	0.1034
QH05_H190K	193.0 ± 2.2	0.1341 ± 0.20%	2.254×10^{-3}	256.75	2.913×10^{20}	0.1084
QH06_H190K	194.4 ± 1.6	0.8063 ± 0.31%	3.384×10^{-4}	416.75	4.237×10^{20}	0.1577
QH07_H190K	191.8 ± 1.5	0.3290 ± 0.19%	8.456×10^{-4}	416.75	4.379×10^{20}	0.1630
QH08_H190K	190.2 ± 1.5	0.1346 ± 0.14%	2.356×10^{-3}	416.75	5.033×10^{20}	0.1873
QH09_H190K	194.1 ± 1.9	0.1400 ± 0.20%	3.312×10^{-2}	64.75	1.120×10^{21}	0.4170
QH10_H190K	196.3 ± 1.7	0.3406 ± 0.42%	1.383×10^{-2}	64.75	1.125×10^{21}	0.4189
QH11_H190K	199.3 ± 1.4	0.8357 ± 0.24%	3.743×10^{-3}	256.75	2.919×10^{21}	1.086
QH13_H190K	201.9 ± 1.9	0.3622 ± 0.26%	4.587×10^{-2}	64.75	3.859×10^{21}	1.436
QH14_H190K	198.3 ± 2.0	0.1553 ± 0.27%	1.109×10^{-1}	64.75	4.074×10^{21}	1.516
QH15_H190K	196.3 ± 1.8	0.3394 ± 0.39%	1.267×10^{-2}	256.75	4.074×10^{21}	1.516
QH16_H190K	196.2 ± 2.4	0.1404 ± 0.34%	3.096×10^{-2}	256.75	4.120×10^{21}	1.533
QH17_H190K	200.2 ± 1.5	0.8330 ± 0.39%	4.015×10^{-3}	416.75	5.043×10^{21}	1.877
QH18_H190K	195.4 ± 1.6	0.3394 ± 0.25%	1.363×10^{-2}	416.75	7.147×10^{21}	2.660
QH19_H190K	191.9 ± 1.7	0.1404 ± 0.16%	3.347×10^{-2}	416.75	7.392×10^{21}	2.751
QH20_H190K	203.2 ± 1.7	0.8657 ± 0.22%	1.789×10^{-2}	256.75	1.417×10^{22}	5.275
QH21_H190K	200.3 ± 2.1	0.3590 ± 0.18%	4.625×10^{-2}	256.75	1.542×10^{22}	5.737
QH22_H190K	200.3 ± 2.6	0.1560 ± 0.21%	1.107×10^{-1}	256.75	1.603×10^{22}	5.967
QH23_H190K	206.8 ± 1.6	0.8723 ± 0.38%	1.729×10^{-2}	416.75	2.202×10^{22}	8.193
QH24_H190K	199.6 ± 1.8	0.3585 ± 0.26%	4.704×10^{-2}	416.75	2.550×10^{22}	9.492
QH25_H190K	194.5 ± 2.0	0.1549 ± 0.19%	1.133×10^{-1}	416.75	2.724×10^{22}	10.14
QH12_H190K	206.3 ± 2.0	0.4877 ± 0.20%	2.771×10^{-1}	64.75	3.072×10^{22}	11.43
QH26_H190K	203.1 ± 2.0	0.2772 ± 0.35%	4.912×10^{-1}	64.75	3.144×10^{22}	11.70
QH27_H190K	208.4 ± 1.6	0.9505 ± 0.26%	1.407×10^{-1}	256.75	1.193×10^{23}	44.42
QH28_H190K	204.2 ± 1.9	0.4840 ± 0.22%	2.805×10^{-1}	256.75	1.236×10^{23}	46.02
QH29_H190K	203.8 ± 2.3	0.2768 ± 0.15%	4.913×10^{-1}	256.75	1.241×10^{23}	46.19
QH30_H190K	204.8 ± 1.8	0.4721 ± 0.25%	2.593×10^{-1}	416.75	1.804×10^{23}	67.15
QH31_H190K	214.3 ± 2.0	0.9495 ± 0.18%	1.366×10^{-1}	416.75	1.827×10^{23}	68.00
QH32_H190K	198.3 ± 2.0	0.2749 ± 0.23%	4.922×10^{-1}	416.75	2.060×10^{23}	76.66

Table A.12: The "190 K" globar H_2-broadened CH_4 spectra and their measurement conditions.

SPECTRUM	T ± 1σ (K)	P_{total}(bar) ± 1σ	P_{CH_4}/P_{total}	L (m)	U(mol/cm²)	U(m · am)
GL01_H190K	193.6 ± 1.6	0.3314 ± 0.19%	8.577×10^{-4}	64.75	6.886×10^{19}	0.02563
GL02_H190K	192.5 ± 1.8	0.1347 ± 0.13%	2.185×10^{-3}	64.75	7.171×10^{19}	0.02669
GL03_H190K	193.8 ± 1.7	0.3313 ± 0.18%	8.182×10^{-4}	256.75	2.601×10^{20}	0.09681
GL04_H190K	196.3 ± 1.1	0.8199 ± 0.31%	3.570×10^{-4}	256.75	2.773×10^{20}	0.1032
GL05_H190K	194.1 ± 2.3	0.1350 ± 0.16%	2.254×10^{-3}	256.75	2.916×10^{20}	0.1085
GL06_H190K	196.7 ± 1.5	0.8151 ± 0.27%	3.384×10^{-4}	416.75	4.233×10^{20}	0.1575
GL07_H190K	192.9 ± 1.5	0.3310 ± 0.15%	8.456×10^{-4}	416.75	4.380×10^{20}	0.1630
GL08_H190K	190.7 ± 1.6	0.1351 ± 0.10%	2.356×10^{-3}	416.75	5.039×10^{20}	0.1875
GL09_H190K	195.4 ± 2.0	0.1409 ± 0.20%	3.312×10^{-2}	64.75	1.120×10^{21}	0.4169
GL10_H190K	198.9 ± 1.6	0.3449 ± 0.33%	1.383×10^{-2}	64.75	1.125×10^{21}	0.4186
GL11_H190K	200.7 ± 1.3	0.8417 ± 0.18%	3.743×10^{-3}	256.75	2.919×10^{21}	1.086
GL13_H190K	203.7 ± 1.7	0.3652 ± 0.21%	4.587×10^{-2}	64.75	3.857×10^{21}	1.435
GL14_H190K	199.9 ± 2.0	0.1565 ± 0.20%	1.109×10^{-1}	64.75	4.072×10^{21}	1.515
GL15_H190K	198.4 ± 1.6	0.3430 ± 0.25%	1.267×10^{-2}	256.75	4.074×10^{21}	1.516
GL16_H190K	198.2 ± 2.3	0.1419 ± 0.24%	3.096×10^{-2}	256.75	4.122×10^{21}	1.534
GL17_H190K	202.6 ± 1.4	0.8429 ± 0.30%	4.015×10^{-3}	416.75	5.043×10^{21}	1.877
GL18_H190K	197.2 ± 1.6	0.3424 ± 0.20%	1.363×10^{-2}	416.75	7.144×10^{21}	2.659
GL19_H190K	192.9 ± 1.8	0.1411 ± 0.13%	3.347×10^{-2}	416.75	7.391×10^{21}	2.750
GL20_H190K	204.7 ± 1.4	0.8717 ± 0.18%	1.789×10^{-2}	256.75	1.417×10^{22}	5.273
GL21_H190K	201.7 ± 1.9	0.3612 ± 0.20%	4.625×10^{-2}	256.75	1.540×10^{22}	5.733
GL22_H190K	201.5 ± 2.6	0.1569 ± 0.14%	1.107×10^{-1}	256.75	1.603×10^{22}	5.966
GL23_H190K	210.8 ± 1.4	0.8894 ± 0.32%	1.729×10^{-2}	416.75	2.202×10^{22}	8.196
GL24_H190K	201.4 ± 1.7	0.3616 ± 0.22%	4.704×10^{-2}	416.75	2.550×10^{22}	9.488
GL25_H190K	195.8 ± 2.1	0.1558 ± 0.14%	1.133×10^{-1}	416.75	2.722×10^{22}	10.13
GL12_H190K	208.0 ± 1.7	0.4906 ± 0.16%	2.771×10^{-1}	64.75	3.065×10^{22}	11.41
GL26_H190K	205.2 ± 1.9	0.2798 ± 0.21%	4.912×10^{-1}	64.75	3.141×10^{22}	11.69
GL27_H190K	210.7 ± 1.5	0.9582 ± 0.20%	1.407×10^{-1}	256.75	1.190×10^{23}	44.29
GL28_H190K	205.9 ± 1.7	0.4872 ± 0.17%	2.805×10^{-1}	256.75	1.234×10^{23}	45.94
GL29_H190K	205.1 ± 2.1	0.2781 ± 0.10%	4.913×10^{-1}	256.75	1.239×10^{23}	46.11
GL30_H190K	206.7 ± 1.7	0.4756 ± 0.20%	2.593×10^{-1}	416.75	1.801×10^{23}	67.03
GL31_H190K	215.8 ± 1.5	0.9547 ± 0.14%	1.366×10^{-1}	416.75	1.824×10^{23}	67.89
GL32_H190K	200.1 ± 2.0	0.2772 ± 0.18%	4.922×10^{-1}	416.75	2.058×10^{23}	76.60

Appendix B

Band-Model Parameters for the Self-Broadened Methane Spectra

The following table lists the band model parameters fitted to the self-broadened CH_4 spectra only, using the Goody-Voigt random band model with $k_\nu(T)$. The equation for transmittance is (Equation 4.28)

$$\overline{\tau}_{Goody-Voigt} = \exp\left(-2k_\nu U \int_0^\infty \frac{V(x,y)}{1+k_\nu U \delta V(x,y)/\alpha_D^0\sqrt{T}}\,dx\right) \qquad (B.1)$$

where

$$y = \frac{\alpha_L}{\alpha_D} = \frac{\alpha_L^0}{\alpha_D^0}\frac{P}{P_0}\frac{\sqrt{T_0}}{T}, \qquad (B.2)$$

$V(x,y) = \alpha_D f_V(\nu)$, and the laboratory conditions T, P, and U are in units of K, bar, and $(\text{molecules/cm}^2)^{-1}$, respectively. For definitions of the variables used in these equations and for details of this fit, see §4.2.4.1 and §7.2. Columns 1 through 6 below are as follows:

1. The midpoint of the degraded 10 cm^{-1} frequency interval: ν (cm^{-1}).
2. The r.m.s. residual error in transmittance: σ.
3. The absorption coefficient at 296 K: $k_\nu(T_0)$ ($\times 10^{24}$ $(\text{molecules/cm}^2)^{-1}$).
4. The parameter δ/α_D^0 ($\text{K}^{-1/2}$).
5. The parameter α_L^0/α_D^0 ($\text{K}^{-1/2}$).
6. The lower state energy: E_L (cm^{-1}).

2000.00	0.55841E-02	0.75716E-02	0.45625E+05	0.39578E+03	0.12012E+03
2005.00	0.65043E-02	0.10727E-01	0.37946E+05	0.39480E+03	0.13017E+03
2010.00	0.59930E-02	0.88029E-02	0.40821E+05	0.39381E+03	0.12969E+03
2015.00	0.54554E-02	0.44925E-02	0.13773E+05	0.39284E+03	0.12001E+03
2020.00	0.57065E-02	0.68434E-02	0.21470E+06	0.39187E+03	0.12001E+03
2025.00	0.56408E-02	0.53295E-02	0.26060E+06	0.39090E+03	0.12002E+03
2030.00	0.56922E-02	0.31420E-02	0.35607E+06	0.38993E+03	0.79988E+02
2035.00	0.59494E-02	0.52319E-02	0.22349E+06	0.38898E+03	0.12003E+03
2040.00	0.60765E-02	0.48111E-02	0.24548E+06	0.38802E+03	0.12002E+03
2045.00	0.63786E-02	0.69335E-02	0.14700E+06	0.38707E+03	0.12268E+03
2050.00	0.63892E-02	0.72945E-02	0.14423E+06	0.38613E+03	0.12621E+03
2055.00	0.74297E-02	0.10414E-01	0.84181E+05	0.38519E+03	0.21000E+03
2060.00	0.75100E-02	0.14623E-01	0.72601E+05	0.38426E+03	0.15061E+03
2065.00	0.63346E-02	0.64435E-01	0.40687E+04	0.37352E+03	0.79376E+03
2070.00	0.60138E-02	0.89387E-01	0.86401E+04	0.38240E+03	0.94492E+03
2075.00	0.60449E-02	0.17604E+00	0.91952E+04	0.38148E+03	0.10101E+04
2080.00	0.63251E-02	0.31795E+00	0.55384E+04	0.37433E+03	0.93879E+03
2085.00	0.60918E-02	0.27689E+00	0.69128E+04	0.37905E+03	0.88786E+03
2090.00	0.64998E-02	0.44199E+00	0.48248E+04	0.38639E+03	0.78953E+03
2095.00	0.63916E-02	0.40943E+00	0.56971E+04	0.38337E+03	0.75907E+03
2100.00	0.70796E-02	0.61572E+00	0.53539E+04	0.37691E+03	0.66838E+03
2105.00	0.61773E-02	0.61259E+00	0.48934E+04	0.37623E+03	0.61640E+03
2110.00	0.83648E-02	0.86097E+00	0.54627E+04	0.37453E+03	0.56737E+03
2115.00	0.13335E-01	0.17061E+01	0.48058E+04	0.37382E+03	0.50164E+03
2120.00	0.98055E-02	0.11624E+01	0.76327E+04	0.37336E+03	0.45266E+03
2125.00	0.10772E-01	0.15526E+01	0.52346E+04	0.37215E+03	0.40255E+03
2130.00	0.10471E-01	0.14094E+01	0.76183E+04	0.37272E+03	0.34918E+03
2135.00	0.13549E-01	0.23472E+01	0.14831E+05	0.36411E+03	0.30107E+03
2140.00	0.23051E-01	0.80064E+01	0.19785E+05	0.42925E+03	0.26051E+03
2145.00	0.13759E-01	0.24958E+01	0.17272E+05	0.36707E+03	0.21888E+03
2150.00	0.12541E-01	0.19686E+01	0.10832E+05	0.37609E+03	0.19110E+03
2155.00	0.10822E-01	0.15284E+01	0.10140E+05	0.37009E+03	0.16389E+03
2160.00	0.11373E-01	0.23588E+01	0.25532E+05	0.36281E+03	0.11543E+03
2165.00	0.19092E-01	0.16784E+02	0.50937E+05	0.35548E+03	0.12125E+03
2170.00	0.94300E-02	0.13274E+01	0.16992E+05	0.36161E+03	0.11537E+03
2175.00	0.66674E-02	0.68347E+00	0.11683E+05	0.36985E+03	0.14501E+03
2180.00	0.84429E-02	0.12560E+01	0.80539E+04	0.36357E+03	0.22722E+03
2185.00	0.77480E-02	0.70010E+00	0.25858E+04	0.36177E+03	0.37982E+03
2190.00	0.77685E-02	0.10401E+01	0.98344E+03	0.35804E+03	0.51811E+03
2195.00	0.60836E-01	0.91871E+01	0.14650E+04	0.35825E+03	0.51042E+03
2200.00	0.66020E-01	0.18063E+02	0.60895E+04	0.37309E+03	0.33618E+03
2205.00	0.87620E-02	0.71720E+00	0.34557E+04	0.36008E+03	0.27059E+03
2210.00	0.85632E-02	0.48280E+00	0.22555E+04	0.35986E+03	0.42785E+03
2215.00	0.73585E-02	0.66241E+00	0.33981E+04	0.35633E+03	0.39173E+03
2220.00	0.81784E-02	0.12212E+01	0.42998E+04	0.35510E+03	0.21377E+03
2225.00	0.71222E-02	0.10445E+01	0.26801E+04	0.35548E+03	0.25197E+03
2230.00	0.11505E-01	0.15874E+01	0.23168E+04	0.35348E+03	0.40789E+03
2235.00	0.19020E-01	0.30730E+01	0.29965E+04	0.35339E+03	0.32318E+03
2240.00	0.16304E-01	0.26019E+01	0.28784E+04	0.35221E+03	0.24877E+03
2245.00	0.11631E-01	0.17586E+01	0.27497E+04	0.35159E+03	0.25017E+03
2250.00	0.20064E-01	0.37515E+01	0.28240E+04	0.35124E+03	0.32383E+03
2255.00	0.25977E-01	0.57938E+01	0.21243E+04	0.35056E+03	0.45092E+03
2260.00	0.15767E-01	0.32342E+01	0.27451E+04	0.34903E+03	0.48483E+03
2265.00	0.13255E-01	0.30439E+01	0.21503E+04	0.34784E+03	0.33424E+03
2270.00	0.20203E-01	0.50685E+01	0.19226E+04	0.34728E+03	0.37880E+03
2275.00	0.19306E-01	0.52988E+01	0.17344E+04	0.35216E+03	0.58140E+03
2280.00	0.11409E-01	0.34687E+01	0.13039E+04	0.34658E+03	0.54962E+03
2285.00	0.59040E-02	0.25628E+01	0.10459E+04	0.34429E+03	0.49466E+03
2290.00	0.80345E-02	0.26802E+01	0.12186E+04	0.34255E+03	0.55040E+03
2295.00	0.89471E-02	0.44579E+01	0.14319E+04	0.34297E+03	0.80993E+03
2300.00	0.95606E-02	0.44464E+01	0.14207E+04	0.34801E+03	0.91681E+03
2305.00	0.93444E-02	0.26594E+01	0.11487E+04	0.34091E+03	0.82170E+03
2310.00	0.95623E-02	0.27199E+01	0.60647E+03	0.34020E+03	0.62524E+03
2315.00	0.12592E-01	0.46928E+01	0.60222E+03	0.33707E+03	0.49890E+03
2320.00	0.14869E-01	0.72246E+01	0.11500E+04	0.34019E+03	0.69071E+03
2325.00	0.10869E-01	0.47989E+01	0.17919E+04	0.33898E+03	0.94954E+03
2330.00	0.12815E-01	0.17700E+01	0.14470E+04	0.34821E+03	0.78829E+03
2335.00	0.16373E-01	0.89015E+00	0.74747E+03	0.34322E+03	0.45974E+03
2340.00	0.16407E-01	0.78860E+01	0.26026E+04	0.33566E+03	0.67992E+03
2345.00	0.92558E-02	0.11734E+02	0.13583E+04	0.34084E+03	0.78082E+03
2350.00	0.99623E-02	0.34673E+01	0.10236E+04	0.33567E+03	0.53361E+03
2355.00	0.13051E-01	0.16901E+01	0.10948E+04	0.33377E+03	0.49917E+03
2360.00	0.27939E-01	0.13209E+02	0.39454E+04	0.33902E+03	0.61822E+03
2365.00	0.11264E-01	0.14938E+02	0.84145E+03	0.35991E+03	0.63969E+03
2370.00	0.14288E-01	0.69804E+01	0.97198E+03	0.33109E+03	0.63172E+03
2375.00	0.12058E-01	0.23291E+01	0.61627E+03	0.33843E+03	0.57628E+03
2380.00	0.86231E-02	0.37375E+01	0.74556E+03	0.33703E+03	0.62230E+03
2385.00	0.20431E-01	0.13373E+02	0.81261E+03	0.32865E+03	0.65350E+03
2390.00	0.16553E-01	0.12060E+02	0.10256E+04	0.33560E+03	0.65743E+03
2395.00	0.14049E-01	0.43224E+01	0.71946E+03	0.33826E+03	0.72173E+03
2400.00	0.10360E-01	0.71069E+01	0.78606E+03	0.33127E+03	0.84235E+03
2405.00	0.12966E-01	0.20489E+02	0.10915E+04	0.32188E+03	0.73747E+03
2410.00	0.80643E-02	0.24780E+02	0.10460E+04	0.43590E+03	0.65525E+03
2415.00	0.11034E-01	0.11302E+02	0.72741E+03	0.32394E+03	0.78412E+03
2420.00	0.17617E-01	0.82891E+01	0.75927E+03	0.33284E+03	0.80428E+03
2425.00	0.15551E-01	0.16598E+02	0.10245E+04	0.33000E+03	0.65862E+03
2430.00	0.20738E-01	0.26086E+02	0.82541E+03	0.32461E+03	0.56240E+03
2435.00	0.10108E-01	0.16283E+02	0.69810E+03	0.32481E+03	0.65212E+03
2440.00	0.15103E-01	0.15075E+02	0.67230E+03	0.33283E+03	0.71771E+03
2445.00	0.13335E-01	0.18073E+02	0.79727E+03	0.32834E+03	0.68996E+03
2450.00	0.18393E-01	0.24128E+02	0.84469E+03	0.32325E+03	0.57554E+03
2455.00	0.13830E-01	0.30549E+02	0.61396E+03	0.31805E+03	0.54180E+03
2460.00	0.15089E-01	0.23886E+02	0.59324E+03	0.32740E+03	0.63624E+03
2465.00	0.19188E-01	0.25573E+02	0.63992E+03	0.33161E+03	0.63121E+03
2470.00	0.10621E-01	0.34812E+02	0.51540E+03	0.29365E+03	0.50568E+03
2475.00	0.94767E-02	0.46809E+02	0.38032E+03	0.27626E+03	0.45898E+03
2480.00	0.10520E-01	0.35465E+02	0.52591E+03	0.34115E+03	0.53082E+03
2485.00	0.21323E-01	0.19193E+02	0.56693E+03	0.33260E+03	0.61966E+03
2490.00	0.22211E-01	0.29558E+02	0.45443E+03	0.31193E+03	0.57892E+03
2495.00	0.94860E-02	0.46953E+02	0.34095E+03	0.30360E+03	0.44177E+03
2500.00	0.91334E-02	0.36447E+02	0.49052E+03	0.41442E+03	0.46939E+03
2505.00	0.15582E-01	0.28910E+02	0.50508E+03	0.32162E+03	0.55982E+03
2510.00	0.16713E-01	0.40020E+02	0.41307E+03	0.30892E+03	0.49778E+03
2515.00	0.13577E-01	0.68099E+02	0.27048E+03	0.23881E+03	0.45974E+03
2520.00	0.15175E-01	0.32582E+02	0.37814E+03	0.32074E+03	0.55269E+03
2525.00	0.83885E-02	0.43475E+02	0.29679E+03	0.32009E+03	0.48319E+03
2530.00	0.74191E-02	0.55259E+02	0.36472E+03	0.35305E+03	0.42626E+03
2535.00	0.96932E-02	0.50822E+02	0.31362E+03	0.26893E+03	0.43476E+03
2540.00	0.10083E-01	0.51705E+02	0.32342E+03	0.25944E+03	0.42039E+03
2545.00	0.10462E-01	0.56042E+02	0.25668E+03	0.19314E+03	0.36348E+03
2550.00	0.10439E-01	0.73567E+02	0.23212E+03	0.22104E+03	0.38240E+03
2555.00	0.12709E-01	0.61813E+02	0.28482E+03	0.32334E+03	0.40507E+03
2560.00	0.10538E-01	0.73566E+02	0.27147E+03	0.32185E+03	0.35844E+03
2565.00	0.13434E-01	0.86977E+02	0.23982E+03	0.30860E+03	0.40529E+03
2570.00	0.84599E-02	0.70264E+02	0.28982E+03	0.37141E+03	0.39903E+03
2575.00	0.90197E-02	0.69368E+02	0.33518E+03	0.52961E+03	0.39843E+03
2580.00	0.81656E-02	0.87996E+02	0.26349E+03	0.55620E+03	0.36749E+03
2585.00	0.80341E-02	0.79117E+02	0.24079E+03	0.48994E+03	0.35802E+03
2590.00	0.99803E-02	0.68892E+02	0.23026E+03	0.39700E+03	0.48321E+03
2595.00	0.12719E-01	0.18066E+03	0.97245E+02	0.90601E+02	0.52847E+03
2600.00	0.11761E-01	0.27165E+03	0.18921E+03	0.32077E+03	0.38490E+03
2605.00	0.77953E-02	0.10500E+03	0.33690E+03	0.55516E+03	0.26407E+03
2610.00	0.85830E-02	0.40057E+02	0.43106E+03	0.48274E+03	0.24066E+03
2615.00	0.10890E-01	0.40255E+02	0.40410E+03	0.43468E+03	0.30352E+03
2620.00	0.14137E-01	0.47721E+02	0.36069E+03	0.44883E+03	0.36710E+03
2625.00	0.14022E-01	0.49781E+02	0.29179E+03	0.38307E+03	0.35985E+03
2630.00	0.11087E-01	0.91100E+02	0.28811E+03	0.44378E+03	0.33359E+03
2635.00	0.11464E-01	0.15997E+03	0.24293E+03	0.34977E+03	0.32912E+03
2640.00	0.11891E-01	0.17547E+03	0.18895E+03	0.33577E+03	0.47692E+03
2645.00	0.11166E-01	0.13916E+03	0.20970E+03	0.46946E+03	0.55221E+03
2650.00	0.10098E-01	0.10814E+03	0.27805E+03	0.54677E+03	0.47458E+03
2655.00	0.96655E-02	0.99406E+02	0.28150E+03	0.49483E+03	0.40953E+03
2660.00	0.10512E-01	0.72879E+02	0.23510E+03	0.37374E+03	0.37472E+03
2665.00	0.10758E-01	0.91925E+02	0.23567E+03	0.37118E+03	0.42930E+03
2670.00	0.10441E-01	0.12245E+03	0.27233E+03	0.52125E+03	0.44371E+03
2675.00	0.11181E-01	0.10398E+03	0.30173E+03	0.63977E+03	0.38514E+03
2680.00	0.10106E-01	0.17673E+03	0.22358E+03	0.50767E+03	0.45817E+03
2685.00	0.14642E-01	0.15161E+03	0.10123E+03	0.14092E+03	0.59810E+03
2690.00	0.11719E-01	0.10274E+03	0.19697E+03	0.35298E+03	0.53980E+03
2695.00	0.95598E-02	0.17362E+03	0.22131E+03	0.40805E+03	0.49423E+03
2700.00	0.10249E-01	0.17863E+03	0.15647E+03	0.24937E+03	0.60652E+03
2705.00	0.10762E-01	0.11043E+03	0.21865E+03	0.41706E+03	0.63393E+03
2710.00	0.12223E-01	0.15326E+03	0.15986E+03	0.26212E+03	0.58098E+03
2715.00	0.11299E-01	0.16751E+03	0.13489E+03	0.22147E+03	0.58050E+03
2720.00	0.12005E-01	0.10673E+03	0.25139E+03	0.53576E+03	0.63676E+03
2725.00	0.11084E-01	0.19330E+03	0.22302E+03	0.39779E+03	0.57942E+03
2730.00	0.12517E-01	0.19583E+03	0.19233E+03	0.34244E+03	0.53240E+03
2735.00	0.15044E-01	0.10561E+03	0.25457E+03	0.57351E+03	0.54756E+03
2740.00	0.12899E-01	0.17458E+03	0.16981E+03	0.30965E+03	0.49856E+03
2745.00	0.12289E-01	0.21210E+03	0.17787E+03	0.39827E+03	0.48124E+03
2750.00	0.12916E-01	0.16250E+03	0.24068E+03	0.59484E+03	0.55617E+03
2755.00	0.13124E-01	0.20959E+03	0.15353E+03	0.40739E+03	0.54255E+03
2760.00	0.12136E-01	0.22026E+03	0.16589E+03	0.57119E+03	0.55622E+03
2765.00	0.13830E-01	0.23249E+03	0.14292E+03	0.44419E+03	0.67877E+03
2770.00	0.14530E-01	0.36997E+03	0.11445E+03	0.41085E+03	0.62906E+03
2775.00	0.11377E-01	0.39820E+03	0.13164E+03	0.48524E+03	0.56845E+03
2780.00	0.14137E-01	0.42082E+03	0.13233E+03	0.35767E+03	0.57451E+03
2785.00	0.12539E-01	0.52183E+03	0.14806E+03	0.43407E+03	0.48413E+03
2790.00	0.11577E-01	0.52627E+03	0.16992E+03	0.51134E+03	0.42003E+03
2795.00	0.12658E-01	0.47685E+03	0.17393E+03	0.49958E+03	0.39812E+03
2800.00	0.13223E-01	0.35415E+03	0.17083E+03	0.45866E+03	0.41740E+03
2805.00	0.13537E-01	0.26815E+03	0.17777E+03	0.41341E+03	0.41236E+03
2810.00	0.12405E-01	0.31611E+03	0.21745E+03	0.55378E+03	0.41673E+03
2815.00	0.13470E-01	0.34347E+03	0.27939E+03	0.79977E+03	0.39129E+03
2820.00	0.13081E-01	0.44115E+03	0.22077E+03	0.87006E+03	0.40996E+03
2825.00	0.11994E-01	0.55741E+03	0.21053E+03	0.97276E+03	0.40920E+03
2830.00	0.12526E-01	0.47438E+03	0.18491E+03	0.66706E+03	0.44858E+03
2835.00	0.14348E-01	0.37921E+03	0.16022E+03	0.53662E+03	0.56978E+03
2840.00	0.16481E-01	0.43580E+03	0.13739E+03	0.35998E+03	0.71664E+03
2845.00	0.14467E-01	0.36360E+03	0.16308E+03	0.46068E+03	0.61730E+03
2850.00	0.14614E-01	0.31429E+03	0.15407E+03	0.45516E+03	0.52332E+03
2855.00	0.14051E-01	0.36346E+03	0.14886E+03	0.49333E+03	0.56059E+03
2860.00	0.14584E-01	0.43870E+03	0.15787E+03	0.56337E+03	0.53942E+03
2865.00	0.16067E-01	0.62079E+03	0.13553E+03	0.49458E+03	0.50801E+03
2870.00	0.16784E-01	0.79508E+03	0.11896E+03	0.40391E+03	0.49276E+03
2875.00	0.17935E-01	0.92642E+03	0.10293E+03	0.44793E+03	0.62414E+03
2880.00	0.15555E-01	0.80134E+03	0.10585E+03	0.47119E+03	0.61877E+03
2885.00	0.15499E-01	0.84012E+03	0.10034E+03	0.42826E+03	0.60744E+03
2890.00	0.17046E-01	0.71045E+03	0.84300E+02	0.25839E+03	0.70361E+03
2895.00	0.17313E-01	0.71864E+03	0.83183E+02	0.27239E+03	0.70230E+03
2900.00	0.15575E-01	0.70089E+03	0.10848E+03	0.56368E+03	0.63140E+03
2905.00	0.15715E-01	0.75563E+03	0.10086E+03	0.53170E+03	0.64357E+03
2910.00	0.15401E-01	0.77002E+03	0.10388E+03	0.49831E+03	0.65725E+03
2915.00	0.15168E-01	0.92136E+03	0.91623E+02	0.40180E+03	0.57622E+03
2920.00	0.14474E-01	0.10336E+04	0.99306E+02	0.46410E+03	0.58915E+03
2925.00	0.14925E-01	0.92823E+03	0.11046E+03	0.50405E+03	0.64094E+03
2930.00	0.14327E-01	0.94439E+03	0.10917E+03	0.46840E+03	0.61184E+03
2935.00	0.11936E-01	0.93047E+03	0.11403E+03	0.54490E+03	0.54192E+03
2940.00	0.12528E-01	0.91093E+03	0.12549E+03	0.63502E+03	0.51479E+03
2945.00	0.14877E-01	0.97305E+03	0.11722E+03	0.58039E+03	0.51816E+03
2950.00	0.16655E-01	0.10151E+04	0.12442E+03	0.68729E+03	0.48052E+03
2955.00	0.15310E-01	0.93963E+03	0.14609E+03	0.90478E+03	0.46381E+03
2960.00	0.14985E-01	0.86178E+03	0.14838E+03	0.83446E+03	0.47428E+03
2965.00	0.14246E-01	0.77518E+03	0.15426E+03	0.92061E+03	0.43905E+03
2970.00	0.13723E-01	0.67601E+03	0.14755E+03	0.10019E+04	0.44941E+03
2975.00	0.13615E-01	0.65167E+03	0.16482E+03	0.97352E+03	0.41887E+03
2980.00	0.13597E-01	0.65293E+03	0.17571E+03	0.10568E+04	0.39892E+03
2985.00	0.13980E-01	0.55019E+03	0.16064E+03	0.10558E+04	0.39816E+03
2990.00	0.16407E-01	0.47382E+03	0.14605E+03	0.99368E+03	0.44905E+03
2995.00	0.26874E-01	0.45346E+03	0.87126E+02	0.75162E+03	0.62672E+03
3000.00	0.33777E-01	0.11169E+04	0.38799E+02	0.49295E+03	0.90807E+03
3005.00	0.82579E-01	0.13744E+04	0.10139E+02	0.28579E+03	0.74599E+03
3010.00	0.11217E+00	0.12419E+04	0.25849E+01	0.25791E+03	0.26999E+03
3015.00	0.93529E-01	0.14297E+04	0.23327E+01	0.27845E+03	0.17000E+03
3020.00	0.77546E-01	0.12725E+04	0.27305E+02	0.39824E+03	0.17854E+03
3025.00	0.24335E-01	0.84748E+03	0.12251E+03	0.55482E+03	0.31584E+03
3030.00	0.26037E-01	0.27798E+03	0.13899E+03	0.11403E+04	0.37121E+03
3035.00	0.25192E-01	0.26255E+03	0.17032E+03	0.10355E+04	0.38705E+03
3040.00	0.23053E-01	0.28362E+03	0.19069E+03	0.11079E+04	0.37472E+03
3045.00	0.18169E-01	0.33207E+03	0.21465E+03	0.13326E+04	0.34735E+03
3050.00	0.25876E-01	0.29578E+03	0.15075E+03	0.11380E+04	0.32947E+03
3055.00	0.18863E-01	0.39808E+03	0.17689E+03	0.15353E+04	0.32613E+03
3060.00	0.30732E-01	0.35465E+03	0.10403E+03	0.11844E+04	0.30348E+03
3065.00	0.17476E-01	0.61731E+03	0.18650E+03	0.13482E+04	0.29002E+03
3070.00	0.17423E-01	0.10384E+04	0.13308E+03	0.91914E+03	0.31520E+03
3075.00	0.19287E-01	0.10888E+04	0.10649E+03	0.70477E+03	0.41667E+03
3080.00	0.18265E-01	0.97441E+03	0.12448E+03	0.88509E+03	0.46075E+03
3085.00	0.17703E-01	0.10033E+04	0.12008E+03	0.84123E+03	0.48543E+03
3090.00	0.17521E-01	0.10119E+04	0.12301E+03	0.80766E+03	0.52270E+03
3095.00	0.19482E-01	0.81955E+03	0.14123E+03	0.86332E+03	0.57359E+03
3100.00	0.19150E-01	0.99396E+03	0.11586E+03	0.54787E+03	0.57722E+03
3105.00	0.19339E-01	0.73755E+03	0.17622E+03	0.87861E+03	0.61685E+03
3110.00	0.18082E-01	0.82417E+03	0.16613E+03	0.80831E+03	0.61977E+03
3115.00	0.16925E-01	0.81668E+03	0.15035E+03	0.56013E+03	0.66976E+03
3120.00	0.18750E-01	0.77085E+03	0.16940E+03	0.66095E+03	0.71950E+03
3125.00	0.18392E-01	0.77204E+03	0.15791E+03	0.55775E+03	0.76986E+03
3130.00	0.19372E-01	0.71401E+03	0.17171E+03	0.43047E+03	0.78339E+03
3135.00	0.18526E-01	0.79529E+03	0.14995E+03	0.41482E+03	0.77949E+03
3140.00	0.18241E-01	0.77019E+03	0.14838E+03	0.23282E+03	0.81885E+03
3145.00	0.24822E-01	0.92476E+03	0.10793E+03	0.16176E+03	0.86188E+03
3150.00	0.21250E-01	0.58025E+03	0.11549E+03	0.14893E+03	0.84529E+03
3155.00	0.19554E-01	0.46992E+03	0.12697E+03	0.14801E+03	0.84904E+03
3160.00	0.24489E-01	0.41327E+03	0.95262E+02	0.58245E+02	0.95156E+03
3165.00	0.23686E-01	0.33525E+03	0.12764E+03	0.69106E+02	0.97831E+03
3170.00	0.20424E-01	0.42921E+03	0.11474E+03	0.58864E+02	0.94771E+03
3175.00	0.20532E-01	0.16617E+03	0.17483E+03	0.13001E+03	0.89131E+03
3180.00	0.20354E-01	0.20665E+03	0.12689E+03	0.65485E+02	0.92305E+03
3185.00	0.25041E-01	0.92152E+02	0.11118E+03	0.43245E+02	0.10019E+04
3190.00	0.26871E-01	0.62724E+02	0.32543E+03	0.23563E+03	0.10301E+04
3195.00	0.21728E-01	0.14199E+03	0.13938E+03	0.81189E+02	0.10152E+04

3200.00	0.28973E-01	0.41271E+02	0.29350E+03	0.24185E+03	0.97617E+03
3205.00	0.26241E-01	0.38135E+02	0.31978E+03	0.23625E+03	0.99922E+03
3210.00	0.30724E-01	0.27994E+02	0.41266E+03	0.24108E+03	0.86848E+03
3215.00	0.31483E-01	0.16030E+02	0.47463E+03	0.24061E+03	0.91913E+03
3220.00	0.31656E-01	0.25102E+02	0.40793E+03	0.24057E+03	0.97127E+03
3225.00	0.39109E-01	0.14867E+02	0.73296E+03	0.24009E+03	0.89891E+03
3230.00	0.33430E-01	0.11035E+02	0.64563E+03	0.24178E+03	0.85941E+03
3235.00	0.30375E-01	0.13455E+02	0.46587E+03	0.24145E+03	0.87363E+03
3240.00	0.32740E-01	0.59253E+01	0.64205E+03	0.24074E+03	0.81954E+03
3245.00	0.31485E-01	0.61379E+01	0.49673E+03	0.23944E+03	0.86839E+03
3250.00	0.28020E-01	0.72106E+01	0.43943E+03	0.23871E+03	0.86769E+03
3255.00	0.31263E-01	0.38751E+01	0.47210E+03	0.23857E+03	0.81026E+03
3260.00	0.32171E-01	0.35024E+01	0.34833E+03	0.23696E+03	0.87587E+03
3265.00	0.28517E-01	0.43463E+01	0.28160E+03	0.23578E+03	0.92993E+03
3270.00	0.29263E-01	0.37062E+01	0.29452E+03	0.23626E+03	0.92891E+03
3275.00	0.31399E-01	0.28209E+01	0.28261E+03	0.23522E+03	0.92254E+03
3280.00	0.30901E-01	0.24468E+01	0.23982E+03	0.23431E+03	0.90252E+03
3285.00	0.30243E-01	0.23615E+01	0.23206E+03	0.23387E+03	0.90972E+03
3290.00	0.30349E-01	0.20066E+01	0.28478E+03	0.23413E+03	0.87427E+03
3295.00	0.30681E-01	0.16226E+01	0.27619E+03	0.23366E+03	0.82502E+03
3300.00	0.29741E-01	0.16316E+01	0.24750E+03	0.23293E+03	0.84677E+03
3305.00	0.28825E-01	0.14162E+01	0.29694E+03	0.23324E+03	0.80038E+03
3310.00	0.27691E-01	0.13004E+01	0.30227E+03	0.23308E+03	0.77612E+03
3315.00	0.26872E-01	0.11458E+01	0.33055E+03	0.23291E+03	0.72963E+03
3320.00	0.26437E-01	0.99198E+00	0.36493E+03	0.24411E+03	0.66771E+03
3325.00	0.25652E-01	0.10234E+01	0.31830E+03	0.23104E+03	0.69620E+03
3330.00	0.25212E-01	0.88226E+00	0.32869E+03	0.23191E+03	0.63560E+03
3335.00	0.23339E-01	0.85757E+00	0.35101E+03	0.24310E+03	0.53267E+03
3340.00	0.22476E-01	0.88891E+00	0.31636E+03	0.23106E+03	0.52924E+03
3345.00	0.22795E-01	0.81364E+00	0.31420E+03	0.24275E+03	0.57773E+03
3350.00	0.22702E-01	0.68382E+00	0.32906E+03	0.23052E+03	0.56677E+03
3355.00	0.22170E-01	0.60269E+00	0.37041E+03	0.24124E+03	0.53077E+03
3360.00	0.21793E-01	0.55827E+00	0.37363E+03	0.23032E+03	0.50814E+03
3365.00	0.20596E-01	0.57269E+00	0.39560E+03	0.24040E+03	0.51450E+03
3370.00	0.19480E-01	0.58872E+00	0.41682E+03	0.23008E+03	0.48028E+03
3375.00	0.18934E-01	0.54531E+00	0.44666E+03	0.23926E+03	0.44764E+03
3380.00	0.17397E-01	0.54680E+00	0.36946E+03	0.23967E+03	0.46632E+03
3385.00	0.17139E-01	0.50434E+00	0.35431E+03	0.22839E+03	0.48102E+03
3390.00	0.16810E-01	0.47711E+00	0.32922E+03	0.22769E+03	0.48634E+03
3395.00	0.16018E-01	0.45690E+00	0.32964E+03	0.23909E+03	0.49044E+03
3400.00	0.16012E-01	0.44855E+00	0.28250E+03	0.22649E+03	0.51198E+03
3405.00	0.15857E-01	0.42116E+00	0.28900E+03	0.23686E+03	0.52652E+03
3410.00	0.15562E-01	0.41251E+00	0.27294E+03	0.22549E+03	0.51159E+03
3415.00	0.14982E-01	0.38265E+00	0.32676E+03	0.22610E+03	0.49636E+03
3420.00	0.14069E-01	0.37965E+00	0.48280E+03	0.23596E+03	0.46365E+03
3425.00	0.13416E-01	0.36901E+00	0.53061E+03	0.23514E+03	0.45068E+03
3430.00	0.12679E-01	0.37388E+00	0.68131E+03	0.23411E+03	0.41609E+03
3435.00	0.11644E-01	0.40614E+00	0.80612E+03	0.23356E+03	0.39058E+03
3440.00	0.11899E-01	0.37013E+00	0.84409E+03	0.23279E+03	0.36968E+03
3445.00	0.11795E-01	0.38910E+00	0.92498E+03	0.22742E+03	0.32237E+03
3450.00	0.11615E-01	0.34557E+00	0.11098E+04	0.23150E+03	0.31677E+03
3455.00	0.11153E-01	0.36996E+00	0.11725E+04	0.23106E+03	0.28317E+03
3460.00	0.11556E-01	0.31158E+00	0.12503E+04	0.22706E+03	0.31100E+03
3465.00	0.11449E-01	0.29579E+00	0.11136E+04	0.23046E+03	0.30256E+03
3470.00	0.11152E-01	0.28481E+00	0.12009E+04	0.23005E+03	0.31459E+03
3475.00	0.11268E-01	0.23940E+00	0.11034E+04	0.22579E+03	0.39005E+03
3480.00	0.10193E-01	0.29410E+00	0.11382E+04	0.22554E+03	0.33539E+03
3485.00	0.10427E-01	0.25524E+00	0.61918E+03	0.22370E+03	0.40422E+03
3490.00	0.95302E-02	0.43975E+00	0.38621E+03	0.22194E+03	0.43352E+03
3495.00	0.73556E-02	0.12619E+01	0.55573E+03	0.22340E+03	0.30325E+03

3500.00	0.96125E-02	0.11112E+01	0.14523E+04	0.22481E+03	0.27656E+03
3505.00	0.10686E-01	0.16758E+00	0.52533E+03	0.22196E+03	0.46146E+03
3510.00	0.97993E-02	0.18046E+00	0.14922E+04	0.22400E+03	0.37064E+03
3515.00	0.10833E-01	0.17359E+00	0.16038E+04	0.21921E+03	0.41375E+03
3520.00	0.10015E-01	0.26102E+00	0.13451E+04	0.22323E+03	0.47316E+03
3525.00	0.90603E-02	0.39632E+00	0.14004E+04	0.22303E+03	0.31851E+03
3530.00	0.87506E-02	0.40010E+00	0.16384E+04	0.22293E+03	0.29022E+03
3535.00	0.88507E-02	0.32300E+00	0.17837E+04	0.22524E+03	0.30959E+03
3540.00	0.81680E-02	0.39218E+00	0.13827E+04	0.22210E+03	0.24517E+03
3545.00	0.77090E-02	0.60181E+00	0.93047E+03	0.22202E+03	0.32961E+03
3550.00	0.75796E-02	0.61560E+00	0.79437E+03	0.22593E+03	0.38802E+03
3555.00	0.71640E-02	0.59978E+00	0.73328E+03	0.22628E+03	0.40993E+03
3560.00	0.72517E-02	0.53981E+00	0.64923E+03	0.21924E+03	0.45773E+03
3565.00	0.75687E-02	0.42866E+00	0.43274E+03	0.21751E+03	0.50078E+03
3570.00	0.75107E-02	0.38380E+00	0.33243E+03	0.21620E+03	0.56181E+03
3575.00	0.72356E-02	0.50142E+00	0.40199E+03	0.21657E+03	0.68112E+03
3580.00	0.73318E-02	0.57512E+00	0.41680E+03	0.21622E+03	0.76648E+03
3585.00	0.82186E-02	0.40034E+00	0.29532E+03	0.21497E+03	0.80907E+03
3590.00	0.85172E-02	0.34646E+00	0.13806E+03	0.21221E+03	0.86416E+03
3595.00	0.86223E-02	0.24606E+00	0.12024E+03	0.21095E+03	0.79554E+03
3600.00	0.86699E-02	0.30999E+00	0.50481E+03	0.21597E+03	0.73370E+03
3605.00	0.82832E-02	0.50282E+00	0.47559E+03	0.21517E+03	0.77256E+03
3610.00	0.87739E-02	0.76099E+00	0.91488E+03	0.21701E+03	0.79106E+03
3615.00	0.95679E-02	0.63178E+00	0.96079E+03	0.21658E+03	0.68849E+03
3620.00	0.92929E-02	0.22878E+00	0.95468E+02	0.20881E+03	0.57265E+03
3625.00	0.91875E-02	0.30431E+00	0.22443E+03	0.21146E+03	0.78718E+03
3630.00	0.87616E-02	0.10065E+01	0.93256E+03	0.21584E+03	0.77441E+03
3635.00	0.73820E-02	0.12980E+01	0.90482E+03	0.21631E+03	0.72379E+03
3640.00	0.83213E-02	0.61529E+00	0.10409E+04	0.21571E+03	0.74310E+03
3645.00	0.94956E-02	0.26292E+00	0.49869E+01	0.21398E+03	0.78283E+03
3650.00	0.10007E-01	0.62076E+00	0.11020E+04	0.21495E+03	0.76084E+03
3655.00	0.92540E-02	0.19376E+01	0.98193E+03	0.21730E+03	0.72555E+03
3660.00	0.72468E-02	0.22785E+01	0.78866E+03	0.23268E+03	0.66892E+03
3665.00	0.88862E-02	0.10640E+01	0.81924E+03	0.21506E+03	0.66321E+03
3670.00	0.10190E-01	0.48515E+00	0.32174E+02	0.20683E+03	0.68794E+03
3675.00	0.11757E-01	0.13709E+01	0.86455E+03	0.21249E+03	0.72459E+03
3680.00	0.11974E-01	0.13511E+01	0.10560E+04	0.21428E+03	0.78246E+03
3685.00	0.11178E-01	0.15194E+01	0.11396E+04	0.21307E+03	0.63589E+03
3690.00	0.10244E-01	0.16967E+01	0.80025E+03	0.21275E+03	0.62712E+03
3695.00	0.11058E-01	0.16002E+01	0.83851E+03	0.21197E+03	0.75394E+03
3700.00	0.11342E-01	0.19626E+01	0.94064E+03	0.21173E+03	0.73892E+03
3705.00	0.10230E-01	0.11080E+01	0.42849E+03	0.21696E+03	0.73031E+03
3710.00	0.11496E-01	0.17652E+01	0.60190E+03	0.21657E+03	0.67545E+03
3715.00	0.11963E-01	0.34154E+01	0.87452E+03	0.21134E+03	0.62179E+03
3720.00	0.11812E-01	0.44011E+01	0.67303E+03	0.21491E+03	0.62329E+03
3725.00	0.10343E-01	0.37485E+01	0.43545E+03	0.21811E+03	0.74709E+03
3730.00	0.11309E-01	0.27747E+01	0.47175E+03	0.21752E+03	0.78243E+03
3735.00	0.12063E-01	0.25635E+01	0.45424E+03	0.21643E+03	0.73672E+03
3740.00	0.14758E-01	0.52699E+01	0.54408E+03	0.20810E+03	0.66557E+03
3745.00	0.17527E-01	0.49177E+01	0.69486E+03	0.20996E+03	0.66719E+03
3750.00	0.13495E-01	0.40857E+01	0.60053E+03	0.20856E+03	0.74675E+03
3755.00	0.96567E-02	0.64734E+01	0.42417E+03	0.22299E+03	0.71527E+03
3760.00	0.11445E-01	0.63641E+01	0.43772E+03	0.21540E+03	0.77461E+03
3765.00	0.12723E-01	0.10866E+02	0.45620E+03	0.22199E+03	0.71963E+03
3770.00	0.11008E-01	0.11933E+02	0.40709E+03	0.23333E+03	0.72467E+03
3775.00	0.12744E-01	0.11249E+02	0.34003E+03	0.20469E+03	0.76275E+03
3780.00	0.10592E-01	0.12018E+02	0.31009E+03	0.22196E+03	0.66300E+03
3785.00	0.10139E-01	0.13715E+02	0.34211E+03	0.22889E+03	0.61294E+03
3790.00	0.11525E-01	0.19242E+02	0.26800E+03	0.19694E+03	0.61451E+03
3795.00	0.11923E-01	0.26707E+02	0.29967E+03	0.21368E+03	0.61517E+03

3800.00	0.93715E-02	0.28171E+02	0.31407E+03	0.26205E+03	0.55818E+03
3805.00	0.95461E-02	0.31783E+02	0.29080E+03	0.30395E+03	0.52754E+03
3810.00	0.11390E-01	0.39302E+02	0.28406E+03	0.33137E+03	0.50870E+03
3815.00	0.12776E-01	0.33859E+02	0.25352E+03	0.25857E+03	0.46732E+03
3820.00	0.12585E-01	0.38848E+02	0.19899E+03	0.20722E+03	0.45828E+03
3825.00	0.13557E-01	0.55224E+02	0.21200E+03	0.26111E+03	0.43444E+03
3830.00	0.13468E-01	0.56985E+02	0.25628E+03	0.35912E+03	0.41354E+03
3835.00	0.13232E-01	0.57898E+02	0.26488E+03	0.43648E+03	0.40180E+03
3840.00	0.11391E-01	0.69084E+02	0.26458E+03	0.49570E+03	0.34499E+03
3845.00	0.96218E-02	0.78762E+02	0.29237E+03	0.52736E+03	0.37980E+03
3850.00	0.10713E-01	0.10123E+03	0.24731E+03	0.37701E+03	0.40546E+03
3855.00	0.12674E-01	0.16631E+03	0.20021E+03	0.26622E+03	0.38306E+03
3860.00	0.13816E-01	0.29592E+03	0.19122E+03	0.25849E+03	0.31712E+03
3865.00	0.17373E-01	0.22745E+03	0.12026E+03	0.13253E+03	0.22061E+03
3870.00	0.13160E-01	0.80148E+02	0.12521E+03	0.11453E+03	0.29391E+03
3875.00	0.10744E-01	0.47028E+02	0.18151E+03	0.27948E+03	0.34867E+03
3880.00	0.87273E-02	0.63907E+02	0.20397E+03	0.38129E+03	0.28990E+03
3885.00	0.90182E-02	0.97686E+02	0.23037E+03	0.42953E+03	0.20166E+03
3890.00	0.12685E-01	0.13049E+03	0.15618E+03	0.20130E+03	0.18365E+03
3895.00	0.13355E-01	0.12805E+03	0.13924E+03	0.15652E+03	0.20829E+03
3900.00	0.12722E-01	0.14270E+03	0.20058E+03	0.22500E+03	0.27136E+03
3905.00	0.12513E-01	0.20176E+03	0.16207E+03	0.17931E+03	0.44484E+03
3910.00	0.10174E-01	0.16349E+03	0.15293E+03	0.16077E+03	0.47641E+03
3915.00	0.85927E-02	0.89382E+02	0.23427E+03	0.26047E+03	0.40853E+03
3920.00	0.82380E-02	0.64869E+02	0.20873E+03	0.25550E+03	0.42553E+03
3925.00	0.91096E-02	0.39406E+02	0.16549E+03	0.22069E+03	0.40217E+03
3930.00	0.85681E-02	0.25721E+02	0.19054E+03	0.21453E+03	0.35191E+03
3935.00	0.12258E-01	0.22482E+02	0.28058E+03	0.25595E+03	0.37139E+03
3940.00	0.10135E-01	0.29365E+02	0.19224E+03	0.20091E+03	0.38397E+03
3945.00	0.99660E-02	0.28641E+02	0.26649E+03	0.28860E+03	0.38108E+03
3950.00	0.13401E-01	0.21467E+02	0.28273E+03	0.24889E+03	0.41075E+03
3955.00	0.10767E-01	0.27687E+02	0.19582E+03	0.20014E+03	0.38346E+03
3960.00	0.10028E-01	0.31724E+02	0.27987E+03	0.33037E+03	0.36619E+03
3965.00	0.11593E-01	0.28746E+02	0.26572E+03	0.28964E+03	0.39454E+03
3970.00	0.10660E-01	0.29474E+02	0.22896E+03	0.24033E+03	0.39971E+03
3975.00	0.97672E-02	0.30049E+02	0.20759E+03	0.24935E+03	0.44710E+03
3980.00	0.10702E-01	0.30119E+02	0.21577E+03	0.29453E+03	0.45898E+03
3985.00	0.10603E-01	0.31347E+02	0.23946E+03	0.30276E+03	0.46359E+03
3990.00	0.98479E-02	0.28451E+02	0.18860E+03	0.24086E+03	0.52720E+03
3995.00	0.11803E-01	0.26917E+02	0.18523E+03	0.26242E+03	0.52737E+03
4000.00	0.11973E-01	0.32632E+02	0.18654E+03	0.26055E+03	0.50132E+03
4005.00	0.10252E-01	0.30458E+02	0.16365E+03	0.21722E+03	0.53381E+03
4010.00	0.93874E-02	0.33285E+02	0.16549E+03	0.24054E+03	0.54565E+03
4015.00	0.10327E-01	0.43204E+02	0.17474E+03	0.24697E+03	0.53791E+03
4020.00	0.10672E-01	0.41200E+02	0.15845E+03	0.23888E+03	0.53550E+03
4025.00	0.12331E-01	0.38643E+02	0.14020E+03	0.21589E+03	0.55061E+03
4030.00	0.13594E-01	0.43116E+02	0.10789E+03	0.16763E+03	0.59189E+03
4035.00	0.11316E-01	0.47979E+02	0.11360E+03	0.17058E+03	0.58938E+03
4040.00	0.10917E-01	0.41971E+02	0.14327E+03	0.23951E+03	0.58988E+03
4045.00	0.11975E-01	0.52797E+02	0.95328E+02	0.14701E+03	0.61207E+03
4050.00	0.15598E-01	0.66536E+02	0.80206E+02	0.10990E+03	0.65134E+03
4055.00	0.13464E-01	0.71735E+02	0.89806E+02	0.16392E+03	0.65027E+03
4060.00	0.11111E-01	0.82033E+02	0.11762E+03	0.21620E+03	0.58599E+03
4065.00	0.10331E-01	0.98335E+02	0.11634E+03	0.21844E+03	0.63075E+03
4070.00	0.10627E-01	0.13562E+03	0.11209E+03	0.21586E+03	0.61653E+03
4075.00	0.11805E-01	0.13352E+03	0.11914E+03	0.18815E+03	0.53284E+03
4080.00	0.13413E-01	0.13372E+03	0.12743E+03	0.20892E+03	0.53624E+03
4085.00	0.14950E-01	0.15480E+03	0.13532E+03	0.24337E+03	0.54088E+03
4090.00	0.15162E-01	0.16556E+03	0.13645E+03	0.24700E+03	0.51149E+03
4095.00	0.15684E-01	0.15564E+03	0.11849E+03	0.22520E+03	0.48170E+03

4100.00	0.17195E-01	0.19097E+03	0.83858E+02	0.17502E+03	0.52929E+03
4105.00	0.17937E-01	0.27965E+03	0.75358E+02	0.20453E+03	0.57509E+03
4110.00	0.16426E-01	0.21079E+03	0.73108E+02	0.15078E+03	0.54547E+03
4115.00	0.16997E-01	0.22089E+03	0.72982E+02	0.15610E+03	0.56480E+03
4120.00	0.18038E-01	0.43742E+03	0.60898E+02	0.14475E+03	0.54944E+03
4125.00	0.17205E-01	0.45798E+03	0.58807E+02	0.13601E+03	0.52583E+03
4130.00	0.15844E-01	0.40946E+03	0.73199E+02	0.13433E+03	0.54859E+03
4135.00	0.14920E-01	0.33479E+03	0.97004E+02	0.18445E+03	0.57480E+03
4140.00	0.14477E-01	0.20252E+03	0.14559E+03	0.32807E+03	0.57642E+03
4145.00	0.15369E-01	0.16250E+03	0.13063E+03	0.25944E+03	0.54665E+03
4150.00	0.14666E-01	0.27306E+03	0.11841E+03	0.24862E+03	0.56220E+03
4155.00	0.13895E-01	0.35804E+03	0.13380E+03	0.39622E+03	0.53983E+03
4160.00	0.14395E-01	0.33855E+03	0.11266E+03	0.35248E+03	0.53591E+03
4165.00	0.13876E-01	0.35808E+03	0.10489E+03	0.40677E+03	0.54347E+03
4170.00	0.16493E-01	0.47612E+03	0.99366E+02	0.32240E+03	0.54758E+03
4175.00	0.18454E-01	0.46514E+03	0.86902E+02	0.25718E+03	0.51898E+03
4180.00	0.14481E-01	0.40694E+03	0.10471E+03	0.52372E+03	0.47837E+03
4185.00	0.14740E-01	0.39254E+03	0.10196E+03	0.53138E+03	0.51340E+03
4190.00	0.18352E-01	0.49251E+03	0.92342E+02	0.34138E+03	0.54317E+03
4195.00	0.25116E-01	0.39939E+03	0.41787E+02	0.13081E+03	0.51529E+03
4200.00	0.23557E-01	0.38797E+03	0.43444E+02	0.14714E+03	0.55693E+03
4205.00	0.21587E-01	0.65542E+03	0.43846E+02	0.12839E+03	0.56064E+03
4210.00	0.23768E-01	0.89295E+03	0.39972E+02	0.12612E+03	0.51325E+03
4215.00	0.27329E-01	0.12723E+04	0.39700E+02	0.16535E+03	0.42348E+03
4220.00	0.24085E-01	0.11149E+04	0.47411E+02	0.17842E+03	0.38176E+03
4225.00	0.17624E-01	0.68123E+03	0.10608E+03	0.32946E+03	0.46565E+03
4230.00	0.19347E-01	0.55770E+03	0.92872E+02	0.24605E+03	0.53085E+03
4235.00	0.18965E-01	0.46552E+03	0.57965E+02	0.15977E+03	0.55756E+03
4240.00	0.18384E-01	0.57155E+03	0.47750E+02	0.14550E+03	0.46475E+03
4245.00	0.24969E-01	0.58609E+03	0.32285E+02	0.11578E+03	0.41500E+03
4250.00	0.24806E-01	0.72123E+03	0.38681E+02	0.13024E+03	0.45015E+03
4255.00	0.26250E-01	0.87116E+03	0.41672E+02	0.13744E+03	0.43120E+03
4260.00	0.30343E-01	0.89642E+03	0.37261E+02	0.12678E+03	0.40880E+03
4265.00	0.26659E-01	0.78026E+03	0.43485E+02	0.12481E+03	0.43947E+03
4270.00	0.27284E-01	0.71631E+03	0.39445E+02	0.11778E+03	0.40525E+03
4275.00	0.23390E-01	0.10092E+04	0.53734E+02	0.14001E+03	0.41199E+03
4280.00	0.20633E-01	0.10064E+04	0.63984E+02	0.14842E+03	0.45039E+03
4285.00	0.22431E-01	0.77588E+03	0.53815E+02	0.12865E+03	0.44926E+03
4290.00	0.22686E-01	0.56631E+03	0.48520E+02	0.12232E+03	0.51041E+03
4295.00	0.21095E-01	0.51300E+03	0.38912E+02	0.12246E+03	0.55583E+03
4300.00	0.20912E-01	0.49567E+03	0.33955E+02	0.12206E+03	0.59569E+03
4305.00	0.21749E-01	0.67692E+03	0.36792E+02	0.11895E+03	0.59197E+03
4310.00	0.25610E-01	0.12420E+04	0.34340E+02	0.13352E+03	0.48710E+03
4315.00	0.26423E-01	0.13991E+04	0.38349E+02	0.14160E+03	0.35824E+03
4320.00	0.25795E-01	0.44776E+03	0.51192E+02	0.51450E+02	0.36497E+03
4325.00	0.15675E-01	0.97379E+02	0.11252E+03	0.61427E+03	0.40777E+03
4330.00	0.15109E-01	0.18087E+03	0.10689E+03	0.59001E+03	0.31438E+03
4335.00	0.34644E-01	0.33929E+03	0.28866E+02	0.94565E+02	0.26625E+03
4340.00	0.30787E-01	0.63877E+03	0.35715E+02	0.11428E+03	0.31402E+03
4345.00	0.24395E-01	0.10048E+04	0.48693E+02	0.14936E+03	0.31067E+03
4350.00	0.23197E-01	0.10281E+04	0.48312E+02	0.14496E+03	0.37618E+03
4355.00	0.22114E-01	0.11300E+04	0.39114E+02	0.13076E+03	0.43454E+03
4360.00	0.20149E-01	0.10323E+04	0.36886E+02	0.12602E+03	0.45507E+03
4365.00	0.20755E-01	0.79074E+03	0.36027E+02	0.12501E+03	0.50311E+03
4370.00	0.19915E-01	0.67145E+03	0.40302E+02	0.12673E+03	0.53165E+03
4375.00	0.21344E-01	0.53666E+03	0.39642E+02	0.11910E+03	0.50137E+03
4380.00	0.22466E-01	0.49440E+03	0.35591E+02	0.11134E+03	0.43698E+03
4385.00	0.19267E-01	0.45489E+03	0.52736E+02	0.13866E+03	0.50673E+03
4390.00	0.20574E-01	0.41581E+03	0.43945E+02	0.12428E+03	0.45987E+03
4395.00	0.21875E-01	0.41141E+03	0.46293E+02	0.13525E+03	0.43229E+03

4400.00	0.20118E-01	0.51633E+03	0.75667E+02	0.19271E+03	0.49558E+03
4405.00	0.22906E-01	0.56576E+03	0.45500E+02	0.12139E+03	0.45853E+03
4410.00	0.20210E-01	0.51642E+03	0.47977E+02	0.12856E+03	0.51249E+03
4415.00	0.19904E-01	0.44054E+03	0.46318E+02	0.12992E+03	0.53251E+03
4420.00	0.24119E-01	0.62117E+03	0.38065E+02	0.11421E+03	0.49011E+03
4425.00	0.19729E-01	0.55726E+03	0.45121E+02	0.12574E+03	0.53667E+03
4430.00	0.18316E-01	0.54999E+03	0.53589E+02	0.14570E+03	0.58705E+03
4435.00	0.20286E-01	0.66266E+03	0.41185E+02	0.13085E+03	0.54383E+03
4440.00	0.19163E-01	0.66260E+03	0.45712E+02	0.13572E+03	0.52532E+03
4445.00	0.17726E-01	0.61257E+03	0.50767E+02	0.13942E+03	0.54853E+03
4450.00	0.18248E-01	0.64805E+03	0.50990E+02	0.12602E+03	0.56867E+03
4455.00	0.18992E-01	0.57231E+03	0.52750E+02	0.11897E+03	0.56848E+03
4460.00	0.18953E-01	0.47947E+03	0.54493E+02	0.12785E+03	0.55758E+03
4465.00	0.18005E-01	0.50173E+03	0.65208E+02	0.14363E+03	0.54344E+03
4470.00	0.17623E-01	0.50308E+03	0.92584E+02	0.19567E+03	0.50696E+03
4475.00	0.17024E-01	0.48116E+03	0.10059E+03	0.18731E+03	0.50154E+03
4480.00	0.16019E-01	0.44596E+03	0.11023E+03	0.17078E+03	0.50796E+03
4485.00	0.15419E-01	0.41345E+03	0.12743E+03	0.17908E+03	0.54681E+03
4490.00	0.15714E-01	0.35976E+03	0.13841E+03	0.21796E+03	0.53633E+03
4495.00	0.13771E-01	0.26600E+03	0.14625E+03	0.20127E+03	0.51629E+03
4500.00	0.12305E-01	0.22203E+03	0.14944E+03	0.19978E+03	0.50713E+03
4505.00	0.12371E-01	0.21967E+03	0.13206E+03	0.19988E+03	0.54462E+03
4510.00	0.12307E-01	0.15023E+03	0.13625E+03	0.24181E+03	0.53582E+03
4515.00	0.11168E-01	0.12048E+03	0.12216E+03	0.19406E+03	0.61776E+03
4520.00	0.12851E-01	0.10233E+03	0.12140E+03	0.25910E+03	0.66624E+03
4525.00	0.14721E-01	0.82015E+02	0.88952E+02	0.30217E+03	0.65253E+03
4530.00	0.20915E-01	0.16241E+03	0.55059E+02	0.12192E+03	0.74636E+03
4535.00	0.22586E-01	0.52595E+03	0.37943E+02	0.46813E+02	0.53230E+03
4540.00	0.22753E-01	0.97649E+03	0.45262E+02	0.12674E+03	0.41886E+03
4545.00	0.21602E-01	0.90365E+03	0.42555E+02	0.11999E+03	0.46820E+03
4550.00	0.19065E-01	0.37033E+03	0.42054E+02	0.49235E+02	0.62130E+03
4555.00	0.14365E-01	0.98134E+02	0.77327E+02	0.16262E+03	0.69560E+03
4560.00	0.18189E-01	0.42646E+02	0.85992E+02	0.14832E+03	0.67410E+03
4565.00	0.19184E-01	0.33282E+02	0.13900E+03	0.20466E+03	0.58248E+03
4570.00	0.20264E-01	0.26301E+02	0.17853E+03	0.18041E+03	0.52973E+03
4575.00	0.16307E-01	0.26545E+02	0.16858E+03	0.19383E+03	0.51320E+03
4580.00	0.14271E-01	0.31016E+02	0.20738E+03	0.19783E+03	0.38420E+03
4585.00	0.14068E-01	0.27735E+02	0.28012E+03	0.25647E+03	0.33097E+03
4590.00	0.11683E-01	0.46447E+02	0.19386E+03	0.22787E+03	0.27509E+03
4595.00	0.11885E-01	0.52977E+02	0.13531E+03	0.13366E+03	0.23480E+03
4600.00	0.11645E-01	0.72606E+02	0.12089E+03	0.10926E+03	0.21736E+03
4605.00	0.10459E-01	0.91659E+02	0.12124E+03	0.12617E+03	0.24566E+03
4610.00	0.98747E-02	0.85325E+02	0.13120E+03	0.16542E+03	0.31576E+03
4615.00	0.10542E-01	0.99399E+02	0.11411E+03	0.15398E+03	0.35894E+03
4620.00	0.16049E-01	0.74019E+02	0.92863E+02	0.68591E+02	0.42988E+03
4625.00	0.17004E-01	0.79604E+02	0.92428E+02	0.62310E+02	0.42922E+03
4630.00	0.15526E-01	0.50959E+02	0.67482E+02	0.28270E+02	0.48287E+03
4635.00	0.15939E-01	0.41283E+02	0.12159E+03	0.84471E+02	0.52349E+03
4640.00	0.17714E-01	0.41896E+02	0.57677E+02	0.25671E+02	0.46652E+03
4645.00	0.14672E-01	0.36420E+02	0.13166E+03	0.69938E+02	0.55678E+03
4650.00	0.13649E-01	0.43793E+02	0.14687E+03	0.99283E+02	0.52118E+03
4655.00	0.11738E-01	0.32423E+02	0.20919E+03	0.14090E+03	0.57491E+03
4660.00	0.12080E-01	0.17456E+02	0.26454E+03	0.18041E+03	0.63134E+03
4665.00	0.13442E-01	0.24120E+02	0.80175E+02	0.35490E+02	0.61501E+03
4670.00	0.31760E-01	0.19594E+02	0.28154E+03	0.15396E+03	0.70466E+03
4675.00	0.12615E-01	0.16142E+02	0.86980E+02	0.35568E+02	0.72001E+03
4680.00	0.23934E-01	0.14787E+02	0.36133E+03	0.15368E+03	0.75457E+03
4685.00	0.12593E-01	0.10876E+02	0.29480E+03	0.16396E+03	0.84375E+03
4690.00	0.12103E-01	0.14785E+02	0.12818E+03	0.49149E+02	0.85287E+03
4695.00	0.12322E-01	0.10080E+02	0.31913E+03	0.16346E+03	0.92248E+03

4700.00	0.17613E-01	0.80053E+01	0.37860E+03	0.16397E+03	0.99661E+03
4705.00	0.20062E-01	0.81148E+01	0.46087E+03	0.16275E+03	0.10229E+04
4710.00	0.20940E-01	0.81263E+01	0.50996E+03	0.16320E+03	0.10785E+04
4715.00	0.18073E-01	0.45563E+01	0.57040E+03	0.16682E+03	0.10877E+04
4720.00	0.17047E-01	0.43032E+01	0.45310E+03	0.16420E+03	0.11429E+04
4725.00	0.16976E-01	0.32134E+01	0.60697E+03	0.16585E+03	0.12303E+04
4730.00	0.17778E-01	0.25773E+01	0.62560E+03	0.16685E+03	0.11711E+04
4735.00	0.17137E-01	0.24327E+01	0.59509E+03	0.16418E+03	0.11723E+04
4740.00	0.17978E-01	0.16832E+01	0.81776E+03	0.16496E+03	0.12605E+04
4745.00	0.17341E-01	0.16017E+01	0.95146E+03	0.16507E+03	0.12011E+04
4750.00	0.16931E-01	0.14600E+01	0.13060E+04	0.16747E+03	0.11715E+04
4755.00	0.17244E-01	0.11188E+01	0.10083E+04	0.16705E+03	0.12027E+04
4760.00	0.16357E-01	0.11395E+01	0.15457E+04	0.16531E+03	0.11453E+04
4765.00	0.15828E-01	0.10733E+01	0.17944E+04	0.16528E+03	0.11714E+04
4770.00	0.16762E-01	0.83976E+00	0.24765E+04	0.16904E+03	0.11738E+04
4775.00	0.16965E-01	0.76840E+00	0.31327E+04	0.16506E+03	0.11116E+04
4780.00	0.16749E-01	0.80610E+00	0.22394E+04	0.16463E+03	0.11220E+04
4785.00	0.17735E-01	0.70761E+00	0.24327E+04	0.16473E+03	0.10913E+04
4790.00	0.18042E-01	0.55213E+00	0.34355E+04	0.16483E+03	0.10114E+04
4795.00	0.17270E-01	0.63577E+00	0.27282E+04	0.16450E+03	0.10827E+04
4800.00	0.17753E-01	0.51624E+00	0.26827E+04	0.16427E+03	0.10126E+04
4805.00	0.18841E-01	0.36141E+00	0.36645E+04	0.16395E+03	0.84223E+03
4810.00	0.17716E-01	0.49355E+00	0.24794E+04	0.16394E+03	0.10523E+04
4815.00	0.17693E-01	0.43378E+00	0.20460E+04	0.16341E+03	0.10111E+04
4820.00	0.19317E-01	0.25635E+00	0.32459E+04	0.16304E+03	0.70539E+03
4825.00	0.19540E-01	0.25199E+00	0.23676E+04	0.17319E+03	0.78175E+03
4830.00	0.19050E-01	0.23973E+00	0.13401E+04	0.16216E+03	0.80145E+03
4835.00	0.19422E-01	0.19169E+00	0.19745E+04	0.15299E+03	0.66007E+03
4840.00	0.18905E-01	0.19650E+00	0.11888E+04	0.16171E+03	0.74296E+03
4845.00	0.18457E-01	0.17870E+00	0.57245E+03	0.16338E+03	0.73620E+03
4850.00	0.18733E-01	0.17554E+00	0.42776E+04	0.15882E+03	0.56093E+03
4855.00	0.18274E-01	0.15296E+00	0.81129E+03	0.15971E+03	0.67626E+03
4860.00	0.18121E-01	0.15746E+00	0.65504E+03	0.16145E+03	0.67949E+03
4865.00	0.17749E-01	0.15311E+00	0.14960E+04	0.16144E+03	0.62426E+03
4870.00	0.15805E-01	0.18359E+00	0.82104E+03	0.16315E+03	0.77350E+03
4875.00	0.15516E-01	0.14606E+00	0.18467E+04	0.15529E+03	0.60985E+03
4880.00	0.15327E-01	0.14646E+00	0.23716E+04	0.15515E+03	0.57888E+03
4885.00	0.13828E-01	0.22818E+00	0.20326E+04	0.16169E+03	0.81186E+03
4890.00	0.12999E-01	0.26163E+00	0.25595E+04	0.16102E+03	0.82669E+03
4895.00	0.13378E-01	0.18898E+00	0.17185E+04	0.15633E+03	0.75517E+03
4900.00	0.13196E-01	0.17314E+00	0.16150E+04	0.16053E+03	0.74599E+03
4905.00	0.12350E-01	0.24763E+00	0.27377E+04	0.16073E+03	0.82184E+03
4910.00	0.11791E-01	0.31905E+00	0.30250E+04	0.16076E+03	0.81099E+03
4915.00	0.12111E-01	0.25415E+00	0.22622E+04	0.16044E+03	0.79067E+03
4920.00	0.12725E-01	0.14348E+00	0.86767E+03	0.15887E+03	0.72218E+03
4925.00	0.11348E-01	0.35512E+00	0.19871E+04	0.15991E+03	0.79061E+03
4930.00	0.11316E-01	0.38553E+00	0.23510E+04	0.15987E+03	0.77050E+03
4935.00	0.11324E-01	0.29136E+00	0.30724E+04	0.15990E+03	0.74070E+03
4940.00	0.10598E-01	0.31383E+00	0.17965E+04	0.15942E+03	0.70035E+03
4945.00	0.10039E-01	0.35602E+00	0.15092E+04	0.15893E+03	0.71088E+03
4950.00	0.10045E-01	0.36488E+00	0.23890E+04	0.15923E+03	0.72029E+03
4955.00	0.95843E-02	0.69107E+00	0.28316E+04	0.16144E+03	0.56995E+03
4960.00	0.96280E-02	0.67787E+00	0.21629E+04	0.16564E+03	0.55343E+03
4965.00	0.10282E-01	0.54257E+00	0.23530E+04	0.15883E+03	0.62183E+03
4970.00	0.94100E-02	0.45414E+00	0.24759E+04	0.15857E+03	0.62916E+03
4975.00	0.88705E-02	0.30195E+00	0.24158E+04	0.15843E+03	0.57338E+03
4980.00	0.94340E-02	0.62997E+00	0.18751E+04	0.16080E+03	0.49465E+03
4985.00	0.10002E-01	0.73355E+00	0.20815E+04	0.15852E+03	0.52551E+03
4990.00	0.92751E-02	0.38280E+00	0.19918E+04	0.15783E+03	0.61172E+03
4995.00	0.91552E-02	0.19898E+00	0.24292E+03	0.15263E+03	0.59935E+03

5000.00	0.95383E-02	0.77085E+00	0.17044E+04	0.16206E+03	0.42938E+03
5005.00	0.95515E-02	0.15229E+01	0.13803E+04	0.16316E+03	0.40106E+03
5010.00	0.12761E-01	0.10133E+01	0.26355E+04	0.15787E+03	0.51335E+03
5015.00	0.10360E-01	0.19475E+00	0.89146E+01	0.14793E+03	0.58040E+03
5020.00	0.10903E-01	0.60619E+00	0.20765E+04	0.16783E+03	0.44575E+03
5025.00	0.10303E-01	0.16082E+01	0.16127E+04	0.15945E+03	0.36620E+03
5030.00	0.11743E-01	0.11144E+01	0.15551E+04	0.15787E+03	0.40832E+03
5035.00	0.10555E-01	0.32673E+00	0.19729E+03	0.15106E+03	0.47086E+03
5040.00	0.10046E-01	0.96276E+00	0.16494E+04	0.16284E+03	0.36422E+03
5045.00	0.89136E-02	0.15696E+01	0.96587E+03	0.15892E+03	0.29424E+03
5050.00	0.10274E-01	0.96704E+00	0.80378E+03	0.15502E+03	0.36667E+03
5055.00	0.97144E-02	0.90964E+00	0.69503E+03	0.15457E+03	0.38235E+03
5060.00	0.95385E-02	0.10769E+01	0.69032E+03	0.16076E+03	0.31970E+03
5065.00	0.96175E-02	0.99263E+00	0.85004E+03	0.16100E+03	0.29902E+03
5070.00	0.98130E-02	0.86197E+00	0.72109E+03	0.16336E+03	0.36716E+03
5075.00	0.10616E-01	0.13124E+01	0.94705E+03	0.15487E+03	0.33768E+03
5080.00	0.93074E-02	0.14382E+01	0.58639E+03	0.15412E+03	0.33385E+03
5085.00	0.90771E-02	0.15544E+01	0.56391E+03	0.15923E+03	0.32295E+03
5090.00	0.94906E-02	0.18006E+01	0.58205E+03	0.16413E+03	0.23502E+03
5095.00	0.10638E-01	0.13420E+01	0.43086E+03	0.16055E+03	0.28656E+03
5100.00	0.86806E-02	0.15571E+01	0.41142E+03	0.15913E+03	0.29278E+03
5105.00	0.89004E-02	0.14736E+01	0.44190E+03	0.15279E+03	0.28398E+03
5110.00	0.90140E-02	0.14555E+01	0.45430E+03	0.15251E+03	0.28073E+03
5115.00	0.85271E-02	0.17341E+01	0.52942E+03	0.16068E+03	0.23449E+03
5120.00	0.95835E-02	0.12867E+01	0.51770E+03	0.16056E+03	0.32502E+03
5125.00	0.12231E-01	0.20795E+01	0.41628E+03	0.15095E+03	0.40535E+03
5130.00	0.67590E-02	0.36285E+01	0.21405E+03	0.11843E+03	0.29211E+03
5135.00	0.70493E-02	0.35521E+01	0.37788E+03	0.19772E+03	0.19202E+03
5140.00	0.78393E-02	0.23448E+01	0.42550E+03	0.15733E+03	0.19527E+03
5145.00	0.86846E-02	0.19435E+01	0.57466E+03	0.16197E+03	0.20177E+03
5150.00	0.91343E-02	0.18135E+01	0.63010E+03	0.15467E+03	0.22943E+03
5155.00	0.81199E-02	0.18121E+01	0.45693E+03	0.15079E+03	0.28773E+03
5160.00	0.71526E-02	0.20554E+01	0.30428E+03	0.16119E+03	0.28699E+03
5165.00	0.77780E-02	0.17993E+01	0.28235E+03	0.15871E+03	0.26887E+03
5170.00	0.74383E-02	0.22658E+01	0.25159E+03	0.17688E+03	0.28571E+03
5175.00	0.66189E-02	0.32274E+01	0.14687E+03	0.13737E+03	0.28693E+03
5180.00	0.10695E-01	0.26771E+01	0.26382E+03	0.14576E+03	0.29903E+03
5185.00	0.86088E-02	0.24491E+01	0.38481E+03	0.15758E+03	0.28754E+03
5190.00	0.83240E-02	0.39583E+01	0.37332E+03	0.17745E+03	0.23378E+03
5195.00	0.69135E-02	0.45313E+01	0.21614E+03	0.12079E+03	0.23317E+03
5200.00	0.78975E-02	0.52926E+01	0.93434E+02	0.57576E+02	0.26055E+03
5205.00	0.91818E-02	0.72378E+01	0.77077E+02	0.59947E+02	0.27780E+03
5210.00	0.11476E-01	0.54287E+01	0.63235E+02	0.23229E+02	0.30233E+03
5215.00	0.77214E-02	0.30648E+01	0.25446E+03	0.12495E+03	0.32181E+03
5220.00	0.74365E-02	0.37366E+01	0.28771E+03	0.14382E+03	0.30190E+03
5225.00	0.68407E-02	0.44638E+01	0.21142E+03	0.13389E+03	0.29220E+03
5230.00	0.82749E-02	0.53002E+01	0.13753E+03	0.77507E+02	0.31080E+03
5235.00	0.91485E-02	0.44131E+01	0.12796E+03	0.64366E+02	0.35671E+03
5240.00	0.77987E-02	0.40060E+01	0.21132E+03	0.15846E+03	0.33536E+03
5245.00	0.84157E-02	0.32058E+01	0.22872E+03	0.16933E+03	0.36333E+03
5250.00	0.92168E-02	0.29251E+01	0.18898E+03	0.15749E+03	0.40066E+03
5255.00	0.88441E-02	0.36275E+01	0.18120E+03	0.16446E+03	0.38400E+03
5260.00	0.99843E-02	0.28822E+01	0.20704E+03	0.15685E+03	0.44245E+03
5265.00	0.11626E-01	0.22972E+01	0.16636E+03	0.15741E+03	0.49260E+03
5270.00	0.10268E-01	0.31558E+01	0.16394E+03	0.14082E+03	0.45586E+03
5275.00	0.11341E-01	0.29811E+01	0.19529E+03	0.14385E+03	0.48054E+03
5280.00	0.12056E-01	0.21685E+01	0.18944E+03	0.15642E+03	0.52493E+03
5285.00	0.10528E-01	0.29072E+01	0.14441E+03	0.15705E+03	0.49640E+03
5290.00	0.97357E-02	0.32300E+01	0.11647E+03	0.15846E+03	0.54272E+03
5295.00	0.10034E-01	0.25613E+01	0.13046E+03	0.15741E+03	0.57122E+03

5300.00	0.99475E-02	0.25987E+01	0.11912E+03	0.15733E+03	0.51633E+03
5305.00	0.10571E-01	0.29416E+01	0.11385E+03	0.15736E+03	0.55049E+03
5310.00	0.96780E-02	0.35943E+01	0.11065E+03	0.15743E+03	0.55538E+03
5315.00	0.83671E-02	0.38393E+01	0.10773E+03	0.17475E+03	0.52787E+03
5320.00	0.91777E-02	0.32915E+01	0.11079E+03	0.15711E+03	0.52254E+03
5325.00	0.93636E-02	0.34774E+01	0.12453E+03	0.15619E+03	0.53780E+03
5330.00	0.90144E-02	0.44692E+01	0.12870E+03	0.15623E+03	0.52706E+03
5335.00	0.85581E-02	0.50639E+01	0.13415E+03	0.17121E+03	0.55542E+03
5340.00	0.83051E-02	0.55103E+01	0.13190E+03	0.16985E+03	0.56730E+03
5345.00	0.75578E-02	0.59463E+01	0.11079E+03	0.16205E+03	0.48084E+03
5350.00	0.78968E-02	0.58367E+01	0.12730E+03	0.17911E+03	0.48007E+03
5355.00	0.69980E-02	0.71733E+01	0.13732E+03	0.17710E+03	0.46901E+03
5360.00	0.55041E-02	0.10869E+02	0.12933E+03	0.17156E+03	0.43410E+03
5365.00	0.68649E-02	0.98918E+01	0.11888E+03	0.11723E+03	0.44071E+03
5370.00	0.85643E-02	0.83197E+01	0.15498E+03	0.14519E+03	0.40068E+03
5375.00	0.82174E-02	0.10738E+02	0.17311E+03	0.18041E+03	0.34625E+03
5380.00	0.80008E-02	0.13948E+02	0.17381E+03	0.19701E+03	0.37856E+03
5385.00	0.86688E-02	0.13568E+02	0.14858E+03	0.19025E+03	0.43394E+03
5390.00	0.92382E-02	0.11218E+02	0.12752E+03	0.18431E+03	0.43576E+03
5395.00	0.86917E-02	0.13210E+02	0.12219E+03	0.18257E+03	0.39338E+03
5400.00	0.78768E-02	0.16942E+02	0.12714E+03	0.19150E+03	0.35634E+03
5405.00	0.68124E-02	0.18906E+02	0.99032E+02	0.18199E+03	0.38228E+03
5410.00	0.72705E-02	0.18159E+02	0.94635E+02	0.20855E+03	0.39800E+03
5415.00	0.80593E-02	0.16364E+02	0.90657E+02	0.15973E+03	0.37013E+03
5420.00	0.83157E-02	0.15147E+02	0.87985E+02	0.11478E+03	0.40366E+03
5425.00	0.95130E-02	0.21185E+02	0.93224E+02	0.12219E+03	0.40903E+03
5430.00	0.73772E-02	0.23516E+02	0.13573E+03	0.20017E+03	0.37457E+03
5435.00	0.67504E-02	0.22807E+02	0.94701E+02	0.15960E+03	0.41154E+03
5440.00	0.61703E-02	0.27108E+02	0.74103E+02	0.16416E+03	0.42752E+03
5445.00	0.66204E-02	0.28262E+02	0.88425E+02	0.18412E+03	0.42465E+03
5450.00	0.65714E-02	0.30576E+02	0.85092E+02	0.15664E+03	0.46257E+03
5455.00	0.64305E-02	0.26983E+02	0.93791E+02	0.16858E+03	0.47830E+03
5460.00	0.73960E-02	0.23893E+02	0.12655E+03	0.23137E+03	0.48087E+03
5465.00	0.66455E-02	0.20165E+02	0.12280E+03	0.19297E+03	0.46062E+03
5470.00	0.12000E-01	0.29134E+02	0.75432E+02	0.92076E+02	0.44999E+03
5475.00	0.70430E-02	0.34758E+02	0.10107E+03	0.16798E+03	0.45409E+03
5480.00	0.91674E-02	0.22402E+02	0.17319E+03	0.32959E+03	0.45748E+03
5485.00	0.74343E-02	0.27554E+02	0.10350E+03	0.18905E+03	0.45372E+03
5490.00	0.98280E-02	0.35676E+02	0.92444E+02	0.13965E+03	0.41564E+03
5495.00	0.11691E-01	0.33636E+02	0.82244E+02	0.10657E+03	0.40011E+03
5500.00	0.96142E-02	0.31368E+02	0.99889E+02	0.14260E+03	0.43511E+03
5505.00	0.75145E-02	0.25070E+02	0.10672E+03	0.19861E+03	0.43515E+03
5510.00	0.10868E-01	0.37916E+02	0.85865E+02	0.15820E+03	0.38959E+03
5515.00	0.11035E-01	0.43782E+02	0.11045E+03	0.15622E+03	0.35821E+03
5520.00	0.11172E-01	0.36127E+02	0.10179E+03	0.14636E+03	0.36160E+03
5525.00	0.10024E-01	0.28642E+02	0.11539E+03	0.19041E+03	0.38671E+03
5530.00	0.87843E-02	0.29732E+02	0.12231E+03	0.18547E+03	0.36280E+03
5535.00	0.10203E-01	0.43793E+02	0.10610E+03	0.15152E+03	0.32110E+03
5540.00	0.93461E-02	0.34618E+02	0.10541E+03	0.19054E+03	0.36078E+03
5545.00	0.10434E-01	0.38107E+02	0.88113E+02	0.17554E+03	0.39222E+03
5550.00	0.97964E-02	0.35997E+02	0.72415E+02	0.17893E+03	0.40979E+03
5555.00	0.87923E-02	0.37056E+02	0.64101E+02	0.17088E+03	0.38589E+03
5560.00	0.87938E-02	0.51261E+02	0.63560E+02	0.15908E+03	0.36889E+03
5565.00	0.88419E-02	0.59884E+02	0.67553E+02	0.15344E+03	0.41048E+03
5570.00	0.10092E-01	0.88808E+02	0.73222E+02	0.14772E+03	0.43719E+03
5575.00	0.12480E-01	0.14422E+03	0.73404E+02	0.14780E+03	0.39197E+03
5580.00	0.14313E-01	0.22486E+03	0.75467E+02	0.12847E+03	0.31363E+03
5585.00	0.15050E-01	0.19870E+03	0.74658E+02	0.11345E+03	0.28422E+03
5590.00	0.13734E-01	0.90917E+02	0.72041E+02	0.13835E+03	0.35875E+03
5595.00	0.10426E-01	0.63064E+02	0.67912E+02	0.20246E+03	0.36836E+03

5600.00	0.11100E-01	0.85498E+02	0.65326E+02	0.16387E+03	0.28671E+03
5605.00	0.11325E-01	0.72487E+02	0.73765E+02	0.16173E+03	0.20881E+03
5610.00	0.92079E-02	0.37808E+02	0.89579E+02	0.19917E+03	0.22649E+03
5615.00	0.88086E-02	0.31051E+02	0.99267E+02	0.18182E+03	0.22880E+03
5620.00	0.10303E-01	0.40251E+02	0.93821E+02	0.13426E+03	0.17807E+03
5625.00	0.96719E-02	0.48253E+02	0.11037E+03	0.21242E+03	0.17642E+03
5630.00	0.12998E-01	0.11029E+03	0.78027E+02	0.12706E+03	0.21047E+03
5635.00	0.12619E-01	0.14809E+03	0.56901E+02	0.14254E+03	0.29958E+03
5640.00	0.11054E-01	0.10107E+03	0.59050E+02	0.17643E+03	0.34853E+03
5645.00	0.12306E-01	0.79245E+02	0.76205E+02	0.21206E+03	0.32562E+03
5650.00	0.10343E-01	0.60711E+02	0.83866E+02	0.18563E+03	0.28867E+03
5655.00	0.11300E-01	0.61379E+02	0.80924E+02	0.14919E+03	0.31184E+03
5660.00	0.12956E-01	0.77458E+02	0.74318E+02	0.13796E+03	0.35998E+03
5665.00	0.10857E-01	0.67966E+02	0.82151E+02	0.16665E+03	0.36000E+03
5670.00	0.10497E-01	0.66157E+02	0.73158E+02	0.15984E+03	0.40974E+03
5675.00	0.10185E-01	0.63001E+02	0.61143E+02	0.14117E+03	0.46207E+03
5680.00	0.87298E-02	0.52960E+02	0.61164E+02	0.17864E+03	0.44121E+03
5685.00	0.87316E-02	0.53996E+02	0.54258E+02	0.19447E+03	0.46591E+03
5690.00	0.85631E-02	0.50343E+02	0.47834E+02	0.16160E+03	0.49502E+03
5695.00	0.90060E-02	0.55513E+02	0.54700E+02	0.17230E+03	0.45575E+03
5700.00	0.97163E-02	0.63410E+02	0.62072E+02	0.17076E+03	0.44516E+03
5705.00	0.91139E-02	0.51442E+02	0.62180E+02	0.17411E+03	0.46723E+03
5710.00	0.91841E-02	0.50563E+02	0.65150E+02	0.18170E+03	0.47437E+03
5715.00	0.10004E-01	0.63180E+02	0.64620E+02	0.15823E+03	0.44518E+03
5720.00	0.88299E-02	0.65561E+02	0.62561E+02	0.16448E+03	0.42883E+03
5725.00	0.85188E-02	0.58236E+02	0.79770E+02	0.18383E+03	0.46819E+03
5730.00	0.87800E-02	0.70768E+02	0.77829E+02	0.15475E+03	0.45380E+03
5735.00	0.84354E-02	0.72477E+02	0.77261E+02	0.17374E+03	0.41930E+03
5740.00	0.88454E-02	0.61778E+02	0.80279E+02	0.18273E+03	0.44871E+03
5745.00	0.10790E-01	0.84288E+02	0.69474E+02	0.16600E+03	0.45393E+03
5750.00	0.12752E-01	0.96576E+02	0.81555E+02	0.27177E+03	0.44443E+03
5755.00	0.11606E-01	0.86342E+02	0.58881E+02	0.18898E+03	0.48377E+03
5760.00	0.12281E-01	0.10181E+03	0.52764E+02	0.16693E+03	0.48775E+03
5765.00	0.13414E-01	0.12014E+03	0.50690E+02	0.18161E+03	0.46026E+03
5770.00	0.13123E-01	0.13413E+03	0.50810E+02	0.14855E+03	0.44903E+03
5775.00	0.15328E-01	0.17936E+03	0.53792E+02	0.14284E+03	0.41664E+03
5780.00	0.15035E-01	0.17692E+03	0.53492E+02	0.14557E+03	0.38732E+03
5785.00	0.14222E-01	0.16229E+03	0.58929E+02	0.13658E+03	0.32555E+03
5790.00	0.14441E-01	0.21358E+03	0.71601E+02	0.13544E+03	0.27260E+03
5795.00	0.13814E-01	0.19525E+03	0.87316E+02	0.16751E+03	0.23407E+03
5800.00	0.13432E-01	0.17003E+03	0.10372E+03	0.20170E+03	0.19526E+03
5805.00	0.12631E-01	0.13813E+03	0.11515E+03	0.19811E+03	0.18419E+03
5810.00	0.11342E-01	0.86414E+02	0.15271E+03	0.31031E+03	0.17956E+03
5815.00	0.10142E-01	0.62149E+02	0.15647E+03	0.33675E+03	0.22096E+03
5820.00	0.11264E-01	0.50182E+02	0.14506E+03	0.32146E+03	0.27564E+03
5825.00	0.10517E-01	0.45547E+02	0.10648E+03	0.26650E+03	0.33368E+03
5830.00	0.95578E-02	0.58945E+02	0.58332E+02	0.16717E+03	0.35835E+03
5835.00	0.13168E-01	0.98409E+02	0.58911E+02	0.19655E+03	0.35401E+03
5840.00	0.14323E-01	0.12735E+03	0.58289E+02	0.17121E+03	0.39389E+03
5845.00	0.14833E-01	0.12174E+03	0.61343E+02	0.16217E+03	0.34306E+03
5850.00	0.18471E-01	0.17195E+03	0.74464E+02	0.13910E+03	0.25346E+03
5855.00	0.19685E-01	0.29065E+03	0.63824E+02	0.12266E+03	0.31709E+03
5860.00	0.17677E-01	0.35487E+03	0.64384E+02	0.12926E+03	0.29725E+03
5865.00	0.15619E-01	0.27498E+03	0.61513E+02	0.13434E+03	0.30737E+03
5870.00	0.14277E-01	0.25277E+03	0.55504E+02	0.13635E+03	0.36146E+03
5875.00	0.14219E-01	0.26074E+03	0.55965E+02	0.14194E+03	0.41225E+03
5880.00	0.13310E-01	0.20060E+03	0.52248E+02	0.14542E+03	0.46145E+03
5885.00	0.11602E-01	0.13990E+03	0.49608E+02	0.14507E+03	0.45642E+03
5890.00	0.14804E-01	0.14314E+03	0.52805E+02	0.13694E+03	0.50073E+03
5895.00	0.15527E-01	0.10559E+03	0.53293E+02	0.13396E+03	0.51446E+03
5900.00	0.15385E-01	0.95975E+02	0.61822E+02	0.13801E+03	0.46894E+03
5905.00	0.16091E-01	0.10876E+03	0.67217E+02	0.14864E+03	0.44502E+03
5910.00	0.13657E-01	0.88809E+02	0.64368E+02	0.14283E+03	0.44732E+03
5915.00	0.14464E-01	0.76421E+02	0.88883E+02	0.13649E+03	0.42099E+03
5920.00	0.12238E-01	0.60602E+02	0.92277E+02	0.16671E+03	0.40873E+03
5925.00	0.12878E-01	0.78741E+02	0.89074E+02	0.16660E+03	0.39860E+03
5930.00	0.11970E-01	0.72342E+02	0.86615E+02	0.19627E+03	0.39233E+03
5935.00	0.98266E-02	0.70362E+02	0.85922E+02	0.15404E+03	0.39765E+03
5940.00	0.99437E-02	0.52940E+02	0.91947E+02	0.16547E+03	0.43234E+03
5945.00	0.94006E-02	0.57678E+02	0.79995E+02	0.16783E+03	0.43288E+03
5950.00	0.97214E-02	0.51620E+02	0.87342E+02	0.16908E+03	0.43714E+03
5955.00	0.13417E-01	0.29516E+02	0.12769E+03	0.31785E+03	0.42870E+03
5960.00	0.99067E-02	0.43770E+02	0.68542E+02	0.13508E+03	0.40661E+03
5965.00	0.10921E-01	0.49290E+02	0.59529E+02	0.12412E+03	0.44565E+03
5970.00	0.99783E-02	0.42708E+02	0.65877E+02	0.10188E+03	0.43024E+03
5975.00	0.12096E-01	0.53006E+02	0.62941E+02	0.10577E+03	0.46653E+03
5980.00	0.13174E-01	0.63058E+02	0.49361E+02	0.15624E+03	0.53433E+03
5985.00	0.13695E-01	0.94711E+02	0.45624E+02	0.13715E+03	0.59095E+03
5990.00	0.15474E-01	0.14638E+03	0.50745E+02	0.12422E+03	0.66640E+03
5995.00	0.20032E-01	0.23470E+03	0.68203E+02	0.11464E+03	0.62690E+03
6000.00	0.23044E-01	0.42013E+03	0.70312E+02	0.11149E+03	0.38668E+03
6005.00	0.23101E-01	0.13899E+03	0.53451E+02	0.41461E+02	0.24208E+03
6010.00	0.14721E-01	0.30375E+02	0.23450E+03	0.41149E+03	0.26730E+03
6015.00	0.10474E-01	0.32185E+02	0.17579E+03	0.29146E+03	0.28396E+03
6020.00	0.12564E-01	0.26968E+02	0.13657E+03	0.20078E+03	0.34940E+03
6025.00	0.12696E-01	0.29323E+02	0.16507E+03	0.29635E+03	0.35630E+03
6030.00	0.12707E-01	0.40867E+02	0.12954E+03	0.32451E+03	0.48552E+03
6035.00	0.15620E-01	0.82173E+02	0.60198E+02	0.10003E+03	0.54906E+03
6040.00	0.12630E-01	0.10715E+03	0.82548E+02	0.11731E+03	0.33633E+03
6045.00	0.10030E-01	0.55573E+02	0.19249E+03	0.25746E+03	0.19820E+03
6050.00	0.12958E-01	0.29774E+02	0.29948E+03	0.45188E+03	0.23547E+03
6055.00	0.14285E-01	0.59226E+02	0.93511E+02	0.90200E+02	0.23565E+03
6060.00	0.11165E-01	0.12702E+03	0.82719E+02	0.13898E+03	0.22807E+03
6065.00	0.13891E-01	0.15612E+03	0.64151E+02	0.11482E+03	0.29238E+03
6070.00	0.13701E-01	0.10390E+03	0.62852E+02	0.11035E+03	0.36205E+03
6075.00	0.11255E-01	0.53976E+02	0.11638E+03	0.32451E+03	0.38161E+03
6080.00	0.12390E-01	0.41762E+02	0.14909E+03	0.32832E+03	0.38638E+03
6085.00	0.14308E-01	0.38921E+02	0.14470E+03	0.27762E+03	0.39245E+03
6090.00	0.12881E-01	0.38718E+02	0.14178E+03	0.19839E+03	0.39645E+03
6095.00	0.14430E-01	0.38468E+02	0.16238E+03	0.19423E+03	0.37552E+03
6100.00	0.14443E-01	0.55031E+02	0.16160E+03	0.17405E+03	0.36552E+03
6105.00	0.12984E-01	0.57581E+02	0.14581E+03	0.14459E+03	0.37792E+03
6110.00	0.16162E-01	0.97973E+02	0.13952E+03	0.90411E+02	0.35061E+03
6115.00	0.12777E-01	0.62747E+02	0.15986E+03	0.14912E+03	0.37573E+03
6120.00	0.14577E-01	0.13659E+03	0.10908E+03	0.66043E+02	0.40684E+03
6125.00	0.15971E-01	0.13645E+03	0.10190E+03	0.59411E+02	0.41344E+03
6130.00	0.13932E-01	0.61767E+02	0.13238E+03	0.11433E+03	0.43853E+03
6135.00	0.15036E-01	0.59770E+02	0.95361E+02	0.65629E+02	0.48529E+03
6140.00	0.13848E-01	0.54375E+02	0.10429E+03	0.92179E+02	0.50111E+03
6145.00	0.14731E-01	0.62996E+02	0.11355E+03	0.93240E+02	0.51680E+03
6150.00	0.14348E-01	0.46165E+02	0.86802E+02	0.76697E+02	0.54505E+03
6155.00	0.14351E-01	0.49890E+02	0.69493E+02	0.57681E+02	0.60655E+03
6160.00	0.98971E-02	0.40342E+02	0.10561E+03	0.10895E+03	0.62946E+03
6165.00	0.79382E-02	0.34529E+02	0.11972E+03	0.12523E+03	0.63091E+03
6170.00	0.97135E-02	0.29274E+02	0.94656E+02	0.77706E+02	0.64559E+03
6175.00	0.92542E-02	0.24725E+02	0.10234E+03	0.11064E+03	0.69176E+03
6180.00	0.12578E-01	0.25067E+02	0.72237E+02	0.59251E+02	0.71991E+03
6185.00	0.12410E-01	0.15935E+02	0.85302E+02	0.52802E+02	0.73516E+03
6190.00	0.10787E-01	0.13624E+02	0.12367E+03	0.11067E+03	0.70479E+03
6195.00	0.13419E-01	0.11995E+02	0.87539E+02	0.71753E+02	0.74620E+03
6200.00	0.18505E-01	0.78868E+01	0.13900E+03	0.11958E+03	0.79611E+03
6205.00	0.16935E-01	0.76946E+01	0.17143E+03	0.11976E+03	0.79888E+03
6210.00	0.18679E-01	0.58051E+01	0.17811E+03	0.12073E+03	0.85657E+03
6215.00	0.22398E-01	0.51824E+01	0.19697E+03	0.12006E+03	0.87318E+03
6220.00	0.21206E-01	0.48106E+01	0.23716E+03	0.12230E+03	0.89833E+03
6225.00	0.25887E-01	0.30720E+01	0.29441E+03	0.13197E+03	0.93822E+03
6230.00	0.27081E-01	0.32315E+01	0.28113E+03	0.12341E+03	0.99891E+03
6235.00	0.25644E-01	0.28271E+01	0.38233E+03	0.12389E+03	0.99016E+03
6240.00	0.29105E-01	0.16357E+01	0.46291E+03	0.12942E+03	0.99620E+03
6245.00	0.28421E-01	0.18126E+01	0.48373E+03	0.12847E+03	0.11032E+04
6250.00	0.26629E-01	0.17372E+01	0.58594E+03	0.12429E+03	0.11194E+04
6255.00	0.27163E-01	0.13257E+01	0.59877E+03	0.12850E+03	0.10513E+04
6260.00	0.26688E-01	0.11873E+01	0.69381E+03	0.12814E+03	0.10962E+04
6265.00	0.27750E-01	0.85803E+00	0.72587E+03	0.12778E+03	0.10620E+04
6270.00	0.28181E-01	0.68041E+00	0.74080E+03	0.12583E+03	0.98801E+03
6275.00	0.30746E-01	0.48157E+00	0.90459E+03	0.12579E+03	0.85494E+03
6280.00	0.31513E-01	0.38186E+00	0.82839E+03	0.12201E+03	0.76402E+03
6285.00	0.31131E-01	0.34637E+00	0.70760E+03	0.12255E+03	0.73776E+03
6290.00	0.32139E-01	0.28264E+00	0.11177E+04	0.12527E+03	0.62660E+03
6295.00	0.32419E-01	0.26571E+00	0.17737E+04	0.12610E+03	0.55332E+03
6300.00	0.30370E-01	0.29267E+00	0.14836E+04	0.12658E+03	0.62971E+03
6305.00	0.31461E-01	0.22185E+00	0.17288E+04	0.12638E+03	0.52718E+03
6310.00	0.32696E-01	0.15689E+00	0.16033E+04	0.12703E+03	0.41122E+03
6315.00	0.30892E-01	0.23194E+00	0.33957E+04	0.13117E+03	0.47994E+03
6320.00	0.31453E-01	0.17634E+00	0.17500E+04	0.12163E+03	0.43642E+03
6325.00	0.33239E-01	0.12668E+00	0.19991E+04	0.12630E+03	0.35050E+03
6330.00	0.33146E-01	0.11193E+00	0.17596E+04	0.11817E+03	0.35648E+03
6335.00	0.32369E-01	0.13663E+00	0.15892E+04	0.12087E+03	0.38696E+03
6340.00	0.31052E-01	0.13989E+00	0.12660E+04	0.12316E+03	0.40071E+03
6345.00	0.31645E-01	0.14344E+00	0.16983E+04	0.11816E+03	0.37811E+03
6350.00	0.31544E-01	0.13194E+00	0.23558E+04	0.11816E+03	0.34237E+03
6355.00	0.30293E-01	0.11888E+00	0.24051E+04	0.12533E+03	0.35612E+03
6360.00	0.28947E-01	0.15829E+00	0.16687E+04	0.11250E+03	0.39247E+03
6365.00	0.27660E-01	0.21057E+00	0.34971E+04	0.12477E+03	0.39409E+03
6370.00	0.26327E-01	0.16177E+00	0.91092E+03	0.13231E+03	0.43317E+03
6375.00	0.24694E-01	0.26272E+00	0.28296E+04	0.11785E+03	0.42907E+03
6380.00	0.24566E-01	0.21157E+00	0.18468E+04	0.12399E+03	0.40895E+03
6385.00	0.24063E-01	0.18707E+00	0.10267E+04	0.12270E+03	0.40943E+03
6390.00	0.22314E-01	0.30716E+00	0.34672E+04	0.12380E+03	0.42174E+03
6395.00	0.21137E-01	0.34180E+00	0.16189E+04	0.12300E+03	0.43029E+03
6400.00	0.20634E-01	0.32928E+00	0.15358E+04	0.12284E+03	0.45027E+03
6405.00	0.20548E-01	0.26769E+00	0.16696E+04	0.12302E+03	0.48147E+03
6410.00	0.20311E-01	0.24263E+00	0.15621E+04	0.12258E+03	0.46159E+03
6415.00	0.20767E-01	0.20490E+00	0.30557E+04	0.12267E+03	0.40204E+03
6420.00	0.21080E-01	0.13628E+00	0.16029E+04	0.12028E+03	0.36532E+03
6425.00	0.19250E-01	0.24462E+00	0.32787E+04	0.12291E+03	0.41099E+03
6430.00	0.18619E-01	0.25759E+00	0.23304E+04	0.12301E+03	0.45156E+03
6435.00	0.19117E-01	0.21442E+00	0.15988E+04	0.13197E+03	0.47331E+03
6440.00	0.19628E-01	0.18245E+00	0.17154E+04	0.11912E+03	0.44201E+03
6445.00	0.20145E-01	0.13039E+00	0.16140E+04	0.12346E+03	0.38225E+03
6450.00	0.17966E-01	0.14006E+00	0.22538E+04	0.11576E+03	0.46947E+03
6455.00	0.18226E-01	0.13246E+00	0.27120E+04	0.10704E+03	0.44274E+03
6460.00	0.19044E-01	0.15062E+00	0.19021E+04	0.12176E+03	0.36530E+03
6465.00	0.17973E-01	0.17094E+00	0.90862E+03	0.12116E+03	0.45560E+03
6470.00	0.17467E-01	0.16698E+00	0.92987E+03	0.12106E+03	0.44257E+03
6475.00	0.16845E-01	0.18604E+00	0.63306E+03	0.12031E+03	0.43116E+03
6480.00	0.17019E-01	0.18811E+00	0.40568E+03	0.11928E+03	0.47132E+03
6485.00	0.17200E-01	0.15395E+00	0.18686E+03	0.11521E+03	0.50200E+03
6490.00	0.16492E-01	0.18900E+00	0.35365E+03	0.11871E+03	0.49040E+03
6495.00	0.16267E-01	0.21137E+00	0.19673E+03	0.11661E+03	0.46517E+03
6500.00	0.16271E-01	0.17918E+00	0.14125E+03	0.11599E+03	0.49791E+03
6505.00	0.15943E-01	0.19846E+00	0.10932E+03	0.11490E+03	0.48530E+03
6510.00	0.15799E-01	0.21447E+00	0.74775E+02	0.11273E+03	0.47686E+03
6515.00	0.15809E-01	0.20038E+00	0.72722E+02	0.13036E+03	0.49473E+03
6520.00	0.16076E-01	0.19052E+00	0.23601E+02	0.12826E+03	0.52214E+03
6525.00	0.16291E-01	0.17421E+00	0.27147E+02	0.13135E+03	0.53375E+03
6530.00	0.15841E-01	0.22277E+00	0.32734E+02	0.12122E+03	0.49987E+03
6535.00	0.15050E-01	0.30848E+00	0.12649E+03	0.10951E+03	0.42371E+03
6540.00	0.15557E-01	0.27355E+00	0.14595E+03	0.11454E+03	0.39467E+03
6545.00	0.16087E-01	0.23052E+00	0.28542E+02	0.13089E+03	0.44933E+03
6550.00	0.15812E-01	0.26214E+00	0.25502E+02	0.12091E+03	0.46781E+03
6555.00	0.15486E-01	0.29441E+00	0.46439E+02	0.12076E+03	0.44042E+03
6560.00	0.15293E-01	0.33499E+00	0.35062E+02	0.12067E+03	0.43916E+03
6565.00	0.15303E-01	0.33255E+00	0.36847E+02	0.11099E+03	0.43006E+03
6570.00	0.15176E-01	0.36043E+00	0.36310E+02	0.11221E+03	0.45918E+03
6575.00	0.14944E-01	0.40942E+00	0.50040E+02	0.11514E+03	0.47397E+03
6580.00	0.14794E-01	0.41679E+00	0.64136E+02	0.11155E+03	0.42785E+03
6585.00	0.14386E-01	0.49011E+00	0.67409E+02	0.12807E+03	0.42580E+03
6590.00	0.14719E-01	0.50257E+00	0.79267E+02	0.11209E+03	0.42020E+03
6595.00	0.14837E-01	0.50339E+00	0.79192E+02	0.11080E+03	0.45088E+03
6600.00	0.14445E-01	0.57305E+00	0.82813E+02	0.11173E+03	0.45002E+03
6605.00	0.14523E-01	0.61447E+00	0.15059E+03	0.11373E+03	0.37993E+03
6610.00	0.13869E-01	0.72897E+00	0.13478E+03	0.11302E+03	0.35629E+03
6615.00	0.14218E-01	0.67893E+00	0.98758E+02	0.11198E+03	0.38360E+03
6620.00	0.15047E-01	0.57390E+00	0.90027E+02	0.11136E+03	0.39758E+03
6625.00	0.14815E-01	0.68040E+00	0.12611E+03	0.11234E+03	0.37990E+03
6630.00	0.14130E-01	0.84235E+00	0.11090E+03	0.11122E+03	0.41472E+03
6635.00	0.14280E-01	0.90340E+00	0.94025E+02	0.11141E+03	0.39626E+03
6640.00	0.13747E-01	0.96817E+00	0.92317E+02	0.11109E+03	0.35318E+03
6645.00	0.14210E-01	0.89080E+00	0.10059E+03	0.11150E+03	0.36486E+03
6650.00	0.15154E-01	0.81423E+00	0.11954E+03	0.11198E+03	0.37121E+03
6655.00	0.14772E-01	0.87481E+00	0.11201E+03	0.11168E+03	0.39698E+03
6660.00	0.14955E-01	0.82187E+00	0.10103E+03	0.11127E+03	0.43424E+03
6665.00	0.15196E-01	0.85242E+00	0.86369E+02	0.11073E+03	0.48042E+03
6670.00	0.14854E-01	0.91431E+00	0.78038E+02	0.11036E+03	0.47039E+03
6675.00	0.14525E-01	0.95453E+00	0.86824E+02	0.11045E+03	0.38427E+03
6680.00	0.13621E-01	0.12896E+01	0.98859E+02	0.10977E+03	0.30656E+03
6685.00	0.12223E-01	0.15783E+01	0.99070E+02	0.11027E+03	0.42864E+03
6690.00	0.12579E-01	0.16353E+01	0.13987E+03	0.10815E+03	0.45888E+03
6695.00	0.14642E-01	0.13104E+01	0.23770E+03	0.11363E+03	0.50796E+03
6700.00	0.13341E-01	0.11462E+01	0.16553E+03	0.11127E+03	0.47889E+03
6705.00	0.10879E-01	0.16504E+01	0.11427E+03	0.11034E+03	0.43123E+03
6710.00	0.89461E-02	0.22618E+01	0.13725E+03	0.13261E+03	0.40708E+03
6715.00	0.88670E-02	0.22489E+01	0.11120E+03	0.12504E+03	0.43231E+03
6720.00	0.95957E-02	0.20955E+01	0.12443E+03	0.12386E+03	0.42994E+03
6725.00	0.83515E-02	0.28421E+01	0.17619E+03	0.12833E+03	0.35917E+03
6730.00	0.83430E-02	0.28430E+01	0.16889E+03	0.12895E+03	0.35013E+03
6735.00	0.84462E-02	0.29335E+01	0.13852E+03	0.11916E+03	0.35631E+03
6740.00	0.78561E-02	0.37874E+01	0.14316E+03	0.13685E+03	0.32232E+03
6745.00	0.88928E-02	0.35137E+01	0.15334E+03	0.12929E+03	0.34017E+03
6750.00	0.87053E-02	0.36218E+01	0.14122E+03	0.12940E+03	0.34058E+03
6755.00	0.73551E-02	0.52806E+01	0.10867E+03	0.13909E+03	0.31736E+03
6760.00	0.60728E-02	0.87077E+01	0.11849E+03	0.14566E+03	0.26718E+03
6765.00	0.75550E-02	0.76283E+01	0.12544E+03	0.12027E+03	0.23303E+03
6770.00	0.10754E-01	0.37516E+01	0.16377E+03	0.18613E+03	0.28103E+03
6775.00	0.10546E-01	0.35715E+01	0.13259E+03	0.13802E+03	0.27554E+03
6780.00	0.98240E-02	0.45481E+01	0.13904E+03	0.13699E+03	0.25324E+03
6785.00	0.94279E-02	0.58980E+01	0.14602E+03	0.16900E+03	0.24090E+03
6790.00	0.96659E-02	0.64978E+01	0.13495E+03	0.18863E+03	0.24470E+03
6795.00	0.75729E-02	0.75795E+01	0.93250E+02	0.13092E+03	0.24097E+03

6800.00	0.74430E-02	0.81521E+01	0.73358E+02	0.11914E+03	0.32102E+03
6805.00	0.81663E-02	0.63461E+01	0.75670E+02	0.15000E+03	0.42083E+03
6810.00	0.98850E-02	0.49553E+01	0.62786E+02	0.14284E+03	0.39070E+03
6815.00	0.13487E-01	0.39330E+01	0.63017E+02	0.13465E+03	0.32448E+03
6820.00	0.13207E-01	0.41983E+01	0.67805E+02	0.14357E+03	0.31314E+03
6825.00	0.11258E-01	0.42362E+01	0.54486E+02	0.13450E+03	0.33877E+03
6830.00	0.12377E-01	0.38432E+01	0.55277E+02	0.12486E+03	0.33206E+03
6835.00	0.11190E-01	0.40457E+01	0.60816E+02	0.14337E+03	0.30514E+03
6840.00	0.11925E-01	0.42122E+01	0.51655E+02	0.13465E+03	0.33566E+03
6845.00	0.11229E-01	0.52518E+01	0.73413E+02	0.14047E+03	0.32697E+03
6850.00	0.96783E-02	0.55047E+01	0.76197E+02	0.16102E+03	0.31297E+03
6855.00	0.10241E-01	0.51154E+01	0.66447E+02	0.16165E+03	0.31321E+03
6860.00	0.10112E-01	0.55398E+01	0.80028E+02	0.16642E+03	0.29337E+03
6865.00	0.96166E-02	0.58740E+01	0.72866E+02	0.16071E+03	0.32421E+03
6870.00	0.82497E-02	0.66734E+01	0.61742E+02	0.17026E+03	0.35193E+03
6875.00	0.82225E-02	0.69843E+01	0.54136E+02	0.15872E+03	0.33010E+03
6880.00	0.87853E-02	0.65625E+01	0.61318E+02	0.16051E+03	0.29738E+03
6885.00	0.81705E-02	0.72437E+01	0.60713E+02	0.16211E+03	0.27410E+03
6890.00	0.87275E-02	0.79443E+01	0.35480E+02	0.10308E+03	0.33579E+03
6895.00	0.88123E-02	0.75751E+01	0.45417E+02	0.11418E+03	0.37916E+03
6900.00	0.99329E-02	0.75047E+01	0.83563E+02	0.18708E+03	0.33082E+03
6905.00	0.94581E-02	0.84918E+01	0.76228E+02	0.18786E+03	0.33259E+03
6910.00	0.69185E-02	0.10964E+02	0.42445E+02	0.13481E+03	0.36499E+03
6915.00	0.70004E-02	0.11554E+02	0.44712E+02	0.15886E+03	0.39777E+03
6920.00	0.89707E-02	0.10048E+02	0.57785E+02	0.20051E+03	0.40276E+03
6925.00	0.97710E-02	0.94180E+01	0.54966E+02	0.19074E+03	0.41629E+03
6930.00	0.84064E-02	0.10308E+02	0.53402E+02	0.14794E+03	0.41326E+03
6935.00	0.64390E-02	0.12948E+02	0.48893E+02	0.13435E+03	0.37886E+03
6940.00	0.69397E-02	0.11381E+02	0.36852E+02	0.12201E+03	0.40089E+03
6945.00	0.72727E-02	0.11183E+02	0.34527E+02	0.11745E+03	0.42171E+03
6950.00	0.67508E-02	0.14427E+02	0.42495E+02	0.14649E+03	0.38067E+03
6955.00	0.70338E-02	0.15548E+02	0.41979E+02	0.13132E+03	0.38639E+03
6960.00	0.72274E-02	0.16261E+02	0.39979E+02	0.12852E+03	0.43369E+03
6965.00	0.66380E-02	0.15177E+02	0.44538E+02	0.15398E+03	0.43975E+03
6970.00	0.60684E-02	0.16673E+02	0.46733E+02	0.15521E+03	0.41502E+03
6975.00	0.61331E-02	0.20447E+02	0.46685E+02	0.15448E+03	0.39677E+03
6980.00	0.61293E-02	0.21979E+02	0.44578E+02	0.13917E+03	0.38439E+03
6985.00	0.57148E-02	0.22166E+02	0.43052E+02	0.14644E+03	0.36281E+03
6990.00	0.61234E-02	0.21071E+02	0.51335E+02	0.16612E+03	0.37078E+03
6995.00	0.74247E-02	0.25821E+02	0.47430E+02	0.12915E+03	0.36664E+03
7000.00	0.70015E-02	0.28475E+02	0.45528E+02	0.14094E+03	0.33344E+03
7005.00	0.61822E-02	0.27817E+02	0.54901E+02	0.19745E+03	0.35647E+03
7010.00	0.71685E-02	0.28247E+02	0.59063E+02	0.19102E+03	0.35681E+03
7015.00	0.68218E-02	0.30221E+02	0.54094E+02	0.16097E+03	0.30865E+03
7020.00	0.75603E-02	0.31562E+02	0.51604E+02	0.14005E+03	0.30632E+03
7025.00	0.69581E-02	0.28065E+02	0.48191E+02	0.14055E+03	0.32264E+03
7030.00	0.73151E-02	0.30465E+02	0.50423E+02	0.16831E+03	0.31831E+03
7035.00	0.81904E-02	0.28466E+02	0.47079E+02	0.13744E+03	0.32883E+03
7040.00	0.88595E-02	0.29904E+02	0.48117E+02	0.13494E+03	0.33441E+03
7045.00	0.94337E-02	0.35640E+02	0.56134E+02	0.16587E+03	0.32210E+03
7050.00	0.94899E-02	0.35673E+02	0.50464E+02	0.16803E+03	0.31741E+03
7055.00	0.96166E-02	0.37772E+02	0.45022E+02	0.13801E+03	0.32125E+03
7060.00	0.97153E-02	0.40609E+02	0.49271E+02	0.13557E+03	0.31240E+03
7065.00	0.94834E-02	0.45400E+02	0.44628E+02	0.15073E+03	0.31141E+03
7070.00	0.10364E-01	0.40302E+02	0.37896E+02	0.12260E+03	0.32626E+03
7075.00	0.99610E-02	0.42301E+02	0.40399E+02	0.12470E+03	0.30422E+03
7080.00	0.89627E-02	0.55217E+02	0.39448E+02	0.14393E+03	0.27315E+03
7085.00	0.87231E-02	0.57393E+02	0.35856E+02	0.15736E+03	0.30801E+03
7090.00	0.96187E-02	0.66552E+02	0.33681E+02	0.16462E+03	0.33373E+03
7095.00	0.13991E-01	0.11069E+03	0.38538E+02	0.13068E+03	0.29798E+03
7100.00	0.15228E-01	0.10862E+03	0.40898E+02	0.12069E+03	0.27804E+03
7105.00	0.10776E-01	0.66062E+02	0.38068E+02	0.14451E+03	0.28492E+03
7110.00	0.10474E-01	0.65559E+02	0.37699E+02	0.15771E+03	0.27366E+03
7115.00	0.11444E-01	0.60831E+02	0.36077E+02	0.14091E+03	0.26566E+03
7120.00	0.11572E-01	0.49343E+02	0.41136E+02	0.15437E+03	0.26966E+03
7125.00	0.13309E-01	0.61420E+02	0.50020E+02	0.15030E+03	0.24154E+03
7130.00	0.12660E-01	0.85013E+02	0.45225E+02	0.14263E+03	0.22524E+03
7135.00	0.11158E-01	0.78825E+02	0.38317E+02	0.15184E+03	0.28512E+03
7140.00	0.11649E-01	0.82408E+02	0.35334E+02	0.14202E+03	0.34027E+03
7145.00	0.12347E-01	0.98604E+02	0.34412E+02	0.13136E+03	0.35338E+03
7150.00	0.11298E-01	0.94633E+02	0.36530E+02	0.13741E+03	0.33264E+03
7155.00	0.11089E-01	0.82675E+02	0.38227E+02	0.14520E+03	0.31025E+03
7160.00	0.10084E-01	0.57465E+02	0.37352E+02	0.16386E+03	0.31990E+03
7165.00	0.86883E-02	0.43997E+02	0.39371E+02	0.17817E+03	0.33964E+03
7170.00	0.90276E-02	0.48847E+02	0.43240E+02	0.15089E+03	0.32483E+03
7175.00	0.10639E-01	0.64638E+02	0.45210E+02	0.16056E+03	0.28454E+03
7180.00	0.11226E-01	0.68355E+02	0.44561E+02	0.14613E+03	0.26572E+03
7185.00	0.12162E-01	0.77829E+02	0.39636E+02	0.13461E+03	0.26483E+03
7190.00	0.12879E-01	0.85912E+02	0.36090E+02	0.16047E+03	0.28437E+03
7195.00	0.13105E-01	0.84525E+02	0.36746E+02	0.15465E+03	0.31504E+03
7200.00	0.12364E-01	0.80748E+02	0.32649E+02	0.14484E+03	0.33911E+03
7205.00	0.12687E-01	0.89550E+02	0.33328E+02	0.15376E+03	0.32936E+03
7210.00	0.12634E-01	0.96083E+02	0.35373E+02	0.15169E+03	0.33735E+03
7215.00	0.11421E-01	0.82531E+02	0.36699E+02	0.14360E+03	0.35513E+03
7220.00	0.12284E-01	0.89766E+02	0.39281E+02	0.13591E+03	0.34354E+03
7225.00	0.12054E-01	0.91001E+02	0.36969E+02	0.13745E+03	0.34183E+03
7230.00	0.12885E-01	0.10162E+03	0.36313E+02	0.13160E+03	0.35722E+03
7235.00	0.12033E-01	0.10138E+03	0.36430E+02	0.13652E+03	0.35993E+03
7240.00	0.12035E-01	0.97483E+02	0.39453E+02	0.13339E+03	0.33508E+03
7245.00	0.11824E-01	0.92646E+02	0.38961E+02	0.13245E+03	0.32544E+03
7250.00	0.10759E-01	0.82122E+02	0.38126E+02	0.13744E+03	0.34226E+03
7255.00	0.12267E-01	0.84441E+02	0.40897E+02	0.13446E+03	0.34029E+03
7260.00	0.11958E-01	0.82213E+02	0.38637E+02	0.13985E+03	0.32562E+03
7265.00	0.12538E-01	0.73270E+02	0.38666E+02	0.13812E+03	0.35161E+03
7270.00	0.11748E-01	0.65820E+02	0.37735E+02	0.15350E+03	0.37216E+03
7275.00	0.10982E-01	0.66122E+02	0.35604E+02	0.15690E+03	0.36846E+03
7280.00	0.11770E-01	0.72233E+02	0.35135E+02	0.14220E+03	0.38509E+03
7285.00	0.11918E-01	0.79561E+02	0.29810E+02	0.14490E+03	0.37443E+03
7290.00	0.13006E-01	0.91628E+02	0.30500E+02	0.13953E+03	0.35027E+03
7295.00	0.14323E-01	0.84294E+02	0.38037E+02	0.11795E+03	0.35378E+03
7300.00	0.99375E-02	0.52561E+02	0.37742E+02	0.12750E+03	0.34900E+03
7305.00	0.95800E-02	0.52636E+02	0.41676E+02	0.13832E+03	0.31985E+03
7310.00	0.96582E-02	0.56229E+02	0.45227E+02	0.13751E+03	0.27269E+03
7315.00	0.96839E-02	0.50895E+02	0.43692E+02	0.12904E+03	0.25305E+03
7320.00	0.12291E-01	0.65399E+02	0.44327E+02	0.11780E+03	0.24768E+03
7325.00	0.11115E-01	0.75878E+02	0.38431E+02	0.13028E+03	0.25359E+03
7330.00	0.92795E-02	0.68277E+02	0.38513E+02	0.13483E+03	0.27658E+03
7335.00	0.12342E-01	0.71033E+02	0.45283E+02	0.11865E+03	0.30414E+03
7340.00	0.14968E-01	0.71377E+02	0.46888E+02	0.11647E+03	0.32339E+03
7345.00	0.12615E-01	0.49405E+02	0.44127E+02	0.13303E+03	0.33169E+03
7350.00	0.11797E-01	0.50053E+02	0.39542E+02	0.13415E+03	0.30597E+03
7355.00	0.11050E-01	0.60359E+02	0.38712E+02	0.16498E+03	0.28774E+03
7360.00	0.10589E-01	0.59446E+02	0.35866E+02	0.16720E+03	0.31762E+03
7365.00	0.17448E-01	0.12065E+03	0.38417E+02	0.12438E+03	0.32402E+03
7370.00	0.14474E-01	0.12418E+03	0.35970E+02	0.13262E+03	0.31498E+03
7375.00	0.93225E-02	0.64364E+02	0.33438E+02	0.14533E+03	0.32882E+03
7380.00	0.10043E-01	0.52373E+02	0.36895E+02	0.13798E+03	0.34618E+03
7385.00	0.10643E-01	0.52376E+02	0.40840E+02	0.14407E+03	0.33252E+03
7390.00	0.10560E-01	0.60305E+02	0.43529E+02	0.16290E+03	0.34328E+03
7395.00	0.94750E-02	0.54620E+02	0.40511E+02	0.14278E+03	0.38480E+03
7400.00	0.84353E-02	0.50139E+02	0.40648E+02	0.15380E+03	0.38731E+03
7405.00	0.84620E-02	0.55376E+02	0.44268E+02	0.15990E+03	0.38704E+03
7410.00	0.87087E-02	0.46144E+02	0.51393E+02	0.13580E+03	0.38224E+03
7415.00	0.96867E-02	0.53614E+02	0.58490E+02	0.13920E+03	0.35783E+03
7420.00	0.99181E-02	0.62392E+02	0.56838E+02	0.15386E+03	0.33802E+03
7425.00	0.10502E-01	0.56884E+02	0.56220E+02	0.13439E+03	0.30975E+03
7430.00	0.10886E-01	0.54683E+02	0.53087E+02	0.12968E+03	0.29693E+03
7435.00	0.10736E-01	0.48773E+02	0.61210E+02	0.15251E+03	0.31428E+03
7440.00	0.11764E-01	0.47510E+02	0.68982E+02	0.16576E+03	0.30535E+03
7445.00	0.11659E-01	0.48377E+02	0.71677E+02	0.15740E+03	0.29532E+03
7450.00	0.11107E-01	0.46461E+02	0.83039E+02	0.17422E+03	0.29337E+03
7455.00	0.10648E-01	0.44419E+02	0.73830E+02	0.17923E+03	0.28938E+03
7460.00	0.13712E-01	0.36781E+02	0.62227E+02	0.11637E+03	0.32048E+03
7465.00	0.11321E-01	0.30106E+02	0.68791E+02	0.11158E+03	0.35022E+03
7470.00	0.10142E-01	0.29042E+02	0.74178E+02	0.12018E+03	0.35018E+03
7475.00	0.11051E-01	0.27774E+02	0.69973E+02	0.11079E+03	0.33547E+03
7480.00	0.10307E-01	0.24557E+02	0.66263E+02	0.11119E+03	0.37417E+03
7485.00	0.96743E-02	0.23263E+02	0.62053E+02	0.12173E+03	0.42047E+03
7490.00	0.89430E-02	0.23328E+02	0.48844E+02	0.12141E+03	0.42925E+03
7495.00	0.83637E-02	0.25131E+02	0.37109E+02	0.11429E+03	0.46954E+03
7500.00	0.87386E-02	0.28112E+02	0.36073E+02	0.13275E+03	0.55339E+03
7505.00	0.26737E-01	0.62720E+02	0.36307E+02	0.33017E+02	0.56672E+03
7510.00	0.27478E-01	0.19079E+03	0.39514E+02	0.30581E+02	0.40079E+03
7515.00	0.20743E-01	0.11834E+03	0.33786E+02	0.31169E+02	0.37627E+03
7520.00	0.13532E-01	0.35953E+02	0.46794E+02	0.76376E+02	0.44279E+03
7525.00	0.10597E-01	0.17152E+02	0.41038E+02	0.67269E+02	0.53022E+03
7530.00	0.13955E-01	0.10298E+02	0.10070E+03	0.15419E+03	0.46659E+03
7535.00	0.20104E-01	0.74538E+01	0.12640E+03	0.16228E+03	0.41572E+03
7540.00	0.16833E-01	0.83109E+01	0.16338E+03	0.18120E+03	0.34996E+03
7545.00	0.12216E-01	0.13064E+02	0.86032E+02	0.10019E+03	0.36619E+03
7550.00	0.14095E-01	0.17942E+02	0.51026E+02	0.60324E+02	0.40002E+03
7555.00	0.14731E-01	0.11180E+02	0.82969E+02	0.50262E+02	0.27249E+03
7560.00	0.13926E-01	0.97386E+01	0.13182E+03	0.65225E+02	0.23830E+03
7565.00	0.14100E-01	0.10869E+02	0.13159E+03	0.69772E+02	0.26768E+03
7570.00	0.13986E-01	0.93781E+01	0.14605E+03	0.79673E+02	0.31187E+03
7575.00	0.11461E-01	0.94184E+01	0.18881E+03	0.12053E+03	0.25948E+03
7580.00	0.10486E-01	0.88945E+01	0.22837E+03	0.22575E+03	0.22809E+03
7585.00	0.11951E-01	0.12575E+02	0.83604E+02	0.93118E+02	0.23982E+03
7590.00	0.14016E-01	0.12462E+02	0.49107E+02	0.36918E+02	0.29851E+03
7595.00	0.14546E-01	0.14256E+02	0.74951E+02	0.58516E+02	0.33788E+03
7600.00	0.16980E-01	0.12313E+02	0.69940E+02	0.29430E+02	0.38287E+03
7605.00	0.15218E-01	0.14479E+02	0.71335E+02	0.25717E+02	0.38559E+03
7610.00	0.16245E-01	0.14020E+02	0.77371E+02	0.20430E+02	0.39592E+03
7615.00	0.13625E-01	0.10896E+02	0.85300E+02	0.35707E+02	0.43445E+03
7620.00	0.81479E-02	0.13577E+02	0.99957E+02	0.72579E+02	0.42599E+03
7625.00	0.81783E-02	0.10321E+02	0.12222E+03	0.89168E+02	0.46785E+03
7630.00	0.81019E-02	0.10712E+02	0.12599E+03	0.11278E+03	0.48083E+03
7635.00	0.99144E-02	0.86307E+01	0.12722E+03	0.10979E+03	0.53278E+03
7640.00	0.11927E-01	0.67814E+01	0.12731E+03	0.12004E+03	0.59503E+03
7645.00	0.12468E-01	0.58285E+01	0.98220E+02	0.11815E+03	0.55514E+03
7650.00	0.17804E-01	0.43960E+01	0.11308E+03	0.95581E+02	0.57318E+03
7655.00	0.19999E-01	0.39942E+01	0.10632E+03	0.10969E+03	0.64914E+03
7660.00	0.17264E-01	0.37420E+01	0.83107E+02	0.11150E+03	0.58794E+03
7665.00	0.19876E-01	0.31024E+01	0.12448E+03	0.11035E+03	0.61548E+03
7670.00	0.22964E-01	0.25932E+01	0.13921E+03	0.96820E+02	0.72588E+03
7675.00	0.23376E-01	0.21205E+01	0.12361E+03	0.11005E+03	0.65028E+03
7680.00	0.23555E-01	0.19126E+01	0.12578E+03	0.96648E+02	0.69602E+03
7685.00	0.26517E-01	0.13800E+01	0.22782E+03	0.99093E+02	0.74493E+03
7690.00	0.25778E-01	0.13909E+01	0.25121E+03	0.99079E+02	0.69771E+03
7695.00	0.24975E-01	0.12609E+01	0.24864E+03	0.99055E+02	0.72007E+03
7700.00	0.26447E-01	0.88715E+00	0.34072E+03	0.99784E+02	0.78105E+03
7705.00	0.26095E-01	0.83301E+00	0.39562E+03	0.10003E+03	0.78330E+03
7710.00	0.25135E-01	0.80803E+00	0.42300E+03	0.99794E+02	0.75275E+03
7715.00	0.26137E-01	0.58014E+00	0.46866E+03	0.10048E+03	0.77695E+03
7720.00	0.26323E-01	0.51297E+00	0.53314E+03	0.10111E+03	0.78189E+03
7725.00	0.25856E-01	0.50070E+00	0.40145E+03	0.98701E+02	0.77327E+03
7730.00	0.27742E-01	0.30557E+00	0.11407E+03	0.98164E+02	0.69405E+03
7735.00	0.28272E-01	0.24930E+00	0.16082E+03	0.95678E+02	0.63391E+03
7740.00	0.28210E-01	0.23349E+00	0.50543E+02	0.99210E+02	0.62126E+03
7745.00	0.30291E-01	0.17045E+00	0.41034E+02	0.92599E+02	0.53201E+03
7750.00	0.30416E-01	0.16790E+00	0.37373E+02	0.95923E+02	0.53946E+03
7755.00	0.25903E-01	0.25021E+00	0.85265E+03	0.10087E+03	0.68946E+03
7760.00	0.26209E-01	0.25127E+00	0.26893E+04	0.10182E+03	0.49072E+03
7765.00	0.26555E-01	0.24381E+00	0.29332E+04	0.10499E+03	0.49142E+03
7770.00	0.26692E-01	0.18531E+00	0.15201E+04	0.10333E+03	0.45922E+03
7775.00	0.25870E-01	0.23572E+00	0.32570E+04	0.10135E+03	0.45064E+03
7780.00	0.25148E-01	0.16154E+00	0.15759E+04	0.10034E+03	0.43070E+03
7785.00	0.23977E-01	0.16599E+00	0.19021E+04	0.10165E+03	0.41000E+03
7790.00	0.23781E-01	0.14240E+00	0.15777E+04	0.10247E+03	0.40792E+03
7795.00	0.23469E-01	0.14857E+00	0.21294E+04	0.95879E+02	0.37545E+03
7800.00	0.22382E-01	0.15014E+00	0.20961E+04	0.91415E+02	0.38018E+03
7805.00	0.22267E-01	0.13797E+00	0.20676E+04	0.10029E+03	0.36212E+03
7810.00	0.22109E-01	0.12151E+00	0.18125E+04	0.10131E+03	0.35009E+03
7815.00	0.22098E-01	0.12737E+00	0.17097E+04	0.10490E+03	0.48059E+03
7820.00	0.21283E-01	0.13238E+00	0.16279E+04	0.10029E+03	0.47597E+03
7825.00	0.20633E-01	0.13215E+00	0.14876E+04	0.90538E+02	0.46479E+03
7830.00	0.19806E-01	0.14347E+00	0.15515E+04	0.99503E+02	0.49036E+03
7835.00	0.19455E-01	0.14922E+00	0.18870E+04	0.90569E+02	0.49334E+03
7840.00	0.18877E-01	0.13826E+00	0.11165E+04	0.10050E+03	0.51519E+03
7845.00	0.16246E-01	0.36131E+00	0.44612E+04	0.10063E+03	0.67046E+03
7850.00	0.15942E-01	0.33801E+00	0.39901E+04	0.99412E+02	0.66135E+03
7855.00	0.16645E-01	0.28182E+00	0.46781E+04	0.10074E+03	0.57464E+03
7860.00	0.15516E-01	0.30749E+00	0.42902E+04	0.10044E+03	0.62123E+03
7865.00	0.15199E-01	0.32287E+00	0.43150E+04	0.10038E+03	0.64190E+03
7870.00	0.14412E-01	0.34372E+00	0.35029E+04	0.10166E+03	0.66998E+03
7875.00	0.14919E-01	0.35304E+00	0.52818E+04	0.91191E+02	0.63441E+03
7880.00	0.16236E-01	0.21166E+00	0.37331E+04	0.95149E+02	0.51739E+03
7885.00	0.13997E-01	0.33222E+00	0.43197E+04	0.10013E+03	0.62583E+03
7890.00	0.13364E-01	0.37177E+00	0.31111E+04	0.99762E+02	0.65054E+03
7895.00	0.13377E-01	0.31978E+00	0.27801E+04	0.10119E+03	0.68687E+03
7900.00	0.13769E-01	0.24779E+00	0.26542E+04	0.99752E+02	0.64230E+03
7905.00	0.13646E-01	0.23126E+00	0.30579E+04	0.99241E+02	0.60282E+03
7910.00	0.12786E-01	0.33110E+00	0.32904E+04	0.99715E+02	0.62101E+03
7915.00	0.17620E-01	0.16906E+00	0.99544E+02	0.93356E+02	0.35216E+03
7920.00	0.13099E-01	0.25789E+00	0.10379E+04	0.98880E+02	0.50025E+03
7925.00	0.12266E-01	0.31040E+00	0.23302E+04	0.99359E+02	0.61111E+03
7930.00	0.13050E-01	0.24048E+00	0.10082E+04	0.98683E+02	0.57113E+03
7935.00	0.12823E-01	0.24586E+00	0.10258E+04	0.97810E+02	0.60037E+03
7940.00	0.12685E-01	0.23670E+00	0.11058E+04	0.98302E+02	0.64165E+03
7945.00	0.12795E-01	0.24009E+00	0.72561E+03	0.98075E+02	0.61208E+03
7950.00	0.12234E-01	0.25084E+00	0.95740E+03	0.98411E+02	0.64200E+03
7955.00	0.11818E-01	0.27260E+00	0.16899E+04	0.98903E+02	0.73186E+03
7960.00	0.12048E-01	0.24760E+00	0.14705E+04	0.97447E+02	0.72279E+03
7965.00	0.12409E-01	0.24815E+00	0.96204E+03	0.98312E+02	0.64077E+03
7970.00	0.16678E-01	0.16490E+00	0.23315E+02	0.89583E+02	0.46671E+03
7975.00	0.16659E-01	0.18801E+00	0.12579E+02	0.10423E+03	0.44977E+03
7980.00	0.16389E-01	0.22655E+00	0.12178E+02	0.90336E+02	0.41317E+03
7985.00	0.16389E-01	0.24346E+00	0.10456E+02	0.98502E+02	0.41248E+03
7990.00	0.16352E-01	0.24882E+00	0.67315E+01	0.10021E+03	0.40430E+03
7995.00	0.16410E-01	0.25106E+00	0.13046E+02	0.99166E+02	0.43277E+03

8000.00	0.16317E-01	0.26916E+00	0.69365E+01	0.98967E+02	0.42595E+03
8005.00	0.16324E-01	0.28059E+00	0.15669E+02	0.88866E+02	0.38619E+03
8010.00	0.16078E-01	0.30014E+00	0.24157E+02	0.10515E+03	0.38766E+03
8015.00	0.15745E-01	0.34862E+00	0.12228E+02	0.89092E+02	0.41559E+03
8020.00	0.15039E-01	0.42160E+00	0.33047E+02	0.10801E+03	0.37543E+03
8025.00	0.14738E-01	0.46140E+00	0.30309E+02	0.88972E+02	0.33237E+03
8030.00	0.14595E-01	0.48733E+00	0.29653E+02	0.88910E+02	0.34625E+03
8035.00	0.14589E-01	0.50185E+00	0.42998E+02	0.89344E+02	0.34751E+03
8040.00	0.14988E-01	0.42572E+00	0.46553E+02	0.89413E+02	0.38365E+03
8045.00	0.15120E-01	0.43907E+00	0.55603E+02	0.89688E+02	0.38220E+03
8050.00	0.14686E-01	0.52998E+00	0.55377E+02	0.89582E+02	0.38085E+03
8055.00	0.14735E-01	0.53269E+00	0.67066E+02	0.90088E+02	0.38810E+03
8060.00	0.14387E-01	0.57821E+00	0.74289E+02	0.89395E+02	0.34128E+03
8065.00	0.14070E-01	0.63089E+00	0.57632E+02	0.89512E+02	0.33991E+03
8070.00	0.13922E-01	0.62937E+00	0.50267E+02	0.89308E+02	0.35713E+03
8075.00	0.13872E-01	0.66531E+00	0.82568E+02	0.90509E+02	0.37425E+03
8080.00	0.13340E-01	0.79797E+00	0.95644E+02	0.90699E+02	0.32159E+03
8085.00	0.12791E-01	0.85860E+00	0.65982E+02	0.89684E+02	0.29433E+03
8090.00	0.12753E-01	0.95191E+00	0.70979E+02	0.89716E+02	0.31321E+03
8095.00	0.12186E-01	0.12931E+01	0.59055E+02	0.87410E+02	0.28632E+03
8100.00	0.12875E-01	0.13255E+01	0.59708E+02	0.88358E+02	0.31136E+03
8105.00	0.13378E-01	0.10795E+01	0.64628E+02	0.89185E+02	0.37479E+03
8110.00	0.13179E-01	0.10677E+01	0.53564E+02	0.88760E+02	0.34972E+03
8115.00	0.12660E-01	0.11624E+01	0.50188E+02	0.88562E+02	0.30822E+03
8120.00	0.12160E-01	0.13496E+01	0.58964E+02	0.96101E+02	0.27181E+03
8125.00	0.11681E-01	0.15193E+01	0.45152E+02	0.83724E+02	0.24920E+03
8130.00	0.12428E-01	0.14285E+01	0.45391E+02	0.88150E+02	0.27137E+03
8135.00	0.13201E-01	0.13092E+01	0.50251E+02	0.88302E+02	0.28727E+03
8140.00	0.13748E-01	0.12415E+01	0.50158E+02	0.88169E+02	0.31197E+03
8145.00	0.13918E-01	0.11449E+01	0.37884E+02	0.87765E+02	0.33593E+03
8150.00	0.14520E-01	0.10854E+01	0.57671E+02	0.10556E+03	0.33790E+03
8155.00	0.15304E-01	0.10594E+01	0.67716E+02	0.10530E+03	0.37289E+03
8160.00	0.15235E-01	0.11601E+01	0.51641E+02	0.88181E+02	0.38578E+03
8165.00	0.15430E-01	0.11335E+01	0.56380E+02	0.88175E+02	0.38092E+03
8170.00	0.15992E-01	0.11359E+01	0.60977E+02	0.89208E+02	0.41024E+03
8175.00	0.16567E-01	0.11703E+01	0.73914E+02	0.87251E+02	0.43425E+03
8180.00	0.17290E-01	0.10692E+01	0.83231E+02	0.89306E+02	0.42887E+03
8185.00	0.17427E-01	0.11215E+01	0.66470E+02	0.88504E+02	0.43652E+03
8190.00	0.16803E-01	0.13532E+01	0.88715E+02	0.10438E+03	0.42409E+03
8195.00	0.17626E-01	0.12637E+01	0.10774E+03	0.10348E+03	0.44516E+03
8200.00	0.18438E-01	0.11489E+01	0.90316E+02	0.10435E+03	0.50267E+03
8205.00	0.18150E-01	0.13169E+01	0.82523E+02	0.10504E+03	0.47060E+03
8210.00	0.16943E-01	0.15860E+01	0.83142E+02	0.10447E+03	0.43595E+03
8215.00	0.16045E-01	0.17460E+01	0.64054E+02	0.10502E+03	0.43718E+03
8220.00	0.16189E-01	0.17526E+01	0.46046E+02	0.10558E+03	0.43658E+03
8225.00	0.15901E-01	0.18625E+01	0.46140E+02	0.10556E+03	0.45182E+03
8230.00	0.17112E-01	0.17624E+01	0.60560E+02	0.10513E+03	0.47758E+03
8235.00	0.16998E-01	0.20505E+01	0.65193E+02	0.10458E+03	0.43930E+03
8240.00	0.13547E-01	0.27791E+01	0.48637E+02	0.10521E+03	0.40173E+03
8245.00	0.13115E-01	0.28878E+01	0.54477E+02	0.10500E+03	0.39456E+03
8250.00	0.14234E-01	0.26597E+01	0.54355E+02	0.10494E+03	0.39752E+03
8255.00	0.14161E-01	0.29201E+01	0.48505E+02	0.10513E+03	0.39854E+03
8260.00	0.13290E-01	0.32606E+01	0.57948E+02	0.11390E+03	0.38587E+03
8265.00	0.13498E-01	0.32902E+01	0.53090E+02	0.10575E+03	0.39419E+03
8270.00	0.14060E-01	0.32287E+01	0.41373E+02	0.10512E+03	0.43525E+03
8275.00	0.13112E-01	0.37742E+01	0.37756E+02	0.10464E+03	0.43186E+03
8280.00	0.10838E-01	0.46681E+01	0.40352E+02	0.13250E+03	0.39039E+03
8285.00	0.10172E-01	0.49598E+01	0.39324E+02	0.13051E+03	0.38607E+03
8290.00	0.10458E-01	0.51767E+01	0.41389E+02	0.14183E+03	0.39435E+03
8295.00	0.90140E-02	0.58255E+01	0.42787E+02	0.16102E+03	0.38435E+03
8300.00	0.87739E-02	0.60984E+01	0.37870E+02	0.16381E+03	0.36030E+03
8305.00	0.83529E-02	0.66818E+01	0.45641E+02	0.17264E+03	0.35368E+03
8310.00	0.76185E-02	0.77070E+01	0.44396E+02	0.14247E+03	0.33690E+03
8315.00	0.75695E-02	0.77132E+01	0.37947E+02	0.13530E+03	0.31731E+03
8320.00	0.73732E-02	0.81092E+01	0.45370E+02	0.16023E+03	0.30956E+03
8325.00	0.75433E-02	0.84903E+01	0.55439E+02	0.16855E+03	0.29933E+03
8330.00	0.67861E-02	0.93294E+01	0.51002E+02	0.15701E+03	0.29763E+03
8335.00	0.71470E-02	0.83950E+01	0.48475E+02	0.14429E+03	0.30585E+03
8340.00	0.75851E-02	0.86313E+01	0.46937E+02	0.13068E+03	0.31837E+03
8345.00	0.72443E-02	0.89650E+01	0.54529E+02	0.18022E+03	0.32919E+03
8350.00	0.74200E-02	0.89763E+01	0.53527E+02	0.17524E+03	0.30410E+03
8355.00	0.67382E-02	0.11094E+02	0.51282E+02	0.15208E+03	0.28419E+03
8360.00	0.60919E-02	0.11211E+02	0.45692E+02	0.15631E+03	0.27695E+03
8365.00	0.64046E-02	0.11402E+02	0.45585E+02	0.17108E+03	0.27145E+03
8370.00	0.66574E-02	0.11603E+02	0.41923E+02	0.15212E+03	0.26920E+03
8375.00	0.65850E-02	0.12563E+02	0.42733E+02	0.15476E+03	0.26168E+03
8380.00	0.62249E-02	0.13528E+02	0.38438E+02	0.15985E+03	0.25867E+03
8385.00	0.60408E-02	0.15786E+02	0.31191E+02	0.15162E+03	0.25649E+03
8390.00	0.64547E-02	0.16904E+02	0.28688E+02	0.15571E+03	0.27805E+03
8395.00	0.66211E-02	0.16382E+02	0.26966E+02	0.16709E+03	0.32053E+03
8400.00	0.67075E-02	0.16558E+02	0.28896E+02	0.16124E+03	0.34897E+03
8405.00	0.68033E-02	0.18107E+02	0.26354E+02	0.12586E+03	0.34399E+03
8410.00	0.66521E-02	0.22524E+02	0.26384E+02	0.13074E+03	0.30359E+03
8415.00	0.77133E-02	0.26746E+02	0.29957E+02	0.14349E+03	0.27364E+03
8420.00	0.98426E-02	0.30685E+02	0.31097E+02	0.12917E+03	0.28103E+03
8425.00	0.10739E-01	0.22122E+02	0.27201E+02	0.10606E+03	0.31150E+03
8430.00	0.75594E-02	0.17920E+02	0.28727E+02	0.14133E+03	0.30378E+03
8435.00	0.72143E-02	0.19785E+02	0.29503E+02	0.14173E+03	0.28559E+03
8440.00	0.67633E-02	0.19100E+02	0.25582E+02	0.14298E+03	0.31105E+03
8445.00	0.66164E-02	0.20331E+02	0.22579E+02	0.14659E+03	0.31381E+03
8450.00	0.68091E-02	0.19874E+02	0.22799E+02	0.16783E+03	0.34170E+03
8455.00	0.70910E-02	0.21721E+02	0.24977E+02	0.17506E+03	0.36286E+03
8460.00	0.71278E-02	0.22708E+02	0.23895E+02	0.16267E+03	0.35231E+03
8465.00	0.69877E-02	0.22595E+02	0.21242E+02	0.16584E+03	0.36911E+03
8470.00	0.74534E-02	0.26712E+02	0.25246E+02	0.17667E+03	0.36877E+03
8475.00	0.69928E-02	0.28744E+02	0.25996E+02	0.16302E+03	0.37261E+03
8480.00	0.65996E-02	0.28754E+02	0.24298E+02	0.15248E+03	0.39762E+03
8485.00	0.66819E-02	0.31944E+02	0.25129E+02	0.15088E+03	0.39822E+03
8490.00	0.62028E-02	0.31707E+02	0.24415E+02	0.16344E+03	0.39227E+03
8495.00	0.60157E-02	0.32092E+02	0.22567E+02	0.15331E+03	0.40674E+03
8500.00	0.65538E-02	0.34165E+02	0.24027E+02	0.13852E+03	0.39945E+03
8505.00	0.73937E-02	0.36802E+02	0.23821E+02	0.13609E+03	0.38839E+03
8510.00	0.65901E-02	0.39150E+02	0.24651E+02	0.15444E+03	0.38051E+03
8515.00	0.65794E-02	0.40460E+02	0.26971E+02	0.15130E+03	0.35761E+03
8520.00	0.68152E-02	0.44304E+02	0.25350E+02	0.15033E+03	0.34494E+03
8525.00	0.71266E-02	0.43853E+02	0.25517E+02	0.15850E+03	0.32594E+03
8530.00	0.91336E-02	0.45732E+02	0.29105E+02	0.14952E+03	0.30574E+03
8535.00	0.10060E-01	0.47634E+02	0.30574E+02	0.14012E+03	0.29780E+03
8540.00	0.11183E-01	0.48883E+02	0.30126E+02	0.15192E+03	0.29993E+03
8545.00	0.13186E-01	0.57531E+02	0.30793E+02	0.14715E+03	0.28369E+03
8550.00	0.12881E-01	0.58285E+02	0.30741E+02	0.14836E+03	0.26225E+03
8555.00	0.11868E-01	0.52504E+02	0.34995E+02	0.15056E+03	0.26498E+03
8560.00	0.11547E-01	0.55284E+02	0.35523E+02	0.14862E+03	0.25475E+03
8565.00	0.11941E-01	0.65959E+02	0.33478E+02	0.15933E+03	0.24604E+03
8570.00	0.11755E-01	0.68511E+02	0.31916E+02	0.16545E+03	0.27202E+03
8575.00	0.11026E-01	0.66979E+02	0.28808E+02	0.16040E+03	0.29263E+03
8580.00	0.11165E-01	0.78195E+02	0.25166E+02	0.15514E+03	0.31212E+03
8585.00	0.12030E-01	0.99292E+02	0.24794E+02	0.14891E+03	0.30929E+03
8590.00	0.11567E-01	0.10091E+03	0.28028E+02	0.14353E+03	0.26101E+03
8595.00	0.12574E-01	0.99273E+02	0.26597E+02	0.14821E+03	0.23785E+03

8600.00	0.14905E-01	0.12406E+03	0.30899E+02	0.13183E+03	0.19941E+03
8605.00	0.14617E-01	0.13019E+03	0.37329E+02	0.13167E+03	0.15887E+03
8610.00	0.14872E-01	0.88963E+02	0.38942E+02	0.12711E+03	0.17059E+03
8615.00	0.13267E-01	0.65515E+02	0.34185E+02	0.14434E+03	0.19927E+03
8620.00	0.13148E-01	0.61576E+02	0.30419E+02	0.14401E+03	0.22906E+03
8625.00	0.10879E-01	0.47357E+02	0.28698E+02	0.16284E+03	0.25352E+03
8630.00	0.11181E-01	0.44956E+02	0.27798E+02	0.15661E+03	0.28583E+03
8635.00	0.12450E-01	0.56243E+02	0.28196E+02	0.15337E+03	0.28861E+03
8640.00	0.13074E-01	0.81597E+02	0.29916E+02	0.15708E+03	0.25811E+03
8645.00	0.13141E-01	0.98955E+02	0.32351E+02	0.14415E+03	0.22879E+03
8650.00	0.12689E-01	0.99488E+02	0.31841E+02	0.13681E+03	0.21081E+03
8655.00	0.12743E-01	0.10145E+03	0.30973E+02	0.14128E+03	0.23023E+03
8660.00	0.12089E-01	0.94452E+02	0.31045E+02	0.14345E+03	0.26266E+03
8665.00	0.11042E-01	0.85141E+02	0.27256E+02	0.14664E+03	0.28694E+03
8670.00	0.11531E-01	0.85499E+02	0.27562E+02	0.13951E+03	0.31273E+03
8675.00	0.11178E-01	0.79582E+02	0.27386E+02	0.13983E+03	0.34002E+03
8680.00	0.94666E-02	0.70910E+02	0.24490E+02	0.15352E+03	0.37033E+03
8685.00	0.86117E-02	0.63865E+02	0.20740E+02	0.15291E+03	0.38523E+03
8690.00	0.92430E-02	0.55702E+02	0.19081E+02	0.15165E+03	0.41036E+03
8695.00	0.84663E-02	0.53262E+02	0.17774E+02	0.15890E+03	0.42830E+03
8700.00	0.89027E-02	0.50392E+02	0.16761E+02	0.15916E+03	0.43554E+03
8705.00	0.86336E-02	0.41773E+02	0.17329E+02	0.16686E+03	0.44469E+03
8710.00	0.83375E-02	0.38507E+02	0.17196E+02	0.15930E+03	0.45139E+03
8715.00	0.80668E-02	0.35686E+02	0.17954E+02	0.16461E+03	0.44400E+03
8720.00	0.77259E-02	0.31799E+02	0.18580E+02	0.16116E+03	0.43237E+03
8725.00	0.79754E-02	0.29593E+02	0.20809E+02	0.14744E+03	0.42958E+03
8730.00	0.83374E-02	0.29233E+02	0.24500E+02	0.14372E+03	0.40184E+03
8735.00	0.86136E-02	0.28332E+02	0.27799E+02	0.14891E+03	0.39579E+03
8740.00	0.83925E-02	0.27019E+02	0.32548E+02	0.16168E+03	0.37165E+03
8745.00	0.88777E-02	0.27819E+02	0.33653E+02	0.13534E+03	0.32371E+03
8750.00	0.10241E-01	0.23752E+02	0.33803E+02	0.11563E+03	0.32865E+03
8755.00	0.90844E-02	0.19593E+02	0.38106E+02	0.13835E+03	0.32359E+03
8760.00	0.96742E-02	0.19525E+02	0.47113E+02	0.14182E+03	0.29361E+03
8765.00	0.93818E-02	0.17785E+02	0.45825E+02	0.14400E+03	0.27747E+03
8770.00	0.10842E-01	0.18100E+02	0.36337E+02	0.11817E+03	0.28507E+03
8775.00	0.11152E-01	0.19727E+02	0.38389E+02	0.12803E+03	0.31422E+03
8780.00	0.96547E-02	0.20368E+02	0.36466E+02	0.14988E+03	0.34409E+03
8785.00	0.96725E-02	0.25382E+02	0.31067E+02	0.14201E+03	0.35317E+03
8790.00	0.10137E-01	0.31090E+02	0.32468E+02	0.13660E+03	0.33149E+03
8795.00	0.11891E-01	0.36601E+02	0.33913E+02	0.12595E+03	0.33525E+03
8800.00	0.10789E-01	0.47999E+02	0.29785E+02	0.13876E+03	0.32967E+03
8805.00	0.13194E-01	0.81143E+02	0.32344E+02	0.12982E+03	0.28672E+03
8810.00	0.14120E-01	0.73414E+02	0.27159E+02	0.32360E+02	0.22602E+03
8815.00	0.89822E-02	0.29764E+02	0.41359E+02	0.12247E+03	0.22540E+03
8820.00	0.76818E-02	0.27372E+02	0.39753E+02	0.13322E+03	0.21070E+03
8825.00	0.82714E-02	0.24632E+02	0.38159E+02	0.12657E+03	0.21063E+03
8830.00	0.83657E-02	0.24631E+02	0.39133E+02	0.13081E+03	0.21811E+03
8835.00	0.88040E-02	0.24340E+02	0.43462E+02	0.14239E+03	0.24130E+03
8840.00	0.99108E-02	0.23838E+02	0.56975E+02	0.14607E+03	0.24147E+03
8845.00	0.95334E-02	0.26962E+02	0.65347E+02	0.15931E+03	0.19769E+03
8850.00	0.10481E-01	0.30431E+02	0.52831E+02	0.14047E+03	0.20524E+03
8855.00	0.11962E-01	0.34209E+02	0.51174E+02	0.12316E+03	0.20604E+03
8860.00	0.10061E-01	0.31798E+02	0.47130E+02	0.13123E+03	0.20203E+03
8865.00	0.10933E-01	0.38968E+02	0.45730E+02	0.12479E+03	0.20858E+03
8870.00	0.10001E-01	0.39871E+02	0.44032E+02	0.13181E+03	0.24573E+03
8875.00	0.89346E-02	0.34789E+02	0.38580E+02	0.15291E+03	0.28211E+03
8880.00	0.94458E-02	0.35565E+02	0.44100E+02	0.14598E+03	0.30198E+03
8885.00	0.80585E-02	0.32334E+02	0.42493E+02	0.13924E+03	0.33273E+03
8890.00	0.83920E-02	0.31979E+02	0.32660E+02	0.12498E+03	0.37175E+03
8895.00	0.94055E-02	0.37082E+02	0.26246E+02	0.12691E+03	0.39346E+03
8900.00	0.98278E-02	0.47314E+02	0.27184E+02	0.14828E+03	0.37427E+03
8905.00	0.13402E-01	0.49012E+02	0.35422E+02	0.11278E+03	0.35211E+03
8910.00	0.13330E-01	0.29640E+02	0.21931E+02	0.36778E+02	0.42184E+03
8915.00	0.81490E-02	0.18728E+02	0.32754E+02	0.12324E+03	0.48520E+03
8920.00	0.91123E-02	0.16048E+02	0.30200E+02	0.11139E+03	0.52575E+03
8925.00	0.89542E-02	0.13790E+02	0.27980E+02	0.10870E+03	0.54859E+03
8930.00	0.10462E-01	0.11508E+02	0.27168E+02	0.84726E+02	0.51660E+03
8935.00	0.99738E-02	0.10660E+02	0.44790E+02	0.15238E+03	0.47251E+03
8940.00	0.11461E-01	0.10236E+02	0.58195E+02	0.16069E+03	0.45182E+03
8945.00	0.13091E-01	0.99003E+01	0.73829E+02	0.15354E+03	0.41300E+03
8950.00	0.12463E-01	0.11517E+02	0.77411E+02	0.11151E+03	0.35772E+03
8955.00	0.12475E-01	0.96037E+01	0.74438E+02	0.11116E+03	0.34712E+03
8960.00	0.12520E-01	0.89066E+01	0.65443E+02	0.10668E+03	0.32915E+03
8965.00	0.14442E-01	0.73814E+01	0.49486E+02	0.61752E+02	0.35198E+03
8970.00	0.14786E-01	0.70036E+01	0.94481E+02	0.11231E+03	0.36400E+03
8975.00	0.11908E-01	0.92087E+01	0.84762E+02	0.12003E+03	0.33328E+03
8980.00	0.14257E-01	0.84744E+01	0.54064E+02	0.53443E+02	0.36178E+03
8985.00	0.15717E-01	0.66142E+01	0.84497E+02	0.82658E+02	0.39968E+03
8990.00	0.13226E-01	0.72297E+01	0.50241E+02	0.66228E+02	0.40635E+03
8995.00	0.18180E-01	0.60288E+01	0.46272E+02	0.33454E+02	0.46934E+03
9000.00	0.18665E-01	0.50201E+01	0.64002E+02	0.75609E+02	0.51425E+03
9005.00	0.16576E-01	0.51848E+01	0.59934E+02	0.10214E+03	0.52024E+03
9010.00	0.20517E-01	0.40795E+01	0.55710E+02	0.10508E+03	0.55819E+03
9015.00	0.22175E-01	0.36471E+01	0.50296E+02	0.97974E+02	0.56839E+03
9020.00	0.23048E-01	0.34898E+01	0.42287E+02	0.97341E+02	0.50456E+03
9025.00	0.20473E-01	0.37108E+01	0.33410E+02	0.97336E+02	0.50343E+03
9030.00	0.22971E-01	0.30340E+01	0.50186E+02	0.97219E+02	0.61057E+03
9035.00	0.29817E-01	0.23544E+01	0.99544E+02	0.95485E+02	0.67001E+03
9040.00	0.27597E-01	0.37205E+01	0.13158E+03	0.84708E+02	0.44259E+03
9045.00	0.25464E-01	0.36047E+01	0.15536E+03	0.81218E+02	0.35588E+03
9050.00	0.30182E-01	0.16929E+01	0.26722E+03	0.90868E+02	0.53167E+03
9055.00	0.34255E-01	0.13071E+01	0.33272E+03	0.90476E+02	0.60115E+03
9060.00	0.33057E-01	0.13172E+01	0.38394E+03	0.90045E+02	0.55500E+03
9065.00	0.32895E-01	0.12393E+01	0.43449E+03	0.90138E+02	0.56951E+03
9070.00	0.31746E-01	0.11067E+01	0.55040E+03	0.89167E+02	0.59196E+03
9075.00	0.30174E-01	0.12174E+01	0.65703E+03	0.86111E+02	0.53064E+03
9080.00	0.29459E-01	0.11212E+01	0.67310E+03	0.86603E+02	0.51053E+03
9085.00	0.30087E-01	0.15940E+01	0.79888E+03	0.84988E+02	0.45590E+03
9090.00	0.27818E-01	0.16137E+01	0.74302E+03	0.86577E+02	0.38478E+03
9095.00	0.25598E-01	0.11291E+01	0.48346E+03	0.88959E+02	0.38865E+03
9100.00	0.25485E-01	0.16370E+01	0.48060E+03	0.85493E+02	0.34122E+03
9105.00	0.25383E-01	0.15763E+01	0.50806E+03	0.85288E+02	0.36861E+03
9110.00	0.25906E-01	0.14176E+01	0.60913E+03	0.88455E+02	0.42549E+03
9115.00	0.25198E-01	0.14443E+01	0.51892E+03	0.88653E+02	0.40005E+03
9120.00	0.25649E-01	0.20309E+01	0.73128E+03	0.85696E+02	0.40266E+03
9125.00	0.24912E-01	0.20652E+01	0.53598E+03	0.84990E+02	0.41152E+03
9130.00	0.23471E-01	0.17983E+01	0.36725E+03	0.89352E+02	0.42604E+03
9135.00	0.25197E-01	0.16886E+01	0.46991E+03	0.85179E+02	0.47559E+03
9140.00	0.24031E-01	0.15672E+01	0.28947E+03	0.89773E+02	0.48551E+03
9145.00	0.24118E-01	0.14533E+01	0.31083E+03	0.89706E+02	0.52547E+03
9150.00	0.24365E-01	0.13113E+01	0.28739E+03	0.89637E+02	0.58270E+03
9155.00	0.23690E-01	0.13420E+01	0.29158E+03	0.89710E+02	0.59503E+03
9160.00	0.24730E-01	0.10455E+01	0.27152E+03	0.89800E+02	0.65776E+03
9165.00	0.24362E-01	0.10812E+01	0.22613E+03	0.90239E+02	0.69097E+03
9170.00	0.25040E-01	0.90987E+00	0.31204E+03	0.89201E+02	0.74061E+03
9175.00	0.23256E-01	0.72233E+00	0.32302E+03	0.83392E+02	0.78097E+03
9180.00	0.23436E-01	0.63225E+00	0.41162E+03	0.84064E+02	0.80077E+03
9185.00	0.23018E-01	0.55445E+00	0.37345E+03	0.83475E+02	0.80645E+03
9190.00	0.23598E-01	0.42179E+00	0.30889E+03	0.81283E+02	0.78012E+03
9195.00	0.23604E-01	0.36040E+00	0.15893E+03	0.78079E+02	0.78225E+03

9200.00	0.24100E-01	0.26506E+00	0.88244E+02	0.77026E+02	0.69382E+03
9205.00	0.25823E-01	0.15815E+00	0.60062E+03	0.93370E+02	0.52475E+03
9210.00	0.25538E-01	0.15451E+00	0.14369E+03	0.80064E+02	0.54117E+03
9215.00	0.22908E-01	0.16894E+00	0.12973E+04	0.84723E+02	0.28099E+03
9220.00	0.22673E-01	0.13408E+00	0.17949E+04	0.81731E+02	0.17294E+03
9225.00	0.20571E-01	0.11545E+00	0.12499E+04	0.74678E+02	0.30562E+03
9230.00	0.19032E-01	0.15362E+00	0.20057E+04	0.83903E+02	0.28177E+03
9235.00	0.18066E-01	0.22618E+00	0.57311E+04	0.77994E+02	0.19704E+03
9240.00	0.17556E-01	0.22035E+00	0.71516E+04	0.86706E+02	0.17666E+03
9245.00	0.18678E-01	0.81936E-01	0.13753E+04	0.82502E+02	0.24854E+03
9250.00	0.17706E-01	0.10619E+00	0.28803E+04	0.77725E+02	0.20821E+03
9255.00	0.17337E-01	0.94862E-01	0.40008E+04	0.75126E+02	0.13753E+03
9260.00	0.17053E-01	0.84779E-01	0.37918E+04	0.70549E+02	0.12559E+03
9265.00	0.16829E-01	0.75952E-01	0.26360E+04	0.83681E+02	0.16864E+03
9270.00	0.16405E-01	0.78021E-01	0.32555E+04	0.77521E+02	0.16077E+03
9275.00	0.15010E-01	0.99403E-01	0.39408E+04	0.74790E+02	0.14639E+03
9280.00	0.14792E-01	0.93165E-01	0.42204E+04	0.68646E+02	0.14155E+03
9285.00	0.14828E-01	0.83199E-01	0.45449E+04	0.74417E+02	0.14260E+03
9290.00	0.15989E-01	0.64416E-01	0.33831E+04	0.78355E+02	0.13777E+03
9295.00	0.15463E-01	0.67717E-01	0.48152E+04	0.85377E+02	0.15030E+03
9300.00	0.15114E-01	0.68519E-01	0.45419E+04	0.78268E+02	0.15915E+03
9305.00	0.14181E-01	0.65996E-01	0.41308E+04	0.79434E+02	0.13985E+03
9310.00	0.13204E-01	0.63198E-01	0.42785E+04	0.77757E+02	0.14017E+03
9315.00	0.12695E-01	0.65061E-01	0.47428E+04	0.77935E+02	0.13269E+03
9320.00	0.12352E-01	0.68265E-01	0.46995E+04	0.69716E+02	0.13212E+03
9325.00	0.12417E-01	0.68796E-01	0.40780E+04	0.80578E+02	0.15419E+03
9330.00	0.12182E-01	0.67018E-01	0.40202E+04	0.78016E+02	0.13693E+03
9335.00	0.14316E-01	0.52092E-01	0.52598E+04	0.77283E+02	0.13155E+03
9340.00	0.14456E-01	0.50666E-01	0.41681E+04	0.75581E+02	0.13297E+03
9345.00	0.13083E-01	0.57487E-01	0.38988E+04	0.79273E+02	0.14130E+03
9350.00	0.12240E-01	0.63631E-01	0.40810E+04	0.77041E+02	0.13664E+03
9355.00	0.12207E-01	0.64392E-01	0.41750E+04	0.77356E+02	0.13843E+03
9360.00	0.11961E-01	0.67517E-01	0.38522E+04	0.78244E+02	0.13892E+03
9365.00	0.11801E-01	0.65012E-01	0.38398E+04	0.76444E+02	0.13998E+03
9370.00	0.11635E-01	0.58466E-01	0.39642E+04	0.81290E+02	0.14118E+03
9375.00	0.11628E-01	0.58291E-01	0.40241E+04	0.79698E+02	0.12956E+03
9380.00	0.11649E-01	0.50527E-01	0.32065E+04	0.78094E+02	0.12872E+03
9385.00	0.11419E-01	0.68134E-01	0.67140E+04	0.81125E+02	0.13059E+03
9390.00	0.12643E-01	0.41630E-01	0.42041E+04	0.82054E+02	0.14874E+03
9395.00	0.12445E-01	0.50095E-01	0.46415E+04	0.80273E+02	0.14157E+03
9400.00	0.12862E-01	0.64550E-01	0.44928E+04	0.81575E+02	0.23024E+03
9405.00	0.12900E-01	0.77661E-01	0.53137E+04	0.80993E+02	0.24032E+03
9410.00	0.12825E-01	0.64471E-01	0.24113E+04	0.69778E+02	0.26061E+03
9415.00	0.13153E-01	0.78283E-01	0.45498E+04	0.73718E+02	0.25634E+03
9420.00	0.13154E-01	0.70572E-01	0.31216E+04	0.80117E+02	0.25054E+03
9425.00	0.13342E-01	0.59181E-01	0.74379E+03	0.83501E+02	0.25283E+03
9430.00	0.13425E-01	0.55270E-01	0.39324E+03	0.81671E+02	0.24227E+03
9435.00	0.13515E-01	0.53865E-01	0.34913E+03	0.83837E+02	0.24254E+03
9440.00	0.13661E-01	0.62118E-01	0.57246E+03	0.83398E+02	0.28393E+03
9445.00	0.13367E-01	0.64470E-01	0.32221E+03	0.82095E+02	0.29140E+03
9450.00	0.13675E-01	0.62182E-01	0.56659E+03	0.82416E+02	0.29188E+03
9455.00	0.12973E-01	0.61169E-01	0.31764E+03	0.86536E+02	0.26416E+03
9460.00	0.12748E-01	0.69702E-01	0.42175E+03	0.81577E+02	0.28189E+03
9465.00	0.12743E-01	0.81194E-01	0.18821E+03	0.81312E+02	0.37129E+03
9470.00	0.12614E-01	0.97687E-01	0.76889E+02	0.91042E+02	0.37248E+03
9475.00	0.12607E-01	0.10320E+00	0.58079E+02	0.90272E+02	0.35113E+03
9480.00	0.12581E-01	0.10316E+00	0.10024E+03	0.91706E+02	0.32413E+03
9485.00	0.13255E-01	0.12308E+00	0.19779E+02	0.90194E+02	0.30465E+03
9490.00	0.13412E-01	0.12179E+00	0.87291E+02	0.92976E+02	0.28968E+03
9495.00	0.12482E-01	0.11127E+00	0.33411E+02	0.93393E+02	0.29860E+03
9500.00	0.12994E-01	0.11625E+00	0.53975E+02	0.92965E+02	0.27625E+03

Appendix C

Band-Model Parameters for the Hydrogen-Broadened Methane Spectra

The following table lists the band model parameters fitted to the combined set of self- and H_2-broadened CH_4 spectra using the Goody-Voigt random band model with $k_\nu(T)$ and SFB. The equation for transmittance is (Equation 4.28)

$$\overline{\tau}_{Goody-Voigt} = \exp\left(-2k_\nu U \int_0^\infty \frac{V(x,y)}{1+k_\nu U \delta V(x,y)/\alpha_D^0\sqrt{T}}\,dx\right) \qquad (C.1)$$

where

$$y = \frac{\alpha_L}{\alpha_D} = \frac{\alpha_L^0}{\alpha_D^0}\frac{P}{P_0}\frac{\sqrt{T_0}}{T}\left[q + \frac{(1-q)}{SFB}\right], \qquad (C.2)$$

$V(x,y) = \alpha_D f_V(\nu)$, and the laboratory conditions T, P, and U are in units of K, bar, and $(\text{molecules/cm}^2)^{-1}$, respectively. For definitions of the variables used in these equations and for details of this fit, see §4.2.4.1 and §7.3. Columns 1 through 7 below are as follows:

1. The midpoint of the degraded 10 cm^{-1} frequency interval: ν (cm^{-1}).
2. The r.m.s. residual error in transmittance: σ.
3. The absorption coefficient at 296 K: $k_\nu(T_0)$ ($\times 10^{24}$ $(\text{molecules/cm}^2)^{-1}$).
4. The parameter δ/α_D^0 ($\text{K}^{-1/2}$).
5. The parameter α_L^0/α_D^0 ($\text{K}^{-1/2}$).
6. The lower state energy: E_L (cm^{-1}).
7. The self-to-foreign broadening parameter: SFB.

2000.00	0.42102E-02	0.99287E-02	0.16243E+05	0.39578E+03	0.14040E+03	0.26620E+00
2005.00	0.45869E-02	0.12914E-01	0.76221E+05	0.39480E+03	0.13071E+03	0.98872E-01
2010.00	0.42509E-02	0.12206E-01	0.12728E+06	0.39381E+03	0.13076E+03	0.11428E+00
2015.00	0.38466E-02	0.96938E-02	0.41661E+06	0.39284E+03	0.13010E+03	0.59322E+00
2020.00	0.40933E-02	0.15260E-01	0.19317E+06	0.39187E+03	0.13000E+03	0.83532E+00
2025.00	0.40477E-02	0.74267E-02	0.52172E+06	0.39090E+03	0.11007E+03	0.93997E+00
2030.00	0.41470E-02	0.54166E-02	0.11486E+07	0.38993E+03	0.84056E+02	0.93675E+00
2035.00	0.43818E-02	0.84263E-02	0.66031E+06	0.38898E+03	0.11534E+03	0.10721E+01
2040.00	0.45015E-02	0.79847E-02	0.75680E+06	0.38802E+03	0.12179E+03	0.99312E+00
2045.00	0.47248E-02	0.95874E-02	0.28894E+06	0.38707E+03	0.13133E+03	0.97990E+00
2050.00	0.47868E-02	0.10388E-01	0.27414E+06	0.38613E+03	0.13024E+03	0.92488E+00
2055.00	0.56364E-02	0.17142E-01	0.10271E+06	0.38519E+03	0.14010E+03	0.13664E+01
2060.00	0.56168E-02	0.16133E-01	0.99070E+05	0.38426E+03	0.13559E+03	0.13969E+01
2065.00	0.48436E-02	0.74760E-01	0.89470E+04	0.38476E+03	0.79000E+03	0.12261E+00
2070.00	0.46289E-02	0.89074E-01	0.94037E+04	0.38240E+03	0.89020E+03	0.38026E+00
2075.00	0.45654E-02	0.18796E+00	0.10099E+05	0.38534E+03	0.10153E+04	0.15744E+01
2080.00	0.47181E-02	0.31728E+00	0.56816E+04	0.38443E+03	0.93169E+03	0.11490E+01
2085.00	0.45234E-02	0.27966E+00	0.71945E+04	0.38315E+03	0.88331E+03	0.13544E+01
2090.00	0.47063E-02	0.44411E+00	0.48384E+04	0.37805E+03	0.78315E+03	0.12051E+01
2095.00	0.45976E-02	0.40775E+00	0.56714E+04	0.38325E+03	0.75504E+03	0.10687E+01
2100.00	0.50798E-02	0.60171E+00	0.51994E+04	0.37637E+03	0.65894E+03	0.10431E+01
2105.00	0.44654E-02	0.60588E+00	0.48159E+04	0.37551E+03	0.61346E+03	0.12171E+01
2110.00	0.59136E-02	0.83854E+00	0.52677E+04	0.37614E+03	0.56315E+03	0.10333E+01
2115.00	0.95479E-02	0.15848E+01	0.43433E+04	0.37300E+03	0.49589E+03	0.93817E+00
2120.00	0.70059E-02	0.10857E+01	0.70126E+04	0.37341E+03	0.44732E+03	0.10201E+01
2125.00	0.78116E-02	0.14852E+01	0.49307E+04	0.37227E+03	0.39718E+03	0.10737E+01
2130.00	0.76078E-02	0.13402E+01	0.70537E+04	0.37167E+03	0.35049E+03	0.11022E+01
2135.00	0.97270E-02	0.16981E+01	0.10866E+05	0.37815E+03	0.30441E+03	0.10459E+01
2140.00	0.16516E-01	0.33352E+01	0.73861E+04	0.37001E+03	0.26030E+03	0.97802E+00
2145.00	0.10131E-01	0.19862E+01	0.13656E+05	0.36966E+03	0.22657E+03	0.10985E+01
2150.00	0.91930E-02	0.18833E+01	0.10117E+05	0.36932E+03	0.18816E+03	0.12010E+01
2155.00	0.80645E-02	0.16563E+01	0.10844E+05	0.36749E+03	0.15215E+03	0.12674E+01
2160.00	0.83295E-02	0.19036E+01	0.20635E+05	0.36962E+03	0.13648E+03	0.12226E+01
2165.00	0.14109E-01	0.36398E+01	0.14582E+05	0.37114E+03	0.13279E+03	0.10838E+01
2170.00	0.71262E-02	0.14699E+01	0.19232E+05	0.37424E+03	0.12363E+03	0.13537E+01
2175.00	0.52331E-02	0.78330E+00	0.13749E+05	0.36441E+03	0.14141E+03	0.15990E+01
2180.00	0.64817E-02	0.13515E+01	0.88591E+04	0.36372E+03	0.21953E+03	0.14593E+01
2185.00	0.59425E-02	0.71564E+00	0.27566E+04	0.36092E+03	0.37516E+03	0.21747E+01
2190.00	0.58215E-02	0.10495E+01	0.10029E+04	0.35803E+03	0.52159E+03	0.34756E+01
2195.00	0.47681E-01	0.17510E+02	0.30575E+04	0.36114E+03	0.51125E+03	0.13834E+01
2200.00	0.49770E-01	0.21709E+02	0.62313E+04	0.35413E+03	0.35425E+03	0.11369E+01
2205.00	0.66355E-02	0.72417E+00	0.35568E+04	0.36139E+03	0.27162E+03	0.40747E+01
2210.00	0.62679E-02	0.48847E+00	0.22946E+04	0.35676E+03	0.43261E+03	0.61604E+01
2215.00	0.55486E-02	0.68552E+00	0.36576E+04	0.35645E+03	0.39190E+03	0.21342E+01
2220.00	0.65144E-02	0.13380E+01	0.49219E+04	0.35541E+03	0.21123E+03	0.14556E+01
2225.00	0.58727E-02	0.11199E+01	0.29985E+04	0.35681E+03	0.26225E+03	0.19275E+01
2230.00	0.92401E-02	0.17351E+01	0.26728E+04	0.35390E+03	0.41351E+03	0.15549E+01
2235.00	0.15287E-01	0.37846E+01	0.39278E+04	0.35474E+03	0.31821E+03	0.13366E+01
2240.00	0.13621E-01	0.33964E+01	0.40115E+04	0.35320E+03	0.25312E+03	0.14123E+01
2245.00	0.98133E-02	0.20203E+01	0.33885E+04	0.35681E+03	0.25525E+03	0.13855E+01
2250.00	0.15241E-01	0.40315E+01	0.30718E+04	0.35099E+03	0.32424E+03	0.12233E+01
2255.00	0.20060E-01	0.63038E+01	0.23875E+04	0.34994E+03	0.43813E+03	0.12562E+01
2260.00	0.12178E-01	0.34463E+01	0.30482E+04	0.35776E+03	0.48425E+03	0.13034E+01
2265.00	0.99050E-02	0.31092E+01	0.22233E+04	0.34837E+03	0.33228E+03	0.12588E+01
2270.00	0.14936E-01	0.50571E+01	0.18856E+04	0.34686E+03	0.38445E+03	0.11559E+01
2275.00	0.14279E-01	0.52761E+01	0.17055E+04	0.35556E+03	0.58563E+03	0.12001E+01
2280.00	0.87053E-02	0.35606E+01	0.13469E+04	0.34565E+03	0.55718E+03	0.13840E+01
2285.00	0.48418E-02	0.25976E+01	0.10675E+04	0.34167E+03	0.49692E+03	0.15543E+01
2290.00	0.62132E-02	0.27297E+01	0.12451E+04	0.34137E+03	0.55577E+03	0.13943E+01
2295.00	0.72198E-02	0.46338E+01	0.15145E+04	0.34315E+03	0.82077E+03	0.13201E+01
2300.00	0.75760E-02	0.47439E+01	0.15420E+04	0.34252E+03	0.92997E+03	0.13412E+01
2305.00	0.74235E-02	0.28059E+01	0.12718E+04	0.34613E+03	0.83908E+03	0.15001E+01
2310.00	0.74317E-02	0.27914E+01	0.64883E+03	0.33813E+03	0.62775E+03	0.16336E+01
2315.00	0.99125E-02	0.49089E+01	0.66381E+03	0.33859E+03	0.50105E+03	0.14757E+01
2320.00	0.11400E-01	0.78185E+01	0.12921E+04	0.34529E+03	0.69927E+03	0.14136E+01
2325.00	0.92198E-02	0.58732E+01	0.23507E+04	0.34731E+03	0.99832E+03	0.14727E+01
2330.00	0.10105E-01	0.19872E+01	0.17745E+04	0.34187E+03	0.81319E+03	0.18140E+01
2335.00	0.11670E-01	0.90323E+00	0.79128E+03	0.33537E+03	0.45926E+03	0.35800E+01
2340.00	0.13521E-01	0.11055E+02	0.36613E+04	0.33902E+03	0.72754E+03	0.13589E+01
2345.00	0.97904E-02	0.16920E+02	0.20044E+04	0.33495E+03	0.82601E+03	0.15475E+01
2350.00	0.97289E-02	0.39553E+01	0.12656E+04	0.33478E+03	0.55144E+03	0.16249E+01
2355.00	0.98616E-02	0.17532E+01	0.12092E+04	0.33199E+03	0.51304E+03	0.18651E+01
2360.00	0.21997E-01	0.24352E+02	0.66975E+04	0.33701E+03	0.64542E+03	0.13286E+01
2365.00	0.14304E-01	0.31421E+02	0.17873E+04	0.33452E+03	0.70847E+03	0.16304E+01
2370.00	0.14314E-01	0.96262E+01	0.14854E+04	0.33301E+03	0.67599E+03	0.15800E+01
2375.00	0.93231E-02	0.23822E+01	0.65408E+03	0.33851E+03	0.58390E+03	0.27553E+01
2380.00	0.86580E-02	0.40747E+01	0.86802E+03	0.33846E+03	0.64488E+03	0.19834E+01
2385.00	0.23089E-01	0.50249E+02	0.32959E+04	0.33633E+03	0.74195E+03	0.18723E+01
2390.00	0.20211E-01	0.41291E+02	0.35938E+04	0.34056E+03	0.72684E+03	0.18097E+01
2395.00	0.11417E-01	0.46149E+01	0.81568E+03	0.33580E+03	0.73669E+03	0.21576E+01
2400.00	0.12395E-01	0.92372E+01	0.11539E+04	0.33349E+03	0.89569E+03	0.18476E+01
2405.00	0.18753E-01	0.93498E+02	0.47791E+04	0.34051E+03	0.80334E+03	0.19430E+01
2410.00	0.13972E-01	0.57940E+02	0.23756E+04	0.40800E+03	0.69207E+03	0.17782E+01
2415.00	0.13076E-01	0.14895E+02	0.10741E+04	0.32643E+03	0.81870E+03	0.17913E+01
2420.00	0.15820E-01	0.97354E+01	0.95432E+03	0.33059E+03	0.83915E+03	0.19980E+01
2425.00	0.21463E-01	0.22202E+03	0.10621E+05	0.32832E+03	0.73627E+03	0.21713E+01
2430.00	0.24277E-01	0.21189E+03	0.63360E+04	0.35726E+03	0.55100E+03	0.20106E+01
2435.00	0.17246E-01	0.38833E+02	0.19155E+04	0.34121E+03	0.71422E+03	0.19814E+01
2440.00	0.16405E-01	0.19582E+02	0.93144E+03	0,32828E+03	0.75174E+03	0.17603E+01
2445.00	0.16206E-01	0.28105E+02	0.13575E+04	0.33707E+03	0.73694E+03	0.17913E+01
2450.00	0.22640E-01	0.15379E+03	0.49723E+04	0.33358E+03	0.59004E+03	0.20312E+01
2455.00	0.21467E-01	0.18622E+03	0.35943E+04	0.34868E+03	0.56985E+03	0.22454E+01
2460.00	0.16085E-01	0.29818E+02	0.80446E+03	0.33688E+03	0.65520E+03	0.16305E+01
2465.00	0.17549E-01	0.28457E+02	0.73378E+03	0.33209E+03	0.63833E+03	0.14477E+01
2470.00	0.18840E-01	0.17978E+03	0.28677E+04	0.33984E+03	0.51225E+03	0.21129E+01
2475.00	0.20124E-01	0.30400E+03	0.28724E+04	0.36984E+03	0.45420E+03	0.22251E+01
2480.00	0.18294E-01	0.92202E+02	0.14568E+04	0.33842E+03	0.52650E+03	0.19815E+01
2485.00	0.18964E-01	0.22391E+02	0.68736E+03	0.32375E+03	0.63379E+03	0.16981E+01
2490.00	0.30146E-01	0.26796E+03	0.42360E+04	0.36105E+03	0.61962E+03	0.24665E+01
2495.00	0.21429E-01	0.23172E+03	0.18022E+04	0.34057E+03	0.44172E+03	0.24466E+01
2500.00	0.16189E-01	0.65186E+02	0.93436E+03	0.39518E+03	0.45876E+03	0.18598E+01
2505.00	0.18046E-01	0.44198E+02	0.87469E+03	0.33672E+03	0.57917E+03	0.18371E+01
2510.00	0.25860E-01	0.26115E+03	0.28384E+04	0.35337E+03	0.50538E+03	0.23829E+01
2515.00	0.23740E-01	0.32437E+03	0.18376E+04	0.35764E+03	0.40016E+03	0.21437E+01
2520.00	0.20898E-01	0.46744E+02	0.60887E+03	0.33648E+03	0.56456E+03	0.18526E+01
2525.00	0.21298E-01	0.14267E+03	0.10548E+04	0.31298E+03	0.47559E+03	0.24894E+01
2530.00	0.15842E-01	0.13533E+03	0.67419E+03	0.25023E+03	0.40424E+03	0.20241E+01
2535.00	0.18334E-01	0.13857E+03	0.99926E+03	0.30815E+03	0.43770E+03	0.21556E+01
2540.00	0.18108E-01	0.15085E+03	0.12178E+04	0.32921E+03	0.40049E+03	0.20793E+01
2545.00	0.20520E-01	0.24179E+03	0.17567E+04	0.32506E+03	0.30721E+03	0.21223E+01
2550.00	0.20080E-01	0.25027E+03	0.11821E+04	0.34410E+03	0.34618E+03	0.21040E+01
2555.00	0.20921E-01	0.20052E+03	0.75858E+03	0.25392E+03	0.36161E+03	0.22624E+01
2560.00	0.20759E-01	0.34564E+03	0.13444E+04	0.34089E+03	0.28526E+03	0.22276E+01
2565.00	0.20460E-01	0.28181E+03	0.61249E+03	0.22984E+03	0.32840E+03	0.19771E+01
2570.00	0.18122E-01	0.21855E+03	0.68164E+03	0.25945E+03	0.34109E+03	0.20474E+01
2575.00	0.18748E-01	0.16862E+03	0.67634E+03	0.37724E+03	0.33666E+03	0.20151E+01
2580.00	0.18467E-01	0.19519E+03	0.46568E+03	0.36361E+03	0.28030E+03	0.20756E+01
2585.00	0.18586E-01	0.18026E+03	0.44332E+03	0.32542E+03	0.28067E+03	0.21507E+01
2590.00	0.19326E-01	0.13079E+03	0.41501E+03	0.31959E+03	0.44772E+03	0.20438E+01
2595.00	0.33403E-01	0.36737E+03	0.54625E+03	0.31245E+03	0.47989E+03	0.23512E+01
2600.00	0.15841E-01	0.56154E+03	0.26544E+03	0.21124E+03	0.30008E+03	0.19723E+01
2605.00	0.16014E-01	0.29703E+03	0.56235E+03	0.30146E+03	0.18117E+03	0.19978E+01
2610.00	0.17866E-01	0.12348E+03	0.12174E+04	0.39066E+03	0.17980E+03	0.20506E+01
2615.00	0.19708E-01	0.14533E+03	0.15071E+04	0.41326E+03	0.26166E+03	0.21431E+01
2620.00	0.22747E-01	0.14992E+03	0.10933E+04	0.38252E+03	0.32573E+03	0.22316E+01
2625.00	0.21837E-01	0.13961E+03	0.76912E+03	0.31926E+03	0.32472E+03	0.21332E+01
2630.00	0.17599E-01	0.29008E+03	0.54247E+03	0.24599E+03	0.27814E+03	0.19663E+01
2635.00	0.15653E-01	0.37825E+03	0.35504E+03	0.21402E+03	0.28518E+03	0.18340E+01
2640.00	0.17510E-01	0.32382E+03	0.26785E+03	0.23640E+03	0.42322E+03	0.19520E+01
2645.00	0.20356E-01	0.28007E+03	0.31140E+03	0.29711E+03	0.49651E+03	0.21156E+01
2650.00	0.20081E-01	0.27567E+03	0.49753E+03	0.33679E+03	0.41160E+03	0.21162E+01
2655.00	0.18747E-01	0.28996E+03	0.54490E+03	0.29060E+03	0.33264E+03	0.20136E+01
2660.00	0.20041E-01	0.23097E+03	0.54926E+03	0.24367E+03	0.30305E+03	0.22135E+01
2665.00	0.18503E-01	0.31175E+03	0.51539E+03	0.22523E+03	0.38272E+03	0.20983E+01
2670.00	0.18586E-01	0.36566E+03	0.50283E+03	0.29744E+03	0.38530E+03	0.19928E+01
2675.00	0.21106E-01	0.30525E+03	0.62598E+03	0.38775E+03	0.29652E+03	0.20531E+01
2680.00	0.18085E-01	0.57623E+03	0.40890E+03	0.27232E+03	0.38482E+03	0.21758E+01
2685.00	0.30321E-01	0.45520E+03	0.60860E+03	0.31383E+03	0.52917E+03	0.23750E+01
2690.00	0.23106E-01	0.28403E+03	0.44758E+03	0.24800E+03	0.46859E+03	0.22119E+01
2695.00	0.20246E-01	0.58263E+03	0.44190E+03	0.23657E+03	0.41814E+03	0.22298E+01
2700.00	0.21211E-01	0.45859E+03	0.29917E+03	0.18529E+03	0.56371E+03	0.23036E+01
2705.00	0.20131E-01	0.23014E+03	0.35434E+03	0.28155E+03	0.60688E+03	0.21072E+01
2710.00	0.23378E-01	0.50443E+03	0.35802E+03	0.17944E+03	0.52535E+03	0.24593E+01
2715.00	0.23789E-01	0.46352E+03	0.29227E+03	0.17692E+03	0.52223E+03	0.25227E+01
2720.00	0.21462E-01	0.20993E+03	0.35771E+03	0.31721E+03	0.60253E+03	0.20004E+01
2725.00	0.20362E-01	0.53795E+03	0.38177E+03	0.23440E+03	0.51701E+03	0.22429E+01
2730.00	0.20762E-01	0.49904E+03	0.31934E+03	0.21424E+03	0.45469E+03	0.23322E+01
2735.00	0.24031E-01	0.27953E+03	0.48358E+03	0.34518E+03	0.49832E+03	0.21075E+01
2740.00	0.24940E-01	0.95974E+03	0.53342E+03	0.19708E+03	0.43041E+03	0.24096E+01
2745.00	0.23438E-01	0.93725E+03	0.44443E+03	0.23712E+03	0.38403E+03	0.24449E+01
2750.00	0.23028E-01	0.43165E+03	0.42170E+03	0.33818E+03	0.46644E+03	0.21156E+01
2755.00	0.24653E-01	0.82401E+03	0.37979E+03	0.24992E+03	0.42988E+03	0.25581E+01
2760.00	0.25613E-01	0.79056E+03	0.35999E+03	0.30442E+03	0.42635E+03	0.26721E+01
2765.00	0.25237E-01	0.47647E+03	0.22459E+03	0.26982E+03	0.56181E+03	0.23055E+01
2770.00	0.28601E-01	0.94491E+03	0.21702E+03	0.28473E+03	0.49833E+03	0.27042E+01
2775.00	0.22374E-01	0.99199E+03	0.21229E+03	0.28443E+03	0.45443E+03	0.25115E+01
2780.00	0.18077E-01	0.76681E+03	0.17844E+03	0.24099E+03	0.48377E+03	0.22201E+01
2785.00	0.17121E-01	0.11619E+04	0.21125E+03	0.27266E+03	0.39253E+03	0.22966E+01
2790.00	0.17400E-01	0.15055E+04	0.26925E+03	0.29662E+03	0.32005E+03	0.23407E+01
2795.00	0.17564E-01	0.13308E+04	0.27204E+03	0.28389E+03	0.28897E+03	0.23482E+01
2800.00	0.20403E-01	0.11777E+04	0.31614E+03	0.26231E+03	0.29112E+03	0.24986E+01
2805.00	0.22057E-01	0.12177E+04	0.43032E+03	0.24309E+03	0.29195E+03	0.24665E+01
2810.00	0.19197E-01	0.10716E+04	0.38713E+03	0.29317E+03	0.29211E+03	0.22724E+01
2815.00	0.19928E-01	0.11572E+04	0.44125E+03	0.37257E+03	0.27081E+03	0.20602E+01
2820.00	0.18552E-01	0.21698E+04	0.38818E+03	0.32976E+03	0.27876E+03	0.22286E+01
2825.00	0.19477E-01	0.28562E+04	0.35522E+03	0.36120E+03	0.27799E+03	0.23078E+01
2830.00	0.21787E-01	0.19213E+04	0.31842E+03	0.30430E+03	0.31524E+03	0.24594E+01
2835.00	0.23067E-01	0.10248E+04	0.25958E+03	0.28891E+03	0.43946E+03	0.24215E+01
2840.00	0.21469E-01	0.76450E+03	0.17933E+03	0.23853E+03	0.61684E+03	0.22469E+01
2845.00	0.23292E-01	0.80564E+03	0.24128E+03	0.27293E+03	0.50277E+03	0.22013E+01
2850.00	0.26537E-01	0.98769E+03	0.31272E+03	0.27849E+03	0.37357E+03	0.26291E+01
2855.00	0.25908E-01	0.12519E+04	0.32192E+03	0.28922E+03	0.40568E+03	0.26295E+01
2860.00	0.23251E-01	0.15119E+04	0.29589E+03	0.29732E+03	0.38932E+03	0.25503E+01
2865.00	0.22059E-01	0.22240E+04	0.24860E+03	0.27080E+03	0.35584E+03	0.26252E+01
2870.00	0.19941E-01	0.24394E+04	0.21142E+03	0.25579E+03	0.34756E+03	0.25831E+01
2875.00	0.22232E-01	0.26519E+04	0.17780E+03	0.26622E+03	0.46917E+03	0.25309E+01
2880.00	0.24953E-01	0.21504E+04	0.17353E+03	0.27778E+03	0.44779E+03	0.26368E+01
2885.00	0.28630E-01	0.20709E+04	0.16161E+03	0.25912E+03	0.45000E+03	0.27189E+01
2890.00	0.35934E-01	0.13756E+04	0.16306E+03	0.26623E+03	0.50452E+03	0.29321E+01
2895.00	0.43360E-01	0.17351E+04	0.16550E+03	0.22332E+03	0.46214E+03	0.26378E+01
2900.00	0.37714E-01	0.22966E+04	0.21609E+03	0.30340E+03	0.38218E+03	0.21657E+01
2905.00	0.44389E-01	0.21508E+04	0.18775E+03	0.29522E+03	0.36352E+03	0.20880E+01
2910.00	0.36933E-01	0.22818E+04	0.19478E+03	0.28752E+03	0.42486E+03	0.24312E+01
2915.00	0.57441E-01	0.18217E+04	0.14710E+03	0.29259E+03	0.28553E+03	0.19586E+01
2920.00	0.72833E-01	0.19870E+04	0.93843E+02	0.38235E+03	0.29188E+03	0.40355E+01
2925.00	0.39570E-01	0.23154E+04	0.17438E+03	0.29474E+03	0.40335E+03	0.21689E+01
2930.00	0.43619E-01	0.21976E+04	0.18827E+03	0.30943E+03	0.35363E+03	0.19850E+01
2935.00	0.47915E-01	0.21622E+04	0.19732E+03	0.38052E+03	0.29018E+03	0.18149E+01
2940.00	0.38364E-01	0.26600E+04	0.21937E+03	0.39332E+03	0.34823E+03	0.19293E+01
2945.00	0.39282E-01	0.27414E+04	0.20751E+03	0.37660E+03	0.33708E+03	0.20407E+01
2950.00	0.82470E-01	0.24560E+04	0.10634E+03	0.51017E+03	0.25299E+03	0.42494E+01
2955.00	0.41335E-01	0.30392E+04	0.26498E+03	0.53530E+03	0.27302E+03	0.20954E+01
2960.00	0.37234E-01	0.29557E+04	0.26741E+03	0.48272E+03	0.33086E+03	0.22287E+01
2965.00	0.33439E-01	0.29470E+04	0.28504E+03	0.46430E+03	0.27963E+03	0.21749E+01
2970.00	0.34043E-01	0.28193E+04	0.27759E+03	0.45613E+03	0.29732E+03	0.21979E+01
2975.00	0.30724E-01	0.26488E+04	0.28619E+03	0.42639E+03	0.27028E+03	0.22384E+01
2980.00	0.29989E-01	0.28524E+04	0.28986E+03	0.44271E+03	0.24625E+03	0.23629E+01
2985.00	0.29729E-01	0.25265E+04	0.30812E+03	0.40335E+03	0.21124E+03	0.22529E+01
2990.00	0.34392E-01	0.20332E+04	0.26085E+03	0.38039E+03	0.25722E+03	0.23668E+01
2995.00	0.43457E-01	0.15879E+04	0.19690E+03	0.34512E+03	0.33091E+03	0.23072E+01
3000.00	0.59649E-01	0.19228E+04	0.68541E+02	0.27496E+03	0.45822E+03	0.21753E+01
3005.00	0.14946E+00	0.15223E+04	0.87352E+01	0.26743E+03	0.13375E+03	0.50773E+C0
3010.00	0.16402E+00	0.36184E+04	0.17775E+02	0.25804E+03	0.10795E+03	0.42128E-01
3015.00	0.17064E+00	0.46352E+04	0.22041E+02	0.26904E+03	0.11931E+03	0.19179E+01
3020.00	0.14683E+00	0.19670E+04	0.19772E+02	0.27728E+03	0.11240E+03	0.11663E+01
3025.00	0.31087E-01	0.29634E+04	0.20847E+03	0.30522E+03	0.21436E+03	0.23457E+01
3030.00	0.36175E-01	0.13552E+04	0.45752E+03	0.72713E+03	0.22909E+03	0.24055E+01
3035.00	0.33705E-01	0.15115E+04	0.40247E+03	0.38330E+03	0.22067E+03	0.21424E+01
3040.00	0.33540E-01	0.15230E+04	0.37196E+03	0.36285E+03	0.24165E+03	0.20505E+01
3045.00	0.31171E-01	0.17956E+04	0.44012E+03	0.56334E+03	0.23475E+03	0.24541E+01
3050.00	0.39428E-01	0.17796E+04	0.43415E+03	0.66345E+03	0.19994E+03	0.22898E+01
3055.00	0.32893E-01	0.25961E+04	0.41653E+03	0.56337E+03	0.19873E+03	0.21750E+01
3060.00	0.39206E-01	0.28388E+04	0.40440E+03	0.59857E+03	0.16364E+03	0.19264E+01
3065.00	0.36153E-01	0.30932E+04	0.30831E+03	0.51327E+03	0.16741E+03	0.20674E+01
3070.00	0.37820E-01	0.33172E+04	0.23357E+03	0.60052E+03	0.17512E+03	0.22469E+01
3075.00	0.41521E-01	0.30219E+04	0.20488E+03	0.52193E+03	0.23517E+03	0.18601E+01
3080.00	0.79165E-01	0.24307E+04	0.10210E+03	0.51847E+03	0.24355E+03	0.37978E+01
3085.00	0.96018E-01	0.21214E+04	0.73740E+02	0.47794E+03	0.23352E+03	0.40058E+01
3090.00	0.75518E-01	0.18584E+04	0.14929E+03	0.39449E+03	0.17867E+03	0.85258E+00
3095.00	0.46851E-01	0.24314E+04	0.20860E+03	0.37035E+03	0.29126E+03	0.15673E+01
3100.00	0.83881E-01	0.18288E+04	0.10066E+03	0.41672E+03	0.23885E+03	0.28593E+01
3105.00	0.43203E-01	0.23597E+04	0.24027E+03	0.30890E+03	0.40174E+03	0.15556E+01
3110.00	0.42363E-01	0.25096E+04	0.21220E+03	0.30687E+03	0.38963E+03	0.16635E+01
3115.00	0.33452E-01	0.25743E+04	0.23879E+03	0.27029E+03	0.48195E+03	0.19082E+01
3120.00	0.35266E-01	0.23828E+04	0.23128E+03	0.27319E+03	0.51468E+03	0.20301E+01
3125.00	0.33470E-01	0.22826E+04	0.24290E+03	0.25360E+03	0.58370E+03	0.19082E+01
3130.00	0.31717E-01	0.19137E+04	0.24877E+03	0.22730E+03	0.61370E+03	0.19895E+01
3135.00	0.28766E-01	0.21775E+04	0.23662E+03	0.22949E+03	0.61650E+03	0.20763E+01
3140.00	0.30474E-01	0.14786E+04	0.25837E+03	0.21851E+03	0.67746E+03	0.20249E+01
3145.00	0.48268E-01	0.13367E+04	0.21414E+03	0.19297E+03	0.57712E+03	0.19099E+01
3150.00	0.31011E-01	0.12801E+04	0.24828E+03	0.16684E+03	0.73569E+03	0.21780E+01
3155.00	0.26021E-01	0.12156E+04	0.24143E+03	0.12558E+03	0.78504E+03	0.21299E+01
3160.00	0.52678E-01	0.60764E+03	0.55077E+03	0.26110E+03	0.82477E+03	0.15686E+01
3165.00	0.41891E-01	0.53531E+03	0.72738E+03	0.27306E+03	0.91183E+03	0.18107E+01
3170.00	0.47091E-01	0.58385E+03	0.71173E+03	0.27829E+03	0.85267E+03	0.16868E+01
3175.00	0.28313E-01	0.40199E+03	0.81014E+03	0.28680E+03	0.90750E+03	0.21283E+01
3180.00	0.34447E-01	0.40350E+03	0.83915E+03	0.26665E+03	0.92999E+03	0.19953E+01
3185.00	0.36793E-01	0.27714E+03	0.14981E+04	0.27720E+03	0.11207E+04	0.21267E+01
3190.00	0.27919E-01	0.15482E+03	0.83835E+03	0.26028E+03	0.11586E+04	0.21979E+01
3195.00	0.30209E-01	0.29177E+03	0.79329E+03	0.26882E+03	0.10438E+04	0.22789E+01

3200.00	0.30199E-01	0.14436E+03	0.10198E+04	0.25513E+03	0.11626E+04	0.23956E+01
3205.00	0.26014E-01	0.77701E+02	0.69728E+03	0.24968E+03	0.11590E+04	0.19383E+01
3210.00	0.29736E-01	0.77126E+02	0.11498E+04	0.24989E+03	0.10417E+04	0.18434E+01
3215.00	0.31929E-01	0.33338E+02	0.10180E+04	0.24052E+03	0.11015E+04	0.16668E+01
3220.00	0.29492E-01	0.48425E+02	0.80515E+03	0.24935E+03	0.11482E+04	0.16821E+01
3225.00	0.35857E-01	0.28445E+02	0.14381E+04	0.24358E+03	0.10404E+04	0.12605E+01
3230.00	0.32768E-01	0.19023E+02	0.11542E+04	0.25166E+03	0.10157E+04	0.14118E+01
3235.00	0.28890E-01	0.22226E+02	0.78520E+03	0.24164E+03	0.10105E+04	0.14854E+01
3240.00	0.33069E-01	0.89748E+01	0.10797E+04	0.24231E+03	0.94365E+03	0.12845E+01
3245.00	0.32077E-01	0.92433E+01	0.87480E+03	0.24198E+03	0.99465E+03	0.12755E+01
3250.00	0.28789E-01	0.10686E+02	0.75541E+03	0.24143E+03	0.99025E+03	0.13143E+01
3255.00	0.31804E-01	0.55560E+01	0.84806E+03	0.24050E+03	0.92537E+03	0.12295E+01
3260.00	0.32335E-01	0.45969E+01	0.60591E+03	0.23905E+03	0.97253E+03	0.11511E+01
3265.00	0.28992E-01	0.56342E+01	0.48122E+03	0.23805E+03	0.10308E+04	0.12181E+01
3270.00	0.29205E-01	0.48135E+01	0.51586E+03	0.23731E+03	0.10302E+04	0.11849E+01
3275.00	0.30629E-01	0.36410E+01	0.53191E+03	0.23967E+03	0.10246E+04	0.11787E+01
3280.00	0.29865E-01	0.30759E+01	0.46731E+03	0.24179E+03	0.99603E+03	0.11482E+01
3285.00	0.29173E-01	0.29604E+01	0.45669E+03	0.23634E+03	0.10001E+04	0.11420E+01
3290.00	0.29030E-01	0.25077E+01	0.54062E+03	0.23653E+03	0.96032E+03	0.10947E+01
3295.00	0.28859E-01	0.20503E+01	0.57354E+03	0.23640E+03	0.91565E+03	0.11729E+01
3300.00	0.27688E-01	0.20140E+01	0.50754E+03	0.23552E+03	0.93033E+03	0.10935E+01
3305.00	0.26799E-01	0.17565E+01	0.59301E+03	0.23579E+03	0.88507E+03	0.11573E+01
3310.00	0.25645E-01	0.16024E+01	0.60282E+03	0.23553E+03	0.85888E+03	0.12181E+01
3315.00	0.24885E-01	0.14085E+01	0.65037E+03	0.23535E+03	0.81075E+03	0.12294E+01
3320.00	0.24069E-01	0.12003E+01	0.66587E+03	0.23481E+03	0.74082E+03	0.13083E+01
3325.00	0.23291E-01	0.12176E+01	0.60448E+03	0.23871E+03	0.76678E+03	0.13753E+01
3330.00	0.22999E-01	0.10416E+01	0.61774E+03	0.23486E+03	0.70064E+03	0.15279E+01
3335.00	0.21591E-01	0.98573E+00	0.56039E+03	0.23296E+03	0.58588E+03	0.20220E+01
3340.00	0.21018E-01	0.10072E+01	0.50756E+03	0.23296E+03	0.57792E+03	0.21802E+01
3345.00	0.20988E-01	0.92800E+00	0.52093E+03	0.23227E+03	0.62986E+03	0.17692E+01
3350.00	0.20665E-01	0.78276E+00	0.61026E+03	0.24049E+03	0.62064E+03	0.20483E+01
3355.00	0.19914E-01	0.68948E+00	0.64971E+03	0.23259E+03	0.58119E+03	0.24759E+01
3360.00	0.19642E-01	0.62918E+00	0.66302E+03	0.23923E+03	0.55446E+03	0.25261E+01
3365.00	0.18669E-01	0.64031E+00	0.64308E+03	0.23861E+03	0.55837E+03	0.29354E+01
3370.00	0.17615E-01	0.65032E+00	0.63965E+03	0.23702E+03	0.51969E+03	0.32981E+01
3375.00	0.16646E-01	0.59850E+00	0.67378E+03	0.24275E+03	0.48136E+03	0.35896E+01
3380.00	0.15468E-01	0.59327E+00	0.52673E+03	0.23069E+03	0.49905E+03	0.35357E+01
3385.00	0.15185E-01	0.54834E+00	0.56527E+03	0.23804E+03	0.51506E+03	0.29139E+01
3390.00	0.14673E-01	0.51928E+00	0.53960E+03	0.22944E+03	0.51844E+03	0.31425E+01
3395.00	0.14051E-01	0.49552E+00	0.51623E+03	0.22909E+03	0.52227E+03	0.32623E+01
3400.00	0.14061E-01	0.48653E+00	0.50770E+03	0.23704E+03	0.54443E+03	0.33940E+01
3405.00	0.13962E-01	0.45759E+00	0.51160E+03	0.22850E+03	0.55807E+03	0.27953E+01
3410.00	0.13490E-01	0.44375E+00	0.49215E+03	0.23652E+03	0.54018E+03	0.32742E+01
3415.00	0.13107E-01	0.40301E+00	0.48217E+03	0.23795E+03	0.52017E+03	0.25648E+01
3420.00	0.12342E-01	0.40539E+00	0.68069E+03	0.23474E+03	0.48943E+03	0.26876E+01
3425.00	0.11789E-01	0.39045E+00	0.70192E+03	0.23435E+03	0.47350E+03	0.36452E+01
3430.00	0.11113E-01	0.39544E+00	0.83119E+03	0.22817E+03	0.43784E+03	0.29819E+01
3435.00	0.10441E-01	0.42846E+00	0.94329E+03	0.22913E+03	0.41029E+03	0.23314E+01
3440.00	0.10474E-01	0.38988E+00	0.10012E+04	0.23249E+03	0.38927E+03	0.25052E+01
3445.00	0.10344E-01	0.40974E+00	0.10992E+04	0.23165E+03	0.33918E+03	0.26087E+01
3450.00	0.10167E-01	0.36342E+00	0.12725E+04	0.23098E+03	0.33377E+03	0.18458E+01
3455.00	0.10090E-01	0.38838E+00	0.13011E+04	0.22758E+03	0.29908E+03	0.17544E+01
3460.00	0.10316E-01	0.32749E+00	0.14272E+04	0.22725E+03	0.32784E+03	0.15864E+01
3465.00	0.10282E-01	0.31150E+00	0.12918E+04	0.22628E+03	0.31829E+03	0.13679E+01
3470.00	0.10157E-01	0.30045E+00	0.13992E+04	0.22894E+03	0.33199E+03	0.12051E+01
3475.00	0.10250E-01	0.25879E+00	0.15377E+04	0.22942E+03	0.40964E+03	0.95045E+00
3480.00	0.93353E-02	0.31172E+00	0.14135E+04	0.22901E+03	0.34921E+03	0.90274E+00
3485.00	0.94401E-02	0.27517E+00	0.97624E+03	0.22527E+03	0.42278E+03	0.56661E+00
3490.00	0.83942E-02	0.45900E+00	0.50350E+03	0.22354E+03	0.44560E+03	0.98046E+00
3495.00	0.66875E-02	0.12966E+01	0.59919E+03	0.22310E+03	0.30656E+03	0.11168E+01
3500.00	0.78786E-02	0.11314E+01	0.14866E+04	0.22481E+03	0.28207E+03	0.92481E+00
3505.00	0.98427E-02	0.19528E+00	0.15712E+04	0.21628E+03	0.49671E+03	0.43836E+00
3510.00	0.87682E-02	0.20467E+00	0.24336E+04	0.22046E+03	0.39756E+03	0.28514E+00
3515.00	0.99820E-02	0.21100E+00	0.31856E+04	0.21853E+03	0.44940E+03	0.42527E+00
3520.00	0.89021E-02	0.28796E+00	0.19127E+04	0.22366E+03	0.49087E+03	0.34019E+00
3525.00	0.80573E-02	0.42013E+00	0.16567E+04	0.22596E+03	0.32820E+03	0.62884E+00
3530.00	0.79016E-02	0.42513E+00	0.18893E+04	0.22525E+03	0.30311E+03	0.63698E+00
3535.00	0.80930E-02	0.34997E+00	0.21452E+04	0.22269E+03	0.32480E+03	0.58158E+00
3540.00	0.74619E-02	0.41622E+00	0.15960E+04	0.22231E+03	0.25663E+03	0.71036E+00
3545.00	0.70168E-02	0.62807E+00	0.10483E+04	0.22237E+03	0.33729E+03	0.70531E+00
3550.00	0.70272E-02	0.64718E+00	0.92043E+03	0.22550E+03	0.39883E+03	0.63126E+00
3555.00	0.69063E-02	0.64270E+00	0.87228E+03	0.22023E+03	0.42984E+03	0.46902E+00
3560.00	0.71204E-02	0.57990E+00	0.83870E+03	0.21970E+03	0.47538E+03	0.32477E+00
3565.00	0.74753E-02	0.46778E+00	0.71216E+03	0.21911E+03	0.51922E+03	0.14423E+00
3570.00	0.75646E-02	0.42752E+00	0.71035E+03	0.21881E+03	0.58608E+03	0.72707E-01
3575.00	0.74923E-02	0.55452E+00	0.69817E+03	0.21859E+03	0.70772E+03	0.17299E+00
3580.00	0.75629E-02	0.62993E+00	0.67301E+03	0.21806E+03	0.78938E+03	0.18950E+00
3585.00	0.82687E-02	0.45863E+00	0.78748E+03	0.21797E+03	0.84482E+03	0.30651E-01
3590.00	0.86518E-02	0.40320E+00	0.72720E+03	0.21807E+03	0.90976E+03	0.29285E-02
3595.00	0.89112E-02	0.29333E+00	0.11304E+04	0.21825E+03	0.84796E+03	0.21294E-02
3600.00	0.86925E-02	0.37367E+00	0.13939E+04	0.21822E+03	0.78007E+03	0.85988E-02
3605.00	0.82882E-02	0.56791E+00	0.85915E+03	0.21733E+03	0.80528E+03	0.22675E+00
3610.00	0.82302E-02	0.84896E+00	0.12368E+04	0.21759E+03	0.81602E+03	0.38895E+00
3615.00	0.86353E-02	0.71854E+00	0.13761E+04	0.21730E+03	0.71765E+03	0.30693E+00
3620.00	0.91457E-02	0.27749E+00	0.11199E+04	0.21634E+03	0.61587E+03	0.16177E+00
3625.00	0.92244E-02	0.37528E+00	0.11502E+04	0.21630E+03	0.84803E+03	0.37379E-03
3630.00	0.81224E-02	0.11040E+01	0.11706E+04	0.21792E+03	0.79579E+03	0.59289E+00
3635.00	0.73196E-02	0.13790E+01	0.10433E+04	0.21842E+03	0.73741E+03	0.74524E+00
3640.00	0.82857E-02	0.69704E+00	0.14681E+04	0.21603E+03	0.76992E+03	0.44386E+00
3645.00	0.96190E-02	0.30309E+00	0.64656E+03	0.21389E+03	0.83510E+03	0.15407E-03
3650.00	0.92477E-02	0.72486E+00	0.16461E+04	0.21567E+03	0.79629E+03	0.37407E+00
3655.00	0.82068E-02	0.20224E+01	0.10538E+04	0.21588E+03	0.73426E+03	0.83346E+00
3660.00	0.73810E-02	0.23618E+01	0.82040E+03	0.22455E+03	0.67643E+03	0.10416E+01
3665.00	0.85317E-02	0.11584E+01	0.10385E+04	0.21860E+03	0.67563E+03	0.71804E+00
3670.00	0.10029E-01	0.54174E+00	0.31669E+03	0.22147E+03	0.71882E+03	0.10492E+00
3675.00	0.99766E-02	0.14970E+01	0.10431E+04	0.21343E+03	0.74469E+03	0.53728E+00
3680.00	0.99744E-02	0.14665E+01	0.12459E+04	0.21352E+03	0.79702E+03	0.53485E+00
3685.00	0.96111E-02	0.16155E+01	0.12881E+04	0.21347E+03	0.64342E+03	0.78901E+00
3690.00	0.93243E-02	0.17943E+01	0.90865E+03	0.21342E+03	0.63439E+03	0.87002E+00
3695.00	0.98223E-02	0.17473E+01	0.10271E+04	0.21416E+03	0.76723E+03	0.76417E+00
3700.00	0.98974E-02	0.21434E+01	0.11275E+04	0.21287E+03	0.74792E+03	0.89430E+00
3705.00	0.99441E-02	0.11841E+01	0.59543E+03	0.22523E+03	0.74329E+03	0.76378E+00
3710.00	0.10161E-01	0.18884E+01	0.70241E+03	0.21328E+03	0.68611E+03	0.94630E+00
3715.00	0.10144E-01	0.35711E+01	0.95367E+03	0.21411E+03	0.62811E+03	0.11489E+01
3720.00	0.99912E-02	0.45689E+01	0.72826E+03	0.21784E+03	0.62447E+03	0.11440E+01
3725.00	0.93485E-02	0.39256E+01	0.48720E+03	0.21724E+03	0.75098E+03	0.11438E+01
3730.00	0.10140E-01	0.29415E+01	0.54006E+03	0.21642E+03	0.79470E+03	0.10888E+01
3735.00	0.10863E-01	0.27467E+01	0.53292E+03	0.21582E+03	0.75417E+03	0.11249E+01
3740.00	0.11934E-01	0.54901E+01	0.59329E+03	0.21123E+03	0.66836E+03	0.11051E+01
3745.00	0.13618E-01	0.51315E+01	0.75678E+03	0.21198E+03	0.66848E+03	0.10366E+01
3750.00	0.11432E-01	0.45426E+01	0.72011E+03	0.20862E+03	0.76750E+03	0.11506E+01
3755.00	0.90682E-02	0.69372E+01	0.49047E+03	0.22950E+03	0.73171E+03	0.13265E+01
3760.00	0.10335E-01	0.67898E+01	0.49737E+03	0.22111E+03	0.79449E+03	0.13111E+01
3765.00	0.11225E-01	0.11726E+02	0.51196E+03	0.22224E+03	0.73096E+03	0.13249E+01
3770.00	0.10460E-01	0.13080E+02	0.45186E+03	0.22424E+03	0.73846E+03	0.13786E+01
3775.00	0.12241E-01	0.13575E+02	0.45857E+03	0.21005E+03	0.79816E+03	0.14409E+01
3780.00	0.11515E-01	0.14405E+02	0.43032E+03	0.23358E+03	0.69353E+03	0.15424E+01
3785.00	0.11881E-01	0.16965E+02	0.45885E+03	0.22503E+03	0.63763E+03	0.15588E+01
3790.00	0.14446E-01	0.28478E+02	0.44753E+03	0.19859E+03	0.65198E+03	0.16637E+01
3795.00	0.16611E-01	0.51747E+02	0.60693E+03	0.20237E+03	0.65117E+03	0.17551E+01
3800.00	0.18077E-01	0.52958E+02	0.63997E+03	0.25045E+03	0.57743E+03	0.17885E+01
3805.00	0.18213E-01	0.64348E+02	0.59279E+03	0.25851E+03	0.53580E+03	0.18809E+01
3810.00	0.19037E-01	0.81332E+02	0.55836E+03	0.26711E+03	0.50448E+03	0.19390E+01
3815.00	0.20251E-01	0.72148E+02	0.61511E+03	0.25345E+03	0.45407E+03	0.18839E+01
3820.00	0.19826E-01	0.98710E+02	0.52539E+03	0.18300E+03	0.43474E+03	0.19445E+01
3825.00	0.21539E-01	0.17308E+03	0.48609E+03	0.17572E+03	0.39580E+03	0.22226E+01
3830.00	0.21771E-01	0.16249E+03	0.55129E+03	0.23566E+03	0.36033E+03	0.21266E+01
3835.00	0.21599E-01	0.14831E+03	0.51880E+03	0.27728E+03	0.35341E+03	0.21084E+01
3840.00	0.20403E-01	0.18935E+03	0.48209E+03	0.27803E+03	0.29545E+03	0.21181E+01
3845.00	0.19250E-01	0.20273E+03	0.48443E+03	0.28020E+03	0.31850E+03	0.19790E+01
3850.00	0.17857E-01	0.25228E+03	0.38374E+03	0.21183E+03	0.33779E+03	0.19574E+01
3855.00	0.16327E-01	0.34943E+03	0.28670E+03	0.17593E+03	0.32257E+03	0.18704E+01
3860.00	0.14844E-01	0.58146E+03	0.25831E+03	0.18438E+03	0.26349E+03	0.18432E+01
3865.00	0.22188E-01	0.59849E+03	0.25121E+03	0.12933E+03	0.14865E+03	0.18903E+01
3870.00	0.28053E-01	0.30788E+03	0.84939E+03	0.23425E+03	0.21449E+03	0.24944E+01
3875.00	0.20449E-01	0.89219E+02	0.31940E+03	0.20996E+03	0.29342E+03	0.21506E+01
3880.00	0.18788E-01	0.13356E+03	0.33626E+03	0.24433E+03	0.22288E+03	0.21295E+01
3885.00	0.17330E-01	0.24479E+03	0.37214E+03	0.25164E+03	0.12936E+03	0.20390E+01
3890.00	0.18397E-01	0.38283E+03	0.30886E+03	0.14667E+03	0.11472E+03	0.20904E+01
3895.00	0.19253E-01	0.38061E+03	0.26453E+03	0.10941E+03	0.13652E+03	0.21059E+01
3900.00	0.15416E-01	0.36040E+03	0.30849E+03	0.14181E+03	0.21817E+03	0.19331E+01
3905.00	0.16284E-01	0.39063E+03	0.23057E+03	0.13306E+03	0.39402E+03	0.18430E+01
3910.00	0.14699E-01	0.27710E+03	0.20236E+03	0.12327E+03	0.43749E+03	0.17988E+01
3915.00	0.13665E-01	0.14282E+03	0.30762E+03	0.20185E+03	0.38504E+03	0.17315E+01
3920.00	0.14200E-01	0.91305E+02	0.26655E+03	0.20838E+03	0.39448E+03	0.17496E+01
3925.00	0.14552E-01	0.52368E+02	0.21878E+03	0.19042E+03	0.37981E+03	0.18134E+01
3930.00	0.13753E-01	0.33603E+02	0.25516E+03	0.19138E+03	0.34090E+03	0.16585E+01
3935.00	0.16671E-01	0.31728E+02	0.38785E+03	0.21799E+03	0.37209E+03	0.15525E+01
3940.00	0.17127E-01	0.50813E+02	0.43297E+03	0.22580E+03	0.37109E+03	0.17491E+01
3945.00	0.18066E-01	0.45761E+02	0.41823E+03	0.24130E+03	0.36778E+03	0.17904E+01
3950.00	0.18582E-01	0.28906E+02	0.37754E+03	0.21361E+03	0.40982E+03	0.15729E+01
3955.00	0.18317E-01	0.47423E+02	0.46320E+03	0.23410E+03	0.35919E+03	0.18173E+01
3960.00	0.18905E-01	0.50173E+02	0.36145E+03	0.21623E+03	0.33976E+03	0.18094E+01
3965.00	0.18931E-01	0.39886E+02	0.31534E+03	0.21173E+03	0.37970E+03	0.16800E+01
3970.00	0.18789E-01	0.45346E+02	0.38869E+03	0.22864E+03	0.38428E+03	0.17525E+01
3975.00	0.18828E-01	0.45838E+02	0.34091E+03	0.22534E+03	0.43586E+03	0.18393E+01
3980.00	0.19194E-01	0.41623E+02	0.26205E+03	0.21507E+03	0.45464E+03	0.17372E+01
3985.00	0.19103E-01	0.43405E+02	0.27508E+03	0.20723E+03	0.44189E+03	0.17102E+01
3990.00	0.19412E-01	0.41874E+02	0.29896E+03	0.21553E+03	0.52826E+03	0.18260E+01
3995.00	0.19770E-01	0.36494E+02	0.24316E+03	0.20695E+03	0.52596E+03	0.16886E+01
4000.00	0.20723E-01	0.45511E+02	0.25477E+03	0.21134E+03	0.48733E+03	0.17783E+01
4005.00	0.19929E-01	0.43658E+02	0.24799E+03	0.19359E+03	0.53693E+03	0.18473E+01
4010.00	0.16580E-01	0.44451E+02	0.22776E+03	0.21294E+03	0.55177E+03	0.17563E+01
4015.00	0.18527E-01	0.59565E+02	0.24242E+03	0.21358E+03	0.52502E+03	0.18358E+01
4020.00	0.19595E-01	0.56198E+02	0.22505E+03	0.21008E+03	0.51914E+03	0.18502E+01
4025.00	0.20525E-01	0.53916E+02	0.20636E+03	0.19183E+03	0.54552E+03	0.19498E+01
4030.00	0.21842E-01	0.66862E+02	0.22134E+03	0.19022E+03	0.59758E+03	0.21405E+01
4035.00	0.18541E-01	0.64285E+02	0.18545E+03	0.18857E+03	0.59212E+03	0.19265E+01
4040.00	0.19639E-01	0.55951E+02	0.18997E+03	0.20284E+03	0.59148E+03	0.18336E+01
4045.00	0.23010E-01	0.82213E+02	0.21278E+03	0.18734E+03	0.60901E+03	0.22588E+01
4050.00	0.23224E-01	0.10428E+03	0.11030E+03	0.81412E+02	0.64051E+03	0.23015E+01
4055.00	0.22314E-01	0.11962E+03	0.17195E+03	0.16560E+03	0.65654E+03	0.23444E+01
4060.00	0.20434E-01	0.12888E+03	0.18417E+03	0.18646E+03	0.56594E+03	0.21459E+01
4065.00	0.19836E-01	0.15153E+03	0.16675E+03	0.17906E+03	0.61939E+03	0.20667E+01
4070.00	0.19605E-01	0.20023E+03	0.15166E+03	0.17785E+03	0.59162E+03	0.19928E+01
4075.00	0.20443E-01	0.22511E+03	0.19048E+03	0.16909E+03	0.49181E+03	0.21627E+01
4080.00	0.21537E-01	0.26747E+03	0.21916E+03	0.16860E+03	0.49953E+03	0.21310E+01
4085.00	0.22373E-01	0.31246E+03	0.22272E+03	0.18164E+03	0.49043E+03	0.21104E+01
4090.00	0.23724E-01	0.31979E+03	0.21470E+03	0.18318E+03	0.43799E+03	0.21346E+01
4095.00	0.25161E-01	0.31560E+03	0.20985E+03	0.17859E+03	0.39350E+03	0.22231E+01
4100.00	0.26827E-01	0.42114E+03	0.19111E+03	0.18551E+03	0.45174E+03	0.24879E+01
4105.00	0.26959E-01	0.50322E+03	0.14062E+03	0.21056E+03	0.49014E+03	0.25749E+01
4110.00	0.27885E-01	0.37744E+03	0.13851E+03	0.15498E+03	0.44702E+03	0.24304E+01
4115.00	0.29403E-01	0.46217E+03	0.16235E+03	0.17465E+03	0.46879E+03	0.26532E+01
4120.00	0.25730E-01	0.79185E+03	0.12729E+03	0.20248E+03	0.44272E+03	0.28054E+01
4125.00	0.23672E-01	0.77715E+03	0.10945E+03	0.17365E+03	0.40799E+03	0.26829E+01
4130.00	0.25121E-01	0.59021E+03	0.10949E+03	0.13978E+03	0.41974E+03	0.24708E+01
4135.00	0.25690E-01	0.67356E+03	0.18113E+03	0.18447E+03	0.48218E+03	0.24723E+01
4140.00	0.26874E-01	0.59285E+03	0.28384E+03	0.21134E+03	0.51164E+03	0.25018E+01
4145.00	0.27466E-01	0.40703E+03	0.24556E+03	0.17871E+03	0.46627E+03	0.23517E+01
4150.00	0.27384E-01	0.75945E+03	0.24624E+03	0.19273E+03	0.47840E+03	0.24196E+01
4155.00	0.27009E-01	0.11076E+04	0.21902E+03	0.20921E+03	0.45260E+03	0.24532E+01
4160.00	0.28672E-01	0.99155E+03	0.20788E+03	0.21953E+03	0.43406E+03	0.26911E+01
4165.00	0.31835E-01	0.10709E+04	0.19054E+03	0.24212E+03	0.43362E+03	0.28519E+01
4170.00	0.33642E-01	0.14126E+04	0.17687E+03	0.21546E+03	0.42712E+03	0.29272E+01
4175.00	0.34798E-01	0.14887E+04	0.18764E+03	0.20208E+03	0.39531E+03	0.26662E+01
4180.00	0.33346E-01	0.18301E+04	0.21371E+03	0.22296E+03	0.31536E+03	0.27417E+01
4185.00	0.37005E-01	0.14458E+04	0.19832E+03	0.24327E+03	0.33031E+03	0.28468E+01
4190.00	0.35136E-01	0.13450E+04	0.17893E+03	0.23943E+03	0.37525E+03	0.30002E+01
4195.00	0.34817E-01	0.14436E+04	0.17614E+03	0.24890E+03	0.35989E+03	0.31234E+01
4200.00	0.36868E-01	0.13146E+04	0.17638E+03	0.24546E+03	0.37062E+03	0.31567E+01
4205.00	0.34998E-01	0.16334E+04	0.12995E+03	0.22209E+03	0.34249E+03	0.34531E+01
4210.00	0.29200E-01	0.24738E+04	0.11530E+03	0.24731E+03	0.35400E+03	0.31511E+01
4215.00	0.11112E+00	0.17200E+04	0.29762E+02	0.27384E+03	0.14890E+03	0.19954E+01
4220.00	0.70183E-01	0.18451E+04	0.92253E+02	0.30245E+03	0.15453E+03	0.13646E+01
4225.00	0.28383E-01	0.15524E+04	0.18611E+03	0.27289E+03	0.30905E+03	0.27523E+01
4230.00	0.31531E-01	0.11853E+04	0.16961E+03	0.21796E+03	0.35687E+03	0.30141E+01
4235.00	0.35605E-01	0.11283E+04	0.14787E+03	0.21378E+03	0.38130E+03	0.36218E+01
4240.00	0.37026E-01	0.16406E+04	0.14901E+03	0.22908E+03	0.26124E+03	0.34616E+01
4245.00	0.30300E-01	0.24263E+04	0.15687E+03	0.27333E+03	0.23043E+03	0.28491E+01
4250.00	0.31623E-01	0.24606E+04	0.14093E+03	0.26037E+03	0.27129E+03	0.30458E+01
4255.00	0.32197E-01	0.28923E+04	0.12944E+03	0.23025E+03	0.25795E+03	0.30826E+01
4260.00	0.27293E-01	0.32285E+04	0.12478E+03	0.24109E+03	0.27141E+03	0.27983E+01
4265.00	0.25308E-01	0.27329E+04	0.13999E+03	0.22854E+03	0.33793E+03	0.29843E+01
4270.00	0.24996E-01	0.29035E+04	0.14739E+03	0.23974E+03	0.30275E+03	0.30561E+01
4275.00	0.21178E-01	0.29214E+04	0.13043E+03	0.20538E+03	0.30910E+03	0.26140E+01
4280.00	0.20233E-01	0.22300E+04	0.12974E+03	0.20224E+03	0.33883E+03	0.25070E+01
4285.00	0.21576E-01	0.19698E+04	0.14225E+03	0.21668E+03	0.29337E+03	0.26975E+01
4290.00	0.28032E-01	0.16108E+04	0.15686E+03	0.22213E+03	0.31983E+03	0.30491E+01
4295.00	0.31715E-01	0.13008E+04	0.13394E+03	0.24816E+03	0.35185E+03	0.36414E+01
4300.00	0.30659E-01	0.12351E+04	0.12914E+03	0.27449E+03	0.40983E+03	0.33260E+01
4305.00	0.28024E-01	0.17055E+04	0.12248E+03	0.24706E+03	0.40122E+03	0.28435E+01
4310.00	0.24613E-01	0.30615E+04	0.91458E+02	0.24560E+03	0.28954E+03	0.26310E+01
4315.00	0.66790E-01	0.17583E+04	0.66928E+02	0.23704E+03	0.14262E+03	0.12092E+01
4320.00	0.60041E-01	0.79214E+03	0.11964E+03	0.15530E+03	0.24699E+03	0.58643E+01
4325.00	0.38080E-01	0.25592E+03	0.20443E+03	0.23819E+03	0.26559E+03	0.27928E+01
4330.00	0.29237E-01	0.91519E+03	0.29543E+03	0.26479E+03	0.13154E+03	0.32063E+01
4335.00	0.24119E-01	0.17599E+04	0.21568E+03	0.30903E+03	0.10012E+03	0.24689E+01
4340.00	0.22053E-01	0.22498E+04	0.13658E+03	0.25245E+03	0.16600E+03	0.25168E+01
4345.00	0.21514E-01	0.25512E+04	0.10951E+03	0.21649E+03	0.17055E+03	0.25456E+01
4350.00	0.23030E-01	0.24820E+04	0.10798E+03	0.20863E+03	0.23206E+03	0.27350E+01
4355.00	0.24884E-01	0.24523E+04	0.85239E+02	0.22904E+03	0.28717E+03	0.34651E+01
4360.00	0.24716E-01	0.21785E+04	0.90988E+02	0.23643E+03	0.30556E+03	0.30423E+01
4365.00	0.26675E-01	0.18667E+04	0.10474E+03	0.24104E+03	0.31412E+03	0.30871E+01
4370.00	0.26964E-01	0.15140E+04	0.10997E+03	0.23217E+03	0.35899E+03	0.31325E+01
4375.00	0.26881E-01	0.14017E+04	0.13998E+03	0.25726E+03	0.32198E+03	0.28622E+01
4380.00	0.26938E-01	0.18716E+04	0.17038E+03	0.27517E+03	0.25633E+03	0.29239E+01
4385.00	0.28864E-01	0.13109E+04	0.16357E+03	0.21432E+03	0.34013E+03	0.31324E+01
4390.00	0.27139E-01	0.15921E+04	0.18763E+03	0.24473E+03	0.30892E+03	0.33815E+01
4395.00	0.27414E-01	0.15037E+04	0.19659E+03	0.26433E+03	0.26767E+03	0.29921E+01

4400.00	0.27457E-01	0.12231E+04	0.17057E+03	0.22127E+03	0.33137E+03	0.30693E+01
4405.00	0.25732E-01	0.16760E+04	0.15452E+03	0.24133E+03	0.30720E+03	0.30290E+01
4410.00	0.26456E-01	0.13330E+04	0.14633E+03	0.23510E+03	0.38333E+03	0.32139E+01
4415.00	0.28727E-01	0.12584E+04	0.15301E+03	0.23175E+03	0.41633E+03	0.32719E+01
4420.00	0.28072E-01	0.20622E+04	0.14381E+03	0.24755E+03	0.35470E+03	0.29744E+01
4425.00	0.27191E-01	0.15366E+04	0.13251E+03	0.21897E+03	0.43030E+03	0.33009E+01
4430.00	0.26887E-01	0.11639E+04	0.12305E+03	0.21140E+03	0.48502E+03	0.30226E+01
4435.00	0.26715E-01	0.15116E+04	0.10862E+03	0.22887E+03	0.43020E+03	0.28856E+01
4440.00	0.24227E-01	0.13086E+04	0.10748E+03	0.23364E+03	0.42779E+03	0.26827E+01
4445.00	0.22655E-01	0.11566E+04	0.10774E+03	0.21212E+03	0.46179E+03	0.27922E+01
4450.00	0.24601E-01	0.12631E+04	0.10704E+03	0.18035E+03	0.46807E+03	0.34289E+01
4455.00	0.26031E-01	0.13260E+04	0.12308E+03	0.17952E+03	0.47104E+03	0.32694E+01
4460.00	0.23685E-01	0.12820E+04	0.14649E+03	0.19221E+03	0.46905E+03	0.28272E+01
4465.00	0.23133E-01	0.11047E+04	0.15489E+03	0.20706E+03	0.43091E+03	0.27235E+01
4470.00	0.22219E-01	0.90504E+03	0.16158E+03	0.21299E+03	0.39664E+03	0.25574E+01
4475.00	0.23235E-01	0.93385E+03	0.17165E+03	0.18464E+03	0.40167E+03	0.23497E+01
4480.00	0.23189E-01	0.88105E+03	0.19548E+03	0.17503E+03	0.41367E+03	0.23199E+01
4485.00	0.22484E-01	0.72929E+03	0.19753E+03	0.16537E+03	0.45620E+03	0.21869E+01
4490.00	0.23571E-01	0.63993E+03	0.20563E+03	0.18457E+03	0.45175E+03	0.22686E+01
4495.00	0.23482E-01	0.46166E+03	0.21839E+03	0.17140E+03	0.43239E+03	0.21455E+01
4500.00	0.24028E-01	0.52479E+03	0.27188E+03	0.16174E+03	0.43302E+03	0.22279E+01
4505.00	0.25097E-01	0.47613E+03	0.22706E+03	0.16134E+03	0.47477E+03	0.22958E+01
4510.00	0.26458E-01	0.33172E+03	0.24212E+03	0.18247E+03	0.47531E+03	0.23301E+01
4515.00	0.28314E-01	0.26566E+03	0.24347E+03	0.16738E+03	0.58533E+03	0.24492E+01
4520.00	0.26852E-01	0.19542E+03	0.19424E+03	0.18193E+03	0.65272E+03	0.22891E+01
4525.00	0.29867E-01	0.14425E+03	0.14248E+03	0.19439E+03	0.64707E+03	0.25263E+01
4530.00	0.30555E-01	0.25158E+03	0.65661E+02	0.64587E+02	0.67996E+03	0.30122E+01
4535.00	0.29140E-01	0.78262E+03	0.56658E+02	0.57914E+02	0.43990E+03	0.29541E+01
4540.00	0.24762E-01	0.14923E+04	0.74714E+02	0.16946E+03	0.28179E+03	0.37608E+01
4545.00	0.25852E-01	0.17343E+04	0.94257E+02	0.20569E+03	0.30982E+03	0.35845E+01
4550.00	0.35315E-01	0.71677E+03	0.73283E+02	0.59154E+02	0.56445E+03	0.34490E+01
4555.00	0.27987E-01	0.15088E+03	0.12869E+03	0.14906E+03	0.66450E+03	0.25619E+01
4560.00	0.31128E-01	0.72158E+02	0.20123E+03	0.16842E+03	0.69434E+03	0.25450E+01
4565.00	0.32206E-01	0.63368E+02	0.33819E+03	0.20185E+03	0.57887E+03	0.22338E+01
4570.00	0.31975E-01	0.58123E+02	0.58014E+03	0.21586E+03	0.52570E+03	0.21617E+01
4575.00	0.32937E-01	0.10027E+03	0.77232E+03	0.19512E+03	0.53297E+03	0.26289E+01
4580.00	0.28920E-01	0.14233E+03	0.91392E+03	0.17486E+03	0.34136E+03	0.24587E+01
4585.00	0.26248E-01	0.81729E+02	0.95143E+03	0.25150E+03	0.28676E+03	0.20921E+01
4590.00	0.25073E-01	0.18341E+03	0.53902E+03	0.14877E+03	0.18372E+03	0.24398E+01
4595.00	0.24635E-01	0.14645E+03	0.32135E+03	0.11148E+03	0.15683E+03	0.24390E+01
4600.00	0.22573E-01	0.16892E+03	0.20857E+03	0.78998E+02	0.14016E+03	0.22293E+01
4605.00	0.21315E-01	0.18859E+03	0.19474E+03	0.96199E+02	0.17375E+03	0.22409E+01
4610.00	0.20732E-01	0.15658E+03	0.21475E+03	0.13643E+03	0.25360E+03	0.22438E+01
4615.00	0.22004E-01	0.19839E+03	0.20140E+03	0.12832E+03	0.29020E+03	0.24226E+01
4620.00	0.30349E-01	0.16923E+03	0.48701E+03	0.18536E+03	0.38019E+03	0.24943E+01
4625.00	0.34882E-01	0.28317E+03	0.81204E+03	0.20053E+03	0.36461E+03	0.24592E+01
4630.00	0.38949E-01	0.29517E+03	0.17607E+04	0.20492E+03	0.45432E+03	0.20211E+01
4635.00	0.30605E-01	0.20952E+03	0.12239E+04	0.18893E+03	0.50518E+03	0.22907E+01
4640.00	0.34248E-01	0.28317E+03	0.16175E+04	0.19941E+03	0.46282E+03	0.22507E+01
4645.00	0.30461E-01	0.22488E+03	0.21461E+04	0.21384E+03	0.54137E+03	0.21626E+01
4650.00	0.28285E-01	0.23209E+03	0.13676E+04	0.19704E+03	0.51376E+03	0.20678E+01
4655.00	0.27798E-01	0.18138E+03	0.15568E+04	0.19463E+03	0.58184E+03	0.20869E+01
4660.00	0.28050E-01	0.46576E+02	0.82847E+03	0.17577E+03	0.69458E+03	0.17394E+01
4665.00	0.31987E-01	0.13792E+03	0.16818E+04	0.17795E+03	0.69964E+03	0.19933E+01
4670.00	0.38179E-01	0.17731E+03	0.29431E+04	0.18882E+03	0.75681E+03	0.18041E+01
4675.00	0.31355E-01	0.50553E+02	0.12522E+04	0.18165E+03	0.81210E+03	0.16378E+01
4680.00	0.33707E-01	0.84133E+02	0.26026E+04	0.18842E+03	0.84084E+03	0.16472E+01
4685.00	0.26415E-01	0.16563E+02	0.56034E+03	0.16938E+03	0.89442E+03	0.11780E+01
4690.00	0.26940E-01	0.25937E+02	0.79323E+03	0.17701E+03	0.91815E+03	0.12760E+01
4695.00	0.27717E-01	0.15312E+02	0.62114E+03	0.16989E+03	0.97227E+03	0.11180E+01

4700.00	0.29190E-01	0.11761E+02	0.69233E+03	0.16686E+03	0.10485E+04	0.90139E+00
4705.00	0.30344E-01	0.12164E+02	0.84418E+03	0.16564E+03	0.10665E+04	0.84751E+00
4710.00	0.31507E-01	0.11987E+02	0.90887E+03	0.16643E+03	0.11154E+04	0.80152E+00
4715.00	0.32338E-01	0.77148E+01	0.12697E+04	0.16949E+03	0.11504E+04	0.71284E+00
4720.00	0.32772E-01	0.67423E+01	0.97375E+03	0.16609E+03	0.12011E+04	0.69954E+00
4725.00	0.33613E-01	0.58285E+01	0.16293E+04	0.16966E+03	0.12827E+04	0.63207E+00
4730.00	0.34290E-01	0.46515E+01	0.19791E+04	0.17444E+03	0.11880E+04	0.46600E+00
4735.00	0.34136E-01	0.49323E+01	0.21712E+04	0.17018E+03	0.11991E+04	0.56887E+00
4740.00	0.35857E-01	0.42086E+01	0.43766E+04	0.16751E+03	0.10821E+04	0.42922E+00
4745.00	0.34420E-01	0.57557E+01	0.69809E+04	0.17969E+03	0.10887E+04	0.40059E+00
4750.00	0.31263E-01	0.42490E+02	0.41527E+05	0.14920E+03	0.10764E+04	0.60795E+00
4755.00	0.37697E-01	0.17423E+02	0.10825E+06	0.16647E+03	0.62419E+03	0.29543E+00
4760.00	0.33215E-01	0.24634E+02	0.80290E+05	0.16630E+03	0.93353E+03	0.35985E+00
4765.00	0.32683E-01	0.34401E+02	0.16739E+06	0.16612E+03	0.72450E+03	0.30907E+00
4770.00	0.42319E-01	0.40093E+00	0.21333E+04	0.17374E+03	0.33258E+03	0.19710E-02
4775.00	0.41680E-01	0.48029E+00	0.64521E+04	0.16863E+03	0.22751E+03	0.12490E+01
4780.00	0.31601E-01	0.27190E+02	0.23872E+06	0.16560E+03	0.66516E+03	0.25904E+00
4785.00	0.40986E-01	0.40201E+00	0.28526E+04	0.15258E+03	0.33321E+03	0.84786E+00
4790.00	0.41284E-01	0.25019E+00	0.30917E+04	0.15731E+03	0.17481E+03	0.22025E+01
4795.00	0.38422E-01	0.36060E+00	0.40475E+04	0.16395E+03	0.28271E+03	0.13291E+00
4800.00	0.37164E-01	0.37162E+00	0.50632E+04	0.15988E+03	0.21050E+03	0.26886E-01
4805.00	0.30343E-01	0.11486E+01	0.39559E+05	0.16545E+03	0.16167E+03	0.19107E+00
4810.00	0.34546E-01	0.47026E+00	0.73341E+04	0.15507E+03	0.22752E+03	0.11283E+00
4815.00	0.35240E-01	0.34022E+00	0.50210E+04	0.15389E+03	0.23227E+03	0.94594E+00
4820.00	0.32205E-01	0.23242E+00	0.81070E+04	0.15650E+03	0.15971E+03	0.39873E+00
4825.00	0.33292E-01	0.17043E+00	0.40429E+04	0.15232E+03	0.15969E+03	0.40375E-02
4830.00	0.32898E-01	0.18028E+00	0.36501E+04	0.14073E+03	0.16660E+03	0.10193E+01
4835.00	0.32070E-01	0.13004E+00	0.17600E+05	0.16372E+03	0.15056E+03	0.43863E+00
4840.00	0.25874E-01	0.34328E+01	0.32830E+06	0.16355E+03	0.15134E+03	0.11827E+00
4845.00	0.27731E-01	0.36162E+00	0.14735E+05	0.15908E+03	0.15077E+03	0.98271E-01
4850.00	0.26470E-01	0.27746E+00	0.13849E+05	0.16108E+03	0.13270E+03	0.13275E+00
4855.00	0.27642E-01	0.18165E+00	0.67663E+04	0.15987E+03	0.15060E+03	0.60802E-01
4860.00	0.27225E-01	0.17093E+00	0.64661E+04	0.16246E+03	0.15245E+03	0.19314E-01
4865.00	0.27413E-01	0.12373E+00	0.59160E+04	0.14908E+03	0.14064E+03	0.53094E+01
4870.00	0.26080E-01	0.16315E+00	0.61565E+04	0.15555E+03	0.17345E+03	0.31328E+00
4875.00	0.24179E-01	0.13956E+00	0.72325E+04	0.16145E+03	0.14036E+03	0.91452E-01
4880.00	0.23186E-01	0.18150E+00	0.89635E+04	0.15241E+03	0.14896E+03	0.19564E-01
4885.00	0.23052E-01	0.24103E+00	0.60945E+04	0.13320E+03	0.24196E+03	0.12853E-01
4890.00	0.22151E-01	0.22000E+00	0.50209E+04	0.14404E+03	0.31235E+03	0.19603E-01
4895.00	0.22273E-01	0.17421E+00	0.62561E+04	0.15146E+03	0.19865E+03	0.39199E-01
4900.00	0.21915E-01	0.16095E+00	0.76376E+04	0.14727E+03	0.16377E+03	0.99695E-01
4905.00	0.20629E-01	0.21345E+00	0.54137E+04	0.13848E+03	0.32218E+03	0.64699E-01
4910.00	0.16164E-01	0.10068E+02	0.18736E+06	0.16280E+03	0.51313E+03	0.41925E+00
4915.00	0.16478E-01	0.35874E+01	0.81699E+05	0.16119E+03	0.60200E+03	0.39424E+00
4920.00	0.21528E-01	0.12213E+00	0.50337E+04	0.15402E+03	0.19965E+03	0.10814E+00
4925.00	0.15782E-01	0.36154E+01	0.38883E+05	0.15969E+03	0.82628E+03	0.57113E+00
4930.00	0.15164E-01	0.21987E+01	0.24142E+05	0.16855E+03	0.87396E+03	0.52834E+00
4935.00	0.14841E-01	0.32460E+01	0.57528E+05	0.16328E+03	0.74782E+03	0.45974E+00
4940.00	0.14853E-01	0.28371E+01	0.33856E+05	0.16240E+03	0.81088E+03	0.61811E+00
4945.00	0.14192E-01	0.11492E+01	0.10297E+05	0.16081E+03	0.84304E+03	0.46013E+00
4950.00	0.13573E-01	0.28145E+01	0.31880E+05	0.17938E+03	0.91878E+03	0.61982E+00
4955.00	0.12806E-01	0.14805E+01	0.73804E+04	0.16379E+03	0.65388E+03	0.64777E+00
4960.00	0.12862E-01	0.12415E+01	0.48463E+04	0.15972E+03	0.62649E+03	0.62875E+00
4965.00	0.12965E-01	0.14134E+01	0.87600E+04	0.16948E+03	0.74774E+03	0.59180E+00
4970.00	0.12604E-01	0.19967E+01	0.16853E+05	0.16773E+03	0.77458E+03	0.66728E+00
4975.00	0.12296E-01	0.27036E+01	0.35787E+05	0.16303E+03	0.71156E+03	0.72884E+00
4980.00	0.12200E-01	0.98825E+00	0.36680E+04	0.15868E+03	0.54985E+03	0.64625E+00
4985.00	0.12114E-01	0.11365E+01	0.38908E+04	0.15860E+03	0.57535E+03	0.61546E+00
4990.00	0.11950E-01	0.93265E+00	0.79380E+04	0.15943E+03	0.72599E+03	0.53852E+00
4995.00	0.12419E-01	0.42500E+00	0.50467E+04	0.15820E+03	0.70203E+03	0.33364E+00

5000.00	0.11640E-01	0.10043E+01	0.25875E+04	0.16163E+03	0.45831E+03	0.78783E+00
5005.00	0.11090E-01	0.17837E+01	0.17542E+04	0.16475E+03	0.41495E+03	0.87707E+00
5010.00	0.12334E-01	0.14305E+01	0.41652E+04	0.16230E+03	0.54376E+03	0.64314E+00
5015.00	0.12803E-01	0.32333E+00	0.25772E+04	0.15731E+03	0.67770E+03	0.24687E+00
5020.00	0.11775E-01	0.86331E+00	0.33632E+04	0.15876E+03	0.47902E+03	0.80245E+00
5025.00	0.10982E-01	0.19491E+01	0.20820E+04	0.15913E+03	0.37935E+03	0.99961E+00
5030.00	0.11780E-01	0.14252E+01	0.22398E+04	0.15722E+03	0.42259E+03	0.81289E+00
5035.00	0.11915E-01	0.41805E+00	0.91986E+03	0.15595E+03	0.51563E+03	0.36951E+00
5040.00	0.11139E-01	0.12694E+01	0.24098E+04	0.15705E+03	0.38496E+03	0.97859E+00
5045.00	0.10620E-01	0.17676E+01	0.12262E+04	0.16298E+03	0.31458E+03	0.10496E+01
5050.00	0.11037E-01	0.11111E+01	0.10725E+04	0.15547E+03	0.37863E+03	0.84046E+00
5055.00	0.10790E-01	0.10233E+01	0.93583E+03	0.16059E+03	0.39672E+03	0.93217E+00
5060.00	0.10760E-01	0.12030E+01	0.87473E+03	0.16044E+03	0.32957E+03	0.11171E+01
5065.00	0.10662E-01	0.11306E+01	0.10922E+04	0.15969E+03	0.30909E+03	0.11390E+01
5070.00	0.10601E-01	0.98022E+00	0.94201E+03	0.15825E+03	0.38154E+03	0.10330E+01
5075.00	0.10480E-01	0.14441E+01	0.11398E+04	0.15674E+03	0.34150E+03	0.96242E+00
5080.00	0.99496E-02	0.15456E+01	0.69989E+03	0.15769E+03	0.33906E+03	0.10789E+01
5085.00	0.10477E-01	0.17218E+01	0.70072E+03	0.16024E+03	0.33263E+03	0.12655E+01
5090.00	0.10635E-01	0.19835E+01	0.70641E+03	0.16549E+03	0.24018E+03	0.14092E+01
5095.00	0.10779E-01	0.14162E+01	0.49728E+03	0.16113E+03	0.29182E+03	0.16996E+01
5100.00	0.97057E-02	0.16491E+01	0.48011E+03	0.16436E+03	0.30280E+03	0.13919E+01
5105.00	0.95962E-02	0.15782E+01	0.51864E+03	0.15349E+03	0.29156E+03	0.11517E+01
5110.00	0.95326E-02	0.15388E+01	0.52297E+03	0.15455E+03	0.28611E+03	0.11833E+01
5115.00	0.96671E-02	0.18952E+01	0.62796E+03	0.15825E+03	0.23942E+03	0.13996E+01
5120.00	0.10129E-01	0.13813E+01	0.62152E+03	0.16092E+03	0.32934E+03	0.13253E+01
5125.00	0.11154E-01	0.22331E+01	0.48815E+03	0.15157E+03	0.41110E+03	0.10650E+01
5130.00	0.85728E-02	0.38505E+01	0.30613E+03	0.14995E+03	0.29491E+03	0.14215E+01
5135.00	0.88292E-02	0.37541E+01	0.34880E+03	0.16117E+03	0.19348E+03	0.14889E+01
5140.00	0.91292E-02	0.25339E+01	0.51781E+03	0.16318E+03	0.19839E+03	0.13355E+01
5145.00	0.95542E-02	0.21165E+01	0.68499E+03	0.16342E+03	0.20305E+03	0.13331E+01
5150.00	0.94687E-02	0.19721E+01	0.73880E+03	0.15522E+03	0.23398E+03	0.12513E+01
5155.00	0.84631E-02	0.18915E+01	0.50042E+03	0.15280E+03	0.29570E+03	0.13181E+01
5160.00	0.83091E-02	0.21551E+01	0.33886E+03	0.15874E+03	0.29169E+03	0.14494E+01
5165.00	0.86550E-02	0.18862E+01	0.32158E+03	0.15806E+03	0.27346E+03	0.15917E+01
5170.00	0.81305E-02	0.23356E+01	0.24721E+03	0.15869E+03	0.29009E+03	0.16850E+01
5175.00	0.77375E-02	0.33330E+01	0.16205E+03	0.13858E+03	0.29149E+03	0.15168E+01
5180.00	0.96680E-02	0.27811E+01	0.28736E+03	0.14598E+03	0.30576E+03	0.12340E+01
5185.00	0.93883E-02	0.25955E+01	0.44306E+03	0.15962E+03	0.29211E+03	0.16031E+01
5190.00	0.93097E-02	0.42117E+01	0.38935E+03	0.16164E+03	0.23259E+03	0.16300E+01
5195.00	0.85612E-02	0.48519E+01	0.28363E+03	0.13858E+03	0.23339E+03	0.15404E+01
5200.00	0.86558E-02	0.55618E+01	0.99978E+02	0.55041E+02	0.25979E+03	0.13493E+01
5205.00	0.93131E-02	0.75785E+01	0.86694E+02	0.61756E+02	0.27872E+03	0.13090E+01
5210.00	0.15368E-01	0.56761E+01	0.30781E+03	0.14399E+03	0.31542E+03	0.12243E+01
5215.00	0.82839E-02	0.32102E+01	0.33283E+03	0.14845E+03	0.32588E+03	0.14308E+01
5220.00	0.80904E-02	0.38982E+01	0.33227E+03	0.15223E+03	0.30427E+03	0.14357E+01
5225.00	0.77910E-02	0.46659E+01	0.23713E+03	0.13618E+03	0.29399E+03	0.14173E+01
5230.00	0.84165E-02	0.55290E+01	0.17104E+03	0.90220E+02	0.31242E+03	0.13007E+01
5235.00	0.92163E-02	0.45793E+01	0.29180E+03	0.14629E+03	0.36173E+03	0.12870E+01
5240.00	0.77875E-02	0.41153E+01	0.23107E+03	0.16176E+03	0.33773E+03	0.14833E+01
5245.00	0.80583E-02	0.32845E+01	0.22766E+03	0.15690E+03	0.36639E+03	0.15286E+01
5250.00	0.84187E-02	0.30005E+01	0.20372E+03	0.15714E+03	0.40514E+03	0.15437E+01
5255.00	0.82274E-02	0.37206E+01	0.18754E+03	0.15731E+03	0.38741E+03	0.15407E+01
5260.00	0.89432E-02	0.29365E+01	0.21896E+03	0.15812E+03	0.44773E+03	0.16009E+01
5265.00	0.99273E-02	0.23378E+01	0.17628E+03	0.15718E+03	0.49908E+03	0.18254E+01
5270.00	0.89499E-02	0.32148E+01	0.17605E+03	0.14342E+03	0.45962E+03	0.13963E+01
5275.00	0.94854E-02	0.30389E+01	0.20828E+03	0.14362E+03	0.48172E+03	0.12884E+01
5280.00	0.10058E-01	0.22038E+01	0.20042E+03	0.15632E+03	0.52957E+03	0.16399E+01
5285.00	0.91077E-02	0.29543E+01	0.15353E+03	0.15689E+03	0.49965E+03	0.15246E+01
5290.00	0.87238E-02	0.32920E+01	0.12402E+03	0.15764E+03	0.54984E+03	0.16600E+01
5295.00	0.94900E-02	0.26076E+01	0.13954E+03	0.15722E+03	0.57883E+03	0.18631E+01

5300.00	0.88571E-02	0.26410E+01	0.12710E+03	0.15718E+03	0.52228E+03	0.18093E+01
5305.00	0.93016E-02	0.29819E+01	0.12199E+03	0.16066E+03	0.55649E+03	0.21153E+01
5310.00	0.87885E-02	0.36486E+01	0.11747E+03	0.15711E+03	0.56054E+03	0.18038E+01
5315.00	0.81381E-02	0.38999E+01	0.10281E+03	0.15738E+03	0.53466E+03	0.17518E+01
5320.00	0.86146E-02	0.33390E+01	0.11620E+03	0.15697E+03	0.52942E+03	0.18558E+01
5325.00	0.86143E-02	0.35157E+01	0.12773E+03	0.15664E+03	0.54479E+03	0.17863E+01
5330.00	0.83225E-02	0.45062E+01	0.12801E+03	0.15071E+03	0.52923E+03	0.15752E+01
5335.00	0.82169E-02	0.50990E+01	0.12500E+03	0.15576E+03	0.55032E+03	0.16049E+01
5340.00	0.80685E-02	0.56023E+01	0.13011E+03	0.15945E+03	0.57336E+03	0.15917E+01
5345.00	0.76535E-02	0.60422E+01	0.12198E+03	0.17066E+03	0.48449E+03	0.15891E+01
5350.00	0.78480E-02	0.59175E+01	0.12696E+03	0.17180E+03	0.48396E+03	0.16038E+01
5355.00	0.73420E-02	0.73606E+01	0.14667E+03	0.17689E+03	0.47433E+03	0.15774E+01
5360.00	0.69567E-02	0.11205E+02	0.13591E+03	0.16819E+03	0.43776E+03	0.15179E+01
5365.00	0.79742E-02	0.10285E+02	0.12723E+03	0.11589E+03	0.44436E+03	0.15093E+01
5370.00	0.92186E-02	0.86492E+01	0.16767E+03	0.14361E+03	0.40166E+03	0.15655E+01
5375.00	0.96223E-02	0.11455E+02	0.18507E+03	0.16666E+03	0.34368E+03	0.15457E+01
5380.00	0.10231E-01	0.15051E+02	0.17462E+03	0.16699E+03	0.37430E+03	0.15293E+01
5385.00	0.10458E-01	0.14058E+02	0.14433E+03	0.16875E+03	0.43148E+03	0.15763E+01
5390.00	0.98033E-02	0.11452E+02	0.12456E+03	0.16894E+03	0.43567E+03	0.16394E+01
5395.00	0.10663E-01	0.13887E+02	0.12903E+03	0.16795E+03	0.38742E+03	0.15704E+01
5400.00	0.10342E-01	0.18028E+02	0.13714E+03	0.17586E+03	0.34573E+03	0.15411E+01
5405.00	0.89618E-02	0.19724E+02	0.10720E+03	0.17499E+03	0.37502E+03	0.15512E+01
5410.00	0.94992E-02	0.18593E+02	0.98688E+02	0.19887E+03	0.39058E+03	0.15280E+01
5415.00	0.10664E-01	0.17046E+02	0.98548E+02	0.15341E+03	0.36854E+03	0.15879E+01
5420.00	0.10685E-01	0.16444E+02	0.97729E+02	0.10509E+03	0.39891E+03	0.16118E+01
5425.00	0.12467E-01	0.24860E+02	0.11648E+03	0.11299E+03	0.39935E+03	0.16726E+01
5430.00	0.11265E-01	0.25856E+02	0.15305E+03	0.18203E+03	0.35485E+03	0.15217E+01
5435.00	0.10186E-01	0.24382E+02	0.10591E+03	0.15062E+03	0.39813E+03	0.15072E+01
5440.00	0.97218E-02	0.29471E+02	0.84347E+02	0.15155E+03	0.41754E+03	0.15775E+01
5445.00	0.10735E-01	0.32410E+02	0.10788E+03	0.16736E+03	0.41551E+03	0.16433E+01
5450.00	0.10710E-01	0.35234E+02	0.10348E+03	0.14315E+03	0.45398E+03	0.16267E+01
5455.00	0.96170E-02	0.29595E+02	0.10809E+03	0.15954E+03	0.47318E+03	0.14975E+01
5460.00	0.10474E-01	0.26594E+02	0.13771E+03	0.20169E+03	0.48243E+03	0.14072E+01
5465.00	0.11776E-01	0.24736E+02	0.15353E+03	0.16491E+03	0.46919E+03	0.15932E+01
5470.00	0.14922E-01	0.40339E+02	0.10812E+03	0.81829E+02	0.45091E+03	0.18371E+01
5475.00	0.12283E-01	0.43764E+02	0.13394E+03	0.15179E+03	0.44820E+03	0.16860E+01
5480.00	0.12599E-01	0.24791E+02	0.15893E+03	0.23737E+03	0.45339E+03	0.13493E+01
5485.00	0.16762E-01	0.39303E+02	0.15815E+03	0.15710E+03	0.45372E+03	0.18628E+01
5490.00	0.16887E-01	0.59588E+02	0.17722E+03	0.13210E+03	0.40350E+03	0.21064E+01
5495.00	0.18472E-01	0.52627E+02	0.13257E+03	0.91688E+02	0.38357E+03	0.21166E+01
5500.00	0.18137E-01	0.45792E+02	0.16671E+03	0.13716E+03	0.42290E+03	0.20896E+01
5505.00	0.13774E-01	0.29799E+02	0.13378E+03	0.17322E+03	0.42382E+03	0.16238E+01
5510.00	0.20245E-01	0.64373E+02	0.16270E+03	0.13535E+03	0.35713E+03	0.22753E+01
5515.00	0.17933E-01	0.75744E+02	0.19356E+03	0.12925E+03	0.30778E+03	0.21391E+01
5520.00	0.20146E-01	0.64328E+02	0.20623E+03	0.13424E+03	0.32014E+03	0.23214E+01
5525.00	0.22388E-01	0.47894E+02	0.20270E+03	0.14881E+03	0.35664E+03	0.21496E+01
5530.00	0.18940E-01	0.44885E+02	0.19561E+03	0.15282E+03	0.32505E+03	0.19397E+01
5535.00	0.17728E-01	0.69598E+02	0.17808E+03	0.13206E+03	0.26307E+03	0.21090E+01
5540.00	0.17722E-01	0.48331E+02	0.15946E+03	0.16083E+03	0.31811E+03	0.19364E+01
5545.00	0.21397E-01	0.58540E+02	0.14828E+03	0.14409E+03	0.34873E+03	0.22278E+01
5550.00	0.20681E-01	0.47676E+02	0.11040E+03	0.15352E+03	0.37360E+03	0.21973E+01
5555.00	0.19056E-01	0.46938E+02	0.93100E+02	0.14684E+03	0.34632E+03	0.21560E+01
5560.00	0.17522E-01	0.67724E+02	0.92331E+02	0.13397E+03	0.31695E+03	0.22311E+01
5565.00	0.15400E-01	0.73569E+02	0.87188E+02	0.13258E+03	0.37645E+03	0.20745E+01
5570.00	0.15514E-01	0.10886E+03	0.90452E+02	0.12680E+03	0.38447E+03	0.21012E+01
5575.00	0.16285E-01	0.17759E+03	0.89990E+02	0.13105E+03	0.32569E+03	0.21695E+01
5580.00	0.16739E-01	0.28811E+03	0.93361E+02	0.11708E+03	0.23391E+03	0.21893E+01
5585.00	0.20184E-01	0.28707E+03	0.92119E+02	0.86332E+02	0.17997E+03	0.23694E+01
5590.00	0.21460E-01	0.14270E+03	0.10310E+03	0.10070E+03	0.26440E+03	0.27567E+01
5595.00	0.18359E-01	0.84820E+02	0.10137E+03	0.16929E+03	0.30734E+03	0.21753E+01

5600.00	0.17449E-01	0.10832E+03	0.89448E+02	0.14824E+03	0.21937E+03	0.21343E+01
5605.00	0.16866E-01	0.97454E+02	0.10346E+03	0.14011E+03	0.13721E+03	0.22244E+01
5610.00	0.17735E-01	0.52624E+02	0.13870E+03	0.16585E+03	0.15916E+03	0.21167E+01
5615.00	0.17448E-01	0.40837E+02	0.14615E+03	0.16016E+03	0.17393E+03	0.19289E+01
5620.00	0.20167E-01	0.75891E+02	0.18304E+03	0.11388E+03	0.10142E+03	0.23545E+01
5625.00	0.18620E-01	0.93042E+02	0.19984E+03	0.15485E+03	0.93535E+02	0.22314E+01
5630.00	0.17905E-01	0.16192E+03	0.10790E+03	0.10706E+03	0.12180E+03	0.22072E+01
5635.00	0.17783E-01	0.18602E+03	0.76427E+02	0.13285E+03	0.20927E+03	0.22515E+01
5640.00	0.18005E-01	0.12643E+03	0.80576E+02	0.15491E+03	0.26763E+03	0.22449E+01
5645.00	0.19745E-01	0.12121E+03	0.11903E+03	0.16305E+03	0.23972E+03	0.24357E+01
5650.00	0.17635E-01	0.92325E+02	0.13051E+03	0.14875E+03	0.21952E+03	0.21893E+01
5655.00	0.17365E-01	0.88586E+02	0.11726E+03	0.12150E+03	0.24500E+03	0.21843E+01
5660.00	0.18688E-01	0.11217E+03	0.10337E+03	0.10708E+03	0.28540E+03	0.23070E+01
5665.00	0.16795E-01	0.97709E+02	0.11760E+03	0.13525E+03	0.30346E+03	0.20928E+01
5670.00	0.15830E-01	0.85066E+02	0.98823E+02	0.13837E+03	0.36296E+03	0.19592E+01
5675.00	0.13923E-01	0.73424E+02	0.73840E+02	0.12288E+03	0.42796E+03	0.18891E+01
5680.00	0.14312E-01	0.61927E+02	0.78246E+02	0.15889E+03	0.40907E+03	0.18171E+01
5685.00	0.16200E-01	0.64240E+02	0.71822E+02	0.16376E+03	0.42802E+03	0.19212E+01
5690.00	0.14127E-01	0.56776E+02	0.59392E+02	0.14232E+03	0.46479E+03	0.18999E+01
5695.00	0.16191E-01	0.65552E+02	0.71062E+02	0.14512E+03	0.40959E+03	0.19169E+01
5700.00	0.17640E-01	0.79265E+02	0.85300E+02	0.14484E+03	0.38732E+03	0.20092E+01
5705.00	0.15933E-01	0.60014E+02	0.80961E+02	0.15558E+03	0.42473E+03	0.19139E+01
5710.00	0.15761E-01	0.62060E+02	0.87912E+02	0.15613E+03	0.43896E+03	0.19796E+01
5715.00	0.16097E-01	0.79921E+02	0.86500E+02	0.13322E+03	0.39808E+03	0.21070E+01
5720.00	0.15681E-01	0.79584E+02	0.81904E+02	0.14195E+03	0.37645E+03	0.20843E+01
5725.00	0.17493E-01	0.84303E+02	0.12127E+03	0.15144E+03	0.43230E+03	0.21675E+01
5730.00	0.16461E-01	0.10010E+03	0.11143E+03	0.12911E+03	0.40804E+03	0.20570E+01
5735.00	0.15507E-01	0.95437E+02	0.10625E+03	0.15067E+03	0.37385E+03	0.20176E+01
5740.00	0.16911E-01	0.87679E+02	0.11764E+03	0.14977E+03	0.40884E+03	0.21299E+01
5745.00	0.18472E-01	0.11850E+03	0.99573E+02	0.13375E+03	0.38975E+03	0.21515E+01
5750.00	0.21549E-01	0.14985E+03	0.12645E+03	0.20024E+03	0.37013E+03	0.22958E+01
5755.00	0.21164E-01	0.12356E+03	0.92273E+02	0.15310E+03	0.41956E+03	0.22478E+01
5760.00	0.22129E-01	0.14465E+03	0.80253E+02	0.13240E+03	0.40954E+03	0.21833E+01
5765.00	0.23382E-01	0.16946E+03	0.81191E+02	0.15576E+03	0.37336E+03	0.21768E+01
5770.00	0.20910E-01	0.17092E+03	0.69680E+02	0.12795E+03	0.36218E+03	0.20880E+01
5775.00	0.21302E-01	0.23761E+03	0.75776E+02	0.13014E+03	0.31840E+03	0.21422E+01
5780.00	0.20836E-01	0.22632E+03	0.74833E+02	0.14084E+03	0.29931E+03	0.22522E+01
5785.00	0.20008E-01	0.22101E+03	0.84517E+02	0.13070E+03	0.24199E+03	0.22768E+01
5790.00	0.18397E-01	0.28290E+03	0.99381E+02	0.13875E+03	0.18739E+03	0.21995E+01
5795.00	0.17433E-01	0.25758E+03	0.12016E+03	0.16920E+03	0.15633E+03	0.21125E+01
5800.00	0.17794E-01	0.24541E+03	0.14481E+03	0.18489E+03	0.11819E+03	0.20583E+01
5805.00	0.17515E-01	0.22751E+03	0.17246E+03	0.16872E+03	0.96472E+02	0.20611E+01
5810.00	0.18036E-01	0.15989E+03	0.21291E+03	0.19252E+03	0.86910E+02	0.20909E+01
5815.00	0.18321E-01	0.10577E+03	0.21350E+03	0.20830E+03	0.13077E+03	0.21088E+01
5820.00	0.20469E-01	0.82562E+02	0.19418E+03	0.19341E+03	0.19451E+03	0.21503E+01
5825.00	0.21785E-01	0.72525E+02	0.16604E+03	0.17891E+03	0.25432E+03	0.22542E+01
5830.00	0.20309E-01	0.82675E+02	0.89645E+02	0.12967E+03	0.28200E+03	0.22445E+01
5835.00	0.22052E-01	0.13309E+03	0.89397E+02	0.16348E+03	0.24578E+03	0.23419E+01
5840.00	0.23478E-01	0.16275E+03	0.85192E+02	0.15241E+03	0.26572E+03	0.22377E+01
5845.00	0.23765E-01	0.18974E+03	0.10780E+03	0.14772E+03	0.20837E+03	0.23462E+01
5850.00	0.22014E-01	0.26757E+03	0.12092E+03	0.13622E+03	0.11956E+03	0.23684E+01
5855.00	0.21196E-01	0.35322E+03	0.81957E+02	0.11911E+03	0.18780E+03	0.23281E+01
5860.00	0.18256E-01	0.38138E+03	0.76211E+02	0.13489E+03	0.19688E+03	0.22260E+01
5865.00	0.17251E-01	0.29838E+03	0.72232E+02	0.13805E+03	0.22858E+03	0.22667E+01
5870.00	0.17440E-01	0.27610E+03	0.65780E+02	0.13725E+03	0.28076E+03	0.22842E+01
5875.00	0.17514E-01	0.29401E+03	0.68678E+02	0.14233E+03	0.32745E+03	0.22830E+01
5880.00	0.18418E-01	0.23227E+03	0.66057E+02	0.13739E+03	0.37141E+03	0.22700E+01
5885.00	0.18359E-01	0.16530E+03	0.63282E+02	0.12647E+03	0.36874E+03	0.21879E+01
5890.00	0.20479E-01	0.17677E+03	0.66902E+02	0.11282E+03	0.41347E+03	0.25436E+01
5895.00	0.22564E-01	0.14256E+03	0.69760E+02	0.96502E+02	0.43272E+03	0.27484E+01

5900.00	0.23122E-01	0.14759E+03	0.91730E+02	0.10161E+03	0.38036E+03	0.26418E+01
5905.00	0.22881E-01	0.17676E+03	0.10643E+03	0.11634E+03	0.35182E+03	0.25524E+01
5910.00	0.21913E-01	0.13504E+03	0.98442E+02	0.11267E+03	0.36871E+03	0.23477E+01
5915.00	0.20744E-01	0.12469E+03	0.13422E+03	0.10708E+03	0.35637E+03	0.22769E+01
5920.00	0.18571E-01	0.90746E+02	0.14025E+03	0.13962E+03	0.35950E+03	0.19922E+01
5925.00	0.19406E-01	0.12122E+03	0.13475E+03	0.13890E+03	0.34666E+03	0.21756E+01
5930.00	0.19345E-01	0.10958E+03	0.13271E+03	0.16344E+03	0.35015E+03	0.22225E+01
5935.00	0.19372E-01	0.11000E+03	0.13276E+03	0.13047E+03	0.35544E+03	0.22256E+01
5940.00	0.21362E-01	0.87471E+02	0.15496E+03	0.13851E+03	0.40355E+03	0.22781E+01
5945.00	0.19701E-01	0.90372E+02	0.12540E+03	0.13186E+03	0.39395E+03	0.22668E+01
5950.00	0.21216E-01	0.87239E+02	0.14982E+03	0.13243E+03	0.39035E+03	0.23713E+01
5955.00	0.21046E-01	0.36129E+02	0.13282E+03	0.21000E+03	0.41801E+03	0.16169E+01
5960.00	0.22884E-01	0.74642E+02	0.12967E+03	0.11228E+03	0.35990E+03	0.25432E+01
5965.00	0.23379E-01	0.75318E+02	0.97362E+02	0.98024E+02	0.39013E+03	0.26878E+01
5970.00	0.23900E-01	0.63114E+02	0.11817E+03	0.15350E+03	0.38028E+03	0.23377E+01
5975.00	0.24735E-01	0.80383E+02	0.11337E+03	0.15206E+03	0.40578E+03	0.23799E+01
5980.00	0.22553E-01	0.81671E+02	0.73714E+02	0.12712E+03	0.47116E+03	0.22551E+01
5985.00	0.22294E-01	0.11185E+03	0.57779E+02	0.10666E+03	0.50661E+03	0.22506E+01
5990.00	0.19878E-01	0.16232E+03	0.51437E+02	0.81929E+02	0.57996E+03	0.23391E+01
5995.00	0.22043E-01	0.34272E+03	0.76801E+02	0.68780E+02	0.54588E+03	0.24538E+01
6000.00	0.30299E-01	0.11797E+04	0.16243E+03	0.13833E+03	0.34155E+03	0.27660E+01
6005.00	0.52838E-01	0.70518E+03	0.28159E+03	0.75442E+02	0.17014E+03	0.21860E+01
6010.00	0.23546E-01	0.44077E+02	0.24664E+03	0.22428E+03	0.21695E+03	0.17733E+01
6015.00	0.21082E-01	0.52842E+02	0.22401E+03	0.16410E+03	0.22277E+03	0.19136E+01
6020.00	0.23573E-01	0.48704E+02	0.25210E+03	0.14793E+03	0.29430E+03	0.20837E+01
6025.00	0.24620E-01	0.58142E+02	0.25177E+03	0.15072E+03	0.29472E+03	0.21351E+01
6030.00	0.26166E-01	0.63649E+02	0.16693E+03	0.17938E+03	0.43455E+03	0.20313E+01
6035.00	0.25975E-01	0.12849E+03	0.81687E+02	0.63272E+02	0.46458E+03	0.23111E+01
6040.00	0.18859E-01	0.16402E+03	0.10807E+03	0.85799E+02	0.25660E+03	0.20421E+01
6045.00	0.18397E-01	0.13655E+03	0.37696E+03	0.18061E+03	0.11799E+03	0.21533E+01
6050.00	0.26251E-01	0.10511E+03	0.52694E+03	0.16949E+03	0.16919E+03	0.24005E+01
6055.00	0.23014E-01	0.14436E+03	0.17706E+03	0.65222E+02	0.14547E+03	0.21528E+01
6060.00	0.18195E-01	0.19698E+03	0.12197E+03	0.12246E+03	0.13984E+03	0.21612E+01
6065.00	0.19330E-01	0.20220E+03	0.77054E+02	0.89906E+02	0.19429E+03	0.23023E+01
6070.00	0.22182E-01	0.15139E+03	0.81793E+02	0.77209E+02	0.26155E+03	0.25830E+01
6075.00	0.26292E-01	0.11548E+03	0.19999E+03	0.17413E+03	0.31379E+03	0.25767E+01
6080.00	0.27760E-01	0.11184E+03	0.30309E+03	0.17017E+03	0.33136E+03	0.25875E+01
6085.00	0.27973E-01	0.10273E+03	0.30362E+03	0.16445E+03	0.35007E+03	0.27912E+01
6090.00	0.25275E-01	0.10073E+03	0.33750E+03	0.14657E+03	0.35168E+03	0.24254E+01
6095.00	0.25349E-01	0.10613E+03	0.36105E+03	0.13341E+03	0.33456E+03	0.24190E+01
6100.00	0.21826E-01	0.14062E+03	0.30445E+03	0.11957E+03	0.32511E+03	0.23022E+01
6105.00	0.20064E-01	0.14714E+03	0.27136E+03	0.10015E+03	0.33920E+03	0.22455E+01
6110.00	0.20511E-01	0.25021E+03	0.22015E+03	0.59634E+02	0.30025E+03	0.22482E+01
6115.00	0.17967E-01	0.11879E+03	0.24926E+03	0.11494E+03	0.33313E+03	0.20014E+01
6120.00	0.15236E-01	0.16755E+03	0.12161E+03	0.57583E+02	0.35912E+03	0.18604E+01
6125.00	0.16216E-01	0.16974E+03	0.11448E+03	0.51799E+02	0.36397E+03	0.20128E+01
6130.00	0.17545E-01	0.11716E+03	0.18631E+03	0.78024E+02	0.40356E+03	0.21308E+01
6135.00	0.18509E-01	0.10257E+03	0.14019E+03	0.54639E+02	0.45977E+03	0.21224E+01
6140.00	0.15965E-01	0.84246E+02	0.13852E+03	0.71300E+02	0.48187E+03	0.19611E+01
6145.00	0.16004E-01	0.10563E+03	0.14235E+03	0.63385E+02	0.50307E+03	0.19035E+01
6150.00	0.16711E-01	0.71418E+02	0.11520E+03	0.58334E+02	0.53628E+03	0.19360E+01
6155.00	0.15694E-01	0.66964E+02	0.92269E+02	0.53767E+02	0.59973E+03	0.18454E+01
6160.00	0.13392E-01	0.52931E+02	0.12925E+03	0.89571E+02	0.62669E+03	0.16571E+01
6165.00	0.10105E-01	0.41159E+02	0.14135E+03	0.11373E+03	0.63632E+03	0.15321E+01
6170.00	0.11266E-01	0.35390E+02	0.11404E+03	0.72193E+02	0.65639E+03	0.15578E+01
6175.00	0.11809E-01	0.27924E+02	0.11669E+03	0.10217E+03	0.69759E+03	0.15335E+01
6180.00	0.12857E-01	0.27699E+02	0.86163E+02	0.62474E+02	0.72843E+03	0.14833E+01
6185.00	0.12517E-01	0.17594E+02	0.94336E+02	0.50536E+02	0.74922E+03	0.15668E+01
6190.00	0.10166E-01	0.14311E+02	0.13252E+03	0.10854E+03	0.71367E+03	0.16168E+01
6195.00	0.11578E-01	0.12199E+02	0.93105E+02	0.74400E+02	0.74703E+03	0.14957E+01

6200.00	0.14161E-01	0.78702E+01	0.13883E+03	0.11933E+03	0.79658E+03	0.16141E+01
6205.00	0.13232E-01	0.76493E+01	0.17146E+03	0.12088E+03	0.79703E+03	0.15674E+01
6210.00	0.14335E-01	0.56238E+01	0.16548E+03	0.12068E+03	0.85050E+03	0.16478E+01
6215.00	0.16628E-01	0.50196E+01	0.18396E+03	0.12063E+03	0.86807E+03	0.18173E+01
6220.00	0.15982E-01	0.46332E+01	0.21723E+03	0.12172E+03	0.89107E+03	0.17045E+01
6225.00	0.19835E-01	0.28450E+01	0.22878E+03	0.12397E+03	0.92400E+03	0.21523E+01
6230.00	0.20477E-01	0.30053E+01	0.25067E+03	0.13221E+03	0.98721E+03	0.21010E+01
6235.00	0.19545E-01	0.26016E+01	0.31398E+03	0.12333E+03	0.98000E+03	0.18232E+01
6240.00	0.22314E-01	0.15121E+01	0.38459E+03	0.13218E+03	0.98881E+03	0.29337E+01
6245.00	0.21738E-01	0.16806E+01	0.39907E+03	0.12943E+03	0.11025E+04	0.22800E+01
6250.00	0.20861E-01	0.15563E+01	0.47698E+03	0.12954E+03	0.11018E+04	0.20005E+01
6255.00	0.21306E-01	0.12564E+01	0.50175E+03	0.12889E+03	0.10733E+04	0.25918E+01
6260.00	0.20769E-01	0.11321E+01	0.60693E+03	0.12850E+03	0.11142E+04	0.18276E+01
6265.00	0.21066E-01	0.88894E+00	0.71118E+03	0.12836E+03	0.11388E+04	0.12470E+01
6270.00	0.21511E-01	0.74110E+00	0.83572E+03	0.12749E+03	0.10826E+04	0.10397E+01
6275.00	0.22877E-01	0.55238E+00	0.10015E+04	0.12388E+03	0.98761E+03	0.36234E+00
6280.00	0.23441E-01	0.47344E+00	0.13001E+04	0.12664E+03	0.89403E+03	0.23974E+00
6285.00	0.23298E-01	0.42529E+00	0.98654E+03	0.11560E+03	0.87748E+03	0.41950E+00
6290.00	0.25837E-01	0.30610E+00	0.14989E+04	0.12105E+03	0.63343E+03	0.37405E+00
6295.00	0.25634E-01	0.28449E+00	0.21929E+04	0.12874E+03	0.58239E+03	0.20532E+00
6300.00	0.24300E-01	0.28853E+00	0.13911E+04	0.13310E+03	0.62952E+03	0.67594E+00
6305.00	0.24628E-01	0.26576E+00	0.29334E+04	0.11924E+03	0.56094E+03	0.39049E-01
6310.00	0.25663E-01	0.26274E+00	0.58710E+04	0.12527E+03	0.42109E+03	0.10841E+00
6315.00	0.24018E-01	0.26719E+00	0.36697E+04	0.12501E+03	0.50600E+03	0.38089E-01
6320.00	0.24274E-01	0.26924E+00	0.52141E+04	0.12513E+03	0.43977E+03	0.12417E+00
6325.00	0.24730E-01	0.18979E+00	0.44371E+04	0.12461E+03	0.36941E+03	0.10481E+01
6330.00	0.24354E-01	0.27113E+00	0.77890E+04	0.12487E+03	0.38256E+03	0.37012E+00
6335.00	0.24255E-01	0.24170E+00	0.57760E+04	0.12508E+03	0.40124E+03	0.16776E+00
6340.00	0.23521E-01	0.23904E+00	0.57036E+04	0.12277E+03	0.40475E+03	0.16092E+00
6345.00	0.23753E-01	0.22947E+00	0.61139E+04	0.13454E+03	0.40792E+03	0.48975E+01
6350.00	0.23936E-01	0.18041E+00	0.38191E+04	0.11136E+03	0.37085E+03	0.10661E+01
6355.00	0.22933E-01	0.21050E+00	0.56702E+04	0.12302E+03	0.37447E+03	0.44247E+01
6360.00	0.22176E-01	0.23484E+00	0.59575E+04	0.13019E+03	0.40782E+03	0.43044E+00
6365.00	0.21559E-01	0.21521E+00	0.34106E+04	0.12380E+03	0.41034E+03	0.61420E-01
6370.00	0.19569E-01	0.23591E+00	0.19531E+04	0.12236E+03	0.46922E+03	0.47747E+00
6375.00	0.18491E-01	0.27196E+00	0.21327E+04	0.12364E+03	0.55209E+03	0.87064E+00
6380.00	0.18152E-01	0.30583E+00	0.31498E+04	0.12317E+03	0.55412E+03	0.15238E+01
6385.00	0.17802E-01	0.31899E+00	0.34574E+04	0.12304E+03	0.56284E+03	0.17494E+01
6390.00	0.17024E-01	0.35170E+00	0.34466E+04	0.12292E+03	0.53975E+03	0.27216E+01
6395.00	0.16588E-01	0.33358E+00	0.15138E+04	0.12297E+03	0.43479E+03	0.46147E+01
6400.00	0.16216E-01	0.33422E+00	0.14379E+04	0.11681E+03	0.47569E+03	0.42627E+01
6405.00	0.15884E-01	0.28354E+00	0.16657E+04	0.12276E+03	0.54098E+03	0.46373E+00
6410.00	0.15690E-01	0.27193E+00	0.17040E+04	0.12278E+03	0.55130E+03	0.31907E+00
6415.00	0.15591E-01	0.27289E+00	0.40489E+04	0.12361E+03	0.54172E+03	0.96884E+00
6420.00	0.16021E-01	0.25487E+00	0.64245E+04	0.12283E+03	0.42079E+03	0.88895E+00
6425.00	0.15041E-01	0.25435E+00	0.29917E+04	0.12259E+03	0.48061E+03	0.90311E+00
6430.00	0.14638E-01	0.26013E+00	0.20966E+04	0.12256E+03	0.50125E+03	0.47251E+00
6435.00	0.14793E-01	0.25168E+00	0.19179E+04	0.12917E+03	0.57746E+03	0.94881E-01
6440.00	0.15300E-01	0.20411E+00	0.22031E+04	0.12223E+03	0.52117E+03	0.27927E-01
6445.00	0.15917E-01	0.19046E+00	0.49527E+04	0.12245E+03	0.40332E+03	0.83375E-01
6450.00	0.13898E-01	0.21308E+00	0.57165E+04	0.12268E+03	0.53081E+03	0.27641E+00
6455.00	0.14233E-01	0.21040E+00	0.75972E+04	0.12110E+03	0.46176E+03	0.40809E+00
6460.00	0.14842E-01	0.19565E+00	0.26850E+04	0.12208E+03	0.51947E+03	0.77180E-03
6465.00	0.14579E-01	0.21102E+00	0.17389E+04	0.12174E+03	0.54336E+03	0.12518E-02
6470.00	0.14201E-01	0.20535E+00	0.18679E+04	0.12171E+03	0.51061E+03	0.48831E-04
6475.00	0.13686E-01	0.20250E+00	0.97603E+03	0.12106E+03	0.45761E+03	0.12486E-04
6480.00	0.13716E-01	0.20936E+00	0.81579E+03	0.12070E+03	0.50263E+03	0.12894E-02
6485.00	0.13970E-01	0.18175E+00	0.88561E+03	0.12074E+03	0.54993E+03	0.16370E-02
6490.00	0.13513E-01	0.20871E+00	0.79977E+03	0.13013E+03	0.51859E+03	0.23555E-02
6495.00	0.13288E-01	0.23220E+00	0.55130E+03	0.11979E+03	0.48557E+03	0.35915E-03

6500.00	0.13382E-01	0.20129E+00	0.59273E+03	0.11980E+03	0.52635E+03	0.84636E-03
6505.00	0.13190E-01	0.21748E+00	0.42640E+03	0.11911E+03	0.51053E+03	0.12173E-01
6510.00	0.13094E-01	0.23577E+00	0.38604E+03	0.11877E+03	0.49785E+03	0.91511E-02
6515.00	0.13149E-01	0.22046E+00	0.31003E+03	0.11793E+03	0.52225E+03	0.58466E+00
6520.00	0.13418E-01	0.20371E+00	0.21168E+03	0.11787E+03	0.54647E+03	0.38042E+00
6525.00	0.13588E-01	0.18762E+00	0.23199E+03	0.12045E+03	0.56628E+03	0.25698E-02
6530.00	0.13198E-01	0.23926E+00	0.23764E+03	0.11811E+03	0.52152E+03	0.10403E-01
6535.00	0.13367E-01	0.30695E+00	0.10106E+03	0.11318E+03	0.43166E+03	0.76457E+00
6540.00	0.13369E-01	0.28417E+00	0.22665E+03	0.11644E+03	0.40419E+03	0.55659E+00
6545.00	0.13675E-01	0.24525E+00	0.16645E+03	0.11493E+03	0.46646E+03	0.19334E+00
6550.00	0.13459E-01	0.26840E+00	0.62412E+02	0.12911E+03	0.47988E+03	0.22864E+01
6555.00	0.13160E-01	0.29987E+00	0.75897E+02	0.12080E+03	0.44683E+03	0.80834E-01
6560.00	0.13310E-01	0.33920E+00	0.38329E+02	0.11121E+03	0.45010E+03	0.90756E-01
6565.00	0.13322E-01	0.33487E+00	0.31648E+02	0.11068E+03	0.43945E+03	0.13808E+00
6570.00	0.13184E-01	0.36602E+00	0.46292E+02	0.11134E+03	0.47029E+03	0.43397E+00
6575.00	0.12956E-01	0.41148E+00	0.42854E+02	0.11059E+03	0.48163E+03	0.24811E+01
6580.00	0.12811E-01	0.41570E+00	0.48384E+02	0.11098E+03	0.43439E+03	0.15495E+00
6585.00	0.12488E-01	0.48653E+00	0.47258E+02	0.12932E+03	0.43040E+03	0.32911E+00
6590.00	0.12693E-01	0.49975E+00	0.63762E+02	0.11168E+03	0.42498E+03	0.37916E+00
6595.00	0.12811E-01	0.49971E+00	0.63053E+02	0.11113E+03	0.45501E+03	0.40460E+00
6600.00	0.12492E-01	0.56829E+00	0.67637E+02	0.11176E+03	0.45586E+03	0.17637E+01
6605.00	0.12580E-01	0.59898E+00	0.11495E+03	0.11588E+03	0.37703E+03	0.81321E+01
6610.00	0.12136E-01	0.72091E+00	0.11888E+03	0.11262E+03	0.35937E+03	0.27524E+01
6615.00	0.12256E-01	0.67325E+00	0.85727E+02	0.11146E+03	0.38658E+03	0.12718E+01
6620.00	0.12846E-01	0.56983E+00	0.73719E+02	0.11045E+03	0.40216E+03	0.23313E+01
6625.00	0.12594E-01	0.67319E+00	0.10987E+03	0.11222E+03	0.38313E+03	0.22117E+01
6630.00	0.12185E-01	0.83076E+00	0.95457E+02	0.11170E+03	0.41707E+03	0.20704E+01
6635.00	0.12273E-01	0.89251E+00	0.80461E+02	0.11109E+03	0.39931E+03	0.16570E+01
6640.00	0.11895E-01	0.96084E+00	0.84488E+02	0.11119E+03	0.35563E+03	0.22209E+01
6645.00	0.12274E-01	0.88389E+00	0.89576E+02	0.11085E+03	0.36793E+03	0.21919E+01
6650.00	0.12862E-01	0.80231E+00	0.10121E+03	0.11152E+03	0.37391E+03	0.14322E+01
6655.00	0.12516E-01	0.86525E+00	0.98078E+02	0.11124E+03	0.40009E+03	0.20108E+01
6660.00	0.12642E-01	0.81308E+00	0.86716E+02	0.11085E+03	0.43781E+03	0.20208E+01
6665.00	0.12796E-01	0.84122E+00	0.82160E+02	0.12711E+03	0.48243E+03	0.10274E+01
6670.00	0.12582E-01	0.89636E+00	0.62635E+02	0.10923E+03	0.47196E+03	0.23896E+01
6675.00	0.12373E-01	0.94309E+00	0.74254E+02	0.11004E+03	0.38703E+03	0.25307E+01
6680.00	0.11625E-01	0.12726E+01	0.87120E+02	0.11034E+03	0.39003E+03	0.24075E+01
6685.00	0.10774E-01	0.15579E+01	0.89776E+02	0.10879E+03	0.42926E+03	0.17430E+01
6690.00	0.11007E-01	0.16061E+01	0.12844E+03	0.11147E+03	0.46260E+03	0.11118E+01
6695.00	0.12413E-01	0.12806E+01	0.21478E+03	0.11305E+03	0.50857E+03	0.74308E+00
6700.00	0.11835E-01	0.11338E+01	0.14242E+03	0.10631E+03	0.48631E+03	0.13477E+01
6705.00	0.10147E-01	0.16323E+01	0.10549E+03	0.11032E+03	0.43432E+03	0.16881E+01
6710.00	0.90032E-02	0.22439E+01	0.12304E+03	0.12507E+03	0.41015E+03	0.16068E+01
6715.00	0.90859E-02	0.22330E+01	0.10548E+03	0.12562E+03	0.43529E+03	0.16503E+01
6720.00	0.95727E-02	0.20784E+01	0.12480E+03	0.13208E+03	0.43318E+03	0.17504E+01
6725.00	0.87542E-02	0.28446E+01	0.17590E+03	0.12878E+03	0.36159E+03	0.16218E+01
6730.00	0.88482E-02	0.28508E+01	0.16165E+03	0.12341E+03	0.35306E+03	0.16335E+01
6735.00	0.88803E-02	0.29244E+01	0.14737E+03	0.12928E+03	0.35757E+03	0.16460E+01
6740.00	0.89184E-02	0.37856E+01	0.13710E+03	0.13001E+03	0.32105E+03	0.16453E+01
6745.00	0.95727E-02	0.34876E+01	0.14407E+03	0.12331E+03	0.33881E+03	0.16334E+01
6750.00	0.91948E-02	0.35776E+01	0.12979E+03	0.12368E+03	0.34061E+03	0.16390E+01
6755.00	0.80774E-02	0.52626E+01	0.10887E+03	0.13931E+03	0.31508E+03	0.15539E+01
6760.00	0.87052E-02	0.88545E+01	0.12288E+03	0.14001E+03	0.25706E+03	0.15190E+01
6765.00	0.94057E-02	0.78199E+01	0.12876E+03	0.11360E+03	0.22477E+03	0.14749E+01
6770.00	0.10867E-01	0.37242E+01	0.13126E+03	0.14775E+03	0.28063E+03	0.18070E+01
6775.00	0.10314E-01	0.35701E+01	0.12700E+03	0.12664E+03	0.26796E+03	0.16731E+01
6780.00	0.10499E-01	0.46803E+01	0.13740E+03	0.12279E+03	0.25108E+03	0.15788E+01
6785.00	0.10982E-01	0.61525E+01	0.13798E+03	0.13783E+03	0.23371E+03	0.15488E+01
6790.00	0.10526E-01	0.67046E+01	0.12633E+03	0.15459E+03	0.23750E+03	0.15447E+01
6795.00	0.91698E-02	0.78564E+01	0.96591E+02	0.11832E+03	0.24212E+03	0.14920E+01

6800.00	0.88489E-02	0.83519E+01	0.76852E+02	0.11258E+03	0.31603E+03	0.14728E+01
6805.00	0.84862E-02	0.63660E+01	0.72784E+02	0.14045E+03	0.42067E+03	0.14919E+01
6810.00	0.95765E-02	0.49352E+01	0.57270E+02	0.13377E+03	0.39126E+03	0.13957E+01
6815.00	0.11875E-01	0.39038E+01	0.56749E+02	0.12527E+03	0.32559E+03	0.16662E+01
6820.00	0.11607E-01	0.41802E+01	0.58718E+02	0.12516E+03	0.31397E+03	0.16272E+01
6825.00	0.10539E-01	0.42013E+01	0.48957E+02	0.12542E+03	0.33820E+03	0.14821E+01
6830.00	0.11263E-01	0.38112E+01	0.52260E+02	0.12517E+03	0.33360E+03	0.15031E+01
6835.00	0.10663E-01	0.39993E+01	0.50416E+02	0.12525E+03	0.30458E+03	0.15557E+01
6840.00	0.11060E-01	0.41629E+01	0.45569E+02	0.12539E+03	0.33526E+03	0.16196E+01
6845.00	0.10868E-01	0.52457E+01	0.71112E+02	0.13291E+03	0.32405E+03	0.15720E+01
6850.00	0.10158E-01	0.54600E+01	0.66705E+02	0.14286E+03	0.30987E+03	0.15432E+01
6855.00	0.10581E-01	0.50407E+01	0.53568E+02	0.13333E+03	0.30992E+03	0.16908E+01
6860.00	0.10521E-01	0.55005E+01	0.66468E+02	0.14194E+03	0.29362E+03	0.14607E+01
6865.00	0.10033E-01	0.58423E+01	0.62117E+02	0.14000E+03	0.31896E+03	0.15168E+01
6870.00	0.93403E-02	0.66517E+01	0.54273E+02	0.15202E+03	0.35280E+03	0.14812E+01
6875.00	0.94108E-02	0.69720E+01	0.49099E+02	0.14204E+03	0.32878E+03	0.15738E+01
6880.00	0.10035E-01	0.65902E+01	0.60839E+02	0.15237E+03	0.29445E+03	0.15475E+01
6885.00	0.98259E-02	0.72410E+01	0.58027E+02	0.15078E+03	0.27046E+03	0.15129E+01
6890.00	0.10009E-01	0.79185E+01	0.35928E+02	0.10467E+03	0.33260E+03	0.14734E+01
6895.00	0.10061E-01	0.75547E+01	0.45226E+02	0.11470E+03	0.37790E+03	0.15547E+01
6900.00	0.10969E-01	0.74045E+01	0.67905E+02	0.14985E+03	0.32265E+03	0.13804E+01
6905.00	0.10510E-01	0.85388E+01	0.71919E+02	0.16925E+03	0.32933E+03	0.15903E+01
6910.00	0.85380E-02	0.10930E+02	0.43623E+02	0.13734E+03	0.36029E+03	0.15579E+01
6915.00	0.89794E-02	0.11518E+02	0.45791E+02	0.16114E+03	0.39323E+03	0.15819E+01
6920.00	0.10361E-01	0.99809E+01	0.49131E+02	0.17098E+03	0.39891E+03	0.14556E+01
6925.00	0.10931E-01	0.94384E+01	0.50131E+02	0.16423E+03	0.41264E+03	0.16048E+01
6930.00	0.98459E-02	0.10469E+02	0.55886E+02	0.14348E+03	0.41127E+03	0.16950E+01
6935.00	0.92348E-02	0.13250E+02	0.51225E+02	0.12606E+03	0.37393E+03	0.16167E+01
6940.00	0.93522E-02	0.11489E+02	0.38422E+02	0.12046E+03	0.39812E+03	0.16241E+01
6945.00	0.94589E-02	0.11267E+02	0.35349E+02	0.11422E+03	0.41933E+03	0.16199E+01
6950.00	0.97239E-02	0.14763E+02	0.44843E+02	0.13480E+03	0.37303E+03	0.15389E+01
6955.00	0.10037E-01	0.16103E+02	0.45728E+02	0.12071E+03	0.37862E+03	0.15527E+01
6960.00	0.10169E-01	0.16638E+02	0.42590E+02	0.12040E+03	0.42583E+03	0.15850E+01
6965.00	0.95609E-02	0.15426E+02	0.46441E+02	0.14508E+03	0.43354E+03	0.15215E+01
6970.00	0.94608E-02	0.17105E+02	0.49730E+02	0.14436E+03	0.40637E+03	0.14766E+01
6975.00	0.10176E-01	0.21122E+02	0.51869E+02	0.14674E+03	0.38328E+03	0.14875E+01
6980.00	0.10562E-01	0.22812E+02	0.48922E+02	0.12739E+03	0.36747E+03	0.15647E+01
6985.00	0.10102E-01	0.22931E+02	0.48333E+02	0.13848E+03	0.34548E+03	0.15614E+01
6990.00	0.10097E-01	0.21871E+02	0.57483E+02	0.15793E+03	0.35703E+03	0.14994E+01
6995.00	0.13049E-01	0.28931E+02	0.58144E+02	0.11217E+03	0.34396E+03	0.18429E+01
7000.00	0.12476E-01	0.31294E+02	0.55906E+02	0.12665E+03	0.30563E+03	0.18984E+01
7005.00	0.10610E-01	0.29239E+02	0.63738E+02	0.18855E+03	0.33671E+03	0.15193E+01
7010.00	0.11903E-01	0.30562E+02	0.71516E+02	0.17931E+03	0.33675E+03	0.14724E+01
7015.00	0.12351E-01	0.32959E+02	0.66472E+02	0.15045E+03	0.27998E+03	0.15473E+01
7020.00	0.12367E-01	0.34267E+02	0.62057E+02	0.12891E+03	0.27238E+03	0.16700E+01
7025.00	0.11710E-01	0.30011E+02	0.57031E+02	0.13056E+03	0.29537E+03	0.15773E+01
7030.00	0.12504E-01	0.33111E+02	0.61960E+02	0.15547E+03	0.28989E+03	0.15212E+01
7035.00	0.13806E-01	0.31613E+02	0.59483E+02	0.12310E+03	0.29523E+03	0.16516E+01
7040.00	0.15659E-01	0.34764E+02	0.64444E+02	0.11829E+03	0.29734E+03	0.17216E+01
7045.00	0.16698E-01	0.42354E+02	0.78465E+02	0.14824E+03	0.27855E+03	0.17335E+01
7050.00	0.17191E-01	0.41960E+02	0.71256E+02	0.14974E+03	0.27077E+03	0.18162E+01
7055.00	0.16950E-01	0.44991E+02	0.63006E+02	0.11897E+03	0.27090E+03	0.20376E+01
7060.00	0.16856E-01	0.49144E+02	0.69356E+02	0.11774E+03	0.25590E+03	0.19790E+01
7065.00	0.16733E-01	0.53421E+02	0.61925E+02	0.13091E+03	0.25149E+03	0.20296E+01
7070.00	0.15627E-01	0.44624E+02	0.47134E+02	0.10338E+03	0.27292E+03	0.21156E+01
7075.00	0.15944E-01	0.47309E+02	0.51301E+02	0.10666E+03	0.24482E+03	0.20339E+01
7080.00	0.15497E-01	0.60357E+02	0.50143E+02	0.13050E+03	0.20713E+03	0.20465E+01
7085.00	0.15292E-01	0.61790E+02	0.45311E+02	0.14149E+03	0.24511E+03	0.20143E+01
7090.00	0.16074E-01	0.72518E+02	0.43031E+02	0.14585E+03	0.27231E+03	0.21372E+01
7095.00	0.17313E-01	0.11242E+03	0.42746E+02	0.11906E+03	0.21934E+03	0.24625E+01
7100.00	0.18066E-01	0.11304E+03	0.44887E+02	0.10262E+03	0.19423E+03	0.26076E+01
7105.00	0.17283E-01	0.75092E+02	0.50118E+02	0.12579E+03	0.21363E+03	0.22215E+01
7110.00	0.17874E-01	0.76676E+02	0.51990E+02	0.13378E+03	0.19850E+03	0.20471E+01
7115.00	0.17782E-01	0.70486E+02	0.48263E+02	0.11811E+03	0.19594E+03	0.22121E+01
7120.00	0.18560E-01	0.59507E+02	0.59990E+02	0.13299E+03	0.20341E+03	0.21411E+01
7125.00	0.18983E-01	0.76891E+02	0.72186E+02	0.12877E+03	0.16181E+03	0.21949E+01
7130.00	0.17143E-01	0.94827E+02	0.56190E+02	0.13132E+03	0.15438E+03	0.21147E+01
7135.00	0.16828E-01	0.87517E+02	0.48767E+02	0.13620E+03	0.21520E+03	0.21116E+01
7140.00	0.17163E-01	0.90790E+02	0.44198E+02	0.12368E+03	0.26968E+03	0.22418E+01
7145.00	0.16751E-01	0.10212E+03	0.39432E+02	0.11673E+03	0.28021E+03	0.22362E+01
7150.00	0.17380E-01	0.10085E+03	0.44568E+02	0.12442E+03	0.25010E+03	0.21743E+01
7155.00	0.18552E-01	0.93031E+02	0.50083E+02	0.12664E+03	0.22071E+03	0.23380E+01
7160.00	0.18218E-01	0.66318E+02	0.51043E+02	0.13422E+03	0.24509E+03	0.23401E+01
7165.00	0.15956E-01	0.48278E+02	0.52178E+02	0.15900E+03	0.28342E+03	0.19745E+01
7170.00	0.16820E-01	0.55349E+02	0.58138E+02	0.14129E+03	0.26187E+03	0.19965E+01
7175.00	0.17896E-01	0.76470E+02	0.62277E+02	0.13967E+03	0.20786E+03	0.21330E+01
7180.00	0.17081E-01	0.77850E+02	0.57886E+02	0.13137E+03	0.19439E+03	0.20786E+01
7185.00	0.17157E-01	0.85589E+02	0.49036E+02	0.12103E+03	0.19355E+03	0.21315E+01
7190.00	0.19503E-01	0.98330E+02	0.48544E+02	0.14345E+03	0.21049E+03	0.21507E+01
7195.00	0.19847E-01	0.98188E+02	0.50653E+02	0.13821E+03	0.23908E+03	0.22093E+01
7200.00	0.18554E-01	0.89018E+02	0.41887E+02	0.12634E+03	0.26697E+03	0.22584E+01
7205.00	0.18914E-01	0.99008E+02	0.42485E+02	0.13090E+03	0.24765E+03	0.22238E+01
7210.00	0.19088E-01	0.10438E+03	0.45133E+02	0.13740E+03	0.25295E+03	0.21959E+01
7215.00	0.17457E-01	0.88602E+02	0.45393E+02	0.13052E+03	0.28145E+03	0.21445E+01
7220.00	0.17724E-01	0.96110E+02	0.47584E+02	0.12213E+03	0.26169E+03	0.22591E+01
7225.00	0.17332E-01	0.97646E+02	0.44995E+02	0.12394E+03	0.26590E+03	0.23241E+01
7230.00	0.16955E-01	0.10800E+03	0.42418E+02	0.11556E+03	0.28287E+03	0.23816E+01
7235.00	0.17167E-01	0.10764E+03	0.43380E+02	0.12134E+03	0.27927E+03	0.23173E+01
7240.00	0.16933E-01	0.10232E+03	0.46069E+02	0.11987E+03	0.25266E+03	0.21816E+01
7245.00	0.16318E-01	0.96759E+02	0.44742E+02	0.11872E+03	0.25057E+03	0.21733E+01
7250.00	0.16463E-01	0.88167E+02	0.45800E+02	0.12199E+03	0.27127E+03	0.21465E+01
7255.00	0.17487E-01	0.92786E+02	0.49538E+02	0.11540E+03	0.26273E+03	0.20785E+01
7260.00	0.16862E-01	0.88617E+02	0.46685E+02	0.12456E+03	0.25413E+03	0.20364E+01
7265.00	0.17347E-01	0.81600E+02	0.47669E+02	0.11792E+03	0.28776E+03	0.21417E+01
7270.00	0.18557E-01	0.76393E+02	0.50955E+02	0.12992E+03	0.30801E+03	0.20712E+01
7275.00	0.17933E-01	0.74245E+02	0.47409E+02	0.13626E+03	0.30083E+03	0.19907E+01
7280.00	0.17169E-01	0.79323E+02	0.43700E+02	0.12148E+03	0.31990E+03	0.20440E+01
7285.00	0.16890E-01	0.85820E+02	0.36968E+02	0.12618E+03	0.31337E+03	0.20358E+01
7290.00	0.17720E-01	0.95893E+02	0.35982E+02	0.12269E+03	0.28043E+03	0.22960E+01
7295.00	0.17237E-01	0.89036E+02	0.41491E+02	0.95399E+02	0.28585E+03	0.25777E+01
7300.00	0.14373E-01	0.58158E+02	0.45901E+02	0.11070E+03	0.30736E+03	0.21638E+01
7305.00	0.15115E-01	0.58659E+02	0.52124E+02	0.12215E+03	0.26914E+03	0.20050E+01
7310.00	0.15480E-01	0.63193E+02	0.57025E+02	0.12191E+03	0.21022E+03	0.20564E+01
7315.00	0.15109E-01	0.56961E+02	0.54439E+02	0.11275E+03	0.19218E+03	0.20570E+01
7320.00	0.15669E-01	0.70439E+02	0.50399E+02	0.10078E+03	0.18274E+03	0.22585E+01
7325.00	0.16105E-01	0.81174E+02	0.45589E+02	0.11602E+03	0.18252E+03	0.23172E+01
7330.00	0.15748E-01	0.72727E+02	0.46539E+02	0.12287E+03	0.20618E+03	0.21333E+01
7335.00	0.16698E-01	0.75011E+02	0.50910E+02	0.10088E+03	0.22521E+03	0.22137E+01
7340.00	0.18836E-01	0.77383E+02	0.52907E+02	0.91954E+02	0.23228E+03	0.24007E+01
7345.00	0.18168E-01	0.55459E+02	0.55845E+02	0.11225E+03	0.25991E+03	0.22694E+01
7350.00	0.17940E-01	0.56844E+02	0.51805E+02	0.11300E+03	0.23420E+03	0.20923E+01
7355.00	0.18831E-01	0.69544E+02	0.53819E+02	0.14147E+03	0.20843E+03	0.20115E+01
7360.00	0.18183E-01	0.66702E+02	0.48808E+02	0.14511E+03	0.24449E+03	0.20057E+01
7365.00	0.19943E-01	0.12269E+03	0.41649E+02	0.10419E+03	0.23127E+03	0.26389E+01
7370.00	0.18332E-01	0.12425E+03	0.40035E+02	0.12252E+03	0.22893E+03	0.25267E+01
7375.00	0.15912E-01	0.68417E+02	0.41153E+02	0.13110E+03	0.26567E+03	0.21178E+01
7380.00	0.16177E-01	0.58068E+02	0.46700E+02	0.11777E+03	0.28830E+03	0.21372E+01
7385.00	0.17967E-01	0.61259E+02	0.55258E+02	0.11946E+03	0.26283E+03	0.21458E+01
7390.00	0.18162E-01	0.71846E+02	0.60574E+02	0.13504E+03	0.26702E+03	0.21555E+01
7395.00	0.16137E-01	0.61213E+02	0.50855E+02	0.12046E+03	0.32617E+03	0.21116E+01
7400.00	0.14625E-01	0.55637E+02	0.50859E+02	0.13180E+03	0.33819E+03	0.19722E+01
7405.00	0.14293E-01	0.61956E+02	0.55482E+02	0.14038E+03	0.34091E+03	0.19368E+01
7410.00	0.13635E-01	0.52145E+02	0.62344E+02	0.11799E+03	0.34345E+03	0.18456E+01
7415.00	0.14487E-01	0.63379E+02	0.74075E+02	0.12244E+03	0.31581E+03	0.18804E+01
7420.00	0.14487E-01	0.73737E+02	0.72300E+02	0.13744E+03	0.29765E+03	0.19148E+01
7425.00	0.14717E-01	0.67599E+02	0.70865E+02	0.11764E+03	0.26712E+03	0.19690E+01
7430.00	0.14940E-01	0.64821E+02	0.66630E+02	0.11231E+03	0.25466E+03	0.20064E+01
7435.00	0.17298E-01	0.65049E+02	0.88522E+02	0.12838E+03	0.27143E+03	0.20440E+01
7440.00	0.18602E-01	0.66431E+02	0.10697E+03	0.14258E+03	0.25914E+03	0.20728E+01
7445.00	0.18951E-01	0.69801E+02	0.11203E+03	0.13286E+03	0.24260E+03	0.21543E+01
7450.00	0.19295E-01	0.73112E+02	0.13731E+03	0.13906E+03	0.23258E+03	0.21754E+01
7455.00	0.19103E-01	0.66042E+02	0.12315E+03	0.14748E+03	0.22734E+03	0.21582E+01
7460.00	0.20216E-01	0.52739E+02	0.99627E+02	0.97256E+02	0.26185E+03	0.22136E+01
7465.00	0.20758E-01	0.46021E+02	0.12100E+03	0.95883E+02	0.29919E+03	0.20736E+01
7470.00	0.20652E-01	0.43049E+02	0.12663E+03	0.10338E+03	0.29889E+03	0.19882E+01
7475.00	0.20511E-01	0.39136E+02	0.11140E+03	0.93898E+02	0.28316E+03	0.20055E+01
7480.00	0.19439E-01	0.31574E+02	0.95923E+02	0.94645E+02	0.33397E+03	0.18884E+01
7485.00	0.16459E-01	0.26992E+02	0.79034E+02	0.10508E+03	0.39286E+03	0.17632E+01
7490.00	0.14743E-01	0.25697E+02	0.58511E+02	0.10511E+03	0.40594E+03	0.16825E+01
7495.00	0.11604E-01	0.26431E+02	0.40730E+02	0.99288E+02	0.45273E+03	0.16668E+01
7500.00	0.11689E-01	0.29370E+02	0.39621E+02	0.11753E+03	0.53979E+03	0.17129E+01
7505.00	0.30844E-01	0.77124E+02	0.48649E+02	0.33543E+02	0.51633E+03	0.39387E+01
7510.00	0.26303E-01	0.20176E+03	0.44017E+02	0.28933E+02	0.29904E+03	0.38126E+01
7515.00	0.21232E-01	0.12205E+03	0.41499E+02	0.35775E+02	0.29255E+03	0.27843E+01
7520.00	0.18358E-01	0.42792E+02	0.56465E+02	0.60089E+02	0.40116E+03	0.18585E+01
7525.00	0.15666E-01	0.19056E+02	0.47555E+02	0.58822E+02	0.52952E+03	0.16587E+01
7530.00	0.15608E-01	0.10911E+02	0.99103E+02	0.12882E+03	0.46838E+03	0.17156E+01
7535.00	0.19300E-01	0.78532E+01	0.12413E+03	0.13647E+03	0.42031E+03	0.18580E+01
7540.00	0.19159E-01	0.92267E+01	0.15090E+03	0.12532E+03	0.34537E+03	0.17700E+01
7545.00	0.18073E-01	0.15693E+02	0.10407E+03	0.80887E+02	0.35633E+03	0.19158E+01
7550.00	0.22439E-01	0.22915E+02	0.76234E+02	0.56776E+02	0.38153E+03	0.19760E+01
7555.00	0.21971E-01	0.15722E+02	0.24466E+03	0.10101E+03	0.26387E+03	0.18735E+01
7560.00	0.24959E-01	0.23683E+02	0.65740E+03	0.11343E+03	0.21653E+03	0.21054E+01
7565.00	0.26318E-01	0.25059E+02	0.62634E+03	0.11220E+03	0.25148E+03	0.20024E+01
7570.00	0.21915E-01	0.16773E+02	0.38675E+03	0.95023E+02	0.30346E+03	0.19904E+01
7575.00	0.19981E-01	0.14287E+02	0.32610E+03	0.10944E+03	0.24368E+03	0.18578E+01
7580.00	0.14445E-01	0.99304E+01	0.20140E+03	0.15373E+03	0.21958E+03	0.16000E+01
7585.00	0.21210E-01	0.17701E+02	0.15240E+03	0.95927E+02	0.21814E+03	0.20454E+01
7590.00	0.22420E-01	0.17435E+02	0.71236E+02	0.29832E+02	0.28274E+03	0.18213E+01
7595.00	0.21810E-01	0.22350E+02	0.22030E+03	0.10044E+03	0.33695E+03	0.19214E+01
7600.00	0.25497E-01	0.20699E+02	0.36461E+03	0.10486E+03	0.40367E+03	0.18596E+01
7605.00	0.16635E-01	0.18385E+02	0.86778E+02	0.22929E+02	0.38124E+03	0.14965E+01
7610.00	0.25622E-01	0.19907E+02	0.37416E+03	0.92638E+02	0.41704E+03	0.17566E+01
7615.00	0.13681E-01	0.12538E+02	0.98340E+02	0.34166E+02	0.44437E+03	0.14672E+01
7620.00	0.10745E-01	0.15288E+02	0.11020E+03	0.65436E+02	0.43011E+03	0.15581E+01
7625.00	0.90602E-02	0.10901E+02	0.12943E+03	0.86123E+02	0.47463E+03	0.15461E+01
7630.00	0.89680E-02	0.11455E+02	0.13333E+03	0.10498E+03	0.48884E+03	0.15756E+01
7635.00	0.94686E-02	0.87755E+01	0.13353E+03	0.11218E+03	0.53604E+03	0.15368E+01
7640.00	0.10208E-01	0.68362E+01	0.12885E+03	0.12166E+03	0.60187E+03	0.15550E+01
7645.00	0.10506E-01	0.59646E+01	0.10816E+03	0.12482E+03	0.56467E+03	0.16219E+01
7650.00	0.13888E-01	0.44210E+01	0.11162E+03	0.95314E+02	0.58120E+03	0.14551E+01
7655.00	0.15492E-01	0.39505E+01	0.99310E+02	0.10971E+03	0.65593E+03	0.15358E+01
7660.00	0.13937E-01	0.37193E+01	0.80584E+02	0.11103E+03	0.59174E+03	0.18733E+01
7665.00	0.15902E-01	0.30024E+01	0.10268E+03	0.11069E+03	0.62383E+03	0.18332E+01
7670.00	0.17929E-01	0.24978E+01	0.11832E+03	0.95944E+02	0.72744E+03	0.15099E+01
7675.00	0.18376E-01	0.20572E+01	0.10391E+03	0.11064E+03	0.65480E+03	0.26712E+01
7680.00	0.18575E-01	0.18492E+01	0.10413E+03	0.94855E+02	0.69735E+03	0.18200E+01
7685.00	0.20475E-01	0.13131E+01	0.18241E+03	0.97904E+02	0.74690E+03	0.18336E+01
7690.00	0.19904E-01	0.13214E+01	0.20487E+03	0.98180E+02	0.69851E+03	0.19302E+01
7695.00	0.19372E-01	0.12077E+01	0.20441E+03	0.98312E+02	0.72490E+03	0.17055E+01
7700.00	0.19982E-01	0.87639E+00	0.30978E+03	0.99703E+02	0.80022E+03	0.10364E+01
7705.00	0.19870E-01	0.82825E+00	0.36411E+03	0.99907E+02	0.80888E+03	0.10281E+01
7710.00	0.19167E-01	0.80392E+00	0.39376E+03	0.10008E+03	0.77648E+03	0.97901E+00
7715.00	0.19795E-01	0.62138E+00	0.52306E+03	0.10049E+03	0.84095E+03	0.32749E+00
7720.00	0.20096E-01	0.54473E+00	0.55710E+03	0.10184E+03	0.86159E+03	0.11694E+00
7725.00	0.19740E-01	0.57369E+00	0.56083E+03	0.10055E+03	0.87062E+03	0.20028E+00
7730.00	0.20583E-01	0.41253E+00	0.64557E+03	0.10030E+03	0.85065E+03	0.18052E-01
7735.00	0.21138E-01	0.30806E+00	0.59956E+03	0.10577E+03	0.73281E+03	0.62908E+00
7740.00	0.20997E-01	0.29017E+00	0.54589E+03	0.10013E+03	0.70259E+03	0.46897E-03
7745.00	0.22880E-01	0.23470E+00	0.15197E+04	0.10139E+03	0.54364E+03	0.18242E-02
7750.00	0.22955E-01	0.23215E+00	0.15509E+04	0.10139E+03	0.53396E+03	0.12283E-02
7755.00	0.18418E-01	0.30301E+00	0.14330E+04	0.10057E+03	0.77628E+03	0.34868E+00
7760.00	0.18721E-01	0.25841E+00	0.22838E+04	0.91824E+02	0.51866E+03	0.17284E-01
7765.00	0.19099E-01	0.25008E+00	0.30359E+04	0.10159E+03	0.49674E+03	0.17206E-02
7770.00	0.18893E-01	0.25330E+00	0.37602E+04	0.10191E+03	0.46116E+03	0.35760E-01
7775.00	0.18378E-01	0.24199E+00	0.34472E+04	0.10046E+03	0.48041E+03	0.62322E-02
7780.00	0.18090E-01	0.21275E+00	0.34803E+04	0.10116E+03	0.43306E+03	0.44362E-01
7785.00	0.17233E-01	0.23350E+00	0.33508E+04	0.93514E+02	0.41807E+03	0.89754E-01
7790.00	0.17121E-01	0.19886E+00	0.33947E+04	0.90175E+02	0.40799E+03	0.21087E+00
7795.00	0.16671E-01	0.29204E+00	0.80205E+04	0.10175E+03	0.40217E+03	0.42302E+00
7800.00	0.16293E-01	0.15250E+00	0.26321E+04	0.10788E+03	0.37896E+03	0.29921E-01
7805.00	0.16244E-01	0.15204E+00	0.20871E+04	0.10147E+03	0.38442E+03	0.76963E+01
7810.00	0.15470E-01	0.16906E+00	0.34762E+04	0.85374E+02	0.37637E+03	0.67863E-02
7815.00	0.15773E-01	0.17809E+00	0.33270E+04	0.93308E+02	0.48445E+03	0.68104E-01
7820.00	0.15147E-01	0.23204E+00	0.58181E+04	0.98597E+02	0.48361E+03	0.22665E-01
7825.00	0.14777E-01	0.26071E+00	0.72211E+04	0.94194E+02	0.47857E+03	0.18509E+00
7830.00	0.14172E-01	0.23032E+00	0.53903E+04	0.10149E+03	0.49126E+03	0.55575E-02
7835.00	0.14001E-01	0.22427E+00	0.51901E+04	0.10083E+03	0.50116E+03	0.15188E-01
7840.00	0.13526E-01	0.27947E+00	0.66238E+04	0.10119E+03	0.54226E+03	0.24273E+00
7845.00	0.11730E-01	0.40832E+00	0.45408E+04	0.10066E+03	0.78162E+03	0.13001E+01
7850.00	0.11537E-01	0.38312E+00	0.42727E+04	0.10058E+03	0.78125E+03	0.94293E+00
7855.00	0.11770E-01	0.30459E+00	0.42311E+04	0.10052E+03	0.72082E+03	0.35855E+00
7860.00	0.11187E-01	0.36750E+00	0.45832E+04	0.10047E+03	0.75098E+03	0.11382E+01
7865.00	0.11002E-01	0.39893E+00	0.47586E+04	0.10051E+03	0.75707E+03	0.14149E+01
7870.00	0.10718E-01	0.38763E+00	0.39110E+04	0.10028E+03	0.74992E+03	0.14967E+01
7875.00	0.10726E-01	0.35043E+00	0.44699E+04	0.10027E+03	0.76174E+03	0.12334E+01
7880.00	0.11215E-01	0.24315E+00	0.39233E+04	0.10075E+03	0.66065E+03	0.19699E+00
7885.00	0.10358E-01	0.35861E+00	0.41589E+04	0.99934E+02	0.70036E+03	0.14624E+01
7890.00	0.10179E-01	0.38051E+00	0.29963E+04	0.97393E+02	0.68119E+03	0.20567E+01
7895.00	0.10115E-01	0.34367E+00	0.29136E+04	0.99641E+02	0.74137E+03	0.12680E+01
7900.00	0.10174E-01	0.30366E+00	0.32546E+04	0.99728E+02	0.75076E+03	0.66856E+00
7905.00	0.10128E-01	0.26627E+00	0.34166E+04	0.99971E+02	0.71053E+03	0.21293E+00
7910.00	0.98440E-02	0.33540E+00	0.31716E+04	0.99369E+02	0.64995E+03	0.11593E+01
7915.00	0.13228E-01	0.19396E+00	0.51667E+03	0.98095E+02	0.37983E+03	0.96015E-03
7920.00	0.99917E-02	0.25508E+00	0.10432E+04	0.99000E+02	0.50510E+03	0.30359E-02
7925.00	0.94184E-02	0.31514E+00	0.22599E+04	0.99402E+02	0.64108E+03	0.69926E+00
7930.00	0.98808E-02	0.25562E+00	0.11344E+04	0.90910E+02	0.59641E+03	0.18065E-01
7935.00	0.97450E-02	0.25368E+00	0.11722E+04	0.98911E+02	0.62066E+03	0.37365E-02
7940.00	0.96339E-02	0.25869E+00	0.14135E+04	0.98996E+02	0.68061E+03	0.27084E-03
7945.00	0.97650E-02	0.26476E+00	0.97643E+03	0.89350E+02	0.64051E+03	0.24158E-01
7950.00	0.94643E-02	0.26878E+00	0.11571E+04	0.98715E+02	0.66506E+03	0.11502E-01
7955.00	0.91295E-02	0.30743E+00	0.20758E+04	0.98848E+02	0.78070E+03	0.53649E+00
7960.00	0.91496E-02	0.29043E+00	0.20479E+04	0.98950E+02	0.79069E+03	0.30509E+00
7965.00	0.94999E-02	0.25765E+00	0.10359E+04	0.89132E+02	0.66076E+03	0.12057E-01
7970.00	0.12482E-01	0.18524E+00	0.24409E+03	0.95823E+02	0.51926E+03	0.10997E-02
7975.00	0.12612E-01	0.21261E+00	0.34570E+03	0.96451E+02	0.48697E+03	0.19267E-02
7980.00	0.12760E-01	0.23925E+00	0.13440E+03	0.93592E+02	0.42710E+03	0.45127E-02
7985.00	0.12782E-01	0.26133E+00	0.12310E+03	0.92778E+02	0.43204E+03	0.63658E+00
7990.00	0.12751E-01	0.26050E+00	0.46158E+02	0.89871E+02	0.42496E+03	0.18531E+01
7995.00	0.12826E-01	0.26276E+00	0.66956E+02	0.91111E+02	0.44842E+03	0.95322E+00

8000.00	0.12703E-01	0.28103E+00	0.67575E+02	0.98946E+02	0.44749E+03	0.64629E-03
8005.00	0.12624E-01	0.30558E+00	0.16715E+03	0.86471E+02	0.39779E+03	0.13497E-01
8010.00	0.12528E-01	0.32104E+00	0.11615E+03	0.92293E+02	0.39984E+03	0.28454E+00
8015.00	0.12186E-01	0.36972E+00	0.80498E+02	0.90232E+02	0.43121E+03	0.92435E-02
8020.00	0.12320E-01	0.43148E+00	0.46790E+02	0.89187E+02	0.38612E+03	0.15832E+01
8025.00	0.12051E-01	0.47127E+00	0.40995E+02	0.89900E+02	0.34279E+03	0.73524E+00
8030.00	0.11997E-01	0.49667E+00	0.38257E+02	0.89259E+02	0.35685E+03	0.16355E+00
8035.00	0.11987E-01	0.50927E+00	0.50780E+02	0.98314E+02	0.35747E+03	0.39565E+00
8040.00	0.12324E-01	0.43710E+00	0.66898E+02	0.89963E+02	0.39542E+03	0.15215E+00
8045.00	0.12431E-01	0.45078E+00	0.71030E+02	0.90129E+02	0.39555E+03	0.92093E-01
8050.00	0.12029E-01	0.54036E+00	0.65297E+02	0.89914E+02	0.39086E+03	0.22014E+00
8055.00	0.12097E-01	0.54360E+00	0.79005E+02	0.90362E+02	0.39794E+03	0.29950E+00
8060.00	0.11884E-01	0.59236E+00	0.87679E+02	0.88425E+02	0.35179E+03	0.80130E+00
8065.00	0.11697E-01	0.64347E+00	0.65090E+02	0.89508E+02	0.34853E+03	0.22103E+01
8070.00	0.11703E-01	0.64546E+00	0.63669E+02	0.89678E+02	0.36737E+03	0.10604E+01
8075.00	0.11660E-01	0.67971E+00	0.94154E+02	0.91036E+02	0.38416E+03	0.58982E+00
8080.00	0.11266E-01	0.80987E+00	0.10028E+03	0.90324E+02	0.32757E+03	0.18934E+01
8085.00	0.10920E-01	0.87313E+00	0.71251E+02	0.89700E+02	0.30216E+03	0.16868E+01
8090.00	0.10813E-01	0.96811E+00	0.75970E+02	0.89271E+02	0.31970E+03	0.25276E+01
8095.00	0.10283E-01	0.13065E+01	0.59626E+02	0.89149E+02	0.29431E+03	0.14699E+01
8100.00	0.10726E-01	0.13466E+01	0.62375E+02	0.88339E+02	0.31742E+03	0.16479E+01
8105.00	0.11155E-01	0.10949E+01	0.68954E+02	0.89452E+02	0.38093E+03	0.14048E+01
8110.00	0.11015E-01	0.10815E+01	0.56457E+02	0.88815E+02	0.35691E+03	0.15169E+01
8115.00	0.10676E-01	0.11782E+01	0.52948E+02	0.90651E+02	0.31575E+03	0.31721E+01
8120.00	0.10300E-01	0.13606E+01	0.54354E+02	0.88618E+02	0.27794E+03	0.25242E+01
8125.00	0.99990E-02	0.15321E+01	0.57461E+02	0.10549E+03	0.25499E+03	0.19839E+01
8130.00	0.10444E-01	0.14471E+01	0.47672E+02	0.87909E+02	0.27742E+03	0.22010E+01
8135.00	0.10986E-01	0.13279E+01	0.52468E+02	0.88331E+02	0.29502E+03	0.15452E+01
8140.00	0.11394E-01	0.12606E+01	0.53748E+02	0.87440E+02	0.31916E+03	0.84426E+00
8145.00	0.11601E-01	0.11646E+01	0.41683E+02	0.87878E+02	0.34493E+03	0.10999E+01
8150.00	0.11957E-01	0.11021E+01	0.50786E+02	0.88327E+02	0.34742E+03	0.13745E+01
8155.00	0.12415E-01	0.10747E+01	0.59546E+02	0.88499E+02	0.38244E+03	0.95457E+00
8160.00	0.12351E-01	0.11752E+01	0.63037E+02	0.10558E+03	0.39498E+03	0.81702E+00
8165.00	0.12465E-01	0.11516E+01	0.59705E+02	0.88352E+02	0.39083E+03	0.73133E+00
8170.00	0.12763E-01	0.11494E+01	0.71770E+02	0.10498E+03	0.42020E+03	0.77174E+00
8175.00	0.13010E-01	0.11875E+01	0.73661E+02	0.88553E+02	0.44146E+03	0.78495E+00
8180.00	0.13566E-01	0.10785E+01	0.83383E+02	0.89303E+02	0.43724E+03	0.68149E+00
8185.00	0.13641E-01	0.11304E+01	0.66129E+02	0.88446E+02	0.44469E+03	0.95773E+00
8190.00	0.13128E-01	0.13629E+01	0.86456E+02	0.10426E+03	0.43338E+03	0.10695E+01
8195.00	0.13818E-01	0.12682E+01	0.10547E+03	0.10361E+03	0.45160E+03	0.93808E+00
8200.00	0.14472E-01	0.11515E+01	0.80567E+02	0.95904E+02	0.50939E+03	0.61330E+00
8205.00	0.14230E-01	0.13228E+01	0.80414E+02	0.10461E+03	0.47802E+03	0.10563E+01
8210.00	0.13402E-01	0.15778E+01	0.80336E+02	0.10477E+03	0.43637E+03	0.12174E+01
8215.00	0.12858E-01	0.17543E+01	0.62877E+02	0.10506E+03	0.44360E+03	0.13210E+01
8220.00	0.13002E-01	0.17623E+01	0.45172E+02	0.10559E+03	0.44333E+03	0.12344E+01
8225.00	0.12846E-01	0.18761E+01	0.46261E+02	0.10551E+03	0.45863E+03	0.13142E+01
8230.00	0.13673E-01	0.17732E+01	0.59958E+02	0.10509E+03	0.48490E+03	0.11141E+01
8235.00	0.13339E-01	0.20590E+01	0.64011E+02	0.10466E+03	0.44534E+03	0.11571E+01
8240.00	0.11206E-01	0.28025E+01	0.49147E+02	0.10528E+03	0.40782E+03	0.15003E+01
8245.00	0.11088E-01	0.29114E+01	0.54636E+02	0.10476E+03	0.40117E+03	0.14285E+01
8250.00	0.11848E-01	0.26767E+01	0.53749E+02	0.10471E+03	0.40443E+03	0.14904E+01
8255.00	0.11732E-01	0.29375E+01	0.47958E+02	0.10507E+03	0.40461E+03	0.16470E+01
8260.00	0.11275E-01	0.32817E+01	0.54080E+02	0.10472E+03	0.39157E+03	0.16863E+01
8265.00	0.11439E-01	0.33002E+01	0.52027E+02	0.10490E+03	0.39975E+03	0.17296E+01
8270.00	0.11805E-01	0.32329E+01	0.39755E+02	0.10524E+03	0.44113E+03	0.18700E+01
8275.00	0.10953E-01	0.37745E+01	0.36725E+02	0.10557E+03	0.43582E+03	0.16590E+01
8280.00	0.94688E-02	0.46974E+01	0.36290E+02	0.11394E+03	0.39443E+03	0.20143E+01
8285.00	0.92200E-02	0.49855E+01	0.37791E+02	0.12457E+03	0.38934E+03	0.16988E+01
8290.00	0.94281E-02	0.52602E+01	0.38889E+02	0.12455E+03	0.40074E+03	0.16151E+01
8295.00	0.86150E-02	0.58829E+01	0.38975E+02	0.14376E+03	0.38915E+03	0.15743E+01
8300.00	0.83334E-02	0.61378E+01	0.33632E+02	0.14428E+03	0.36448E+03	0.13908E+01
8305.00	0.83262E-02	0.68152E+01	0.44526E+02	0.15195E+03	0.35782E+03	0.14400E+01
8310.00	0.82281E-02	0.79162E+01	0.48625E+02	0.13757E+03	0.33865E+03	0.15518E+01
8315.00	0.79220E-02	0.78816E+01	0.40146E+02	0.12802E+03	0.31923E+03	0.15385E+01
8320.00	0.77105E-02	0.82576E+01	0.46469E+02	0.14871E+03	0.31040E+03	0.14878E+01
8325.00	0.82770E-02	0.86982E+01	0.58229E+02	0.15777E+03	0.29928E+03	0.15873E+02
8330.00	0.79448E-02	0.95681E+01	0.54228E+02	0.14885E+03	0.29716E+03	0.15944E+01
8335.00	0.77530E-02	0.85624E+01	0.50267E+02	0.13764E+03	0.30755E+03	0.16202E+01
8340.00	0.79949E-02	0.88580E+01	0.48826E+02	0.12217E+03	0.32006E+03	0.16185E+01
8345.00	0.77922E-02	0.91836E+01	0.56805E+02	0.16873E+03	0.33074E+03	0.16642E+01
8350.00	0.84823E-02	0.92446E+01	0.55885E+02	0.15883E+03	0.30388E+03	0.17269E+01
8355.00	0.87300E-02	0.11545E+02	0.54581E+02	0.13676E+03	0.28045E+03	0.17158E+01
8360.00	0.78694E-02	0.11531E+02	0.48855E+02	0.14639E+03	0.27379E+03	0.17132E+01
8365.00	0.78505E-02	0.11585E+02	0.47801E+02	0.16309E+03	0.26696E+03	0.15910E+01
8370.00	0.82033E-02	0.11789E+02	0.44712E+02	0.14766E+03	0.26440E+03	0.15694E+01
8375.00	0.86465E-02	0.12925E+02	0.46651E+02	0.14532E+03	0.25475E+03	0.15281E+01
8380.00	0.86347E-02	0.13914E+02	0.41874E+02	0.14724E+03	0.25036E+03	0.14555E+01
8385.00	0.91089E-02	0.16295E+02	0.34460E+02	0.13581E+03	0.24488E+03	0.14751E+01
8390.00	0.95243E-02	0.17385E+02	0.32686E+02	0.14547E+03	0.26598E+03	0.14828E+01
8395.00	0.89661E-02	0.16712E+02	0.29143E+02	0.15279E+03	0.31257E+03	0.14520E+01
8400.00	0.89900E-02	0.16904E+02	0.31612E+02	0.15187E+03	0.34158E+03	0.15653E+01
8405.00	0.90529E-02	0.18695E+02	0.28952E+02	0.11375E+03	0.33519E+03	0.17943E+01
8410.00	0.95679E-02	0.23453E+02	0.30547E+02	0.12101E+03	0.28967E+03	0.19043E+01
8415.00	0.12125E-01	0.28780E+02	0.37746E+02	0.13024E+03	0.25084E+03	0.20007E+01
8420.00	0.13376E-01	0.33183E+02	0.38427E+02	0.11378E+03	0.24990E+03	0.24276E+01
8425.00	0.12660E-01	0.23554E+02	0.29850E+02	0.82779E+02	0.29113E+03	0.25118E+01
8430.00	0.10165E-01	0.18577E+02	0.32787E+02	0.12865E+03	0.29051E+03	0.19036E+01
8435.00	0.98931E-02	0.20429E+02	0.33348E+02	0.12973E+03	0.26953E+03	0.18562E+01
8440.00	0.92191E-02	0.19483E+02	0.28772E+02	0.13635E+03	0.29810E+03	0.17757E+01
8445.00	0.96741E-02	0.20850E+02	0.25781E+02	0.13414E+03	0.29868E+03	0.18689E+01
8450.00	0.96358E-02	0.20292E+02	0.25223E+02	0.14916E+03	0.32813E+03	0.15740E+01
8455.00	0.11705E-01	0.22915E+02	0.30288E+02	0.14802E+03	0.34723E+03	0.16005E+01
8460.00	0.12252E-01	0.24217E+02	0.30275E+02	0.13750E+03	0.33441E+03	0.16902E+01
8465.00	0.11104E-01	0.23649E+02	0.25862E+02	0.14193E+03	0.35337E+03	0.15479E+01
8470.00	0.12390E-01	0.28112E+02	0.31014E+02	0.15202E+03	0.34521E+03	0.15511E+01
8475.00	0.11488E-01	0.29982E+02	0.31517E+02	0.14947E+03	0.34969E+03	0.16339E+01
8480.00	0.10212E-01	0.29609E+02	0.28214E+02	0.14354E+03	0.38056E+03	0.16626E+01
8485.00	0.10715E-01	0.33217E+02	0.30136E+02	0.14299E+03	0.37894E+03	0.17938E+01
8490.00	0.10176E-01	0.32960E+02	0.28614E+02	0.14865E+03	0.37467E+03	0.19958E+01
8495.00	0.90745E-02	0.33393E+02	0.26039E+02	0.14007E+03	0.39618E+03	0.23162E+01
8500.00	0.93494E-02	0.35521E+02	0.28045E+02	0.13216E+03	0.38646E+03	0.23751E+01
8505.00	0.10196E-01	0.38448E+02	0.28258E+02	0.12739E+03	0.37066E+03	0.25760E+01
8510.00	0.10213E-01	0.41105E+02	0.29126E+02	0.14022E+03	0.36292E+03	0.25223E+01
8515.00	0.10572E-01	0.42397E+02	0.31734E+02	0.13827E+03	0.33440E+03	0.24245E+01
8520.00	0.10677E-01	0.46301E+02	0.30220E+02	0.14038E+03	0.31970E+03	0.24158E+01
8525.00	0.11339E-01	0.46518E+02	0.31126E+02	0.14347E+03	0.30092E+03	0.22912E+01
8530.00	0.13627E-01	0.50281E+02	0.36977E+02	0.12996E+03	0.27292E+03	0.22830E+01
8535.00	0.13938E-01	0.52040E+02	0.38263E+02	0.12399E+03	0.26172E+03	0.23207E+01
8540.00	0.14807E-01	0.54876E+02	0.38786E+02	0.12663E+03	0.26383E+03	0.23140E+01
8545.00	0.17372E-01	0.66215E+02	0.41555E+02	0.12383E+03	0.23527E+03	0.25007E+01
8550.00	0.17240E-01	0.66342E+02	0.41112E+02	0.12610E+03	0.21060E+03	0.25421E+01
8555.00	0.16665E-01	0.60019E+02	0.47637E+02	0.13382E+03	0.21433E+03	0.23137E+01
8560.00	0.16610E-01	0.62340E+02	0.47530E+02	0.13327E+03	0.19761E+03	0.22012E+01
8565.00	0.17392E-01	0.74821E+02	0.44867E+02	0.13708E+03	0.17913E+03	0.23073E+01
8570.00	0.17855E-01	0.77432E+02	0.43409E+02	0.14174E+03	0.20042E+03	0.24994E+01
8575.00	0.17021E-01	0.74628E+02	0.38572E+02	0.13671E+03	0.22987E+03	0.25888E+01
8580.00	0.16281E-01	0.86054E+02	0.32254E+02	0.12845E+03	0.25826E+03	0.26778E+01
8585.00	0.15921E-01	0.10318E+03	0.28945E+02	0.13248E+03	0.25439E+03	0.29673E+01
8590.00	0.15686E-01	0.10307E+03	0.32422E+02	0.13966E+03	0.20592E+03	0.26933E+01
8595.00	0.16104E-01	0.10547E+03	0.31809E+02	0.13204E+03	0.18243E+03	0.27205E+01
8600.00	0.17298E-01	0.12670E+03	0.34793E+02	0.12517E+03	0.13870E+03	0.28541E+01
8605.00	0.17365E-01	0.13213E+03	0.42002E+02	0.13090E+03	0.94614E+02	0.25685E+01
8610.00	0.17217E-01	0.95166E+02	0.44958E+02	0.11457E+03	0.10727E+03	0.25929E+01
8615.00	0.17990E-01	0.74183E+02	0.44799E+02	0.12586E+03	0.13435E+03	0.24115E+01
8620.00	0.18280E-01	0.68911E+02	0.40555E+02	0.12395E+03	0.16138E+03	0.26506E+01
8625.00	0.17071E-01	0.52524E+02	0.38095E+02	0.13480E+03	0.19992E+03	0.25004E+01
8630.00	0.17323E-01	0.50602E+02	0.37905E+02	0.12759E+03	0.23585E+03	0.24518E+01
8635.00	0.17758E-01	0.63282E+02	0.37364E+02	0.12031E+03	0.22718E+03	0.25699E+01
8640.00	0.19238E-01	0.91866E+02	0.40453E+02	0.13695E+03	0.18416E+03	0.25133E+01
8645.00	0.18474E-01	0.10513E+03	0.40008E+02	0.13761E+03	0.15596E+03	0.24368E+01
8650.00	0.16761E-01	0.10111E+03	0.36900E+02	0.13530E+03	0.14726E+03	0.25552E+01
8655.00	0.16671E-01	0.10759E+03	0.36764E+02	0.12833E+03	0.16526E+03	0.27491E+01
8660.00	0.16614E-01	0.10212E+03	0.37733E+02	0.12675E+03	0.19719E+03	0.27339E+01
8665.00	0.15249E-01	0.89070E+02	0.32077E+02	0.13120E+03	0.23325E+03	0.26881E+01
8670.00	0.15404E-01	0.90101E+02	0.32977E+02	0.12696E+03	0.26115E+03	0.27987E+01
8675.00	0.15213E-01	0.84960E+02	0.33261E+02	0.12542E+03	0.29237E+03	0.27374E+01
8680.00	0.13394E-01	0.74365E+02	0.28529E+02	0.13100E+03	0.33116E+03	0.25027E+01
8685.00	0.12781E-01	0.66108E+02	0.24573E+02	0.13654E+03	0.34982E+03	0.25295E+01
8690.00	0.12662E-01	0.57914E+02	0.22520E+02	0.13055E+03	0.38243E+03	0.24389E+01
8695.00	0.12300E-01	0.55462E+02	0.22003E+02	0.14487E+03	0.40358E+03	0.22187E+01
8700.00	0.12665E-01	0.52308E+02	0.20995E+02	0.14341E+03	0.40917E+03	0.22576E+01
8705.00	0.11816E-01	0.43489E+02	0.20591E+02	0.13814E+03	0.42443E+03	0.22625E+01
8710.00	0.11468E-01	0.39870E+02	0.21071E+02	0.14529E+03	0.43306E+03	0.20592E+01
8715.00	0.11335E-01	0.36767E+02	0.21412E+02	0.14980E+03	0.42635E+03	0.18768E+01
8720.00	0.10640E-01	0.32533E+02	0.20992E+02	0.14272E+03	0.41579E+03	0.20752E+01
8725.00	0.10630E-01	0.30548E+02	0.24024E+02	0.13388E+03	0.41533E+03	0.21446E+01
8730.00	0.11091E-01	0.30392E+02	0.28309E+02	0.12914E+03	0.38452E+03	0.23446E+01
8735.00	0.12039E-01	0.29834E+02	0.32891E+02	0.13254E+03	0.37681E+03	0.23234E+01
8740.00	0.12115E-01	0.28302E+02	0.38085E+02	0.14641E+03	0.35106E+03	0.21035E+01
8745.00	0.11901E-01	0.28937E+02	0.38975E+02	0.12674E+03	0.29839E+03	0.22302E+01
8750.00	0.12679E-01	0.25145E+02	0.37960E+02	0.99012E+02	0.30656E+03	0.22487E+01
8755.00	0.12705E-01	0.20973E+02	0.44918E+02	0.12126E+03	0.30570E+03	0.19192E+01
8760.00	0.14652E-01	0.21682E+02	0.58057E+02	0.12075E+03	0.26998E+03	0.18741E+01
8765.00	0.13684E-01	0.19175E+02	0.53902E+02	0.12531E+03	0.25774E+03	0.17711E+01
8770.00	0.14483E-01	0.19490E+02	0.41567E+02	0.97644E+02	0.26435E+03	0.18382E+01
8775.00	0.15237E-01	0.21445E+02	0.44464E+02	0.10268E+03	0.29005E+03	0.17938E+01
8780.00	0.13396E-01	0.21527E+02	0.41900E+02	0.12865E+03	0.32415E+03	0.15711E+01
8785.00	0.13463E-01	0.26927E+02	0.36213E+02	0.11987E+03	0.32880E+03	0.17122E+01
8790.00	0.14034E-01	0.33134E+02	0.38502E+02	0.11721E+03	0.29797E+03	0.18971E+01
8795.00	0.15816E-01	0.39853E+02	0.41524E+02	0.10670E+03	0.29220E+03	0.20979E+01
8800.00	0.15225E-01	0.51477E+02	0.37088E+02	0.12345E+03	0.28494E+03	0.22789E+01
8805.00	0.16523E-01	0.84810E+02	0.37014E+02	0.11331E+03	0.22464E+03	0.28473E+01
8810.00	0.15272E-01	0.71783E+02	0.29842E+02	0.35034E+02	0.17742E+03	0.26139E+01
8815.00	0.12396E-01	0.31777E+02	0.48197E+02	0.11338E+03	0.19882E+03	0.23219E+01
8820.00	0.11923E-01	0.29439E+02	0.48083E+02	0.12580E+03	0.18777E+03	0.21870E+01
8825.00	0.11801E-01	0.26576E+02	0.45455E+02	0.11519E+03	0.18954E+03	0.23197E+01
8830.00	0.12843E-01	0.27196E+02	0.48752E+02	0.11600E+03	0.19259E+03	0.22995E+01
8835.00	0.13934E-01	0.27034E+02	0.55099E+02	0.12607E+03	0.21209E+03	0.21232E+01
8840.00	0.16065E-01	0.27931E+02	0.77385E+02	0.12976E+03	0.20688E+03	0.19709E+01
8845.00	0.15398E-01	0.31842E+02	0.89247E+02	0.14638E+03	0.16207E+03	0.18302E+01
8850.00	0.15044E-01	0.35302E+02	0.69894E+02	0.12764E+03	0.17007E+03	0.18728E+01
8855.00	0.15141E-01	0.39923E+02	0.65330E+02	0.10799E+03	0.16819E+03	0.18997E+01
8860.00	0.14337E-01	0.36247E+02	0.59992E+02	0.11815E+03	0.17100E+03	0.18097E+01
8865.00	0.14562E-01	0.44361E+02	0.56525E+02	0.11066E+03	0.17567E+03	0.18935E+01
8870.00	0.14337E-01	0.45143E+02	0.55151E+02	0.11889E+03	0.21513E+03	0.18514E+01
8875.00	0.14390E-01	0.38721E+02	0.48987E+02	0.13863E+03	0.25952E+03	0.18407E+01
8880.00	0.14405E-01	0.40123E+02	0.56244E+02	0.13448E+03	0.28132E+03	0.18784E+01
8885.00	0.12224E-01	0.35196E+02	0.50995E+02	0.13049E+03	0.31866E+03	0.17890E+01
8890.00	0.11099E-01	0.33929E+02	0.37365E+02	0.11497E+03	0.36014E+03	0.21044E+01
8895.00	0.11548E-01	0.39362E+02	0.30151E+02	0.11225E+03	0.38158E+03	0.25039E+01
8900.00	0.12975E-01	0.50610E+02	0.31940E+02	0.12773E+03	0.35212E+03	0.24994E+01
8905.00	0.14736E-01	0.51872E+02	0.38124E+02	0.92305E+02	0.31604E+03	0.29863E+01
8910.00	0.14347E-01	0.30591E+02	0.23957E+02	0.35973E+02	0.40595E+03	0.21232E+01
8915.00	0.97970E-02	0.19800E+02	0.35924E+02	0.10843E+03	0.48774E+03	0.20440E+01
8920.00	0.10777E-01	0.17150E+02	0.28855E+02	0.75984E+02	0.53114E+03	0.19646E+01
8925.00	0.10287E-01	0.14441E+02	0.28458E+02	0.88230E+02	0.55517E+03	0.20041E+01
8930.00	0.11671E-01	0.12087E+02	0.25759E+02	0.60424E+02	0.52157E+03	0.18693E+01
8935.00	0.12101E-01	0.11259E+02	0.49528E+02	0.13282E+03	0.47885E+03	0.17919E+01
8940.00	0.13577E-01	0.10835E+02	0.58896E+02	0.13241E+03	0.45936E+03	0.17408E+01
8945.00	0.15592E-01	0.10774E+02	0.75768E+02	0.11855E+03	0.41720E+03	0.17954E+01
8950.00	0.15907E-01	0.12952E+02	0.86087E+02	0.90790E+02	0.35282E+03	0.16963E+01
8955.00	0.14621E-01	0.10510E+02	0.78157E+02	0.89958E+02	0.34690E+03	0.17184E+01
8960.00	0.14324E-01	0.97443E+01	0.67894E+02	0.84274E+02	0.33239E+03	0.18379E+01
8965.00	0.14614E-01	0.79293E+01	0.50928E+02	0.51352E+02	0.35880E+03	0.18018E+01
8970.00	0.14619E-01	0.75437E+01	0.98404E+02	0.96979E+02	0.37229E+03	0.20222E+01
8975.00	0.12623E-01	0.99271E+01	0.90523E+02	0.10574E+03	0.33833E+03	0.19497E+01
8980.00	0.13097E-01	0.88616E+01	0.57615E+02	0.52011E+02	0.36838E+03	0.16902E+01
8985.00	0.13691E-01	0.69041E+01	0.88376E+02	0.78962E+02	0.40722E+03	0.18639E+01
8990.00	0.11770E-01	0.74365E+01	0.52077E+02	0.64488E+02	0.41314E+03	0.18759E+01
8995.00	0.14837E-01	0.61855E+01	0.47574E+02	0.32874E+02	0.47670E+03	0.17692E+01
9000.00	0.15078E-01	0.51252E+01	0.68592E+02	0.78863E+02	0.52338E+03	0.19093E+01
9005.00	0.13899E-01	0.53130E+01	0.63450E+02	0.10227E+03	0.52867E+03	0.19768E+01
9010.00	0.16501E-01	0.41123E+01	0.51252E+02	0.96952E+02	0.56850E+03	0.28645E+01
9015.00	0.17664E-01	0.36851E+01	0.50651E+02	0.96901E+02	0.57748E+03	0.33297E+01
9020.00	0.18289E-01	0.35308E+01	0.42850E+02	0.97012E+02	0.51499E+03	0.43676E+01
9025.00	0.16610E-01	0.37569E+01	0.33777E+02	0.97296E+02	0.51459E+03	0.44189E+01
9030.00	0.18239E-01	0.30623E+01	0.50404E+02	0.96612E+02	0.62188E+03	0.35983E+01
9035.00	0.22728E-01	0.23575E+01	0.96227E+02	0.94998E+02	0.68183E+03	0.47683E+01
9040.00	0.20888E-01	0.36670E+01	0.11810E+03	0.79581E+02	0.44111E+03	0.16418E+01
9045.00	0.19602E-01	0.35506E+01	0.14870E+03	0.81564E+02	0.35774E+03	0.13014E+01
9050.00	0.23022E-01	0.16781E+01	0.25449E+03	0.91152E+02	0.54142E+03	0.25160E+01
9055.00	0.25873E-01	0.13146E+01	0.31847E+03	0.90324E+02	0.63000E+03	0.51125E+01
9060.00	0.25018E-01	0.12931E+01	0.35862E+03	0.90169E+02	0.56525E+03	0.65679E+01
9065.00	0.25184E-01	0.12229E+01	0.40156E+03	0.88512E+02	0.58377E+03	0.48955E+01
9070.00	0.24556E-01	0.11246E+01	0.54069E+03	0.89091E+02	0.62086E+03	0.46364E+01
9075.00	0.23476E-01	0.11892E+01	0.61712E+03	0.87392E+02	0.54569E+03	0.34126E+01
9080.00	0.23128E-01	0.11321E+01	0.65042E+03	0.85377E+02	0.53251E+03	0.36894E+01
9085.00	0.23251E-01	0.15671E+01	0.76908E+03	0.86407E+02	0.46653E+03	0.18879E+01
9090.00	0.21448E-01	0.16451E+01	0.73750E+03	0.86111E+02	0.40094E+03	0.19037E+01
9095.00	0.20160E-01	0.11588E+01	0.49127E+03	0.89744E+02	0.40921E+03	0.42684E+01
9100.00	0.19937E-01	0.17366E+01	0.50886E+03	0.84755E+02	0.35944E+03	0.18393E+01
9105.00	0.19914E-01	0.16862E+01	0.54403E+03	0.84767E+02	0.38998E+03	0.17560E+01
9110.00	0.20169E-01	0.14981E+01	0.64399E+03	0.88767E+02	0.44811E+03	0.19448E+01
9115.00	0.19602E-01	0.15104E+01	0.54035E+03	0.88730E+02	0.42061E+03	0.20469E+01
9120.00	0.19704E-01	0.21027E+01	0.74017E+03	0.85771E+02	0.42358E+03	0.14914E+01
9125.00	0.19104E-01	0.21125E+01	0.53709E+03	0.84829E+02	0.42651E+03	0.14846E+01
9130.00	0.18266E-01	0.18310E+01	0.36586E+03	0.88968E+02	0.44148E+03	0.20692E+01
9135.00	0.19320E-01	0.16997E+01	0.46067E+03	0.85036E+02	0.48924E+03	0.18904E+01
9140.00	0.18582E-01	0.15804E+01	0.28481E+03	0.89765E+02	0.49797E+03	0.26831E+01
9145.00	0.18636E-01	0.14681E+01	0.30713E+03	0.88644E+02	0.53669E+03	0.28715E+01
9150.00	0.18897E-01	0.13226E+01	0.28406E+03	0.89844E+02	0.59722E+03	0.39014E+01
9155.00	0.18690E-01	0.13612E+01	0.29260E+03	0.89334E+02	0.60866E+03	0.36037E+01
9160.00	0.19407E-01	0.10674E+01	0.27975E+03	0.89612E+02	0.67401E+03	0.49317E+01
9165.00	0.19131E-01	0.11064E+01	0.23656E+03	0.89963E+02	0.70694E+03	0.52829E+01
9170.00	0.19286E-01	0.96330E+00	0.36088E+03	0.88943E+02	0.76268E+03	0.33966E+01
9175.00	0.18207E-01	0.79589E+00	0.42884E+03	0.84279E+02	0.81340E+03	0.38772E+01
9180.00	0.18132E-01	0.72585E+00	0.56722E+03	0.84167E+02	0.86035E+03	0.25128E+01
9185.00	0.17981E-01	0.66289E+00	0.62662E+03	0.84465E+02	0.86284E+03	0.15719E+01
9190.00	0.18019E-01	0.53874E+00	0.70173E+03	0.83020E+02	0.86808E+03	0.13253E+01
9195.00	0.17814E-01	0.47238E+00	0.61654E+03	0.84653E+02	0.89298E+03	0.11561E+01

9200.00	0.17915E-01	0.35423E+00	0.64213E+03	0.84437E+02	0.78483E+03	0.98130E-02
9205.00	0.19694E-01	0.42693E+00	0.59467E+04	0.84341E+02	0.46090E+03	0.75981E+00
9210.00	0.19708E-01	0.26571E+00	0.29004E+04	0.86578E+02	0.48141E+03	0.32664E+00
9215.00	0.17183E-01	0.60422E+00	0.10235E+05	0.86211E+02	0.26142E+03	0.17206E+01
9220.00	0.16867E-01	0.13400E+01	0.29017E+05	0.79989E+02	0.16830E+03	0.14509E+01
9225.00	0.15938E-01	0.27112E+00	0.50980E+04	0.81457E+02	0.21392E+03	0.10815E+01
9230.00	0.15116E-01	0.74755E+00	0.18507E+05	0.85194E+02	0.21503E+03	0.16775E+01
9235.00	0.15356E-01	0.20051E+00	0.51591E+04	0.77921E+02	0.12768E+03	0.52349E+01
9240.00	0.14949E-01	0.19063E+00	0.53723E+04	0.85654E+02	0.14869E+03	0.14617E+01
9245.00	0.15535E-01	0.11603E+00	0.41371E+04	0.72969E+02	0.14982E+03	0.33396E+00
9250.00	0.14846E-01	0.14129E+00	0.56784E+04	0.79427E+02	0.15071E+03	0.31841E+00
9255.00	0.14555E-01	0.13529E+00	0.70375E+04	0.87410E+02	0.15268E+03	0.21813E+00
9260.00	0.14377E-01	0.13557E+00	0.78155E+04	0.84086E+02	0.14877E+03	0.18582E+00
9265.00	0.14326E-01	0.14647E+00	0.78442E+04	0.86734E+02	0.13794E+03	0.45872E+01
9270.00	0.14084E-01	0.10772E+00	0.57531E+04	0.84496E+02	0.16598E+03	0.33526E-01
9275.00	0.13344E-01	0.11647E+00	0.52648E+04	0.78621E+02	0.15091E+03	0.10745E+00
9280.00	0.13018E-01	0.15593E+00	0.80824E+04	0.66912E+02	0.14010E+03	0.39416E+00
9285.00	0.12998E-01	0.13204E+00	0.85520E+04	0.74716E+02	0.12728E+03	0.40236E+00
9290.00	0.14069E-01	0.91279E-01	0.60160E+04	0.82283E+02	0.14327E+03	0.45259E+00
9295.00	0.13927E-01	0.94485E-01	0.76161E+04	0.85992E+02	0.13290E+03	0.67628E+00
9300.00	0.13729E-01	0.94279E-01	0.73374E+04	0.78207E+02	0.14668E+03	0.36070E+01
9305.00	0.13046E-01	0.92764E-01	0.77917E+04	0.85225E+02	0.13128E+03	0.11738E+01
9310.00	0.12331E-01	0.79949E-01	0.75068E+04	0.94244E+02	0.14094E+03	0.36335E+00
9315.00	0.11784E-01	0.11315E+00	0.11390E+05	0.90295E+02	0.15290E+03	0.26928E+01
9320.00	0.11799E-01	0.93223E-01	0.93453E+04	0.85559E+02	0.14130E+03	0.13990E+00
9325.00	0.12014E-01	0.89787E-01	0.74890E+04	0.79498E+02	0.13033E+03	0.99938E+01
9330.00	0.11822E-01	0.11306E+00	0.93104E+04	0.77791E+02	0.13620E+03	0.88293E+00
9335.00	0.13395E-01	0.13145E+00	0.25758E+05	0.84796E+02	0.14976E+03	0.10503E+02
9340.00	0.13243E-01	0.89711E-01	0.10882E+05	0.86766E+02	0.13921E+03	0.25161E-01
9345.00	0.12589E-01	0.94028E-01	0.88713E+04	0.84126E+02	0.13882E+03	0.12035E+01
9350.00	0.11802E-01	0.11667E+00	0.11111E+05	0.81871E+02	0.14213E+03	0.40310E+00
9355.00	0.11910E-01	0.97764E-01	0.98426E+04	0.91554E+02	0.13897E+03	0.17110E+00
9360.00	0.11837E-01	0.79147E-01	0.55404E+04	0.73180E+02	0.13696E+03	0.50303E+00
9365.00	0.11653E-01	0.88650E-01	0.61050E+04	0.71417E+02	0.14762E+03	0.56654E+00
9370.00	0.11579E-01	0.12054E+00	0.12853E+05	0.83611E+02	0.14456E+03	0.75128E+01
9375.00	0.11900E-01	0.50705E-01	0.62826E+04	0.81123E+02	0.15046E+03	0.24072E+01
9380.00	0.11570E-01	0.71899E-01	0.70383E+04	0.83785E+02	0.14087E+03	0.35951E-01
9385.00	0.11552E-01	0.79053E-01	0.84682E+04	0.81437E+02	0.14151E+03	0.24418E+01
9390.00	0.12669E-01	0.31436E-01	0.80166E+04	0.84299E+02	0.13915E+03	0.38023E-01
9395.00	0.12050E-01	0.68874E-01	0.94490E+04	0.82878E+02	0.15027E+03	0.36939E+00
9400.00	0.12427E-01	0.85362E-01	0.81153E+04	0.75798E+02	0.14654E+03	0.21010E-01
9405.00	0.12876E-01	0.73158E-01	0.58159E+04	0.84302E+02	0.15161E+03	0.89195E+00
9410.00	0.13026E-01	0.81354E-01	0.59122E+04	0.80520E+02	0.15702E+03	0.10041E+00
9415.00	0.13011E-01	0.10929E+00	0.10654E+05	0.91437E+02	0.16198E+03	0.15732E-01
9420.00	0.13406E-01	0.77867E-01	0.44205E+04	0.86181E+02	0.16404E+03	0.14840E+00
9425.00	0.13311E-01	0.95772E-01	0.54093E+04	0.76356E+02	0.16103E+03	0.54460E-02
9430.00	0.13343E-01	0.10503E+00	0.64913E+04	0.64588E+02	0.15218E+03	0.11039E+01
9435.00	0.12923E-01	0.81419E+00	0.68154E+05	0.84092E+02	0.13114E+03	0.60958E+00
9440.00	0.13007E-01	0.55010E+00	0.42573E+05	0.82582E+02	0.16081E+03	0.71496E+00
9445.00	0.13160E-01	0.98673E-01	0.56033E+04	0.85790E+02	0.21440E+03	0.67413E+00
9450.00	0.13441E-01	0.91211E-01	0.59064E+04	0.83156E+02	0.18509E+03	0.55083E-01
9455.00	0.12750E-01	0.12483E+00	0.79960E+04	0.83468E+02	0.16232E+03	0.26690E+01
9460.00	0.12541E-01	0.96051E-01	0.38234E+04	0.84295E+02	0.21110E+03	0.32841E-01
9465.00	0.12597E-01	0.72564E-01	0.44348E+02	0.89292E+02	0.28324E+03	0.27988E+01
9470.00	0.12201E-01	0.10190E+00	0.48313E+02	0.74360E+02	0.39725E+03	0.76198E+01
9475.00	0.12312E-01	0.11404E+00	0.26534E+03	0.82190E+02	0.40061E+03	0.11248E-01
9480.00	0.12342E-01	0.11436E+00	0.23332E+03	0.83502E+02	0.37631E+03	0.10659E+01
9485.00	0.12864E-01	0.12960E+00	0.14399E+02	0.93325E+02	0.33687E+03	0.25002E+01
9490.00	0.13088E-01	0.12596E+00	0.41741E+01	0.93397E+02	0.32060E+03	0.57270E+00
9495.00	0.12703E-01	0.12443E+00	0.21117E+03	0.78358E+02	0.34147E+03	0.63920E+00
9500.00	0.13043E-01	0.12698E+00	0.17526E+03	0.84152E+02	0.31930E+03	0.29750E-01

References

Allen, C.W. (1973). *Astrophysical Quantities. Third Edition.* London: The Athlone Press, University of London.

Allison, M., and Travis, L.D. (1986). Astronomical, Physical, and Meteorological Parameters for Planetary Atmospheres. In *The Jovian Atmospheres* (M. Allison and L.D. Travis, Eds.), p.293–319. NASA CP–2441.

Apt, J., Martonchik, J.V., and Brown, L.R. (1981). Comparison of Band Model and Integrated Line-by-Line Synthetic Spectra for Methane in the 2.3 μm Region. *J.Q.S.R.T.* **26** 431.

Armstrong, B.H. (1967). Spectrum Line Profiles: The Voigt Function. *J.Q.R.S.T.* **7** 61.

Armstrong, K.R., Harper, D.A. Jr., and Low, F.J. (1972). Far-Infrared Temperature of the Planets. *Astrophys. J.* **178** L89.

Atreya, S.K. (1986). *Atmospheres and Ionospheres of the Outer Planets and Their Satellites.* Berlin: Springer-Verlag.

Atreya, S.K., and Romani, P.N. (1985). Photochemistry and Clouds of Jupiter, Saturn, and Uranus. In *Recent Advances in Planetary Meteorology* (G.E. Hunt, Ed.), p.17–68. Cambridge: Cambridge University Press.

Atreya, S.K., Donahue, T.M., Sandel, B.R., Broadfoot, A.I., and Smith, G.R. (1979). Jupiter Upper Atmosphere Temperature Measurement by the Voyager 1 UVS Experiment. *Geophys. Res. Lett.* **6** 795.

Atreya, S.K., Donahue, T.M., and Festou, M.C. (1981). Jupiter: Structure and Composition of the Upper Atmosphere. *Astrophys. J.* **247** L43.

Aumann, H.H., and Gillespie, C.M. Jr. (1969). The Internal Powers and Effective Temperatures of Jupiter and Saturn. *Astrophys. J.* **157** L69.

Baines, K.H., Cochran, W.D., and Smith, W.H. (1983). Aerosols in the Jovian Equatorial Troposphere. An Analysis of Center-to-Limb (CTL) H_2 and NH_3 Features. *Bull. Amer. Astron. Soc.* **15** 833.

Ballard, J., and Johnston, W.B. (1986). Self-Broadened Widths and Absolute Strengths of $^{12}CH_4$ Lines in the 1310–1370 cm^{-1} Region. *J.Q.S.R.T.* **36** 365.

Banwell, C.N. (1983). *Fundamentals of Molecular Spectroscopy. Third Edition.* London: McGraw-Hill Book Company (UK) Limited.

Bar-Nun, A., and Podolak, M. (1985). The Contribution by Thunderstorms to the Abundances of CO, C_2H_2, and HCN on Jupiter. *Icarus* **64** 112.

Barshay, S.S., and Lewis, J.S. (1978). Chemical Structure of the Deep Atmosphere of Jupiter. *Icarus* **33** 593.

B.D.H. Crystran Crystals Handbook (1988). Poole: B.D.H. Advanced Materials Division, B.D.H. Limited.

Beatty, J.K., O'Leary, B., and Chaikin, A. (1981). *The New Solar System.* Cambridge: Cambridge University Press.

Beebe, R.F., and Youngblood, L.A. (1979). Pre-Voyager Velocities, Accelerations and Shrinkage Rates of Jovian Cloud Features. *Nature* **280** 771.

Beer, R. (1975). Detection of Carbon Monoxide in Jupiter. *Astrophys. J.* **200** L169.

Beer, R., and Taylor, F.W. (1978). The Abundance of Carbon Monoxide in Jupiter. *Astrophys. J.* **221** 1100.

Beer, R., Farmer, C.B., Norton, R.H., Martonchik, J.V., and Barnes, T.G. (1972). Jupiter: Observation of Deuterated Methane in the Atmosphere. *Science* **175** 1360.

Bender, M.L., Callaway, P.W., Chase, S.C., Moore, G.F., and Ruiz, R.D. (1974). Infrared Radiometer for the Pioneer 10 and 11 Missions to Jupiter. *Appl. Opt.* **13** 2623.

Benner, D.C. (1979). The Visual and Near Infrared Spectrum of Methane and Its Application to Uranus, Neptune, Triton, and Pluto. *Ph.D. Dissertation,* University of Arizona.

Benner, D.C., and Fink, U. (1980). Analysis of Infrared Laboratory CH_4 Spectra. *Bull. Am. Astron. Soc.* **12** 697.

Berstein, H.J., and Herzberg, G. (1948). Rotation-Vibration Spectra of Diatomic and Simple Polyatomic Molecules with Long Absorbing Paths. I. The Spectrum of Fluoroform (CHF_3) from 2.4 μ to 0.7 μ. *J. Chem. Phys.* **16** 30.

Bézard, B., Baluteau, J.P., and Marten, A. (1983a). Study of the Deep Cloud Structure in the Equatorial Region of Jupiter from Voyager Infrared and Visible Data. *Icarus* **54** 434.

Bézard, B., Marten, A., Baluteau, J.P., Gautier, D., Flaud, J.M., Camy-Peyret, C. (1983b). On the Detectability of H_2S in Jupiter. *Icarus* **55** 259.

Bjoraker, G.L., Larson, H.P., and Kunde, V.G. (1986a). The Gas Composition of Jupiter Derived from 5–μm Airborne Spectroscopic Observations. *Icarus* **66** 579.

Bjoraker, G.L., Larson, H.P., and Kunde, V.G. (1986b). Water Vapour in Jupiter's Atmosphere. In *The Jovian Atmospheres* (M. Allison and L.D. Travis, Eds.), p.48–52. NASA CP–2441.

Bomem DA3.002 Spectrophotometer System Manual (1981). Vanier, Québec: Bomem Inc..

Brault, J.W., Fox, K., Jennings, D.E., and Margolis, J.S. (1981). Anomalous $^{12}CH_4$:$^{13}CH_4$ Strengths in $3\nu_3$. *Astrophys. J.* **247** L101.

Brown, L.R. (1988). Methane Line Parameters from 3700 to 4136 cm^{-1}. *Appl. Opt.* **27** 3275.

Brown, L.R., and Rothman, L.S. (1982). Methane Line Parameters for the 2.3–μm Region. *Appl. Opt.* **21** 2425.

Buriez, J.C., and de Bergh, C. (1980). Methane Line Profiles Near 1.1 μ as a Probe of the Jupiter Cloud Structure and C/H Ratio. *Astron. Astrophys.* **83** 149.

Busse, F.H. (1976). A Simple Model of Convection in the Jovian Atmosphere. *Icarus* **29** 255.

Busse, F.H. (1983). A Model of Mean Zonal Flows in the Major Planets. *Geophys. Astrophys. Fluid Dynamics* **23** 153.

Calcutt, S.B. (1984). The Infrared Spectrum of the Atmosphere of Jupiter. *D.Phil. Thesis,* University of Oxford.

Calcutt, S.B., Ballard, J., Johnston, W.B., and Taylor, F.W. (1988). Spectroscopic Parameters for Methane from 1 to 2.5 Microns with Applications to Remote Sensing of the Atmosphere of Jupiter. Unpublished.

Cameron, A.G.W., and Pollack, J.B. (1976). On the Origin of the Solar System and of Jupiter and Its Satellites. In *Jupiter* (T. Gehrels, Ed.), p.61–84. Tucson: University Of Arizona Press.

Chackerian, C., Jr., and Guelachvili, G. (1980). Ground-State Rotational Constants of $^{12}CH_3D$. *J. Mol. Spec.* **84** 447.

Chackerian, C., Jr., and Guelachvili, G. (1983). Direct Retrieval of Lineshape Parameters: Absolute Line Intensities for the ν_2 Band of CH_3D. *J. Mol. Spec.* **97** 316.

Chamberlain, J. (1979). *The Principles of Interferometric Spectroscopy.* Chichester: John Wiley & Sons.

Chedin, A., Husson, N., Scott, N.A., Jobard, I., Cohen-Hallaleh, J., and Berroir, A. (1980). La Banque des Données GEISA. Description et Logiceil d'Utilisation. *Laboratoire de Météorogie Dynamique du CNRS Internal Note 108.* Ecole Polytechnique, France.

Chedin, A., Husson, N., Scott, N.A., Cohen-Hallaleh, J., and Berroir, A. (1981). **La Banque des Données GEISA. Mise à Jour No. 2.** *Laboratoire de Météorogie Dynamique du CNRS Internal Note 113.* Ecole Polytechnique, France.

Chedin, A., Husson, N., Scott, N.A., Cohen-Hallaleh, J., and Berroir, A. (1985). The GEISA Databank: 1984 Version. *Laboratoire de Météorogie Dynamique du CNRS Internal Note 127.* Ecole Polytechnique, France.

Childs, W. (1936). The Structure of the Near Infrared Bands of Methane. I. General Survey and a New Band at 1.1050 Å. *Proc. Roy. Soc. London A* **153** 555.

Clark, F.R.S., and Moffatt, D.J. (1978). The Elimination of Interference Fringes from Infrared Spectra. *Appl. Spec.* **32** 547.

Cochran, W.D. (1977). Jupiter: An Inhomogeneous Atmospheric Model Analysis of Spatial Variations of the Jovian H_2 Quadrupole Lines. *Icarus* **31** 325.

Coffeen, D.L. (1974). Optical Polarization Measurements of the Jupiter Atmosphere at 103° Phase Angle. *J.G.R.* **79** 3645.

Combes, M., and Encrenaz, T. (1979). A Method for the Determination of Abundance Ratios in the Outer Planets – Application to Jupiter. *Icarus* **39** 1.

Combes, M., Encrenaz, T., Vapillon, L., Zéau, Y., and Lesqueren, C. (1974). Confirmation of the Identification of C_2H_2 and C_2H_6 in the Jovian Atmosphere. *Astron. Astrophys.* **34** 33.

Combes, M., Maillard, J.P., and de Bergh, C. (1977). Evidence for a Telluric Value of the $^{12}C/^{13}C$ Ratio in the Atmospheres of Jupiter and Saturn. *Astron. Astrophys.* **61** 531.

Conrath, B.J. (1982). Radiative Transfer and Remote Sensing. In *Vibrational-Rotational Spectroscopy for Planetary Atmospheres* (M.J. Mumma, K. Fox, and J. Hornstein, Eds.), p.47–62. NASA CP–2223.

Conrath, B.J., and Gierasch, P.J. (1984). Global Variation of the para Hydrogen Fraction in Jupiter's Atmosphere and Implications for Dynamics on the Outer Planets. *Icarus* **57** 184.

Conrath, B.J., Gautier, D., Hanel, R.A., and Hornstein, J.S. (1984). The Helium Abundance of Saturn from Voyager Measurements. *Astrophys. J.* **282** 807.

Coustenis, A., Lellouch, E., Maillard, J.-P., Griffith, C., Schmitt, B., Lemmon, M., Tomasko, M., Doose, L., and Strong, K. (1991). High-Resolution Observations of Titan in the 1 to 1.3 Micron Region: Preliminary Study. *Paper presented at the 23rd Annual DPS Meeting, Palo Alto, California.*

Courtin, R., Gautier, D., Marten, A., and Kunde, V. (1983). The $^{12}C/^{13}C$ Ratio in Jupiter from the Voyager Infrared Investigation. *Icarus* **53** 121.

Cruikshank, D.P., and Apt, J. (1984). Methane on Triton: Physical State and Distribution. *Icarus* **58** 306.

Cruikshank, D.P., and Silvaggio, P.M. (1979). Triton: A Satellite with an Atmosphere. *Astrophys. J.* **233** 1016.

Cruikshank, D.P., Brown, R.P., Giver, L.P., and Tokunaga, A.T. (1989). Triton: Do We See to the Surface? *Science* **245** 283.

Cunningham, C.C., Hunten, D.M., and Tomasko, M.G. (1988). H_2 Spectroscopy and a Diurnally Changing Cloud on Jupiter. *Icarus* **75** 324.

Curtis, A.R. (1952). Discussion of "A Statistical Model for Water Vapor Absorption" by R. M. Goody. *Quart. J. Roy. Met. Soc.* **78** 638.

Danielson, R.E. (1974). The Visible Spectrum of Uranus. *Astrophys. J. Lett.* **192** L107.

Davis, G.R. (1987). Remote Sensing of Atmospheric Water Vapour by Pressure Modulator Radiometry. *D.Phil. Thesis,* University of Oxford.

de Bergh, C., Maillard, J.P., Lecacheaux, J., and Combes, M. (1976). A Study of the $3\nu_3$-CH_4 Region in a High-Resolution Spectrum of Jupiter Recorded by Fourier Transform Spectroscopy. *Icarus* **29** 307.

de Pater, I. (1986). Jupiter's Zone-Belt Structure at Radio Wavelengths. II. Comparison of Observations with Model Atmosphere Calculations. *Icarus* **68** 344.

Dick, K.A., and Fink, U. (1977). Photoelectric Absorption Spectra of Methane, Methane and Hydrogen Mixtures, and Ethane. *J.Q.S.R.T.* **18** 433.

Drayson, S.R. (1976). Rapid Computation of the Voigt Profile. *J.Q.S.R.T.* **16** 611.

Drossart, P., and Encrenaz, T. (1982). The Abundance of Water on Jupiter from the Voyager IRIS Data at 5 μm. *Icarus* **52** 483.

Drossart, P., Encrenaz, T., Kunde, V., Hanel, R., and Combes, M. (1982). An Estimate of the PH_3, CH_3D, and GeH_4 Abundances on Jupiter from the Voyager IRIS Data at 4.5 μm. *Icarus* **49** 416.

Drossart, P., Encrenaz, T., and Tokunaga, A.T. (1984). Variability of Phosphine on Jupiter from 5-μm Spectroscopy. *Icarus* **60** 613.

Drossart, P., Encrenaz, T., and Combes, M. (1985). The $^{14}N/^{15}N$ Ratio in the Jovian Atmosphere. *Astron. Astrophys.* **146** 181.

Drossart, P., Bézard, B., Atreya, S.K., Lacy, J., Serabyn, E.,Tokunaga, A., and Encrenaz, T. (1986). Enhanced Acetylene Emission near the North Pole of Jupiter. *Icarus* **66** 610.

Drossart, P., Courtin, R., Atreya, S., Tokunaga, A. (1989) Variations in the Jovian Atmospheric Composition and Chemistry. In *Time-Variable Phenomena in the Jovian System.* (M.J.S. Belton, R.A. West, and J. Rahe, Eds.), p.211–220. NASA SP–494.

Dunham, T., Jr. (1952). Spectroscopic Observations of the Planets at Mount Wilson. In *The Atmospheres of the Earth and Planets, Second Edition.* (G.P. Kuiper, Ed.), p.288–305. Chicago: University of Chicago Press.

Edwards, D.P. (1987). GENLN2: The New Oxford Line-By-Line Atmospheric Transmission/Radiance Model. Description and User's Guide. *Internal Memorandum 87.2.* Dept. of Atmospheric, Oceanic, and Planetary Physics, University of Oxford.

Edwards, D.P. (1988a). Atmospheric Transmittance and Radiance Calculations Using Line-By-Line Computer Models. *SPIE Critical Review of Technology: Modelling of the Atmosphere.* Orlando, Florida.

Edwards, D.P. (1988b). GENLN2: The New Oxford Line-By-Line Atmospheric Transmission/Radiance Model. Update of Description and User's Guide for Version 2.2. Hooke Institute for Cooperative Atmospheric Research, University of Oxford.

Elsasser, W.M. (1938). Mean Absorption and Equivalent Absorption Coefficient of a Band Spectrum. *Phys. Rev.* **54** 126.

Elsasser, W.M. (1942). *Heat Transfer by Infrared Radiation in the Atmosphere.* Harvard Meteorological Studies No. 6. Harvard University Press.

Encrenaz, T. (1984). Primordial Matter in the Outer Solar System: A Study of Its Chemical Composition from Remote Spectroscopic Analysis. *Space Sci. Rev.* **38** 35.

Encrenaz, T., Combes, M., and Zéau, Y. (1978). The Spectrum of Jupiter Between 10 and 13 μ: An Estimate of the Jovian $^{15}N/^{14}N$ Ratio. *Astron. Astrophys.* **70** 29.

Encrenaz, T., Combes, M., and Zéau, Y. (1980). The Spectrum of Jupiter Between 8 and 9 μ: Estimates of the Jovian C/H and D/H Ratios. *Astron. Astrophys.* **84** 148.

Erickson, E.F., Goorvitch, D., Simpson, J.P., and Stecker, D.W. (1978). Far Infrared Brightness Temperature of Jupiter and Saturn. *Icarus* **35** 61.

Eshleman, V.R., Tyler, G.L., Wood, G.E., Lindal, G.F., Anderson, J.D., Levy, G.S., and Croft, T.A. (1979). Radio Science with Voyager 1 at Jupiter: Preliminary Profiles of the Atmosphere and Ionosphere. *Science* **204** 976.

Festou, M.C., Atreya, S.K., Donahue, T.M., Sandel, B.R., Shemansky, D.E., and Broadfoot, A.L. (1981). Composition and Thermal Profiles of the Jovian Upper Atmosphere Determined by the Voyager Ultraviolet Stellar Occultation Experiment. *J.G.R.* **86** 5715.

Fink, U. (1982). Current Band Model Studies of CH_4 at Wavelengths Less than 2.5 Microns. In *Vibrational-Rotational Spectroscopy for Planetary Atmospheres* (M. J. Mumma, K. Fox, J. Hornstein, Eds.), p.559–583. NASA CP–2223.

Fink, U., and Larson, H. P. (1979). The Infrared Spectra of Uranus, Neptune, and Titan from 0.8–2.5 Microns. *Astrophys. J.* **233** 1021.

Fink, U., Benner, D.C., and Dick, K.A. (1977). Band Model Analysis of Laboratory Methane Absorption Spectra from 4500 to 10500 Å. *J.Q.S.R.T.* **18** 447.

Fink, U., Larson, H.P., and Treffers, R.R. (1978). Germane in the Atmosphere of Jupiter. *Icarus* **34** 344.

Fink, U., Smith, B.A., Benner, C.D., Johnson, J.R., and Reitsema, H.J. (1980). Detection of a CH_4 Atmosphere on Pluto. *Icarus* **44** 62.

Fox, K. (1984). Symmetry-Dependent Broadening Parameters for Methane. *J. Chem. Phys.* **80** 1367.

Fox, K., and Jennings, D.E. (1990). Spectroscopic Studies of Methane in Collisions with Rare Gas Atoms and Diatomic Molecules. *J. Mol. Struct.* **224** 1.

Fox, K., Mantz, A.E., Owen, T., and Rae, K.N. (1972). A Tentative Identification of $^{13}CH_4$ and an Estimate of $^{12}C/^{13}C$ in the Atmosphere of Jupiter. *Astrophys. J.* **176** L81

Fox, K., Jennings, D.E., Stern, E.A., and Hubbard, R. (1988). Measurements of Argon-, Helium-, Hydrogen-, and Nitrogen-Broadened Widths of Methane Lines Near 9000 cm^{-1}. *J.Q.S.R.T.* **39** 473.

Fox, K., Quillen, D.T., Jennings, D.E., Wagner, J., and Plymate, C. (1991). Methane Spectral Line Widths and Shifts, and Dependences on Physical Parameters. *J.G.R.* **96 (E2)** 17483.

Gautier, D., and Owen, T. (1983). Cosmogonical Implications of Elemental and Isotopic Abundances in Atmospheres of the Giant Planets. *Nature* **304** 691.

Gautier, D., Conrath, B., Flasar, M., Hanel, R., Kunde, V., Chedin, A., and Scott, N. (1981). The Helium Abundance of Jupiter from Voyager. *J.G.R.* **86** 8713.

Gautier, D., Bézard, B., Marten, A., Baluteau, J.P., Scott, N., Chedin, A., Kunde, V., and Hanel, R. (1982). The C/H Ratio in Jupiter from the Voyager Infrared Investigation. *Astrophys. J.* **257** 901.

Gibson, G.A., and Pierluissi, J.H. (1971). Accurate Formula for Gaseous Transmittance in the Infrared. *Appl. Opt.* **10** 1509.

Giess, J., and Reeves, H. (1972). Cosmic and Solar System Abundances of Deuterium and Helium, 3. *Astron. Astrophys.* **18** 126.

Gill, P.E., and Murray, W. (1978). Algorithms for the Solution of the Nonlinear Least-Squares Problem. *SIAM J. Numer. Anal.* **15** 977.

Gillett, F.C., Low, F.J., and Stein, W.A. (1969). The 2.8–14 Micron Spectrum of Jupiter. *Astrophys J.* **157** 925.

Giver, L.P. (1978). Intensity Measurements of the CH_4 Bands in the Region of 4350 Å to 10,600 Å. *J.Q.S.R.T.* **19** 311.

Giver, L.P., Benner, D.C., and Boese, R.W. (1984). Band Model Coefficients of Methane from 4000 to 9200 cm^{-1}, Determined at 112, 188, and 294 K. *Bull. Amer. Astron. Soc.* **16** 711.

Giver, L.P., Benner, D.C., ad Suárez, C.B. (1988). Band Models of Methane Gas Phase Spectra, 2.1–2.5 μm, Extrapolated to T=55 K for Analysis of Triton's Spectrum. *Bull. Amer. Astron. Soc.* **20** 838.

Giver, L.P., Benner, D.C., Tomasko, M.G., Fink, U., and Kerola, D. (1990). Gaussian Quadrature Exponential Sum Modeling of Near Infrared Methane Laboratory Spectra Obtained at Temperatures from 106 to 297 K. In *First International Conference on Laboratory Research for Planetary Atmospheres* (K. Fox, J.E. Allen, Jr., and D.T. Quillen, Eds.), p.147–156. NASA CP–3077.

Gladstone, G.R., and Yung, Y.L. (1983). An Analysis of the Reflection Spectrum of Jupiter from 1500 Å to 1740 Å. *Astrophys. J.* **266** 415.

Godson, W.L. (1954). Spectral Models and the Properties of Transmission Functions. *Proc. Toronto Meteor. Conf. 1953,* 35.

Godson, W.L. (1955). The Computation of Infrared Transmission by Atmospheric Water Vapour. *J. of Meteorology* **12** 272.

Goody, R.M. (1952). A Statistical Model for Water-Vapour Absorption. *Quart. J. Roy. Met.*

Soc. **78** 165.

Goody, R.M. (1964). *Atmospheric Radiation. I. Theoretical Basis.* Oxford: The Clarendon Press.

Goody, R., West, R., Chen, L., and Crisp, D. (1989). The Correlated-k Method for Radiation Calculations in Nonhomogeneous Atmospheres. *J.Q.S.R.T.* **42** 539.

Griffith, C.A., and Owen, T. (1991). Observing the Surface of Titan Through Near-Infrared Windows in Its Atmosphere. *Proceedings of Symposium on Titan.* E.S.A. Publication. In press.

Griffiths, P.R., and de Haseth, J.A. (1986). *Fourier Transform Infrared Spectroscopy.* New York: John Wiley & Sons.

Hanel, R.A. (1982). Molecular Spectroscopy and Planetary Exploration from Space. In *Vibrational-Rotational Spectroscopy for Planetary Atmospheres* (M.J. Mumma, K. Fox, and J. Hornstein, Eds.), p.29–46. NASA CP–2223.

Hanel, R., Conrath, B., Flasar, M., Kunde, V., Lowman, P., Maguire, W., Pearl, J., Pirraglia, J., Samuelson, R., Gautier, D., Gierasch, P., Kumar, S., and Ponnamperuma, C. (1979a). Infrared Observations of the Jovian System from Voyager 1. *Science* **204** 972.

Hanel, R., Conrath, B., Flasar, M., Herath, L., Kunde, V., Lowman, P., Maguire, W., Pearl, J., Pirraglia, J., Samuelson, R., Gautier, D., Gierasch, P., Horn, L., Kumar, S., and Ponnamperuma, C. (1979b). Infrared Observations of the Jovian System from Voyager 2. *Science* **206** 952.

Hanel, R.A., Crosby, D., Herath, L., Vanous, D., Collins, D., Croswick, H., Harris, C., and Rhodes, M. (1980). Infrared Spectrometer for Voyager. *Appl. Opt.* **19** 1391.

Hanel, R.A., Conrath, B.J., Herath, L.W., Kunde, V.G., and Pirraglia, J.A., (1981). Albedo, Internal Heat, and Energy Balance of Jupiter: Preliminary Results of the Voyager Infrared Investigation. *J.G.R.* **86** 8705.

Hansen, J.E. (chairman), Belton, M.J.S., Carlson, R.W., Chapman, C.R., Encrenaz, T., Esh-leman, V.R., Gierasch, P.J., Hord, C.W., Howard, H.T., Orton, G.S., Owen, T., Pilcher, C.B., Pollack, J.B., Rossow, W.B., Stewart, A.I., Stone, P.H., and Taylor, F.W. (1980). Jupiter's Atmosphere: Exploration by the Galileo Mission. *Report of a subcommittee of the Galileo Atmospheric Working Group.*

Hecht, E., and Zajac, A. (1974). *Optics.* Reading, Masssachusetts: Addison-Wesley Publishing Company, Inc..

Herzberg, G. (1945). *Molecular Spectra and Molecular Structure. II. Infrared and Raman Spectra of Polyatomic Molecules.* New York: D. Van Nostrand Reinhold Company.

Herzberg, G. (1950). *Molecular Spectra and Molecular Structure. I. Spectra of Diatomic Molecules. Second Edition.* New York: D. Van Nostrand Reinhold Company.

Hide, R., and Stannard, D. (1976). Jupiter's Magnetism: Observations and Theory. In *Jupiter* (T. Gehrels, Ed.), p.767–787. Tucson: University of Arizona Press.

Hildebrand, R.H., Loewenstein, R.F., Harper, D.A., Orton, G.S., Keene, J., and Whitcomb, S.E. (1985). Far-Infrared and Submillimeter Brightness Temperatures of the Giant Planets. *Icarus* **64** 64.

Hogan, J.S., Rasool, S.I., and Encrenaz, T. (1969). The Thermal Structure of the Jovian Atmosphere. *J. Atmos. Sci.* **26** 898.

Hornstein, J., Fox, K., and Mumma, M.J. (1982). Summary of the Working Session. In *Vibrational-Rotational Spectroscopy for Planetary Atmospheres* (M.J. Mumma, K. Fox, and J. Hornstein, Eds.), p.747–761. NASA CP–2223.

Houghton, J.T. (1986). *The Physics of Atmospheres. Second Edition.* Cambridge: Cambridge University Press.

Houghton, J.T., Taylor, F.W., and Rodgers, C.D. (1984). *Remote Sounding of Atmospheres. Second Edition.* Cambridge: Cambridge University Press.

Hubbard, W.B. (1984). *Planetary Interiors.* New York: Van Nostrand Reinhold Company Inc..

Hunt, G. E. (1981). Atmospheres of Jupiter and Saturn. *Phil. Trans. R. Soc. Lond.* **303** 225.

Hunt, G.E., Godfrey, D., Haines, K., and Moore, V. (1985). The Meteorology of Jupiter and Saturn. In *Recent Advances in Planetary Meteorology* (G.E. Hunt, Ed.), p.101–120. Cambridge: Cambridge University Press.

Hunten, D.M. (1976). Atmospheres and Ionospheres. In *Jupiter* (T. Gehrels, Ed.), p.22–31. Tucson: University of Arizona Press.

Hunten, D.M., Tomasko, M., and Wallace, L. (1980). Low-Latitude Thermal Structure of Jupiter in the Region 0.1–5 Bars. *Icarus* **43** 143.

Hunten, D.M., Colin, L., and Hansen, J.E. (1986). Atmospheric Science on the Galileo Mission. *Space Sci. Rev.* **44** 191.

Husson, N., Chedin, A., Scott, N.A., Cohen-Hallaleh, I., and Berroir, A. (1982). La Banque des Données GEISA. Mise à Jour No. 3. *Laboratoire de Météorogie Dynamique du CNRS Internal Note 116.* Ecole Polytechnique, France.

Husson, N., *et al.* (1986). The GEISA Spectroscopic Line Parameters Data Bank in 1984. *Annales Geophysicae* **86A** 185.

Ingersoll, A.P. (1981). Jupiter and Saturn. In *The New Solar System* (J.K. Beatty, B. O'Leary, and A. Chaikin, Eds.), p.117–128. Cambridge: Cambridge University Press.

Ingersoll, A.P., and Miller, R.L. (1986). Motions in the Interiors and Atmospheres of Jupiter and Saturn. 2. Barotropic Instabilities and Normal Modes of an Adiabatic Planet. *Icarus* **65** 370.

Ingersoll, A.P., and Pollard, D. (1982). Motion in the Interiors and Atmospheres of Jupiter and Saturn: Scale Analysis, Anelastic Equations, Barotropic Stability Criterion. *Icarus* **52** 62.

Ingersoll, A.P., and Porco, C.C. (1978). Solar Heating and Internal Heat Flow on Jupiter. *Icarus* **35** 27.

Ingersoll, A.P., Münch, G., Neugebauer, G., Diner, D.J., Orton, G.S., Schupler, B., Schroeder, M., Chase, S.C., Ruiz, R.D., and Trafton, L.M. (1975). Pioneer 11 Infrared Radiometer Experiment: The Global Heat Balance of Jupiter. *Science* **188** 472.

Ingersoll, A.P., Münch, G., Neugebauer, G., and Orton, G.S. (1976). Results of the Infrared Radiometer Experiment on Pioneers 10 and 11. In *Jupiter* (T. Gehrels, Ed.), p.197–205. Tucson: University of Arizona Press.

Ingersoll, A.P., Beebe, R.F., Collins, S.A., Hunt, G.E., Mitchell, J.L., Müller, J.-P., Smith, B.A., and Terrile, R.J. (1979). Zonal Velocity and Texture in the Jovian Atmosphere Inferred from Voyager Images. *Nature* **280** 773.

Ingersoll, A.P., Beebe, R.F., Mitchell, J.L., Garneau, G.W., Yagi, G.M., and Müller, J.-P. (1981). Interaction of Eddies and Mean Zonal Flow on Jupiter as Inferred from Voyager 1 and 2 Images. *J.G.R.* **86** 8733.

Ingersoll, A.P., Beebe, R.F., Conrath, B.J., and Hunt, G.E. (1984). Structure and Dynamics of Saturn's Atmosphere. In *Saturn* (T. Gehrels and M.S. Matthews, Eds.), p.195–238. Tucson: University of Arizona Press.

Jenkins, F.A., and White, H.E. (1950). *Fundamentals of Optics.* New York: McGraw-Hill Book Company, Inc..

Jones, B.W. (1984). *The Solar System.* Oxford: Pergamon Press Ltd..

Jones, R.L. (1983). Measurement of the Atmospheric Distribution of CH_4 and N_2O from Satellites. *D.Phil. Thesis,* University of Oxford.

Judge, D.L., and Carlson, R.W. (1974). Pioneer 10 Observations of the Ultraviolet Glow in the Vicinity of Jupiter. *Science* **183** 317.

Kaye, J.A. (1987). Mechanisms and Observations for Isotope Fractionation of Molecular Species in Planetary Atmospheres. *Rev. of Geophysics* **25** 1609.

Kaye, J.A., and Strobel, D.F. (1983). HCN Formation on Jupiter: The Coupled Photochemistry of Ammonia and Acetylene. *Icarus* **54** 417.

Keay, C.S.L., Low, F.J., Rieke, G.H., and Minton, R.B. (1973). High-Resolution Maps of Jupiter at Five Microns. *Astrophys. J.* **183** 1063.

Kiess, C.C., Corliss, C.H., and Kiess, H.K. (1960). High Dispersion Spectra of Jupiter. *Astrophys. J.* **132** 221.

Kim, S.J., Caldwell, J., Rivolo, A.R., Wagener, R., and Orton, G.S. (1985). Infrared Polar Brightening on Jupiter. III. Spectrometry from the Voyager 1 IRIS Experiment. *Icarus* **64** 233.

King, J.I.F. (1964). Band Absorption Model for Arbitrary Line Variance. *J.Q.S.R.T.* **4** 705.

Knacke, R.F., Kim, S.J., Ridgway, S.T., and Tokunaga, A.T. (1982). The Abundances of CH_4, CH_3D, NH_3, and PH_3 in the Troposphere of Jupiter Derived from High-Resolution 1100–1200 cm^{-1} Spectra. *Astrophys. J.* **262** 388.

Kostiuk, T., Mumma, M.J., Espenak, F., Deming, D., Jennings, D.E., Maguire, W., and Zipoy, D. (1983). Measurements of Stratospheric Ethane in the Jovian South Polar Region from Infrared Heterodyne Spectroscopy of the ν_9 Band near 12 Microns. *Astrophys. J.* **265** 564.

Kuiper, G.P. (1950). Planetary and Satellite Atmospheres. *Reports on Progress in Physics* **13** 247.

Kuiper, G.P. (1952). Planetary Atmospheres and Their Origin. In *The Atmospheres of the Earth and Planets* (G.P. Kuiper, Ed.), p.306–405. Chicago: University of Chicago Press.

Kunde, V.G. (1982). Voyager IRIS Measurements of the Jovian Atmosphere. In *Vibrational-Rotational Spectroscopy for Planetary Atmospheres* (M.J. Mumma, K. Fox, and J. Hornstein, Eds.), p.387–405. NASA CP–2223.

Kunde, V., Hanel, R., Maguire, W., Gautier, D., Baluteau, J.P., Marten, A., Chedin, A., Husson, N., and Scott, N. (1982). The Tropospheric Gas Composition of Jupiter's North Equatorial Belt (NH_3, PH_3, CH_3D, GeH_4, H_2O) and the Jovian D/H Isotopic Ratio. *Astrophys. J.* **263** 443.

Lacy, J.H., Larabee, A.I., Wollman, E.R., Geballe, T.R., Townes, C.H., Bregman, J.D., and Rank, D.M. (1975). Observations and Analysis of the Jovian Spectrum in the 10 Micron ν_2 Band of NH_3. *Astrophys. J.* **198** L145.

Lambert, D. (1978). The Abundance of the Elements in the Solar Photosphere. VIII. Revised Abundances of Carbon, Nitrogen, and Oxygen. *Mon. Not. Roy. Astron. Soc.* **82** 249.

Ladenburg, R., and Reiche, F. (1913). Über Selektive Absorption. *Ann. Phys.* **42** 181.

Larson, H.P. (1982). Jupiter and Saturn from 2 to 6 μm. In *Vibrational-Rotational Spectroscopy for Planetary Atmospheres* (M.J. Mumma, K. Fox, and J. Hornstein, Eds.), p.407–427. NASA CP–2223.

Larson, H.P., Fink, U., Treffers, R., and Gautier, T.N. III (1975). Detection of Water Vapor on Jupiter. *Astrophys. J.* **197** L137.

Larson, H.P., Fink, U., and Treffers, R.R. (1978). Evidence for CO in Jupiter's Atmosphere from Airborne Spectroscopic Observations at 5 Microns. *Astrophys. J.* **219** 1084.

Larson, H.P., Davis, D.S., Hofmann, R., and Bjoraker, G.L. (1984). The Jovian Atmospheric Window at 2.7 μm: A Search for H_2S. *Icarus* **60** 621.

Lellouch, E., Drossart, P., Encrenaz, T., Guelachvili, G., Lacome, N., and Tarrago, G. (1989). A New Analysis of the Jovian 5–μm IRIS Spectra. In *Time-Variable Phenomena in the Jovian System.* (M.J.S. Belton, R.A. West, and J. Rahe, Eds.), p.371–373. NASA SP–494.

Lellouch, E., Coustenis, A., Maillard, J.-P., Strong, K., Demé, N. Griffith, C., and Schmitt, B. (1991). The Spectrum of Titan in the 1.06 and 1.28 Micron Windows. *Proceedings of Symposium on Titan.* E.S.A. Publication. In press.

Lewis, J.S. (1969a). The Clouds of Jupiter and the NH_3–H_2 and NH_3–H_2S Systems. *Icarus* **10** 365.

Lewis, J.S. (1969b). Observability of Spectroscopically Active Compounds in the Atmosphere of Jupiter. *Icarus* **10** 393.

Lewis, J.S., and Prinn, R.G. (1970). Jupiter's Clouds: Structure and Composition. *Science* **169** 972.

Lewis, J.S., and Prinn, R.G. (1984). *Planets and Their Atmospheres: Origin and Evolution.* London: Academic Press Inc. Ltd..

Lewis, S.R. (1988). Long-Lived Eddies in the Atmosphere of Jupiter. *D.Phil. Thesis*, University of Oxford.

Lindal, G.F., Wood, G.E., Levy, G.S., Anderson, J.D., Sweetnam, D.N., Hotz, H.B., Buckles, B.J., Holmes, D.P., Doms, P.E., Eshleman, V.R., Tyler, G.L., and Croft, T.A. (1981). The Atmosphere of Jupiter: An Analysis of the Voyager Radio Occultation Measurements. *J.G.R.* **86** 8721.

Lorentz, H.A. (1906). The Absorption and Emission Lines of Gaseous Bodies. *Proc. Amst. Akad. Sci.* **8** 591.

Low, F.J. (1965). Planetary Radiation at Infrared and Millimeter Wavelengths. *Lowell Observ. Bull.* **128** 184.

Lutz, B., and Ramsay, D.A. (1972). New Observations on the Kuiper Bands of Uranus. *Astrophys. J.* **176** 521.

Lutz, B.L., Owen, T., and Cess, R.D. (1976). Laboratory Band Strengths of Methane and Their Application to the Atmospheres of Jupiter, Saturn, Uranus, Neptune, and Titan. *Astrophys. J.* **203** 541.

Lutz, B.L., Owen, T., and Cess, R.D. (1982). Laboratory Band Strengths of Methane and Their Application to the Atmospheres of Jupiter, Saturn, Uranus, Neptune, and Titan. II. The Red Region 6000–7000 Å. *Astrophys. J.* **258** 886.

Maguire, W.C., Samuelson, R.E., Hanel, R.A., and Kunde, V.G. (1984). Latitudinal Variation of the Acetylene and Ethane in the Jovian Atmosphere from Voyager IRIS Observation. *Bull. Amer. Astron. Soc.* **16** 647.

Maillard, J.P., Combes, M., Encrenaz, T., and Lecacheaux, J. (1973). New Infrared Spectra of the Jovian Planets from 12,000 to 4000 cm^{-1} by Fourier Transform Spectroscopy. I. Study of Jupiter in the $3\nu_3$ CH_4 Band. *Astron. Astrophys.* **25** 219.

Malkmus, W. (1967). Random Lorentz Band Model with Exponential-Tailed S^{-1} Line-Intensity Distribution Function. *J. Opt. Soc. Am.* **57** 323.

Margolis, J.S. (1971). Self-Broadened Half-Widths and Pressure Shifts for the R-Branch J-Manifolds of the $3\nu_3$ Methane Band. *J.Q.S.R.T.* **11** 69.

Margolis, J. (1982). H_2 and HD Spectroscopic Status. In *Vibrational-Rotational Spectroscopy for Planetary Atmospheres* (M.J. Mumma, K. Fox, and J. Hornstein, Eds.), p.431–437. NASA CP–2223.

Margolis, J.S., and Fox, K. (1969a). Studies of Methane Absorption in the Jovian Atmosphere. I. Rotational Temperature from the $3\nu_3$ Band. *Astrophys. J.* **157** 935.

Margolis, J.S., and Fox, K. (1969b). Studies of Methane Absorption in the Jovian Atmosphere. II. Abundance from the $3\nu_3$ Band. *Astrophys. J.* **158** 1183.

Margolis, J.S., and Fox, K. (1969c). Extension of Calculations of Rotational Temperature and Abundance of Methane in the Jovian Atmosphere. *J. Atmos. Sci.* **26** 862.

Marks, L.S., Ed. (1941). *Mechanical Engineer's Handbook. Fourth Edition.* McGraw-Hill Books Company, Inc..

Marten, A., Courtin, R., Gautier, D., and Lacombe, A. (1980). Ammonia Vertical Density Profiles in Jupiter and Saturn from Their Radioelectric and Infrared Emissivities. *Icarus* **41** 410.

Marten, A., Rouan, D., Baluteau, J.P., Gautier, D., Conrath, B.J., Hanel, R. A., Kunde, V., Samuelson, R., Chedin, A., and Scott, N. (1981). Study of the Ammonia Ice Cloud Layer in the Equatorial Region of Jupiter from the Infrared Interferometric Experiment on Voyager. *Icarus* **46** 233.

Mayer, H.L. (1947). Methods of Opacity Calculations. *LA-647.* Los Alamos.

McClatchey, R.A., Benedict, W.S., Clough, S.A., Burch, D.E., Calfee, R.F., Fox, K., Rothman, L.S., and Garing, J.S. (1973). AFCRL Atmospheric Absorption Line Compilation. *AFCRL–TR–73–0096.* Bedford, MA.: Air Force Cambridge Research Laboratories.

McCleese, D.J. (1976). A Study of Radiative Transfer in Cloudy Atmospheres. *D.Phil. Thesis*, University of Oxford.

McKay, C.P., Pollack, J.B., and Courtin, R. (1989). The Thermal Structure of Titan's Atmosphere. *Icarus* **80** 23.

McKellar, A.R.W. (1989). The Spectrum of Gaseous Methane at 77 K in the 1.1–2.6 μm Region: A Benchmark for Planetary Astronomy. *Can. J. Phys.* **67** 1027.

Mecke, R. (1933). Neue Absorptionsbanden des Methans im nahen Ultraroten. *Z. Astrophys.* **6** 144.

Menzel, D.H., Coblentz, W.W., and Lampland, C.O. (1926). Planetary Temperatures Derived from Water-Cell Transmissions. *Astrophys. J.* **63** 177.

Michelson, A.A. (1895). On the Broadening of Spectral Lines. *Astrophys. J.* **2** 251.

Mickelson, M.E., Larson, L.E., and Schubert, A. (1991). New Measurements of the 6190-Å Band of Methane. *J.G.R.* **96 (E2)** 17507.

Mitchell, R. (1988). [Galileo] Mission Design Status Report. *Internal JPL Report presented at a NIMS Science Team Meeting, 21 March 1988, Pasadena, California.*

Mitchell, J.L., Terrile, R.J., Smith, B.A., Müller, J.-P., Ingersoll, A.P., Hunt, G.E., Collins, S.A., and Beebe, R.F. (1979). Jovian Cloud Structure and Velocity Fields. *Nature* **280** 776.

Moreno, F., Molina, A., and Ortiz, J.L. (1991). Near-Infrared CVF Spectrophotometry of Selected Areas of Jupiter During the 1991 Apparition. *Icarus*. In press.

Multipoint Data Recorder PM8237A/02 Operating Manual. Philips Scientific & Industrial Equipment Division.

Mumma, M.J., Fox, K., and Hornstein, J., Eds. *Vibrational-Rotational Spectroscopy for Planetary Atmospheres.* NASA CP–2223.

Murphy, R.E., and Fesen, R.A. (1974). Spatial Variations in the Jovian 20-Micrometer Flux. *Icarus* **21** 42.

Murray, B.C., and Wildey, R.L. (1963). Stellar and Planetary Observations at 10 Microns. *Astrophys. J.* **137** 692.

NAG FORTRAN Library Manual, Mark 10, Volume 3. E04 — Minimising or Maximising a Function (1983). Oxford: Numerical Algorithms Group.

Near-Infrared Mapping Spectrometer System Description (1978). Gardena, California: Ball Aerospace Systems Division, Western Laboratories.

Noll, K.S., Knacke, R.F., Tokunaga, A.T., Lacy, J.H., Beck, S., and Serabyn, E. (1986). The Abundances of Ethane and Acetylene in the Atmospheres of Jupiter and Saturn. *Icarus* **65** 257.

Noll, K.S., Geballe, T.R., and Knacke, R.F. (1989). Arsine in Saturn and Jupiter. *Astrophys. J.* **338** L71.

Norton, R.H., and Beer, R. (1976). New Apodizing Functions for Fourier Spectrometry. *J. Opt. Soc. Am.* **66** 259.

Ockman, N. (1958). The Infra-Red and Raman Spectra of Ice. *Adv. Cry. Eng.* **7** 199.

Orton, G.S. (1975a). The Thermal Structure of Jupiter: I. Implications of Pioneer 10 Infrared Radiometer Data. *Icarus* **26** 125.

Orton, G.S. (1975b). The Thermal Structure of Jupiter: II. Observations and Analysis of 8–14 Micron Radiation. *Icarus* **26** 142.

Orton, G.S. (1981). Atmospheric Structure in the Equatorial Region of Jupiter: A Report of the Galileo Working Group on Atmospheres, Subcommittee on Atmospheric Structure. *NASA-JPL Report 1625–125.* Pasadena, California: Jet Propulsion Laboratory.

Orton, G.S., and Ingersoll, A.P. (1976). Pioneer 10 and 11 and Groundbased Infrared Data on Jupiter: The Thermal Structure and He–H_2 Ratio. In *Jupiter* (T. Gehrels, Ed.), p.206–215. Tucson: University of Arizona Press.

Owen, T. (1965). Comparisons of Laboratory and Planetary Spectra. II. The Spectrum of Jupiter from 9700 to 11,200 Å. *Astrophys. J.* **141** 444.

Owen, T. (1967). Comparisons of Laboratory and Planetary Spectra. IV. The Identification of

the 7500–Å Bands in the Spectra of Uranus and Neptune. *Icarus* **6** 108.

Owen, T. (1969). The Spectra of Jupiter and Saturn in the Photographic Infrared. *Icarus* **10** 355.

Owen, T. (1972). The Composition of Planetary Atmospheres. In *Physics of the Solar System* (S.I. Rasool, Ed.), p.243–268. NASA SP–300.

Owen, T., and Terrile, R.J. (1981). Colors on Jupiter. *J.G.R.* **86** 8797.

Owen, T., Lutz, B.L., Porco, C.C., and Woodman, J.H. (1974). On the Identification of the 6420 Å Absorption Feature in the Spectra of Uranus and Neptune. *Astrophys. J.* **189** 379.

Owen, T., Caldwell, J., Rivolo, A.R., Moore, V., Lane, A.L., Sagan, C., Hunt, G., and Ponnamperuma, C. (1980). Observations of the Spectrum of Jupiter from 1500 to 2000 Å with the IUE. *Astrophys. J.* **236** L39.

Palik, E.D. (1985). Gallium Arsenide. In *Handbook of Optical Constants of Solids* (E.D. Palik, Ed.), p.429–443. London: Academic Press Inc. Ltd..

Peek, B.M. (1958). *The Planet Jupiter.* London: Faber and Faber Ltd..

Penner, S.S. (1959). *Quantitative Molecular Spectroscopy and Gas Emissivities.* Reading, Massachusetts: Addison-Wesley Publishing Company, Inc..

Pirraglia, J.A. (1984). Meridional Energy Balance of Jupiter. *Icarus* **59** 169.

Plass, G.N. (1958). Models for Spectral Band Absorption. *J. Opt. Soc. Am.* **48** 690.

Podolak, M, and Giver, L.P. (1979). On Inhomogeneous Scattering Models of Titan's Atmosphere. *Icarus* **37** 361.

Prather, M.J., Logan, J.A., and McElroy, M.B. (1978). Carbon Monoxide in Jupiter's Upper Atmosphere: An Extraplanetary Source. *Astrophys. J.* **223** 1072.

Press, W.H., Flannery, B.P., Teulosky, S.A., and Vetterling, W.T. (1986). *Numerical Recipes: The Art of Scientific Computing.* Cambridge: Cambridge University Press.

Prinn, R.G., and Barshay, S.S. (1977). Carbon Monoxde on Jupiter and Implications for Atmospheric Convection. *Science* **198** 1031.

Prinn, R.G., and Lewis, J.S. (1975). Phosphine on Jupiter and Implications for the Great Red Spot. *Science* **190** 274.

Prinn, R.G., and Owen, T. (1976). Chemistry and Spectroscopy of the Jovian Atmosphere. In *Jupiter* (T. Gehrels, Ed.), p.319–371. Tucson: University of Arizona Press.

Ramaprasad, K.R., Caldwell, J., and McClure, D.S. (1978). The Vibrational Overtone Spectrum of Liquid Methane in the Visible and Near Infrared: Applications to Planetary Studies. *Icarus* **35** 400.

Rank, D.H., Fink, U., and Wiggins, T.A. (1966). Measurements on Spectra of Gases of Planetary Interest. II. H_2, CO_2, NH_3, and CH_4. *Astrophys. J.* **143** 980.

Remedios, J.J. (1990). Spectroscopy for Remote Sounding of the Atmosphere. *D.Phil. Thesis,* University of Oxford.

Richards, P.L. (1967). Fourier Transform Spectroscopy. In *Spectroscopic Techniques* (D.H. Martin, Ed.), p.31–66. Amsterdam: North-Holland Publishing Company.

Ridgway, S.T. (1974a). Jupiter: Identification of Ethane and Acetylene. *Astrophys. J.* **187** L41.

Ridgway, S.T. (1974b). The Infrared Spectrum of Jupiter, 750–1200 cm^{-1}. *Bull. Amer. Astron. Soc.* **6** 376.

Ridgway, S.T., Larson, H.P., and Fink, U. (1976a). The Infrared Spectrum of Jupiter. In *Jupiter* (T. Gehrels, Ed.), p.384–417. Tucson: University of Arizona Press.

Ridgway, S.T., Wallace, L., and Smith, G.R. (1976b). The 800–1200 Inverse Centimeter Absorption Spectrum of Jupiter. *Astrophys. J.* **207** 1002.

Rodgers, C.D. (1966). Laboratory Measurements of Weighting Functions. *Internal Memorandum 66.12.* Dept. of Atmospheric Physics. University of Oxford.

Rodgers, C.D. (1976). Approximate Methods of Calculating Transmission by Bands of Spectral

Lines. *NCAR/TN-116+1A*. Boulder, Colorado: National Center for Atmospheric Research.

Ross, J.E., and Aller, L.H. (1976). The Chemical Composition of the Sun. *Science* **191** 1223.

Rossi, B. (1965). *Optics*. Reading, Massachusetts: Addison-Wesley Publishing Company, Inc..

Rothman, L.S. (1978). Update of the AFGL Atmospheric Absorption Line Parameters Compilation. *Appl. Opt.* **17** 3517.

Rothman, L.S. (1981). AFGL Atmospheric Absorption Line Parameters Compilation: 1980 Version. *Appl. Opt.* **20** 791.

Rothman, L.S., and McClatchey, R.A. (1976). Updating of the AFCRL Atmospheric Absorption Line Parameters Compilation. *Appl. Opt.* **15** 2616.

Rothman, L.S., Gamache, R.R., Barbe, A., Goldman, A., Gillis, J.R., Brown, L.R., Toth, R.A., Flaud, J.-M., and Camy-Peyret, C. (1983). AFGL Atmospheric Absorption Line Parameters Compilation: 1982 Edition. *Appl. Opt.* **22** 2247.

Rothman, L.S., Gamache, R.R., Goldman, A., Gillis, J.R., Brown, L.R., Toth, R.A., Pickett, H.M., Poynter, R.L., Flaud, J.-M., Camy-Peyret, C., Barbe, A., Husson, N., Rinsland, C.P., and Smith, M.A.H. (1987). The HITRAN Database: 1986 Edition. *Appl. Opt.* **26** 4058.

Rothman, L.S., *et al.* (1991). The HITRAN Database: 1991 Edition. In press.

Russell, C.T. (1988). A Program for Studying Temporal Variations in the Jovian System (TVJS). *Report prepared by the International Jupiter Watch.*

Sato, M., and Hansen, J.E. (1979). Jupiter's Atmospheric Composition and Cloud Structure Deduced from Absorption Bands in Reflected Sunlight. *J. Atmos. Sci.* **36** 1133.

Silvaggio, P. (1977). Experimental Determination of Molecular Absorption Coefficients for Methane and Ammonia at Low Temperatures and Model Atmospheres for the Major Planets. *Ph.D. Thesis*, Cornell University.

Silvaggio, P. (1982). Long-Pathlength Absorption Spectroscopy of CH_4. In *Vibrational-Rotational Spectroscopy for Planetary Atmospheres* (M.J. Mumma, K. Fox, and J. Hornstein, Eds.), p.585–598. NASA CP–2223.

Silvaggio, P.M., Boese, R.W., and Nanes, R. (1980). Band Model Calculations for $CFCl_3$ in the 8–12 μm Region. *J.Q.R.S.T.* **23** 221.

Smith, B.A., and Hunt, G.E. (1976). Motions and Morphology of Clouds in the Atmosphere of Jupiter. In *Jupiter* (T. Gehrels, Ed.), p.564–585. Tucson: University of Arizona Press.

Smith, B.A., Soderblom, L.A., Johnson, T.V., Ingersoll, A.P., Collins, S.A., Shoemaker, E.M., Hunt, G.E., Masursky, H., Carr, M.H., Davies, M.E., Cook, A.F. II, Boyce, J., Danielson, G.E., Owen, T., Sagan, C., Beebe, R.F., Ververka, J., Strom, R.G., McCauley, J.F., Morrison, D., Briggs, G.A., and Suomi, V.E. (1979a). The Jupiter System Through the Eyes of Voyager. *Science* **204** 951.

Smith, B.A., Soderblom, L.A., Beebe, R.F., Boyce, J., Briggs, G.A., Carr, M., Collins, S.A., Cook, A.F. II, Danielson, G.E., Davies, M.E., Hunt, G.E., Ingersoll, A.P., Johnson, T.V., Masursky, H., McCauley, J.F., Morrison, D., Owen, T., Sagan, C., Shoemaker, E.M., Strom, R.G., Suomi, V.E. and Ververka, J. (1979b). The Galilean Satellites and Jupiter: Voyager 2 Imaging Science Results. *Science* **206** 927.

Smith, D.W., and Greene, T.F. (1980). Galilean Satellite Eclipse Studies. III. Jovian Methane Abundance. *Icarus* **44** 134.

Smith, P.H. (1986). The Vertical Structure of the Jovian Atmosphere. *Icarus* **65** 264.

Smith, W.H., Conner, C.P., and Baines, K.H. (1990). Absorption Coefficients for the 6190-Å CH_4 Band Between 290 and 100°K with Application to Uranus' Atmosphere. *Icarus* **85** 58.

Smith, W.L. (1969). Polynomial Representation of Carbon Dioxide and Water Vapour Transmission. *ESSA Technical Report NESC47.*

Smoluchowski, R. (1976). Origin and Structure of Jupiter and Its Satellites. In *Jupiter* (T. Gehrels, Ed.), p.3–21. Tucson: University of Arizona Press.

Spehalski, R.J., Ausman, N.E. Jr., Yeates, C.M., O'Neil, W.J., and Johnson, T.V. (1989). *Galileo Science Requirements Document PD 625-50, Revision D.* Pasadena, California: Jet

Propulsion Laboratory.

Stevenson, D.J., and Salpeter, E.E. (1976). Interior Models of Jupiter. In *Jupiter* (T. Gehrels, Ed.), p.85–112. Tucson: University of Arizona Press.

Stone, E.C., and Lane, A.L. (1979a). Voyager 1 Encounter with the Jovian System. *Science* **204** 945.

Stone, E.C., and Lane, A.L. (1979b). Voyager 2 Encounter with the Jovian System. *Science* **206** 925.

Strobel, D.F., and Yung, Y.L. (1979). The Galilean Satellites as a Source of CO in the Jovian Upper Atmosphere. *Icarus* **37** 256.

Strong, K. (1991). Operation of the Rutherford Appleton Laboratory Long White Cell Using Methane and Hydrogen: Development and Implementation of Safety Measures and Operating Procedures. *Rutherford Appleton Laboratory Internal Report RAL-91-015.* Chilton, Didcot: RAL, Science and Engineering Research Council.

Taylor, F.W. (1972). Temperature Sounding Experiments for the Jovian Planets. *J. Atmos. Sci.* **29** 950.

Taylor, F.W., and Calcutt, S.B. (1984). Near-Infrared Spectroscopy of the Atmosphere of Jupiter. *J.Q.S.R.T.* **32** 463.

Taylor, F.W., and McCleese, D.J. (1977). Multiple Scattering in Broad Spectral Bands. In *Proceedings of the Symposium on Radiation in the Atmosphere.* (H.-J. Bolle, Ed.), p.271–273. Princeton: Science Press.

Tejwani, G.D.T., and Varanasi, P. (1971). Calculation of Collision-Broadened Linewidths in the Infrared Bands of Methane. *J. Chem. Phys.* **55** 1075.

Terrile, R.J., and Beebe, R.F. (1979). Summary of Historical Data: Interpretation of the Pioneer and Voyager Cloud Configurations in a Time-Dependent Framework. *Science* **204** 948.

Terrile, R.J., and Westphal, J.A. (1977). The Vertical Cloud Structure of Jupiter from 5 μm Measurements. *Icarus* **30** 274.

Terrile, R.J., Capps, R.W., Becklin, E.E., and Cruikshank, D.P. (1979). Jupiter's Cloud Distribution Between the Voyager 1 and 2 Encounters: Results from 5-Micrometer Imaging. *Science* **206** 995.

Tokunaga, A.T., Knacke, R.F., and Ridgway, S.T., and Wallace, L. (1979). High-Resolution Spectra of Jupiter in the 744–980 Inverse Centimeter Spectral Range *Astrophys. J.* **232** 603.

Tokunaga, A.T., Knacke, R.F., and Ridgway, S.T. (1980). High Spatial and Spectral Resolution 10-μm Observations of Jupiter. *Icarus* **44** 93.

Tokunaga, A.T., Beck, S.C., Geballe, T.R., Lacy, J.H., and Serabyn, E. (1981). The Detection of HCN on Jupiter. *Icarus* **48** 283.

Tomasko, M.G. (1974). Ammonia Absorption Relevant to the Albedo of Jupiter. II. Interpretation. *Astrophys. J.* **187** 641.

Tomasko, M.G., West, R.A., and Castillo, N.D. (1978). Photometry and Polarimetry of Jupiter at Large Phase Angles. *Icarus* **33** 558.

Trafton, L.M., and Wildey, R. (1974). A Comment on the 8 to 14 Micron Limb Darkening. *Astrophys. J.* **194** 499.

Trauger, J.T., Roesler, F.L., Carleton, N.P., and Traub, W.A. (1973). Observation of HD on Jupiter and the D/H Ratio. *Astrophys. J.* **184** L137.

Treffers, R.R., Larson, H.P., Fink, U., and Gautier, T.N. (1978). Upper Limits to Trace Constituents in Jupiter's Atmosphere from an Analysis of Its 5–μm Spectrum. *Icarus* **34** 331.

Vandergraft, J.S. (1983). *Introduction to Numerical Computations. Second Edition.* New York: Academic Press, Inc..

Varanasi, P., and Chudmani, S. (1990). The Temperature Dependence of Lineshifts, Linewidths, and Line Intensities of Methane at Low Temperatures. *J.Q.S.R.T.* **43** 1.

Varanasi, P., and Tejwani, G.D.T. (1972). Experimental and Theoretical Studies on Collision-

Broadened Lines in the ν_4 Fundamental of Methane. *J.Q.S.R.T.* **12** 849.

Varanasi, P., Sarangi, S., and Pugh, L. (1973). Measurements on the Infrared Lines of Planetary Gases at Low Temperatures. I. ν_3-Fundamental of Methane. *Astrophys. J.* **179** 977.

Wagener, R., Caldwell, J., Owen, T., Kim, S.J., Encrenaz, T., and Combes, M. (1985). The Jovian Stratosphere in the Ultraviolet. *Icarus* **63** 222.

Wallace, L. (1980). The Structure of the Uranus Atmosphere. *Icarus* **43** 231.

Wallace, L., and Smith, G.R. (1977). The Interpretation of Jovian Methane Absorptions. *Astrophys. J.* **212** 252.

Wallace, L., Prather, M., and Belton, M.J.S. (1974). The Thermal Structure of the Atmosphere of Jupiter. *Astrophys. J.* **193** 481.

Weidenschilling, S.J., and Lewis, J.S. (1973). Atmospheric and Cloud Structures of the Jovian Planets. *Icarus* **20** 465.

West, R.A. (1979). Spatially Resolved Methane Band Photometry of Jupiter. II. Analysis of the South Equatorial Belt and South Tropical Zone Reflectivity. *Icarus* **38** 34.

West, R.A., Kupferman, P.N., and Hart, H. (1985). Voyager 1 Imaging and IRIS Observations of Jovian Methane Absorption and Thermal Emission: Implications for Cloud Structure. *Icarus* **61** 311.

West, R.A., Strobel, D.F., and Tomasko, M.G. (1986). Clouds, Aerosols, and Photochemistry in the Jovian Atmosphere. *Icarus* **65** 161.

West, R.A., Crisp, D., and Chen, L. (1990). Mapping Transformations for Broadband Atmospheric Radiation Calculations. *J.Q.S.R.T.* **43** 191.

Westphal, J.A. (1969). Observations of Localized 5-Micron Radiation from Jupiter. *Astrophys. J.* **157** L63.

Westphal, J.A., Matthews, D., and Terrile, R.J. (1974). 5-Micron Pictures of Jupiter. *Astrophys. J.* **188** L111.

Wetherill, G.W. (1989). The Formation of the Solar System: Consensus, Alternatives, and Missing Factors. In *The Formation and Evolution of Planetary Systems* (H.A. Weaver and L. Danly, Eds.), p.1–30. Cambridge: Cambridge University Press.

White, J. (1942). Long Optical Paths at Large Aperture. *J. Opt. Soc. Am.* **32** 285.

Wildt, R. (1932). Absorptions Spektren und Atmosphären der Grossen Planeten. *Veröff. Univ. Sternwarte Göttingen* **2** 171.

Williams, G.P. (1978). Planetary Circulations: 1. Barotropic Representation of Jovian and Terrestrial Turbulence. *J. Atmos. Sci.* **35** 1399.

Williams, G.P. (1979). Planetary Circulations: 2. The Jovian Quasi-Geostrophic Regime. *J. Atmos. Sci.* **36** 932.

Wolfe, W.L., and Zissis, G.J., Eds. (1978). *The Infrared Handbook.* Washington, D.C.: Office of Naval Research, Dept. of the Navy.

Woodman, J.M. (1976). Jupiter: Observations of Spatial Variations of Methane and Ammonia Interpreted as a Cloud Deck with Elevated Haze. *Dissertation*, University of Texas at Austin.

Yeates, C.M., Johnson, T.V., Colin, L., Fanale, F.P., Frank, L., and Hunten, D.M. (1985). *Galileo: Exploration of Jupiter's Solar System.* NASA SP-479.

Zachor, A.S. (1968a). A General Approximation for Gaseous Absorption. *J.Q.S.R.T.* **8** 771.

Zachor, A.S. (1968b). Equations for the Transmittance of the 2 μ CO_2 Bands. *J.Q.S.R.T.* **8** 1341.